



# RESEARCH REPORT

---

---

## IDENTIFICATION OF CAUSES AND SOLUTION STRATEGIES FOR DECK CRACKING IN JOINTLESS BRIDGES

by

David J. Stringer

Rigoberto Burgueño

Report No. CEE-RR – 2012/04

July 2012

Research Report for MDOT under Contract No. 2009-0746/Z1  
SPR No. 108522

---

**Department of Civil and Environmental Engineering  
Michigan State University  
East Lansing, Michigan**

<b>1. Report No.</b> RC-1571	<b>2. Government Accession No.</b> N/A	<b>3. MDOT Project Manager</b> Eric Burns	
<b>4. Title and Subtitle</b> Identification of Causes and Solution Strategies for Deck Cracking in Jointless Bridges		<b>5. Report Date</b> July 30, 2012	
		<b>6. Performing Organization Code</b> N/A	
<b>7. Author(s)</b> David J. Stringer and Rigoberto Burgueño		<b>8. Performing Org. Report No.</b> CEE-RR – 2012/04	
<b>9. Performing Organization Name and Address</b> Michigan State University 3546 Engineering Building East Lansing, MI 48824-1226		<b>10. Work Unit No. (TRAIS)</b> N/A	
		<b>11. Contract No.</b> 2009-0746	
		<b>11(a). Authorization No.</b> Z1	
<b>12. Sponsoring Agency Name and Address</b> Michigan Department of Transportation Research Administration 8885 Ricks Rd. P.O. Box 30049 Lansing MI 48909		<b>13. Type of Report &amp; Period Covered</b> Final Report 10/20/2009 – 5/31/2012	
		<b>14. Sponsoring Agency Code</b> N/A	
<b>15. Supplementary Notes</b>			
<b>16. Abstract</b> Bridges have traditionally relied on a system of expansion joints and flexible bearings to accommodate movements due to temperature, creep, and shrinkage loading. Joints and elements in their vicinity experience a high amount of degradation; thus modern design approaches are advocating their removal, with movement accommodated through flexible piles and abutment walls. While jointless bridges have been performing well, many of them suffer from widespread early-age transverse deck cracking. Restrained concrete shrinkage was identified as the most dominant source for the noted damage based on a literature review and a field investigation. Deck cracking is caused by the build-up of tensile forces resulting from the increased rigidity in jointless bridges. Experimentally calibrated finite-element models were used to predict deck cracking in two bridge systems under shrinkage-induced loading and a parametric study was conducted to investigate the influence of design parameters on restrained shrinkage cracking. Simulation results confirmed that the increase of system restraint increases the tendency for cracking. Models for steel and concrete beam bridges showed that both systems were equally susceptible to deck cracking due to restrained concrete shrinkage. The lowest amount of cracking was predicted for bridges with non-integral abutments, higher shear connector spacing, and a low-shrinkage concrete mix. Changing the deck reinforcement configuration had little effect on the predicted damage patterns. Use of a low-shrinkage concrete mix had the greatest impact on minimizing deck cracking. Overall, the computational simulations indicated that restrained shrinkage cracking in the decks of jointless bridges is unavoidable, but that modifying design details and improving concrete mixture designs can help reduce its extent.			
<b>17. Key Words</b> bridge; jointless; deck; cracking; shrinkage; experiment; finite element.		<b>18. Distribution Statement</b> No restrictions. This document is available to the public through the Michigan Department of Transportation.	
<b>19. Security Classification - report</b> Unclassified	<b>20. Security Classification - page</b> Unclassified	<b>21. No. of Pages</b> 216	<b>22. Price</b> N/A

Report No. CE-RR – 2012/04

**IDENTIFICATION OF CAUSES AND SOLUTION STRATEGIES FOR  
DECK CRACKING IN JOINTLESS BRIDGES**

by

**David J. Stringer**

*Graduate Research Assistant*

**Rigoberto Burgueño**

*Associate Professor of Structural Engineering*

Research Report to Michigan DOT under Contract No. 2009-0746/Z1  
SPR No. 108522

Department of Civil and Environmental Engineering  
Michigan State University  
East Lansing, MI 48824-1226

July 2012

## **DISCLAIMER**

The opinions, findings, conclusions and recommendations presented in this report are those of the authors alone and do not necessarily represent the views and opinions of Michigan State University or the Michigan Department of Transportation.

Most of this report has also been published as the MS Thesis of Mr. David J. Stringer under the following reference:

Stringer, D.J. Effects of Design Parameters on Deck Cracking from Restrained Concrete Shrinkage in Jointless Bridges. MS Thesis, Department of Civil and Environmental Engineering, Michigan State University, 2012.

## **ABSTRACT**

### **IDENTIFICATION OF CAUSES AND SOLUTION STRATEGIES FOR DECK CRACKING IN JOINTLESS BRIDGES**

By

**David J. Stringer**

*Graduate Research Assistant*

**Rigoberto Burgueño, Ph.D.**

*Associate Professor of Structural Engineering*

Bridges have traditionally relied on a system of expansion joints and flexible bearings to accommodate movements due to temperature, creep, and shrinkage loading. Joints and elements in their vicinity experience a high amount of degradation; thus modern design approaches are advocating their removal, with movement accommodated through flexible piles and abutment walls. While jointless bridges have been performing well, many of them suffer from widespread early-age transverse deck cracking. Restrained concrete shrinkage was identified as the most dominant source for the noted damage based on a literature review and a field investigation. Deck cracking is caused by the build-up of tensile forces resulting from the increased rigidity in jointless bridges. Experimentally calibrated finite-element models were used to predict deck cracking in two bridge systems under shrinkage-induced loading and a parametric study was conducted to investigate the influence of design parameters on restrained shrinkage cracking. Simulation results confirmed that the increase of system restraint increases the tendency for cracking. Models for steel and concrete beam bridges showed that both systems were equally susceptible to deck cracking due to restrained concrete shrinkage. The lowest amount of cracking was predicted for bridges with non-integral abutments, higher shear connector spacing, and a low-shrinkage concrete mix. Changing the deck reinforcement configuration had little effect on the predicted damage patterns. Use of a low-shrinkage concrete mix had the greatest impact on minimizing deck cracking. Overall, the computational simulations indicated that restrained shrinkage cracking in the decks of jointless bridges is unavoidable, but that modifying design details and improving concrete mixture designs can help reduce its extent.

# TABLE OF CONTENTS

DISCLAIMER .....	iv
ABSTRACT.....	v
TABLE OF CONTENTS.....	vi
LIST OF TABLES .....	ix
LIST OF FIGURES .....	xi
1 INTRODUCTION.....	1
1.1 Background .....	1
1.2 Motivation .....	4
1.3 Research Objectives .....	5
1.4 Report Organization .....	6
2 LITERATURE REVIEW .....	7
2.1 Sources Contributing to Deck Cracking .....	7
2.1.1 <i>Material Properties and Mix Design</i> .....	7
2.1.2 <i>Soil-Structure Interaction and Abutment Movement</i> .....	8
2.1.3 <i>Temperature, Creep, and Shrinkage effects</i> .....	9
2.1.4 <i>Bridge Design Features</i> .....	13
2.2 Concrete Shrinkage Standard Tests.....	18
2.3 Questions and Outstanding Issues Remaining .....	19
2.4 Conclusions, Recommendations, and Suggestions for Prototype Bridge System .....	19
3 FIELD INSPECTION .....	21
3.1 Past Field Investigation Studies that have been Performed .....	21
3.2 Bridge Information Provided by MDOT.....	22
3.3 Parameters Considered and Bridges Visited .....	23
3.4 Field Inspection Results .....	25
3.4.1 <i>Transverse Cracking</i> .....	29
3.4.2 <i>Longitudinal Cracking</i> .....	29
3.5 Summary and Conclusions.....	29
4 EXPERIMENTAL EVALUATION .....	31
4.1 Original Approach.....	31
4.2 Revised Approach .....	32
4.3 Test Unit Design Parameters.....	34
4.3.1 <i>Steel Beam Size Determination</i> .....	35
4.3.2 <i>Diaphragm Section Determination</i> .....	36
4.3.3 <i>Shear Connector Layout Determination</i> .....	38
4.3.4 <i>Deck Reinforcing Steel Determination</i> .....	40
4.3.5 <i>Weld Design</i> .....	41

4.3.6	<i>Pin Support Design</i> .....	43
4.3.7	<i>Test Unit Design Summary</i> .....	44
4.3.8	<i>Ring Test</i> .....	45
4.4	<i>Instrumentation Layout</i> .....	46
4.4.1	<i>Strain Gages</i> .....	46
4.4.2	<i>LVDT's</i> .....	49
4.4.3	<i>Thermocouples</i> .....	49
4.4.4	<i>Instrumentation Naming Scheme</i> .....	50
4.5	<i>Test Unit Construction and Casting</i> .....	51
4.5.1	<i>Formwork</i> .....	52
4.5.2	<i>Reinforcing Steel</i> .....	56
4.5.3	<i>Instrumentation Installation</i> .....	58
4.5.4	<i>Test unit Casting</i> .....	61
4.5.4.1	<i>Concrete Mix Design</i> .....	61
4.5.4.2	<i>Concrete casting</i> .....	62
4.5.5	<i>Completed test units</i> .....	64
4.5.6	<i>Concrete Shrinkage Ring Tests</i> .....	66
4.6	<i>Results</i> .....	67
4.6.1	<i>Data Acquisition</i> .....	67
4.6.2	<i>Concrete Material Testing</i> .....	68
4.6.3	<i>Ambient temperature and relative humidity</i> .....	72
4.6.4	<i>Thermocouples</i> .....	77
4.6.5	<i>LVDT's</i> .....	81
4.6.6	<i>Strain Gages</i> .....	83
4.6.7	<i>Ring Test Crack Growth</i> .....	90
4.7	<i>Data Analysis</i> .....	91
4.7.1	<i>Temperature</i> .....	92
4.7.2	<i>Vertical Displacements</i> .....	92
4.7.3	<i>Strains</i> .....	93
5	<b>COMPUTATIONAL EVALUATION</b> .....	94
5.1	<i>Modeling Approach</i> .....	94
5.1.1	<i>Free shrinkage model</i> .....	96
5.2	<i>Computer Modeling Features</i> .....	97
5.3	<i>Material Properties</i> .....	100
5.4	<i>Laboratory Models</i> .....	103
5.4.1	<i>Concrete Shrinkage Ring Test</i> .....	103
5.4.2	<i>Lab Test Unit Test unit Models</i> .....	108
5.4.3	<i>Discussion</i> .....	122
5.4.3.1	<i>Validation of Computer Modeling Approach</i> .....	122
5.4.3.2	<i>Effects of Design Parameters at the Sub-assembly level</i> .....	123
6	<b>PARAMETRIC STUDY ON FULL BRIDGE MODELS</b> .....	125
6.1	<i>Parameters Considered</i> .....	127
6.2	<i>Loading method</i> .....	128
6.2.1	<i>Shrinkage loading</i> .....	128
6.2.2	<i>Gravity/self weight loading</i> .....	130

6.2.3	<i>Pour sequencing</i> .....	130
6.2.4	<i>Concrete barrier walls</i> .....	130
6.2.5	<i>Concrete/soil friction at approach slabs</i> .....	131
6.2.6	<i>Soil/structure interaction at the piles</i> .....	133
6.2.7	<i>Random load application for full bridge models</i> .....	136
6.3	Concrete Spread Box Beam Bridge.....	139
6.3.1	<i>Parts and element types</i> .....	139
6.3.2	<i>Concrete box beam equivalent section</i> .....	141
6.3.3	<i>Constraints, boundary conditions, and other model features</i> .....	141
6.3.4	<i>Parametric evaluation features</i> .....	142
6.4	Steel Girder Bridge.....	143
6.4.1	<i>Parts and element types</i> .....	143
6.4.2	<i>Constraints, boundary conditions and other model features</i> .....	145
6.4.3	<i>Parametric evaluation features</i> .....	145
6.5	Results.....	146
6.5.1	<i>Box Beam Bridge Model Overall Results</i> .....	146
6.5.2	<i>Steel Girder Bridge Model Overall Results</i> .....	161
6.5.3	<i>Concrete box beam bridge parametric study comparison results</i> .....	174
6.5.3.1	<i>Effect of Increasing Deck Reinforcement</i> .....	182
6.5.4	<i>Steel girder bridge parametric study comparison results</i> .....	193
6.5.4.1	<i>Effect of shear connector re-distribution</i> .....	203
6.5.5	<i>Effect of concrete tensile strength</i> .....	203
6.5.6	<i>Discussion</i> .....	208
7	CONCLUSIONS AND RECOMMENDATIONS.....	211
7.1	Conclusions.....	211
7.2	Recommendations.....	212
8	REFERENCES.....	214
9	APPENDICES.....	217



## LIST OF TABLES

Table 1. Bridges visited for field investigation.....	24
Table 2. Field investigation results .....	28
Table 3. Experimental Test Matrix for Sub-Assembly Evaluation of Shrinkage Effects.....	34
Table 4. Test Unit Reinforcement Details (Derived from Reference).....	40
Table 5. Test Unit Design Summary.....	44
Table 6. MDOT Grade D Concrete Mix Design.....	61
Table 7. MDOT Modified Grade D Slag Replacement Mix Design .....	61
Table 8. Concrete Fresh Property Characteristics.....	62
Table 9. Shrinkage strain calculation constants .....	95
Table 10. Element types used in computational evaluation.....	98
Table 11. Material properties used in the computer analyses .....	102
Table 12. Concrete spread box beam bridge properties [24] .....	126
Table 13. Steel girder bridge properties [23] .....	127
Table 14. Analyses run for full bridge parametric study .....	128
Table 15. Values used to calculate shrinkage load temperatures.....	129
Table 16. Assumed soil foundation properties [9][27] .....	133
Table 17. Element types utilized for concrete box beam bridge.....	139
Table 18. Concrete box beam transformed section moment of inertia calculation .....	141
Table 19. Concrete box beam parametric evaluation analyses details.....	142
Table 20. Concrete box beam reinforcement arrangements .....	142
Table 21. Element types utilized for concrete steel girder bridge .....	143
Table 22. Steel girder parametric evaluation analyses details .....	145
Table 23. Steel girder bridge reinforcement arrangement .....	146
Table 24. Nomenclature used for box beam parametric study results .....	175

Table 25. Box beam bridge parametric study overall results.....	182
Table 26. Nomenclature used for steel girder parametric study results.....	193
Table 27. Steel girder bridge parametric study overall results .....	202
Table 28. Shear stud size and volume determination for parametric study .....	203

## LIST OF FIGURES

Figure 1. Jointless bridges vs. bridges with expansion joints (adapted from [6]) .....	1
Figure 2. Integral bridges vs. jointless decks (adapted from [10]) .....	2
Figure 3. Jointless Bridge Abutment Details (Adapted from [10]) .....	3
Figure 4. Shrinkage-induced stress development in concrete bridge decks [30].....	10
Figure 5. Simplified Shrinkage Cracking [16].....	10
Figure 6. Cracking in continuously restrained concrete test unit [16].....	10
Figure 7. Curling of concrete deck due to sealed bottom surface [16] .....	11
Figure 8. Development of Free Shrinkage Strain with Time [21] .....	18
Figure 9. Field investigation locations.....	23
Figure 10. Semi-integral abutment connection (Bridge No. 13, 26 Mile Rd. over M-53) .....	25
Figure 11. Fully-integral abutment connection (Bridge No. 4, US-10 over Sanford Lake).....	26
Figure 12. Transverse cracking over pier/negative moment region (Bridge No. 13, 26 mile Rd. over M-53) .....	26
Figure 13. Typical transverse cracking in deck surface (Bridge No. 5: M-57 over US-127).....	27
Figure 14. Typical longitudinal cracking (Bridge No. 11: Burlingame Rd. over M-6).....	27
Figure 15. Region of bridge to model in the original laboratory investigation approach.....	31
Figure 16. Loading approach for original laboratory investigation .....	32
Figure 17. Steel beams selected, with welded extension plates.....	35
Figure 18. MDOT cross-bracing standard specifications (adapted from ref. [25]) .....	36
Figure 19. Halsted Bridge cross-bracing dimensions and SAP 2000 model .....	37
Figure 20. Cross-bracing displacement results .....	37
Figure 21. Gusset Plate Dimensions .....	38
Figure 22. Shear Connector Spacing over Top Flange .....	39
Figure 23. Shear Connector Detail 1(Test units 1, 3, and 4) .....	39

Figure 24. Shear Connector Detail 2 (Test Unit 2).....	39
Figure 25. Deck Reinforcement Detail 1 (Test units 1, 2, and 4).....	40
Figure 26. Deck Reinforcement Detail 2 (Test Unit 3) .....	41
Figure 27. Welded connection configurations.....	42
Figure 28. Pin plate details.....	43
Figure 29. Pin connection setup.....	43
Figure 30. Test Unit Overall View .....	44
Figure 31. Ring Test Setup (adapted from ref. [5]) .....	45
Figure 32. Example Ring Test Strain Output [5].....	46
Figure 33. Reinforcing steel top mat strain gage locations.....	47
Figure 34. Reinforcing steel bottom mat strain gage locations .....	47
Figure 35. Steel beam strain gage locations.....	48
Figure 36. Diaphragm strain gage locations .....	48
Figure 37. LVDT Locations.....	49
Figure 38. X-Y orientation for instrumentation.....	50
Figure 39. Depth locations for instrumentation .....	51
Figure 40. Test Unit Steel Frame Assemblies (Test units 1, 2, and 4) .....	51
Figure 41. Test Unit 3 Steel Frame Assembly.....	52
Figure 42. SIP forms front view .....	53
Figure 43. SIP forms Styrofoam fillers.....	53
Figure 44. Spot-welding of the forms (typical) .....	54
Figure 45. Schematic for the cantilevered section formwork (note these forms are removable) .....	54
Figure 46. Cantilever forms bottom section .....	55
Figure 47. Completed cantilever forms .....	55
Figure 48. Completed formwork (all lumber forms are removable) .....	56

Figure 49. Concrete spacers for reinforcing steel (typical).....	57
Figure 50. Spacing between reinforcing steel mats (typical).....	57
Figure 51. Reinforcing steel side cover (typical).....	58
Figure 52. Example strain gage installation process (typical for all strain gages) .....	59
Figure 53. LVDT placed underneath mid-test unit.....	60
Figure 54. LVDT in place (mid-span of beam) .....	60
Figure 55. Placing and vibrating the concrete (test unit 3) .....	63
Figure 56. Bull floating the concrete surface (test unit 3) .....	63
Figure 57. Timeline of events between casting to the end of moist curing (typical).....	64
Figure 58. Completed test unit overall view (test unit 4) .....	64
Figure 59. Completed test unit cantilever section (test unit 3) .....	65
Figure 60. Close-up of completed test unit top surface (test unit 4).....	65
Figure 61. Test unit cross-section (test unit 4).....	66
Figure 62. Overall view of shrinkage rings .....	67
Figure 63. Concrete split tensile strength testing.....	68
Figure 64. Concrete compressive strength testing .....	68
Figure 65. Test units 1 and 2 (MDOT Grade D mix) .....	69
Figure 66. Test unit 3 (MDOT Grade D mix).....	70
Figure 67. Test unit 4 (Modified MDOT Grade D mix).....	71
Figure 68. Ambient temperature values, first set of tests .....	73
Figure 69. Relative humidity percentage, first set of tests.....	74
Figure 70. Ambient temperature values, second set of tests.....	75
Figure 71. Relative humidity percentage, second set of tests .....	76
Figure 72. Concrete deck temperatures at the bottom mat of reinforcing steel (test units 1 and 2) .....	77
Figure 73. Lab ambient temperature, first set of test units .....	78

Figure 74. Maximum temperature gradient through the depth of the test unit (test units 1 and 2)	78
Figure 75. Concrete deck temperatures at the bottom mat of reinforcing steel (test units 3 and 4)	79
Figure 76. Lab ambient temperature, second set of test units	80
Figure 77. Maximum temperature gradient through the depth of the test unit (test units 3 and 4)	81
Figure 78. Girder 1 mid-span displacement (L-G1-1/2)	82
Figure 79. Mid-test unit displacement (L-1/2-1/2)	82
Figure 80. Mid-test unit quarter-span displacement (L-1/2-3/4)	83
Figure 81. Top mat longitudinal rebar strains, middle of test unit (S-Tp-1/2-1/2-L)	84
Figure 82. Bottom mat longitudinal rebar strains, middle of test unit (S-Bt-1/2-1/2-L)	84
Figure 83. Top mat transverse rebar strains, middle of test unit (S-Tp-1/2-1/2-T)	85
Figure 84. Bottom mat transverse rebar strains, middle of test unit (S-Bt-1/2-1/2-T)	85
Figure 85. Beam top flange, mid-span longitudinal strains (S-G1-Tf-M-G1-1/2-L)	86
Figure 86. Beam mid-web longitudinal strains (S-G1-W-O-G1-1/2-L)	86
Figure 87. Beam bottom flange, mid-span longitudinal strains (S-G1-Bf-M-G1-1/2-L)	87
Figure 88. Beam bottom flange, mid-span longitudinal strain inside and outside comparison	88
Figure 89. Diaphragm strain data comparison	89
Figure 90. Maximum Strain Gradient, Test unit 3	89
Figure 91. Maximum Strain Gradient, Test unit 4 (tension plotted on the right)	90
Figure 92. Concrete ring crack growth, Rings 1 to 4 (Grade D Mix)	90
Figure 93. Ring test cracking (Ring 2)	91
Figure 94. Concrete ring crack growth, Rings 5 to 8	92
Figure 95. Concrete free shrinkage block overall model	96
Figure 96. Free shrinkage model strains and deflected shape	97

Figure 97. Schematic representation of elements used [36] .....	99
Figure 98. Concrete damaged plasticity stress/strain curves .....	102
Figure 99. Concrete ring test assembly .....	103
Figure 100. Material Imperfection Assignment.....	104
Figure 101. ACI 209 Temperature values (applied to outside surface of concrete ring) [2].....	104
Figure 102. Temperature distribution through the rings .....	105
Figure 103. Concrete Ring plastic strain PE, Max Principal at time of 17 days .....	105
Figure 104. Plastic strain magnitude outputs through for the region of damage.....	106
Figure 105. Steel ring strain output through time .....	106
Figure 106. Concrete ring strain output through time.....	107
Figure 107. Lab test unit test unit models overall view .....	108
Figure 108. Temperature loading values for lab test unit analyses.....	109
Figure 109. Test Unit Models Overall Deflected Shape and Vertical Displacement [35] .....	109
Figure 110. Beam mid-span deflection data comparison (L-G1-1/2).....	111
Figure 111. Mid-test unit deflection data comparison (L-1/2-1/2).....	112
Figure 112. Reinforcing Steel Top Mat Long. Strain Data Comparison (S-Tp-1/2-1/2-L).....	113
Figure 113. Reinforcing Steel Bott. Mat Long. Strain Data Comparison (S-Bt-1/2-1/2-L).....	113
Figure 114. Reinforcing Steel Top Mat Trans. Strain Data Comparison (S-Tp-G1-1/2-T) .....	114
Figure 115. Reinforcing Steel Bott. Mat Trans. Strain Data Comparison (S-Bt-G1-1/2-T) .....	114
Figure 116. Beam Top Flange Strain Data Comparison (S-G1-Tf-M-G1-1/2-L) .....	115
Figure 117. Beam Mid-Web Strain Data Comparison (S-G1-W-O-G1-1/2-L).....	115
Figure 118. Beam Bottom Flange Strain Data Comparison (S-Bf-M-G1-1/2-L).....	116
Figure 119. Depth through beam/slab assembly slab strain data comparisons (time=20 days)	116
Figure 120. Computer model data comparison, beam mid-span deflection (L-G1-1/2) .....	117
Figure 121. Computer model data comparison, test unit mid-span deflection (L-1/2-1/2).....	117

Figure 122. Computer model data comparison, rebar top mat long. strains (S-Tp-1/2-1/2-L)..	118
Figure 123. Computer model data comparison, rebar bott. mat long. strains (S-Bt-1/2-1/2-L)	118
Figure 124. Computer model data comparison, rebar top mat trans. strains (S-Tp-1/2-1/2-T).	119
Figure 125. Computer model data comparison, rebar bott. mat trans. strains (S-Bt-1/2-1/2-T)	119
Figure 126. Computer model data comparison, beam top flange strains (S-G1-Tf-M-1/2-L) ..	120
Figure 127. Computer model data comparison, beam mid-web strains (S-G1-W-O-1/2-L).....	120
Figure 128. Computer model data comparison, beam bott. flange strains (S-G1-Bf-M-1/2-L)	121
Figure 129. Longitudinal Strains through the depth of the beam/test unit section .....	121
Figure 130. Strain behavior through the depth of the slab.....	124
Figure 131. Concrete spread box beam bridge (M-57 over US-127) elevation and cross-section [24].....	125
Figure 132. Steel beam bridge (Kensington Rd. over I-96) elevation and cross-section [23]...	126
Figure 133. Shrinkage load temperature values for bridge deck and barrier wall (standard mix) .....	129
Figure 134. Barrier wall equivalent rectangular cross section [23].....	131
Figure 135. Typical approach slab connection with bridge deck [25].....	131
Figure 136. Approach slab friction force-displacement curve for each 2'-wide segment.....	132
Figure 137. P-Y curves for soil/pile interaction.....	134
Figure 138. Pile lateral displacement values (as-built box beam model) .....	135
Figure 139. Literature pile lateral displacement values [9] .....	135
Figure 140. Deck top temperature values for random load approach (box beam bridge) [35]..	136
Figure 141. Deck max principal plastic strains with random load approach [35] .....	137
Figure 142. Deck max principal stresses with random load approach [35].....	137
Figure 143. Correct random temperature distribution application for bridge slabs.....	138
Figure 144. Concrete box beam bridge overall views .....	140
Figure 145. Concrete box beam bridge overall views .....	144



Figure 146. Box beam as-built model deflected shape and vertical displacements (t=45 days)	147
Figure 147. Box beam as-built model maximum principal tensile stresses (t=45 days) .....	148
Figure 148. Box beam as-built model maximum principal plastic strains (t=45 days) .....	149
Figure 149. Box beam as-built model plastic strain global X-direction (1-1) output.....	150
Figure 150. Box beam as-built model plastic strain global Y-direction (2-2) output.....	150
Figure 151. Box beam as-built model plastic strain global Z-direction (3-3) output .....	151
Figure 152. Box beam as-built model plastic shear strain (1-3) output.....	151
Figure 153. Vertical displacement through time in bridge longitudinal direction.....	153
Figure 154. Maximum principal tensile stresses through time in bridge longitudinal direction	153
Figure 155. Maximum principal plastic strains through time in bridge longitudinal direction.	154
Figure 156. Maximum principle plastic strain output in positive moment region (span 2).....	155
Figure 157. Development of maximum principal tensile stresses in full bridge deck.....	156
Figure 158. Development of maximum principal plastic strains in full bridge deck .....	157
Figure 159. Maximum principle tensile stresses along longitudinal direction, bottom of deck	158
Figure 160. Maximum principle plastic strains along longitudinal direction, bottom of deck..	158
Figure 161. Vertical displacements along bridge transverse direction (time=45 days).....	159
Figure 162. Maximum principle tensile stresses along bridge transverse direction (t=45 days)	160
Figure 163. Maximum principle plastic strains along bridge transverse direction (time=45 days) .....	160
Figure 164. Steel girder as-built model deflected shape and vertical displacements (t=45 days) .....	161
Figure 165. Steel girder as-built model maximum principal tensile stresses (t=45 days) .....	162
Figure 166. Steel girder as-built model maximum principal plastic strains (t=45 days).....	163
Figure 167. Steel girder as-built model plastic strain global X-direction (1-1) output.....	164
Figure 168. Steel girder as-built model plastic strain global Y-direction (2-2) output.....	165
Figure 169. Steel girder as-built model plastic strain global Z-direction (3-3) output .....	165

Figure 170. Steel girder as-built model plastic shear strain (1-3) output.....	166
Figure 171. Vertical displacement through time in bridge longitudinal direction.....	167
Figure 172. Maximum principal tensile stresses through time in bridge longitudinal direction	168
Figure 173. Maximum principal plastic strains through time in bridge longitudinal direction.	168
Figure 174. Maximum principle plastic strain output in positive moment region (span 2).....	169
Figure 175. Development of maximum principal tensile stresses in full bridge deck.....	170
Figure 176. Development of maximum principal plastic strains in full bridge deck .....	171
Figure 177. Maximum principle tensile stresses along longitudinal direction, bottom of deck	172
Figure 178. Vertical displacements along bridge transverse direction (time=45 days).....	173
Figure 179. Maximum principle tensile stresses along bridge transverse direction (t=45 days)	173
Figure 180. Maximum principle plastic strains along bridge transverse direction (time=45 days) .....	174
Figure 181. Max principal tensile stresses through the depth of the slab, between beams (t=45) .....	175
Figure 182. Max principal plastic strains through the depth of the slab, between beams (t=45) .....	175
Figure 183. Max principal tensile stresses through depth of beam/slab assembly (t=45) .....	176
Figure 184. Max principal plastic strains through depth of slab, over beams (t=45) .....	176
Figure 185. Vertical displacements along the longitudinal direction, span 2 (t=45 days).....	177
Figure 186. Max principal stresses along the longitudinal direction, span 2 (t=45 days) .....	177
Figure 187. Max principal plastic strains along the longitudinal direction, span 2 (t=45 days)	178
Figure 188. Vertical displacements along the transverse direction (t=45 days).....	178
Figure 189. Max principal stresses along the transverse direction (t=45 days).....	179
Figure 190. Max principal plastic strains along the transverse direction (t=45 days).....	179
Figure 191. Vertical displacements through time, between beams, span 2 .....	180
Figure 192. Max principal stresses through time, between beams, span 2.....	181

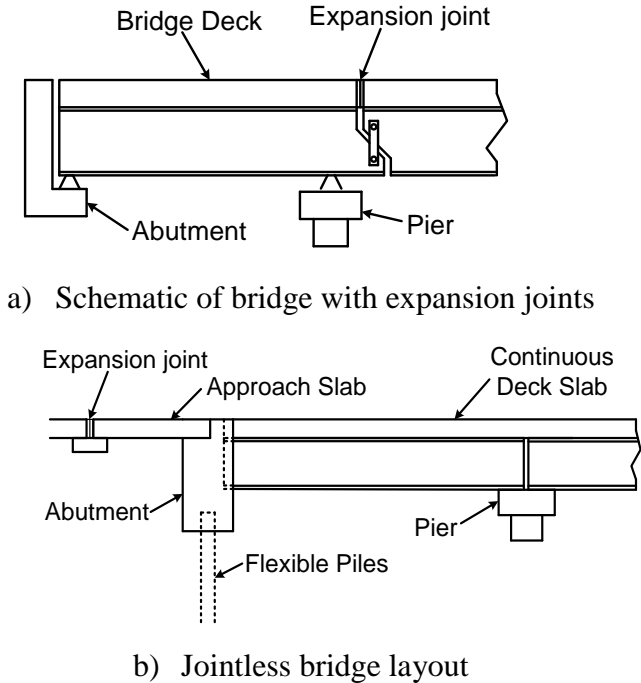
Figure 193. Max principal plastic strains through time, between beams, span 2 .....	181
Figure 194. Prism model setup for investigating effect of reinforcement .....	183
Figure 195. Maximum principal plastic strain output, unreinforced prism .....	184
Figure 196. Maximum principal plastic strain output, #3 embedded bar .....	185
Figure 197. Maximum principal plastic strain output, #8 embedded bar .....	186
Figure 198. Development of stresses with time in prism.....	187
Figure 199. Prism with #3 reinforcement plastic strain output at various times .....	188
Figure 200. Prism with #8 reinforcement plastic strain output at various times .....	188
Figure 201. Prism plastic strain values with time in concentrated cracking areas .....	189
Figure 202. Prism reinforcing bar longitudinal stresses with time .....	190
Figure 203. #3 prism with ‘rebar layer’ approach maximum principal plastic strains (t=30 days) .....	191
Figure 204. #8 prism with ‘rebar layer’ approach maximum principal plastic strains (t=30 days) .....	191
Figure 205. Plastic strains along longitudinal path for prisms with rebar layer approach (t=30) .....	192
Figure 206. Max principal tensile stresses through the depth of the slab, between beams (t=45) .....	194
Figure 207. Max principal plastic strains through the depth of the slab, between beams (t=45) .....	194
Figure 208. Max principal tensile stresses through depth of beam/slab assembly (t=45) .....	195
Figure 209. Max principal plastic strains through depth of slab, over beams (t=45) .....	196
Figure 210. Vertical displacements along the longitudinal direction (t=45 days).....	197
Figure 211. Max principal stresses along the longitudinal direction (t=45 days).....	197
Figure 212. Max principal plastic strains along the longitudinal direction (t=45 days).....	198
Figure 213. Vertical displacements along the transverse direction (t=45 days).....	198
Figure 214. Max principal stresses along the transverse direction (t=45 days).....	199

Figure 215. Max principal plastic strains along the transverse direction (t=45 days) .....	199
Figure 216. Vertical displacements through time, between beams .....	200
Figure 217. Max principal stresses through time, between beams .....	201
Figure 218. Max principal plastic strains through time, between beams, span 2 .....	201
Figure 219. Maximum principal stress contours (time=30 days) .....	204
Figure 220. Concrete maximum principal tensile stresses, middle of the slab on top.....	205
Figure 221. Vertical displacements, middle of slab on top.....	205
Figure 222. Maximum principle tensile stress values through time, tensile strength comparison .....	206
Figure 223. Maximum principle plastic strain values through time, tensile strength comparison .....	206
Figure 224. Maximum principle plastic strain values along longitudinal direction (t=45 days).....	207
Figure 225. Longitudinal strains through the depth of the slab .....	209

# 1 INTRODUCTION

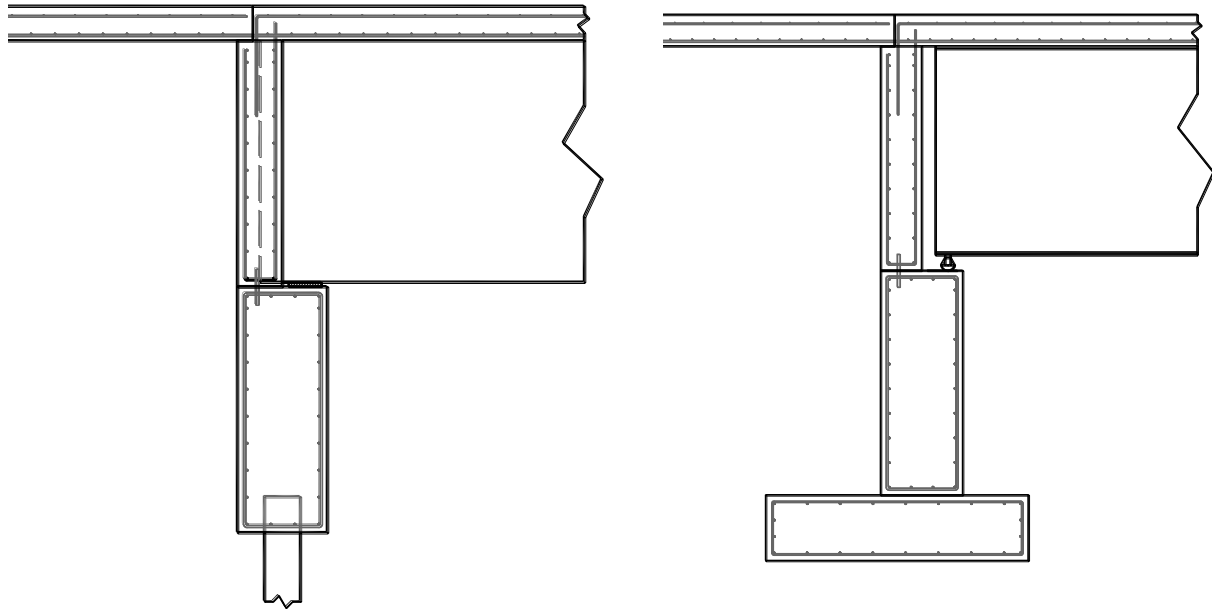
## 1.1 Background

Traditionally, highway bridges have relied on a system of expansion joints, rockers, and other structural releases to accommodate expansion and contraction movements due to temperature, creep, and shrinkage loading [10][29]. These expansion joints have been the cause of many deterioration problems, as deicing chemicals and other debris prevent the joints from functioning properly and lead to the corrosion of the structure beneath. This leads to high maintenance and rehabilitation costs, and reduces the service level for the bridge [10][19]. Due to these issues, recent measures have been taken to eliminate these joints and allow the bridge to function as a continuous structural system. These are referred to as *integral* or *jointless* bridges [10][14][40]. In jointless bridges, the expansion joints over the piers are eliminated and the deck is made continuous, as shown in Figure 1.



**Figure 1.** Jointless bridges vs. bridges with expansion joints (adapted from [6])

Newly designed bridges are connected with the abutment walls, allowing the structure to act as a single system. Jointless bridge systems are either considered integral bridges (where the girders are cast into the abutment wall), or non-integral bridges (where the substructure is traditional, while the deck is continuous and cast with the abutment wall) [10]. See Figure 2.



(a) *Integral Bridge Abutment Detail*

(b) *Non-integral Bridge Abutment Detail*

**Figure 2.** Integral bridges vs. jointless decks (adapted from [10])

Non-integral bridges do not have girders cast into the abutment wall, and the substructure is a traditional design with roller, pin, or fixed supports. The bridge deck either rests on top of the abutment wall and is allowed to slide, or is cast monolithically with the abutment [20]. In either case, the movement is accommodated by placing expansion joints beyond the abutment walls, and the deck behaves as a continuous system.

While the design guidelines vary from state to state, integral bridges are grouped into two major categories: (1) Fully-integral (full moment transfer) abutment systems, and (2) Semi-integral (shear transfer only) abutment systems. In fully-integral systems, the abutment is connected rigidly to a single row of flexible piles, which move to accommodate full shear and moment transfer. In semi-integral systems, the backwall is allowed to move or rotate on top of the abutment wall, creating a shear transfer but no moment transfer [10][29][40], see Figure 3.

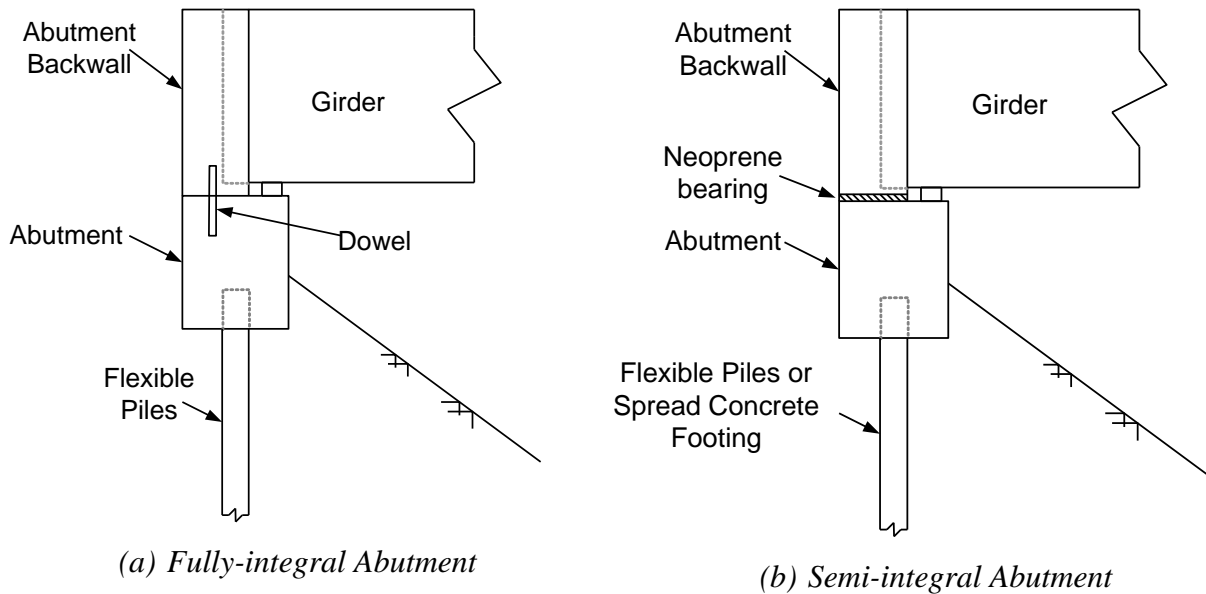


**Figure 3.** Jointless Bridge Abutment Details (Adapted from [10])

A fully-integral abutment is designed by placing position bars in between the top and bottom sections of the abutment backwall, preventing it from sliding. These bars are placed along the centerline of each beam bearing. The bars provide added restraint between the abutment wall and the backwall and full moment transfer. The entire abutment is designed to move and rotate as a single system, transferring movements to the flexible piles oriented in weak-axis bending. Semi-integral abutments are designed the same as fully-integral abutments, with the exception that semi-integral abutments do not have the presence of the position dowels. The bottom of the backwall is allowed to move with frictional resistance, thus transferring only shear forces due to the frictional resistance between the bottom of the backwall and the top of the abutment wall.

At least 32 states use jointless bridges. The overall designs consist of continuous decks with capped pile stub-type abutments resting on steel H-piles oriented in weak-axis bending [19]. While the maximum length constraints vary from state to state, typical ranges for total bridge lengths are 200' to 500' for steel girders, and 150' to 800' for concrete girders [10]. Many types of jointless bridge systems have been studied, with varying designs regarding fully-integral abutments, semi-integral abutments, concrete girders, steel girders, maximum skew angle, span length, and number of spans [6][14][15][19][29][30][34].

## 1.2 Motivation

Jointless bridges are overall performing well, and they have alleviated the deterioration problems experienced in conventional bridge design. Eliminating expansion joints has provided increased ride quality, less required maintenance, and overall increased longevity of the structure [10][20][29][40]. A survey conducted by the New York State Department of Transportation (NYSDOT) found that at least 30 states use integral abutment bridges, most of which are considered to be in ‘good’ or ‘excellent’ condition [19]. While jointless bridges are overall performing as designed and are better than bridges with joints, there is interest in investigating the various problems that have arisen in these new bridges [6][10][29][40]. Most of the problems are attributed to the increased rigidity of the system, resulting in less freedom of movement and higher stress levels due to temperature, creep, and shrinkage movements. Problems that have arisen include settlement and cracking of approach test units, separation of the approach test unit to the abutment, cracking in abutment end diaphragms, and transverse cracking in bridge decks [6][10][16][29][30][39][40]. Transverse cracking in bridge decks is a common problem for both jointless bridges and bridges with joints, and has been studied extensively.

However, transverse cracking in bridge decks has been found to be the most common problem experienced by jointless bridges, when the restrained mass of concrete experiences a change of volume and generates additional stresses due to the restraint in movement. Transverse cracking occurs when the longitudinal tensile stresses exceed the concrete modulus of rupture. Studies have shown that more than 100,000 bridges in the United States experience transverse deck cracking.[15][16][17][28][30][34][39]. Cracks often appear at an early age, sometimes before the bridge is open to traffic. The cracks are often full-depth, spaced 3-9 feet apart, and will continue growing with time. This could potentially lead to further deterioration problems within the deck and supporting girders [10][15][16][17][30][39]. Cracks are typically concentrated over transverse rebar in negative moment regions and along the longitudinal edge of girders. These areas are more susceptible to forming a plane of weakness in the concrete [28]. Cracking is greater in longer spans and older decks [15][28]. Additionally, cracking has often occurred in approach test units as soil backfill settles and resultant forces are transferred into the approaches [19][20][29]. Longitudinal cracking has been a common problem in concrete girder bridges along the edges of the girders, due to the formation of weak planes at the girder edges



[16]. This type of cracking can be attributed to the bridge geometry, and is not due to restrained concrete shrinkage.

Overall, deck cracking can be attributed to the build-up of forces induced by the secondary effects of temperature, creep, and shrinkage. Current designs account for dead and live loading, as well as for temperature loads. However, many agencies do not account for concrete creep and shrinkage in bridge deck design, which may explain the presence of cracking [19][29][39].

### 1.3 Research Objectives

The overall objective of this research project is to investigate the performance of jointless bridges, identifying the causes that lead to early-age deck cracking, and develop solution strategies to minimize or eliminate this damage. This was accomplished through experimentally-calibrated finite-element computer simulations and field assessments. The overall objective was completed through the following tasks:

- **Task 1: Literature Review.** Determine the current state-of-the-art on the behavior of jointless bridges, indentifying the existing knowledge on the causes for deck cracking, as well as any potential solution strategies.
- **Task 2: Field Inspection.** Perform field inspections on jointless bridges in Michigan that are known to suffer from deck cracking. Identify the parameters and conditions that could predict the cause of the distress. Develop a matrix of bridge design features and cracking patters to summarize the predominant parameters. This information is used to verify the findings from the literature review, and to develop a prototype system for the experimental and computational evaluation.
- **Task 3: Experimental Evaluation.** Experimentally evaluate the behavior of jointless bridges at the sub-assembly level through four different test unit systems. Determine the relative differences between the test units, and use the experimental data to validate the computer modeling approach.
- **Task 4: Computational Evaluation.** Evaluate the behavior of jointless bridges through experimentally-calibrated finite element models. Verify the modeling approach through smaller sub-assembly models, and implement the approach for full bridge systems. Perform a parametric study to evaluate the bridge behavior for different bridge design features.

This research study provides an in-depth analysis of the behavior of jointless bridges and identifies the predominant causes that lead to early-age deck cracking. Solution strategies for future bridge design and construction are also developed and proposed. The information presented in this report is immediately applicable to the work of MDOT and bridge engineers.

#### **1.4 Report Organization**

This report is organized to highlight the results of each of the four tasks outlined in the previous section. A literature review is presented in Chapter 2 to present the current state-of-the-art on deck cracking in jointless bridges. Chapter 3 presents the results and conclusions of the field investigation. Chapter 4 discusses the experimental evaluation, including the methods, approach, and results. Chapter 5 discuss the computer modeling approach, and the verification of the computer modeling through comparison with experimental data. Chapter 6 presents and discusses the results from the series of finite-element computer simulations with different bridge design parameters. Each task will be presented as an individual chapter, followed by a summary of the overall conclusions and recommendations in Chapter 7.

## 2 LITERATURE REVIEW

### 2.1 Sources Contributing to Deck Cracking

Due to the increased rigidity created by eliminating expansion joints, jointless bridge systems have less freedom of movement and thus less opportunity to relieve the stresses induced by temperature, creep, and shrinkage effects. The behavior of jointless bridges is complex and requires an investigation of many parameters affecting the stiffness of the overall system, which dictates the amount of deck cracking. These parameters include material properties and mix design, soil-structure interaction/abutment movement, temperature, creep, and shrinkage loading effects, and bridge design features.

#### 2.1.1 *Material Properties and Mix Design*

Much research has been performed on the effect concrete material properties and mix design has on deck cracking. A study was performed on 40 steel girder bridges in Kansas to investigate the relationship of material properties to deck cracking [14]. While the bridges selected were not all jointless, the effects of material properties apply to all types of bridges. The study found that the amount of cracking increased with an increase in slump (although zero slump was found to be worse due to the lack of consolidation), water content, compressive strength, and a decrease in air content. Although this was not always the case, the study also found that the higher w/c ratio, the more cracking. Most of the cracking occurred along transverse reinforcement, in the areas of concrete settlement adjacent to reinforcement [28][34]. Other studies suggested that cracking increases with higher w/c ratio, cement content, and air content [15][17]. The same studies also found that larger aggregate volume would minimize cracking due to the reduction in cement content.

Overall, the underlying premise behind the effects of material properties and mix design is that the higher content of water and cement, the more concrete shrinkage that will occur, which will lead to higher restraint forces from volume changes and in turn increase the amount of cracking [15][34]. Research has found that limiting the w/c ratio, lowering the cement content, lowering the air content, and increasing the aggregate content will reduce the amount of deck cracking [15][28][34]. Reduced cement paste volume and low cement contents are associated with reduced heat of hydration, which leads to reduced thermal stresses and reduced cracking

[15]. Specifically, it has been found that low shrinkage aggregates with the largest possible size should be used. Type II cement should be used due to its reduced early thermal gradient [17][28]. Compressive strength should be limited. Finally, set retarding admixtures should be used, as they reduce the rate of early temperature change [17].

### ***2.1.2 Soil-Structure Interaction and Abutment Movement***

Cracking in bridge decks relates heavily to the overall stiffness of the system, which is partially dictated by the soil-structure interaction at the abutment and supporting piles. This issue has been investigated to a moderate extent, although further research is needed. The largest induced movement for jointless bridge systems is found to occur at the abutments. Therefore, a large stress concentration is formed in this region of the bridge deck [29]. The overall length limitations for jointless bridges are often dependent on soil/structure interaction, and how much lateral movement can be accommodated without compromising the structure serviceability [9][14]. In addition to the bridge decks, the approach slabs in jointless bridges also exhibit cracking problems as stress levels increase due to settling of soil backfill and restrained movement of the bridge system [19]. Since most approach slabs rest on top of the abutment backwalls and extend longitudinally from the decks, stresses are induced due to load transfer at the abutment.

The behavior of a prototype integral abutment bridge in Minnesota was studied through instrumentation during and after construction. The bridge was a 3-span, simply supported concrete girder system with a continuous deck. The study found that abutment movement behaved in translation instead of rotation, and that the tops of piles deformed in double curvature. The study also found that the lower the freedom of movement, the higher the induced stress levels and the higher the amount of cracking [20].

Most agencies simplify soil pressure behind the abutment and supporting piles as a linear, triangular pressure distribution. The calculation of the soil stiffness involves an iterative procedure, where the magnitude of the soil lateral loads are estimated and applied with linear springs [14]. However, this is not the case, as the true soil reaction is inherently non-linear and varies with the depth, amount, and mode of pile displacement. The amount of soil pressure will increase as a function of the pile displacement. Nonlinear p-y design curves, developed by the

American Petroleum Institute, can be used to model nonlinear soil behavior [4]. The behavior of soil is very complex, and current methods over-simplify soil/structure response.

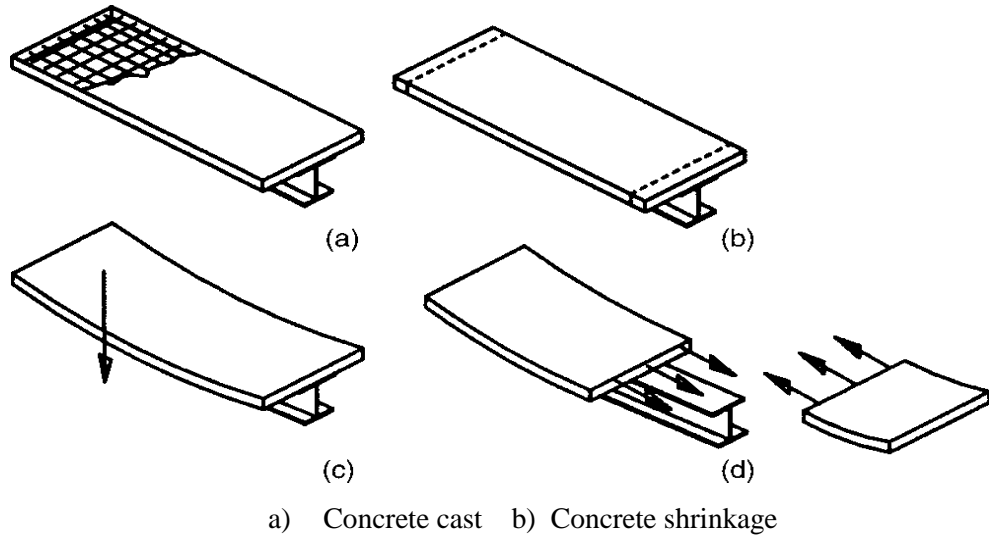
A 3D Finite-Element model was created for the Bemis Road Bridge in Fitchburg, Massachusetts [14]. The Bemis Road Bridge is a 3-span fully-integral abutment steel girder bridge that is 150' long. The soil response was modeled as a series of “Winkler” springs, and p-y design curves were used to model the nonlinear springs at the abutment wall and pile nodes. The soil compaction levels were varied: loose/dense, loose/loose, dense/loose, and dense/dense. The analysis results indicated the level of soil compaction behind the abutment wall is of utmost importance, as the axial forces and bending moments in the deck more than doubled when the soil compaction was varied from loose to dense [14]. Overall, it was found that the larger the soil compaction level, the more rigidity within the system and the larger the amount of cracking. While having looser soil may help mitigate some of the deck cracking issues, it is necessary to have enough compaction to support the approach test unit. Soil-structure interaction is a parameter that is currently simplified and not much research has been conducted on its behavior [9][14][20].

### ***2.1.3 Temperature, Creep, and Shrinkage effects***

Temperature effects have been studied, and it has been determined that both daily and seasonal temperature fluctuations create movement within the structure. Daily fluctuations create a thermal gradient through the cross section of the structure, while seasonal fluctuations lead to overall structural expansion and contraction. [20][29]. Temperature effects are taken into account in current designs, and use the equation for thermal expansion,  $\Delta L=L\Delta T\alpha$  [19]. The effects of temperature have been found to be as much as the effects of live loading [20].

Volume change in concrete is unavoidable, resulting from drying of concrete materials and internal chemical reactions which lead to concrete shrinkage. The amount of concrete shrinkage is dictated by mix design and construction practices, and is considered to be the most dominant source of deck cracking in jointless bridges due to the restraint in volume change [10][15][16][28][34][39]. Restrained concrete shrinkage causes early-age cracking in particular, since most shrinkage magnitude and strength gain occurs within the first few weeks [15][16][20][38]. Concrete shrinkage is resisted by girder stiffness, shear connectors, and reinforcing steel. The downward deflection of the deck-girder system creates restraint in

concrete shrinkage, inducing tensile stresses within the deck, which leads to cracking [16][17]. This is illustrated below in Figure 4.



a) Concrete cast b) Concrete shrinkage  
 c) Girder restraint produces a downward displacement d) Tensile stresses are induced  
**Figure 4.** Shrinkage-induced stress development in concrete bridge decks [30]

Consider a regular reinforced concrete section supported on its two ends. When undergoing restrained shrinkage, the specimen will first crack in the center, as shown in Figure 5. After this, the two cracked pieces will act as individual pieces and shrinkage-induced cracking will continue at the quarter points. Cracking will continue until the total shrinkage strain is accommodated, and the length of the un-cracked section is small enough to allow tensile stresses to be accommodated by the concrete. This is shown in Figure 6. This mechanism possibly explains the equal spacing of early-age transverse cracks in bridge deck systems.

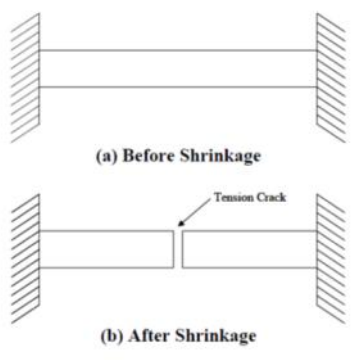


**Figure 5.** Simplified Shrinkage Cracking [16]

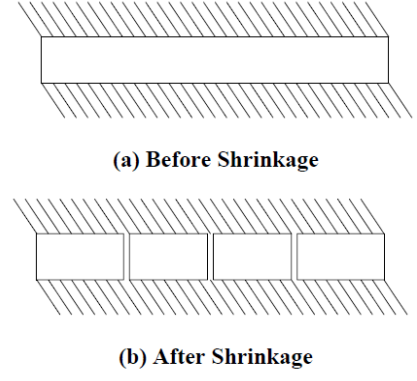


**Figure 6.** Cracking in continuously restrained concrete test unit [16]

In bridges, restraint is only provided at the bottom surface, and cracking initiates at the bottom surface and increases in depth until the total shrinkage strains are accommodated. Since the bottom surface is sealed while the top surface is free to shrinkage, differential shrinkage strains form through the depth of the deck, causing curling. This creates additional tensile stresses in the bottom surface of the deck. These stresses are higher for systems more susceptible to this differential shrinkage, such as bridges with steel girders, concrete girder bridges with overlays, and bridges with stay-in-place (SIP) deck forms [16].

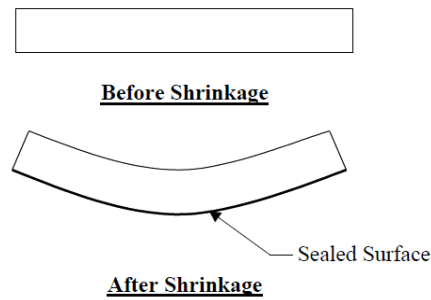


**Figure 7.** Curling of concrete deck due to sealed bottom surface [16]

There are four major types of concrete shrinkage, all of which contribute to inducing tensile stresses. These include plastic shrinkage (moisture loss from concrete before it sets), autogenous shrinkage (loss of water from capillary pores due to hydration), carbonation shrinkage (chemical reaction of hydration with the air, which occurs on exposed concrete surfaces), and drying shrinkage (long-term volumetric change due to drying of concrete). While total shrinkage is the sum of all four types, carbonation and autogenous shrinkage does not contribute significantly to deck cracking [16][17][18][30][39]. Since early age cracking is of particular interest, the effects of creep can be neglected. Creep is a long-term effect due to the deck self-weight, and cracking most often occurs before creep is able to take place [18][30][39].

Concrete shrinkage is a parameter that is not always taken into account in design. A survey performed by the NYSDOT revealed that 75% of agencies do not take into account shrinkage of concrete in design, and those that do confine it only to prestressed-concrete bridges [19]. If shrinkage is evaluated, it is taken into account over the long-term, while short-term volume changes due to shrinkage are overlooked and dismissed as insignificant. Current design practices consider shrinkage as a secondary, long-term effect, and use only the long-term drying shrinkage

component as the ultimate shrinkage value. However, this is inaccurate, since most concrete shrinkage occurs at an early age, and exceeds the amount of long-term shrinkage. Shrinkage stresses can potentially exceed even traffic loading conditions, so it is therefore inappropriate to consider it as a secondary effect [15][16][18][19][30][39]. Early age volume change due to drying shrinkage is of great importance, and should be considered in design. Drying shrinkage magnitude is dependent on the amount of water lost during placement and the rate of evaporation. Typical values are around 1 mm/m or less over the long-term, but short-term values could be 5 mm/m or greater during accelerated drying. This is often equal to or greater than the 28-day drying shrinkage measurements [18].

The University of West Virginia performed a study to investigate the effects of early age shrinkage stresses [39]. The researchers instrumented a 3-span continuous steel-girder bridge with fully integral abutments. Sensors were placed along half the length of the first stage of the bridge deck construction to monitor strain and temperature in the deck and reinforcing steel, and overall expansion and contraction of the bridge system. Strain data was taken every 30 minutes, which was used to analyze the stresses. It was discovered that the strain at the top of the deck was higher than the strain at the bottom, since the bottom is more constrained due to formwork and shear connectors. This produced tensile stresses at the top of the deck, which exceeded the concrete modulus of rupture and led to cracking. The study found that as the concrete ages, the stresses due to shrinkage stabilize. However, it was discovered that the magnitude of the shrinkage stresses exceeded the concrete modulus of rupture and produced cracking. Overall, the study confirmed that the volume changes and induced stresses due to drying shrinkage is of paramount importance, and the stresses that develop are relatively high even compared to the traffic loading. The study suggested that the effect of shrinkage be considered in design as a primary load [39].

Research on the specific effects of concrete shrinkage on deck cracking is limited, and its behavior is largely unknown [29]. However, all the studies agreed that the higher the shrinkage rate and the higher amount of shrinkage, the more deck cracking [10][15][16][17][18][29][30][39]. Gaining an understanding of early age shrinkage is of increasing concern, and studying it in more detail could help mitigate the problem of early-age cracking.



#### **2.1.4 Bridge Design Features**

Many different types of bridge designs and the effects of those designs on early-age deck cracking have been studied. There is much disparity in design requirements, which vary from state to state. A field investigation and parametric study performed by the Minnesota Department of Transportation (MNDOT) investigated the effects of bridge design on deck cracking. Seventy-two bridges were investigated, including 34 with concrete girders, 34 with steel girders, and 4 with W-shaped steel beams [15]. The top and bottom deck crack patterns were documented and summarized, and the bridge decks were given a rating from '5' to '9', with 9 being no cracking. While the field investigation was able to consider the entire system as a whole, the parametric study was used to isolate individual factors.

Overall, the more restraint that was present in the system, the more cracking that occurred. The field study found that concrete girder bridges performed better than steel girder bridges. Of the 34 concrete girder bridges studied, 25 had ratings of '8' or better, while of the 38 steel girder bridges studied, only 12 had ratings of '8' or better. This was attributed to reduced end restraint provided by simply supported concrete girders with continuous decks and the beneficial shrinkage characteristics of the concrete girders [15]. Steel girder bridges have differential shrinkage characteristics between the deck and the girders, while concrete girder bridges exhibit shrinkage of both the deck and the girders. Since steel girders do not shrink, they create increased rigidity in the system, thus leading to higher stresses and lower overall deck ratings. This phenomenon can also be seen in deck reconstruction on concrete girder bridges, which had more cracking than on new bridges. This is because the shrinkage characteristics of girders for the reconstructed deck bridges had already been stabilized, thus restraining the shrinkage of the deck and having a similar effect to steel girder bridges. Other conclusions drawn through the field study was that longitudinal restraint should be limited by increasing girder spacing and the number of shear connectors used should be limited. It was concluded that thicker decks should also be used, and should be above 6 ¼" thick. Additionally, the transverse bar size should be limited while the spacing should be maximized. It was recommended to use No. 5 bars spaced at 5.5" or No. 6 bars spaced at 7". Crack concentrations were found to occur in the area of cross-frames and diaphragms. For steel structures, the larger the girder spacing, the less cracking that occurred. The field study found that multiple factors exist, making it difficult to pinpoint individual parameters [15].

For the parametric study, computational analysis was performed using the finite-element program *PBEAM* [15]. Fiber or layered analysis approach was used, and the cross section of the girders and test unit were divided into layers. The bridge boundary conditions were modeled as fixed, pinned, or roller supports. A prestressed concrete girder bridge was modeled, as well as a continuous steel girder bridge. Nonlinear static analysis was conducted, varying the key parameters of shrinkage, end conditions, girder stiffness, cross-frames, splices, and the value of the deck modulus [15]. Differential shrinkage between the concrete deck and supporting girders was the primary cause of cracking, which was especially evident in steel and reconstructed concrete bridges. Additionally, the rate of shrinkage had a large impact on deck cracking. Reducing the initial rate of shrinkage reduced early transverse cracking. For end boundary conditions, the most extensive cracking was found with the fixed-fixed case. The end boundary conditions had the greatest effect on the extent of cracking, while girder stiffness, cross-frames, and splices dictated the crack locations. The study found that crack concentrations were increased in areas of cross-frames and splices. Additionally, stiffer girders produced more uniform cracking, while flexible girders exhibited increased crack concentrations at midspan. The study also found that the smaller the value of the deck modulus, the more allowed shrinkage deformation and the less cracking. The parametric study correlated well with the field study [15].

Purdue University also performed a field investigation and created laboratory models to investigate the effect of design factors on bridge deck cracking [16]. The field investigation involved visually inspecting twenty bridges, which included eleven steel-girder bridges and nine concrete-girder bridges. The most transverse cracking was observed on steel girder bridges incorporating composite action and SIP forms, while the least amount of cracking was observed on bridge decks cast monolithically with concrete superstructures. More longitudinal cracking was observed on concrete girder bridges than steel girder bridges, likely due to the planes of weakness formed along the edges of the concrete girders [16]. Nine of the eleven steel-girder bridges experienced transverse cracking, while only four of the nine concrete-girder bridges had transverse cracking. Interestingly, one of the concrete-girder bridges only experienced cracking on a newly widened portion of the bridge deck. Since the original portion of the deck had already undergone shrinkage, it created an additional restraint for the shrinkage movement in the widened portion. The original portion prevented the widened portion from shrinking freely, thus

inducing cracking in that region. This observation is similar to the observations noted with reconstructed decks cast on concrete-girder bridges in the MNDOT study, where the new deck portion experiences restrained shrinkage, leading to the build-up of tensile forces and deck cracking [15][16].

The study performed at Purdue also included a field instrumentation and extensive laboratory investigation into the effects of design factors on concrete shrinkage and deck cracking [16]. For the field instrumentation, a series of strain gages were placed in the deck and supporting girders of a new bridge to measure thermal and strain gradients through the deck and girders. A dramatic increase in strain in the deck reinforcement was noted 19 days after casting, while there was no change in the steel girder strain, likely indicating the development of transverse cracking. It was determined that once the deck cracked, the stress in the concrete was transferred to the reinforcing steel and eventually decreased over time due to force redistribution [16]. The laboratory investigation consisted of three parts. The first part involved creating cut models from the instrumented bridge deck, the second part involved creating small shrinkage models to investigate various design parameters, and the third part involved creating reinforced concrete test unit models to investigate the effect of reinforcing bar size, spacing, and epoxy-coating thickness [16]. In the first part, it was determined that moisture loss and drying shrinkage commenced at the completion of curing, and that the primary cause of deck cracking is the restraint of drying shrinkage of concrete. In the second part, it was determined that sealing the bottom surface of the deck (through SIP forms) significantly influences the amount of concrete shrinkage, increased deck thickness leads to reduced shrinkage, and increasing the reinforcement reduces the total shrinkage, but increases the amount of curling. In the third part, it was determined that as the reinforcement spacing was decreased, the spacing and size of primary cracks decreased but the number of cracks increased. As reinforcement spacing was increased, the number of cracks decreased but the crack width increased. Additionally, it was determined that as epoxy coating thickness was increased, the average and maximum crack widths also increased [16].

Another study developed a 2D and 3D finite-element model to examine the effects of changing various design factors and boundary conditions [30]. The computer program *ANSYS* was used to model the Hackensack Avenue Bridge over New Jersey Route 4. An increasing uniform shrinkage loading was applied, and cracking was assumed to occur at sudden jumps in

the shrinkage strain curves. The study revealed that cracks develop suddenly from the bottom to the top, and are full-depth. The more rigid the boundary conditions and end restraint conditions, the lower the amount of shrinkage required to cause cracking [30]. For the 2D model, different design parameters were varied for each boundary condition. An increase in overall stress levels led to an increase in the amount of cracking. The analysis revealed the following:

- Increasing boundary restraints increased tensile shrinkage stresses.
- Span length had no effect on shrinkage stresses.
- Increasing deck thickness reduced shrinkage stresses.
- Increasing girder spacing reduced shrinkage stresses.
- Increasing ratio of girder to deck moment of inertia increased shrinkage stresses. It is desirable to have flexible supporting girders.
- Increasing area of longitudinal reinforcement increased shrinkage stresses.
- Changing the distribution of reinforcement had no effect on shrinkage stresses. [30]

The study also investigated the effect of shear connectors on deck cracking. It was determined that reducing the number of connectors would be beneficial in reducing the rigidity of the system. However, the current number is required in design to allow for composite action. The study proposed a mechanism be employed to prevent composite action at the early stages (during early age shrinkage), but will initiate when higher service loads and ultimate loads are applied. The idea was proposed to wrap the shear connectors in a hyperelastic material, which compress during early age shrinkage and provide enough resistance at later times to provide full composite action [30]. Overall, the study proposed the following conclusions:

- Stresses between the deck and girders are concentrated at the two ends.
- Time-dependent volume change due to shrinkage should be considered in the design of bridges.
- Construction practices should not introduce unnecessary boundary condition restraint on the girders.
- Ratio of girder/deck stiffness should be minimized.
- More flexible superstructures are recommended: have a minimum deflection requirement, and increase the maximum limit.
- Uniform reinforcement is recommended, and increasing reinforcement volume above code is not beneficial.

- Controlled composite action (wrapped shear connectors) should be investigated. [30]

Most jointless bridges use piles in favor of spread footings, as translationally stiff foundations induce greater superstructure loads due to less freedom of movement. Current designs assume axial pile loads are distributed evenly, and over 50% of agencies design for vertical eccentric loading at the tops of the piles [14][19]. Expansion for jointless bridges is provided at the far end of the approach test unit or between the abutment and the approach test unit. For steel structures, having expansion joints beyond the backwall produced less deck cracking [6][19].

A research study was also performed at Marquette University through the Wisconsin Department of Transportation to investigate early-age deck cracking. The effects of design parameters, construction practices, and concrete mix design on early-age cracking were all investigated by means of a field investigation and finite-element computer modeling [38]. The field investigation showed a varied trend in cracking patterns, and not all bridge properties were able to be investigated. However, the study found that bridges with concrete girders exhibited the most cracking, which is in conflict with previous research findings [38]. It was determined that the type of superstructure can greatly influence the amount of cracking, and is important to consider.

Finite-element computer modeling was also performed to simulate concrete shrinkage and traffic loading. Shrinkage loading was applied through temperature, while traffic loads were simulated through pressure points. The analysis did not use full inelastic material behavior. Instead, cracking was determined to occur when the concrete stress exceeded the concrete modulus of rupture. The analysis found that longitudinal stresses were larger than transverse stresses, so transverse cracking would dominate. It also found that even if deck cracking does not occur due to shrinkage loading alone, the added stresses due to traffic loading may be high enough to cause cracking [38].

Design criteria vary considerably from state to state, and every bridge investigated in the literature contained different types of designs. Overall, it was determined that the more restraint in the system, the more susceptible it was to deck cracking. In general, concrete girder bridges experienced less cracking than steel girder bridges, larger skews produced more cracking (especially in steel girder bridges), larger span lengths produced more cracking, and the closer the girder spacing, the more cracking that occurred [6][15][16][17][19][28][40].

## 2.2 Concrete Shrinkage Standard Tests

Many standard tests exist for studying concrete shrinkage and for determining restrained shrinkage strain and cracking. The most common test is the “ring test.” Literature describing ring test experiments is widely available and many results are available for comparison [8][21][32][33]. The literature focused mostly on the effects of concrete material properties, fibers and shrinkage-reducing admixtures on shrinkage strain and crack width, which goes beyond the scope of this research [32][33]. However, the literature revealed that most free shrinkage strain occurs during the first month of drying and levels out with time [21][32][33]. This is illustrated below in Figure 8. Additionally, the literature indicated that cracking occurred fairly consistently at a steel ring strain of 100 to 120 $\mu$ -strain [8][21][32][33].

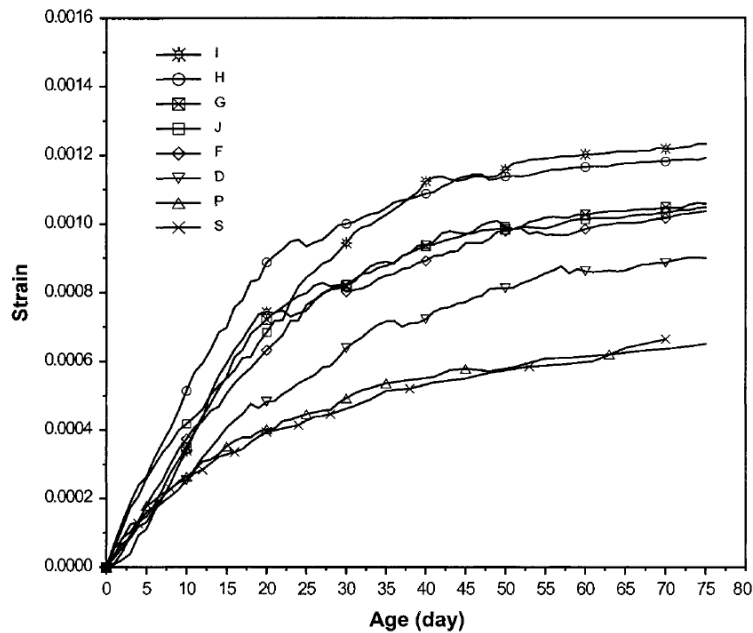


**Figure 8.** Development of Free Shrinkage Strain with Time [21]

While the literature obtained on concrete shrinkage standard testing focused on material properties and mix design, it was determined that the ring test is able to predict cracking potential and restrained shrinkage strain reasonably well. The results from the literature are used further as a comparison for computer modeling, and to verify modeling approaches.

### **2.3 Questions and Outstanding Issues Remaining**

Overall, the behavior of jointless bridges has been considerably investigated, and research is widely available on the effects of mix design and primary loading. However, more work and research is needed for the behavior due to the secondary forces of temperature, creep, and shrinkage, particularly in the area of shrinkage. While temperature effects have been studied to some extent, the effects of concrete creep and shrinkage are still largely unknown, and need further investigation. Specifically, the effect of bridge design factors on concrete shrinkage needs further investigation, as the effect of mix design on concrete shrinkage has been studied in more detail.

Conducting more research in all these areas will shed light on the issues currently facing jointless bridges, specifically in the area of deck cracking. This research can be used to develop new designs that could help mitigate the problem of deck cracking in jointless bridges.

### **2.4 Conclusions, Recommendations, and Suggestions for Prototype Bridge System**

It is hypothesized that evenly-spaced early-age transverse cracking in jointless bridge decks are primarily caused by restrained concrete shrinkage. The amount of shrinkage is dictated primarily by concrete material properties and mix design, but bridge design factors can also have an effect. Overall, it is predicted that the more restraint present in the bridge system, the more cracking that will occur. Bridge designs can be modified to reduce the amount of restraint, which will decrease the amount of early-age cracking.

Deck cracking appears to be more prevalent in bridges supported by steel girders due to differential shrinkage and temperature characteristics through the section depth, along with the added restraint provided by the shear connectors. Reconstructed bridge decks supported by concrete girders also experience deck cracking, as they behave similar to steel girder bridges. Therefore, further research focuses on steel girder bridges. The effects of boundary conditions, girder spacing, rebar size and spacing, deck thickness and cover, and the effects of shear connectors are studied.

The nature of the focus of the research project dictates the features of the recommended prototype bridge system. The prototype bridge is a continuous steel-girder bridge with multiple spans. The length and width is large enough to fall within the typical range values, but small enough to be able to instrument in the laboratory study. The focus is on new bridges with no

skew. The various design parameters suggested above are implemented, and their effect on concrete shrinkage and deck cracking is investigated. Using this type of prototype bridge system will allow conclusions to be drawn on what parameters contribute to deck cracking in jointless bridges, from which recommendations can be made to alleviate the problem.



### 3 FIELD INSPECTION

A field inspection was conducted to examine several jointless bridges in Michigan that are known to have suffered from early-age deck cracking. A total of fifteen bridges were visited, including four different types of superstructures. The field inspection was used to identify the parameters and conditions that could cause distress in bridge decks. The findings were compared to the results from the literature review, and used to develop a prototype bridge system for further research tasks.

#### 3.1 Past Field Investigation Studies that have been Performed

A number of other field investigation studies have been performed to determine the parameters causing deck cracking in jointless bridges. The study performed by the Minnesota Department of Transportation outlined in the literature review involved an extensive field investigation [15]. Seventy-two bridges in the Minneapolis/St. Paul area were investigated, including 34 with concrete girders, 34 with steel girders, and 4 with wide-flanged steel beams. A wide range of roadway types, ages, lengths and deck conditions were chosen. The design, material, and construction data were collected for each bridge and documented. This included information on the year of construction, overlay/redecking, dimensions, average daily traffic, span lengths, girder spacing, deck reinforcement and shear connector details, cement supplier and detailed mix design, deck contractor, joint type, and high and low temperature during the day of deck placement. The top crack patterns in the deck were examined, as well as the bottom crack patterns by fascia girders, joints in parapets, cross frames, and field splices. Crack patterns were documented and given a deck rating similar to the rating system used by MNDOT. The rating was on a scale from '5' to '9'. The detailed criteria are presented below: [15]

'9' – No cracks

'8' –A few single cracks less than 0.03'' wide

'7' –Single cracks with crack width less than 0.03'' and crack spacing greater than 6'

'6' –Areas with high crack density. Crack width less than 0.03'' and crack spacing from 3' to 6'

'5' –Areas with high crack density and large crack width. Crack with greater than 0.03'' and crack spacing less than 3'

The deck condition rating was compared to the design, material, and construction data, and relationships between the deck rating and various parameters were plotted on 2D graphs. Linear regression was used to determine cracking tendency [15].

Another field investigation was conducted by researchers at Purdue University [16]. The field investigation involved visually inspecting and documenting cracking tendencies on bridges in two regional transportation districts. Bridges chosen were either newly constructed, or older bridges known to be experiencing deck cracking. Both concrete and steel girder bridges were investigated. A total of twenty bridges were inspected, which included 11 steel girder bridges and 9 concrete girder bridges. The top surface of the bridge deck was visually inspected by walking the entire length of the bridge. Any type of cracking or deterioration was noted and documented. The bottom surface of the bridge was also examined. Cracking was recorded for bridges not using stay-in-place (SIP) forms, while the use of these forms was also noted. Photographs were taken to capture the deterioration, and crack width/spacing was measured. Pertinent information recorded was the Indiana Department of Transportation (INDOT) structure number, date of construction, date of rehabilitation or widening (if applicable), date inspected, type of girder, skew angle, use of SIP forms, and cracking type. Major concerns observed were also documented and summarized [16].

### **3.2 Bridge Information Provided by MDOT**

MDOT provided information on several bridges in Michigan that have experienced deck cracking. Information provided included bridge inspection reports and photographs of damage. The bridge information was reviewed and a matrix of the deck cracking was developed. General bridge information was recorded, including the bridge ID number, location, date of construction, date of inspection, repair actions taken, skew angle, and type of deck forms used. A description of the type of cracking was then provided, along with the MDOT deck rating. A summary of the provided information was made to determine the structures to visit for the field investigation. Please refer to the appendix for a summary of the bridge information provided by MDOT.

### 3.3 Parameters Considered and Bridges Visited

The bridge inspection reports and photographs provided by MDOT were used to predict whether or not transverse cracking was evident. A decision was then made whether or not each bridge was a potential candidate to visit. Bridges selected to visit were ones that appeared to have widespread transverse cracking, indicating restrained concrete shrinkage. Bridges with recent deck replacements that were known to experience cracking were of particular interest, since these would have early-age cracking. Bridges with large skew angles (greater than 20 degrees) were discarded, along with bridges known to have part-width construction. The bridges visited are summarized below in Table 1. The bridge locations are shown in Figure 9.

The field investigation examined a wide variety of bridge superstructure types and a variety of locations. Most of the bridges provided by MDOT are supported by concrete beams, since that is the most common construction practice for new bridges in Michigan.

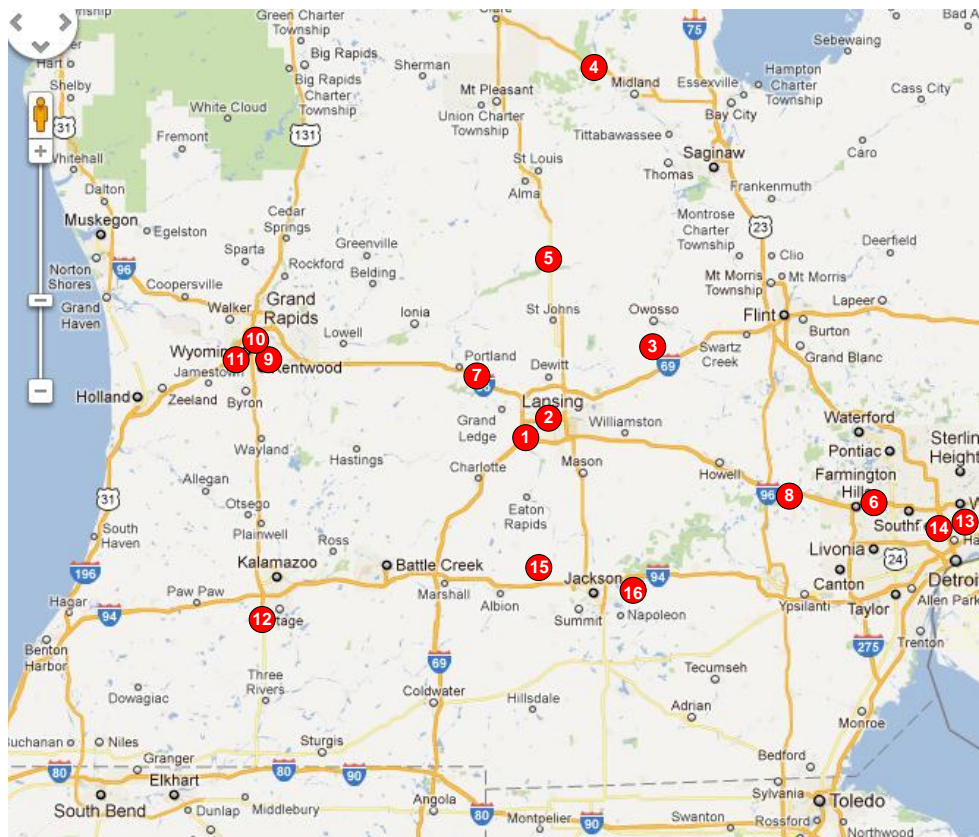


**Figure 9.** Field investigation locations

(For interpretation of the references to color in this and all other figures, the reader is referred to the electronic version of this report)

**Table 1.** Bridges visited for field investigation

<b>Bridge Location</b>	<b>Bridge ID Number</b>	<b>Girder Type</b>	<b>Reason to visit</b>
I-96 wb @ Lansing Rd.	1a	Side-by-side box beams	Cracking pattern of interest, close proximity to MSU
I-96 eb @ Lansing Rd.	1b	Side-by-side box beams	Cracking pattern of interest, close proximity to MSU
I-496 eb @ Pennsylvania Ave.	2a	Side-by-side box beams	Cracking pattern of interest, close proximity to MSU
I-496 wb @ Pennsylvania Ave.	2b	Side-by-side box beams	Cracking pattern of interest, close proximity to MSU
M-52 over Looking Glass River	3	Spread box beams	Extensive transverse cracking is evident
US-10 eb over Sanford Lake	4	Concrete I-beams	Extensive transverse cracking, spaced at 10', interestingly the westbound counterpart has no cracking
M-57 over US-127	5	Spread box beams	Based on photos and inspection report, there is extensive cracking
Halsted Rd. over I-696	6	Steel girders	Cracking evident prior to recent concrete overlay
I-96 eb over Grange Rd.	7a	Concrete I-beams	Cracking possibly widespread, close proximity to MSU
I-96 wb over Grange Rd.	7b	Concrete I-beams	Cracking possibly widespread, close proximity to MSU
Kensington Rd. over I-96	8	Steel girders	Photos indicate possible transverse cracking, has a high deck rating
M-6 eb over Buck Creek	9	Concrete I-beams	Need photos to document the damage, extensive cracking not evident
44 <sup>th</sup> Street over US-131	10	Steel Girders	Widespread transverse cracking, may be affected by part-width construction
Burlingame Rd. over M-6	11	Concrete I-beams	Transverse cracking appears concentrated at the piers
Milham Rd. over US-131	12	Spread box beams	Photos and inspection report indicate widespread cracking
26 Mile Rd. over M-53	13	Spread box beams	Some cracking over piers, recent bridge replacement
Walton Blvd. over I-75	14	Spread box beams	Some cracking throughout, recent bridge replacement
Hawkins Rd. over I-94	15	Spread box beams	Inspection photos indicate cracking, recent bridge replacement
I-94 over Sandstone Creek	16	Steel Girders	Transverse cracking evident, recent overlay and deck widening

### 3.4 Field Inspection Results

All of the bridges for the field investigation were visited during a one-week period in October, 2011. The visits occurred between mid-morning to late-afternoon, in weather ranging from sunny to overcast/light rain. Cracks were able to be observed on all days the bridges were visited. Pertinent bridge information was recorded, such as superstructure type, number of spans, type of abutment, use of stay-in-place forms, and skew angle. Next, photographs were taken of the overall bridge deck top surface and elevation to verify the overall design parameters. The bottom surface of the bridge deck was then inspected and photographed, and evidence of visible cracks was documented. Most bridges employed stay-in-place forms, which prevented cracking on the bottom surface. Finally, the entire top surface was visually inspected by walking the length of the bridge. All crack types were documented and photographed. Based on the photographs, a qualitative assessment of the damage was developed, and a prediction was made on whether or not cracking was onset by restrained concrete shrinkage. Typical photographs of damage are shown below in Figure 10 to Figure 14. Please refer to the Appendix for detailed photographs for each bridge. The results of each bridge inspection are summarized in Table 2.



**Figure 10.** Semi-integral abutment connection (Bridge No. 13, 26 Mile Rd. over M-53)



**Figure 11.** Fully-integral abutment connection (Bridge No. 4, US-10 over Sanford Lake)



**Figure 12.** Transverse cracking over pier/negative moment region (Bridge No. 13, 26 mile Rd. over M-53)



**Figure 13.** Typical transverse cracking in deck surface (Bridge No. 5: M-57 over US-127)



**Figure 14.** Typical longitudinal cracking (Bridge No. 11: Burlingame Rd. over M-6)

**Table 2.** Field investigation results

<i>Bridge</i>	<i>Type</i>	<i>Abutment Type</i>	<i>Cracking Type</i>		<i>Shrinkage-Induced?</i>	<i>Possibly Recently Re-constructed?</i>
			<i>Transverse</i>	<i>Longitudinal</i>		
I-96 @ Lansing Rd.	Adjacent Box Beam	Integral	Yes, at piers and joints	Yes, evenly spaced	Not likely	No
I-496 @ Pennsylvania	Adjacent Box Beam	Integral	Yes, at piers and joints	Yes	Not likely	No
<i>M-52 over Looking Glass River</i>	<i>Spread Box Beam</i>	<i>Integral</i>	<i>Yes</i>	<i>Yes</i>	<i>Yes</i>	<i>No</i>
<i>M-57 over US-127*</i>	<i>Spread Box Beam</i>	<i>Integral</i>	<i>Yes, widespread</i>	<i>Not much</i>	<i>Yes</i>	<i>No</i>
I-96 over Grange Road	I-beam	Integral	Yes, only at piers	Not much	No	Yes
Hawkins Rd. over I-94	Spread Box Beam	Integral	Yes, especially at piers	Yes, evenly spaced	Possibly	No
I-94 over Sandstone Creek	Steel beams	Non-integral	No	No	No	Yes
US-10 over Sanford Lake	MI-1800 I-girder	Integral	Yes, at piers	Yes	Possibly	No
<i>Kensington Rd. over I-96*</i>	<i>Steel beams</i>	<i>Integral</i>	<i>Yes, at piers and joints</i>	<i>Yes, spaced randomly</i>	<i>Yes</i>	<i>Yes</i>
26-Mile Rd. over M-53	Spread Box Beam	Non-integral	Yes, at pier	Yes, evenly spaced	No	No
Walton Blvd. over I-75	Spread Box Beam	Non-integral	Yes, at pier	Yes, evenly spaced	No	No
Halsted Rd. over I-696	Steel beams	Non-integral	No	No	No	Yes
<i>M-6 over Buck Creek</i>	<i>MI-1800 I-girder</i>	<i>Non-integral</i>	<i>Yes, at piers and in-between</i>	<i>No</i>	<i>Yes</i>	<i>No</i>
<i>44th Street over US-131</i>	<i>Steel beams</i>	<i>Non-integral</i>	<i>Yes, at piers</i>	<i>No</i>	<i>Yes</i>	<i>No</i>
Burlingame Rd. over M-6	MI-1800 I-girder	Integral	Yes at piers	Yes, evenly spaced	No	No
<i>Milham Rd. over US-131*</i>	<i>Spread Box Beam</i>	<i>Integral</i>	<i>Yes, widespread</i>	<i>Yes, spaced randomly</i>	<i>Yes</i>	<i>Yes (part-width construction)</i>

*Note: "Integral" refers to beams cast into the abutment, while "non-integral" refers to beams not cast into abutment.*



### **3.4.1 *Transverse Cracking***

Transverse cracking was evident in the negative moment regions (over the piers) in almost all of the bridges inspected. Transverse cracks in these regions were likely caused by the negative bending moment, rather than induced tensile forces from restrained concrete shrinkage. Restrained shrinkage cracking was indicated by the presence of evenly-spaced transverse cracks throughout the entire bridge surface. This appeared to have occurred in bridges 5, 8, 9, 10, and 12. Interestingly, it was evident in bridges with three different superstructure types (spread box beams, concrete I-beams, steel girders). It was only not evident in side-by-side box beam bridges.

### **3.4.2 *Longitudinal Cracking***

Longitudinal cracking was common in bridges with side-by-side box beams and spread box beams. The cracks typically spanned the entire length of the bridge, and were spaced at the same spacing of the beams. The longitudinal cracks in the side-by-side beam bridges were likely due to either differential settlement between the beams and the grout filler, or loss of post-tension force between the beams. For the spread box beam bridges, longitudinal cracking likely occurred due to a concentration of longitudinal shear forces at the edges of the beams. This is predicted since the spacing of the cracks match the beam spacing. These types of cracks are not due to restrained concrete shrinkage.

## **3.5 Summary and Conclusions**

Based on the field investigation, some general trends and conclusions were observed.

- Bridges with fully integral abutments (beams cast directly into the abutment) experienced more cracking than bridges with non-integral abutments (beams not cast into the abutment). This is expected, since bridges with fully integral abutments have more restraint.
- Bridges with larger spans and larger girders experienced more cracking.
- Part-width construction on Bridge 12 may have had an influence on the extent of cracking.

- Bridges with spread box beams had the largest extent of transverse cracking among the bridges visited. These bridges also had longitudinal cracking, spaced at the same spacing of the beams.
- Bridges with steel girders also had extensive transverse cracking, but did not experience longitudinal cracking.
- Bridges with side-by-side box beams did not experience transverse cracking.

In general, the information obtained from the field inspection correlated well with the information provided by MDOT. It is difficult to pin-point which type of bridge will experience the most restrained shrinkage cracking, since transverse cracking was evident on a wide variety of superstructure types, and each bridge is unique. However, the field investigation was able to confirm the hypothesis that the more restraint present in the system, the more cracking. Overall, it appears that bridges with spread box beams and steel girders are most susceptible to restrained shrinkage cracking.

Based on the results of the field investigation, two prototype bridges were chosen to develop finite-element computer modeling at the global/system level. It was initially understood that the Halsted Rd. over I-696 bridge experienced a heavy amount of transverse cracking, and was considered as a prototype for the steel-girder laboratory models. However, based on the field investigation, that was not the case. Of the steel bridges visited, the Kensington Rd. over I-96 bridge (Bridge 8) appeared to be the best candidate to use as a prototype for computer modeling, since it had the largest extent of transverse cracking among the steel girder bridges. Of the spread box beam bridges visited, M-57 over US-127 had the most amount of cracking. These two bridges are used as prototypes for further computer modeling.

## 4 EXPERIMENTAL EVALUATION

The experimental evaluation was used to investigate the behavior of jointless bridges at the material and sub-assembly levels. This was completed by constructing four different full-scale test unit slabs. The data is used to compare the relative differences in the shrinkage behavior of each test unit, and to validate the computer modeling approach.

### 4.1 Original Approach

The originally-proposed experimental task focused on the evaluation of shrinkage effects and early-age deck cracking on two scaled segments of different jointless bridges. The models were to be approximately  $\frac{1}{2}$ -scale, where continuity with the remaining bridge was to be simulated through boundary restraints and shrinkage effects were to be simulated by mechanically-equivalent external loads. The models would be created to simulate  $\frac{1}{4}$  of the entire bridge, as shown below in Figure 15.

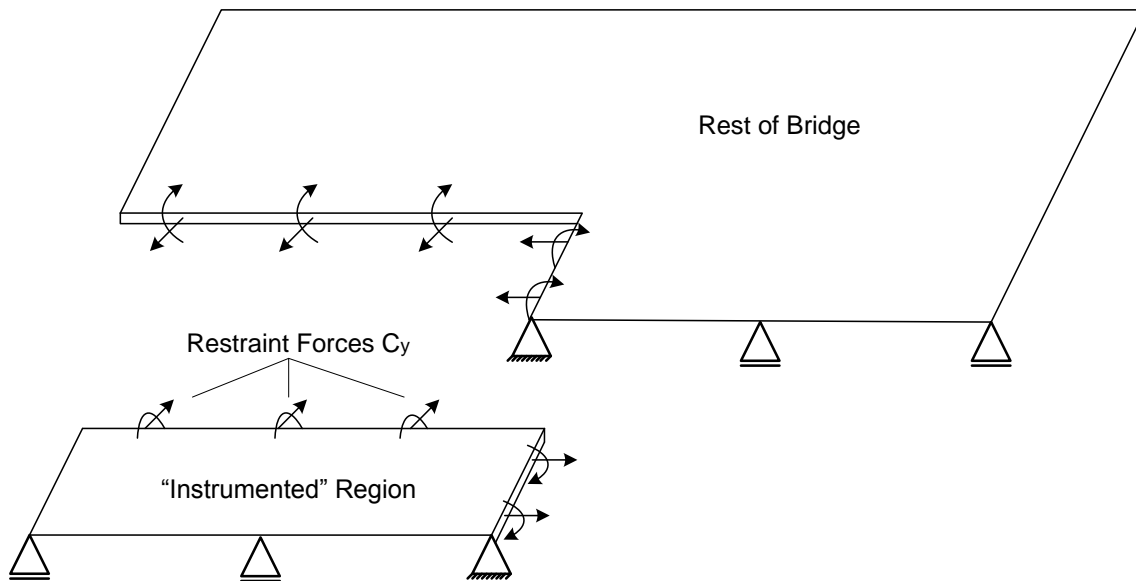


**Figure 15.** Region of bridge to model in the original laboratory investigation approach

In order to determine the required loading for the laboratory investigation, the non-mechanical (shrinkage) loads had to be converted into equivalent mechanical loads (forces and moments) to be applied externally to the test unit. Additionally, since only a section of the

bridge was to be modeled, the restraint provided by the rest of the bridge had to be calculated and applied externally as well. This overall procedure is shown below in Figure 16.

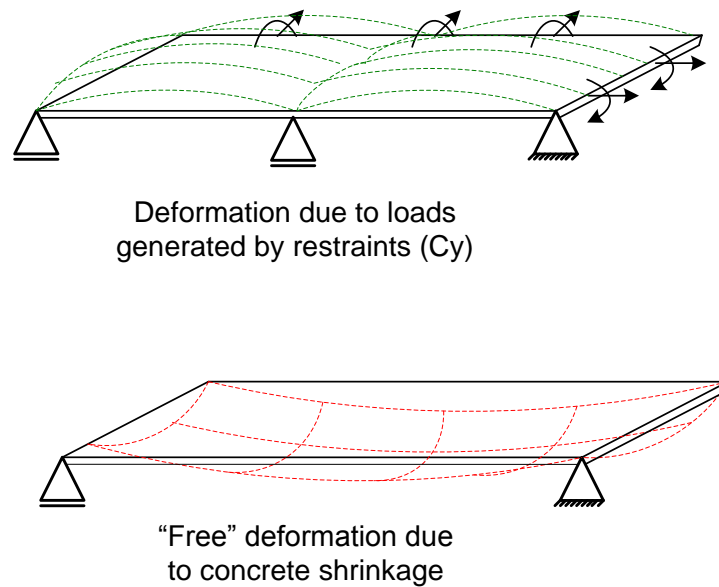


**Figure 16.** Loading approach for original laboratory investigation

As shown, two types of loading were to be combined together to obtain the correct response for the laboratory test units. The first was mechanically-equivalent shrinkage loads, while the second was the effects of the restraint provided by the rest of the bridge. The aim of the original approach was to validate the computer models by comparing simulated and real data on the scaled bridge segments at the global (full-bridge) level.

## 4.2 Revised Approach

Much difficulty arose in finding the mechanically-equivalent shrinkage loads in a rational manner. The complexity arose due to the high number of indeterminacies present in the bridge segment under consideration due to the interaction between the test unit, girders, diaphragms and boundary conditions. While the equivalent shrinkage-inducing loads could have been found through the solution of an inverse problem using the developed finite element models, they would have lacked a physical justification. Without rational physical justification, the value of the experimental data and research findings would have been severely compromised, so a change of strategy was thus needed.

The causes behind restrained shrinkage cracking may be grouped at three levels: (i) material, (ii) sub-assembly, and (iii) system. Material effects on concrete shrinkage have been studied considerably and are not in the scope of the current project. Sub-assembly level effects include structural design features such as girder type, diaphragms, deck forms, deck reinforcement details, and shear connector configuration. System level effects include those from support conditions, soil/structure interaction, and interaction between sub-assembly units.

Instead of evaluating behavior at the global level, which was the original approach, the laboratory investigation was revised to assess behavior at the sub-assembly level. The approach was similar to a laboratory investigation performed at Purdue University, which consisted of square deck test unit segments attached to longitudinal edge girders and incorporating relevant design features such as transverse diaphragms, shear connectors and formwork panels [16].

The effects of restrained shrinkage were evaluated by means of the actual volume change of the concrete in the deck test unit. Thus, no attempt was made to simulate restraining effects from the rest of the bridge or to introduce mechanically equivalent shrinkage loads. The smaller size of the test units allowed the testing of four beam/test unit assemblies, creating the opportunity to experimentally evaluate the effects of different design parameters. The following parameters were considered be important to shrinkage restraint at the sub-assembly level:

- Deck-girder shear interaction: shear connector spacing and amount
- Transverse system stiffness: diaphragm type (e.g., channel vs. x-bracing)
- Deck reinforcement: mainly transverse reinforcement size and spacing.
- Deck thickness
- Formwork system

Of these parameters, deck thickness was eliminated since it is constant for modern MDOT bridge designs. Also, the effects of formwork were evaluated by the work at Purdue University [16] and

no repetition was needed. While this the focus of this research is mainly on the effects of design factors on restraining concrete shrinkage, MDOT was also interested in studying one optimized mix design, which would contain less cement and therefore theoretically experience less shrinkage.

Based on these considerations, the experimental test matrix shown in Table 3 was developed. The baseline details for deck reinforcement, shear connector density, and size and girder spacing was obtained from the Halsted Rd. over I-696 bridge.

**Table 3.** Experimental Test Matrix for Sub-Assembly Evaluation of Shrinkage Effects

<b>Test No.</b>	<b>Girder Type</b>	<b>Diaphragm Type</b>	<b>Shear Connectors</b>	<b>Reinforcement Detail</b>	<b>Concrete Mix</b>	<i>Unique Parameter</i>
1	Steel	C-Channel	Studs-Density 1	Detail 1	Standard	<i>Standard Design</i>
2	Steel	C-Channel	Studs-Density 2	Detail 1	Standard	<i>Shear Connector Density</i>
3	Steel	X-Bracing	Studs-Density 1	Detail 2	Standard	<i>Diaphragm Type and Reinforcement Density</i>
4	Steel	C-Channel	Studs-Density 1	Detail 1	Optimized	<i>Concrete Mix</i>

The experimental data obtained from the experimental tests was used to calibrate material and shrinkage simulation finite element models. The finite element models for the sub-assemblies were further used to evaluate variations on the design parameters. Evaluation of system-level effects, such as soil-structure interaction and skew angle were done on finite element models of full bridge systems using the calibrated material and shrinkage modeling approach used for the sub-assembly models.

### **4.3 Test Unit Design Parameters**

Based on the revised approach described above, designs were developed for all four test units. As previously stated, the originally-considered prototype bridge (Halsted Rd. over I-696) was

used as a basis for the designs. Each test unit consisted of a 10-ft by 10-ft test unit cast on two beams, spaced apart by 7'-0" on center. The Halsted Road Bridge has a girder spacing of 9'-4" on center. However, due to laboratory size constraints and typical bridge girder spacing from the literature, a 7'-0" spacing was chosen. The overall test unit size was based on the beam spacing and space constraints in the lab. The design development for each parameter shown in Table 3 is described in the following sections.

#### 4.3.1 Steel Beam Size Determination

The two parameters considered in determining the steel beam size was axial stiffness and top flange width. The beams had to be as stiff or stiffer than the girders used in the Halsted Bridge, and the top flange width had to be the same in order to match the interaction between the steel and concrete. Since the span length of the test units were very small compared to the actual span length in the prototype bridge, the governing criteria was to match the top flange width. The flange width of the girders used in the Halsted Bridge is 14", so the smallest wide flange beam section with a 14-in. flange was desired. This yielded a W14x176 beam. However, this section yielded a large cross-sectional area and would have produced much larger axial stiffness than the actual prototype bridge, and was also above the budget for the project. Therefore, the beam selection was modified.

Instead of using a W14x176 beam with a 14-in. flange, the design was modified to choose a smaller section, and weld extension plates to the top flange to obtain the correct width. A W12x40 section was thus chosen, which is the smallest section with 8"-wide flanges. In order to reach the required 14"-width on top, 3" extension plates were welded on either side of the top flange, as shown below in Figure 17.

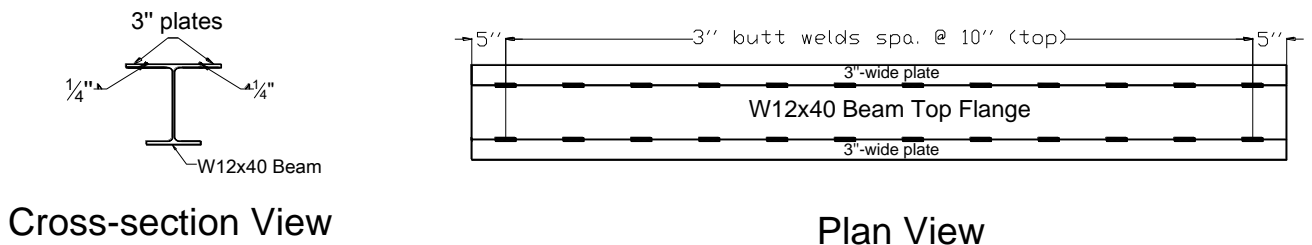


**Figure 17.** Steel beams selected, with welded extension plates

### 4.3.2 Diaphragm Section Determination

As shown in Table 3, two different types of diaphragms are used for the test units. The diaphragms were selected to match the axial stiffness of the C-channels used in the prototype bridge, which were C12x25 shapes with a cross-sectional area of 7.34 in<sup>2</sup>. The transverse spacing of the beams in the laboratory test units was the same as the actual bridge. Therefore, the cross sectional area of the chosen diaphragm shape had to be the same to match the axial stiffness. Double angle sections were used in lieu of C-channels, since the available C-channel sections were too tall for the W12x40 beams. The 2L5x5x3/8, with a cross-sectional area of 7.3 in<sup>2</sup> was thus chosen.

MDOT specifications and structural analysis were used to determine the angle size to produce equivalent stiffness for the cross-bracing diaphragms. First, a cross-bracing design for the Halsted Bridge was determined according to the MDOT standard specifications, as shown below in Figure 18.

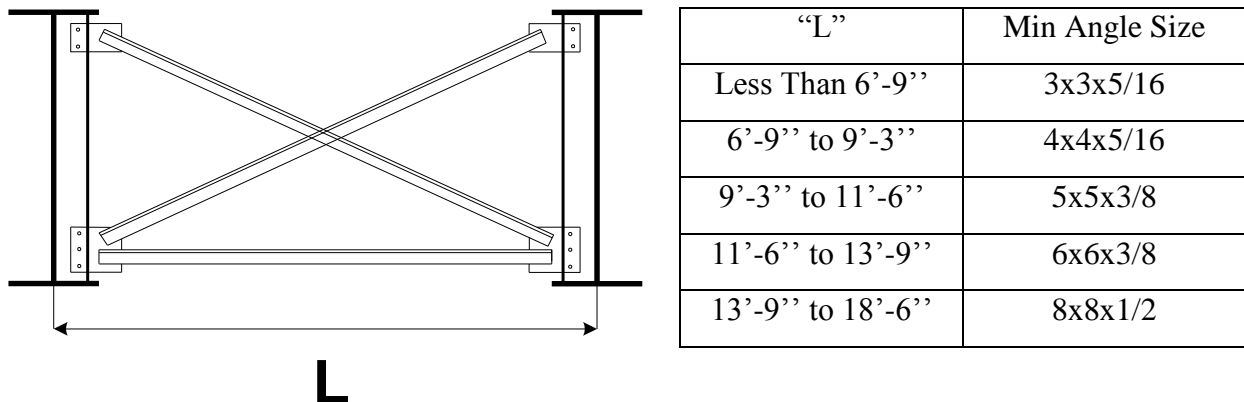
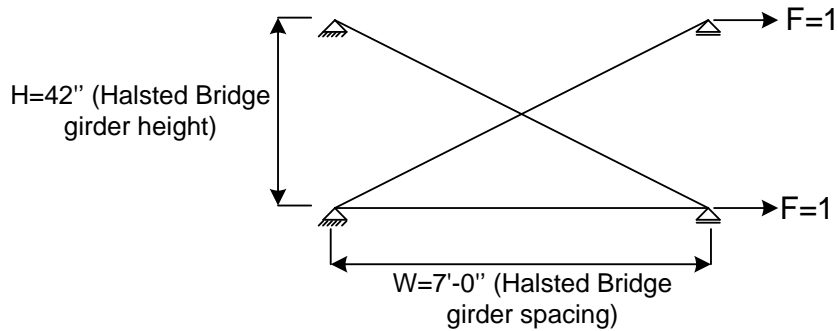


**Figure 18.** MDOT cross-bracing standard specifications (adapted from ref. [25])

Since the girder spacing, "L", is 7'-0" in the Halsted Bridge, the angle size that would be used in a cross-bracing diaphragm is L4x4x5/16. This cross-bracing for the Halsted Bridge was then modeled in SAP2000 with a unit force, as shown below in Figure 19. The corresponding displacements are shown below in Figure 20.





Note: MDOT specs. require two cross-members, as well as a straight member across the bottom, as shown

**Figure 19.** Halsted Bridge cross-bracing dimensions and SAP 2000 model

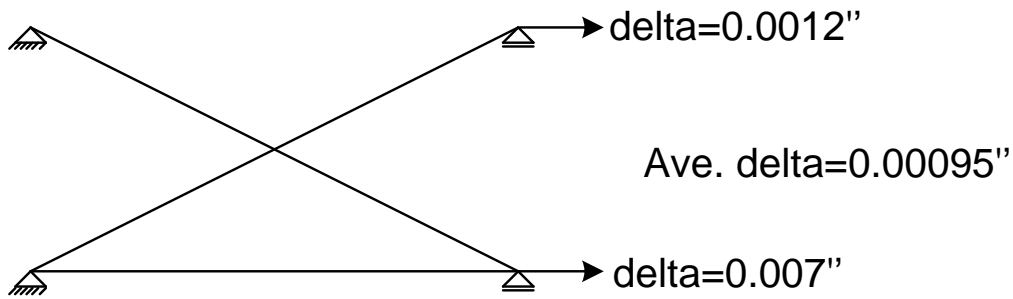


**Figure 20.** Cross-bracing displacement results

The shapes for the lab model cross-bracing were selected so that the overall axial stiffness was equivalent to the prototype bridge. The process for determining the correct shapes is summarized below in Equations 4-1 to 4-7.

$$\text{Stiffness, } k = \frac{F}{\delta} = \frac{2}{\delta} \quad (4-1)$$

$$k = \frac{EA}{L} \text{ (axial stiffness)} \quad (4-2)$$

$$k_{\text{bottom}} = \frac{F_b}{\delta_b} = \frac{1}{0.007} = 1429 \quad (4-3)$$

$$k_{\text{top}} = \frac{F_{\text{top}}}{\delta_{\text{top}}} = \frac{1}{0.0012} = 833 \quad (4-4)$$

$$k_{bottom} = 1429 = \frac{29000 * A}{L} \rightarrow A_{bottom} = 3.73 \text{ sq. in.} \quad (4-5)$$

$$k_{top} = 833 = \frac{29000 * A}{L} \rightarrow A_{top} = 2.18 \text{ sq. in.} \quad (4-6)$$

$$A_{total} = 5.49 \text{ in}^2 \rightarrow 2.75 \text{ in}^2 \text{ per angle in lab bracing} \quad (4-7)$$

Note that two angles were chosen for the lab cross-bracing instead of three due to the height of the beams. With 2.75 in<sup>2</sup> required per angle, a shape of L3x3x1/2 was selected for the cross-bracing members in the laboratory models.

Two sets of diaphragms were placed for each test unit, 1-ft. inward from the ends of the beams. The diaphragms were attached to the beams at gusset plates. The plate dimensions were chosen to be 3/8"-thick fit in-between the top and bottom flanges of the beams. The gusset plate details are shown below in Figure 21.

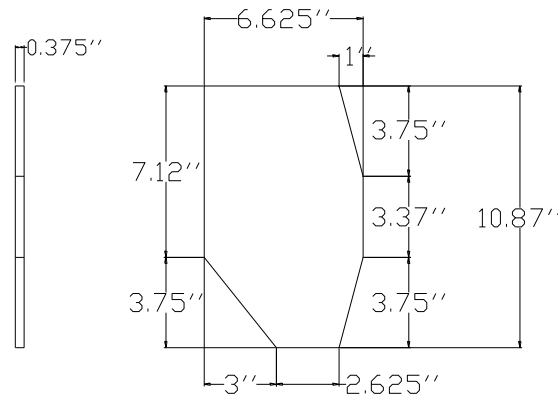


**Figure 21.** Gusset Plate Dimensions

### 4.3.3 Shear Connector Layout Determination

Two different shear connector configurations were welded to the top flange of the beams. The shear stud spacing in the Halsted Bridge varied from 6'' to 2'-0''. Therefore, to examine the effect of shear stud density, both extremes were used. The 6-in. spacing was used for test unit 2, while the 2'-0'' spacing were used for test units 1, 3, and 4. The same 3/4-in. diameter by 6-in. tall shear connectors were used in the test units. The same 5-in. spacing across the width of the flange was also used. The shear connector configurations are shown below in Figure 22 to Figure 24.

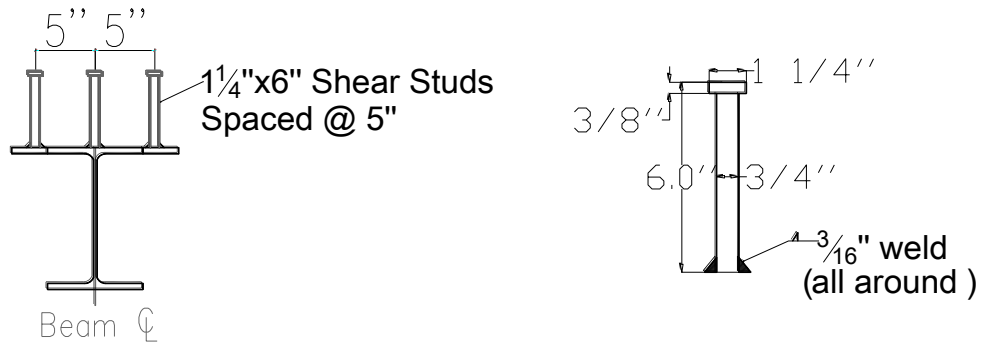


**Figure 22.** Shear Connector Spacing over Top Flange

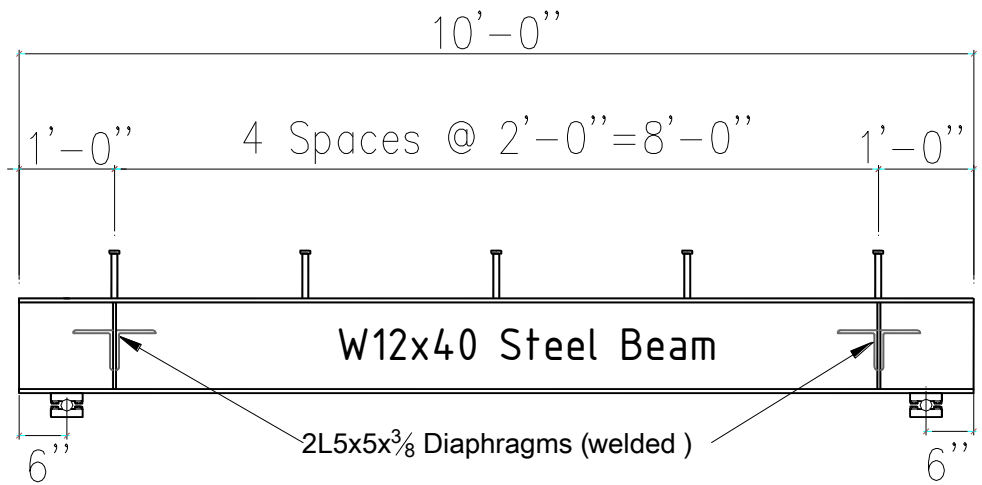


**Figure 23.** Shear Connector Detail 1 (Test units 1, 3, and 4)

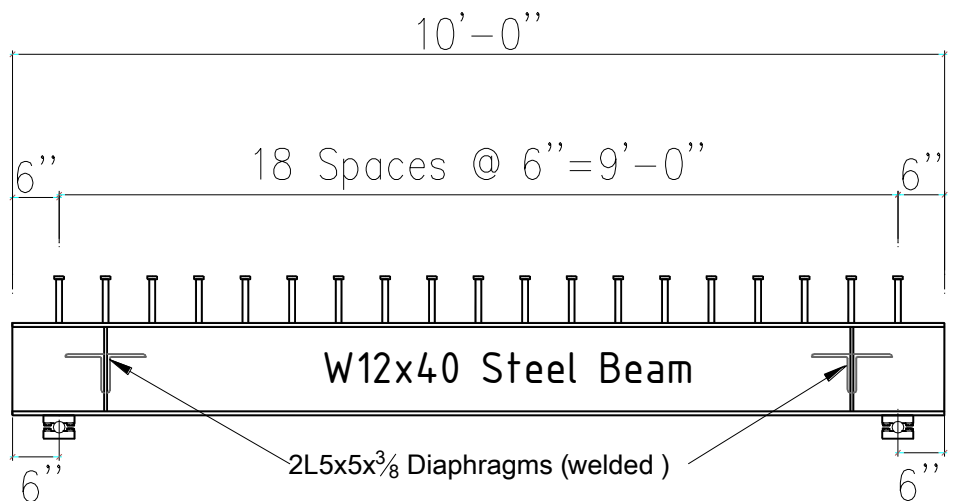


**Figure 24.** Shear Connector Detail 2 (Test Unit 2)

#### 4.3.4 Deck Reinforcing Steel Determination

Two different reinforcing steel configurations were used for the test units. The first configuration matched the MDOT specifications for the 7'-0" beam spacing used in the lab test units. This was used for test units 1, 2, 3, 5, and 6. The second configuration matched the Halsted Bridge reinforcement, which was derived from the girder spacing of 9'-4" in the actual bridge. This was used for test unit 4. The two reinforcement configurations are summarized below in Table 4, and are visually represented in Figure 25 and Figure 26.

**Table 4.** Test Unit Reinforcement Details (Derived from Reference)

Reinforcement Type	Top Longitudinal	Top Transverse	Bottom Longitudinal	Bottom Transverse
Detail 1	#3 Bars Spa. @ 10.5"	#5 Bars Spa. @ 8"	#4 Bars Spa. @ 8.5"	#5 Bars Spa. @ 8"
Detail 2	#3 Bars Spa. @ 10"	#6 Bars Spa. @ 8.5"	#5 Bars Spa. @ 9"	#6 Bars Spa. @ 8.5"

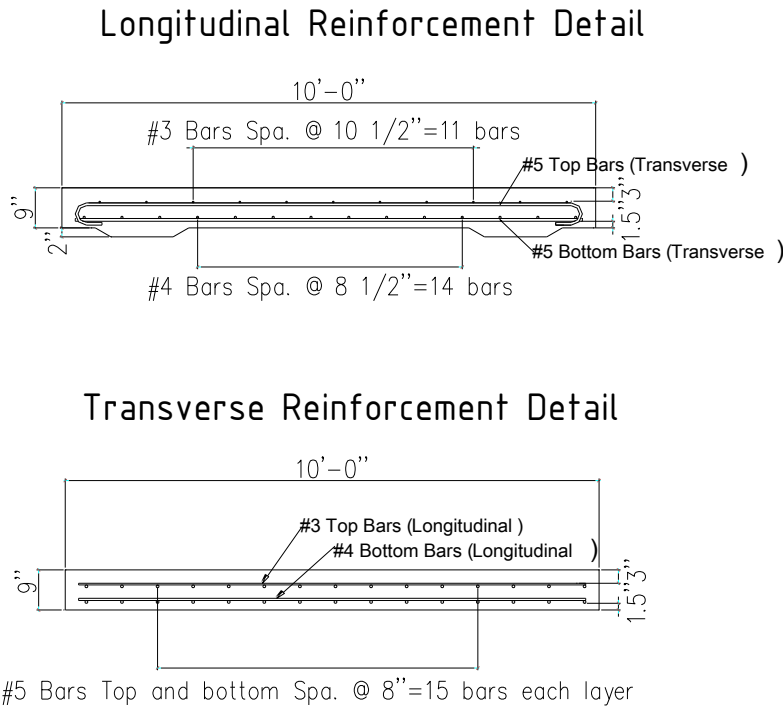
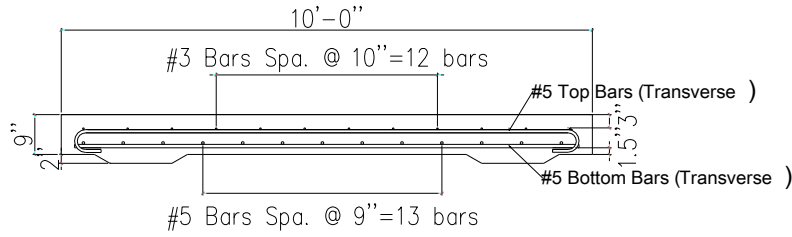


**Figure 25.** Deck Reinforcement Detail 1 (Test units 1, 2, and 4)

### Longitudinal Reinforcement Detail



### Transverse Reinforcement Detail

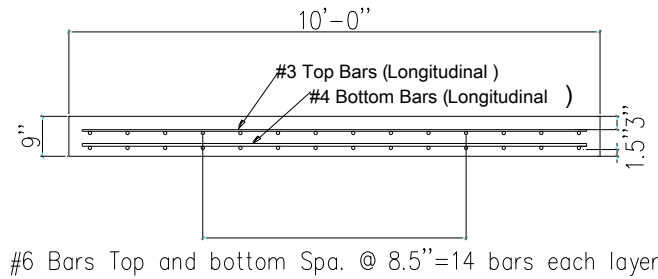


**Figure 26.** Deck Reinforcement Detail 2 (Test Unit 3)

#### 4.3.5 Weld Design

The connections for the gusset plates, shear studs, and diaphragms were welded together using the AISC minimum weld size specifications. According to the AISC manual, for a plate and angle thickness of 3/8", the minimum weld size is 3/16" [3]. The weld strength is specified below in Equation 4-8.

$$P_{weld} = 0.75(0.707 * t * L * 0.6 * 60ksi) = 19.089 * L * t \quad (4-8) [3]$$

Assuming 3/16"-thick welds, the weld strength is:

$$P_{weld} = 3.58 * L \quad (4-9) [3]$$

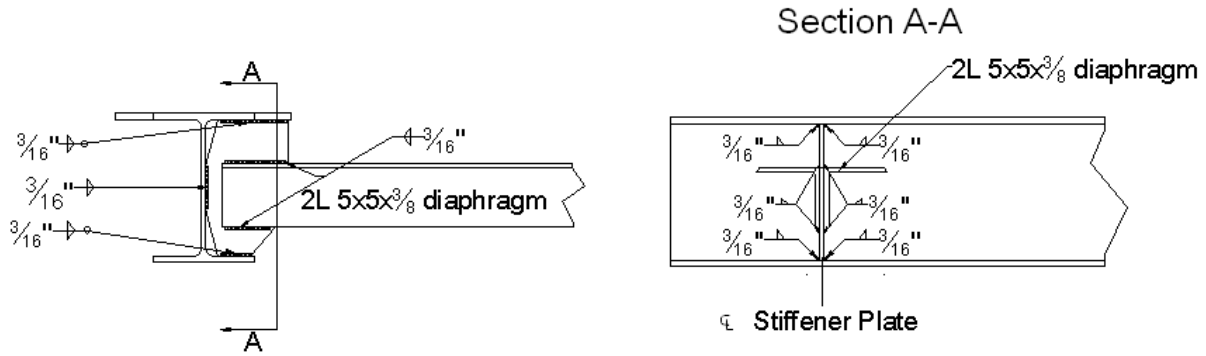
The weld lengths were dictated by the required connection details. Using Equation 9, the weld strength for each the connection is given as:

$$P_{weld\_gusset} = 3.58 * (2 * [6'' + 6'' + 5'']) = 121.72 \text{ kips} = 121,720 \text{ lbs} \quad (4-10)$$

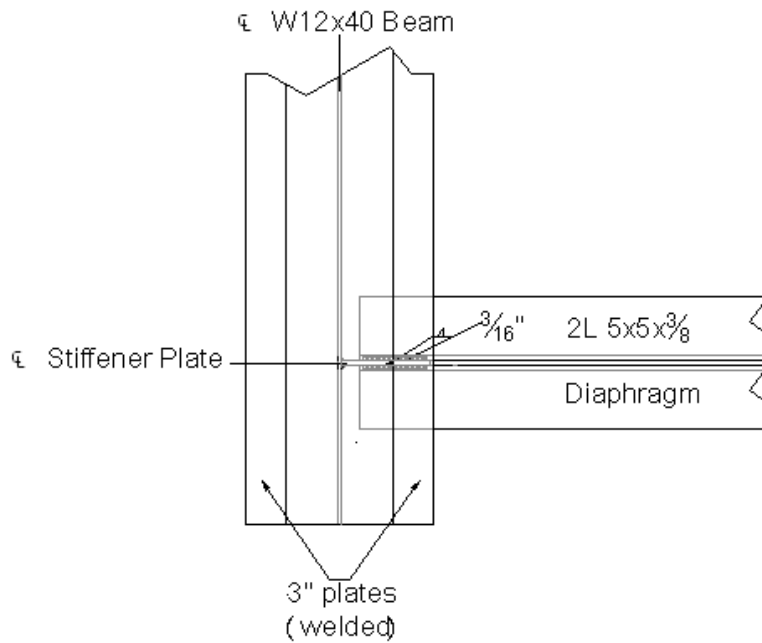
$$P_{weld\_diaphragms} = 3.58 * (2 * [2 * 5.5'']) = 78.76 \text{ kips} = 78,760 \text{ lbs} \quad (4-11)$$

$$P_{weld\_x-bracing} = 3.58 * (2 * [2 * 5.5'']) = 78.76 \text{ kips} = 78,760 \text{ lbs} \quad (4-12)$$

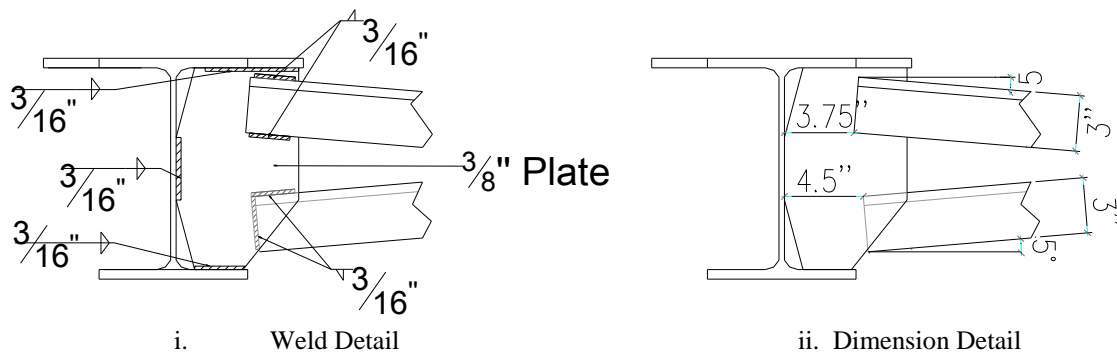
Since these strengths are much higher than the anticipated forces expected for the lab models, it was determined that using 3/16" welds would be adequate. The weld details are shown below in Figure 27.



a) Gusset Plate and Diaphragm Connection Cross-Section View



b) Diaphragm Connection Plan View



c) Cross Bracing Connection

**Figure 27.** Welded connection configurations

### 4.3.6 Pin Support Design

The beams were set on pin supports at each end. The bases for the supports were made from cut sections of W8x31 beams. Grooved steel plates and round steel bars were utilized to simulate the standard rocker bearings used in bridges. Since the anticipated rotations at the supports were small, the pin dimensions did not need to match the dimensions of the rocker bearings used in the Halsted Bridge. The pin support details are shown below in Figure 28 and Figure 29. The supports were placed 6'' from the ends of each beam. Bolted connections were used so that the plates could be re-used.

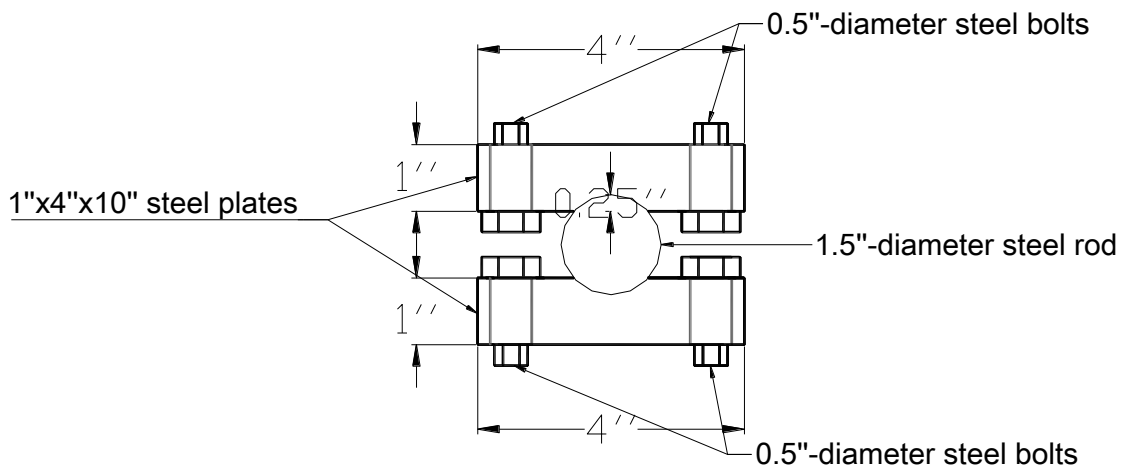


**Figure 28.** Pin plate details

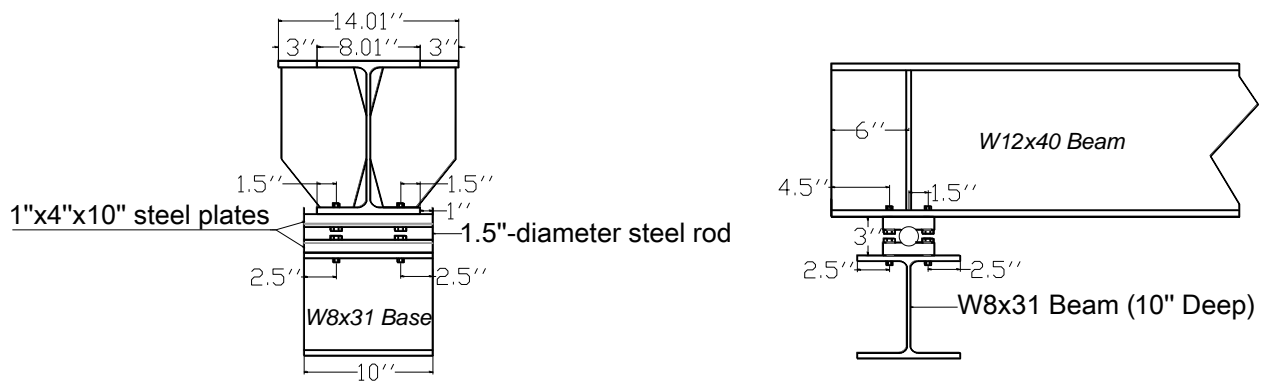


**Figure 29.** Pin connection setup

#### 4.3.7 Test Unit Design Summary

The overall designs for all four test units are summarized below in Table 5. A three-dimensional drawing of the test unit is shown in Figure 30.

**Table 5.** Test Unit Design Summary

Test No.	Girder Type	Diaphragm Type	Shear Connectors	Reinforcement Detail	Concrete Mix
1	W14x176	2L 5x5x3/8 angles	1.25x6'' studs spa. @ 2'-0''	Detail 1	Standard
2	W14x176	2L 5x5x3/8 angles	1.25x6'' studs spa. @ 6''	Detail 1	Standard
3	W14x176	L 3x3x1/2 X-bracing	1.25x6'' studs spa. @ 2'-0''	Detail 1	Standard
4	W14x176	2L 5x5x3/8 angles	1.25x6'' studs spa. @ 2'-0''	Detail 2	Optimized

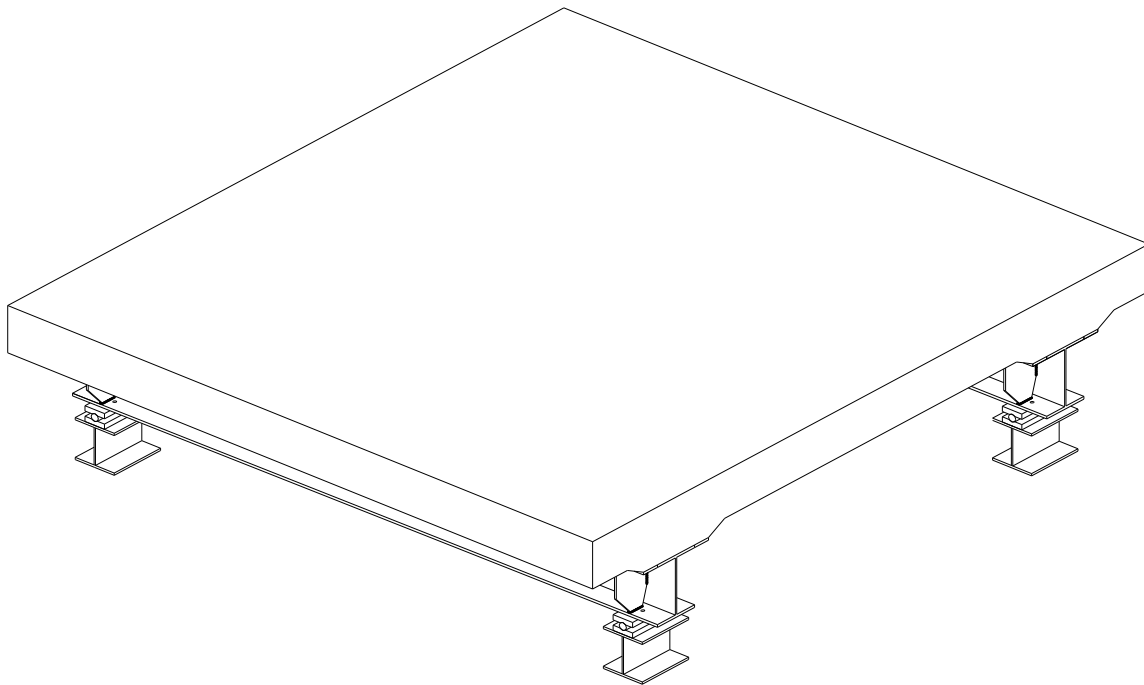


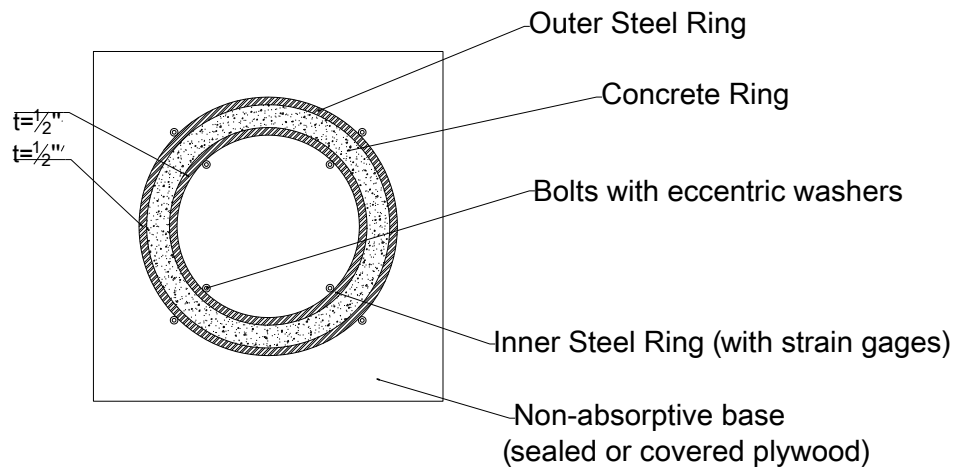
**Figure 30.** Test Unit Overall View



### 4.3.8 Ring Test

In addition to the four test units, a concrete shrinkage ring test was performed to test the shrinkage properties and cracking potential of the concrete. The test setup was based on ASTM C1581-04. In the test, a ring-shaped sample of concrete is cast between an instrumented steel ring and a circular mold. After the specimens have cured, the circular mold is removed and the top surface is sealed, which allows free shrinkage only on the exterior surface of the concrete ring. The interior steel ring restrains the shrinkage of the concrete ring, and compressive strain and stress is induced [5]. The test setup is shown in Figure 31.

#### Overall Test Setup (Plan View)



#### Overall Test Setup (Section View)

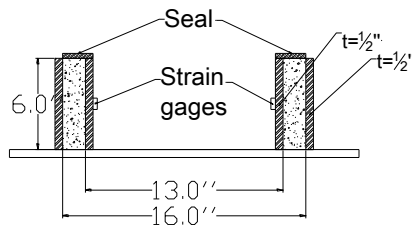


**Figure 31.** Ring Test Setup (adapted from ref. [5])

Strain gages are placed on the interior of steel ring to measure strain in the circumferential direction. As the concrete shrinks, it compresses the inner steel ring, inducing compressive strains. The steel ring restrains the shrinkage movement of the concrete ring, and the

compressive strains increase until cracks form in the concrete ring [5]. Compressive strain is measured from the time of casting, and cracking is indicated by a sudden decrease in strain. An example strain output is shown in Figure 32. Three rings were cast for each batch of concrete.

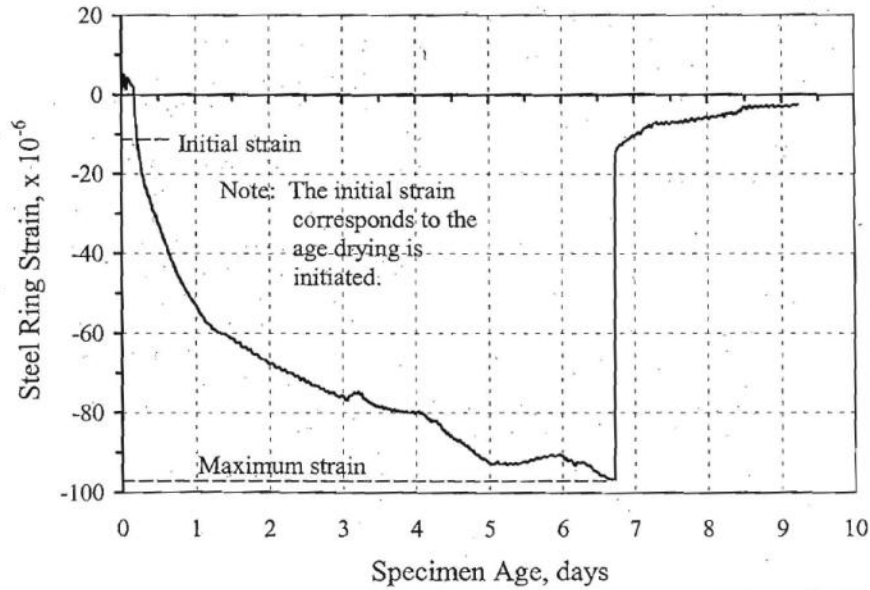


**Figure 32.** Example Ring Test Strain Output [5]

#### 4.4 Instrumentation Layout

A combination of LVDTs, Thermocouples, and Strain Gages were used to monitor the early-age concrete behavior in the test units, and to measure the effect of concrete shrinkage. Instrumentation was placed so that an overall representative behavior of each test unit could be obtained and used to calibrate the computer models.

##### 4.4.1 Strain Gages

Wire-resistant strain gages were attached on both mats of reinforcing steel and through the depth of the beams to determine the strain gradient through the depth of the test units. The strain gage locations are shown below in Figure 33 to Figure 36.

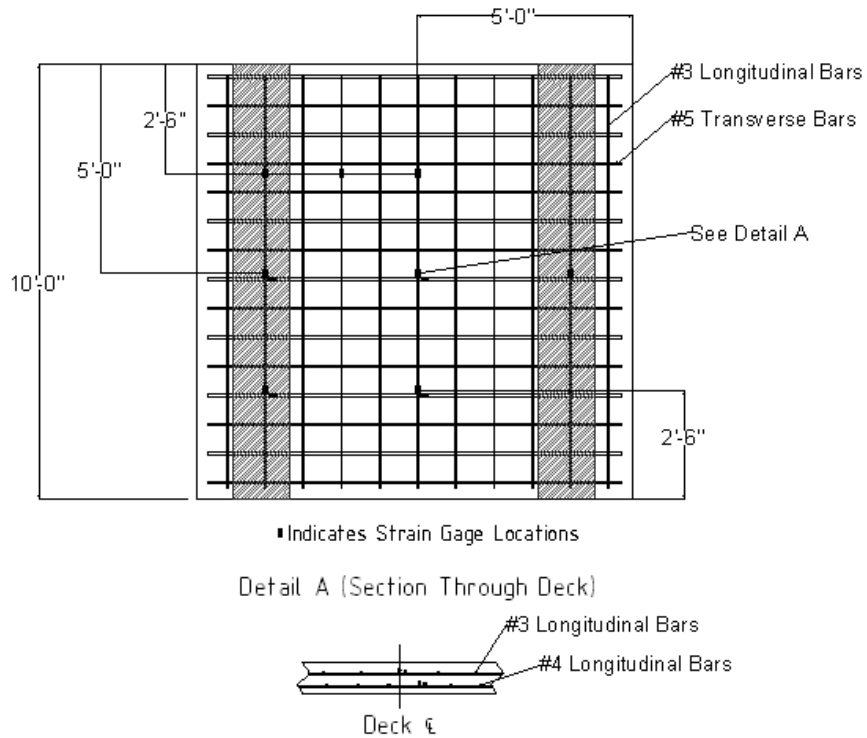


**Figure 33.** Reinforcing steel top mat strain gage locations

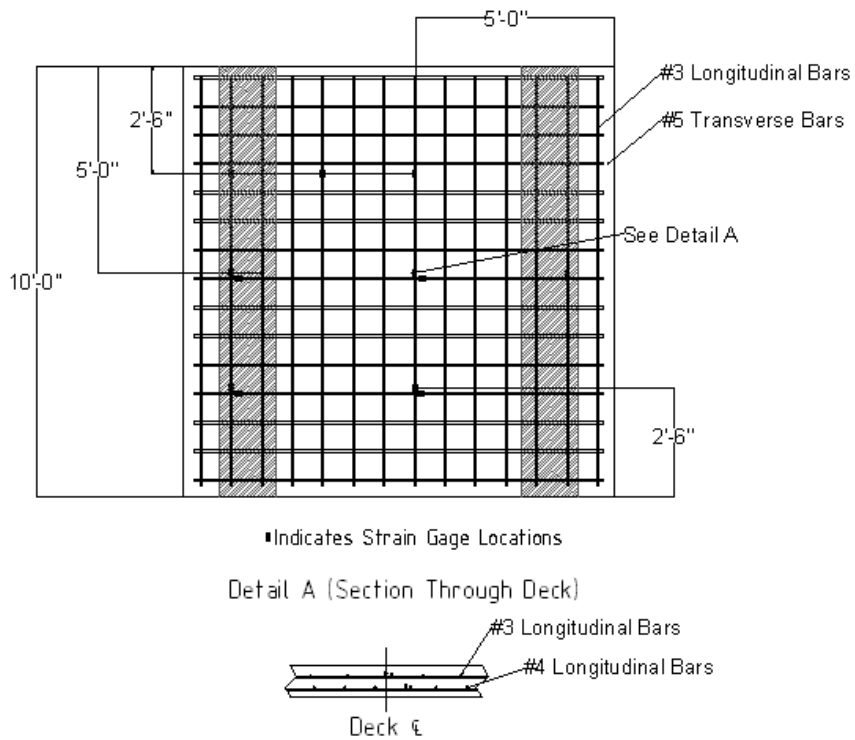
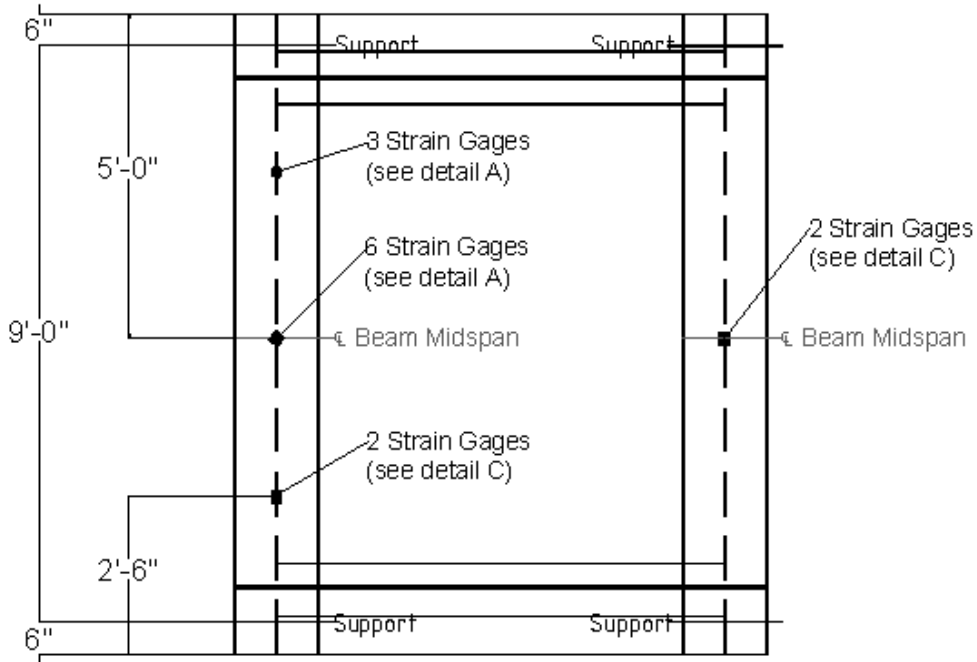
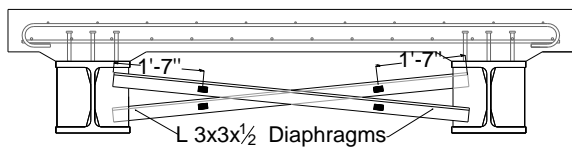


**Figure 34.** Reinforcing steel bottom mat strain gage locations



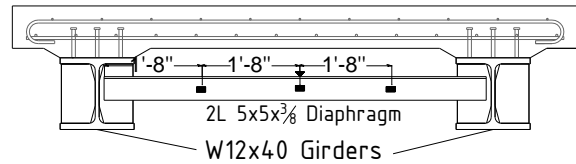
• Indicates Strain Gage Locations

**Figure 35.** Steel beam strain gage locations



■ Indicates Strain Gage Locations

Note: Strain gages shall be placed at the quarter-span and three-quarter span of each diaphragm, measuring strains in the local longitudinal direction



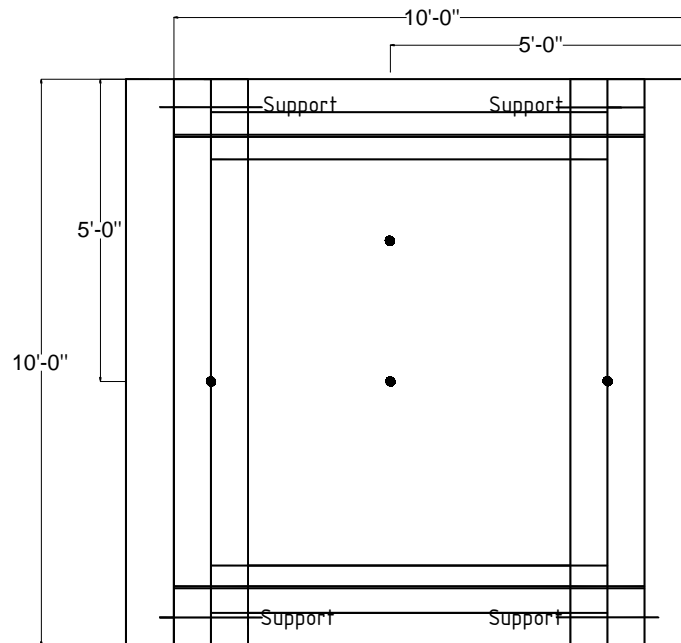
■ Indicates Strain Gage Locations

Note: Strain gages shall be placed at the quarter-span and three-quarter span of each diaphragm, measuring strains in the local longitudinal direction

**Figure 36.** Diaphragm strain gage locations

#### 4.4.2 LVDT's

Several 0.05-in. LVDT's were used to measure the deflection of the laboratory models. The LVDT's were calibrated using plates with known heights, which was required to convert output voltage to displacement. The LVDT layout is shown below in Figure 37. As shown, LVDT's were placed underneath each beam at mid-span, as well as two locations in the center of the test unit.



• Indicates LVDT Locations

**Figure 37.** LVDT Locations

#### 4.4.3 Thermocouples

Type K Thermocouples were used to measure the temperature change in the concrete during curing, as well as the ambient temperature. The thermocouples were positioned at the same level as the top and bottom mats of reinforcing steel in the test unit, while the ambient thermocouple was placed close to the test units.

#### 4.4.4 Instrumentation Naming Scheme

The following naming scheme was used to identify the locations of each instrument. This naming scheme is utilized in all the data outputs.

**(Test Unit)-(Type)-(X-coordinate)-(Y-coordinate)-(Depth)-(Orientation)**

- Test Unit: 1, 2, 3, or 4
- Type: LVDT (D), Strain gage (S), Thermocouple (T)
- X-coordinate: See Figure 38
- Y-coordinate: See Figure 38
- Depth: See Figure 39
- Orientation: Transverse (T), Longitudinal (L)

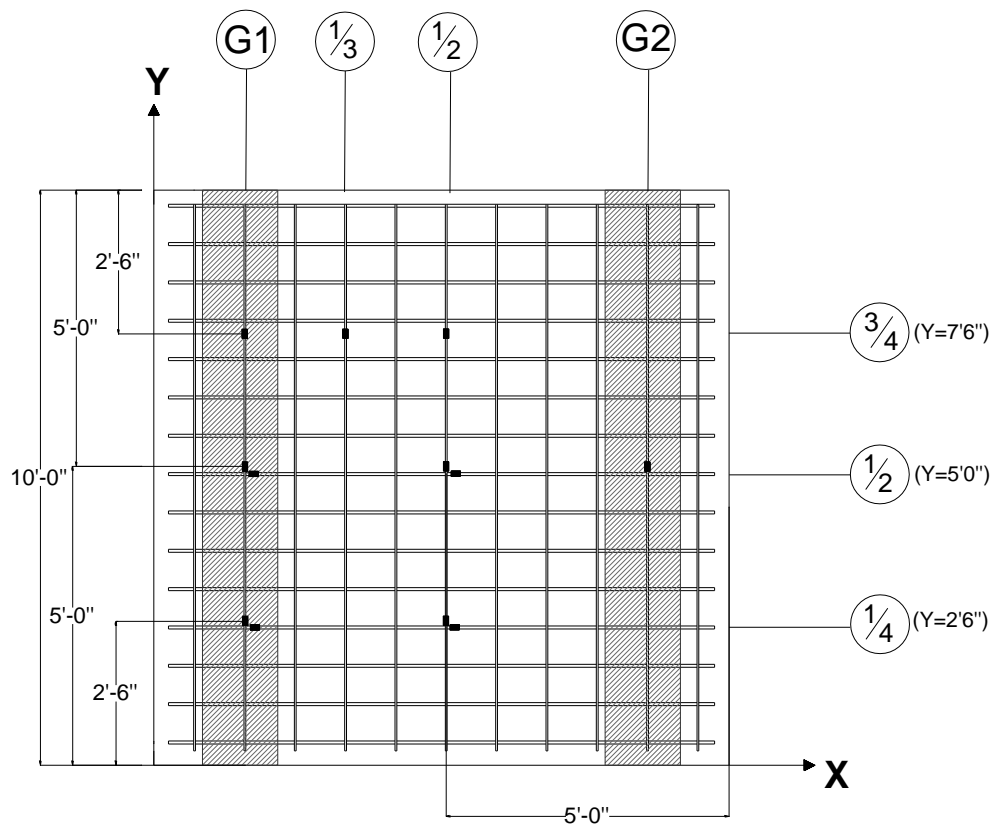


**Figure 38.** X-Y orientation for instrumentation

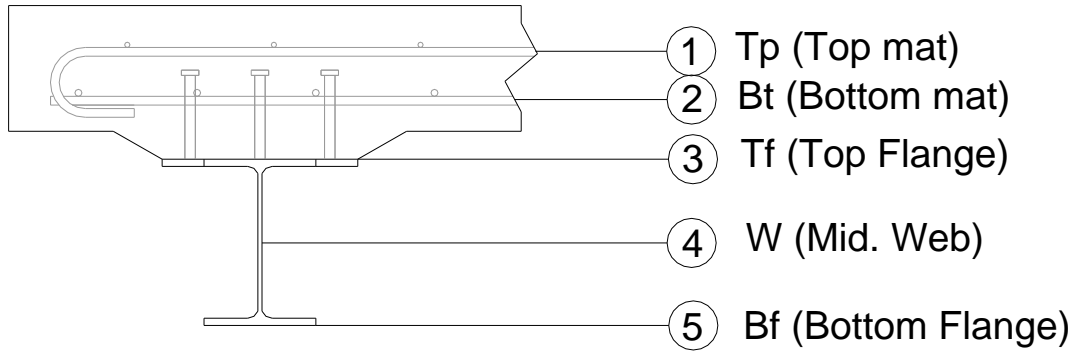


**Figure 39.** Depth locations for instrumentation

#### 4.5 Test Unit Construction and Casting

The construction process of the laboratory test units is described in the following sections. Please refer to the appendix for detailed photographs of the construction process. Due to space constraints, two test units were constructed and tested the same time at the lab. A local fabricator assembled the steel girder/diaphragm assemblies and attached the shear studs. The test unit steel frames were then brought into the lab and set on the supports, as shown below in Figure 40 and Figure 41.



**Figure 40.** Test Unit Steel Frame Assemblies (Test units 1, 2, and 4)



**Figure 41.** Test Unit 3 Steel Frame Assembly

#### ***4.5.1 Formwork***

Standard stay-in-place metal bridge deck forms were used in between the steel beams, and were spot-welded in place on the top flange of the beams. The corrugations of the forms were filled with Styrofoam inserts, which is typical for MDOT bridges. The metal form installation is shown below in Figure 42 to Figure 44.





**Figure 42.** SIP forms front view

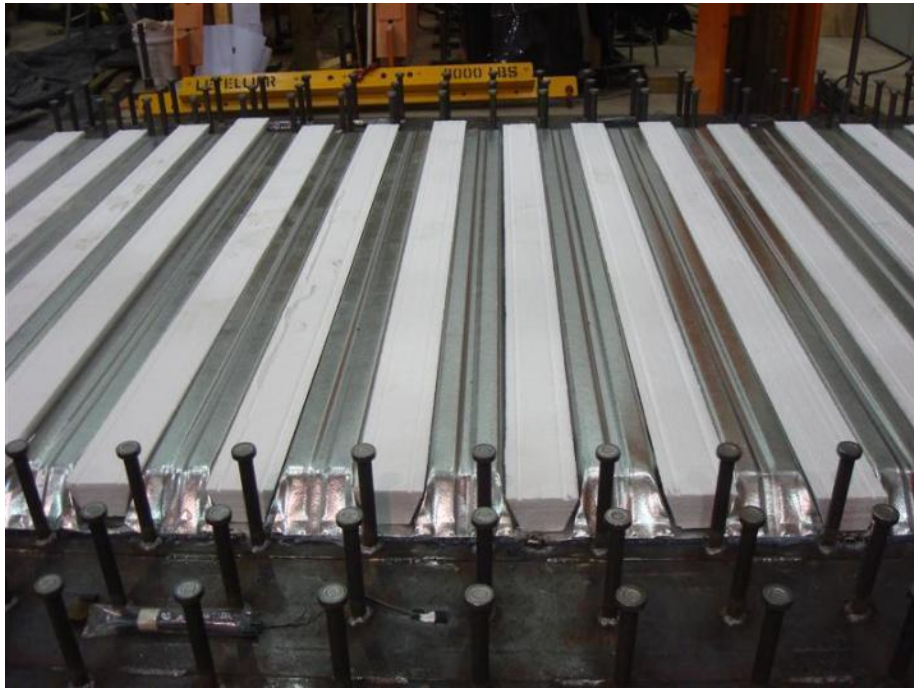


**Figure 43.** SIP forms Styrofoam fillers

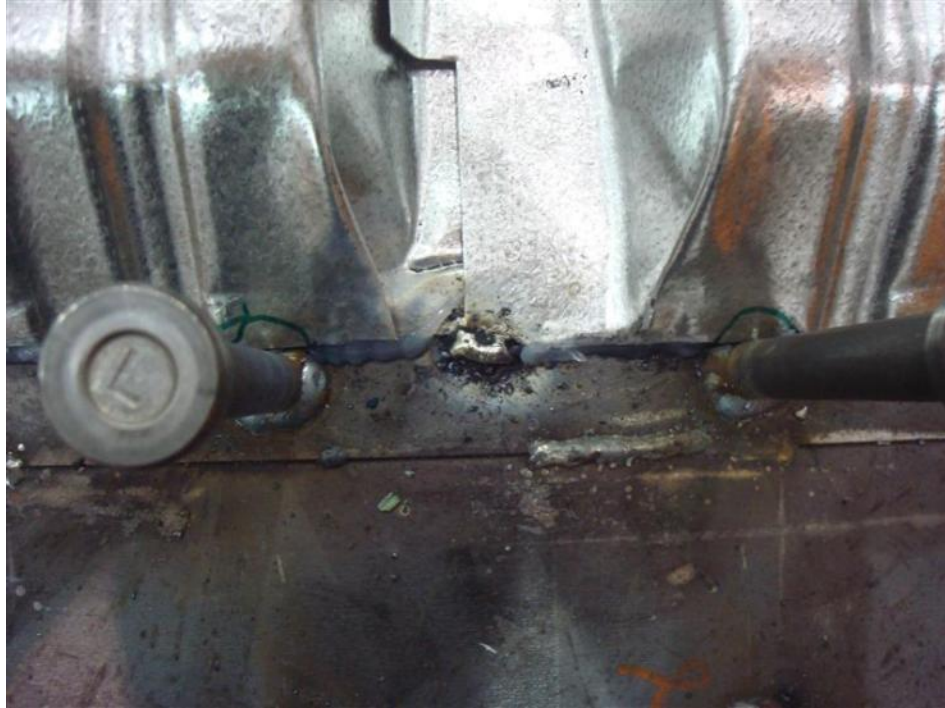


**Figure 44.** Spot-welding of the forms (typical)

Removable lumber forms were used for the edges of the test units, as well as the cantilevered sections. A schematic of the formwork for the cantilevered section is shown below in Figure 45.

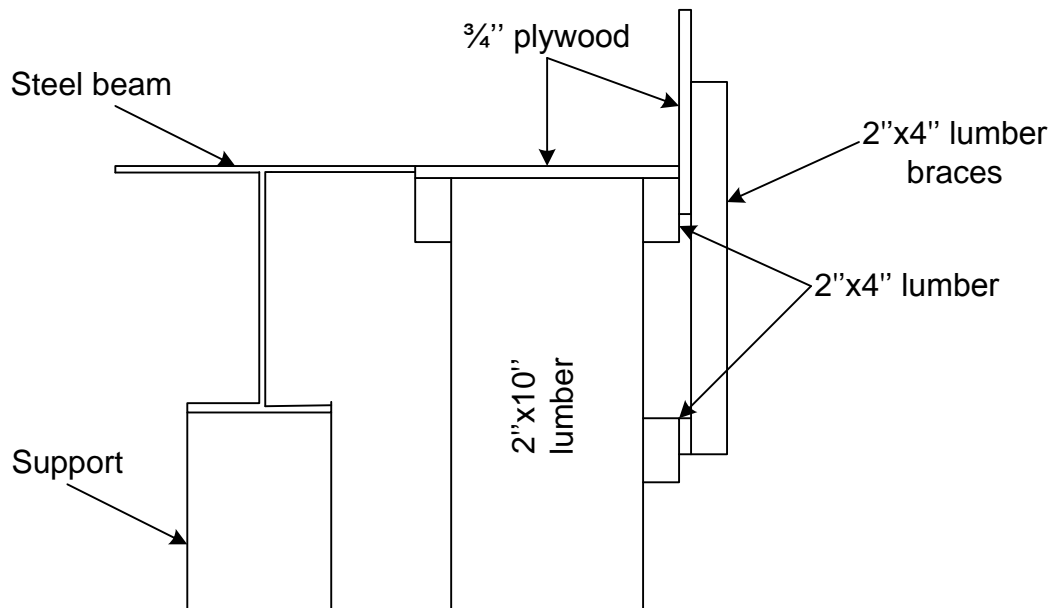


**Figure 45.** Schematic for the cantilevered section formwork (note these forms are removable)

Photos of the formwork construction are shown in Figure 46 to Figure 48.



**Figure 46.** Cantilever forms bottom section



**Figure 47.** Completed cantilever forms



**Figure 48.** Completed formwork (all lumber forms are removable)

#### ***4.5.2 Reinforcing Steel***

The mats of reinforcing steel were tied together with steel wire and then positioned in the test units. Each intersection of the bars was tied and secured, ensuring the bars did not move. Concrete spacers were cut to provide the required cover for both mats of steel, as shown in Figure 49 to Figure 51.



**Figure 49.** Concrete spacers for reinforcing steel (typical)

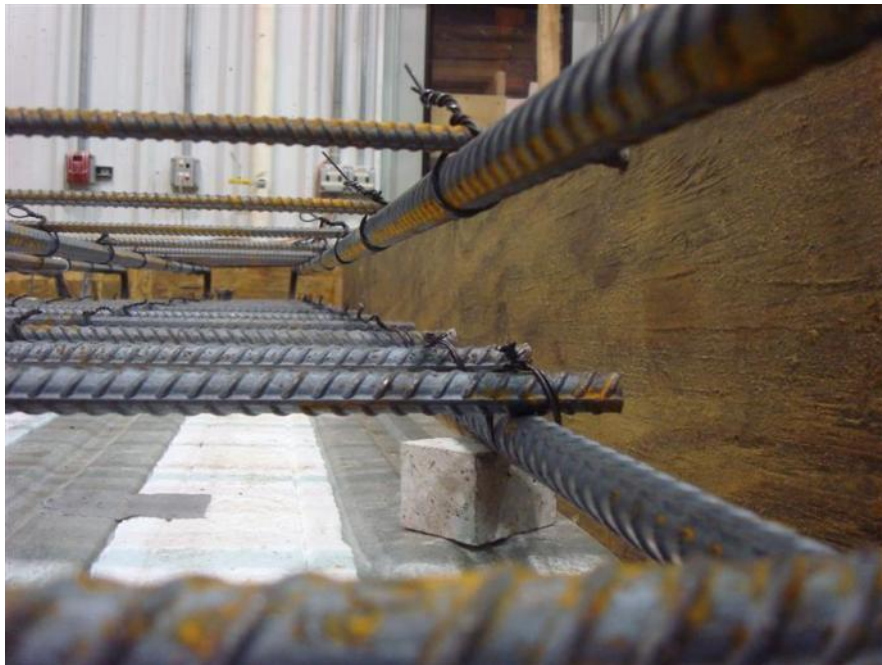


**Figure 50.** Spacing between reinforcing steel mats (typical)



**Figure 51.** Reinforcing steel side cover (typical)

#### ***4.5.3 Instrumentation Installation***

Strain gages were attached directly to the reinforcing steel and structural steel. The installation followed the procedure outlined below.

- The installation surface was ground smooth, and wiped with rubbing alcohol to ensure a clean surface.
- The strain gage was taped to the surface using cellophane tape
- The tape was pulled back from one end to expose the bottom of the strain gage. Then, M-Bond adhesive was applied to the bottom of the strain gage, which was pressed down for at least one minute.
- The cellophane tape was removed, and the lead wires were adjusted, ensuring they did not touch one another or the steel surface.
- The entire assembly was covered with M-Coat D acrylic paint.
- Electrical tape was placed over the strain gage to provide further protection.

This process is shown below in Figure 52.



a) Ground and cleaned surface



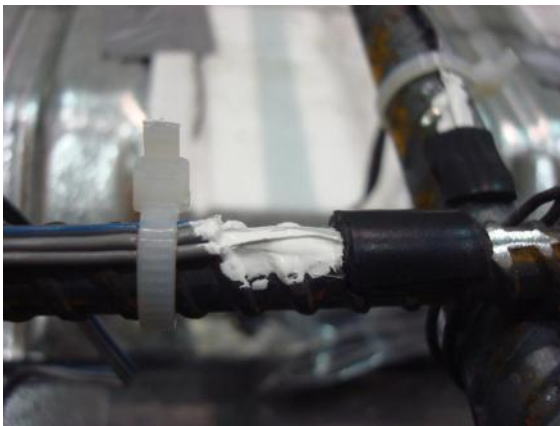
b) Strain gage attached to steel bar



c) Lead wires adjusted so they do not touch the steel



d) Assembly covered with M-Coat D



e) Electrical tape placed to protect strain gage

**Figure 52.** Example strain gage installation process (typical for all strain gages)

LVDT's were positioned directly underneath the bottom flanges of the beams to record midspan deflections. Wooden stands were constructed to hold the LVDT's in place. For the LVDT's in the middle of the test unit, a small steel rod with an aluminum plate was positioned into the deck. The LVDT's were positioned underneath the aluminum plate, so that deflections of the concrete test unit could be directly measured. This was done in case the concrete deck and formwork became separated. The LVDT placement is shown below in Figure 53 and Figure 54.



a) LVDT stand setup



b) Steel bonding rod

**Figure 53.** LVDT placed underneath mid-test unit



**Figure 54.** LVDT in place (mid-span of beam)



#### 4.5.4 Test unit Casting

##### 4.5.4.1 Concrete Mix Design

Two different types of concrete mixes were used in the test units. For the first three test units, the MDOT standard Grade D concrete mix was used, while a modified Grade D mix was used for the fourth test unit. Both mixes had a design compressive strength of 4,500 psi and maximum aggregate size of 1". The only differences between the two mixes were in the cement content and aggregate gradation. The modified mix had a 30% slag cement replacement and an optimized aggregate gradation. MDOT was interested in testing this mix, since it would theoretically perform better due to the lower cement content. The details for each mix are summarized below in Table 6 and Table 7.

**Table 6.** MDOT Grade D Concrete Mix Design

<b>Material</b>	<b>Quantity</b>
Portland Cement	658 lb/yd <sup>3</sup>
Fly Ash	None
Lafarge Slag	None
Sand (2NS)	1195 lb/yd <sup>3</sup>
Gravel (26A)	None
Gravel (6AA)	1740 lb/yd <sup>3</sup>
Water	270 lb/yd <sup>3</sup>
W/C ratio	0.41
Air content (%)	6.5
Slump (in.)	4.5
Fine agg./total agg percentage	0.41

**Table 7.** MDOT Modified Grade D Slag Replacement Mix Design

<b>Material</b>	<b>Quantity</b>
Portland Cement	461 lb/yd <sup>3</sup>
Fly Ash	None
Lafarge Slag	197 lb/yd <sup>3</sup>
Sand (2NS)	1088 lb/yd <sup>3</sup>
Gravel (26A)	508 lb/yd <sup>3</sup>
Gravel (6AA)	1306 lb/yd <sup>3</sup>
Water	270 lb/yd <sup>3</sup>
W/C ratio	0.41
Air content (%)	6.5
Slump (in.)	5.25
FA./TA percentage	0.55

#### 4.5.4.2 Concrete casting

The first two test units were cast at the same time to ensure they experienced the same shrinkage characteristics. The concrete was obtained from Shafer's, a local redi-mix company. The concrete was mechanically vibrated during casting to ensure proper consolidation. The test unit surfaces were then finished with a bull float. The first two test units were cast in the morning of February 10, 2012. The third test unit was cast in the morning of March 23, 2012, and the fourth test unit was cast in the morning of March 26, 2012. Casting took about 30-45 minutes for each test unit. The casting and finishing work is shown below in Figure 55 and Figure 56.

Fresh concrete properties (air and slump) were tested for each concrete mix using standard test methods. The results are summarized in Table 8.

**Table 8.** Concrete Fresh Property Characteristics

<b>Mix</b>	<b>Slump (in)</b>	<b>Air content (%)</b>
Test unit 1 and 2 (Grade D)	4.5	5.5
Test unit 3 (Grade D)	4.25	6.5
Test unit 4 (Grade D-Mod.)	4.25	6.5

After the concrete initial set, the test unit surfaces were covered with wet burlap and plastic to provide a seven-day wet cure in accordance with MDOT standard specifications [25]. This was done four hours after the concrete surface was finished. The burlap was examined daily to ensure it was kept saturated, and was re-wetted when necessary. All wooden forms were removed after three days. A typical timeline of events from casting to the end of curing is shown below in Figure 57. The times listed are approximate and varied slightly for each test unit.



**Figure 55.** Placing and vibrating the concrete (test unit 3)



**Figure 56.** Bull floating the concrete surface (test unit 3)

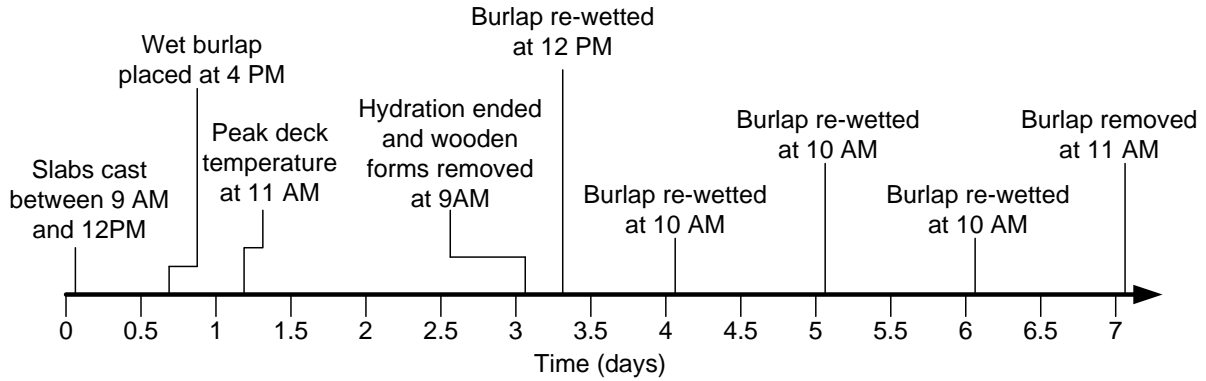


**Figure 57.** Timeline of events between casting to the end of moist curing (typical)

#### 4.5.5 Completed test units

After the seven-day wet cure, the burlap and plastic was removed and the top and outside surfaces of the test units were exposed to drying shrinkage. The completed test units are shown below in Figure 58 to Figure 61.



**Figure 58.** Completed test unit overall view (test unit 4)



**Figure 59.** Completed test unit cantilever section (test unit 3)



**Figure 60.** Close-up of completed test unit top surface (test unit 4)



**Figure 61.** Test unit cross-section (test unit 4)

#### ***4.5.6 Concrete Shrinkage Ring Tests***

Concrete rings were cast for each mix in order to determine the shrinkage characteristics and cracking potential at the material level. For the first two test units, three rings were moist-cured for seven days, while one ring was moist-cured for 24 hours. For the second set of test units, two rings were cast using the standard Grade D mix (test unit 3), and two rings were cast using the modified Grade D mix (test unit 4). These four rings were moist-cured for seven days. The rings were placed in a separate room where a constant temperature and humidity was maintained. After the moist-cure period was completed, the top surfaces of the rings were sealed with silicone, thus only allowing shrinkage from the outside surface. An overall view of the completed rings is shown below.



**Figure 62.** Overall view of shrinkage rings

## 4.6 Results

The data obtained from the laboratory investigation was used to both calibrate the material and shrinkage simulation of the finite element computer models and analyze the effect of bridge design parameters at the sub-assembly level. The experimental data was used to verify the computer modeling approach, and validate its use for full bridge models at the global level.

### 4.6.1 Data Acquisition

Data was collected on two *National Instruments SCXI-1001* data acquisition systems. Data was collected continuously, starting within two hours after the top surface of the concrete was finished. Readings were taken once every minute during the duration of the test. The system was tested prior to casting to ensure all instrumentation and connections were properly working. Since early-age behavior was of interest, the tests were run for a period of three weeks, including the one week of wet curing.

#### **4.6.2 Concrete Material Testing**

Standard compressive and split tensile strength tests were performed on 4''x8'' concrete cylinders at ages of 3, 7, 14, 21, and 28 days. The cylinders were de-molded three days after casting and placed in a curing room with a constant temperature of 72°F and constant relative humidity of 80%. The cylinder strength testing is shown below in Figure 63 and Figure 64.



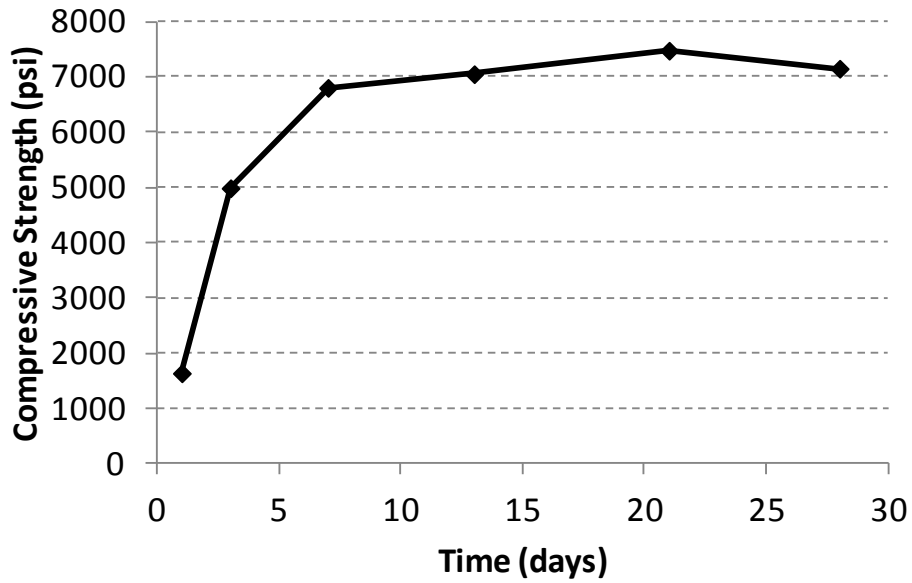
**Figure 63.** Concrete split tensile strength testing



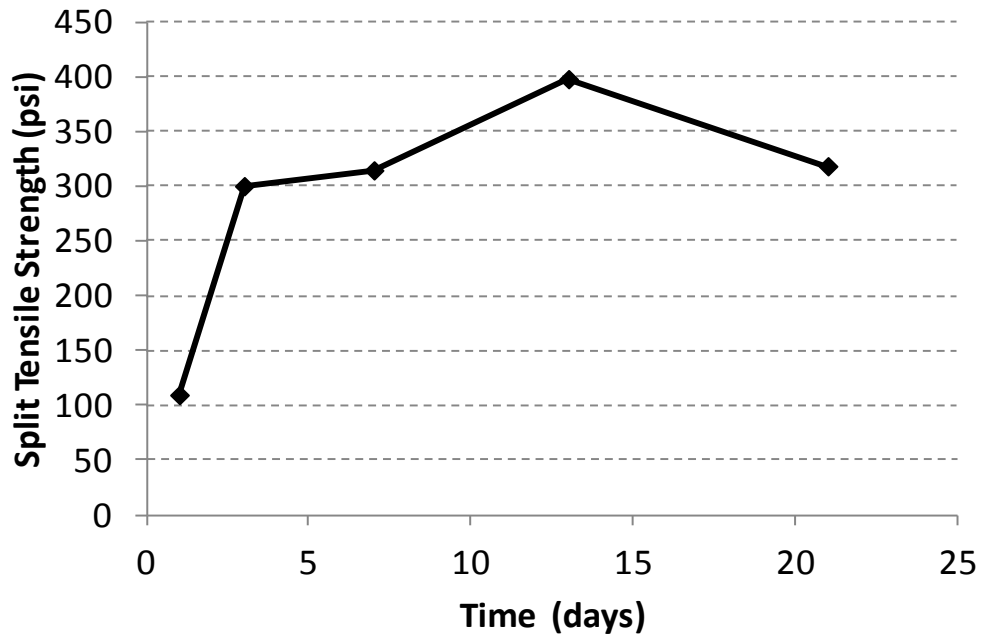
**Figure 64.** Concrete compressive strength testing



The compressive and split tensile strength gain curves for each mix are shown below in Figure 65 to Figure 67.

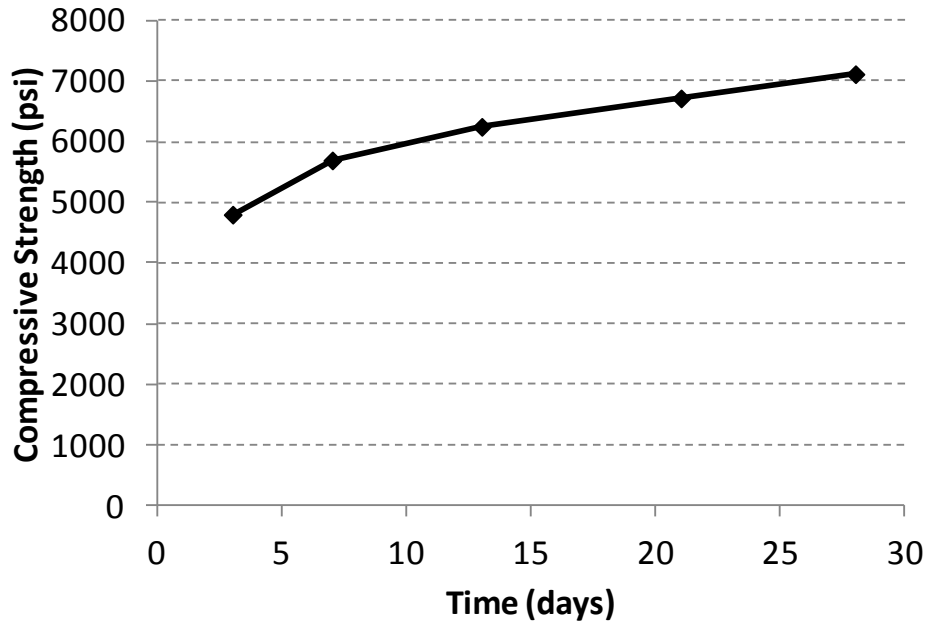


a) Compressive

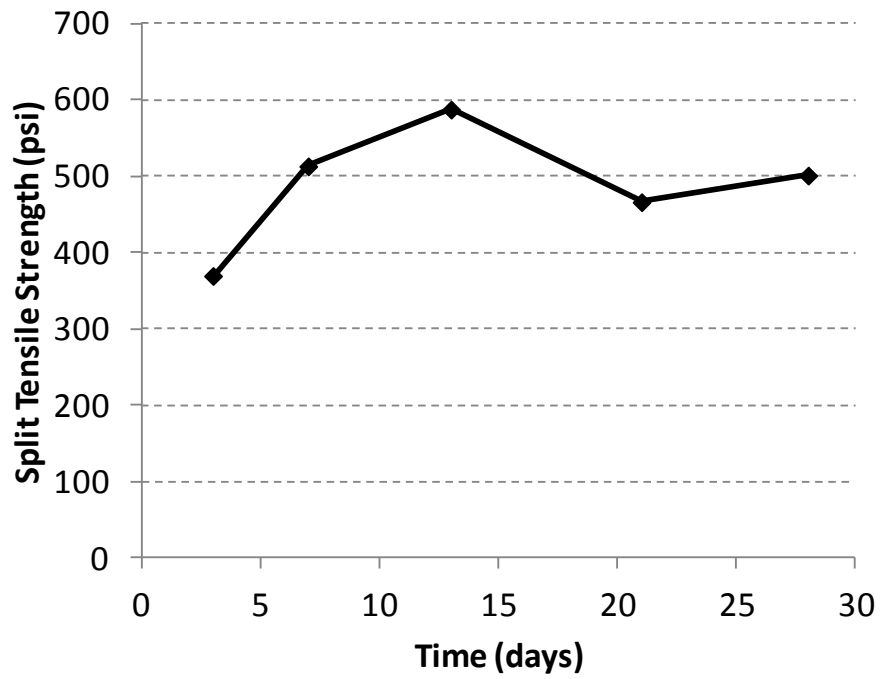


b) Split Tensile

**Figure 65.** Test units 1 and 2 (MDOT Grade D mix)

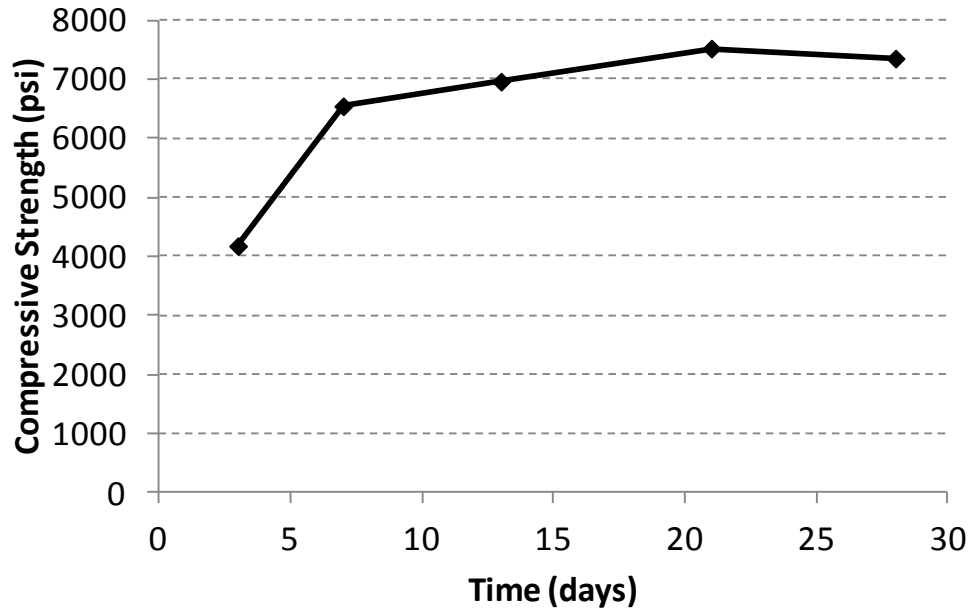


a) Compressive

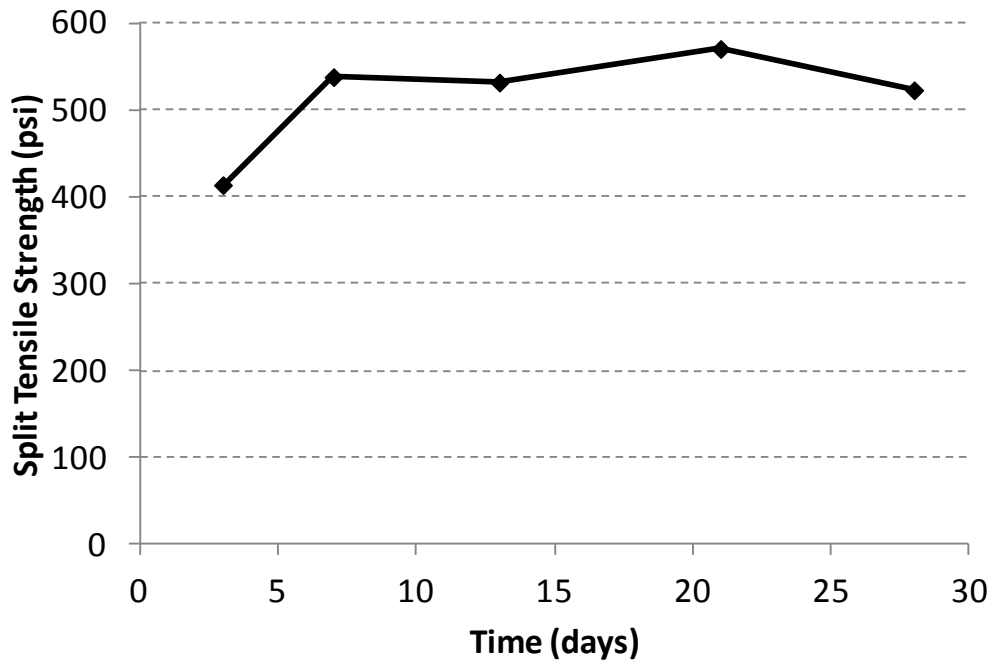


b) Split Tensile

**Figure 66.** Test unit 3 (MDOT Grade D mix)



a) Compressive



b) Split Tensile

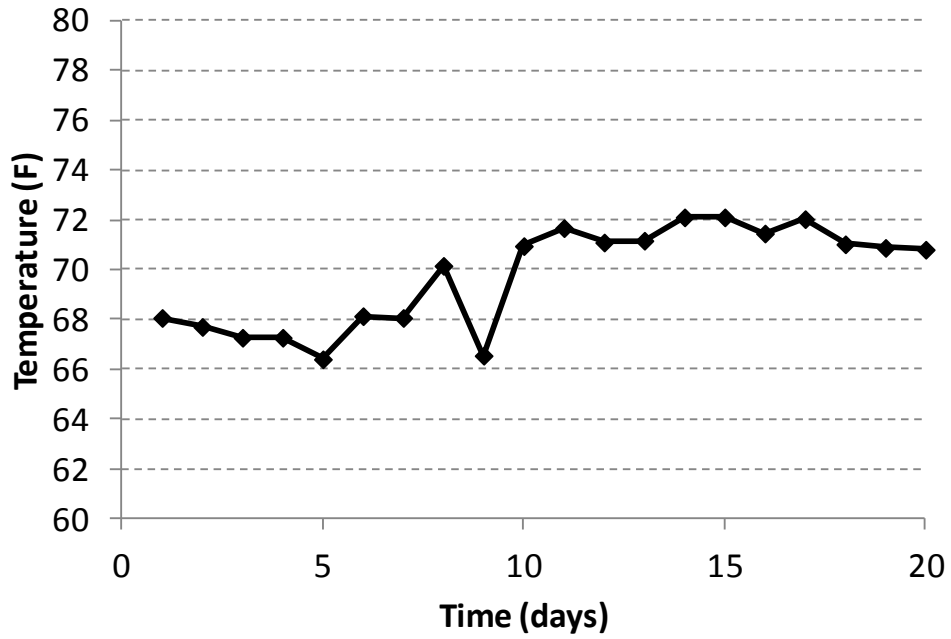
**Figure 67.** Test unit 4 (Modified MDOT Grade D mix)

As shown, the compressive and split tensile strength values were fairly consistent for all of the concrete mixes. The peak compressive strength was around 7,000 psi for all mixes, which was 2,500 psi higher than the design compressive strength. The modified Grade D mix had similar material strength characteristics to the standard mix, so the mix design modifications did not have an effect on the concrete strength. The concrete strength data was used further to develop the concrete inelastic material properties in the computational evaluation.

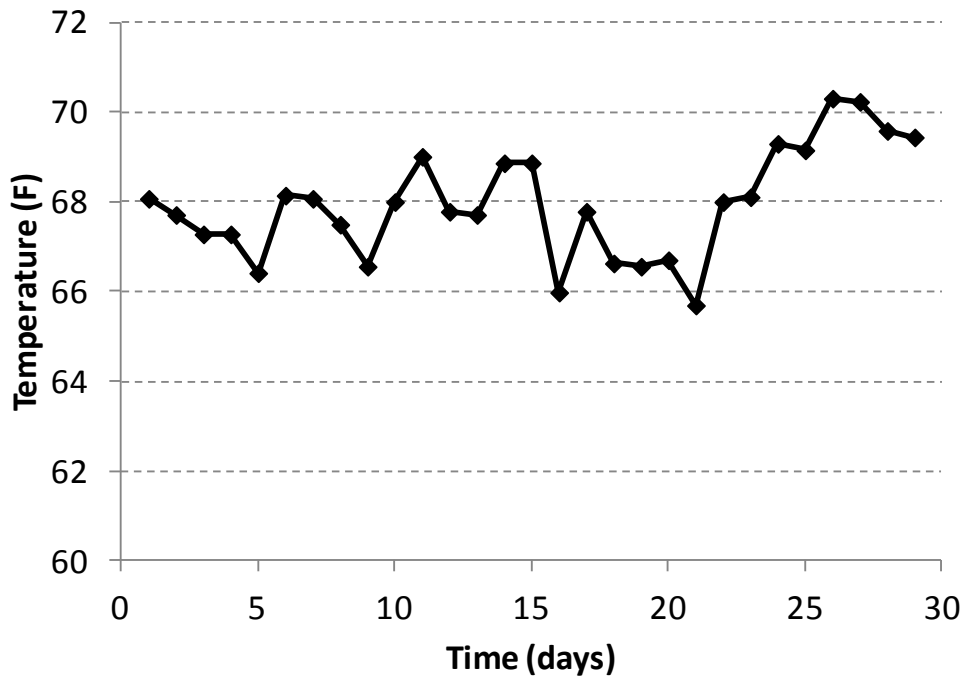
#### ***4.6.3 Ambient temperature and relative humidity***

The ambient temperature and relative humidity was monitored daily in the main lab and in the ring test room. The data was used in developing the shrinkage loading characteristics in the computational evaluation. The temperatures and relative humidity for the first set of test units are shown below in Figure 68 and Figure 69. The temperatures and relative humidity for the second set of test units are shown in Figure 70 and Figure 71. Note that 100% relative humidity was assumed during the time of wet curing.

As shown, the temperature and relative humidity remained fairly consistent in both the main lab and the ring test room. A humidifier was placed in the ring test room to try to maintain a consistent humidity of 50%. However, due to the heaters running and the size of the room, this was difficult to achieve. The temperature and humidity data were used further to calculate the required loads for the computational evaluation.

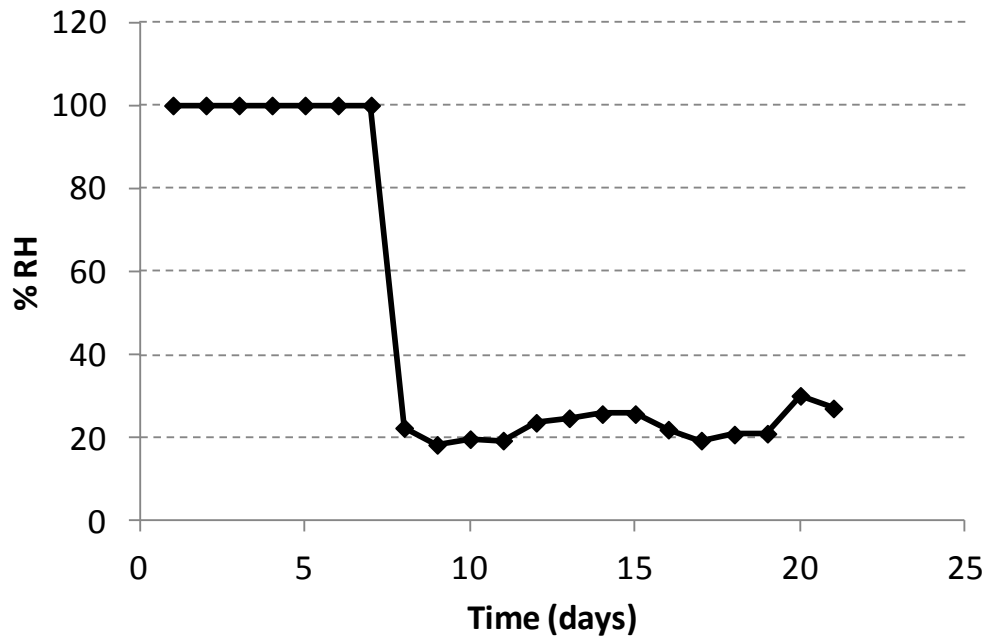


a) Main Lab

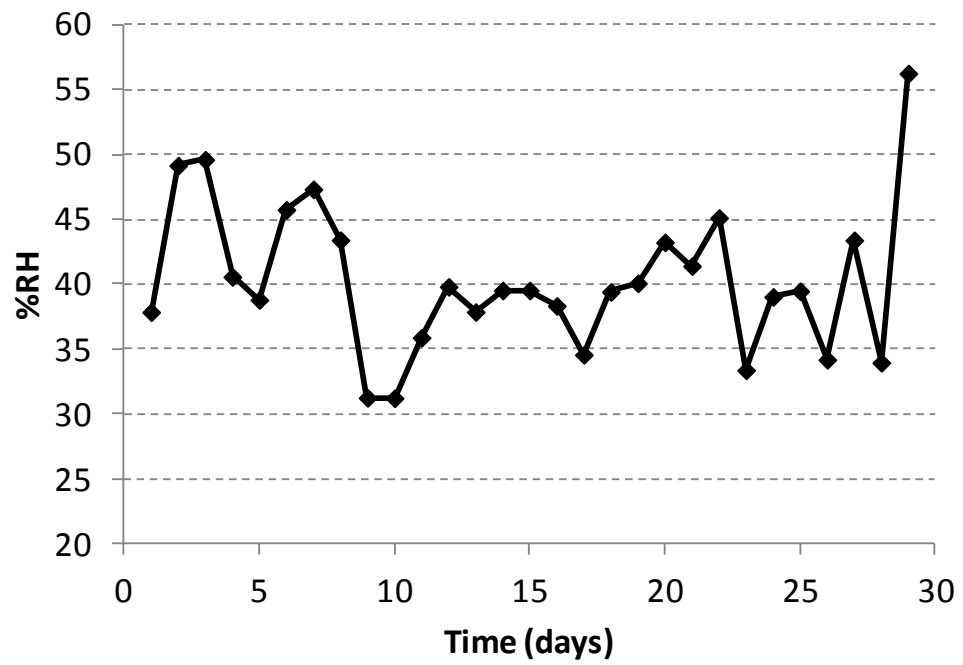


b) Ring Test Room

**Figure 68.** Ambient temperature values, first set of tests

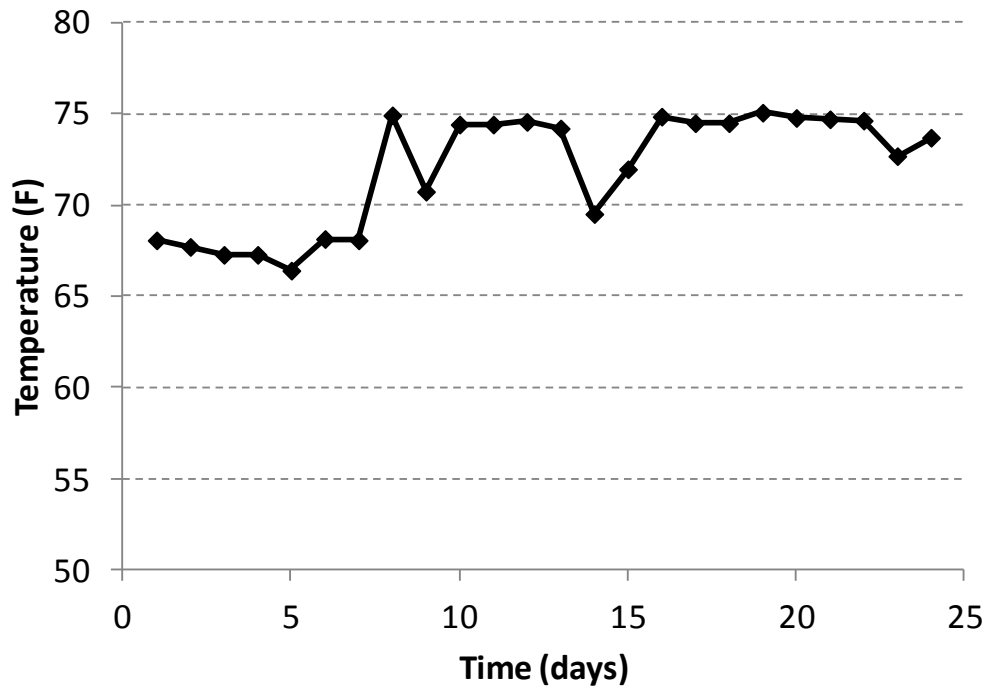


a) Main Lab

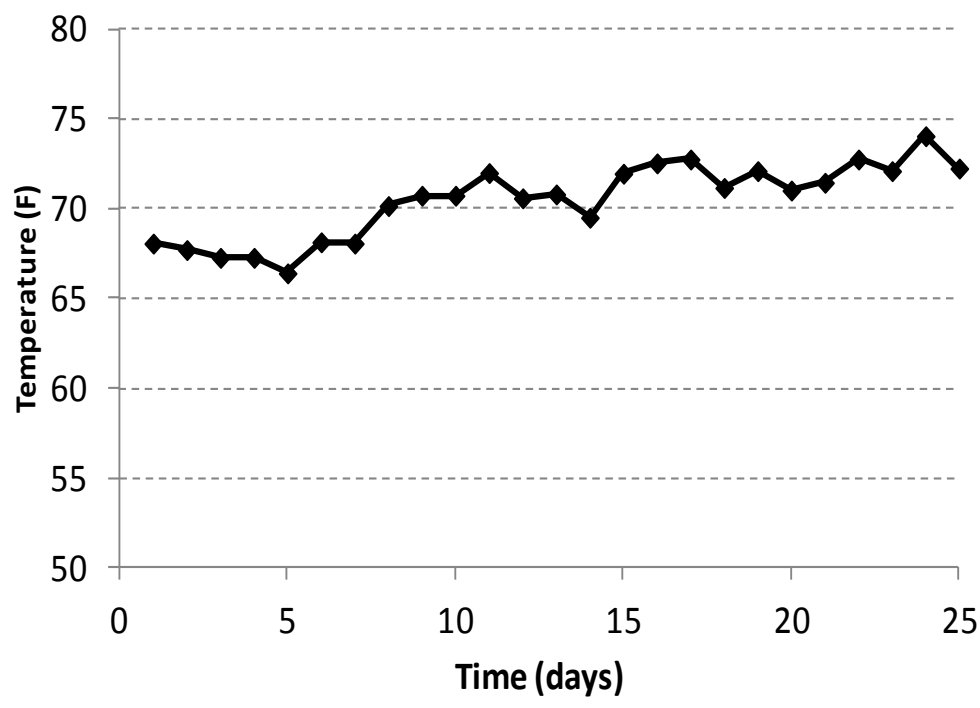


b) Ring Test Room

**Figure 69.** Relative humidity percentage, first set of tests

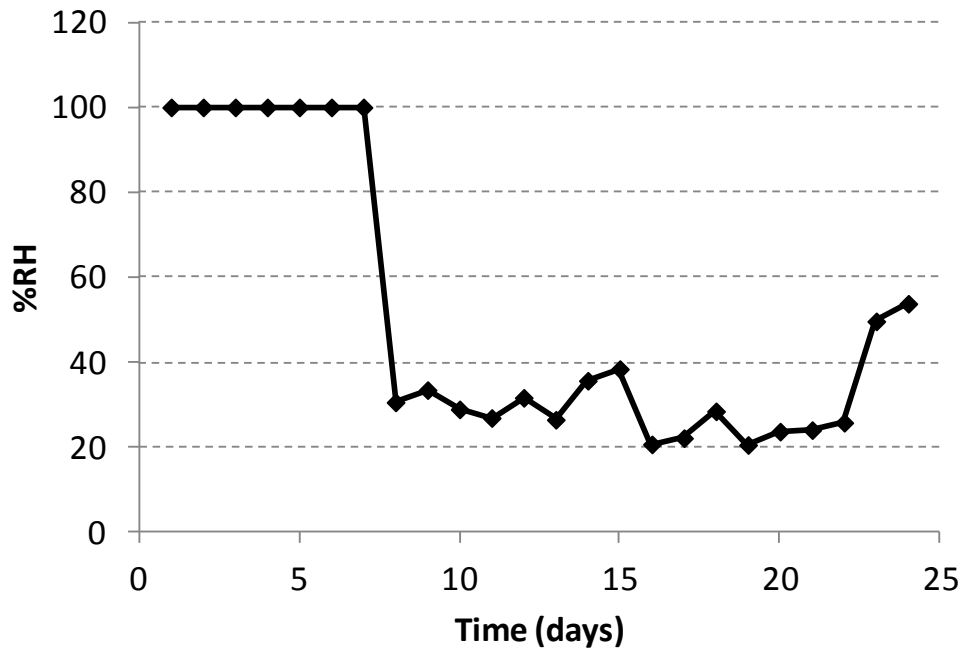


a) Main Lab

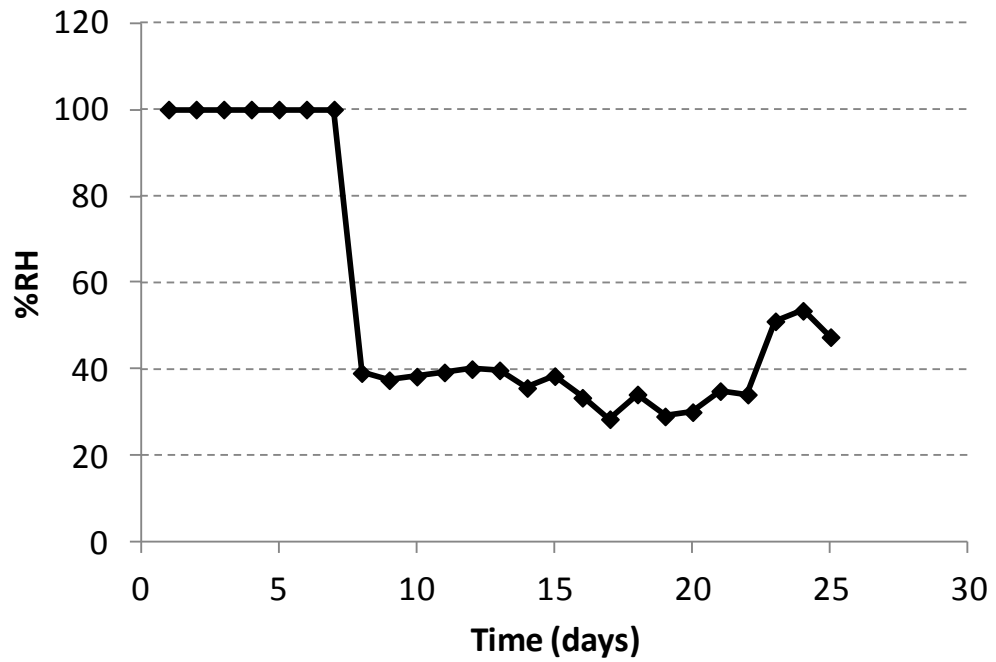


b) Ring Test Room

**Figure 70.** Ambient temperature values, second set of tests



a) Main Lab



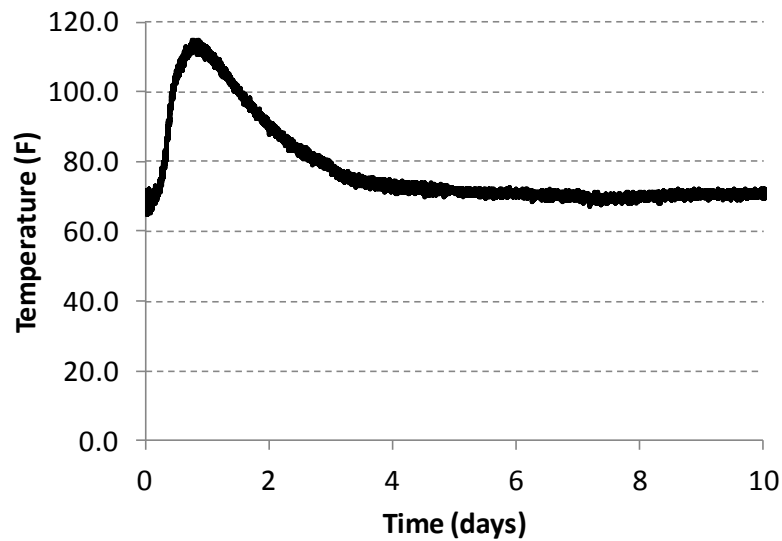
b) Ring Test Room

**Figure 71.** Relative humidity percentage, second set of tests

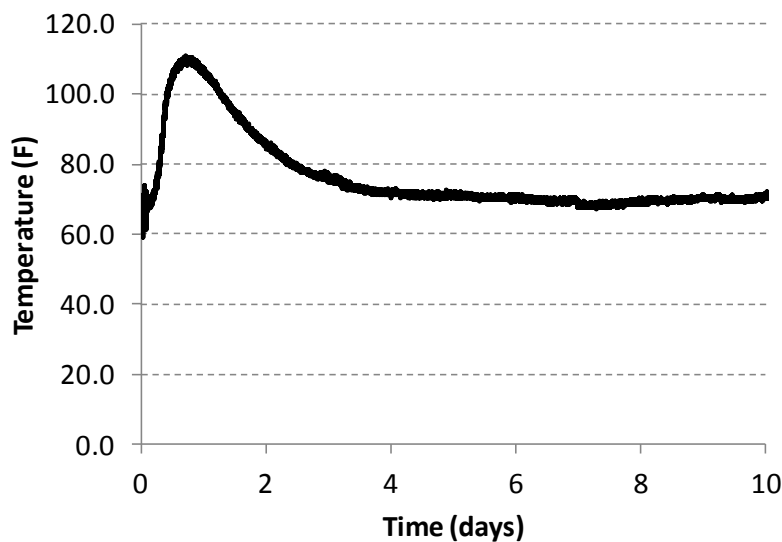


#### 4.6.4 Thermocouples

Thermocouples were positioned at the top and bottom mats of reinforcing steel, the beam top flange, and the beam bottom flange. This allowed temperature profiles through the depth of the test units to be measured. An ambient thermocouple was also positioned next to the test units to monitor the temperature variation in the lab. The temperature in the deck for test units 1 and 2 are shown below in Figure 72, while the lab ambient temperature is shown in Figure 73.



a) Test Unit 1



b) Test Unit 2

**Figure 72.** Concrete deck temperatures at the bottom mat of reinforcing steel (test units 1 and 2)

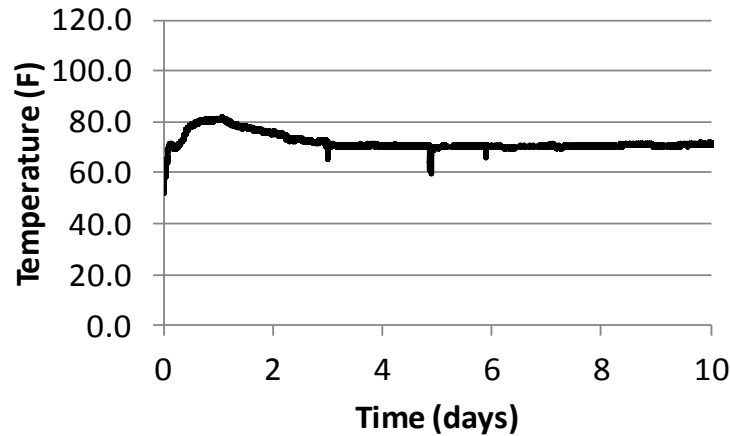


**Figure 73.** Lab ambient temperature, first set of test units

The concrete temperatures of the two test units remained consistent. This was expected, since the two test units contained the same concrete mix. The maximum deck temperature was reached about 24 hours after casting, and the hydration period ended at about three days. The lab ambient temperature remained fairly consistent for the duration of the test. The drops shown were times when the door was opened and the lab was allowed to cool. The initial increase in temperature was due to the thermocouple being placed underneath the plastic which was covering the two test units. After the hydration period, the concrete temperature was about the same as the ambient temperature of the lab.

The temperature gradient through the depth of the test unit is shown below in Figure 74. As shown, the thermocouples at the top and bottom mats of steel were very similar, the beam top flange was slightly cooler, and the beam bottom flange was very close to the ambient temperature.

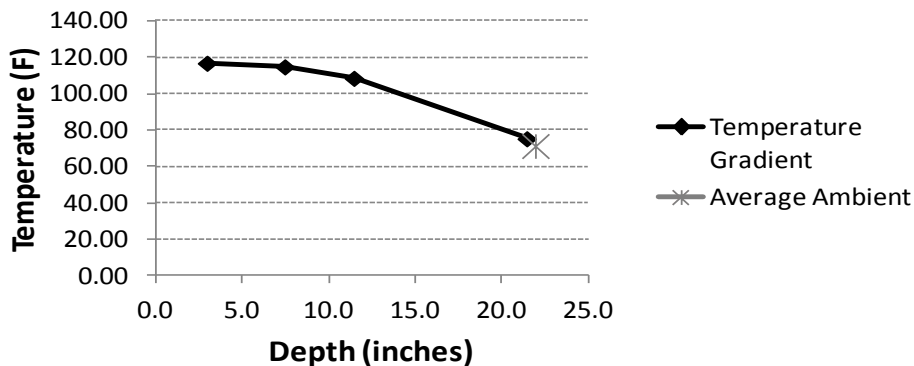
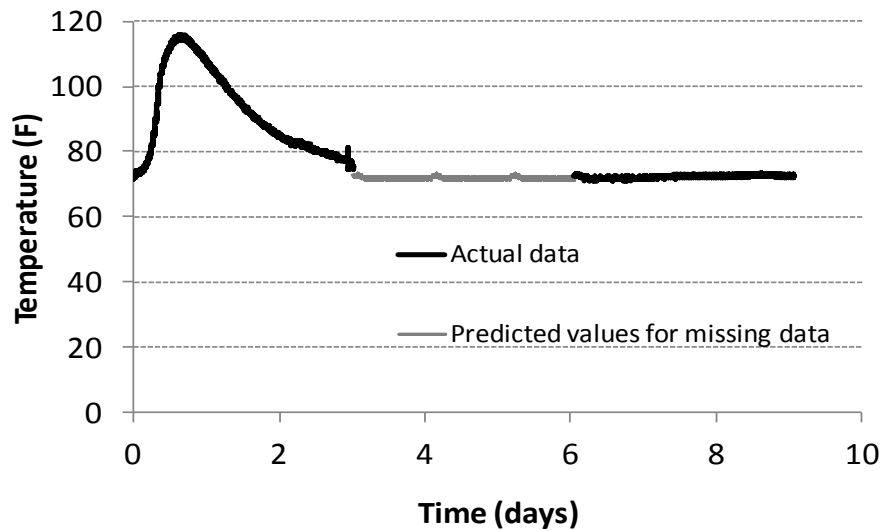
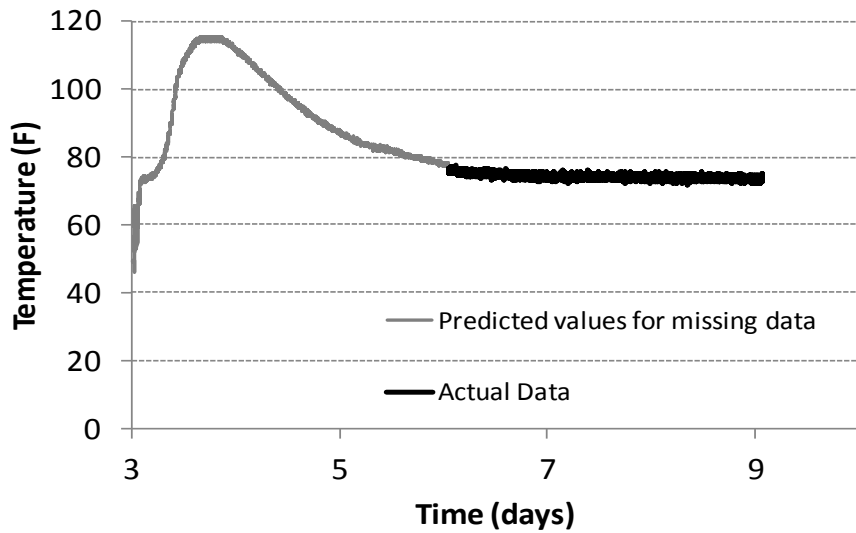


**Figure 74.** Maximum temperature gradient through the depth of the test unit (test units 1 and 2)

The temperature in the deck for test units 3 and 4 are shown in Figure 75, while the lab ambient temperature is shown in Figure 76. During the test, the data acquisition system was accidentally unplugged, so some of the values shown are predictions for the missing data.



a) Test Unit 3



b) Test Unit 4

**Figure 75.** Concrete deck temperatures at the bottom mat of reinforcing steel (test units 3 and 4)

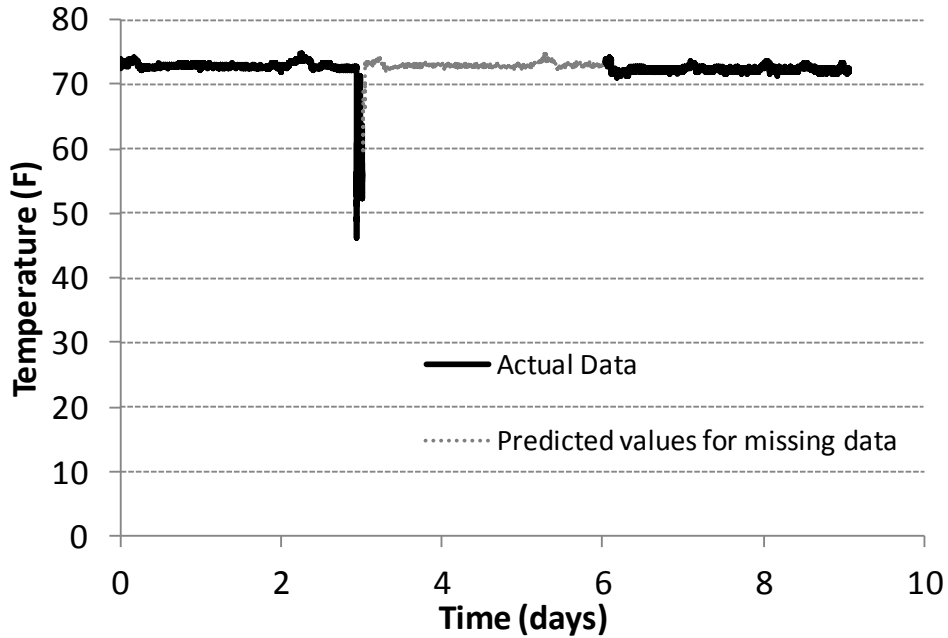


**Figure 76.** Lab ambient temperature, second set of test units

The concrete temperature maximum range for the two mixes was about the same, while the hydration period for the slag mix (test unit 4) was slightly longer and the concrete remained at the peak temperature longer. The initial set time in test unit 4 also took longer than in the first three test units. The concrete temperature distribution was very similar between test unit 3 and the first two test units, since they were made with the same concrete mix. The lab ambient temperature remained fairly consistent for the duration of the test, except during the casting of test unit 4. The large temperature drop shown is when the door to the lab was left open during the casting of test unit 4, allowing the lab to cool. After the hydration period, the concrete temperature was about the same as the ambient temperature of the lab. The temperature gradient through the depth of the test unit is shown below in Figure 77.

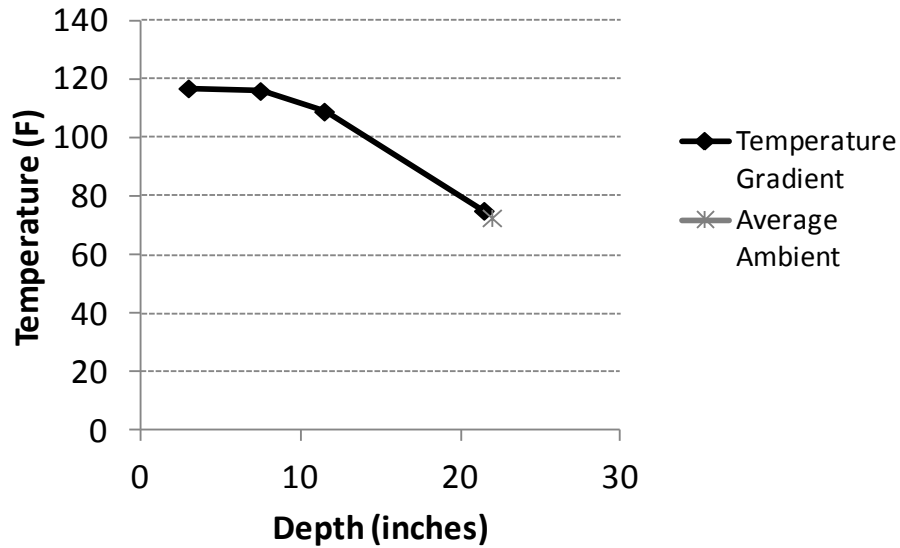


**Figure 77.** Maximum temperature gradient through the depth of the test unit (test units 3 and 4)

The maximum temperature distribution through the depth of the test units was very similar to the distribution for the first two test units. The concrete temperature at the top and bottom mats of steel were similar, followed by a slight decrease at the top flange, and the bottom flange was consistent with the average ambient temperature. Overall, the temperature distribution is consistent with what was expected.

#### 4.6.5 LVDT's

The vertical displacements for all four test units are shown below in Figure 78 to Figure 80. Note that negative values indicate downward movement, while positive values indicate upward movement. Also note that the LVDT's were not positioned until after the concrete initial set, so they do not show an initial downward deflection that would have occurred due to the concrete dead load.

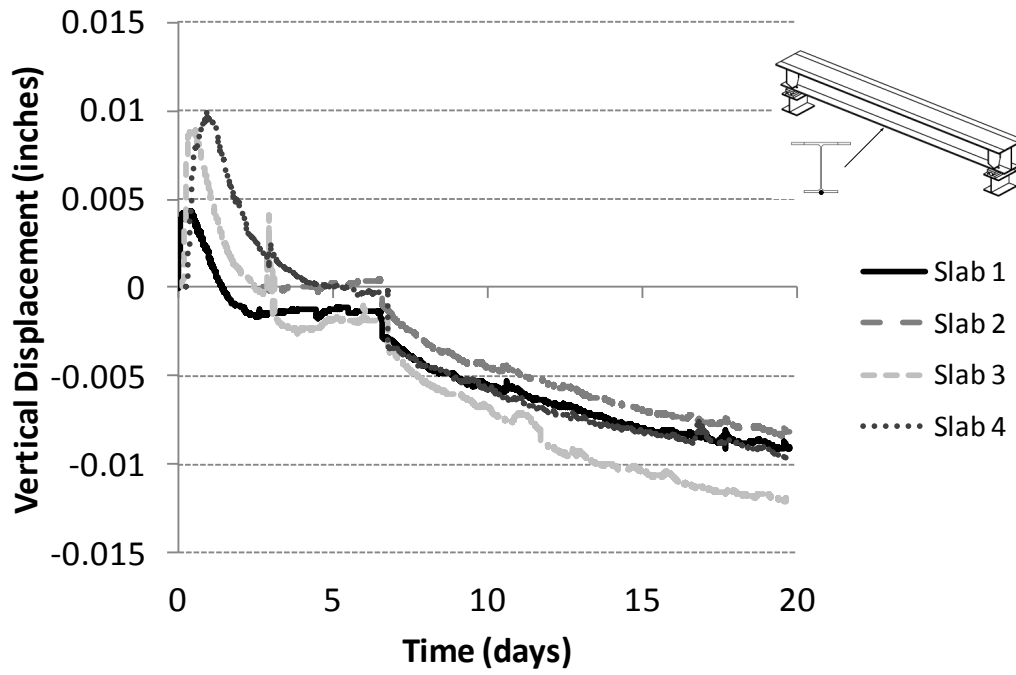


**Figure 78.** Girder 1 mid-span displacement (L-G1-1/2)

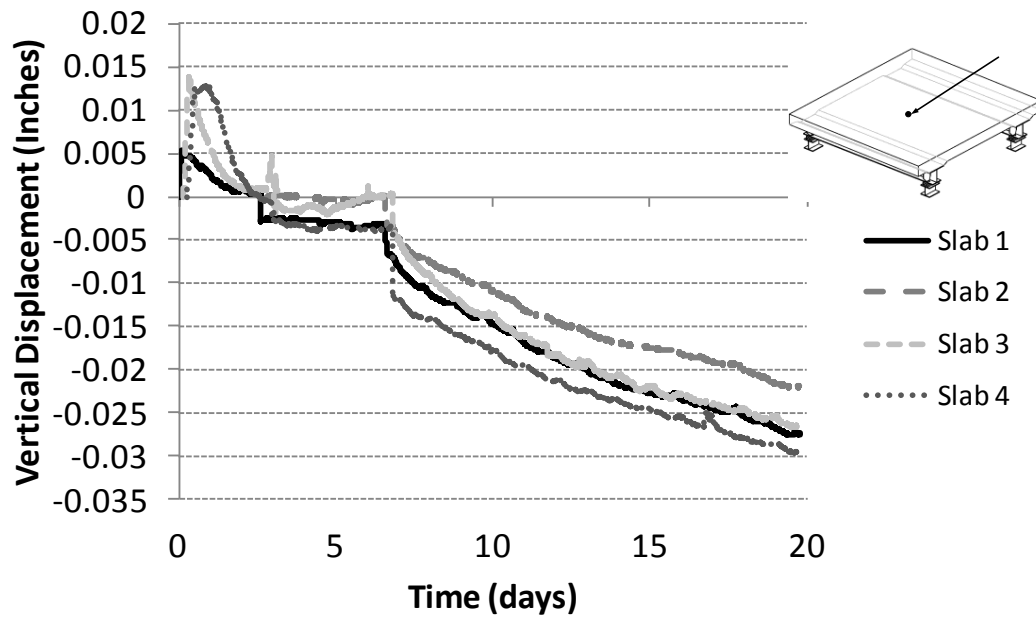


**Figure 79.** Mid-test unit displacement (L-1/2-1/2)

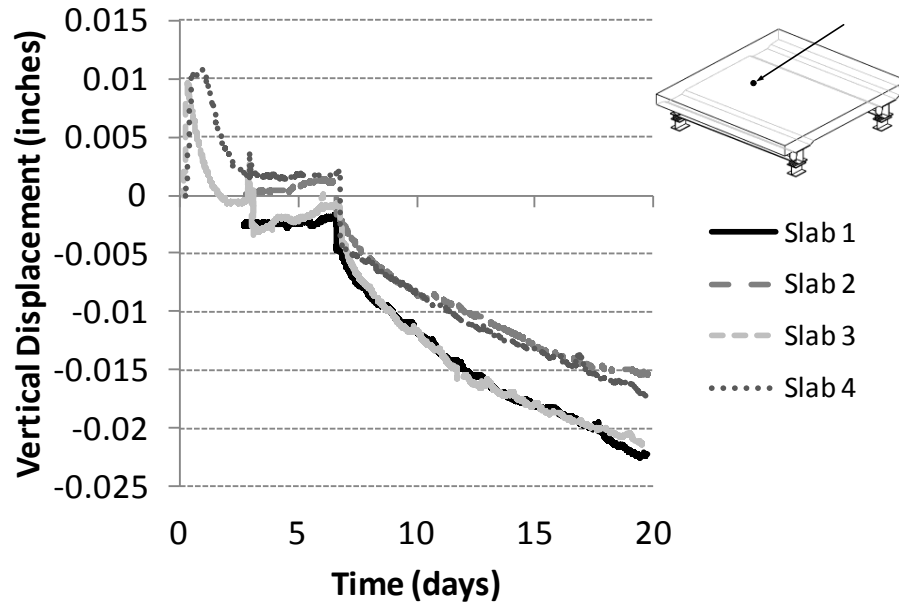


**Figure 80.** Mid-test unit quarter-span displacement (L-1/2-3/4)

At each LVDT location, the test units underwent the same general behavior. The upward displacement corresponds well with the concrete temperature values. The concrete expanded due to the temperature rise during hydration, causing an upward displacement. There was then a slight drop in the displacement due to the removal of the wooden forms. The displacements then remained level while the concrete surface remained covered during the remainder of the seven-day wet cure. When the burlap was removed, there was a sudden drop in the displacements due to immediate drying of the concrete. The displacements then decreased steadily due to drying shrinkage.

#### 4.6.6 Strain Gages

There were several errors in the strain gage data for the first two test units. Since the data was taken continuously and the system was not re-set during the test, the system became saturated and skewed the data points after the first few days. For test units 3 and 4, the system was stopped and re-set daily, and the strain data turned out much better overall. Selected strain plots for test units 3 and 4 are presented below. Please refer to the appendix for the full data output. Note that in the following plots, compressive strains are negative and tensile strains are positive. Recall that the instrumentation naming scheme is presented in Figure 38 and Figure 39.

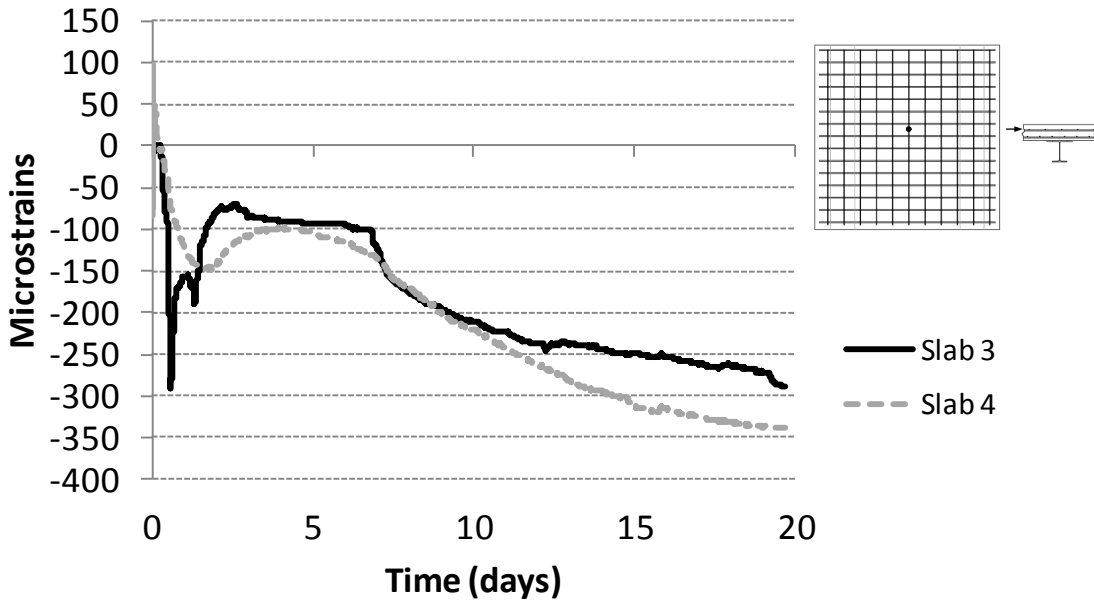


**Figure 81.** Top mat longitudinal rebar strains, middle of test unit (S-Tp-1/2-1/2-L)

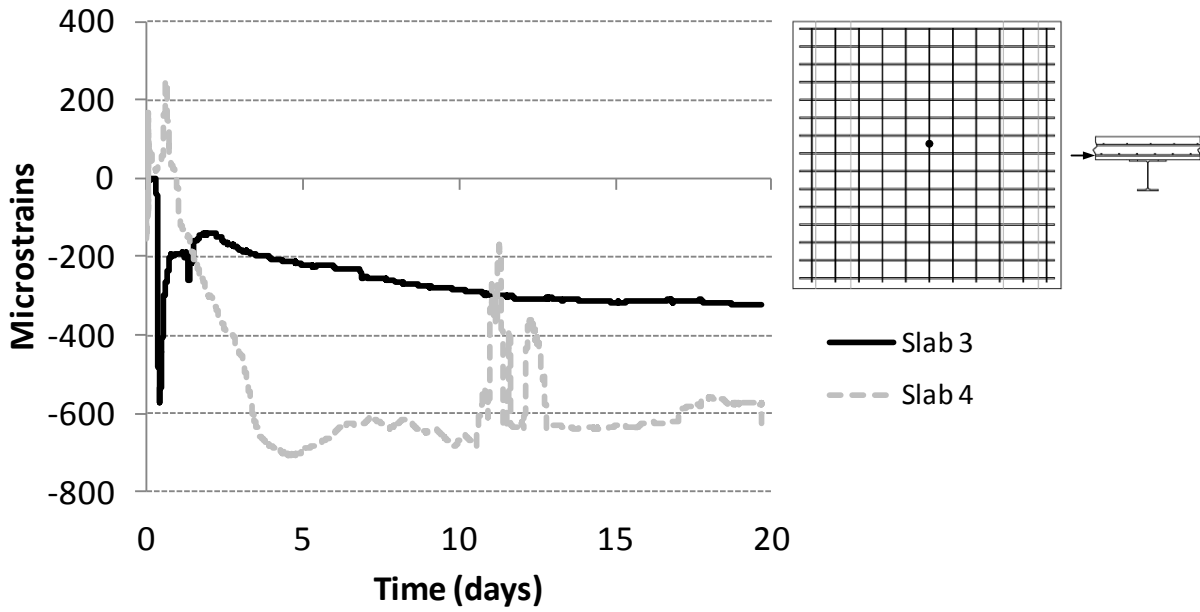


**Figure 82.** Bottom mat longitudinal rebar strains, middle of test unit (S-Bt-1/2-1/2-L)



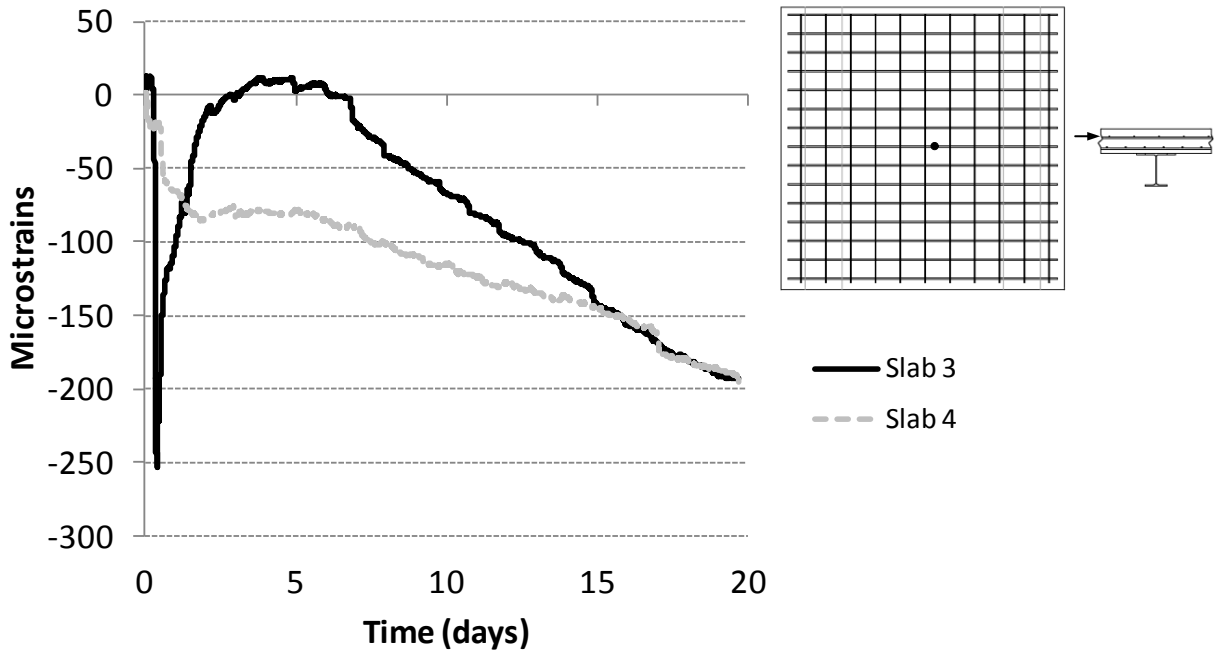


**Figure 83.** Top mat transverse rebar strains, middle of test unit (S-Tp-1/2-1/2-T)

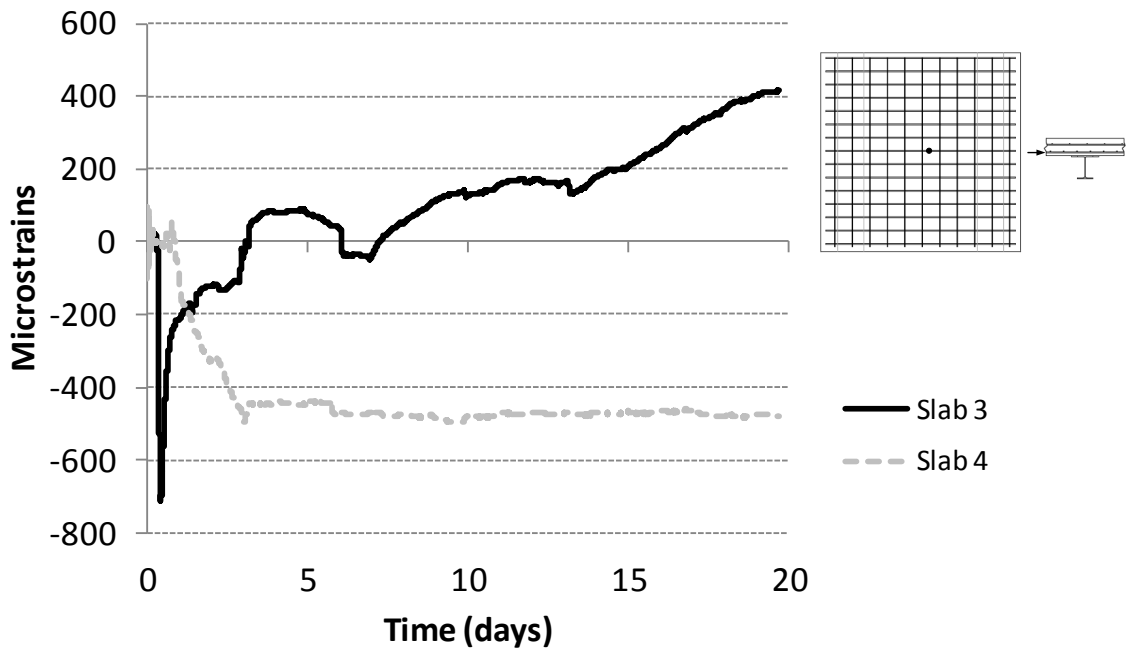


**Figure 84.** Bottom mat transverse rebar strains, middle of test unit (S-Bt-1/2-1/2-T)

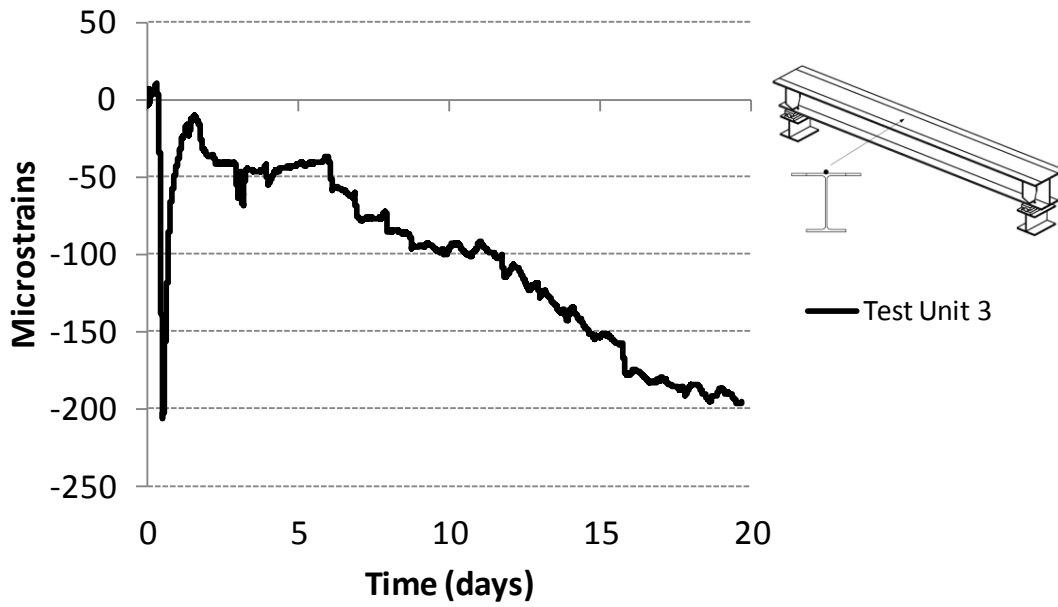


**Figure 85.** Beam top flange, mid-span longitudinal strains (S-G1-Tf-M-G1-1/2-L)

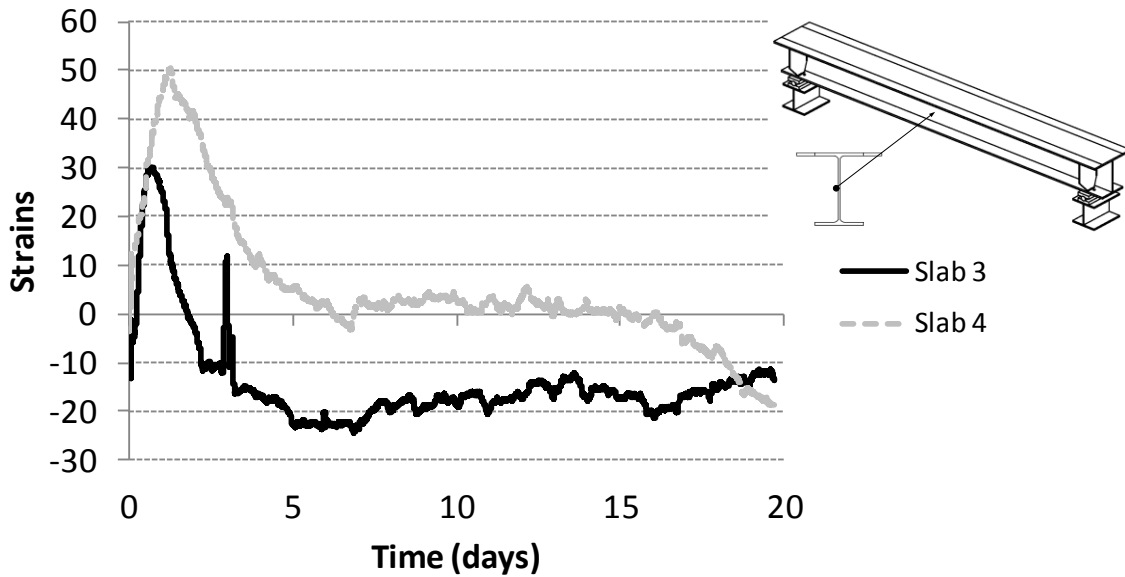


**Figure 86.** Beam mid-web longitudinal strains (S-G1-W-O-G1-1/2-L)

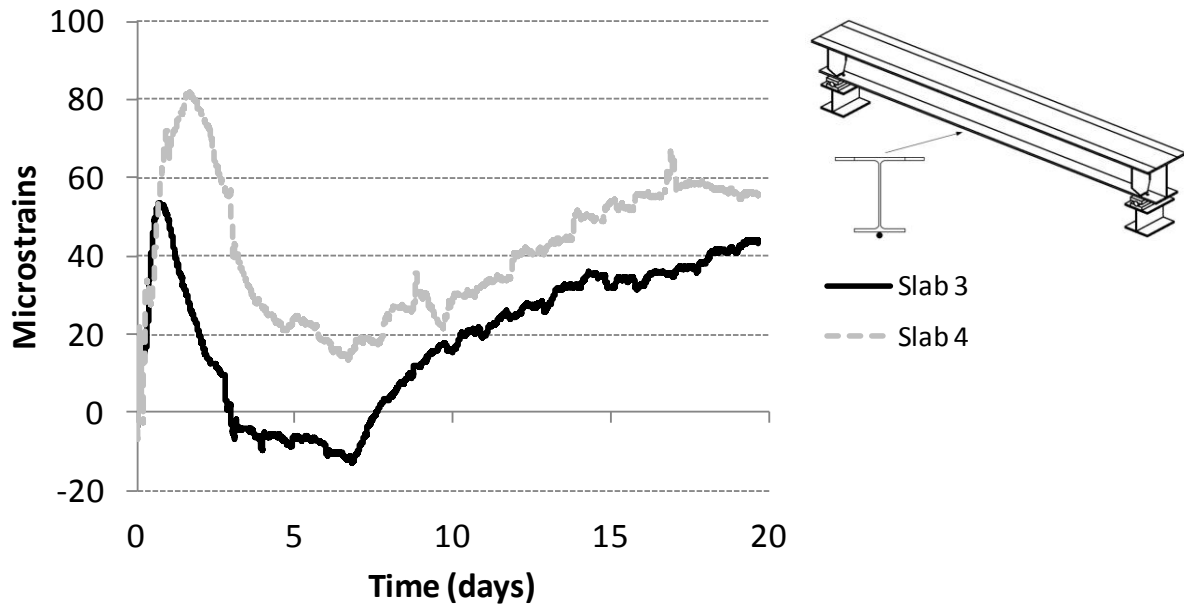


**Figure 87.** Beam bottom flange, mid-span longitudinal strains (S-G1-Bf-M-G1-1/2-L)

The strain output behavior is summarized below:

- *Longitudinal Strains:* All of the longitudinal strain gages showed a large spike in compressive strain during the concrete hydration period, followed by a leveling-off during the remainder of the wet-cure period, then a steady increase in compressive strain due to drying shrinkage.
- *Transverse Strains:* The transverse strains exhibited similar overall behavior to the longitudinal strains, but were smaller in magnitude. This was expected, since the bar size for the transverse steel was larger than the longitudinal steel.
- *Top Flange Strains:* The beam top flange strains were very similar to the rebar strains, and also smaller in magnitude.
- *Mid-Web Strains:* In the web, there was a large increase in tensile strain due to the beam expansion during hydration. The strains then leveled off to close to zero, and remained there for the remainder of the test.
- *Bottom Flange Strains:* Like the web, in the bottom flange there was a large increase in tensile strain due to beam expansion during hydration. The strains then leveled off, followed by a steady increase in tensile strain during drying shrinkage.

To determine if the beams were bending inward or outward, longitudinal strain gages were placed at the inside and outside of the bottom flange. The bottom flange inside and outside strains for test unit 3 are shown below in Figure 88.

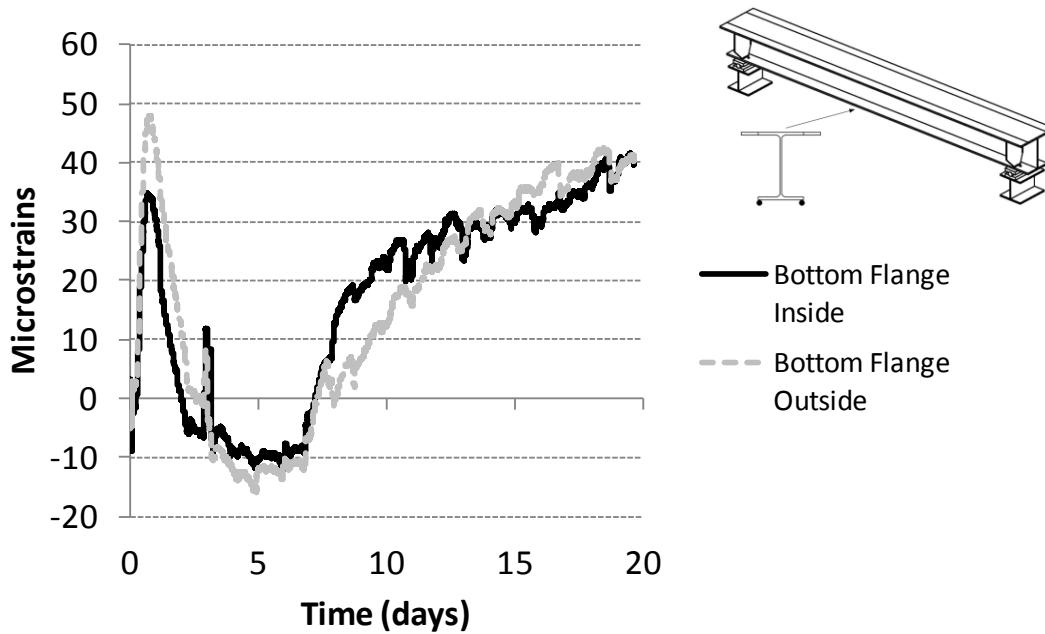


**Figure 88.** Beam bottom flange, mid-span longitudinal strain inside and outside comparison

As shown, the strains at the outside of the bottom flange remain slightly higher than the strains at the inside of the bottom flange. This indicates that the bottom flange not only experienced positive bending, but also bent slightly inward.

To determine the effect of using straight diaphragms verses cross-bracing, the diaphragm strain data was compared. The strains on the outside front surface are compared below in Figure 89. As shown, both sets of diaphragms behave in tension during the initial deck expansion due to hydration, then undergo compression due to concrete shrinkage. The strain values were for each diaphragm, although the straight diaphragm had slightly larger strain magnitudes. The cross-bracing diaphragms likely created slightly more restraint in the system than the straight diaphragms.

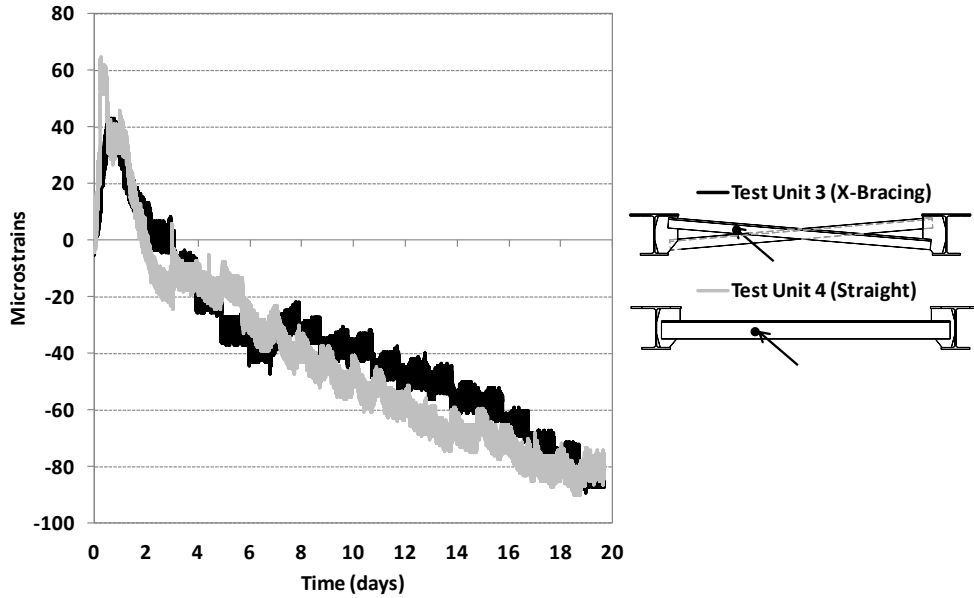


**Figure 89.** Diaphragm strain data comparison

The maximum strain gradients through the depth of both test units were extracted at the mid-span of Girder 1. They are presented below in Figure 90 and Figure 91. Note that tension is plotted to the right (high) side of the x-axis. As shown, both mats of reinforcing steel bent in compression, while the beams deformed in positive bending, with compressive strains on top, nearly zero strain in the web, and tensile strains on the bottom. The maximum strain gradient was larger for test unit 4 than test unit 3, which was likely due to the smaller bar sizes that were used.

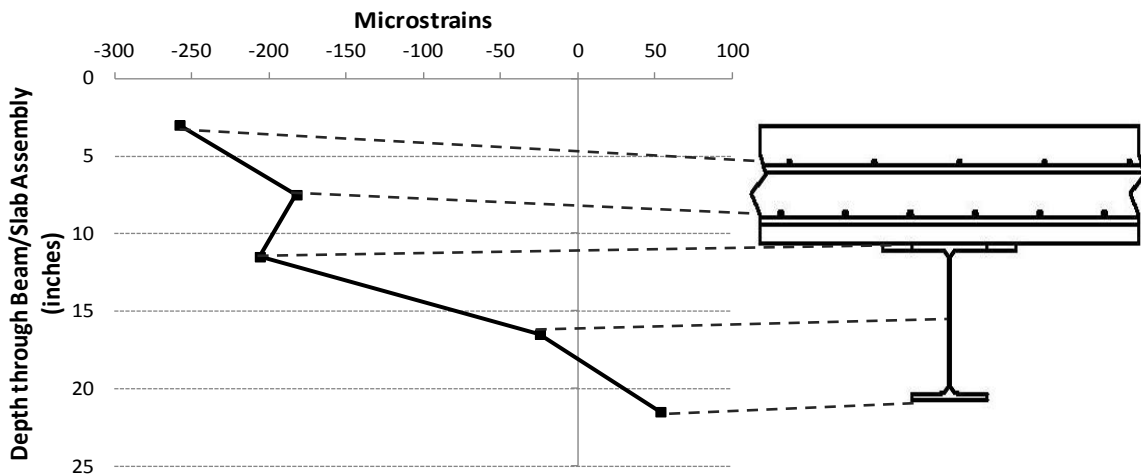


**Figure 90.** Maximum Strain Gradient, Test unit 3

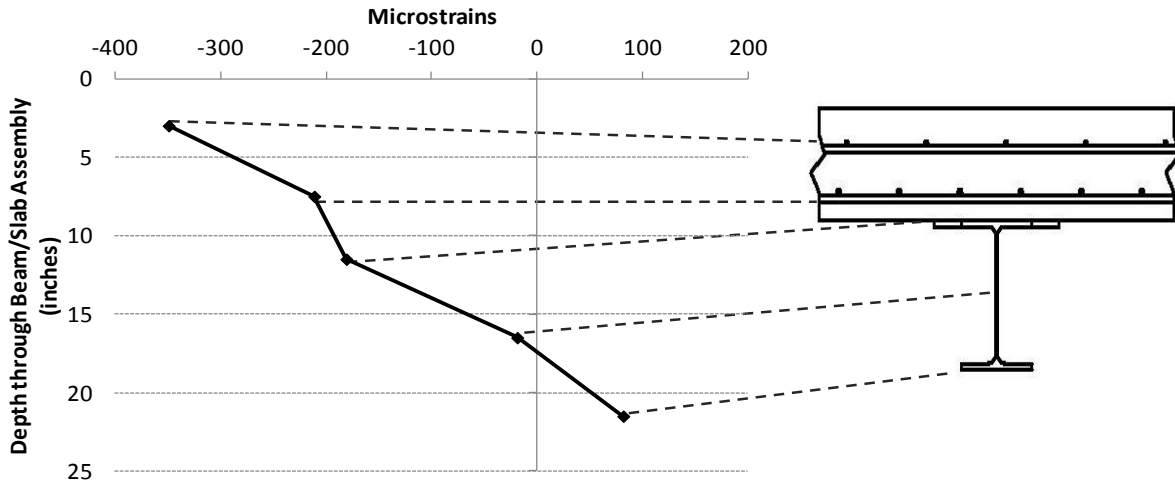


**Figure 91.** Maximum Strain Gradient, Test unit 4 (tension plotted on the right)

#### 4.6.7 Ring Test Crack Growth

The shrinkage rings were monitored daily for cracking. Once the presence of cracking was detected, the cracks were measured and crack growth plots were developed. The crack growth plots for Rings 1 to 4 (corresponding to the concrete used in Test units 1 and 2) are shown below in Figure 92.

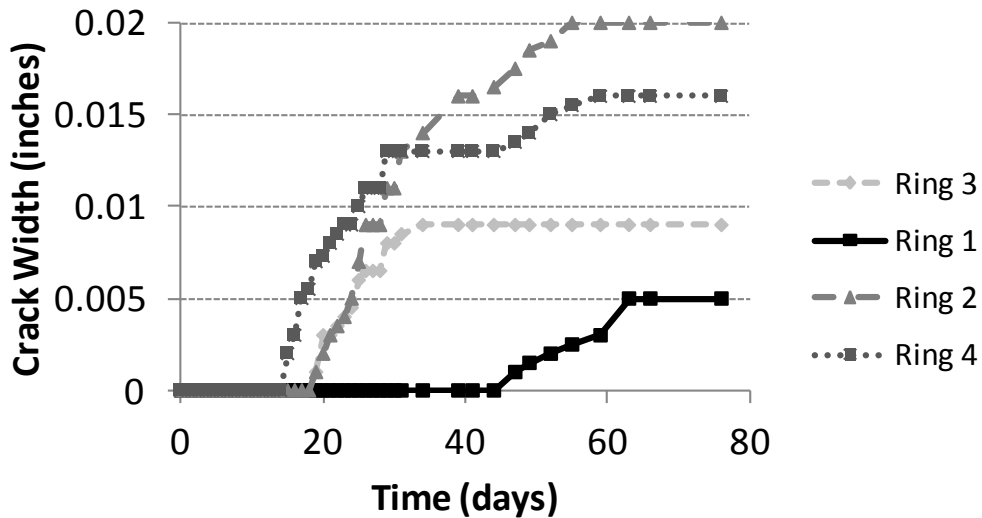


**Figure 92.** Concrete ring crack growth, Rings 1 to 4 (Grade D Mix)

As expected, Ring 4 was the first ring to crack, since it only underwent moist curing for 24 hours. Rings 2 and 3 experienced a similar cracking trend for the first few days, while the crack width for Ring 2 continued growing. Ring 1 did not crack until much later. In general, the rings began to crack at around 15-20 days after casting. Each ring contained one vertical crack, which kept growing as the rings continued to undergo shrinkage. An example ring crack is shown below in Figure 93.



**Figure 93.** Ring test cracking (Ring 2)

For test units 3 and 4, two rings were cast for each concrete mix and moist-cured for seven days. Rings 7 and 8, the rings made with the modified Grade D mix did not crack. The rings made with the standard Grade D mix began showing evidence of cracking at around 18 days, which was consistent with the first set of rings. The crack growth plots for Rings 5 to 8 is shown below in Figure 94.

#### **4.7 Data Analysis**

Overall, the data matched what was expected for the testing. The data revealed the test units initially expand due to the concrete heat of hydration, then leveled off while they remained covered during wet curing. Once the wet burlap was removed, drying was initiated, and the test units steadily curled inward in a bowl-shaped pattern. The overall trends and analyses for each type of instrument are presented below. Variations in behavior due to different design parameters at the sub-assembly level are presented in the computational analysis section.

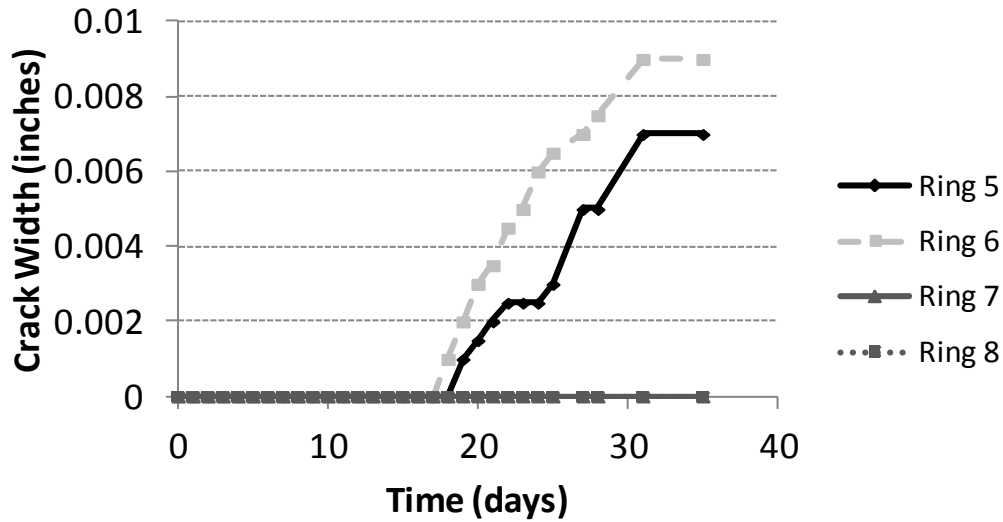


**Figure 94.** Concrete ring crack growth, Rings 5 to 8

#### 4.7.1 Temperature

Overall, each test unit exhibited the same general temperature behavior. In the concrete, there was a large increase in temperature during the first 24 hours of hydration, followed by a decrease until the end of hydration at three days. The steel top flange temperature was slightly cooler than the concrete, while the steel bottom flange temperature remained close to ambient. After the hydration period, the concrete internal temperature was slightly warmer than the lab ambient temperature.

All three test units made with the standard MDOT Grade D mix exhibited very similar temperature trends, indicating consistency in the mix. The modified Grade D mix had a similar temperature magnitude to the other mixes, but had a longer initial set time and remained at the peak temperature longer.

#### 4.7.2 Vertical Displacements

As expected, the overall deflection magnitudes were larger underneath the test unit than underneath the steel beams, and were largest in the middle of the test unit. This behavior matched the overall deflected “bowl-shaped” pattern of the beam/slab assembly due to concrete shrinkage, with the largest displacement in the middle.



Overall, test units 2 and 4 exhibited very similar displacement trends, as well as test units 1 and 3. The high shear stud density in test unit 2 likely produced added restraint, thus limiting the overall amount of displacement, and the low-shrinkage mix for test unit 4 also limited the displacement. Test units 1 and 3 had the same type of concrete, with different rebar configurations and diaphragm types. From a displacement point of view, these design features do not appear to have a large effect. Since test unit 2 had the smallest overall displacements, it can be seen that increasing the shear stud density decreases the overall displacements.

#### **4.7.3 Strains**

Overall, the strain behavior was as expected, and matched well with the deflection and temperature data. All of the reinforcing steel strains remained in compression, which was consistent with the expected “bowl-shaped” displacement of the test unit. The beams initially showed a combination of positive bending (due to concrete dead load) and expansion (due to heat of hydration). After the hydration period was over, the beams continued to experience positive bending, with compressive strain in the top flange, nearly zero strain in the web, and tensile strain in the bottom flange. Based on the bottom flange strain gage data, the beams also bent inward slightly. The overall strain magnitudes in test unit 4 were higher than in test unit 3. This was slightly surprising, since test unit 4 had a lower-shrinkage concrete mix. However, test unit 3 had a heavier reinforcement scheme, which may have caused lower values of strain. The diaphragm strain values were similar for both types of diaphragms, although the cross-bracing diaphragms likely created slightly more restraint than the straight diaphragms.

## 5 COMPUTATIONAL EVALUATION

Finite-element computer models were developed to simulate restrained concrete shrinkage in jointless bridge systems. An approach was developed to simulate concrete shrinkage through temperature loading. The approach was verified by comparing the experimental data to the computer model data. The approach was then implemented for full bridge systems, and results were compared for different bridge design features.

### 5.1 Modeling Approach

A method was developed for modeling and evaluating restrained concrete shrinkage through finite-element simulations. The finite-element program *ABAQUS* was used for all computational evaluations. The method utilizes temperature loading on exposed concrete surfaces to simulate free shrinkage strain. The free shrinkage strain at time  $t$  is calculated using the relationship given by ACI 209, as shown in Equation 5-1 below [2].

$$(\varepsilon_{sh})_t = \frac{t}{35 + t} * (\varepsilon_{sh})_u \quad (5-1)$$

where  $(\varepsilon_{sh})_t$  is the free shrinkage strain,  $t$  is the time (in days), and  $(\varepsilon_{sh})_u$  is the ultimate shrinkage strain. The ultimate shrinkage strain is based on a number of factors related to relative humidity and mix design as shown in Equation 5-2 below.

$$(\varepsilon_{sh})_u = 780 * \lambda_{cp} * \lambda_{\lambda} * \lambda_{vs} * \lambda_s * \lambda_{\psi} * \lambda_c * \lambda_{\alpha} * 10^{-6} \quad (5-2)$$

where  $\lambda_{cp}$  depends on the number of days of moist curing,  $\lambda_{\lambda}$  depends on the percentage of relative humidity,  $\lambda_{vs}$  depends on the volume/surface area ratio (inches),  $\lambda_s$  depends on the slump (in.),  $\lambda_{\psi}$  depends on the percentage of fine aggregate to total aggregate,  $\lambda_c$  depends on the cement content (lb./yd.<sup>3</sup>), and  $\lambda_{\alpha}$  depends on the air content (%). Equations for each of these parameters are listed below.

$$\lambda_{cp} = 1.0 \text{ for } 7 - \text{ day moist cure} \quad (5-3)$$

$$\lambda_{\lambda} = \begin{cases} 1.4 - 0.01 * \lambda, & \text{for } 40\% \leq \lambda \leq 80\% \\ 3.0 - 0.03 * \lambda, & \text{for } 80\% < \lambda \leq 80\% \end{cases} \quad (5-4)$$

$$\lambda_{v_s} = 1.2 * e^{-0.12 * v/s}, \quad \text{where } v/s \text{ is volume to surface area (inches)} \quad (5-5)$$

$$\lambda_s = 0.89 * 0.041 * s, \quad \text{where } s \text{ is the slump (in.)} \quad (5-6)$$

$$\lambda_{\psi} = \begin{cases} 0.3 + 0.014 * \psi, & \text{for } \psi \leq 50\% \\ 3.0 - 0.03 * \psi, & \text{for } \psi > 50\% \end{cases} \quad (5-7)$$

$$\lambda_c = 0.75 + 0.00036 * c, \quad \text{where } c \text{ is the cement content in } lb/yd^3 \quad (5-8)$$

$$\lambda_a = 0.95 + 0.008 * a, \quad \text{where } a \text{ is the air content percentage} \quad (5-9)$$

Values for all these constants were calculated for each of the four laboratory test units, and are listed below in Table 9.

**Table 9.** Shrinkage strain calculation constants

Constant	Test units 1 and 2 (Standard Mix)	Test Unit 3 (Standard Mix)	Test Unit 4 (Modified Mix)
$\lambda_{cp}$	1.0	1.0	1.0
$\lambda_{\lambda}$	Varies, dependent on humidity (see Figure 69)	Varies, depends on humidity (see Figure 71)	Varies, depends on humidity (see Figure 71)
$\lambda_{v_s}$	1.114	1.114	1.114
$\lambda_s$	1.075	1.064	1.064
$\lambda_{\psi}$	0.874	0.874	0.874
$\lambda_c$	0.987	0.987	0.916
$\lambda_a$	0.986	1.002	1.002

After calculating the above values, the free shrinkage strain at time t,  $(\epsilon_{sh})_t$ , was able to be determined. To apply this strain through temperature loading, Equation 5-1 was set equal to the equation for free thermal expansion, as shown below in Equation 5-10.

$$(\epsilon_{sh})_t = \alpha * T \quad (5-10)$$

where  $\alpha$  is the coefficient of thermal expansion (1/°F) and T is the temperature (°F). Finally, the temperature loading to be applied in the finite-element modeling was determined by solving Equation 5-10 for T.

$$T = -\frac{(\epsilon_{sh})_t}{\alpha} \quad (5-11)$$

The temperature values calculated in Equation 5-11 were applied to exposed concrete surfaces to simulate free shrinkage strain, while a temperature of zero degrees was applied to restrained concrete surfaces. The temperature values were applied using transient coupled temperature-displacement loading in ABAQUS.

### 5.1.1 Free shrinkage model

To verify the approach in Equation 5-11, a simplified concrete block model was created and simulated. The block model is shown below in Figure 95.

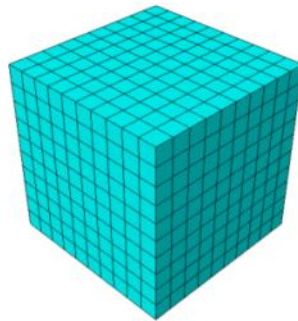


**Figure 95.** Concrete free shrinkage block overall model

Assuming a shrinkage strain  $((\epsilon_{sh})_t)$  of  $100\mu$  and concrete coefficient of thermal expansion ( $\alpha$ ) of  $6.0 \times 10^{-6}$ , the applied temperature loading was  $-16.67$  °F. This was applied to the outside of the block on all surfaces. The strain values and deflected shape are shown below in Figure 96.

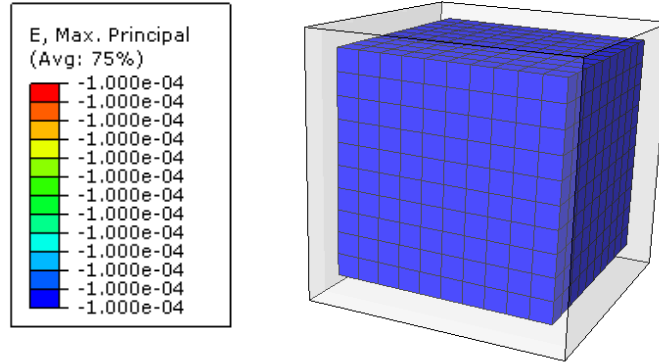


**Figure 96.** Free shrinkage model strains and deflected shape

As shown, the strain throughout the entire block was the assumed free shrinkage strain of  $100\mu$ . Additionally, the stress throughout the block was zero, since the block was completely free to contract. This analysis indicated that the temperature equation (Equation 5-11) could be used to successfully simulate free shrinkage strain.

## 5.2 Computer Modeling Features

As previously stated, the finite-element program *ABAQUS* was used in all computational evaluations. Transient coupled temperature-displacement analysis was used to model concrete shrinkage through temperature loading. The analysis procedure allows for the simultaneous solution of stresses, strains, and displacement with the changes in temperature. The system is solved by using Newton's method, as illustrated below [36].

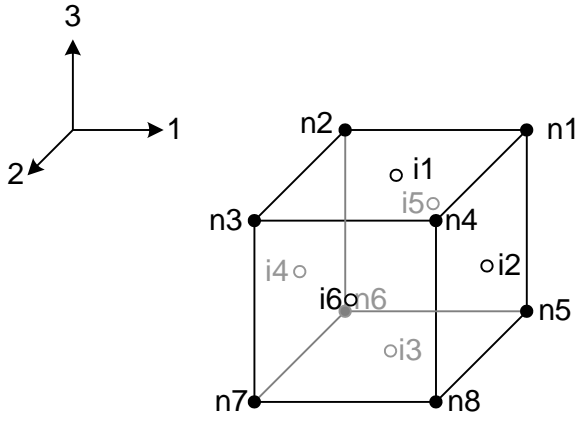
$$\begin{bmatrix} K_{uu} & K_{u\theta} \\ K_{\theta u} & K_{\theta\theta} \end{bmatrix} * \begin{pmatrix} \Delta u \\ \Delta \theta \end{pmatrix} = \begin{pmatrix} R_u \\ R_\theta \end{pmatrix} \quad (5-12)$$

where  $\Delta u$  and  $\Delta \theta$  are the corrections for incremental displacement and temperature,  $K$  are the stiffness values for the Jacobian matrix, and  $R_u$  and  $R_\theta$  are the mechanical and thermal vectors.

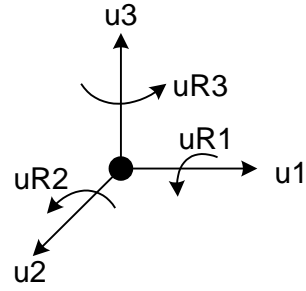
Different types of elements were used for the various parts in the models. Reduced integration was used for all analyses. The element types used for each part are summarized below in Table 10. Schematics and available degrees of freedom for each element type are illustrated in Figure 97.

**Table 10.** Element types used in computational evaluation

<b>Part</b>	<b>Element Type</b>	<b>Abaqus Element Designation</b>	<b>Number of Nodes Per Element</b>
Concrete Deck	3D Thermally-Coupled Solid Brick	C3D8T	8
Steel Beams	2D Shell	S4R	4
Diaphragms	2D Shell	S4R	4
Stay-in-place deck forms	2D Shell	S4R	4
Reinforcement	1D Truss	T3D2	2
Shear Connectors	1D Truss	T3D2	2

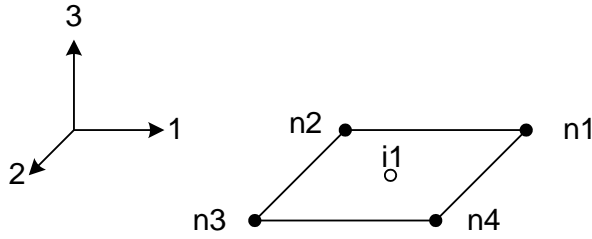


i) Element Nodes and Integration Points

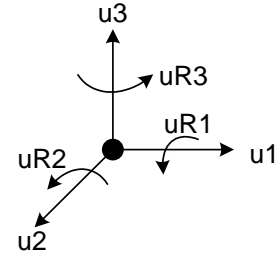


ii) Nodal Degrees of Freedom

a) C3D8T

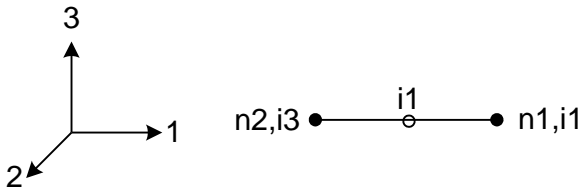


i) Element Nodes and Integration Points

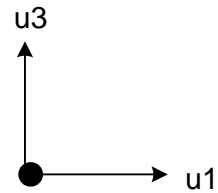


ii) Nodal Degrees of Freedom

b) S4R



i) Element Nodes and Integration Points



ii) Nodal Degrees of Freedom

c) T3D2

**Figure 97.** Schematic representation of elements used [36]

### 5.3 Material Properties

Inelastic concrete behavior was implemented by using the ‘concrete damaged plasticity’ material property. The material is a plasticity-based damage model for concrete, and is good to use for concrete in all types of structures under low confining pressures [36]. It can be used in both plain and reinforced concrete models, although it is primarily used to model reinforced concrete. It is able to model the irreversible damage that occurs when concrete cracks through strain softening. While it does not introduce cracking directly at material integration points, cracks can be visualized to occur in locations where plastic strain outputs are larger than zero. To model the inelastic concrete behavior, it implements damaged elasticity, along with tensile and compressive plasticity, and requires the input of concrete stress/strain curves in tension and compression.

The concrete stress-strain curves were generated by using the model proposed by Collins, et. al. [13]. The compressive stress/strain equations are shown below [13].

$$\frac{f_c}{f'_c} = \frac{\varepsilon_c}{\varepsilon'_c} * \frac{n}{(n-1) + (\varepsilon_c/\varepsilon'_c)^{n*k}} \quad (5-13)$$

where  $f_c$  is the compressive stress (psi),  $f'_c$  is the compressive strength (psi),  $\varepsilon$  is the compressive strain (in/in),  $\varepsilon'_c$  is the strain where  $f_c$  reaches  $f'_c$  (in/in), and  $n$  and  $k$  are curve-fitting factors, as shown below. For  $\varepsilon_c/\varepsilon'_c > 1$ ,

$$k = 0.67 + \frac{f'_c}{9000} \text{ (psi)} \quad (5-14)$$

$$n = 0.8 + \frac{f'_c}{2500} \text{ (psi)} \quad (5-15)$$



The equation for  $\varepsilon'_c$  is given as

$$\varepsilon'_c = \frac{f'_c}{E_c} \cdot \frac{n}{n-1} \quad (in/in) \quad (5-16)$$

The concrete modulus of elasticity,  $E_c$ , was predicted using the ACI code.

$$E_c = 57,000\sqrt{f'_c} \quad (psi) \quad (5-17)$$

The tensile stress-strain relationship proposed by Vecchico and Collins [37] was used. The stress-strain behavior of the concrete in tension was assumed to be linear-elastic, with modulus  $E_c$ , up to cracking. After cracking, the average tensile stress was calculated to be

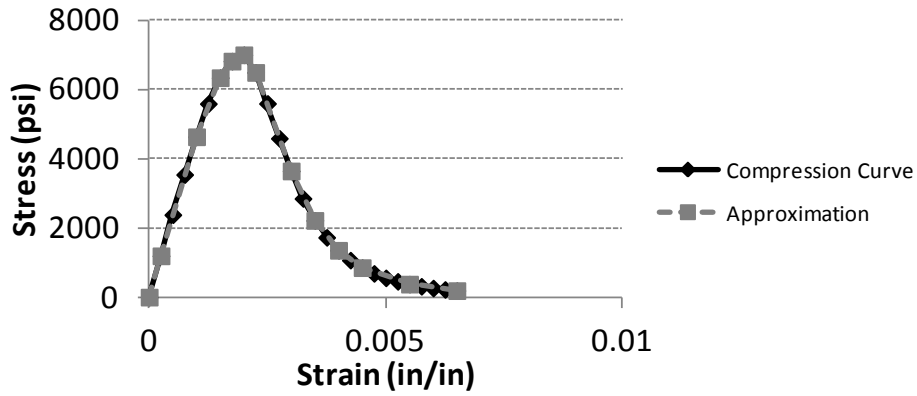
$$\sigma_c = \frac{f_{cr}}{1 + \sqrt{500 * \varepsilon_{cr}}} \quad (psi) \quad (5-18)$$

Here,  $\sigma_c$  is the concrete stress (psi),  $f_{cr}$  is the concrete tensile strength (psi), and  $\varepsilon_{cr}$  is the concrete strain after cracking. The concrete tensile strength varies greatly, and several different equations are proposed for calculating the tensile strength. For the computer modeling, the following relationship was used.

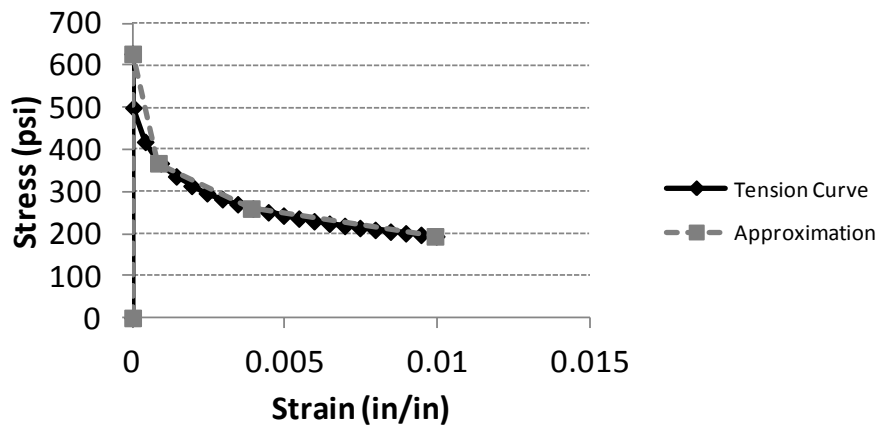
$$f_{cr} = 7.5 * \sqrt{f'_c} \quad (5-19)$$

This relationship was used in lieu of actual strength data from the laboratory, due to the scatter in the data output.

For the computer modeling, a concrete compressive strength of 7,000 psi was assumed for all of the analyses, since all the concrete had a 28-day compressive strength of 7,000 psi or slightly higher. The concrete stress/strain curves were generated using the method described above, and are shown below in Figure 98.



a) Compression



b) Tension

**Figure 98.** Concrete damaged plasticity stress/strain curves

In addition to the concrete inelastic behavior, several elastic material properties were modeled for both the concrete and the steel. Note that all steel was modeled as elastic. The material properties for the steel and concrete are shown below in Table 11.

**Table 11.** Material properties used in the computer analyses

Material Property	Concrete	Steel
Modulus of Elasticity E (psi)	4,768,962	29,000,000
Poisson's Ratio $\nu$	0.2	0.3
Mass density $\rho$ (slugs/in <sup>3</sup> )	0.00261	0.00881
Coefficient of thermal expansion $\alpha$ (per °F)	$6.0 \times 10^{-6}$	$6.5 \times 10^{-6}$
Thermal conductivity $\kappa$ (Btu/in*hr*°F)	0.15	2.5

## 5.4 Laboratory Models

Before implementing the loading approach to full bridge models, it had to first be calibrated and validated. This was completed by comparing the computer model data to the results obtained from the laboratory investigation. Models were created to simulate both the ring test and the four test unit slabs.

### 5.4.1 Concrete Shrinkage Ring Test

A computer model was first created to simulate the shrinkage rings cast in the lab. Separate parts were created for the concrete and steel rings, and the dimensions corresponded to those shown in Figure 31. Both the concrete and steel were made of solid 3D elements, with six elements through the depth of the concrete ring and five elements through the depth of the steel ring. Friction interaction was implemented in the tangential direction between the concrete and steel, with a friction coefficient of 0.45. “Hard” contact was used for the interaction between the steel and concrete in the normal direction. Fixed boundary conditions were placed at the four contact points where the bolts were located at the inner steel ring. The ring test assembly setup is shown below in Figure 99

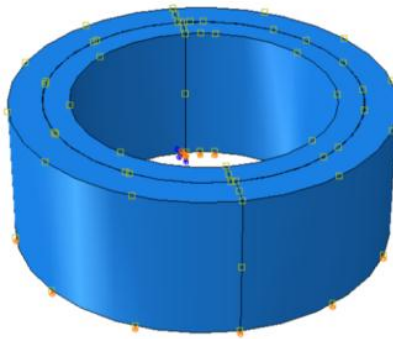


**Figure 99.** Concrete ring test assembly

A zero-degree boundary condition was implemented for the steel ring, as well as the inside, top, and bottom surfaces of the concrete ring, since these drying was prevented from these surfaces. The outside surface of the concrete ring had time-dependent tabular temperature values applied, corresponding to the calculated ACI 209 free shrinkage strain values [2]. The temperature values were calculated as described in Section 5.1.

Originally, the entire outside surface of the concrete ring had a uniform temperature distribution applied. With this approach, the entire ring would show cracking without a small imperfection being introduced. Instead of damage being concentrated in a specific region of high stress, the entire ring would become damaged, since it has uniform material properties and loading. Therefore, a material imperfection was created along a small strip in the concrete ring. This was done to provide a stress concentration and produce cracking in a specified region of damage. An arbitrary value of  $8 \times 10^{-6}$  was chosen for the imperfection region. This is illustrated below in Figure 100.

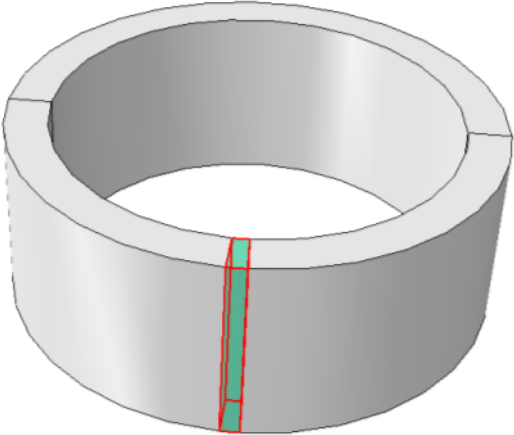


**Figure 100.** Material Imperfection Assignment

The calculated temperature values applied to the outside surface are shown below in Figure 101 and Figure 102.

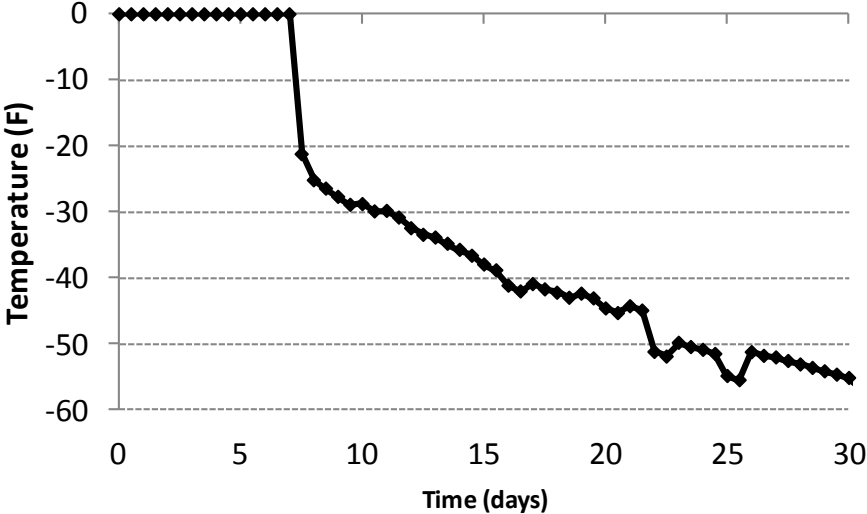


**Figure 101.** ACI 209 Temperature values (applied to outside surface of concrete ring) [2]

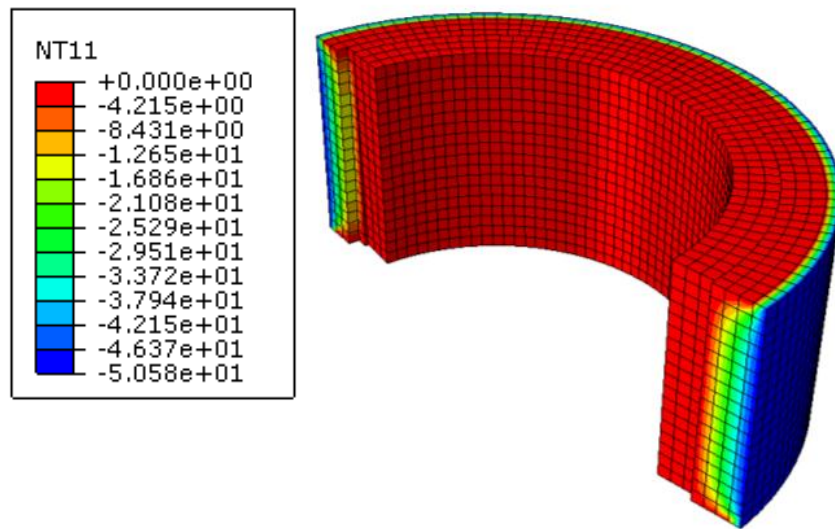


**Figure 102.** Temperature distribution through the rings

The analysis was run for the entire time period, and the plastic strains were monitored for cracking. According to the results, cracking began at a temperature value of -45 °F, corresponding to a time of 17 days. This was very similar to the time for cracking in the actual laboratory models. The plastic strain magnitudes at that time are shown below in Figure 103.

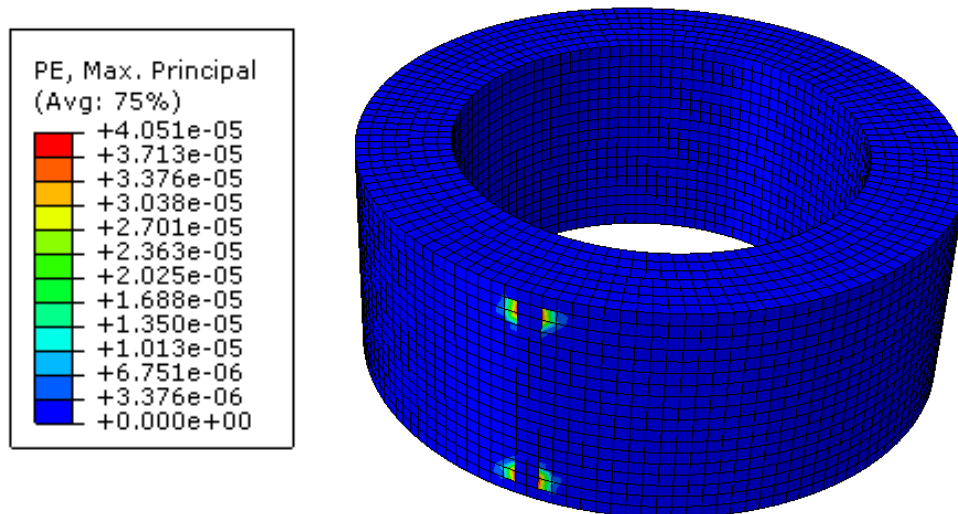


**Figure 103.** Concrete Ring plastic strain PE, Max Principal at time of 17 days

The plastic strain output through time in the region of imperfection was extracted, and is shown in Figure 104. The strains through time at the inside middle surface of the ring is shown

in Figure 105. This is the same location where strain gages were placed for the ring test. Additionally, the concrete ring strains in the location of damage were extracted and they are shown in Figure 106.

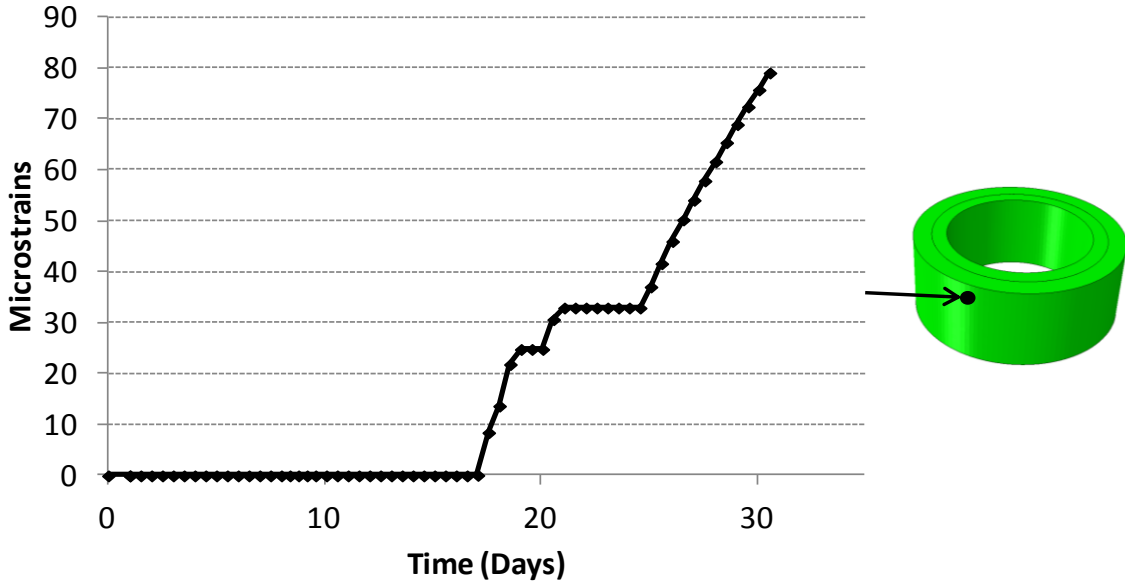


**Figure 104.** Plastic strain magnitude outputs through for the region of damage

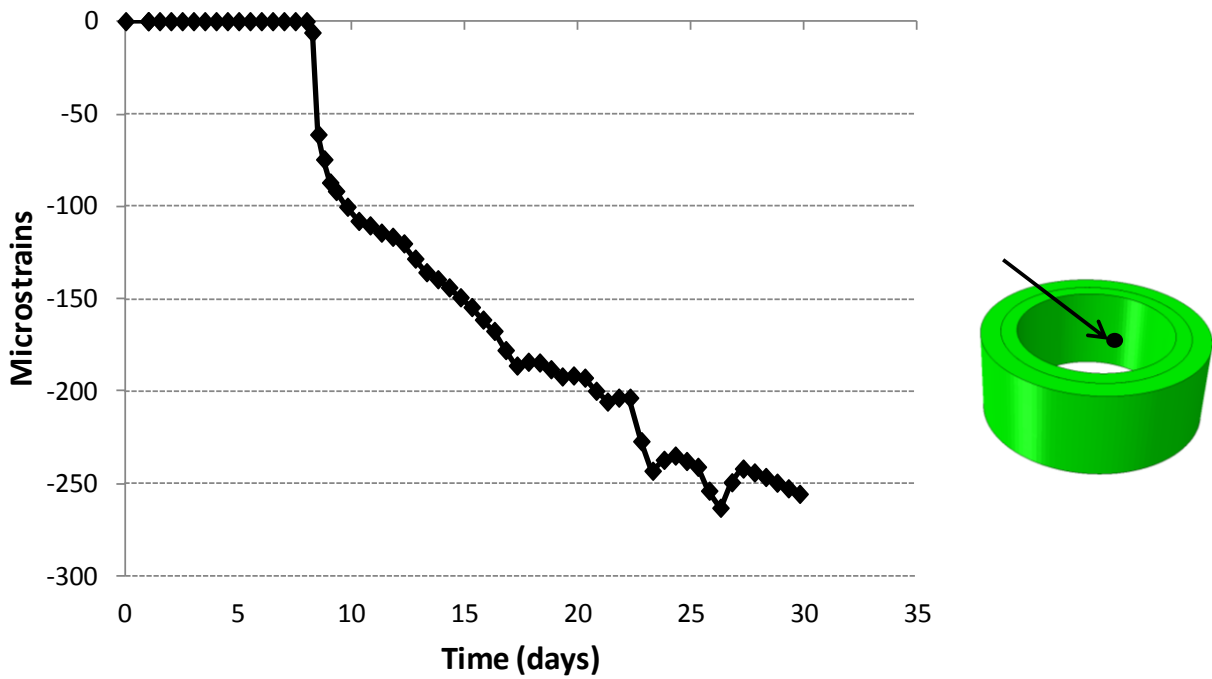


**Figure 105.** Steel ring strain output through time

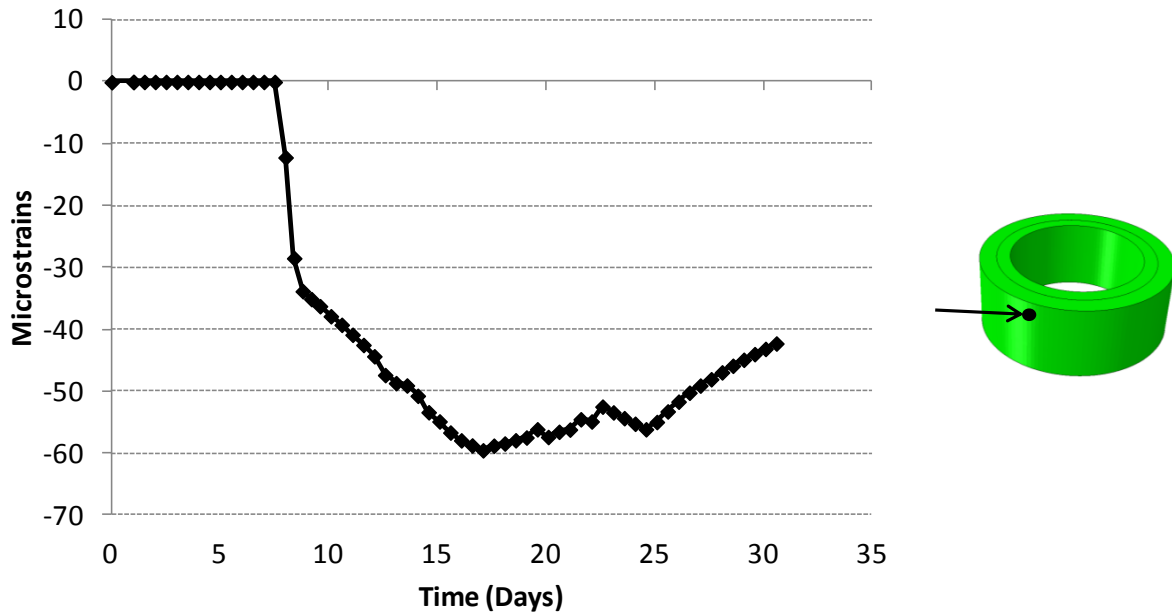


**Figure 106.** Concrete ring strain output through time

As shown, the steel ring compressive strains increased with time, but did not experience a sudden drop, which would in reality happen when cracking occurs. However, in looking at the concrete ring strains, it can be seen that softening occurs, and the strains drop after cracking occurs. The reason why the steel ring strains did not drop may be due to the plastic strains not being full-depth, and other issues with how finite-element simulations are run. The material imperfection approach was successfully able to concentrate the plastic strains in one particular region where cracking would occur, instead of having evenly-distributed damage throughout the entire ring. It can be seen that introducing random imperfections needed to be implemented in the full bridge parametric studies to produce accurate cracking distributions, and prevent uniform damage from occurring throughout the entire model.

The time for cracking matched well with the results for the laboratory, and the steel ring strain results matched the overall magnitude of the results from the lab. Overall the approach was shown to be logical, and correctly implemented the concrete material properties and damage.

#### 5.4.2 Lab Test Unit Test unit Models

Computer models were next created to simulate the test unit test units that were created in the lab. Each model consisted of the same design and layout as the test units. The effect of different design parameters at the sub-assembly level was examined, along with the validity of the overall computer modeling approach. An overall view of the model is shown below in Figure 107.

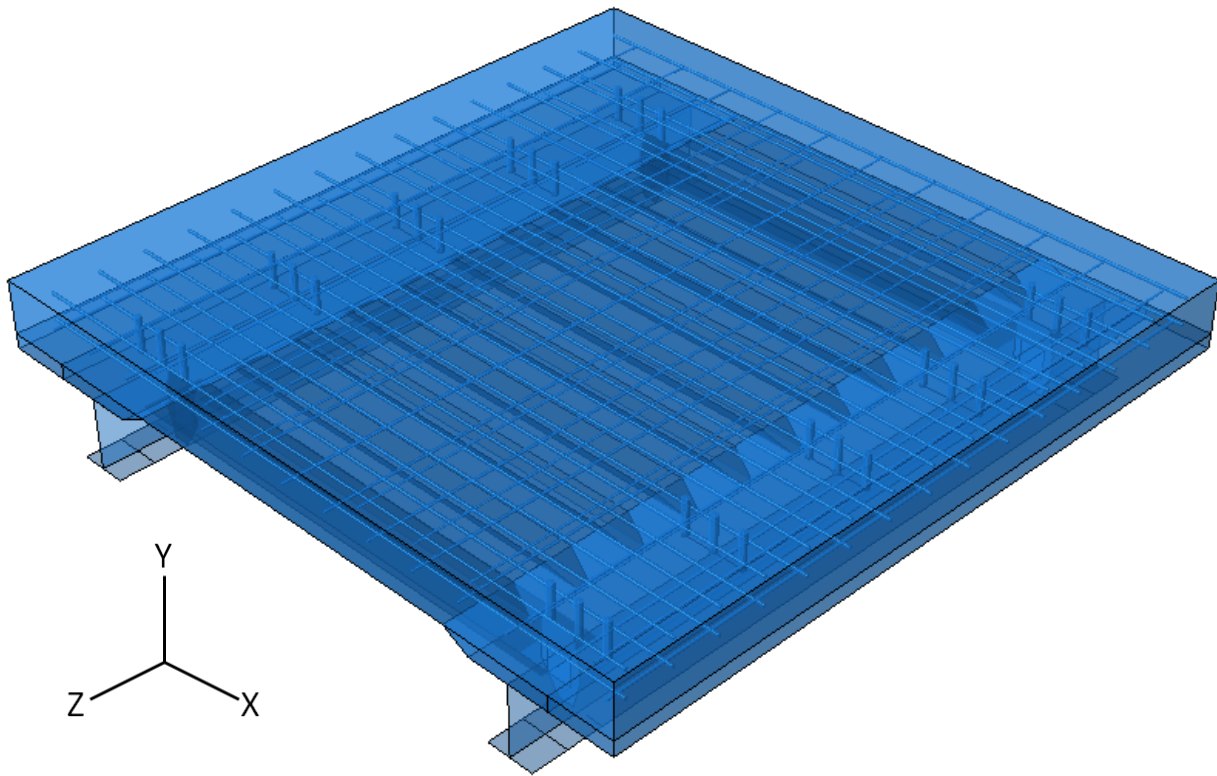


**Figure 107.** Lab test unit test unit models overall view

Tie constraints were used to simulate all welded connections. This included the connections between the stiffener plates and beams, diaphragms and stiffener plates, metal forms and beam top flanges, and the shear studs and beam top flanges. The reinforcing steel and shear studs were embedded in the concrete using the ‘embedded region’ constraint. Friction interaction was modeled between the steel and concrete with a friction coefficient of 0.45. Since the effects of the concrete dead load were not monitored during the laboratory testing, self-weight loading was not included in the computational analyses. The pin bearings from the lab were simulated through boundary conditions along a path at the bottom flanges of the beams, where rotation in the x-direction was allowed and all other degrees of freedom were fixed. To simulate shrinkage, temperature loading was applied to the top and side surfaces of the test units, while the bottom



surface had a temperature of zero degrees. This created a linear temperature distribution through the depth of the test units. The temperature loading values that were applied are shown below in Figure 108. The overall deflected shape for the test unit models at the end of the analysis is shown in Figure 109. Note the presence of the “bowl-shape” pattern as discussed in Chapter 4.

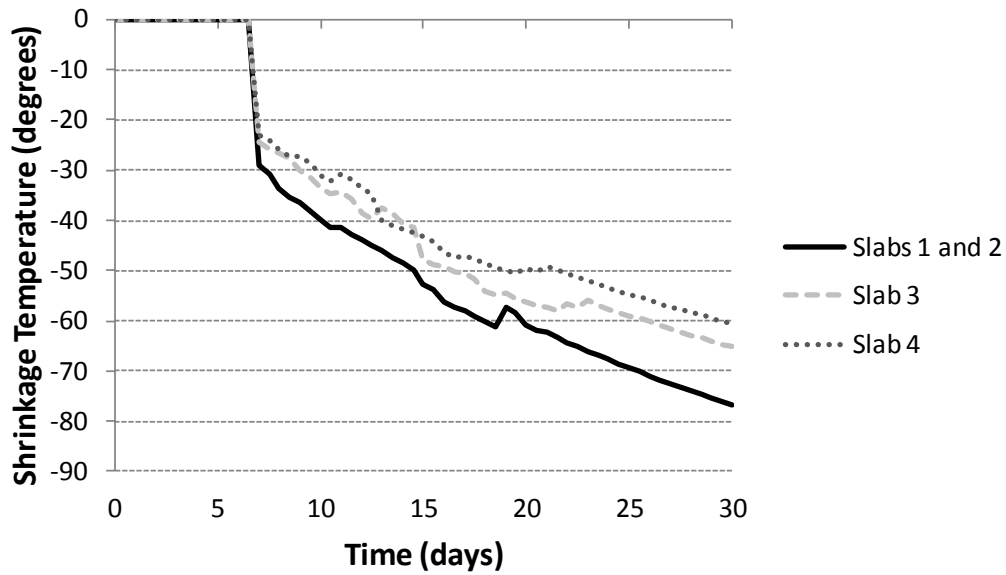


**Figure 108.** Temperature loading values for lab test unit analyses

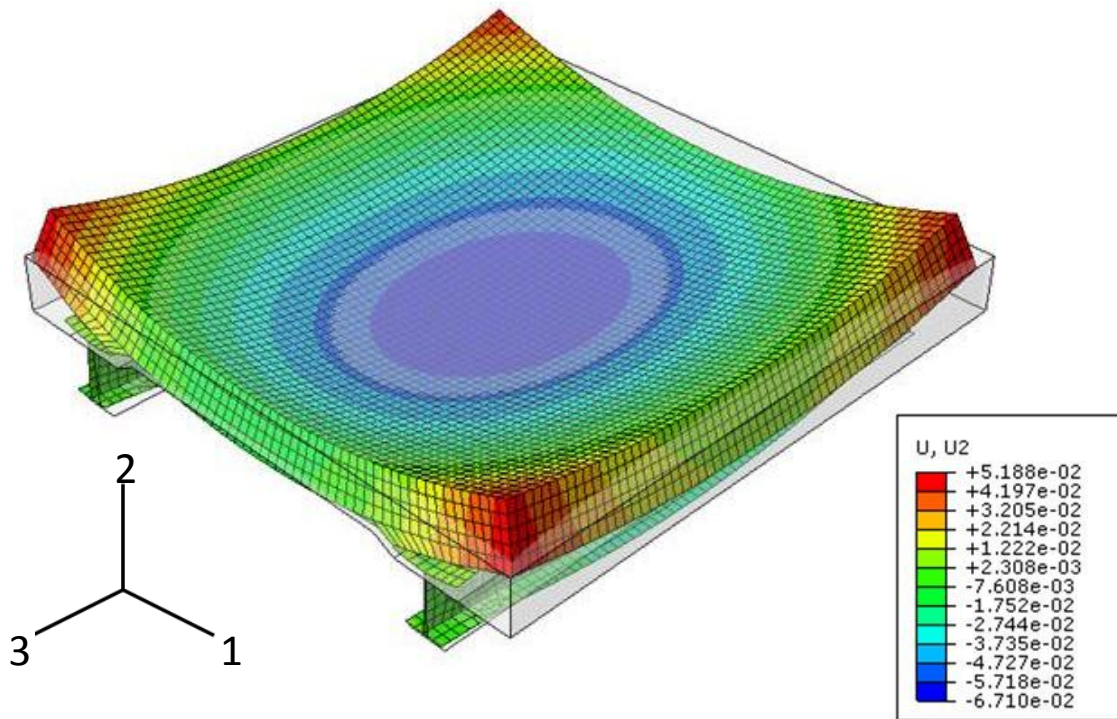
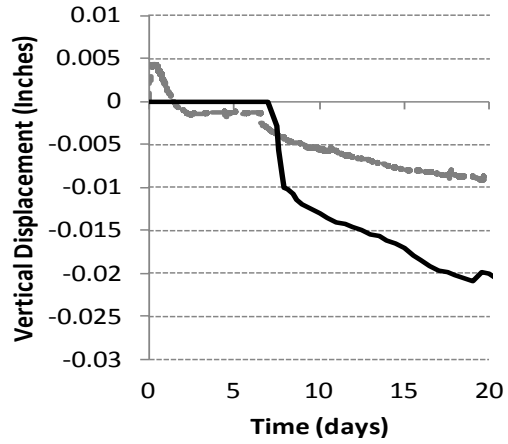


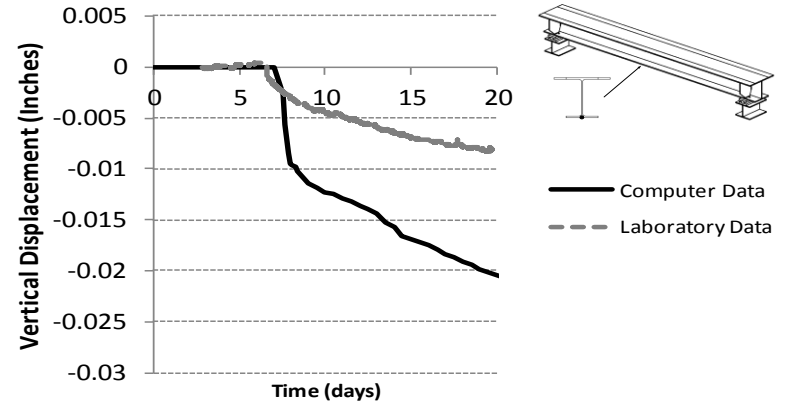
**Figure 109.** Test Unit Models Overall Deflected Shape and Vertical Displacement [35]

To validate the computer modeling approach, the computational analysis results were compared with the laboratory data. Selected comparison plots shown in Figure 110 to Figure 119 (refer to Figure 38 and Figure 39 for the instrumentation naming scheme.) As shown, the computer model data corresponded to the laboratory data reasonably well

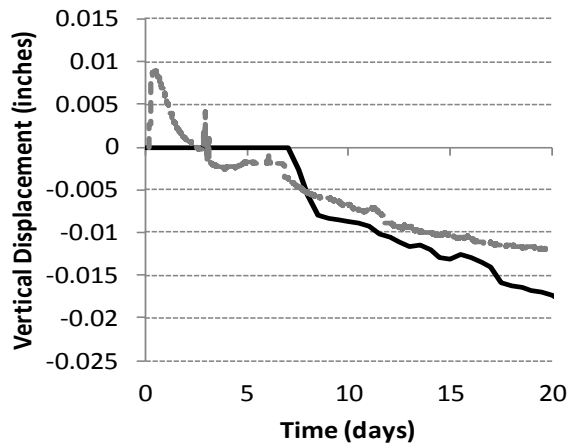
The computer model data for each test unit was also extracted to determine the relative differences at the sub-assembly level. Selected plots are shown in Figure 120 to Figure 128.



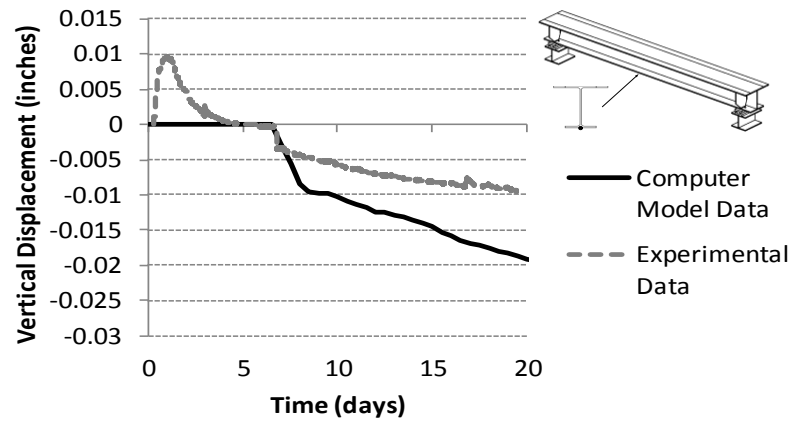
a) Test Unit 1



b) Test Unit 2

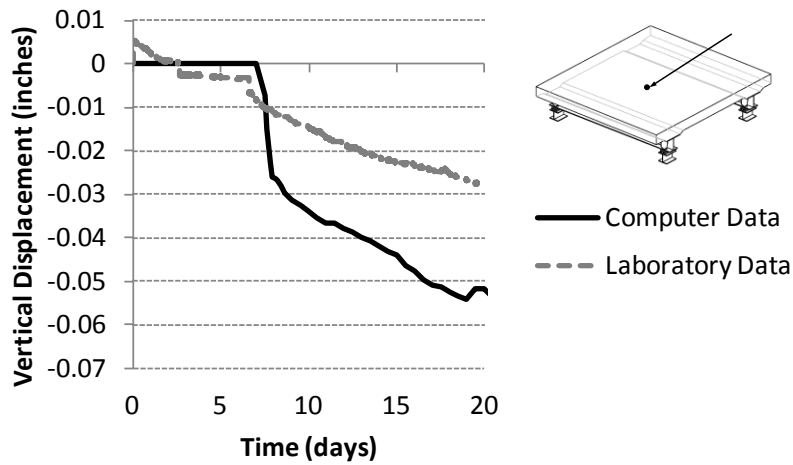


c) Test Unit 3

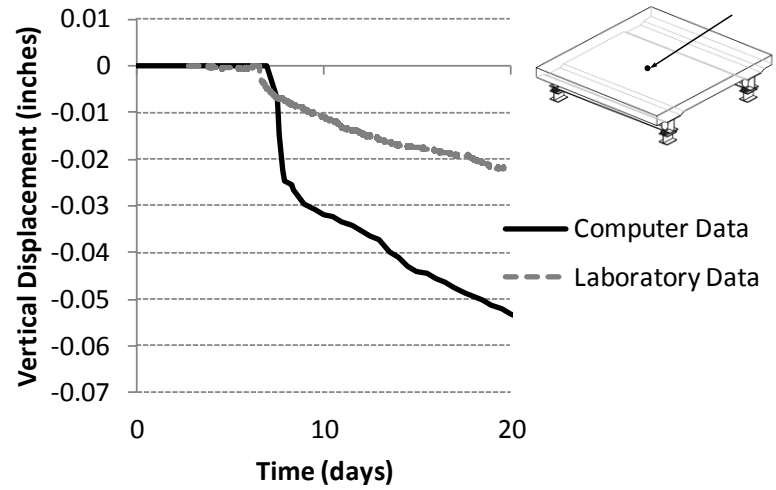


d) Test Unit 4

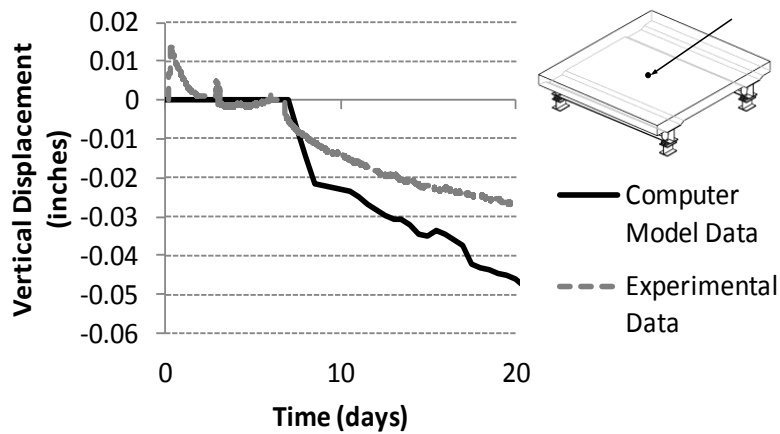
**Figure 110.** Beam mid-span deflection data comparison (L-G1-1/2)



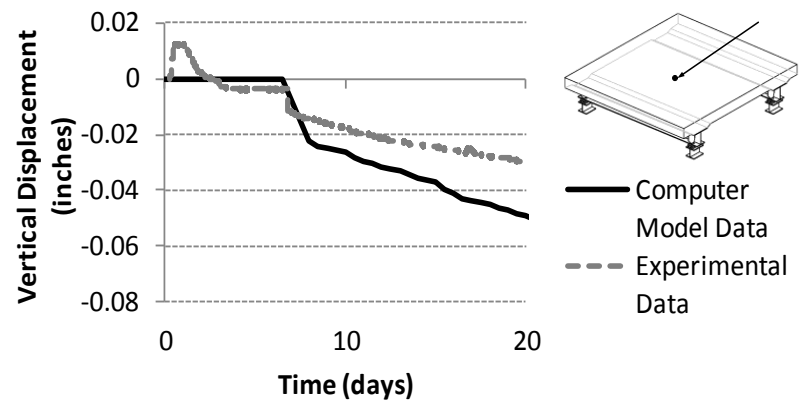
a) Test Unit 1



b) Test Unit 2

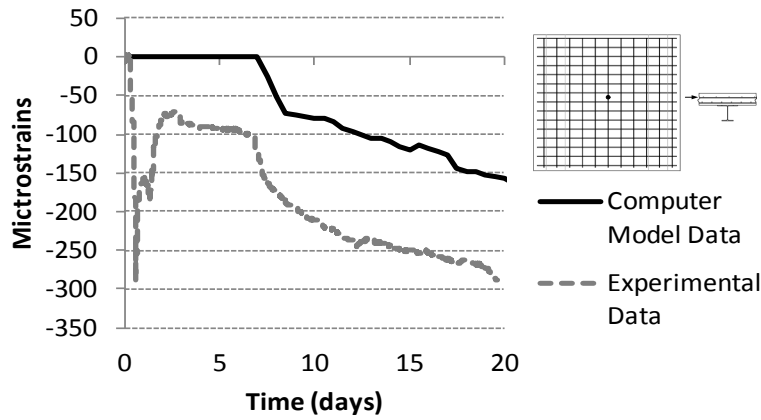


c) Test Unit 3

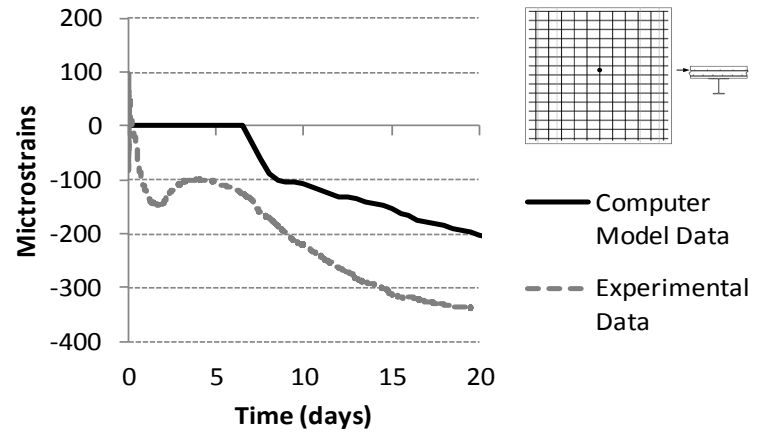


d) Test Unit 4

**Figure 111.** Mid-test unit deflection data comparison (L-1/2-1/2)

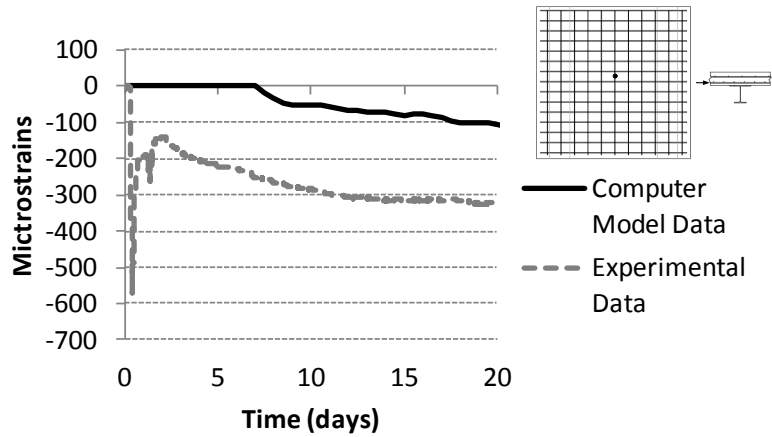


a) Test Unit 3

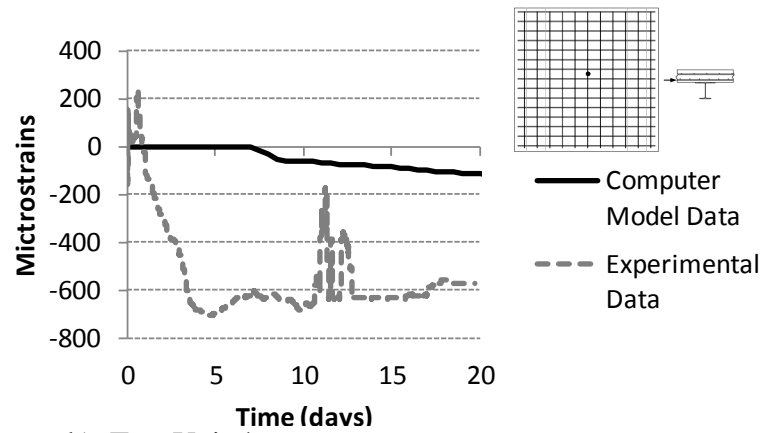


b) Test Unit 4

**Figure 112.** Reinforcing Steel Top Mat Long. Strain Data Comparison (S-Tp-1/2-1/2-L)

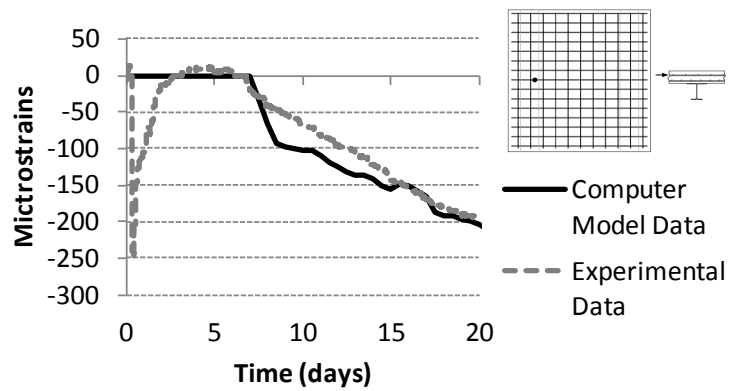


a) Test Unit 3

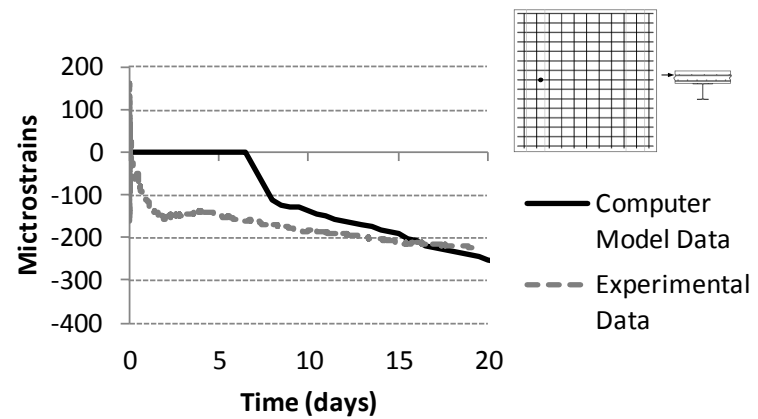


b) Test Unit 4

**Figure 113.** Reinforcing Steel Bott. Mat Long. Strain Data Comparison (S-Bt-1/2-1/2-L)

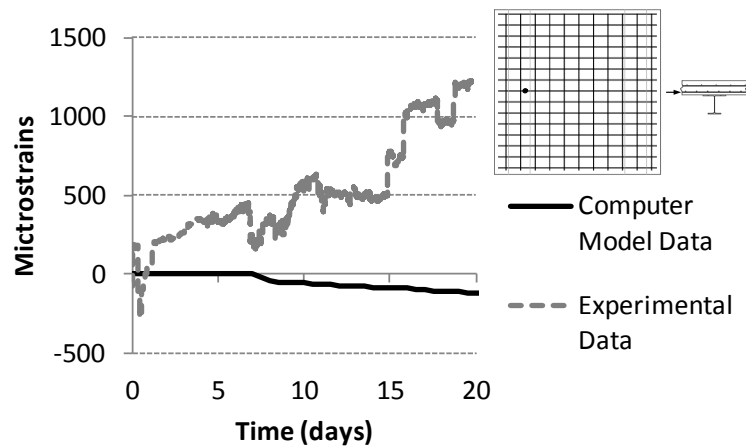


a) Test Unit 3

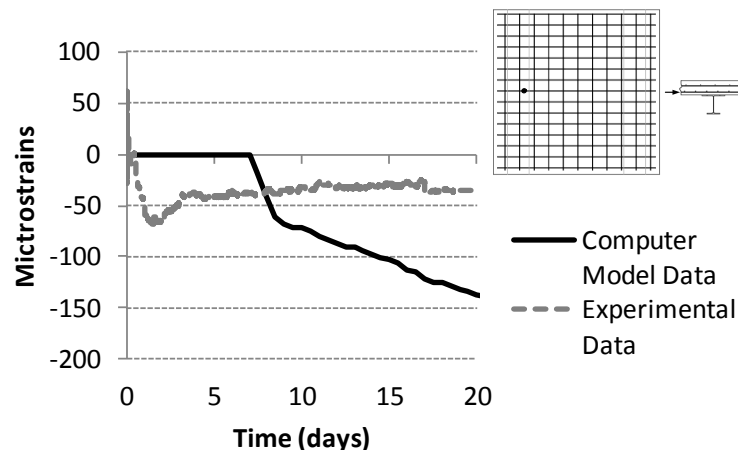


b) Test Unit 4

**Figure 114.** Reinforcing Steel Top Mat Trans. Strain Data Comparison (S-Tp-G1-1/2-T)

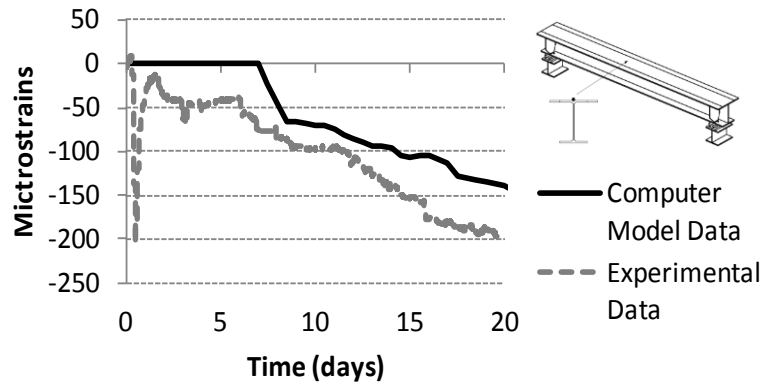


a) Test Unit 3

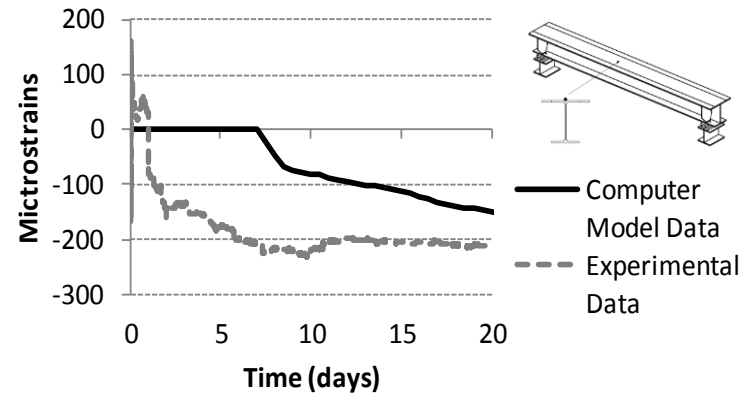


b) Test Unit 4

**Figure 115.** Reinforcing Steel Bott. Mat Trans. Strain Data Comparison (S-Bt-G1-1/2-T)

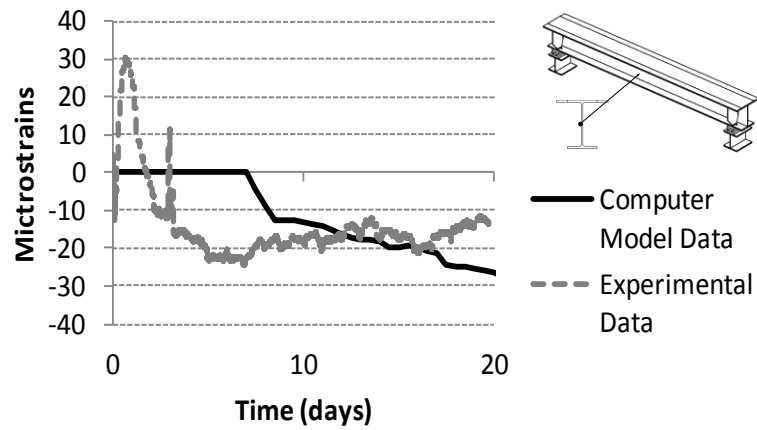


a) Test Unit 3

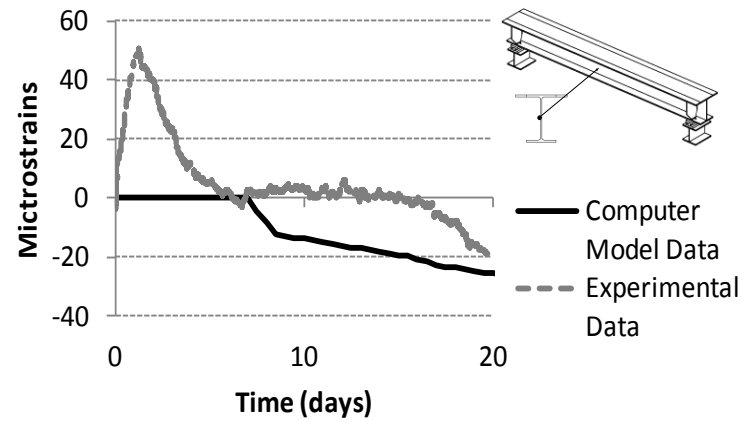


b) Test Unit 4

**Figure 116.** Beam Top Flange Strain Data Comparison (S-G1-Tf-M-G1-1/2-L)

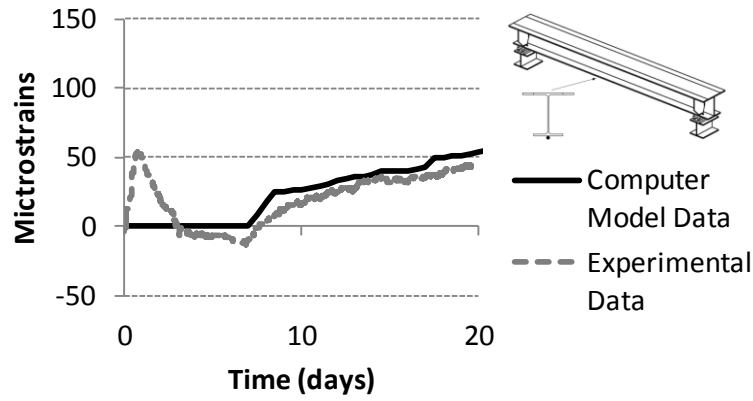


a) Test Unit 3

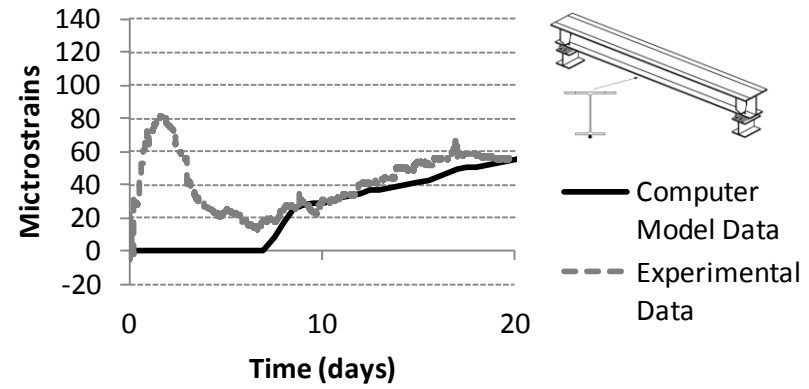


b) Test Unit 4

**Figure 117.** Beam Mid-Web Strain Data Comparison (S-G1-W-O-G1-1/2-L)

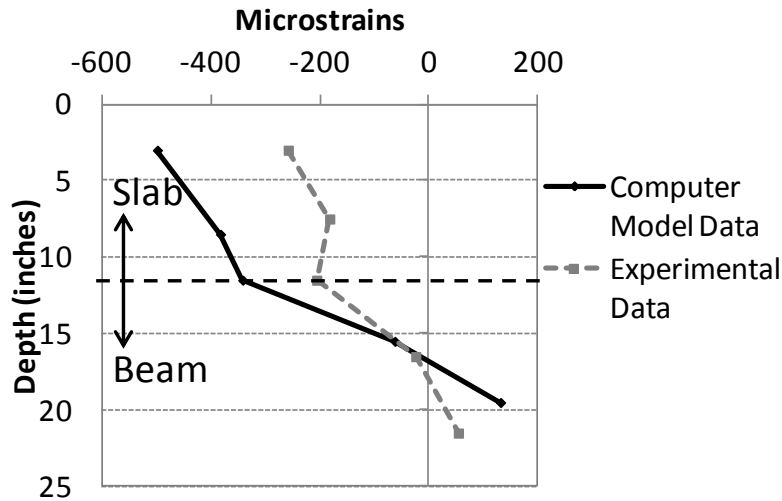


a) Test Unit 3

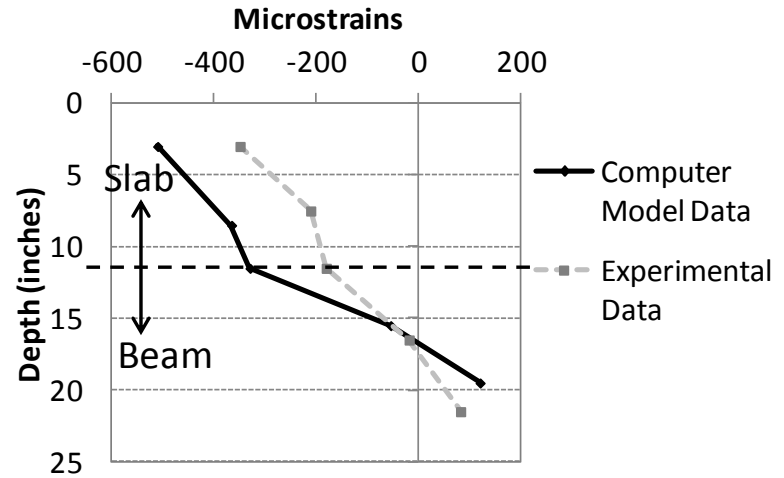


b) Test Unit 4

**Figure 118.** Beam Bottom Flange Strain Data Comparison (S-Bf-M-G1-1/2-L)



a) Test Unit 3



b) Test Unit 4

**Figure 119.** Depth through beam/slab assembly slab strain data comparisons (time=20 days)



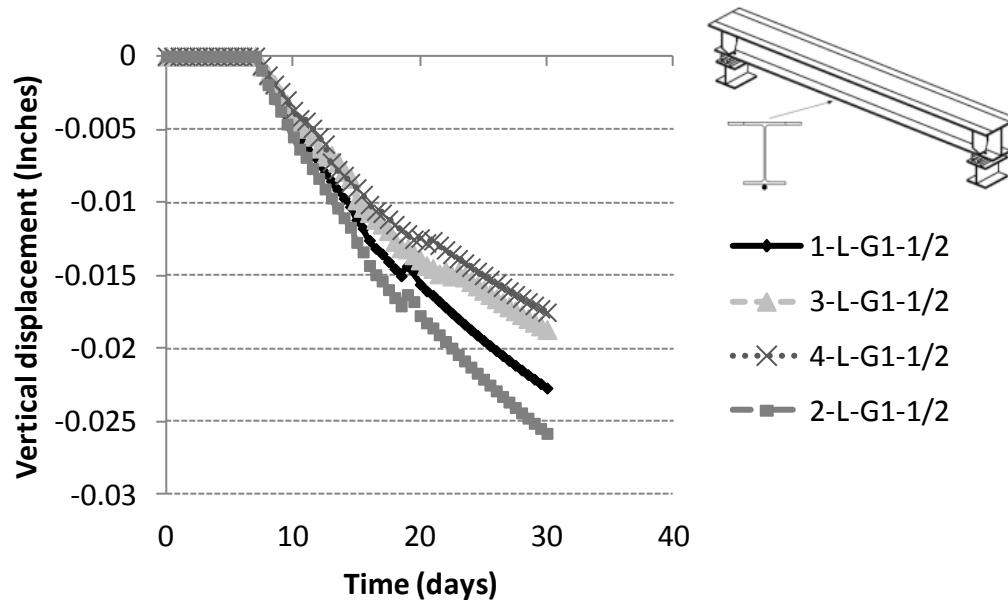


**Figure 120.** Computer model data comparison, beam mid-span deflection (L-G1-1/2)

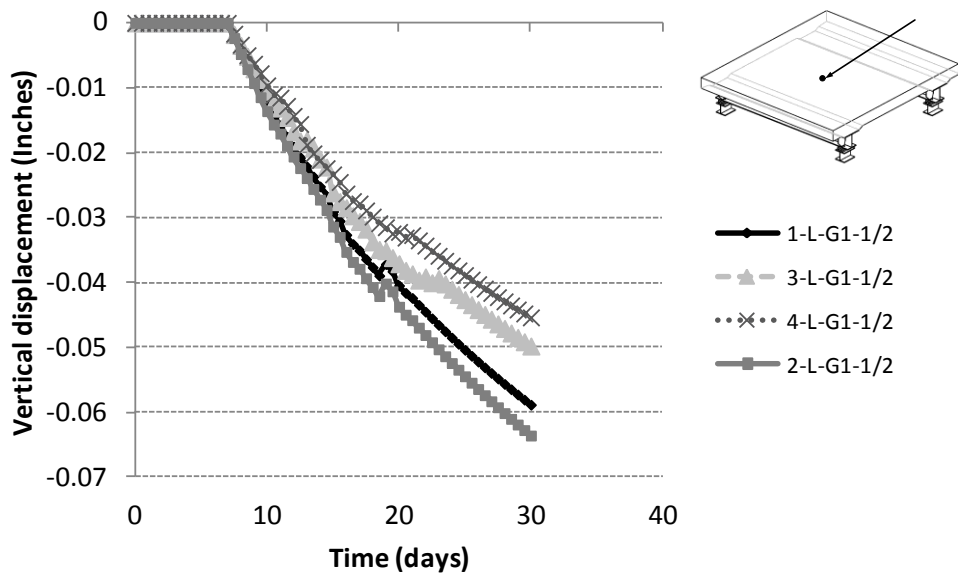


**Figure 121.** Computer model data comparison, test unit mid-span deflection (L-1/2-1/2)

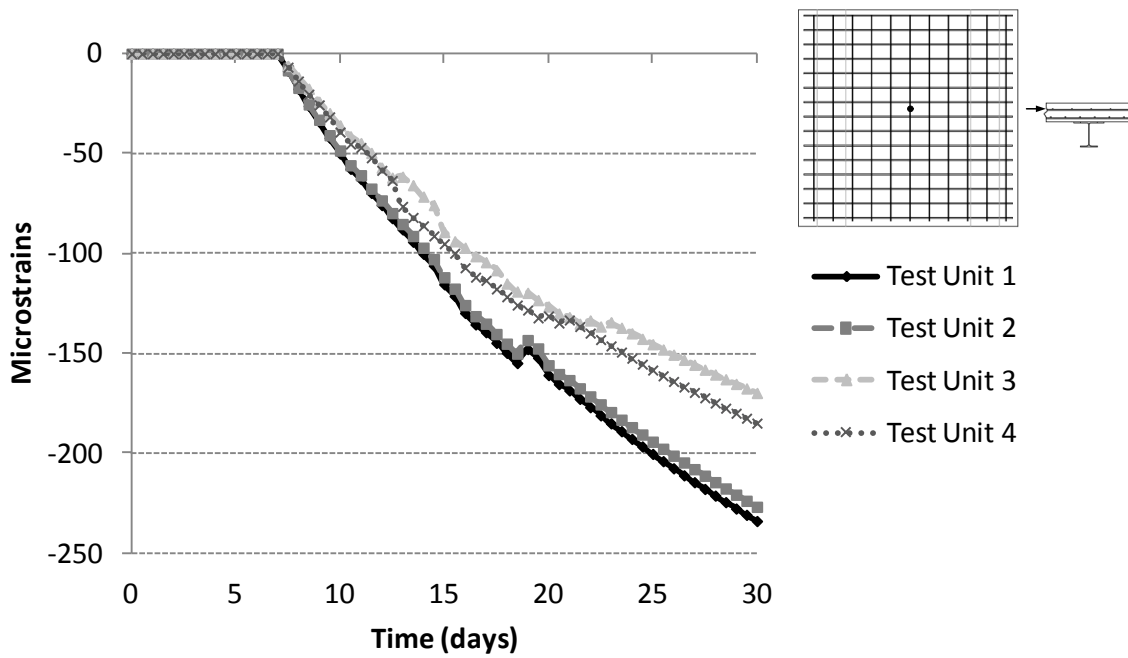


**Figure 122.** Computer model data comparison, rebar top mat long. strains (S-Tp-1/2-1/2-L)

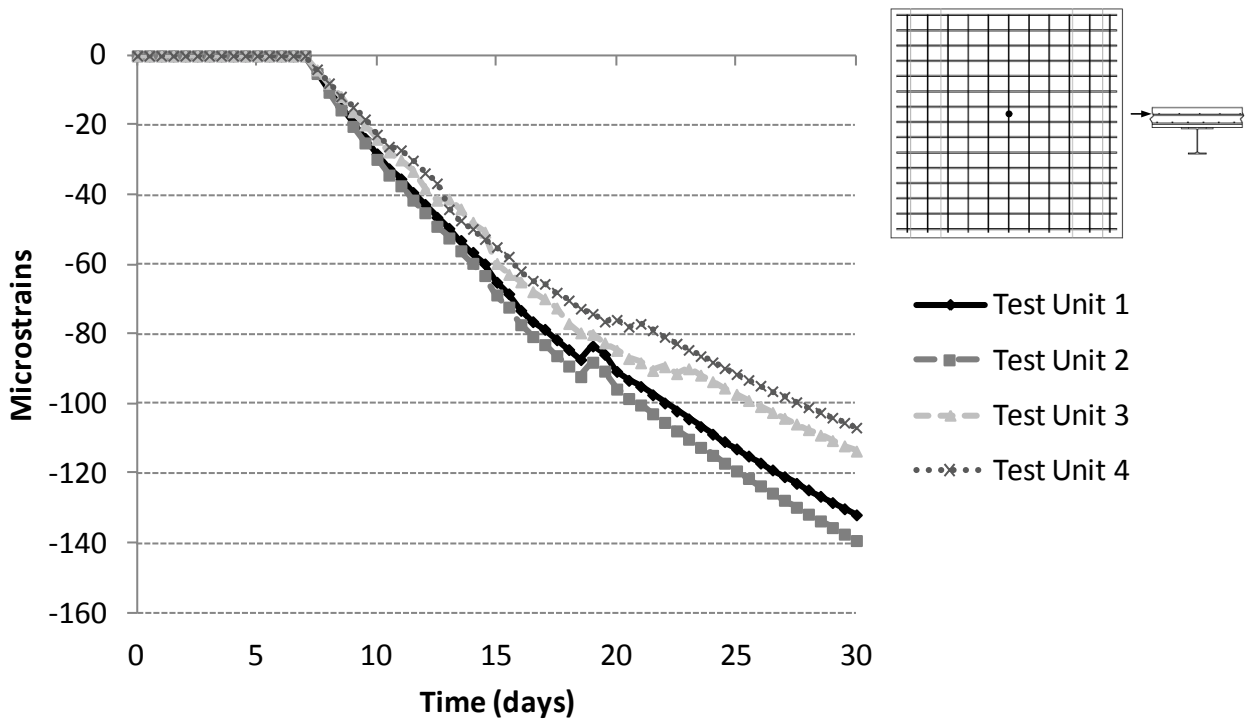


**Figure 123.** Computer model data comparison, rebar bott. mat long. strains (S-Bt-1/2-1/2-L)

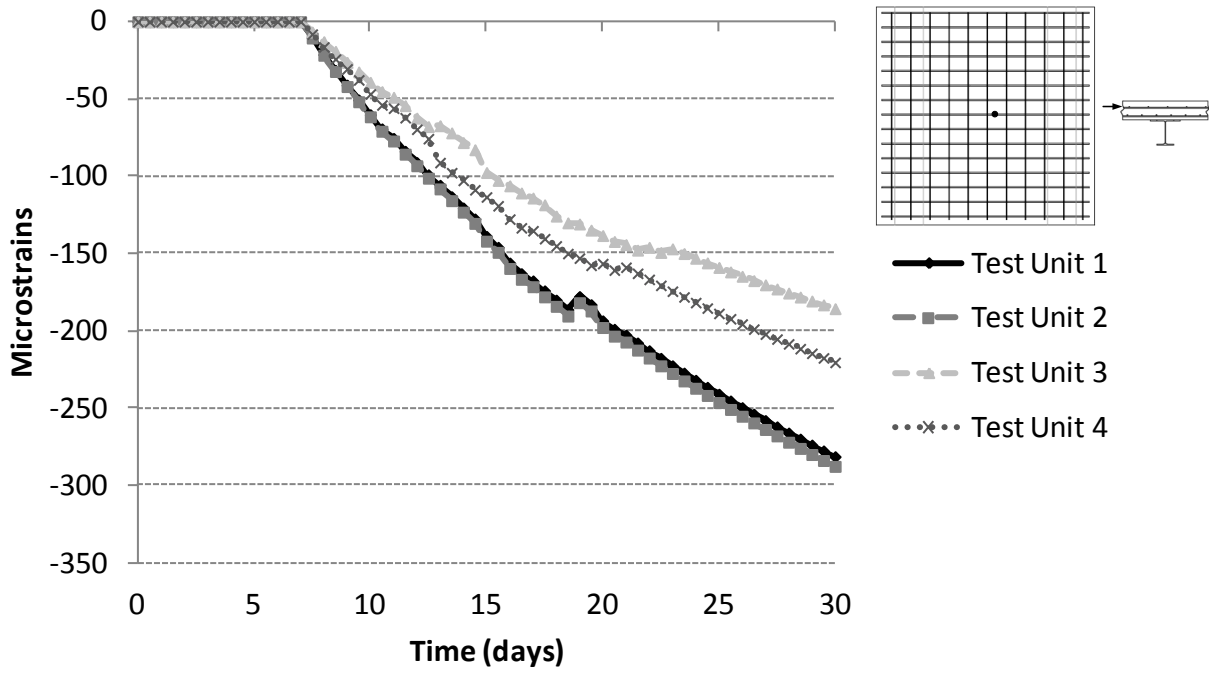


**Figure 124.** Computer model data comparison, rebar top mat trans. strains (S-Tp-1/2-1/2-T)

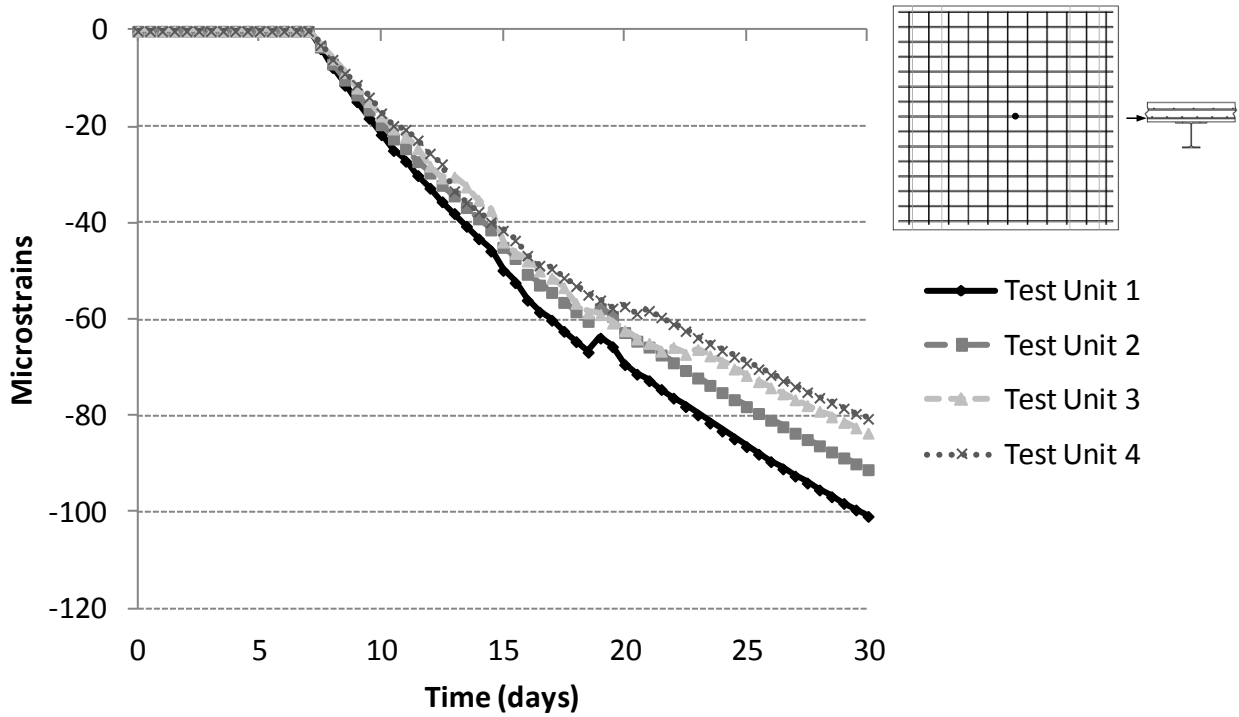


**Figure 125.** Computer model data comparison, rebar bott. mat trans. strains (S-Bt-1/2-1/2-T)

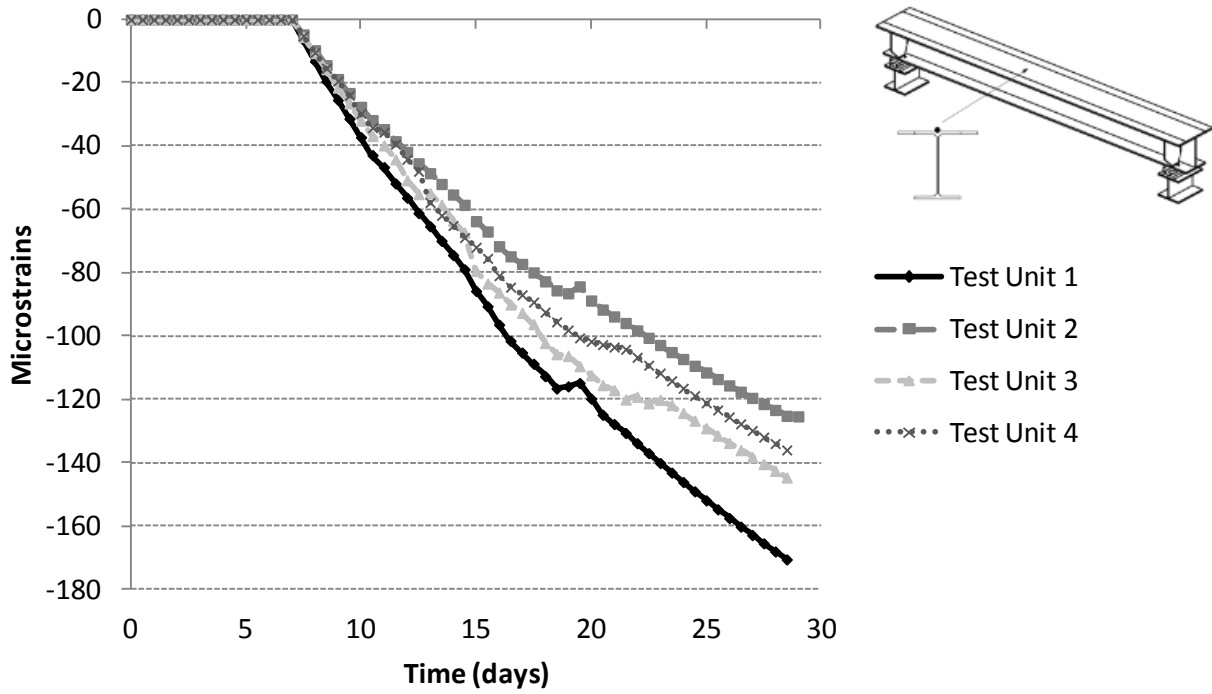


**Figure 126.** Computer model data comparison, beam top flange strains (S-G1-Tf-M-1/2-L)

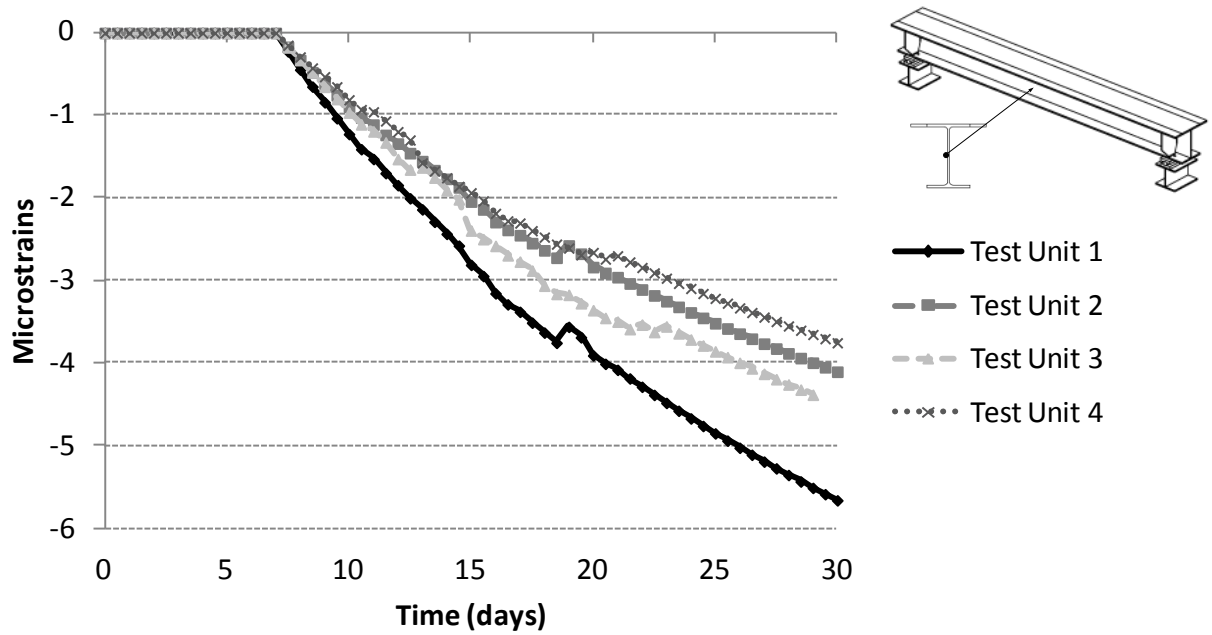


**Figure 127.** Computer model data comparison, beam mid-web strains (S-G1-W-O-1/2-L)

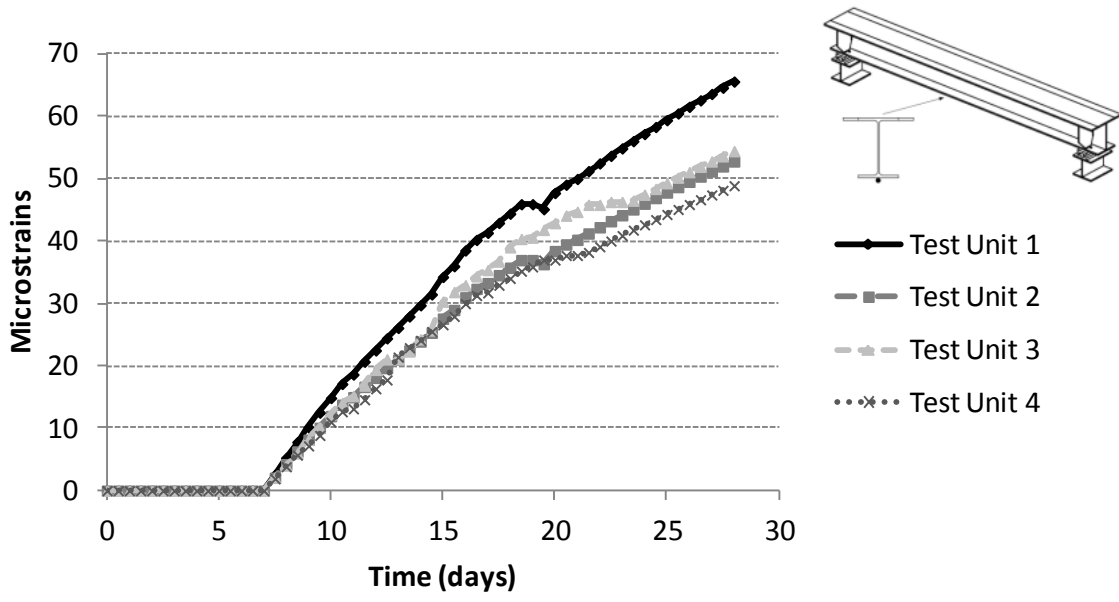


**Figure 128.** Computer model data comparison, beam bott. flange strains (S-G1-Bf-M-1/2-L)

The strains through the depth of the beam/test unit sections were also determined, and are shown below in Figure 129. Compression is plotted to the left and tension is plotted to the right.

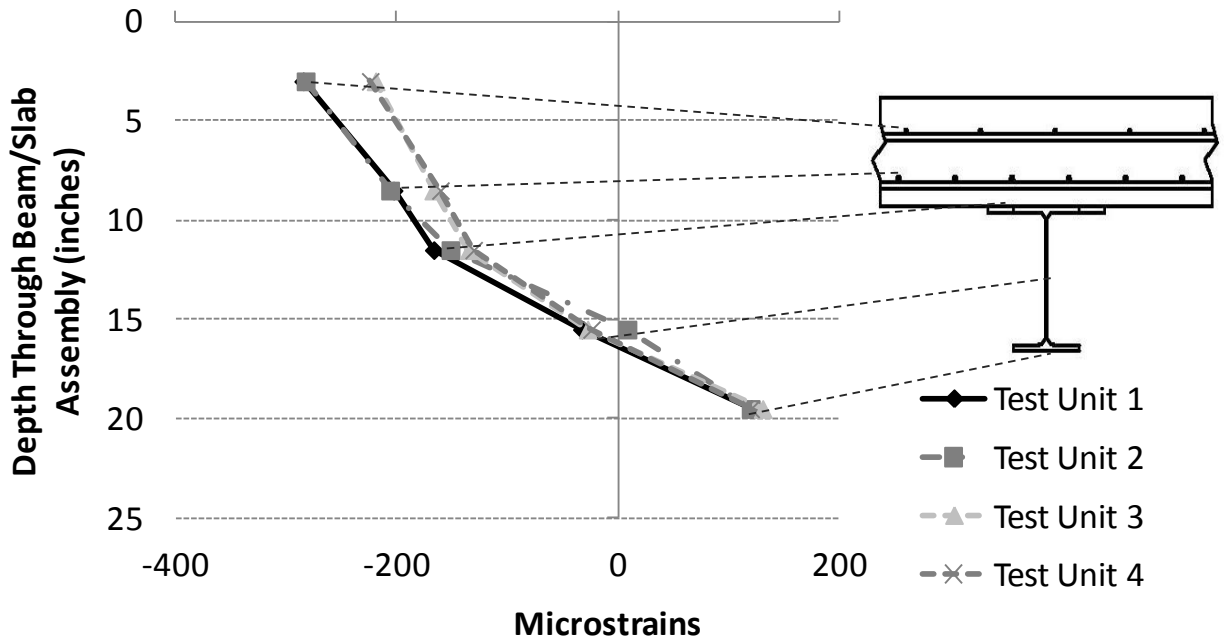


**Figure 129.** Longitudinal Strains through the depth of the beam/test unit section

### **5.4.3 Discussion**

#### *5.4.3.1 Validation of Computer Modeling Approach*

As shown in Figure 110 to Figure 119, the computer model data correlated reasonably well with the experimental data. In general, the computer model data slightly over-predicted the deflection outputs, while it slightly under-predicted the strain data.

The computer modeling approach did not take into account the spike in strains and deflections caused by the expansion of the concrete due to the heat of hydration. Instead, the model assumed zero loading during the initial seven-day wet cure, followed by the temperature loads to simulate drying shrinkage (see Figure 108). After the initial spike in strains and deflections due to hydration, most of the experimental data leveled off to around zero, followed by a steady increase/decrease due to shrinkage. The data overall had similar trends/slopes, but different magnitudes. The difference in the magnitudes between the computer simulations and lab data was likely due to assuming that strains and deflections were equal to zero after the hydration period is over. This behavior is especially prevalent in Figure 112. The data matches the best when the experimental readings dropped back to zero following the initial spike due to hydration. This can be seen in Figure 114.

Overall, the computer model data matched reasonably well with the experimental data. The data followed the same trends and were close to the same magnitude. The biggest discrepancy is likely due to the absence of modeling concrete hydration, as this creates an initial jump in some of the strain data. Other reasons for the discrepancy could have been due to small changes in the lab ambient temperature not being taken into account, friction behavior at the pin supports, and other areas where the computer modeling simplified actual experimental behavior. Despite the discrepancies, the computer modeling approach was shown to be valid, and comparing to the experimental data proved the approach and implementation was valid. Since the ring test and test unit slab data matched with the experimental data, the computer modeling approach was justified to be applied to the parametric study on full bridge models.

#### 5.4.3.2 *Effects of Design Parameters at the Sub-assembly level*

While the overall trends and effects of design parameters at the sub-assembly level can be evaluated using the lab shrinkage test unit models, their effect on the cracking potential for full jointless bridges are evaluated using the parametric study on full bridge models.

In general, the reinforcing steel top and bottom mat strains were very similar for test units 1 and 2, and also test units 3 and 4. The rebar strains in test units 1 and 2 were overall higher than the rebar strains in test units 3 and 4. Test unit 3 most likely had lower strain values since it had a denser reinforcement configuration, and test unit 4 most likely had lower strain values since it had a lower-shrinkage concrete mix. It was expected that test units 1 and 2 would have similar reinforcement strain gage behavior, since they had the same concrete mix and reinforcement arrangement. For the strains in the top flange, test unit 2 had the lowest values. This was likely due to the added restraint caused by the denser shear stud configuration. Test units 1 and 3 had similar top flange strain values, while test unit 4 had lower values due to the lower-shrinkage mix. The strains in the web were nearly zero for all of the test units. For the bottom flange strains, test unit 4 had the lowest values, while test unit 1 had the highest values. This was likely because test unit 1 had the least amount of overall restraint with the regular Grade D mix, while test unit 4 had the low-shrinkage mix.

In looking at the strain data through the depth of the test units, it can be seen that both mats of steel underwent compression, while the beams behaved in positive bending, with compressive strains on the top flange, nearly zero strains in the web, and tensile strains on the bottom flange. The compressive strain in the reinforcing steel was due to the pure compression caused by the shrinkage of the concrete, as well as bending strain induced by the curling of the deck. A schematic of this is illustrated below for test unit 1. Note that all the test units had a similar behavior.

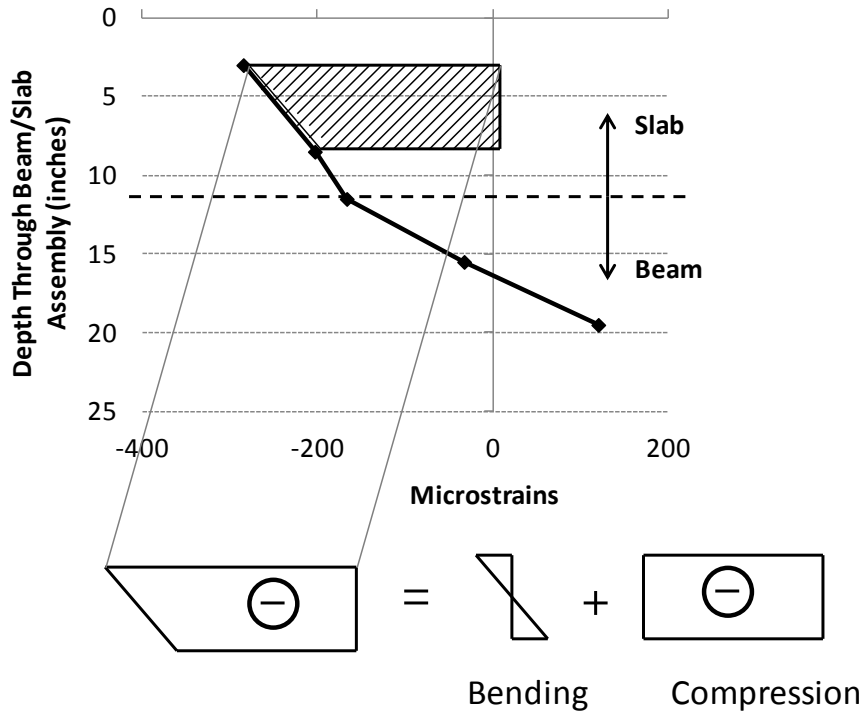


**Figure 130.** Strain behavior through the depth of the slab

As shown, the strains through the depth of the slab are due to a combination of bending and compression. In looking at the strain values, it can be seen that most of the strains are pure compressive, caused by the shrinkage of the concrete. The bending effect due to the curling of the deck has a much smaller contribution. Overall, test units 3 and 4 had a very similar trend, while test units 1 and 2 also had a very similar trend.



## 6 PARAMETRIC STUDY ON FULL BRIDGE MODELS

To evaluate the effect of bridge design factors on restraining concrete shrinkage and producing cracking at the global level, a parametric study was performed on full bridge models. Two types of bridges were studied: one concrete spread box beam bridge (M-57 over US-127) and one steel girder bridge (Kensington Rd. over I-96). These bridges were selected due to their similarity in size and layout, and due to the presence of transverse deck cracking discovered in the field investigation. Elevation and cross-section views of both bridges are shown in Figure 131 and Figure 132, and details for each bridge are summarized in Table 12 and Table 13.

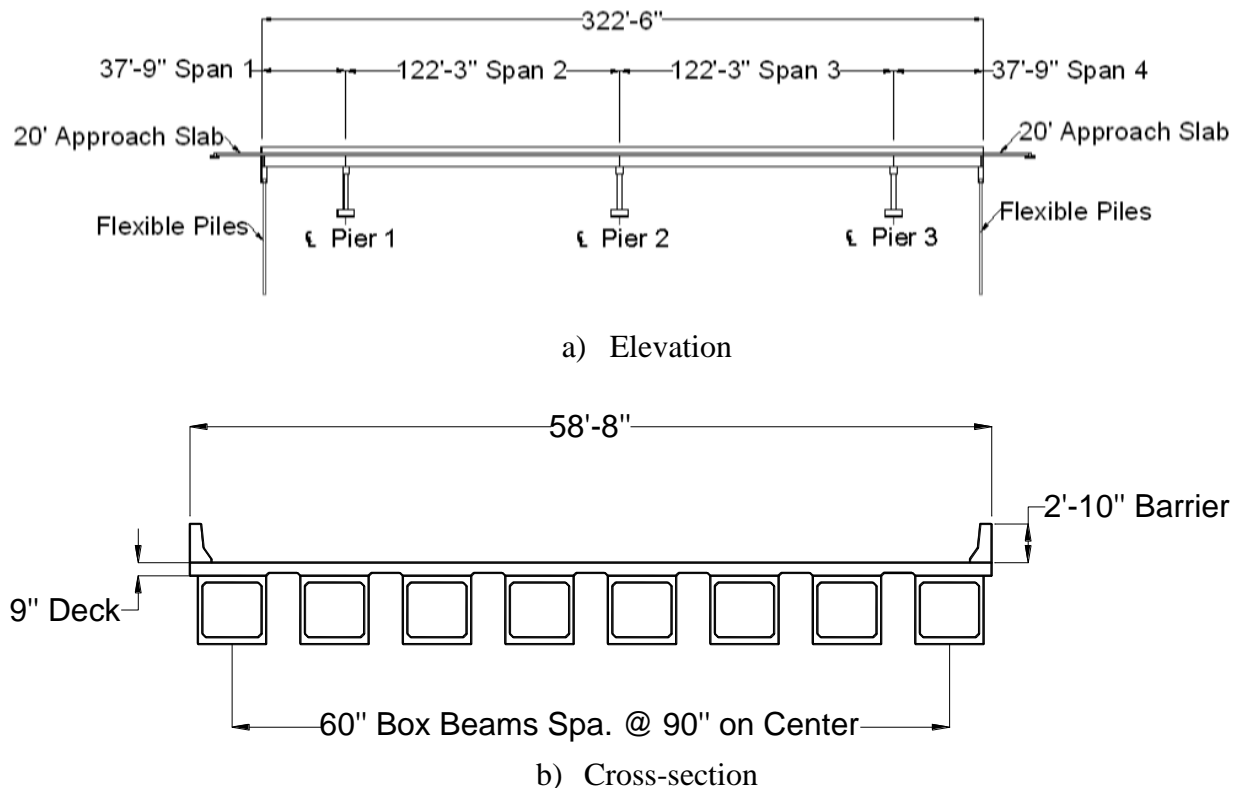
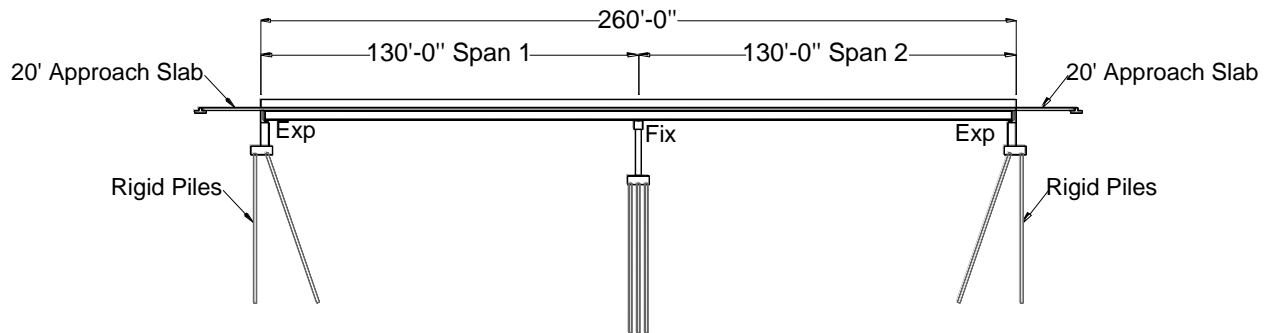


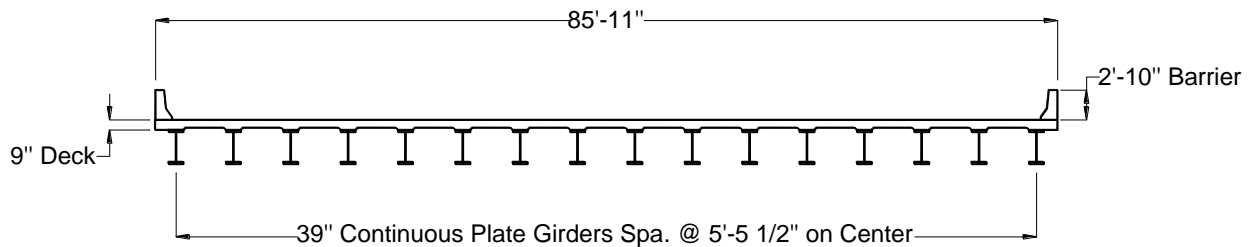
**Figure 131.** Concrete spread box beam bridge (M-57 over US-127) elevation and cross-section [24]

**Table 12.** Concrete spread box beam bridge properties [24]

<b>Beam Type</b>	60'' Prestressed Concrete Box Beams
<b>Beam Spacing</b>	90'' on center
<b>Beam Support Conditions</b>	Simply Supported on Elastomeric Bearings
<b>Number of Spans</b>	Four
<b>Bridge Length</b>	322'-6''
<b>Bridge Width</b>	58'-8''
<b>Abutment Type</b>	Fully Integral, with piles oriented in weak axis bending
<b>Skew Angle</b>	Zero Degrees



a) Elevation



b) Cross-section

**Figure 132.** Steel beam bridge (Kensington Rd. over I-96) elevation and cross-section [23]

**Table 13.** Steel girder bridge properties [23]

<b>Girder Type</b>	39'' Continuous Plate Girders
<b>Girder Spacing</b>	5'-5 1/2'' on center
<b>Girder Support Conditions</b>	Rocker Bearings at abutments, Fixed at the central pier
<b>Number of Spans</b>	Two
<b>Bridge Length</b>	260'-0''
<b>Bridge Width</b>	85'-11''
<b>Abutment Type</b>	Fully Integral, with rigid piles oriented in strong axis bending
<b>Skew Angle</b>	22 Degrees

### 6.1 Parameters Considered

Each bridge was analyzed using *ABAQUS*, and the cracking potential was determined for various design parameters. The following design parameters were investigated:

- Reinforcement density/distribution
- Shear connector density
- Girder and diaphragm axial stiffness
- Skew angle
- Abutment Details (Integral vs. Non-Integral)
- Concrete mix (standard D mix vs. modified D mix)

The parameters were studied by running several analyses for each full bridge model, with each analysis containing a different design parameter. The analyses run are summarized below in Table 14. The stress output and cracking potential was extracted for each analysis, which are used to develop overall recommendations and conclusions for the research.

**Table 14.** Analyses run for full bridge parametric study

<b>Bridge Type</b>	<b>Analysis Type</b>	<b>Parameter Studied</b>
Box Beam	As-built	Overall bridge performance
Box Beam	Different reinforcement configuration	Effect of keeping same reinforcement ratio, different configuration
Box Beam	Denser reinforcement configuration	Effect of increasing the reinforcement
Box Beam	Low-shrinkage	Effect of using the low-shrinkage slag mix
Steel Girder	As-built	Effect of girder and diaphragm axial stiffness
Steel Girder	Shear connector spacing	Effect of changing the spacing of shear connectors
Steel Girder	Abutment Detail	Effect of changing abutment connection from integral to non-integral
Steel Girder	Skew	Effect of changing the skew angle

## **6.2 Loading method**

### *6.2.1 Shrinkage loading*

The loading method utilized to simulate concrete shrinkage is the same method described and validated in Sections 5.1 and 5.2. Shrinkage is simulated through time-dependent negative temperature loading applied to the exposed concrete surfaces. A uniform average relative humidity value was assumed for the entire analysis process. The overall average was taken for humidity values in Lansing and in Detroit for the months of May through October, during which deck casting would most likely occur. Humidity values were obtained from the National Climactic Data Center [26]. The average humidity value calculated for the analyses was 71%. The other values that were implemented to calculate the shrinkage loading are summarized in Table 15.

**Table 15.** Values used to calculate shrinkage load temperatures

Parameter	Value
Wet Cure Time	7 days
Percent Relative Humidity	71% (calculated average value for lower Michigan)
Deck Volume/Surface Area	1.2 inches
Barrier Wall Volume/Surface Area	5.7 inches
Cement Content (Grade D Mix)	658 lb/yd <sup>3</sup>
Cement Content (Low Shrinkage Mix)	461 lb/yd <sup>3</sup>
Slump	4.5 inches
Fine Agg./Total Agg. Percentage	41%
Air Content	6.5%

Using the values noted in Table 15,  $(\epsilon_{sh})_u$  (Equation 5-2) was calculated to be 514 microstrains for the deck, and 299 microstrains for the barrier wall. These values varied slightly for the low-shrinkage mix. Plots of the temperature load applied for the deck and barrier walls in the full bridge models are shown below. Note that these values are different with the low shrinkage mix.

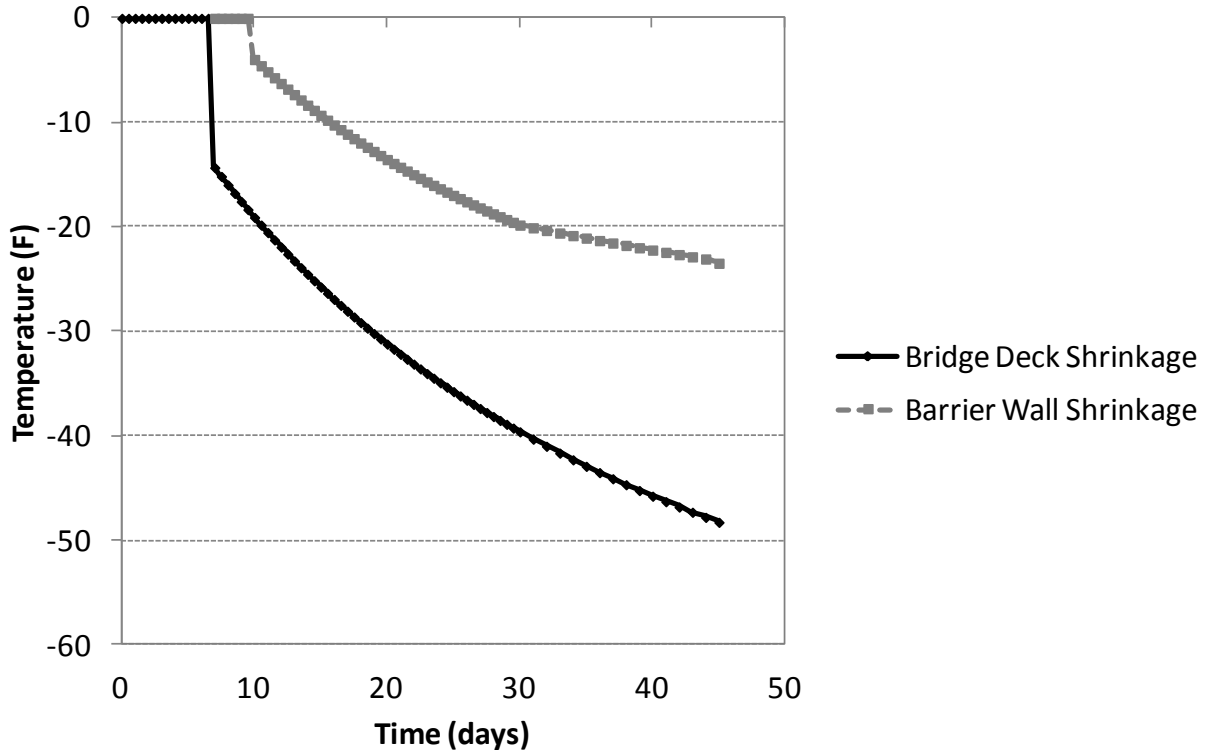


**Figure 133.** Shrinkage load temperature values for bridge deck and barrier wall (standard mix)

### 6.2.2 Gravity/self weight loading

Gravity loading and the effects of self-weight were ignored in the computer modeling. The reasoning behind this was because the camber of the beams and girders would account for the deflections due to self-weight and bridge dead load. Since early-age shrinkage is the parameter of interest, the effects of traffic loading were also able to be neglected.

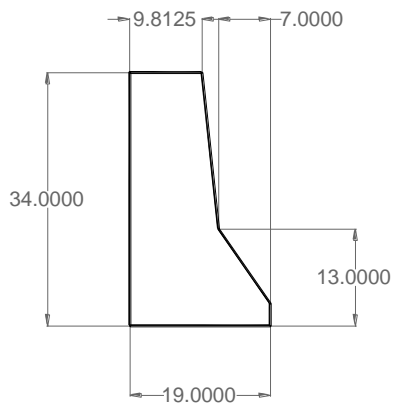
### 6.2.3 Pour sequencing

Pour sequencing is an important parameter affecting bridge deck performance, and was included in the modeling. While the exact pour sequences vary for different bridge plans, MDOT has specified that positive moment regions be cast 24 hours prior to negative moment regions [25]. This is implemented to reduce the amount of negative moment that is induced by pouring over the supports. Shrinkage will begin to occur in the region of the first pour one day prior to shrinkage in the second pour, after the seven-day wet curing period. Therefore, pour sequencing was implemented in the computer models using the ‘model change’ feature in Abaqus [35]. The sections of the bridge deck were partitioned into different segments to account for the different pour sequence regions. The elements associated with the second pour were then de-activated until one day after the first pour.

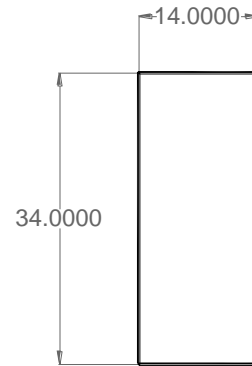
### 6.2.4 Concrete barrier walls

In Michigan, concrete barrier walls are typically cast immediately after the seven-day wet cure for the decks [25]. At this time, the deck concrete has cured sufficiently and gained enough strength to handle the load of the barrier walls. Like the deck, the walls are cast continuously, with expansion provided at the two ends of the bridge. Since barrier walls are cast during the early-age time region of interest, they were included in the modeling. To simplify the mesh, the actual barrier wall cross section was simplified to a rectangular section, as shown below in Figure 134.

Again, the ‘model change’ feature was utilized to implement the barrier wall elements after the initial seven-day wet cure. Shrinkage was assumed to commence at a time of three days, when the forms would be removed.



a) Original (per plan) Dimensions



b) Equivalent Dimensions used in Computer Modeling

**Figure 134.** Barrier wall equivalent rectangular cross section [23]

### 6.2.5 Concrete/soil friction at approach slabs

Since the approach slab is cast monolithically with the bridge for both the box beam bridge and the steel girder bridge, the friction between the approach slab surface and approach fill has an effect on the bridge restraint, and needed to be accounted for in modeling. The connection detail is shown below in Figure 135.

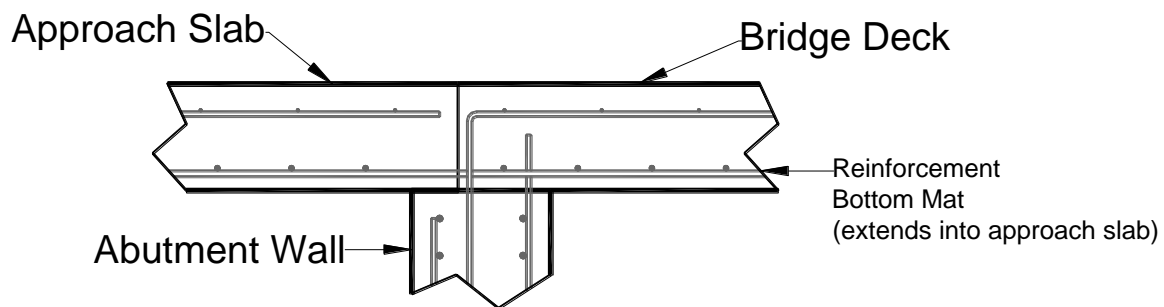


**Figure 135.** Typical approach slab connection with bridge deck [25]

This was implemented by using a series of nonlinear springs at the bottom of the deck slab. The springs spaced at two-foot increments, and were modeled using a nonlinear force-displacement response. The force-displacement behavior was determined as follows.

$$\text{Slab Weight} = \gamma_{\text{concrete}} * (w * L * t) \quad (6-1)$$

where  $\gamma$  is the unit weight of concrete (taken to be 145 pcf),  $w$  is the width of the strip in consideration (taken to be 2'), and  $t$  is the slab thickness (taken to be 0.75'). The friction force due to the weight of the slab is shown below.

$$F_{friction} = \mu * Slab Weight \tag{6-2}$$

Here, the coefficient of friction,  $\mu$ , between the concrete and approach fill was taken to be 0.6. Note that this relationship assumed that the soil was densely compacted for the approach fill. Solving for equations 6-1 and 6-2, the friction force for each 2'-wide segment was calculated to be 2,610 lbs.

Once the friction force was determined the soil spring curve was able to be developed. A non-linear force-displacement relationship was assumed, where the displacement was zero up to the calculated friction force, after which nearly free deformation can occur. An arbitrary small slope of 0.25 was assigned to the curve after the force exceeded the calculated friction force. The developed spring curve for each 2'-wide segment of the approach slab is shown below in Figure 136.

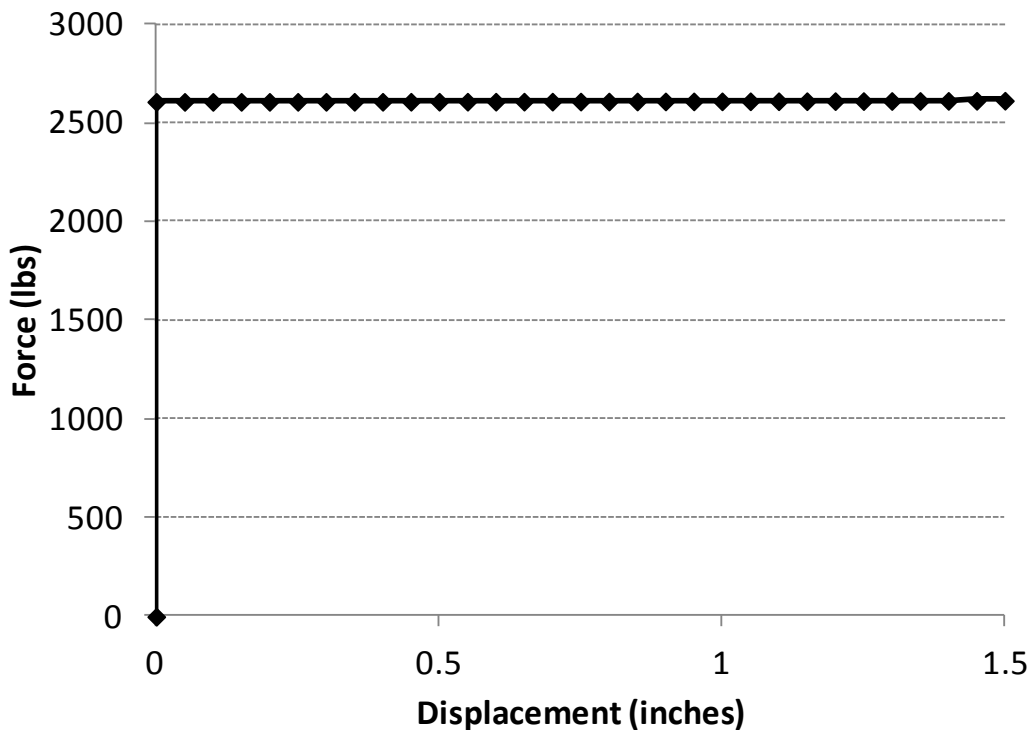


**Figure 136.** Approach slab friction force-displacement curve for each 2'-wide segment



Tabular values from the force-displacement response were applied to the bottom of the deck slab by using the ‘connector builder’ feature in Abaqus. *CONN3D2* elements were applied at various nodal locations, representing the center of each 2’-wide strip. The force-displacement response was activated for the global Z-direction (bridge longitudinal direction).

### 6.2.6 Soil/structure interaction at the piles

Soil-structure interaction at the piles was modeled through nonlinear soil springs with varying force-displacement responses for different depths. Piles were considered to be 50’-deep as stated in the bridge design plans [24]. The natural soil properties were assumed to vary from ‘loose’ to ‘dense’ below the abutments. The assumed soil characteristics for each type of soil were obtained from the National Cooperative Highway Research Program design curves [27] and are summarized below in Table 16.

**Table 16.** Assumed soil foundation properties [9][27]

Depth	Friction Angle	Density
0’ to 15’	29 degrees	110 pcf
15’ to 30’	35 degrees	125 pcf
30’ to 50’	40 degrees	140 pcf

From the assumed soil properties, nonlinear force-displacement responses could be developed for varying depths through the soil. The p-y design curves recommended by the American Petroleum Institute were utilized to model soil behavior [4].

$$P = A * p_u * \tanh \left[ \frac{k * H}{A * p_u} * y \right] \quad (6-3)$$

Here,  $P$  is the soil resistance force (lbs),  $A$  is a factor to account for cyclic or static loading (see equation 5-16),  $p_u$  is the ultimate soil bearing capacity at various depths (lbs/in.),  $k$  is the initial modulus subgrade reaction (lb/in.<sup>3</sup>), determined from Figure 6.8.7-1 in reference [4],  $y$  is the lateral pile deflection (in.), and  $H$  is the depth below the surface (in.). The ultimate soil bearing capacity,  $p_u$ , varies for shallow depths verses deep depths. It is given as the smallest of  $p_{us}$  and  $p_{ud}$ , shown below.

$$p_{us} = (C1 * H + C2 * D) * \gamma * H \quad (6-4)$$

$$p_{ud} = C3 * D * \gamma * H \quad (6-5)$$

where  $p_{us}$  is the ultimate soil resistance (lb/in) at shallow depths,  $p_{ud}$  is the ultimate soil resistance (lb/in) at deep depths,  $\gamma$  is the soil unit weight (lb/in.<sup>3</sup>),  $H$  is the depth (in.),  $D$  is the average pile

diameter (in.), and C1, C2, and C3 are coefficients determined from Figure 6.8.6-1 in reference [4]. The factor to account for cyclic or static loading, A, is given below.

$$A = \begin{cases} 0.9 \text{ for cyclic loading} \\ \left(3.0 - 0.8 \frac{H}{D}\right) \geq 0.9 \text{ for static loading} \end{cases} \quad (6-6)$$

P-y design curves were developed at 2'-incremental depths along the length of the piles. The developed curves are shown below in Figure 137.

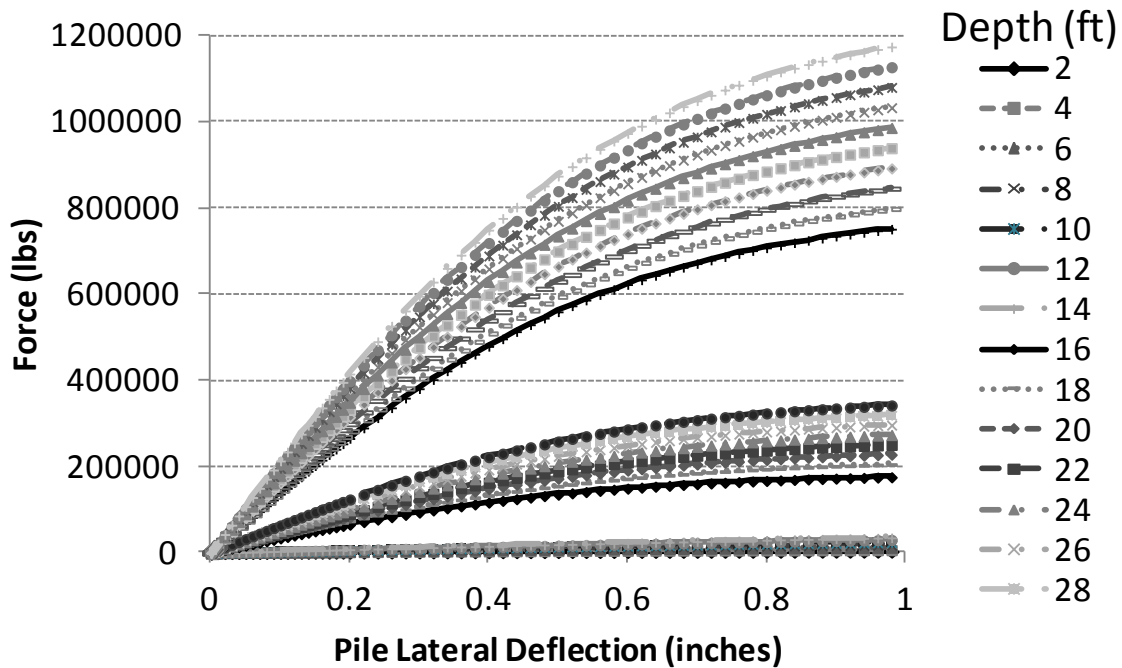


**Figure 137.** P-Y curves for soil/pile interaction

To assess the accuracy of the developed p-y design curves, the pile displacement results for the as-built box beam model was compared to results obtained from reference [9]. In the literature, various temperature values were monitored on a fully-integral bridge in the field, and the pile displacement profiles were developed. The pile lateral displacements are compared below in Figure 138 and Figure 139.

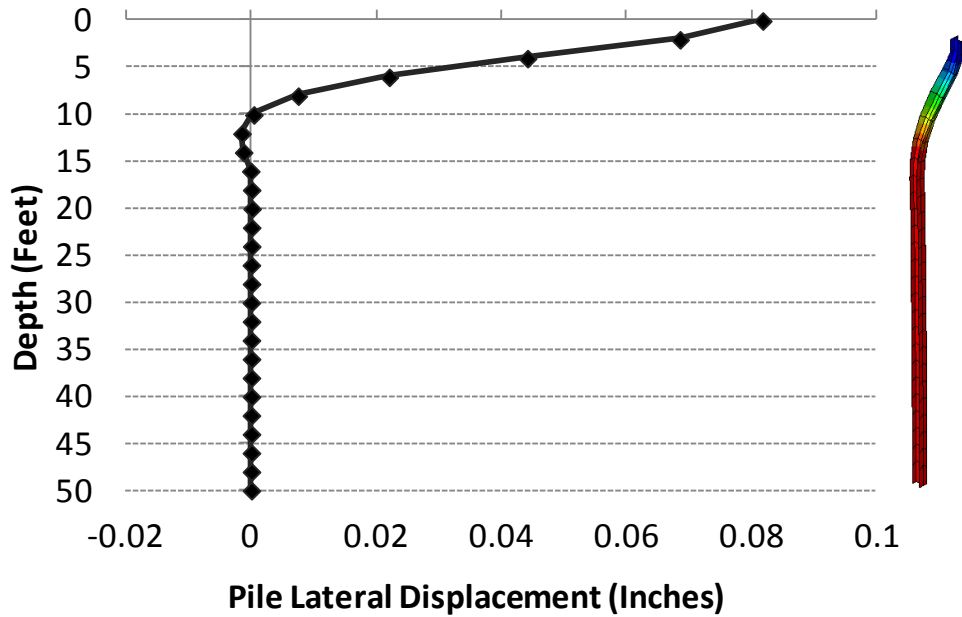


Figure 138. Pile lateral displacement values (as-built box beam model)

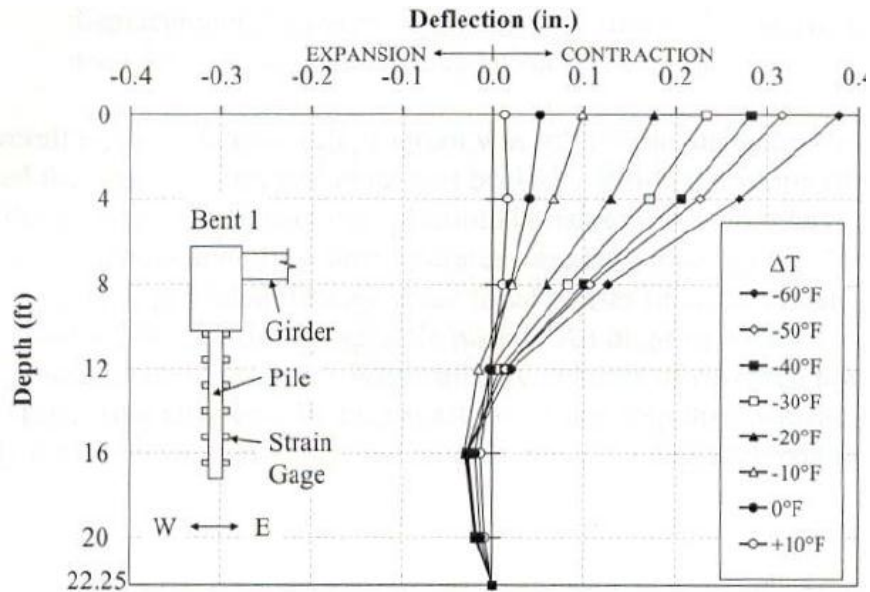
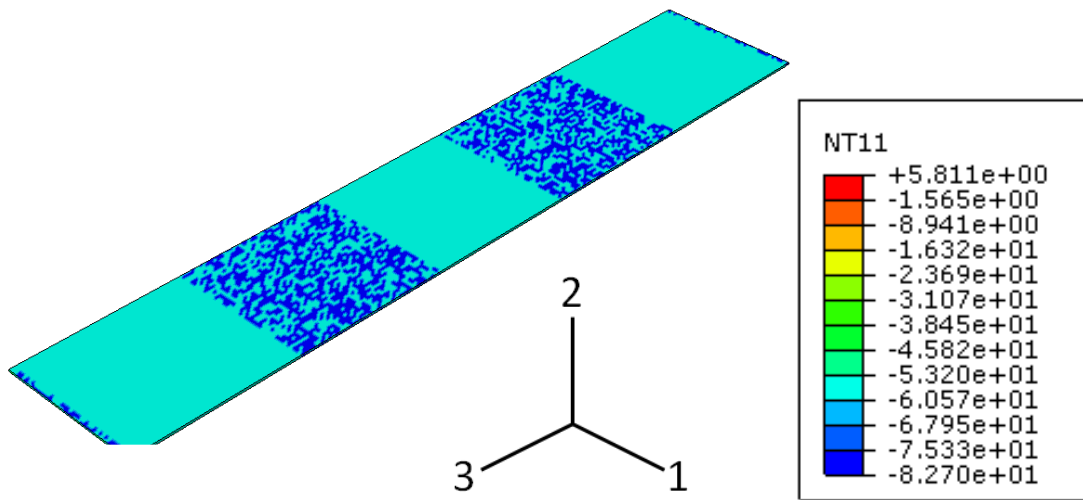


Figure 139. Literature pile lateral displacement values [9]

As shown, the piles experience lateral displacement up to a depth of around 10 feet, after which the piles bend in double curvature, followed by remaining essentially rigid in the deeper soil strata. Since the pile behavior in the computational analysis follows closely with literature values, and has a deflection profile as expected, it can be seen that the p-y curves are correctly implemented.

### 6.2.7 Random load application for full bridge models

As described in Section 5.4.1, it was necessary to investigate a random load distribution for correctly implementing stress concentrations and damage in the deck due to shrinkage loading. With a uniform load application, it was expected that uniform plastic strains would be present throughout the entire deck, and damage would not be concentrated in specified regions. To apply random loading, a code was developed to randomly select half of the nodes in the sets where temperature is applied. These randomly-selected nodes had time-dependent temperature values of 1.5-times larger than the standard temperature according to the ACI 209 equations. It was anticipated that this approach would concentrate stresses randomly throughout the entire model, allowing for areas of restraint to dominate cracking behavior. To determine the accuracy of this approach, it was only utilized for the “first pour” region. Selected outputs are given below in Figure 140 to Figure 142.



**Figure 140.** Deck top temperature values for random load approach (box beam bridge) [35]

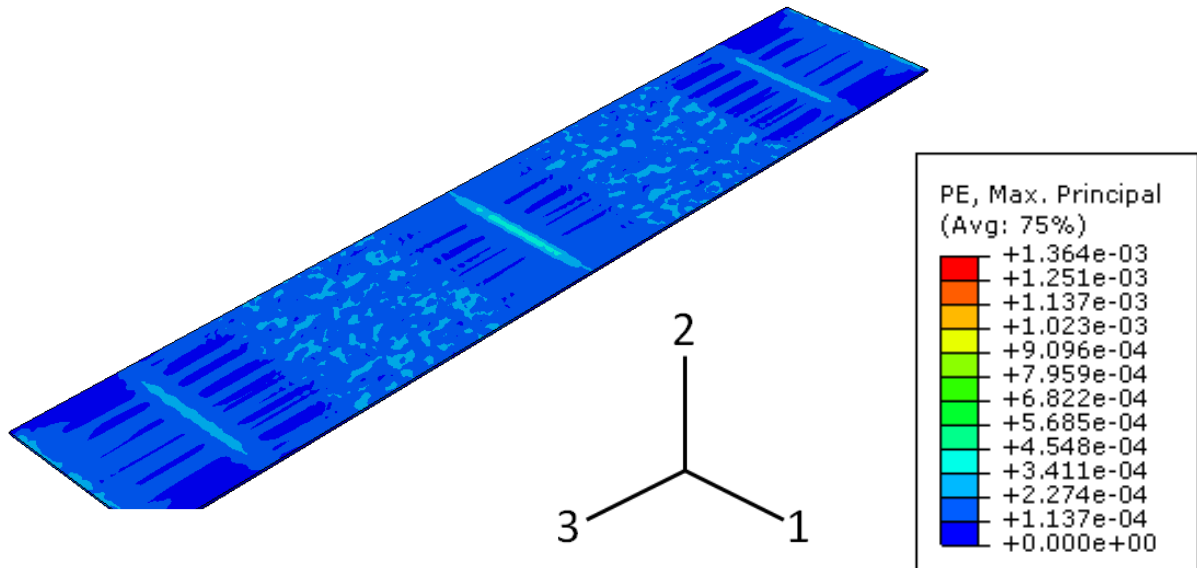


**Figure 141.** Deck max principal plastic strains with random load approach [35]

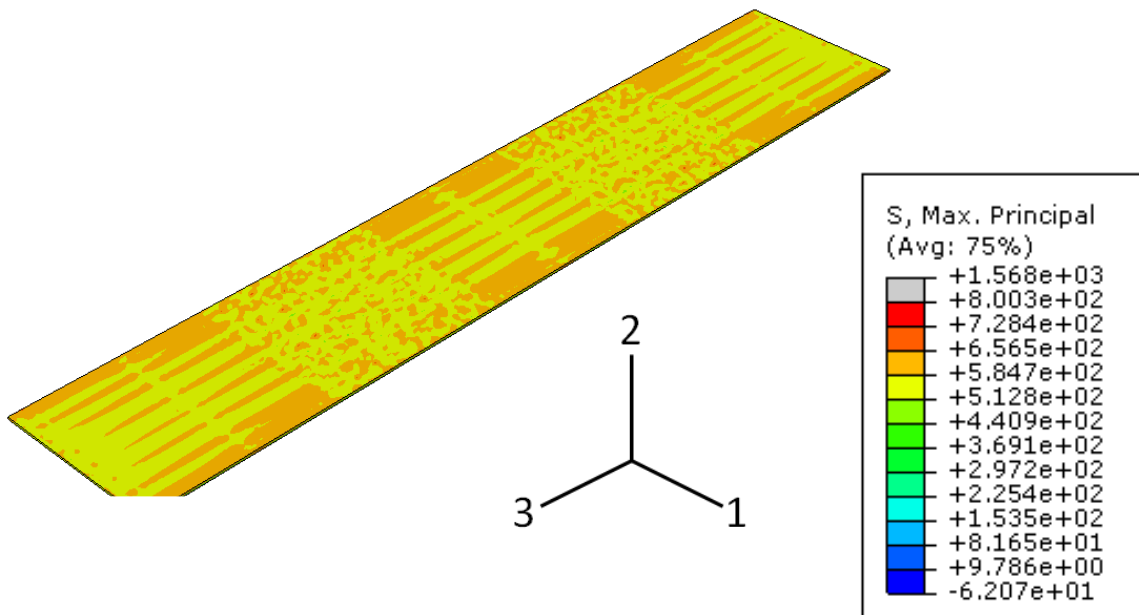


**Figure 142.** Deck max principal stresses with random load approach [35]

As shown, the approach did not produce the results that would be expected. It was thought that the random temperature loading would allow for stress concentrations and cracking in the areas of restraint in the bridge. However, it can be seen that cracking occurs randomly, at the

same locations where the higher temperature values are applied. Instead of the areas of restraint dominating the bridge behavior, the random locations where higher temperature load is applied dominate the behavior. In order to correctly use a random load distribution, each element would have to have a completely different temperature application. The temperatures would need to be applied such that the overall collective average temperature of all the elements followed a normal distribution, with the highest frequency matching the ACI 209 temperature equivalent values. This is illustrated below in Figure 143.

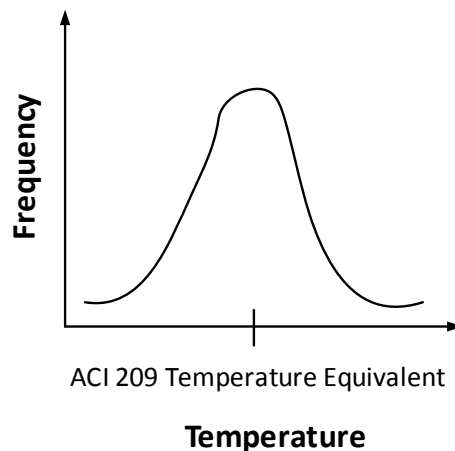


**Figure 143.** Correct random temperature distribution application for bridge slabs

In the approach implemented, half of the elements followed the ACI 209 temperature equivalent, while the other half had higher temperature values. Creating a random temperature distribution that follows a normal bell-curve collectively for all the elements would be very complicated, as each element would require its own set of time-dependent temperature values. While this would be possible to implement, it may still produce incorrect results, and the same random cracking patterns, and would also be time-consuming. Therefore, it was determined to use the uniform temperature application to simulate shrinkage in the full bridge systems. While the uniform application would not yield completely correct results, it could still be utilized for comparison-sake for different design parameters in the parametric evaluation.

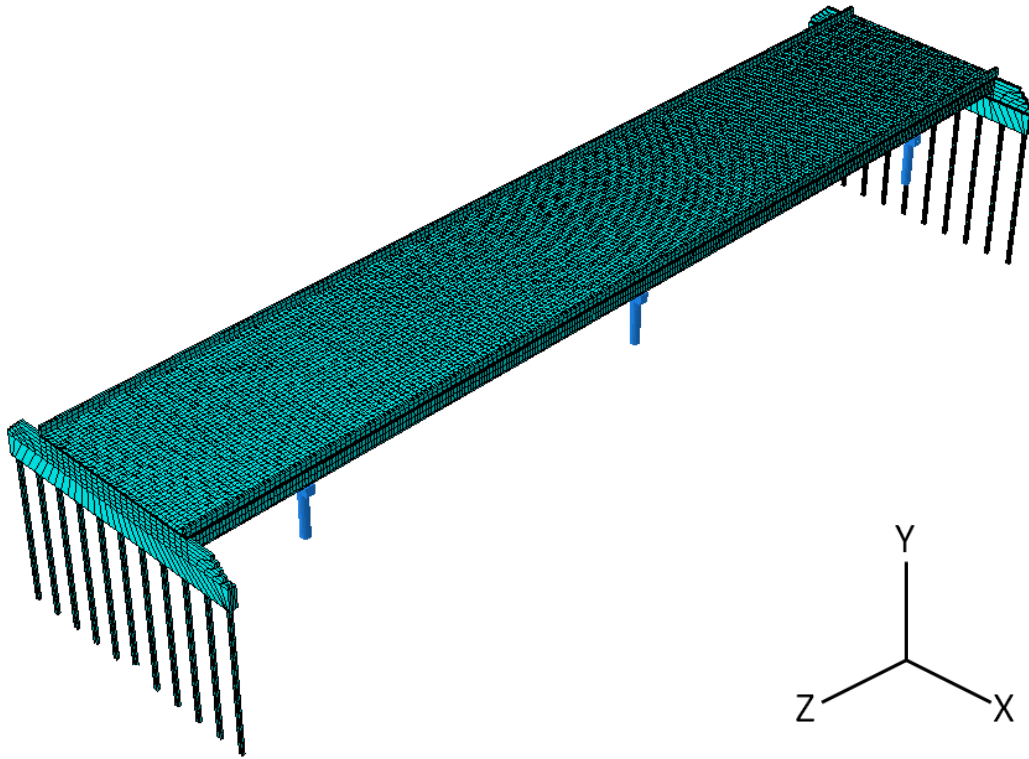
## 6.3 Concrete Spread Box Beam Bridge

### 6.3.1 Parts and element types

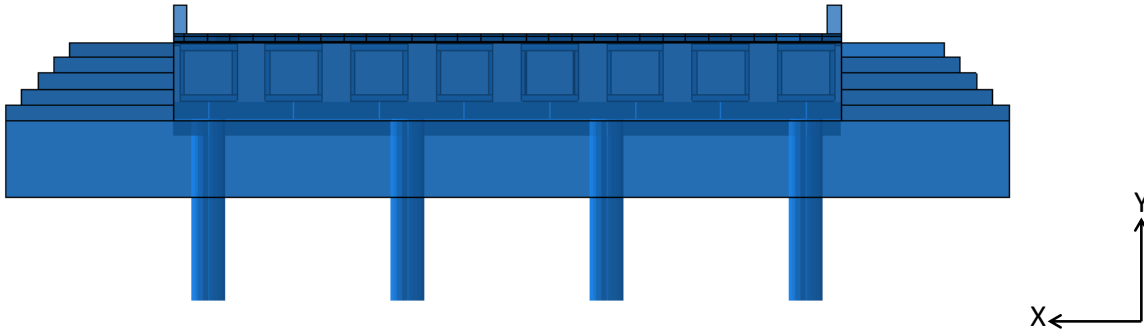
A model was first developed for the concrete spread box beam bridge (M-57 over US-127). The as-built model followed the geometry and design details specified in Figure 131 and Table 12. Separate parts were created for the deck, abutment, piles, box beams, deck reinforcement, and piers. The element types utilized in the model are summarized below in Table 17. The elements were meshed so that the global element size was 20". Overall views of the model are shown below in Figure 144.

**Table 17.** Element types utilized for concrete box beam bridge

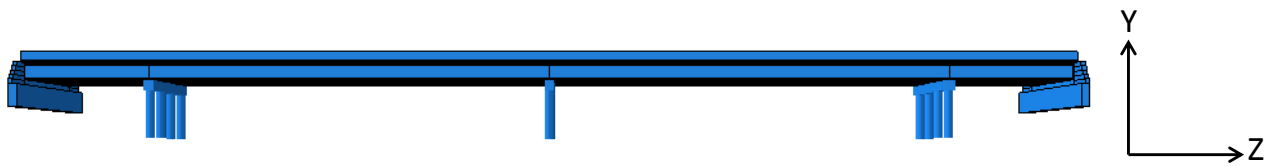
<b>Part</b>	<b>Element Type</b>	<b>Abaqus Element Designation</b>	<b>Mesh Size</b>
Concrete Deck and Barrier Wall	3D Thermally-Coupled Solid Brick	C3D8T	6 elements through depth
Box Beams	3D Thermally-Coupled Solid Brick	C3D8T	1 element through thickness, 3 elements through the depth
Abutment	3D Thermally-Coupled Solid Brick	C3D8T	2 elements through thickness, 6 elements through height
Piles	2D Shell	S4R	25 elements through height
Reinforcement	2D Shell, with 'Rebar Layer' Option	S4R	Global element size of 20"
Piers	1D Beam	B31	8 elements through column height



a) Isometric view of meshed assembly



b) End view (piles not shown)



c) Elevation view (piles not shown)

**Figure 144.** Concrete box beam bridge overall views



### 6.3.2 Concrete box beam equivalent section

In lieu of modeling the actual reinforcement in the concrete box beams, the beams were modeled by using the equivalent stiffness of the concrete/steel composite beam. The calculation for the equivalent stiffness involved calculating the transformed section modulus of elasticity and moment of inertia, as outlined below.

$$E_{transformed} = \left( \frac{A_c}{A_{tot}} * E_c \right) + \left( \frac{A_s}{A_{tot}} * E_s \right) \quad (6-7)$$

Here,  $E_{transformed}$  is modulus of the transformed section (psi),  $E_c$  is the concrete modulus of elasticity (psi),  $E_s$  is the steel modulus of elasticity (psi),  $A_c$  is the concrete area (in.<sup>2</sup>),  $A_s$  is the steel area (in.<sup>2</sup>), and  $A_{tot}$  is the total area (in.<sup>2</sup>).

**Table 18.** Concrete box beam transformed section moment of inertia calculation

	$n (E_s/E_c)$	$A$ (in. <sup>2</sup> )	$n*A$ (in. <sup>2</sup> )	depth (in.)	$d*n*A$	$I_{section}$ (in. <sup>4</sup> )	$y_{bar}$ (in.)	$y_{bar}^2 * n * A$
Top Steel	6.080988	1.4	8.513382726	3	25.54015	0	-25.8571	5691.981
Bottom Steel	6.080988	9.548	58.06127019	57	3309.492	0	28.14285	45985.69
Concrete	1	1104	1104	30	33120	600768	-1.14285	1441.945
$\Sigma$	-	-	1170.574653	-	36455.03	600768	-	53119.62

The transformed section moment of inertia was calculated according to Equation 6-8 below.

$$I_{section} = \Sigma I_i + \Sigma (A * n * y_{bar}^2) \quad (6-8)$$

This yielded a calculated section moment of inertia of 653,888 in<sup>4</sup>. The beam side thicknesses were changed to 4.5'' (instead of 4'' per plan), and the beam top and bottom thicknesses were changed to 6.75'' (instead of 6'' per plan). This yielded a section moment of inertia of 652,685 in<sup>4</sup>, which is only an error of 0.18%.

### 6.3.3 Constraints, boundary conditions, and other model features

Surface-to-surface tie constraints were implemented to model the connection between the bottom of the deck and the top of the abutment. Node-to-surface tie constraints were also used to model the shear stirrups in lieu of actual embedded truss elements. The elastomeric bearings were modeled using MPC link constraints. This allows for free translation in the longitudinal

direction, and creates rollers at the supports. Embedded region constraints were implemented for the deck reinforcement rebar layers, the beam end embedment into the abutment, and the pile top embedment into the abutment. The piles were oriented such that bending occurs about the weak axis, as stated in the design plans. Connector sections were implemented at locations spaced at 2' along the length of the piles to simulate nonlinear soil response. The force-displacement response followed the developed p-y design curves shown in Figure 137, and activated for the global Z-direction (bridge longitudinal direction). Fully-fixed boundary conditions were applied at the bottom of the pier columns and the bottom of the piles. Additionally, vertical displacements were restrained for the bottom of the abutment, since abutment movement behaves mostly in translation [9][14][17].

#### 6.3.4 Parametric evaluation features

The parametric evaluation for the concrete box beam bridge studied the effects of the low-shrinkage concrete mix and reinforcement arrangement. The design details for each parametric study are summarized below in Table 19. The reinforcement arrangements are summarized in Table 20. Deck reinforcement was implemented using the 'rebar layer' feature.

**Table 19.** Concrete box beam parametric evaluation analyses details

<b>Analysis</b>	<b>Shear Stirrup Spacing</b>	<b>Reinforcement Detail</b>	<b>Concrete Mix</b>
As-built	12''	Detail 1 (see Table 20)	Standard D-mix
Reinforcement Redistribution	12''	Detail 2 (see Table 20)	Standard D-mix
Reinforcement Density	12''	Detail 3 (see Table 20)	Standard D-mix
Low-Shrinkage Mix	12''	Detail 1 (see Table 20)	Low-shrinkage mix

**Table 20.** Concrete box beam reinforcement arrangements

<b>Reinforcement Detail</b>	<b>Top Mat Transverse</b>	<b>Top Mat Longitudinal</b>	<b>Bottom Mat Transverse</b>	<b>Bottom Mat Longitudinal</b>
Detail 1	#5 Spa. @ 9''	#3 Spa. @ 10''	#5 Spa. @ 9''	#5 Spa. @ 9''
Detail 2 (increased by 50%)	#6 Spa. @ 9''	#4 Spa. @ 10''	#6 Spa. @ 9''	#6 Spa. @ 9''
Detail 3 (same $\rho$ )	#6 Spa. @ 12.75''	#4 Spa. @ 18''	#6 Spa. @ 12.75''	#6 Spa. @ 13''

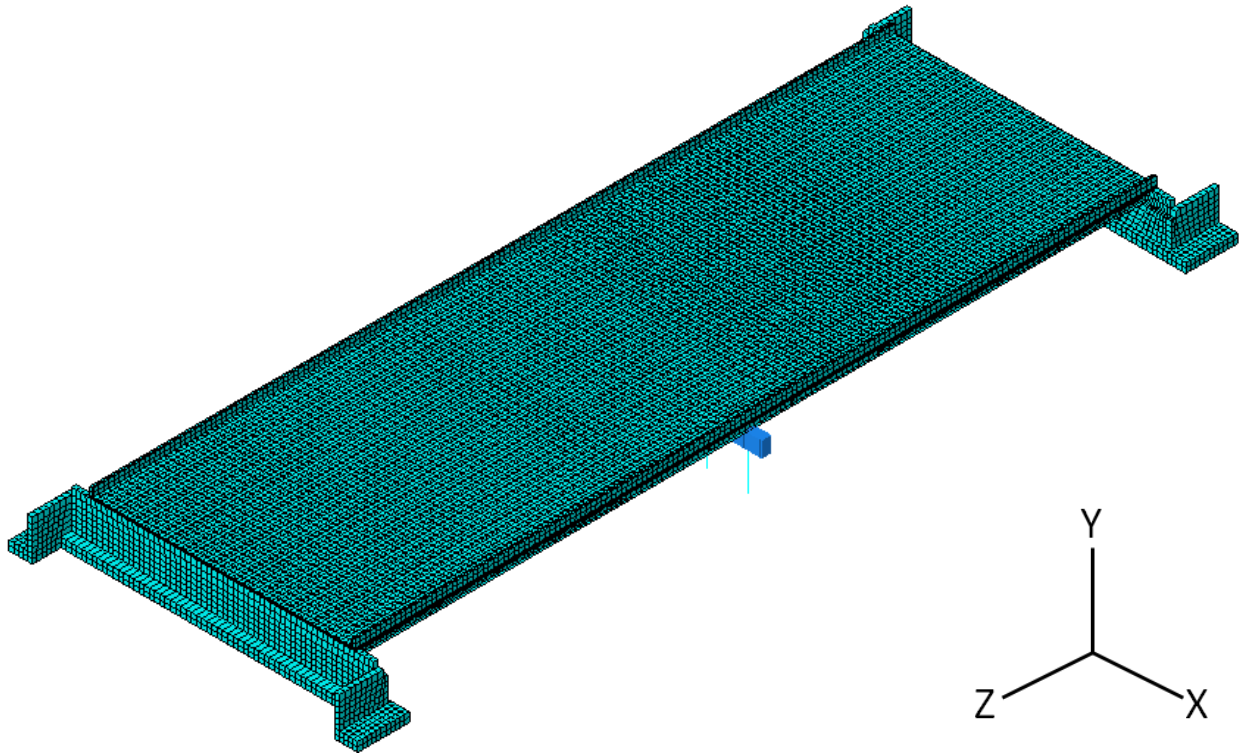
## 6.4 Steel Girder Bridge

### 6.4.1 Parts and element types

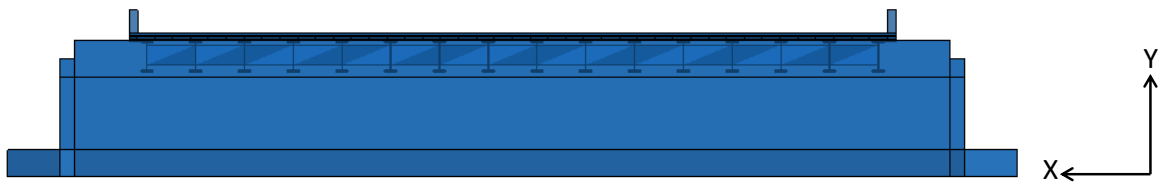
A model was then developed for the steel girder bridge (Kensington Road over I-96). The as-built model followed the geometry and design details specified in Figure 132 and Table 13. Separate parts were created for the deck, abutment, steel girders, deck reinforcement, and piers. The element types utilized in the model are summarized below in Table 21. The elements were meshed so that the global element size was 20''. Overall views of the model are shown below in Figure 145.

**Table 21.** Element types utilized for concrete steel girder bridge

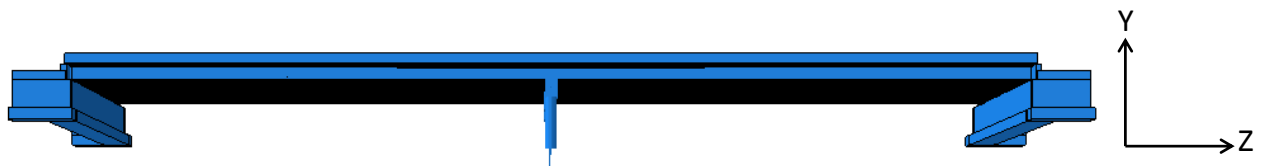
<b>Part</b>	<b>Element Type</b>	<b>Abaqus Element Designation</b>	<b>Mesh Size</b>
Concrete Deck and Barrier Wall	3D Thermally-Coupled Solid Brick	C3D8T	6 elements through depth
Steel Girder	2D Shell	S4R	2 elements through height and width
Diaphragms	2D Shell	S4R	1 element through height and width
Abutment	3D Thermally-Coupled Solid Brick	C3D8T	2 elements through thickness, 9 elements through height
Reinforcement	2D Shell, with 'Rebar Layer' Option	S4R	Global element size of 20''
Piers	1D Beam	B31	8 elements through column height



a) Isometric view of meshed assembly



b) End view



c) Elevation view

**Figure 145.** Concrete box beam bridge overall views

#### 6.4.2 Constraints, boundary conditions and other model features

Surface-to-surface tie constraints were implemented to model the connection between the bottom of the deck and the top of the abutment. Node-to-surface tie constraints were also used to model the shear studs at individual points in lieu of actual embedded beam elements (as used in the laboratory test unit models). The rocker bearings were modeled using MPC link constraints. This allows for free translation in the longitudinal direction, and creates pins at the supports. The fixed bearings at the pier were modeled using MPC rigid constraints. Embedded region constraints were implemented for the deck reinforcement rebar layers and the girder end embedment into the abutment. Fully-fixed boundary conditions were applied at the bottom of the pier columns and at the bottom surface of the abutment footings. Since the piles for this bridge are oriented in strong axis bending, it was assumed that the abutment footing would remain fully fixed, and abutment translation would be restrained.

#### 6.4.3 Parametric evaluation features

The parametric evaluation for the steel girder bridge studied the effects of the girder axial stiffness and diaphragms, shear connector density, abutment type (integral vs. non-integral), and skew angle. The design details for each parametric study are summarized below in Table 22. Note that the Standard Grade D mix was used for all steel girder bridge analyses.

**Table 22.** Steel girder parametric evaluation analyses details

<b>Analysis</b>	<b>Shear Stud Spacing</b>	<b>Skew Angle</b>	<b>Abutment Type</b>
As-built	6'' in positive moment, 2' in negative moment	Zero Degrees	Integral
Shear Connector Density	12'' in positive moment, 2' in negative moment	Zero Degrees	Integral
Abutment Configuration	6'' in positive moment, 2' in negative moment	Zero Degrees	Non-integral
Skew Angle	6'' in positive moment, 2' in negative moment	22 Degrees	Integral

In Table 22 “Integral” refers to the girder ends being embedded into the abutment, while “Non-integral” refers to the girder ends not being embedded into the abutment. This is illustrated in Figure 2.

The deck reinforcement arrangement followed the arrangement specified in the bridge plans, and was implemented using the ‘rebar layer’ feature. The reinforcement configuration is summarized below in Table 23.

**Table 23.** Steel girder bridge reinforcement arrangement

<b>Top Longitudinal</b>	<b>Top Transverse</b>	<b>Bottom Longitudinal</b>	<b>Bottom Transverse</b>
#3 Bars Spa. @ 10’’	#5 Bars Spa. @ 8.5’’	#5 Bars Spa. @ 5’’	#5 Bars Spa. @ 8.5’’

## 6.5 Results

### 6.5.1 Box Beam Bridge Model Overall Results

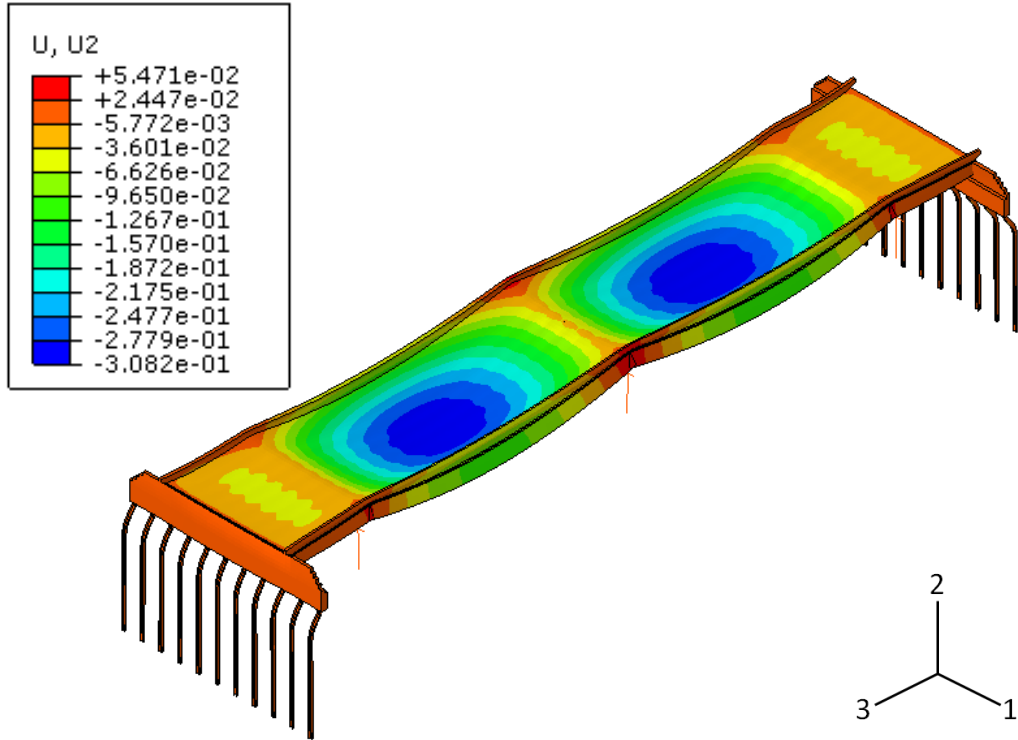
The overall behavior of the box beam bridge was similar for each parametric analysis that was simulated. The bridge deflected shape and vertical displacements for the as-built model are shown below in Figure 146.

As shown, the ends of the bridge move inward, while the two central spans deflect in a “bowl-shaped” pattern. To examine the cracking behavior for the deck, the maximum principal tensile stresses and plastic strain outputs at the end of the analysis were extracted. They are shown below in Figure 147 and Figure 148, respectively.

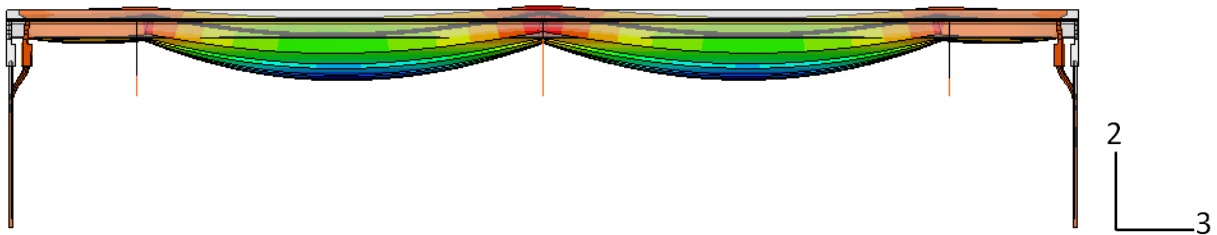
The overall behavior shown in Figure 146 to Figure 148 was similar for all parametric analyses. The regions of damage in the deck can be seen by examining the maximum principal plastic strain output. As shown, most of the damage occurs on the top of the deck, while the bottom of the deck experiences some damage at the piers. The highest levels of damage are concentrated at the piers and the abutment, in the negative moment region. Additionally, damage can be seen in-between the piers, throughout the entire deck. As expected, the stresses are higher in the regions over the beams, and lower in-between the beams. The stresses are lower in regions corresponding to higher plastic strains, indicating softening behavior.

While the maximum principal tensile stress and plastic strain output is able to show overall regions of damage, the directions of cracking are not able to be determined. In order to determine the cracking directions, the plastic strain outputs for the different components needed to be extracted, to derive the direction of the maximum principal plastic strains. Cracking would

occur perpendicular to the direction of maximum principal plastic strains. The plastic strain component outputs at a time of 45 days are shown below in Figure 149 to Figure 152.

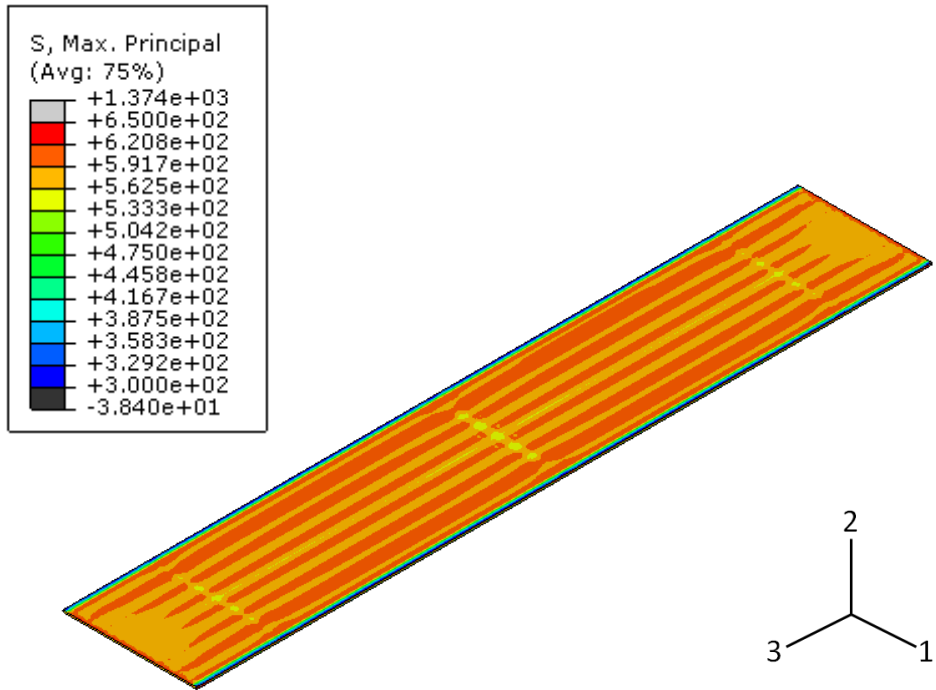


a) Isometric View (deformation scale factor=500)

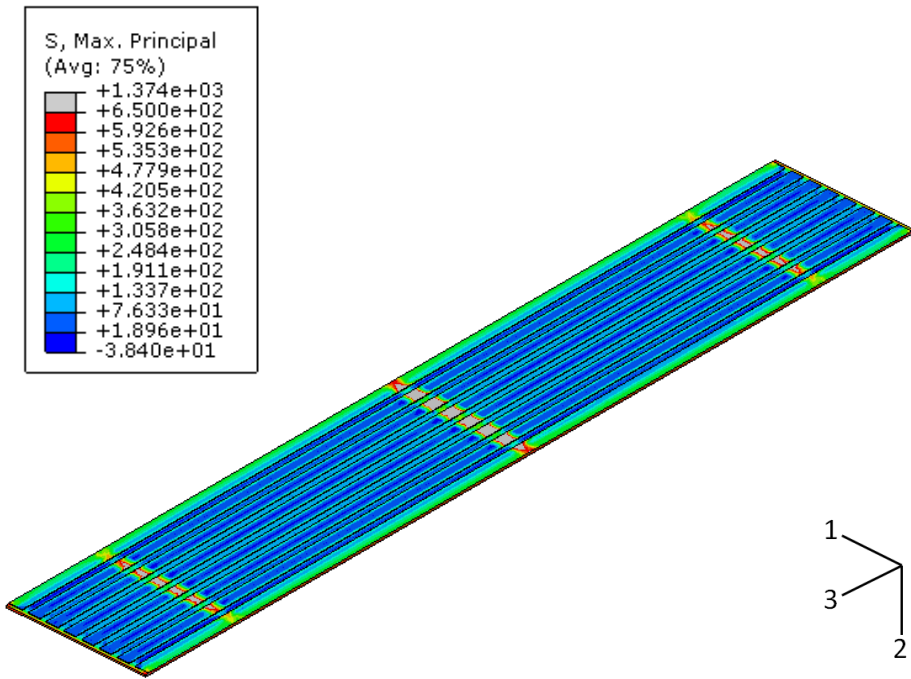


b) Elevation View (deformation scale factor=500)

**Figure 146.** Box beam as-built model deflected shape and vertical displacements (t=45 days)



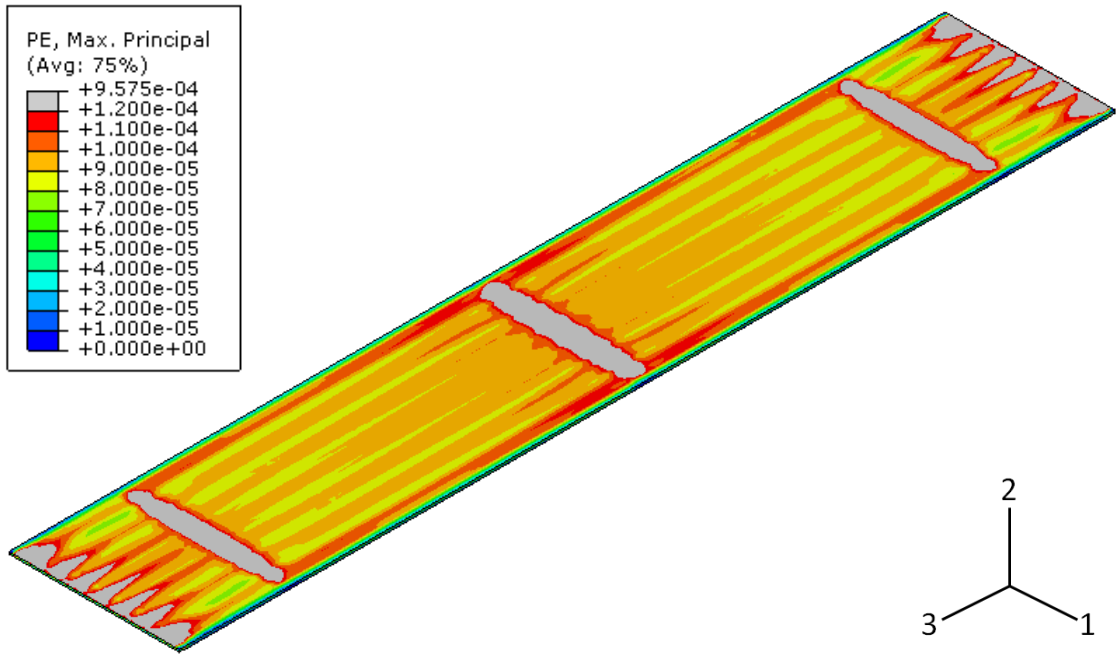
a) Top of Deck



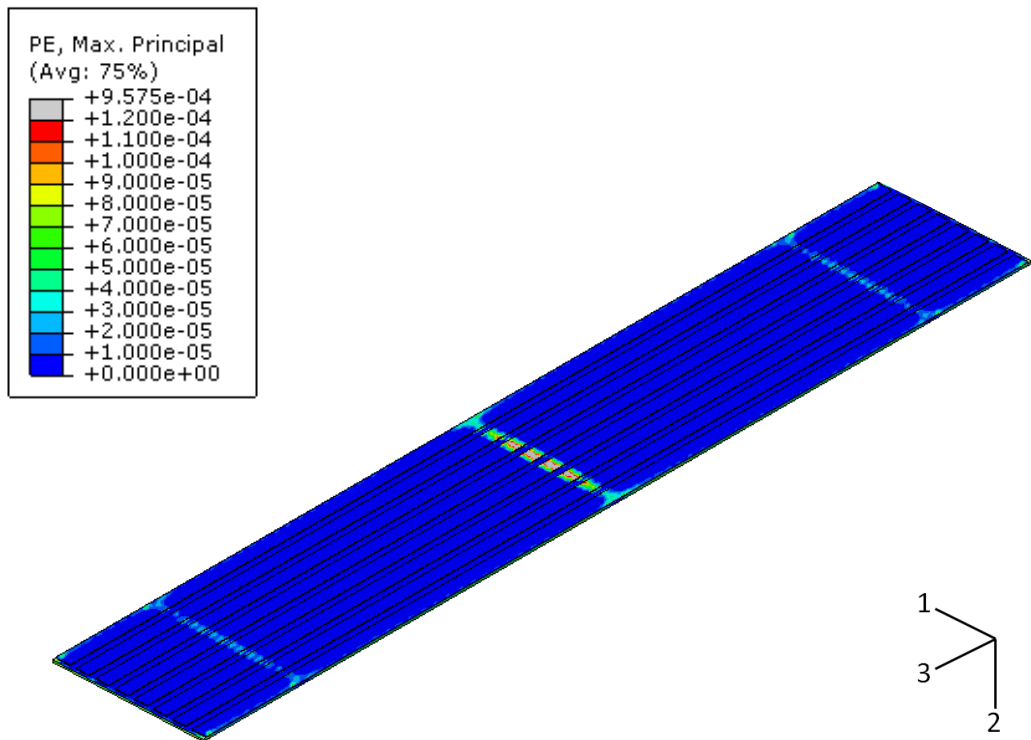
b) Bottom of Deck

**Figure 147.** Box beam as-built model maximum principal tensile stresses (t=45 days)





a) Top of Deck



b) Bottom of Deck

**Figure 148.** Box beam as-built model maximum principal plastic strains (t=45 days)

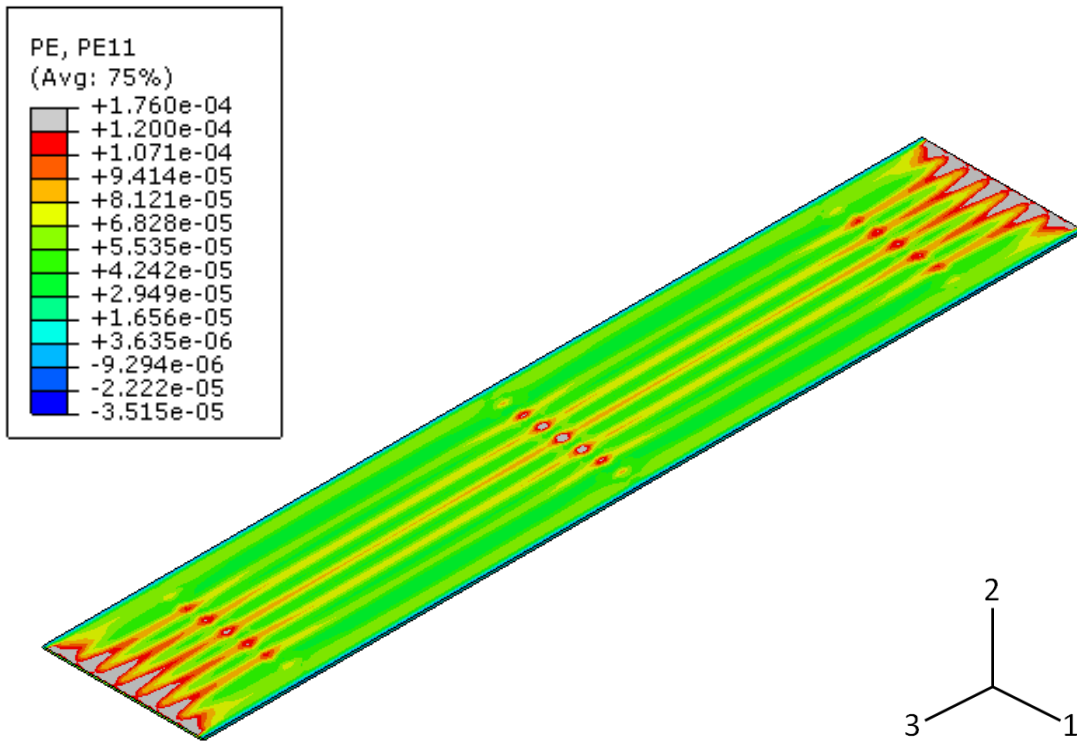


**Figure 149.** Box beam as-built model plastic strain global X-direction (1-1) output

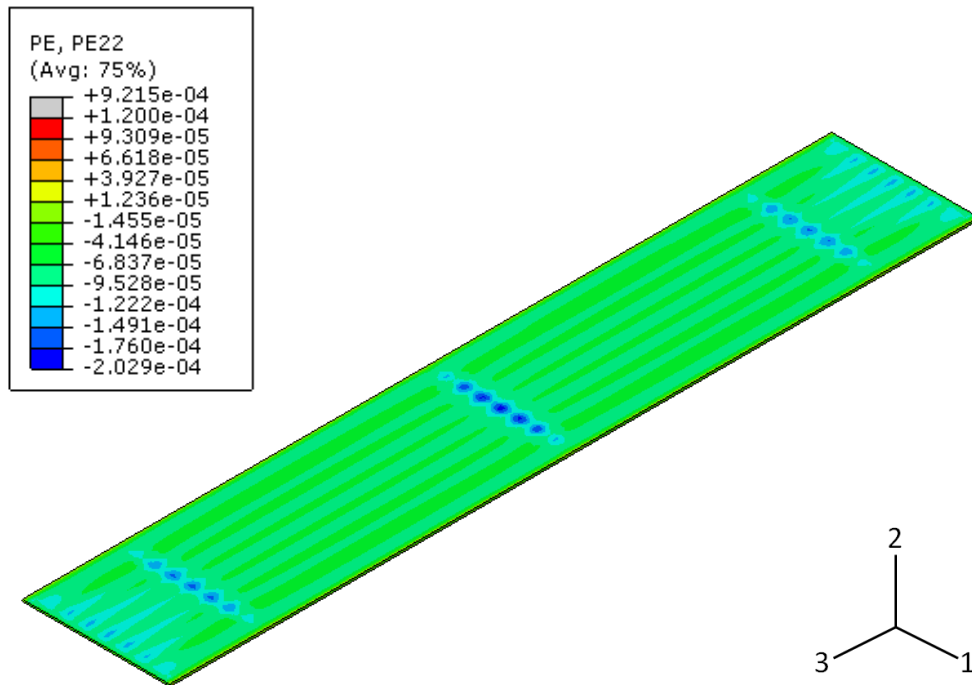


**Figure 150.** Box beam as-built model plastic strain global Y-direction (2-2) output

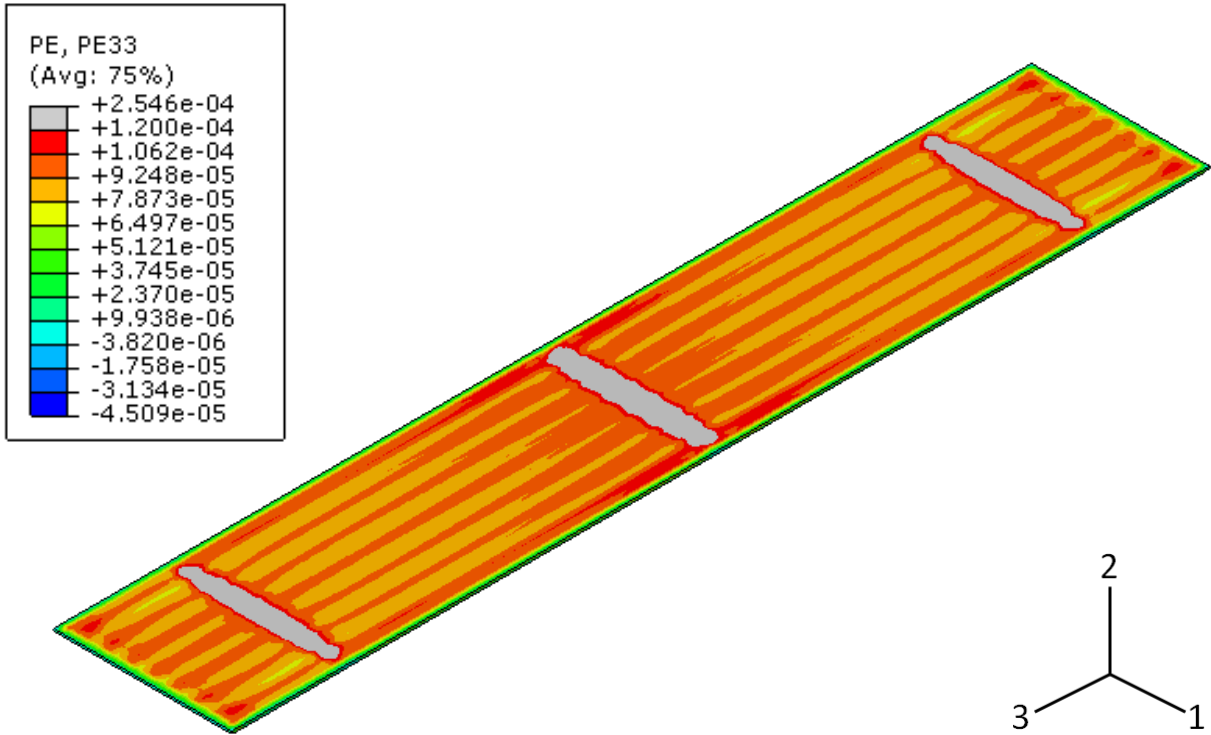


**Figure 151.** Box beam as-built model plastic strain global Z-direction (3-3) output

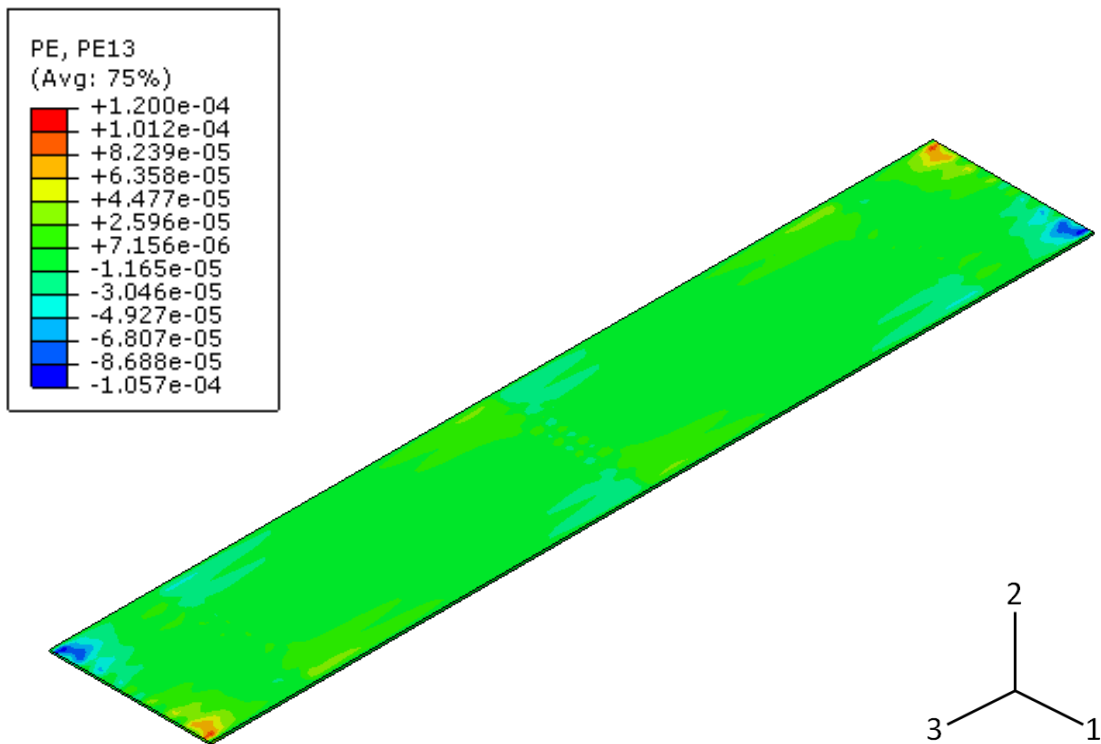


**Figure 152.** Box beam as-built model plastic shear strain (1-3) output

As shown in the results highlighted above, the maximum principal plastic strains are mostly influenced by the longitudinal (PE33) plastic strains in the positive moment regions, and are mostly influenced by the transverse (PE11) plastic strains in the negative moment regions. The vertical plastic strains (PE22) are nearly zero, and therefore do not contribute heavily to the maximum principal plastic strains. It can also be seen that shear strain (PE13) contributes in four corners of the bridge, by the abutment. This is attributed to the additional transverse restraint created by the abutment.

Since cracking occurs perpendicular to the direction of plastic strain, it can be seen that transverse cracking is predicted in the positive moment regions (since the plastic strain is mostly in the longitudinal direction), and both longitudinal and transverse cracking occurs in the negative moment regions, by the piers and the abutment (since the plastic strain is in both the longitudinal and transverse direction). Additionally, the transverse plastic strain output (PE11) predicts longitudinal cracking along the beams, across the entire length of the bridge. There is also a concentration of shear cracking at the corners of the deck, near the abutment, as predicted by the shear strain (PE13) output. These cracking patterns match well with the overall field observations.

To determine overall bridge behavior through time, the vertical displacements, maximum principal stresses, and maximum principal strains were extracted along a longitudinal path in along the middle of the bridge at various times. These outputs are shown below in Figure 153 to Figure 155.

As shown in Figure 153, the overall vertical displacement profile remains the same for each time step, while the magnitudes continue to increase. This is as expected, since the overall deflections increase as the amount of shrinkage increases. The maximum principal tensile stresses continuously grow with time up until the point of cracking, when they decrease due to softening. The tensile stresses are highest in the negative moment regions at the piers and the abutments during the first part of the analysis, after which the tensile stress becomes uniform due to cracking throughout the deck. The plastic strains remain zero up until the point of cracking, where they steadily continue to grow. The negative moment regions over the piers and the abutments experience cracking before the other regions, and have the highest overall plastic strain magnitudes.

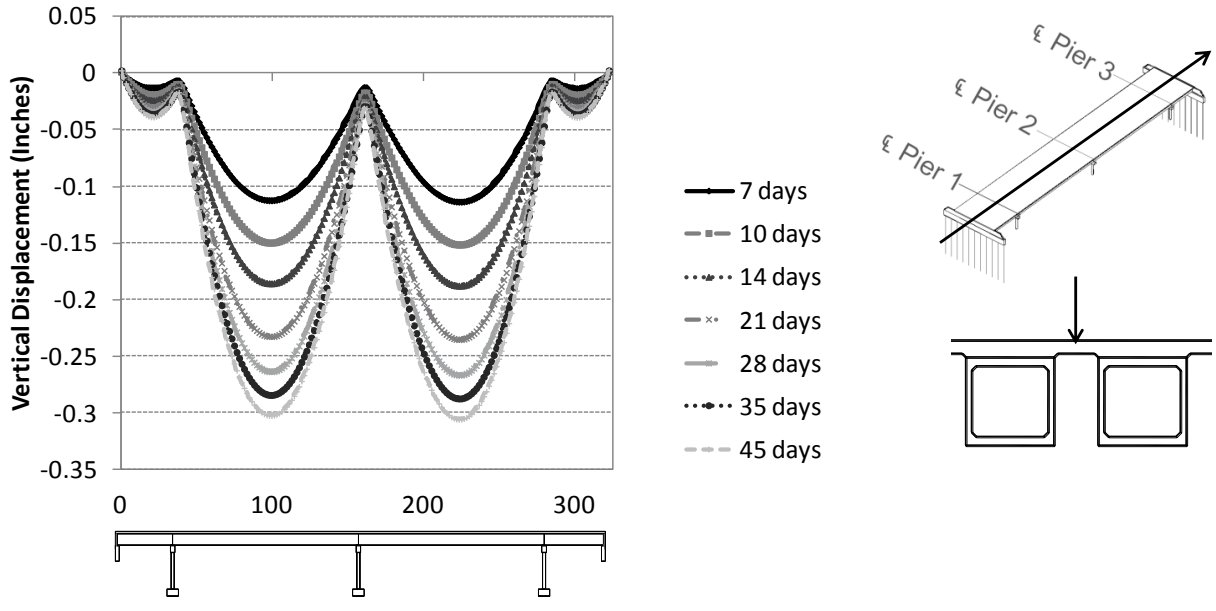


**Figure 153.** Vertical displacement through time in bridge longitudinal direction

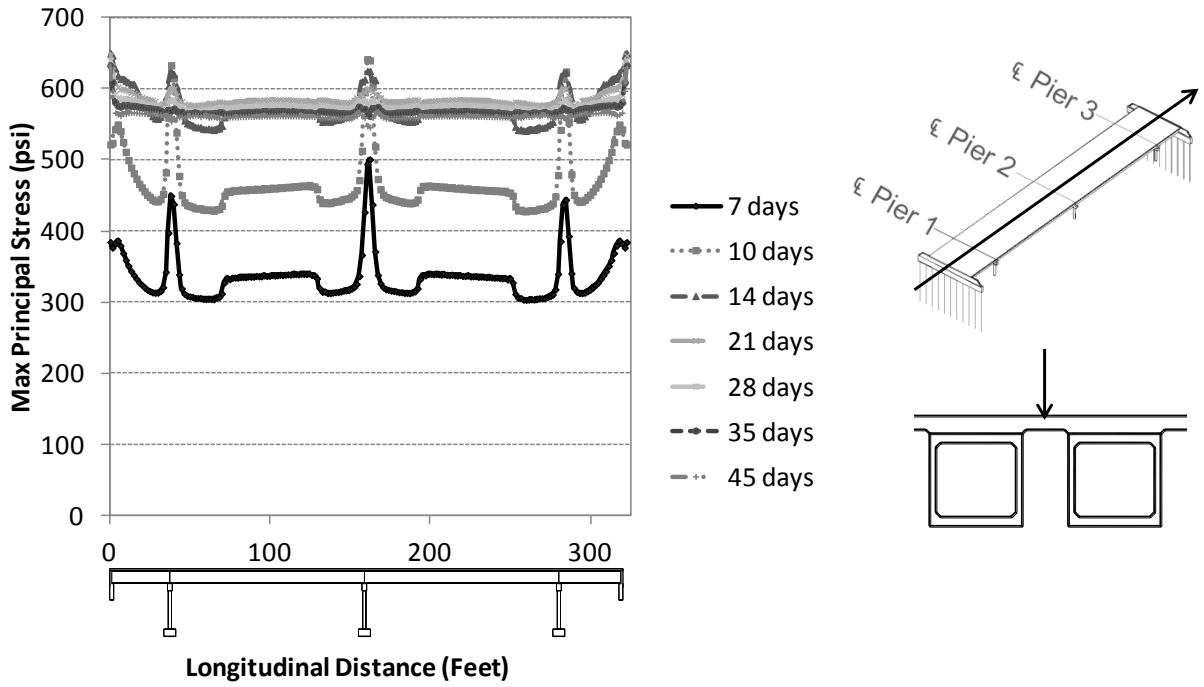


**Figure 154.** Maximum principal tensile stresses through time in bridge longitudinal direction

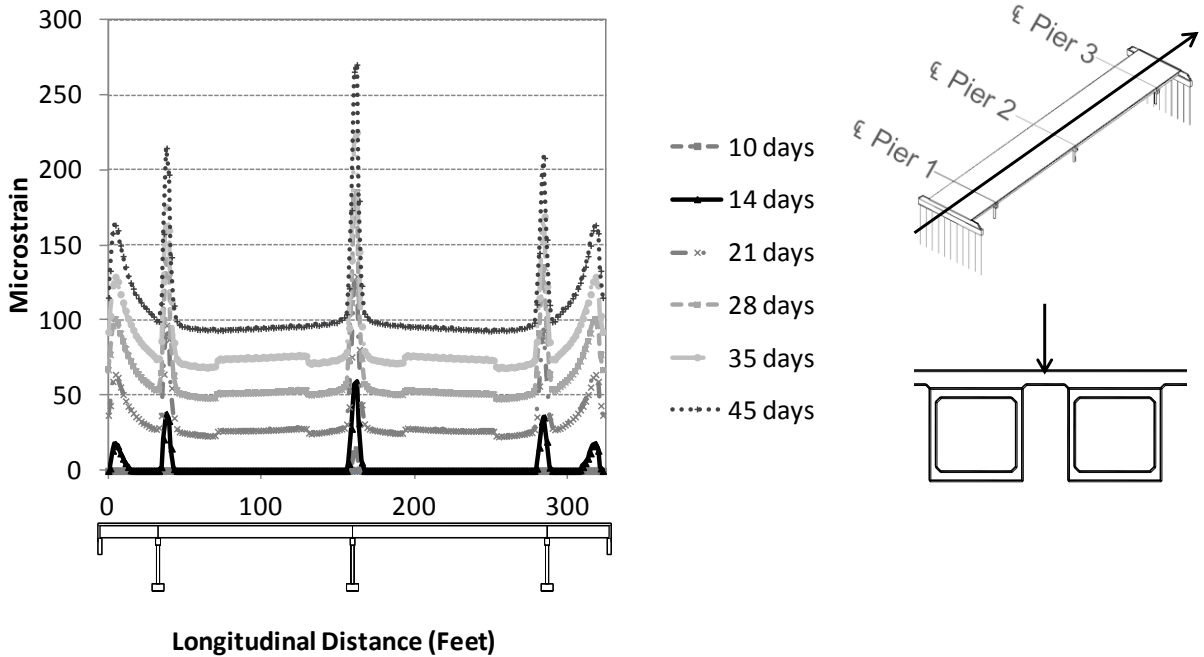


**Figure 155.** Maximum principal plastic strains through time in bridge longitudinal direction

To determine the presence of localization of damage and evenly-spaced transverse cracking, the maximum principle plastic strain outputs were extracted in the positive moment region at the end of the analysis. Jumps in the strain outputs would indicate presence of local cracking. The output is shown below in Figure 156. As shown, there is a steady increase in plastic strains towards the central pier, since that region has more restraint. The jumps in the strain data indicate the presence of localized damage and transverse cracking. The jumps are spaced at 3-5', which is consistent with the spacing of transverse cracks in the field.

The development of maximum principal stresses and plastic strains in the depth through time are shown with full contour plots below in Figure 157 and Figure 158. As shown the maximum principle tensile stresses and plastic strains begin to grow in the negative moment regions near the beginning of the analysis, and then continue to propagate through the deck. Transverse and longitudinal cracking begins over the piers at around 14 days, then continues into the deck at 21 days.

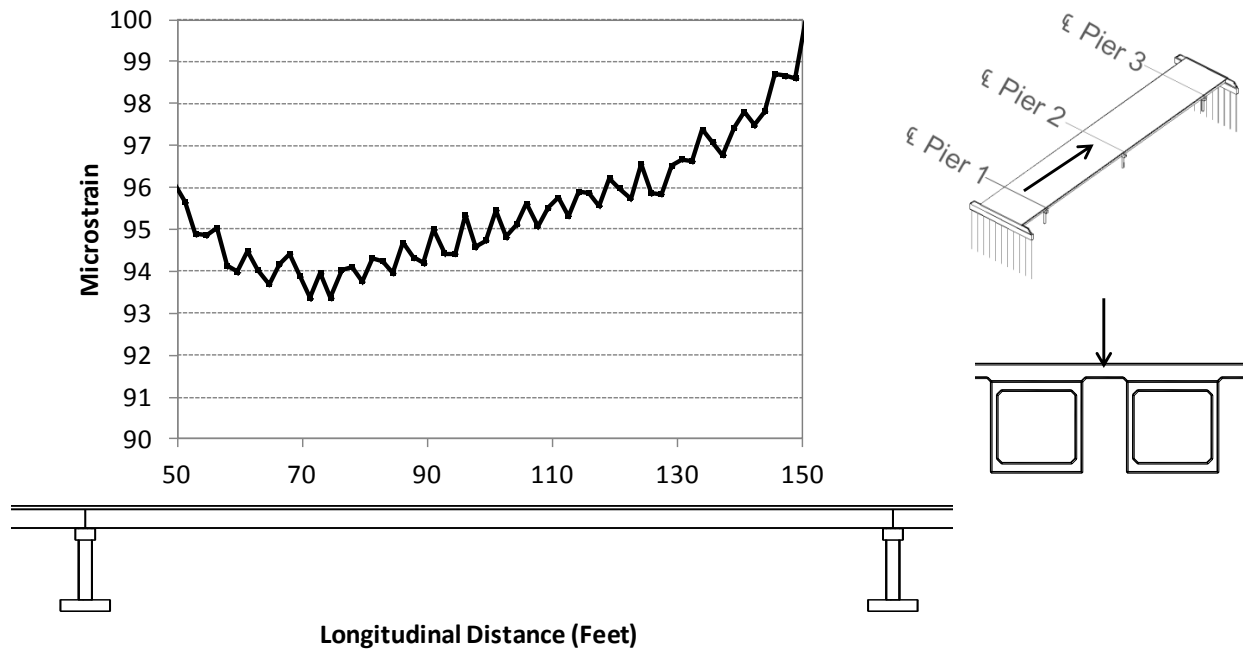
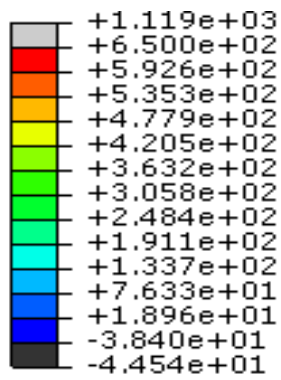
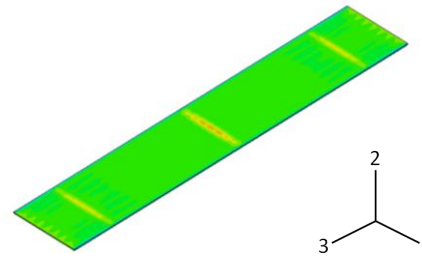


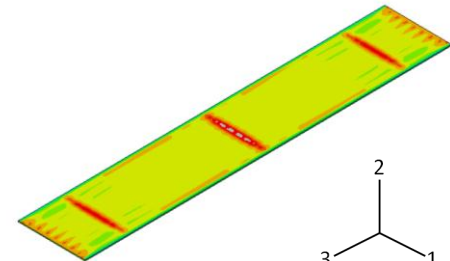
**Figure 156.** Maximum principle plastic strain output in positive moment region (span 2)



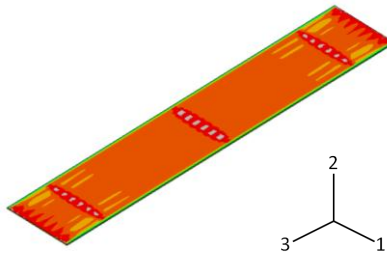
a) Legend



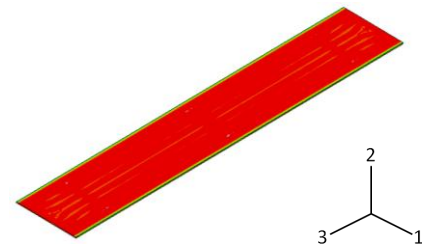
b) Time=7 days



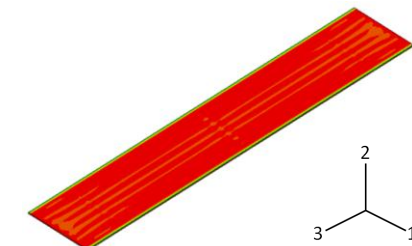
c) Time=10 days



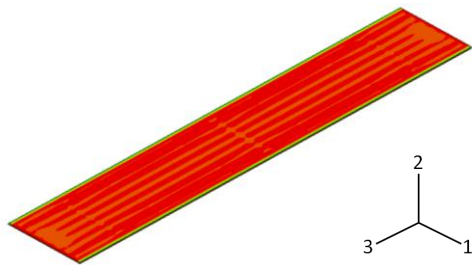
d) Time=14 days



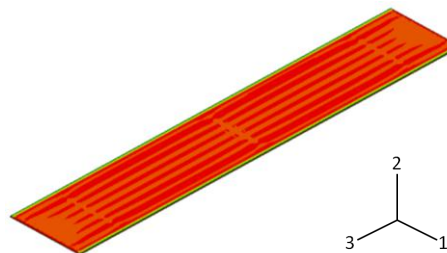
e) Time=21 days



f) Time=28 days



g) Time=35 days



h) Time=45 days

**Figure 157.** Development of maximum principal tensile stresses in full bridge deck



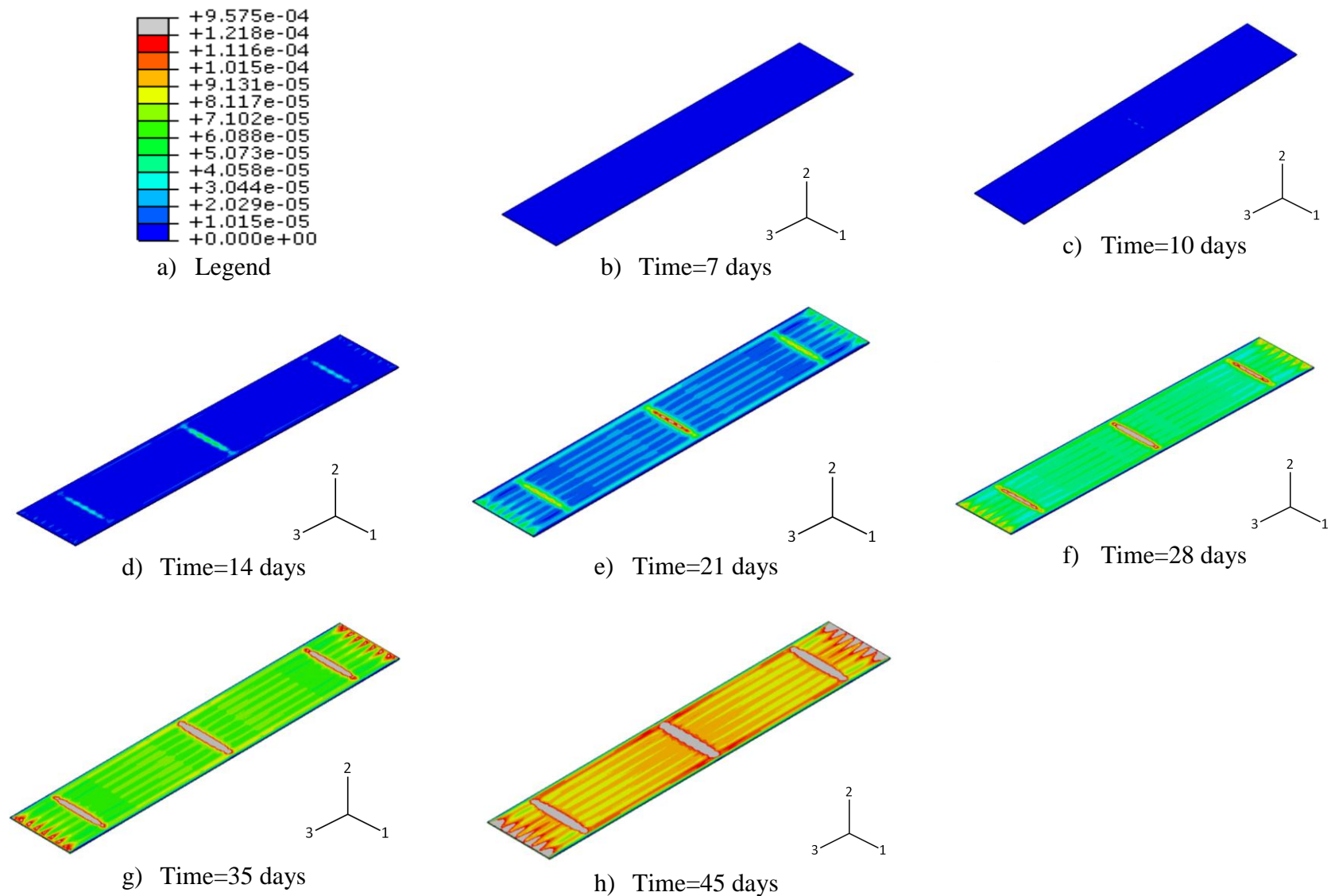


**Figure 158.** Development of maximum principal plastic strains in full bridge deck

The maximum principle stresses and plastic strains were also extracted along the longitudinal direction at the bottom of the deck at the end of the analysis (time=45 days). The outputs are shown below in Figure 159 and Figure 160.

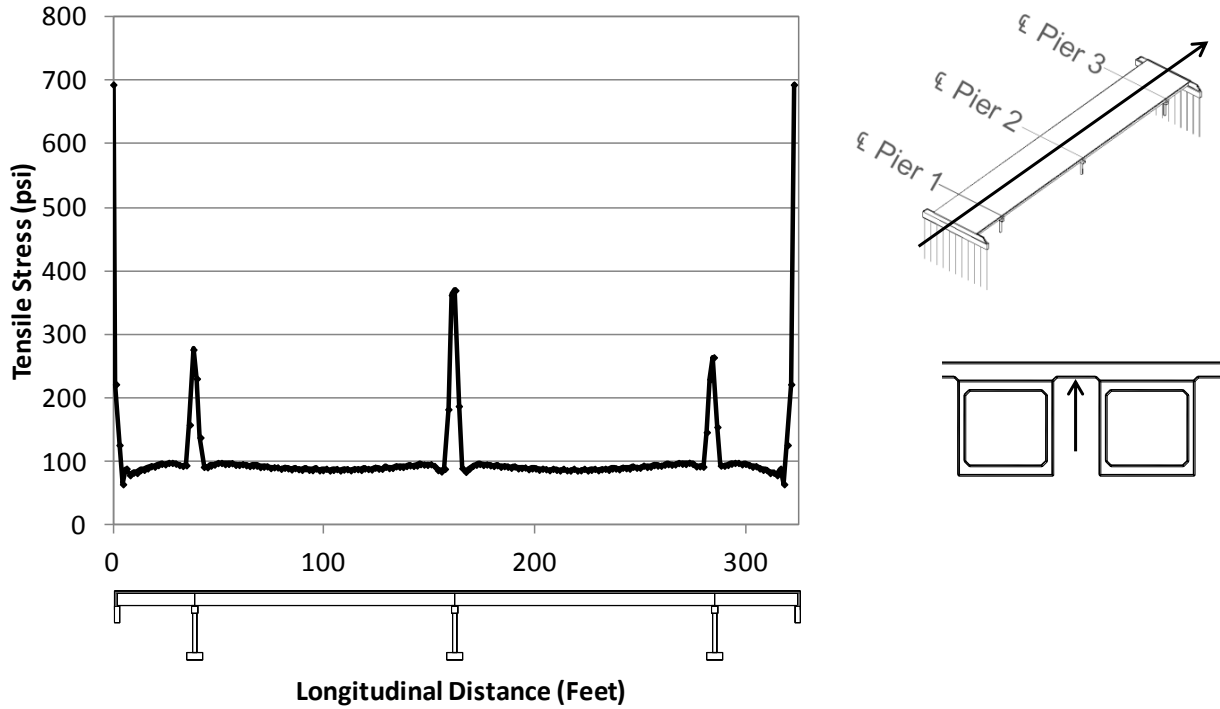


**Figure 159.** Maximum principle tensile stresses along longitudinal direction, bottom of deck

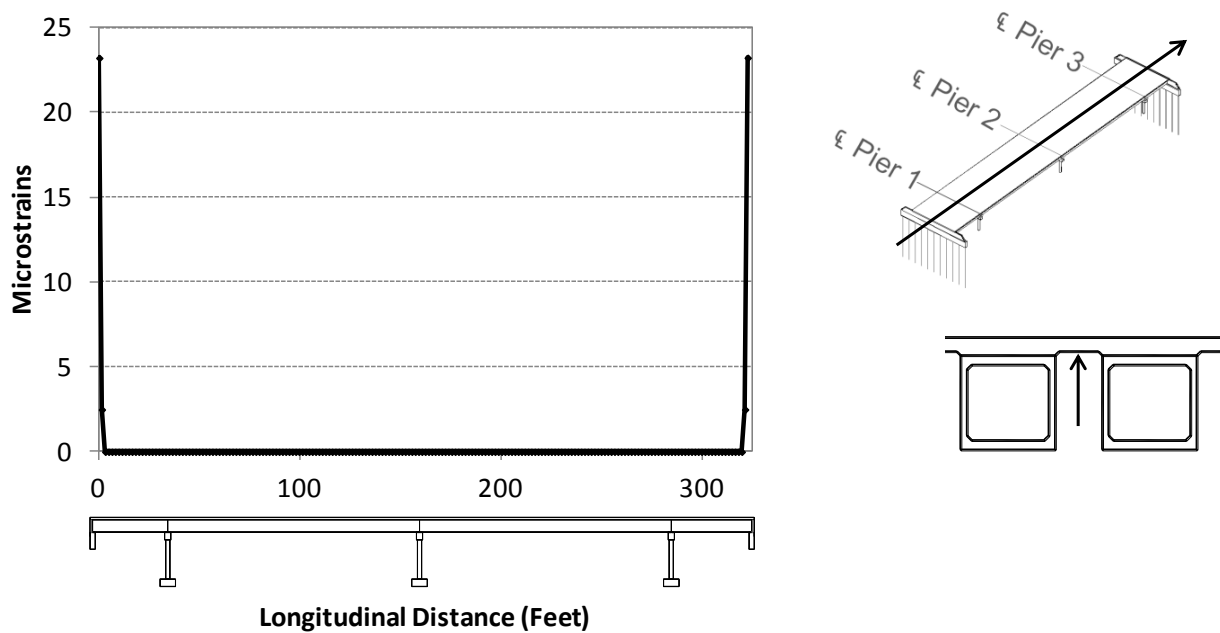


**Figure 160.** Maximum principle plastic strains along longitudinal direction, bottom of deck

As in the top of the deck, the regions over the piers and the abutments show the highest levels of stress. The plastic strains are around zero through the entire length of the bridge, except for at the abutment connection. These areas show increased damage, since they are areas of high restraint due to the deck connection with the abutment backwall.

The maximum principle stresses, maximum principle strains, and deflections were also extracted along the transverse direction, midway between Pier 1 and Pier 2. The plots are shown below in Figure 161 to Figure 163. As shown, the bridge deck displaces in a “bowl-shaped” pattern along the transverse direction, with maximum displacement in the middle. The jumps in the plastic strain and tensile stresses at the two ends are likely due to the restraint provided by the concrete barrier walls. Additionally, jumps can be seen in the plastic strain plot through the width of the deck, indicating longitudinal cracking between beams.

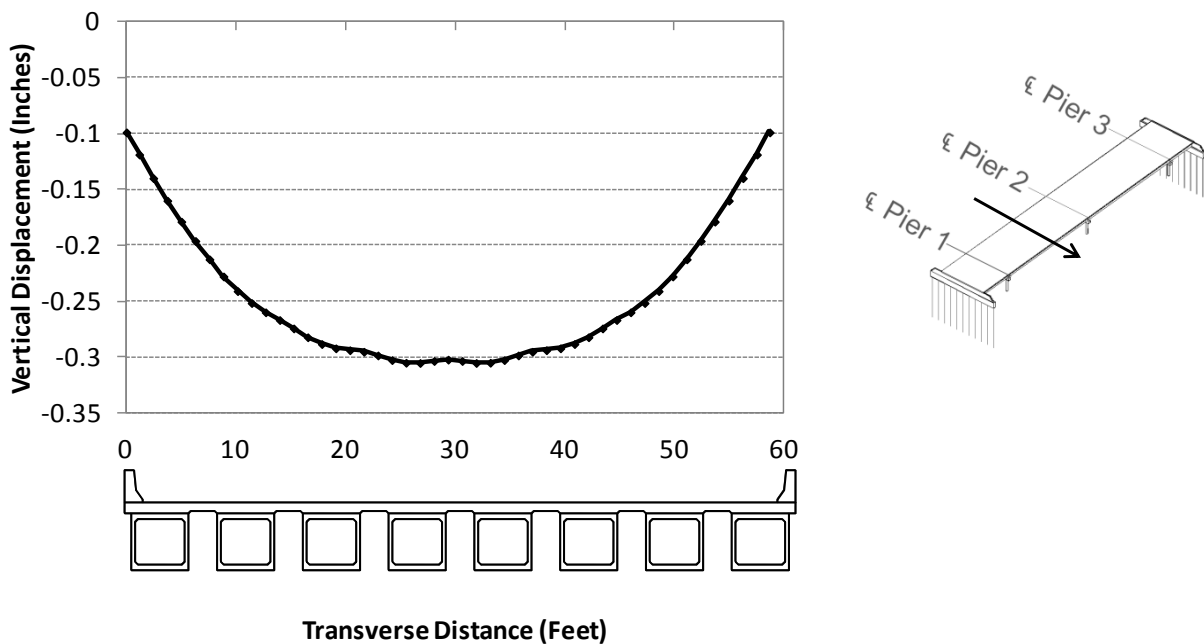


**Figure 161.** Vertical displacements along bridge transverse direction (time=45 days)

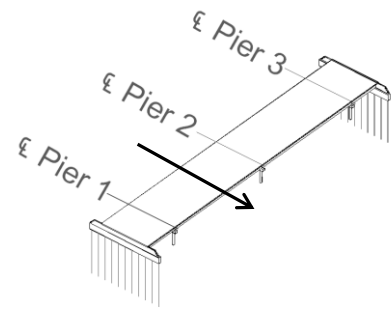
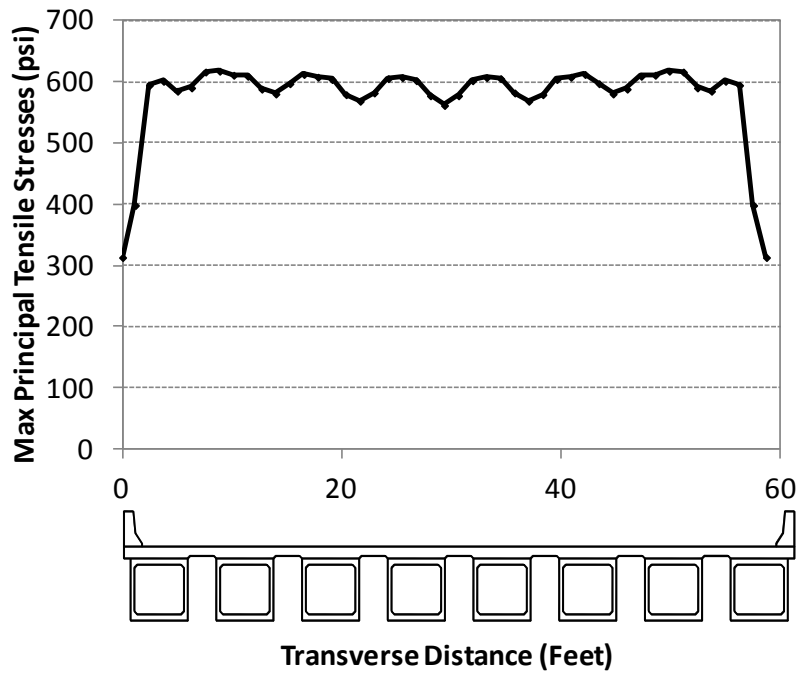


**Figure 162.** Maximum principle tensile stresses along bridge transverse direction (t=45 days)

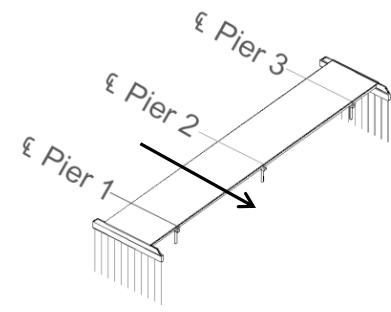
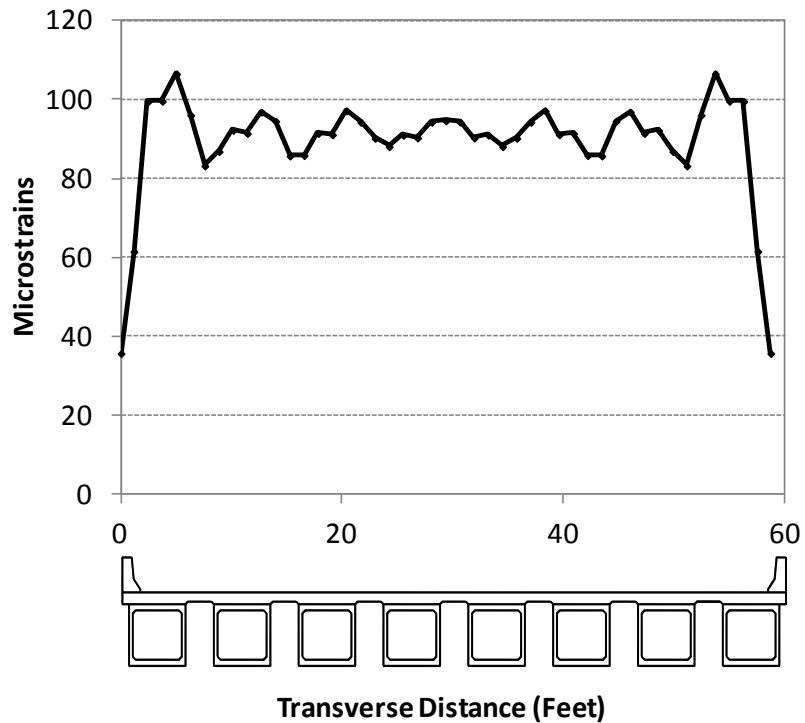


**Figure 163.** Maximum principle plastic strains along bridge transverse direction (time=45 days)

### 6.5.2 Steel Girder Bridge Model Overall Results

The overall behavior of the steel girder bridge was also similar for each parametric analysis that was simulated. The bridge deflected shape and vertical displacements for the as-built model are shown below in Figure 164. As shown, the two spans deflect in a similar “bow-shaped” pattern as the box beam bridge. Since the abutments are more rigid due to the pile configuration, there is less inward movement than in the box beam bridge. To examine the cracking behavior for the deck, the maximum principal tensile stresses and plastic strain outputs at the end of the analysis were extracted. They are shown below in Figure 165 and Figure 166, respectively.

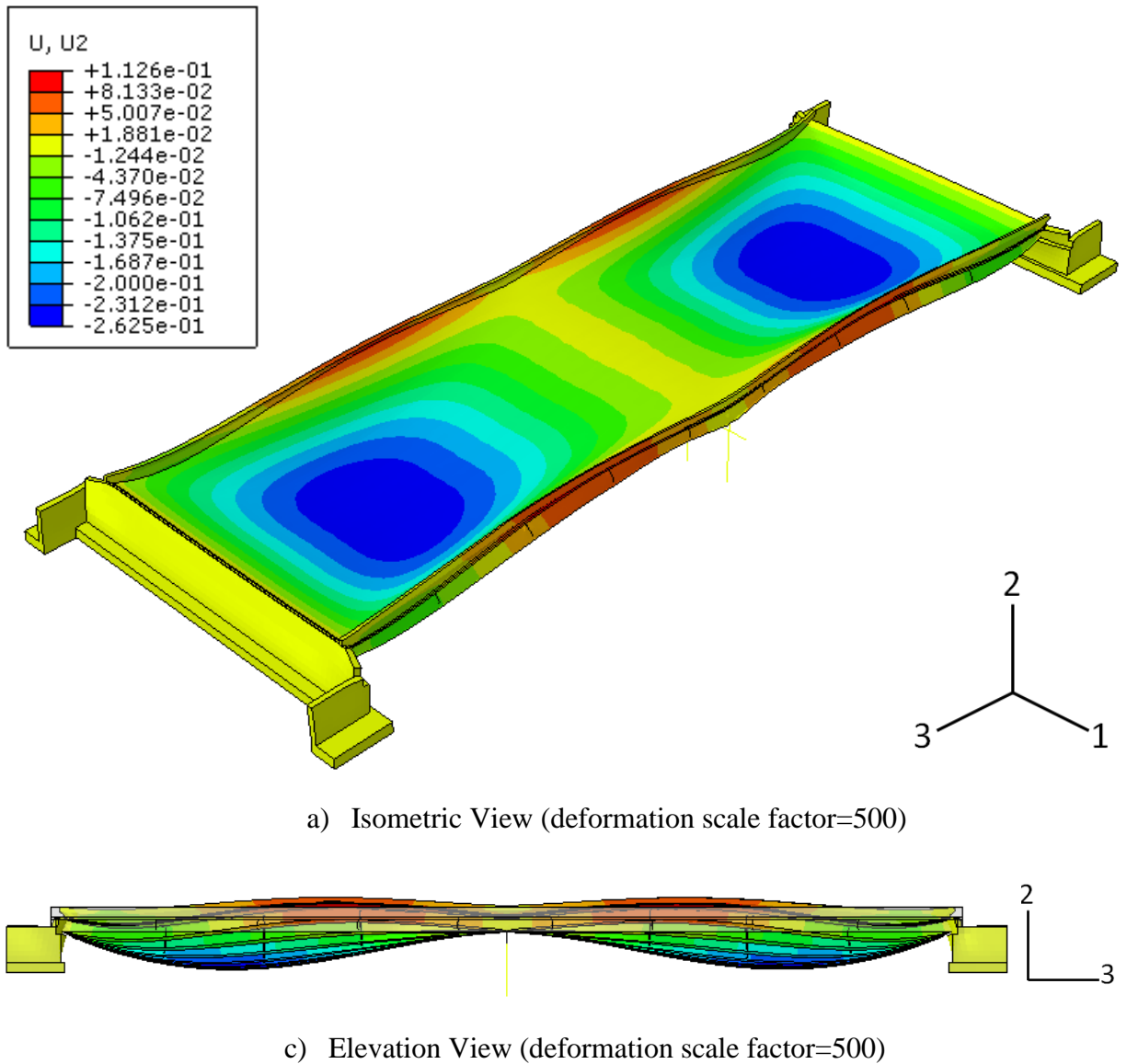
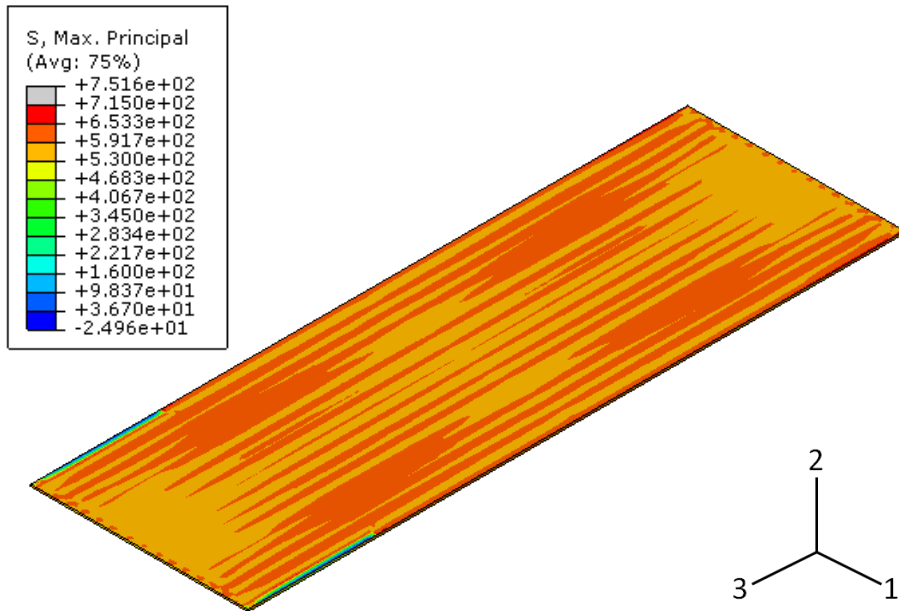
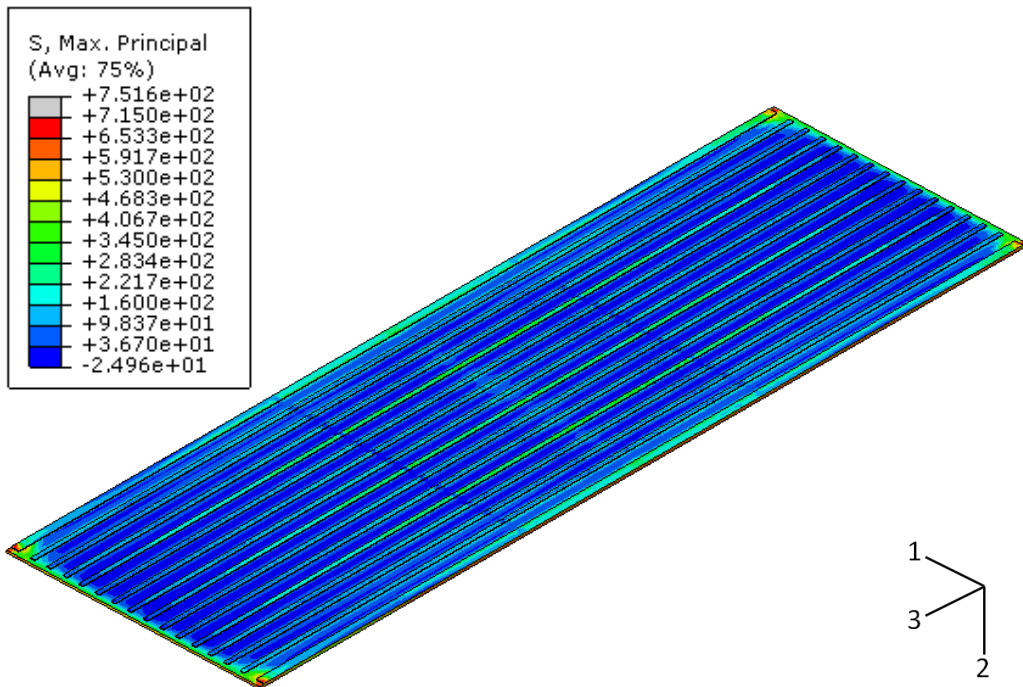


**Figure 164.** Steel girder as-built model deflected shape and vertical displacements (t=45 days)



a) Top of Deck



b) Bottom of Deck

**Figure 165.** Steel girder as-built model maximum principal tensile stresses (t=45 days)

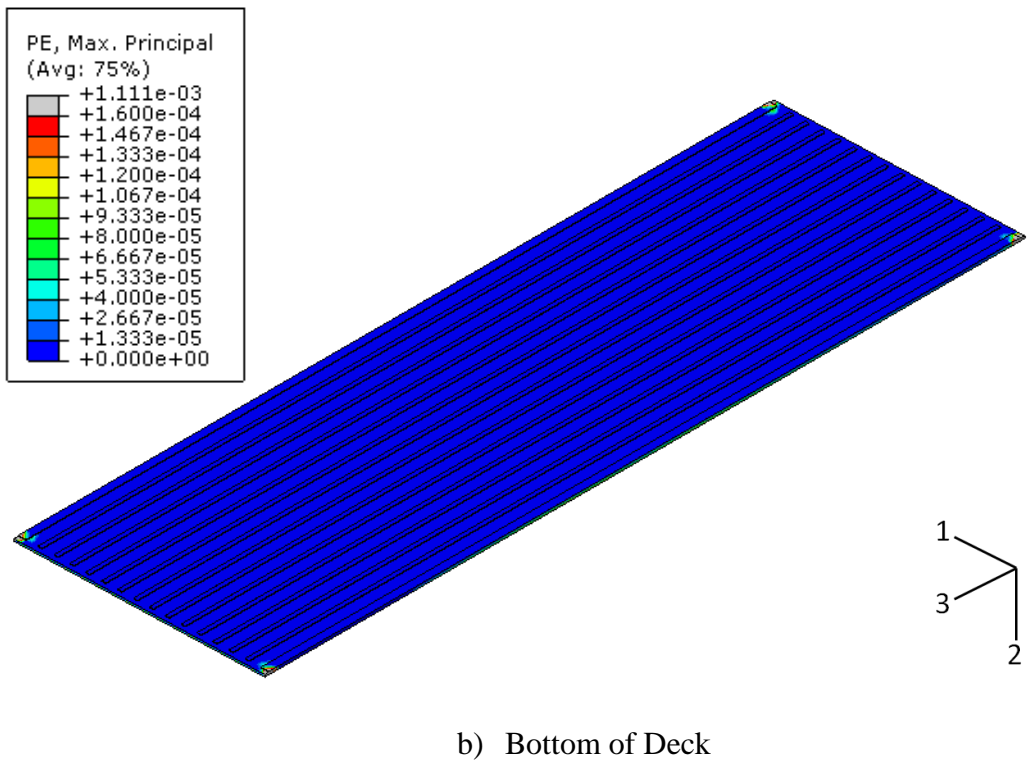
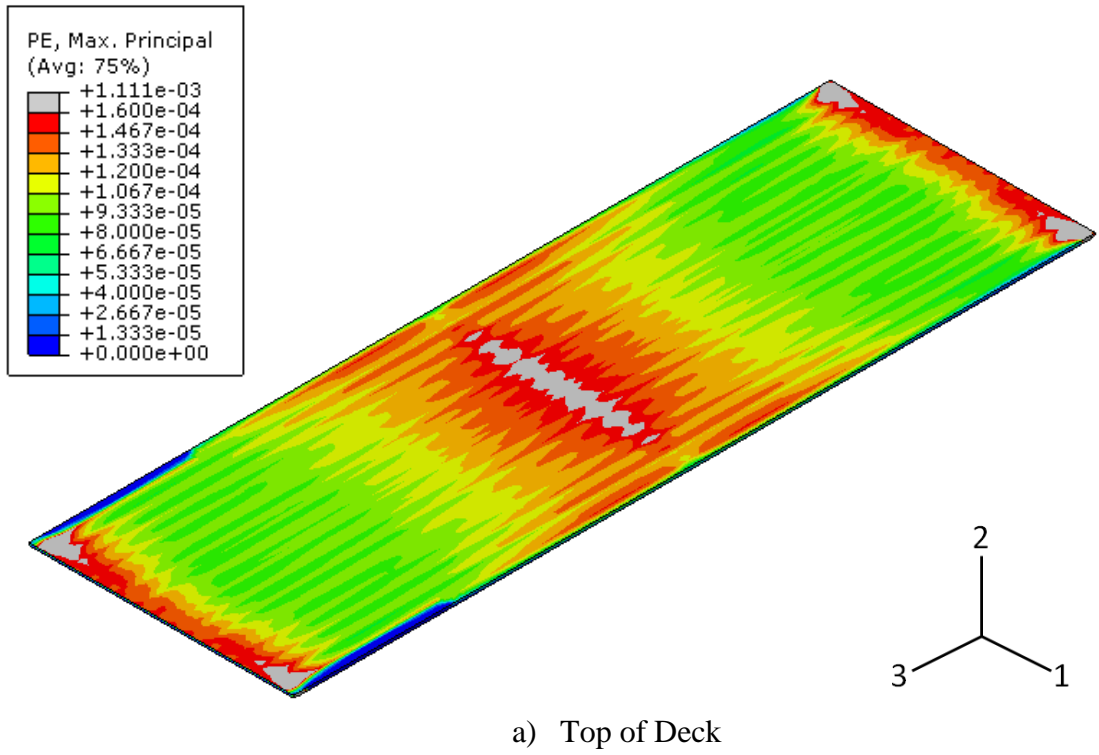


**Figure 166.** Steel girder as-built model maximum principal plastic strains (t=45 days)

The overall behavior shown in Figure 164 to Figure 166 was similar for all parametric analyses for the steel girder bridge. The regions of damage in the deck can be seen by examining the maximum principal plastic strain output. As shown, almost all of the damage occurs on the top of the deck, while the bottom of the only experiences damage in the corners, by the connection with the abutment. The highest levels of damage are concentrated at the pier and the abutments, in the negative moment region. Additionally, some damage is being captured in-between the piers, throughout the entire deck. The stresses are higher in the regions over the beams, and lower in-between the beams. Regions where the plastic strains are higher correspond with lower stresses, which indicate softening behavior.

As with the box beam bridge output, the plastic strains were extracted for each component to derive the directions of the maximum principle tensile stresses and determine the directions for cracking. The plastic strain component outputs at a time of 45 days are shown below in Figure 167 to Figure 170.

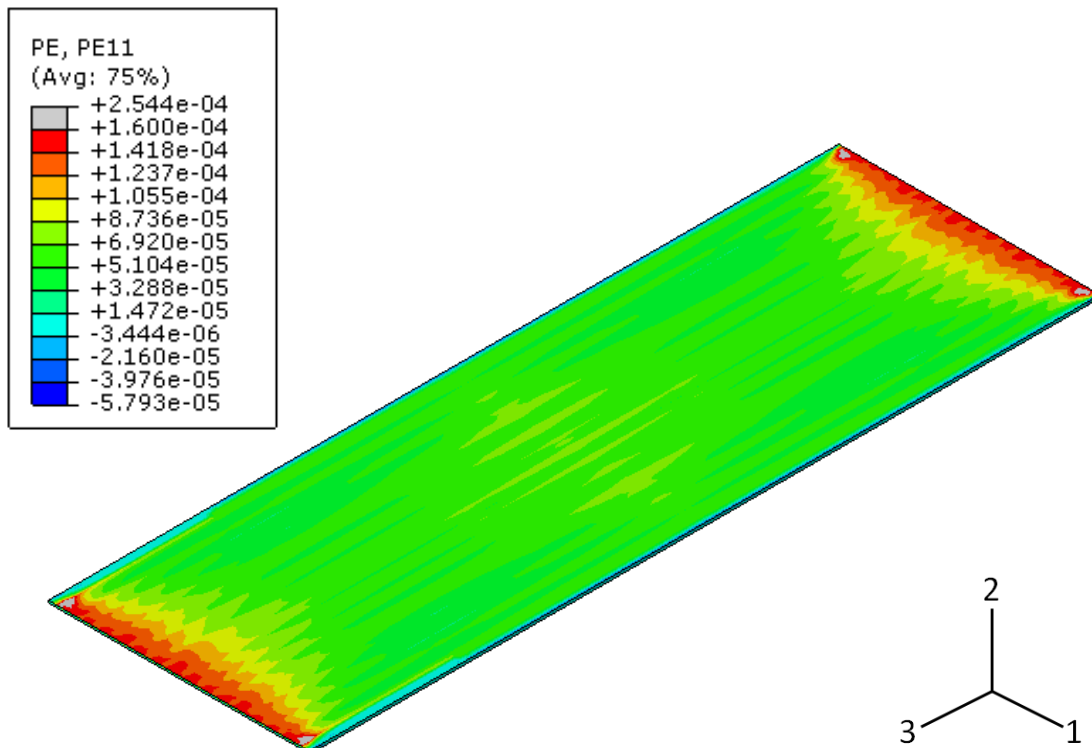


**Figure 167.** Steel girder as-built model plastic strain global X-direction (1-1) output



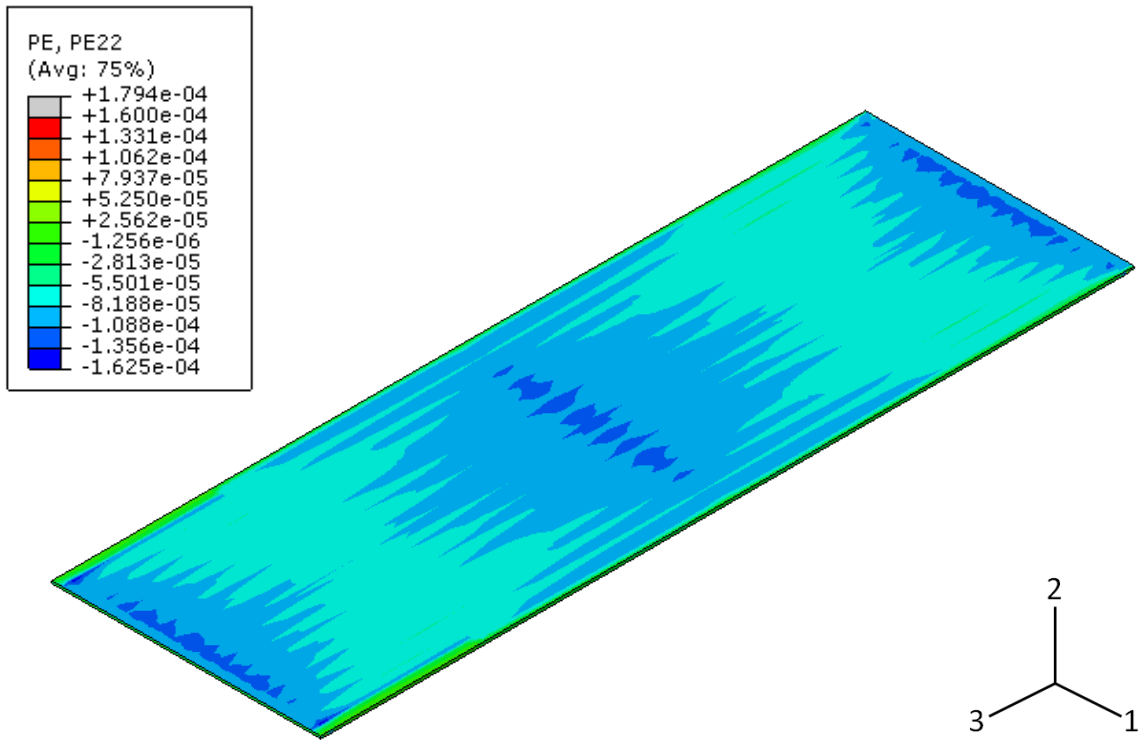


**Figure 168.** Steel girder as-built model plastic strain global Y-direction (2-2) output

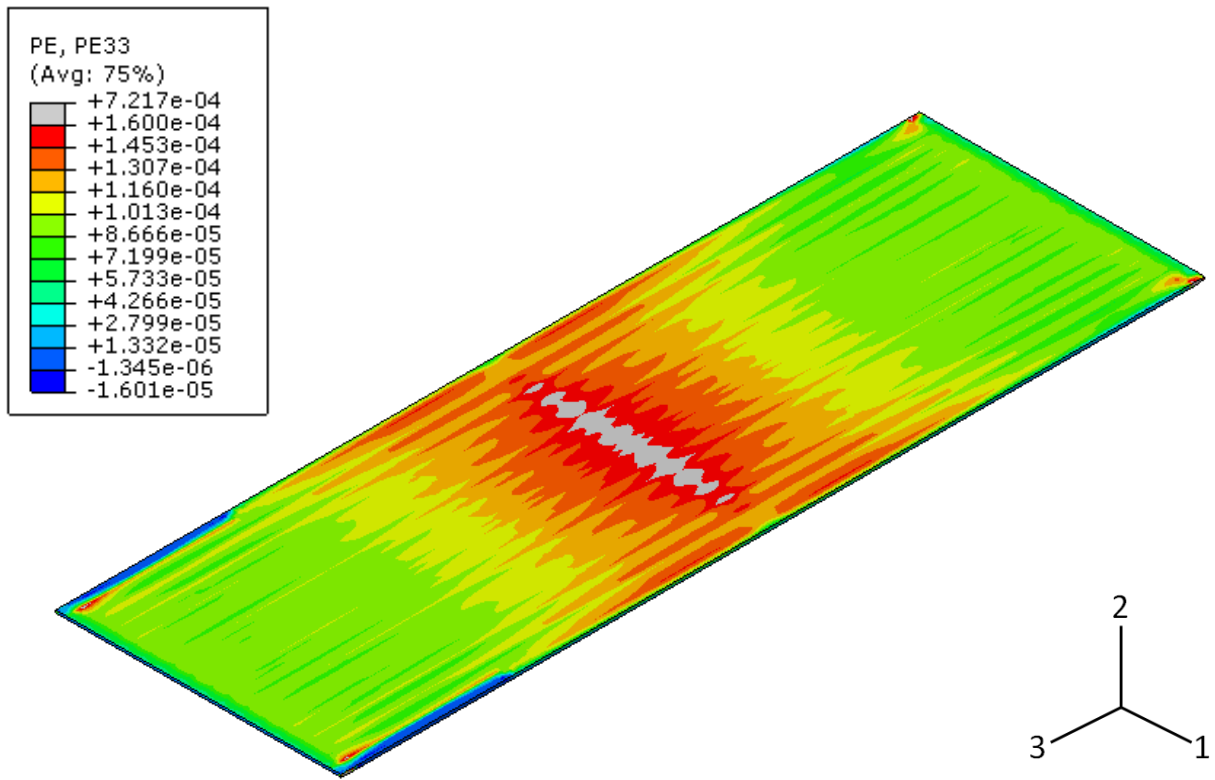


**Figure 169.** Steel girder as-built model plastic strain global Z-direction (3-3) output

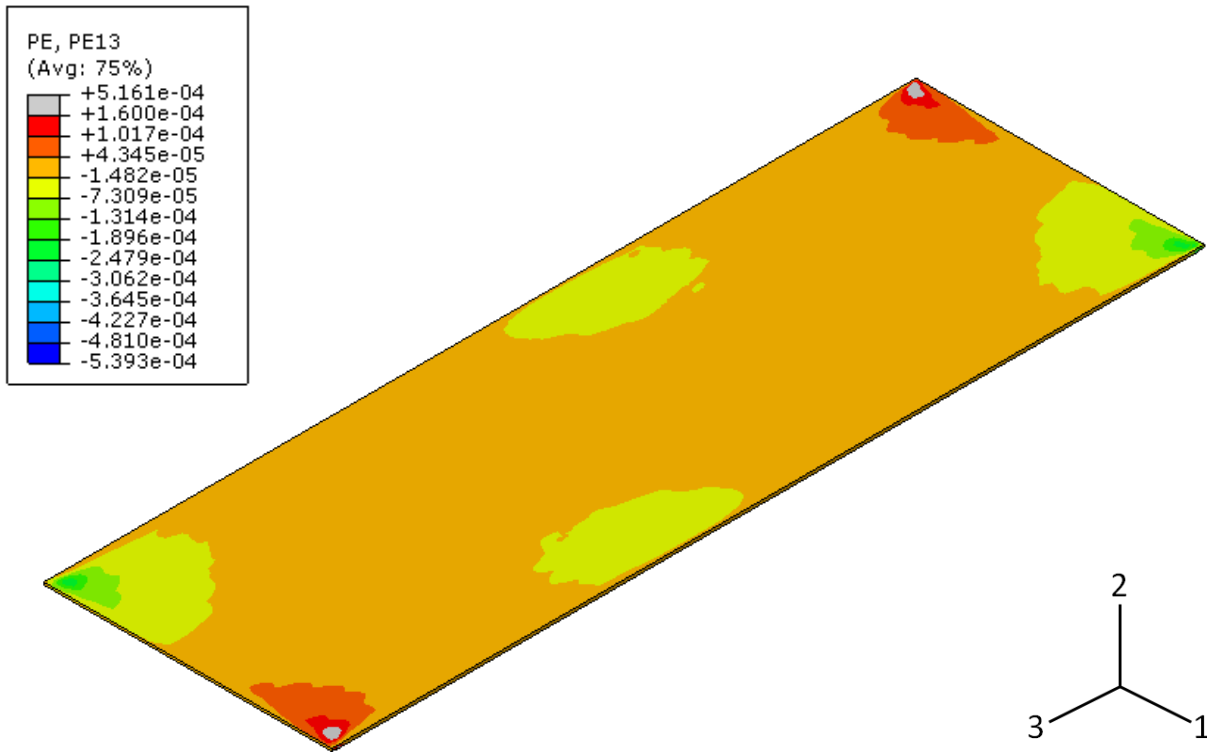


**Figure 170.** Steel girder as-built model plastic shear strain (1-3) output

As shown above, the maximum principal plastic strains are mostly influenced by the longitudinal (PE33) plastic strains in the positive moment regions and over the pier, and are mostly influenced by the transverse (PE11) plastic strains in the regions over the abutments. It can also be seen that shear strain (PE13) contributes in four corners of the bridge, by the abutment, as well as on the two edges of the bridge, by the pier. This is due to the increased transverse restraint caused by the pier and the abutment in those regions.

Since cracking occurs perpendicular to the direction of plastic strain, it can be seen that transverse cracking is predicted in the positive moment regions and over the pier, and longitudinal cracking is predicted over the abutments. The concentration of transverse cracking is predicted to be highest over the pier. This matched the field observations of closer-spaced cracking over the pier. Unlike the box beam bridge output, the steel bridge does not have the presence of longitudinal cracking along the entire length of the bridge, which is consistent with field observations. Shear cracking is concentrated at the corners of the deck and near the edges of the piers, as predicted by the shear strain (PE13) output. These overall cracking patterns match well with the overall field observations.

To determine overall bridge behavior through time, the vertical displacements, maximum principal stresses, and maximum principal strains were extracted along a longitudinal path in along the middle of the bridge at various times. These outputs are shown below in Figure 171 to Figure 173.

As shown in Figure 171, the overall vertical displacement profile remains the same for each time step, while the magnitudes continue to increase. This is as expected, since the overall deflections increase as the amount of shrinkage increases. The maximum principal tensile stresses continuously grow with time up until the point of cracking, when they decrease due to softening. The tensile stresses are highest in the negative moment regions at the pier and the abutments during the first part of the analysis, after which they become uniform due to cracking throughout the deck. The plastic strains remain zero up until the point of cracking, where they steadily continue to grow. The negative moment regions over the pier and the abutments experience cracking before the other regions, and have the highest overall plastic strain magnitudes.

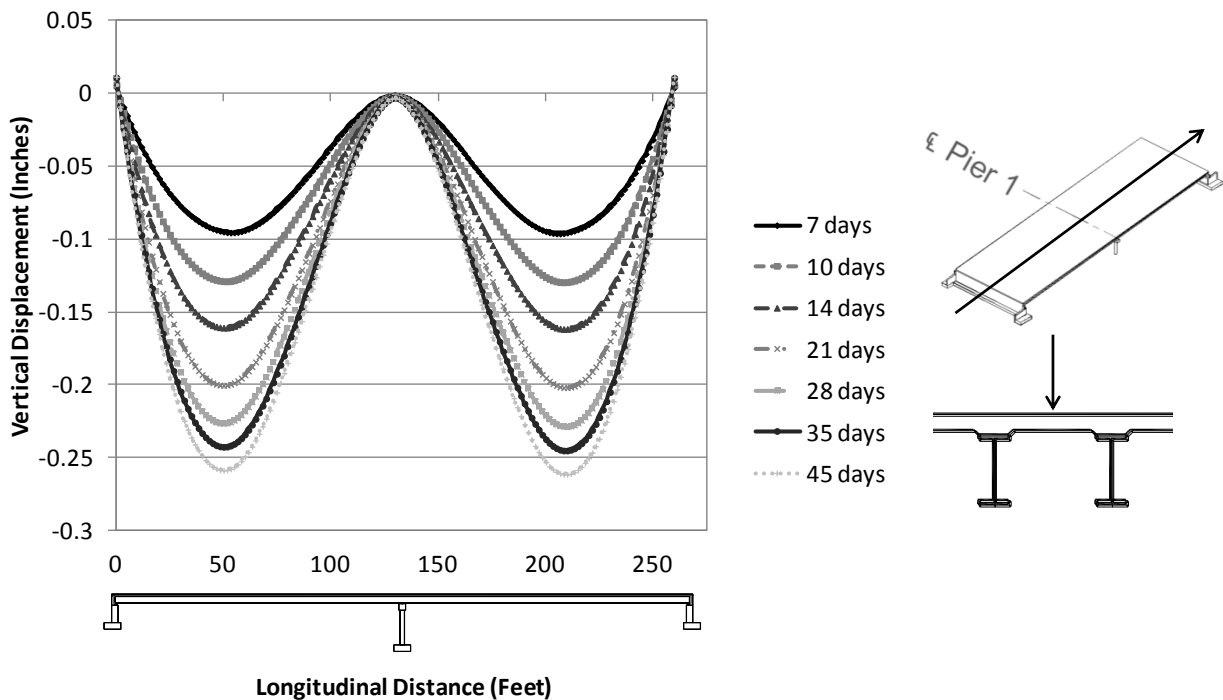


**Figure 171.** Vertical displacement through time in bridge longitudinal direction

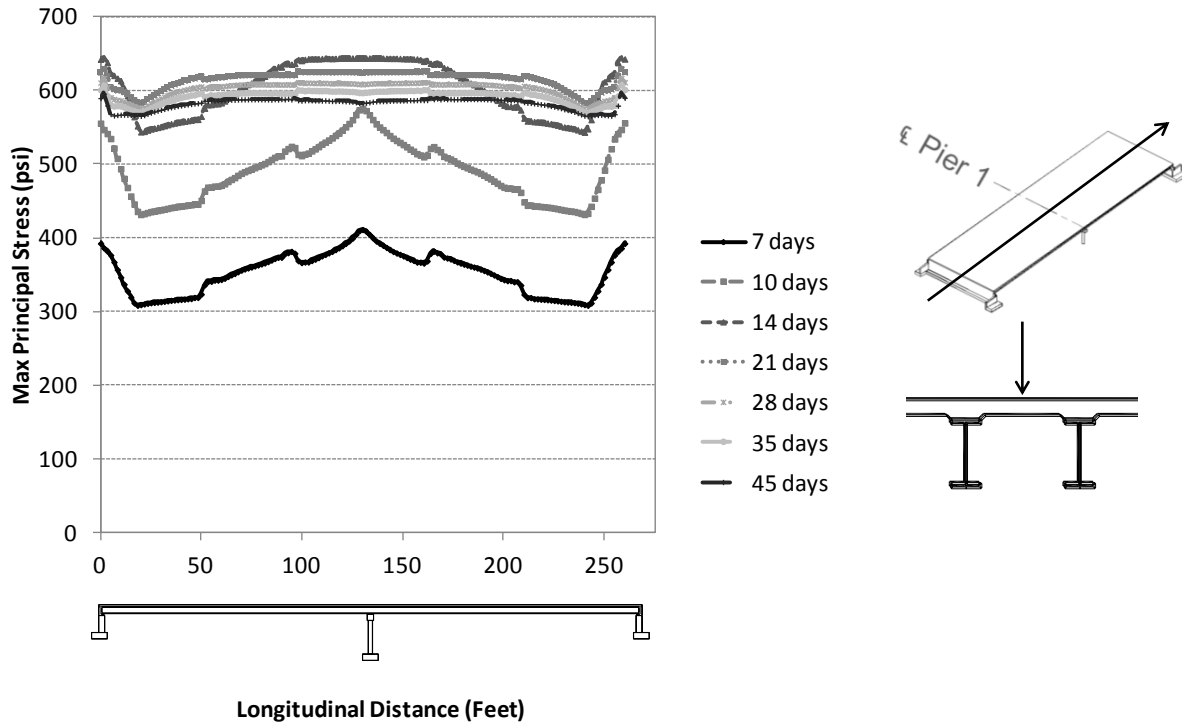


**Figure 172.** Maximum principal tensile stresses through time in bridge longitudinal direction

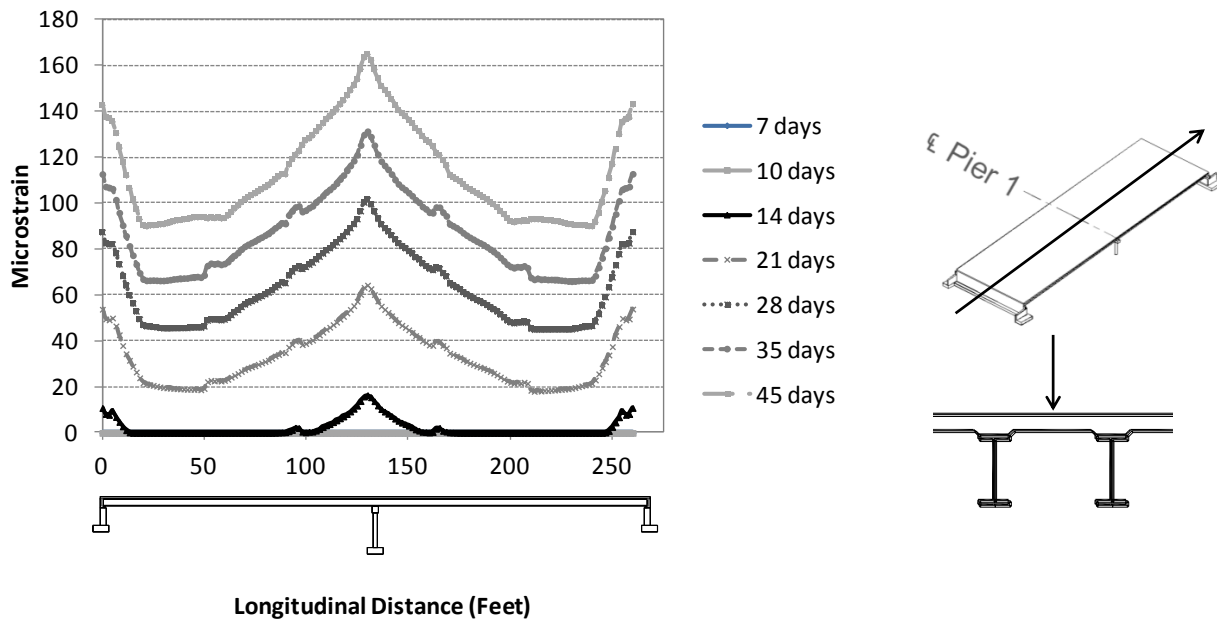


**Figure 173.** Maximum principal plastic strains through time in bridge longitudinal direction

To determine the presence of localization of damage and evenly-spaced transverse cracking, the maximum principle plastic strain outputs were extracted in the positive moment region at the end of the analysis. Jumps in the strain outputs would indicate presence of local cracking. The output is shown below in Figure 174.

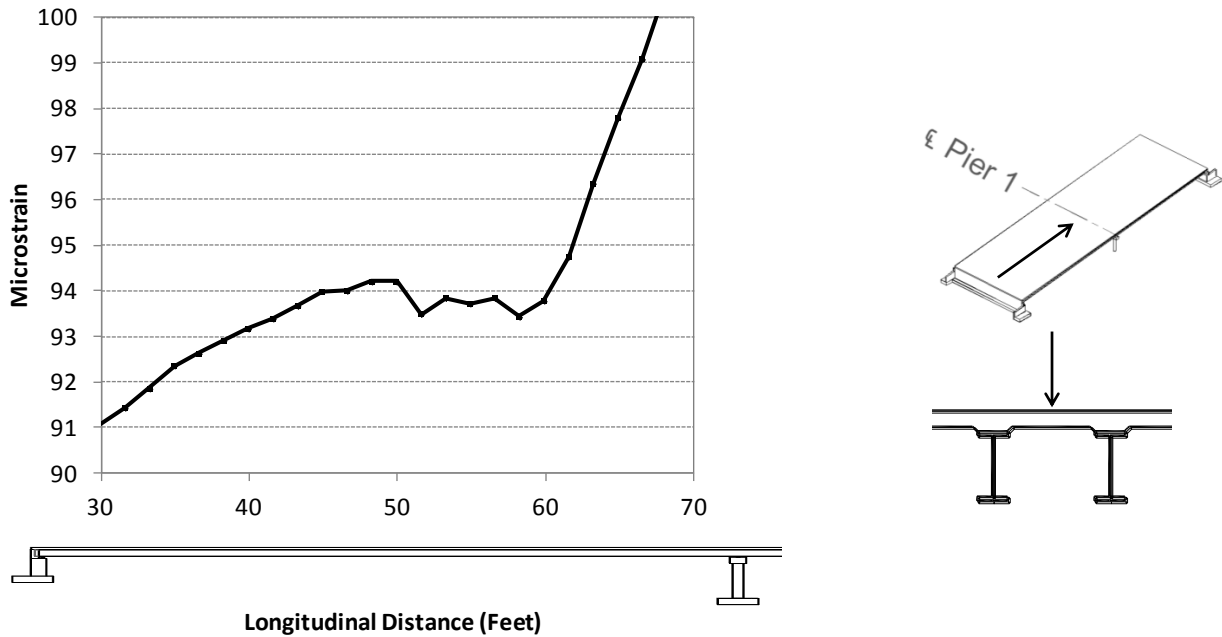


**Figure 174.** Maximum principle plastic strain output in positive moment region (span 2)

As shown, there is a steady increase in plastic strain towards the pier, since that region has more restraint. There is not an obvious presence of jumps in the strain data as there was for the box beam bridge output. The analysis is capturing uniform damage throughout the entire deck, instead of evenly-spaced localized areas of cracking.

The development of maximum principal stresses and plastic strains in the depth through time are shown with full contour plots below in Figure 175 and Figure 176.

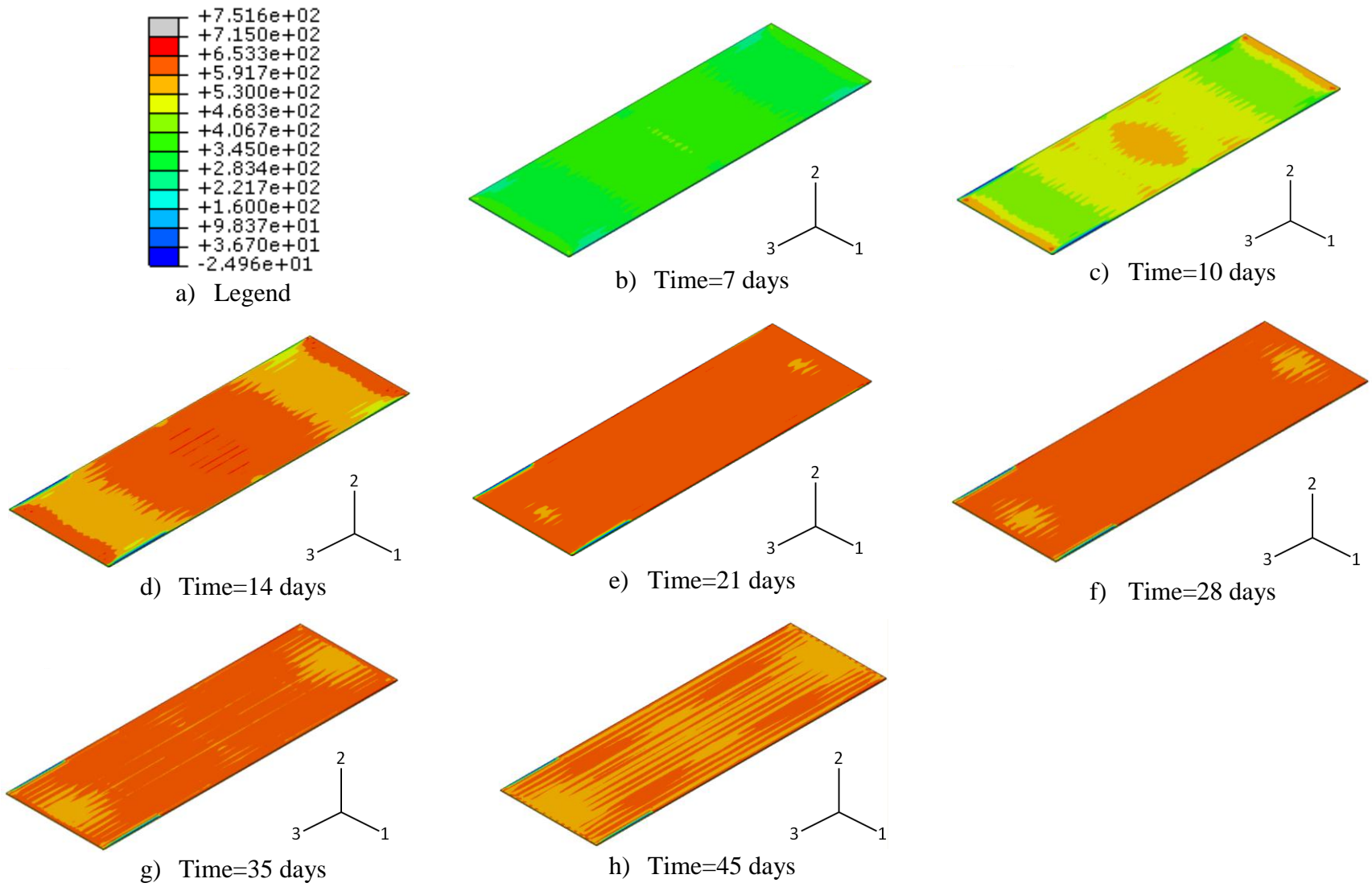


**Figure 175.** Development of maximum principal tensile stresses in full bridge deck

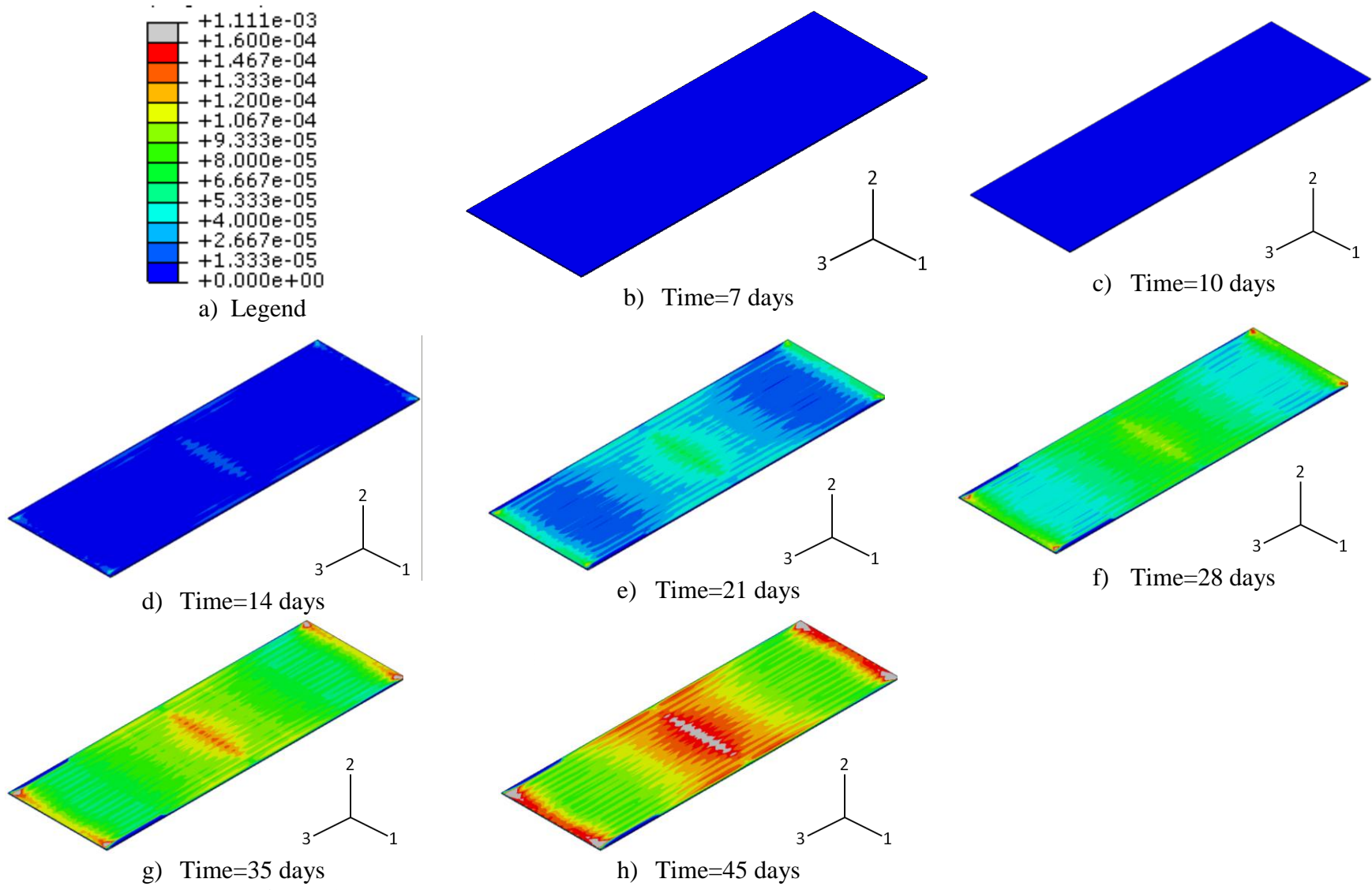


**Figure 176.** Development of maximum principal plastic strains in full bridge deck

As shown the maximum principle tensile stresses and plastic strains begin to grow in the negative moment regions near the beginning of the analysis, and then continue to propagate through the deck. At 14 days, the plastic strains originate as shear cracks at the corners of the deck, by the abutment, and as transverse cracks in the negative moment region over the pier. Longitudinal cracking then develops over the abutments, followed by transverse cracking in the positive moment regions at 21 days. It can be seen that less localization of damage is being captured in this model, as the tensile stresses remain fairly uniform throughout the deck.

The maximum principle stresses were also extracted along the longitudinal direction at the bottom of the deck at the end of the analysis (time=45 days), as shown below in Figure 177.

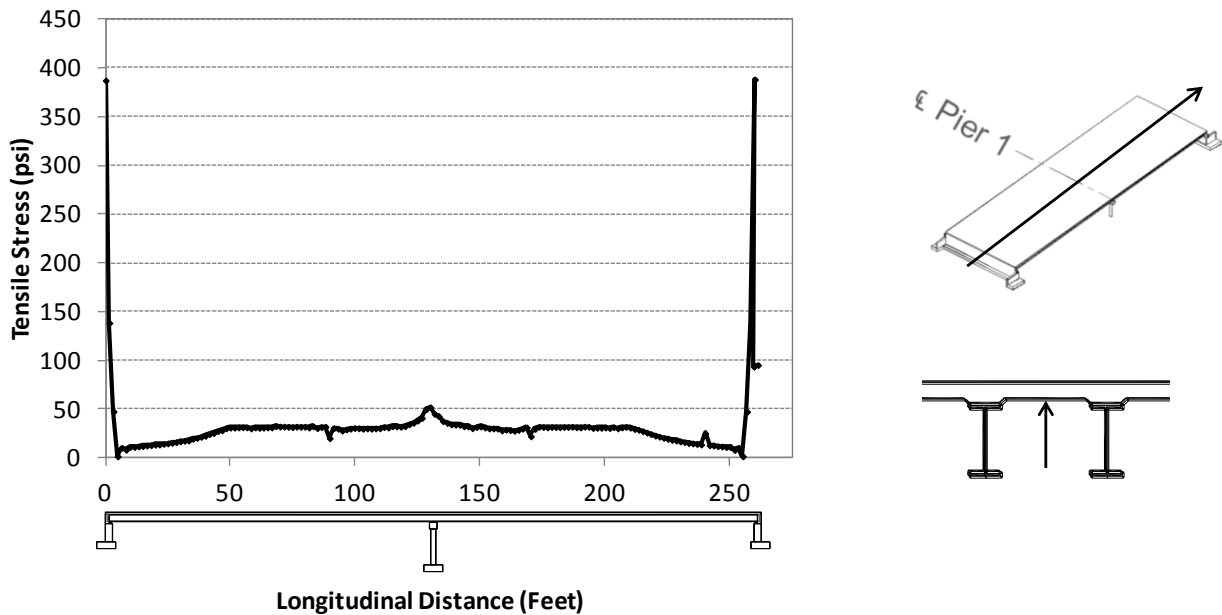


**Figure 177.** Maximum principle tensile stresses along longitudinal direction, bottom of deck

The regions over the piers abutments show the highest levels of stress, due to the high restraint present in those regions. The plastic strains were zero along this entire length, indicating that cracking did not occur on the bottom surface.

The maximum principle stresses, maximum principle strains, and deflections were also extracted along the transverse direction, midway between Abutment A and Pier 1. The plots are shown below in Figure 178 to Figure 180.



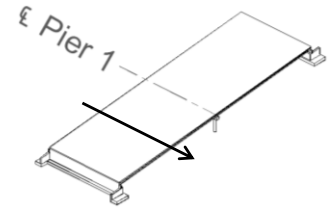
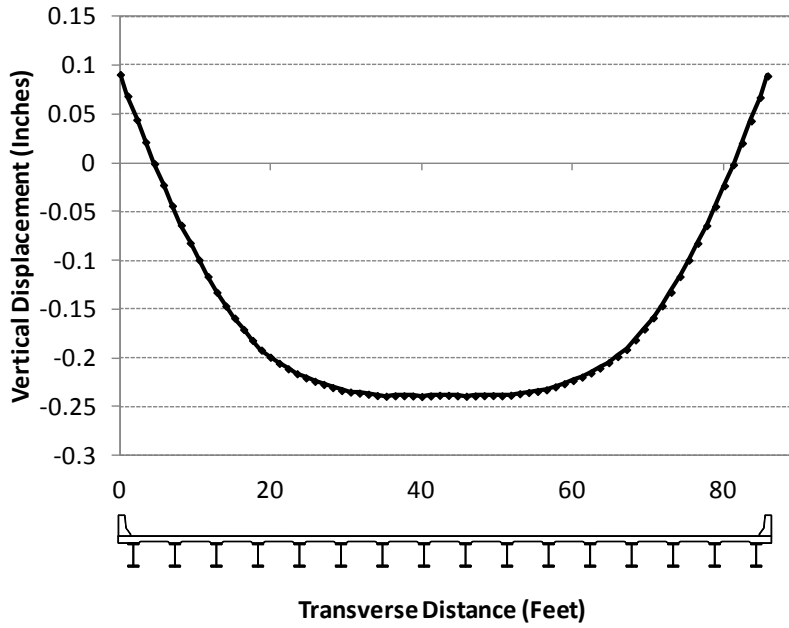


**Figure 178.** Vertical displacements along bridge transverse direction (time=45 days)

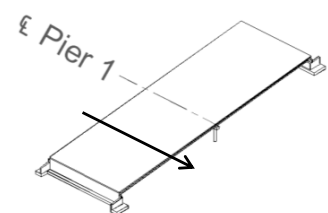
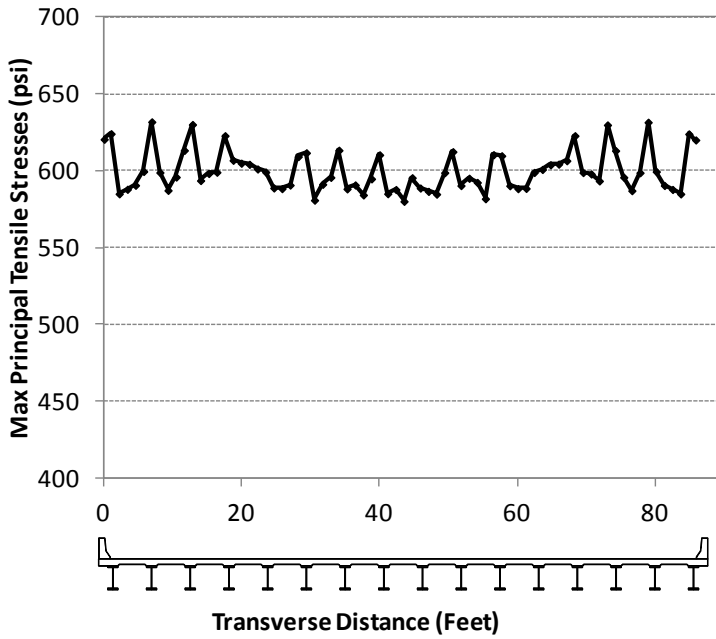


**Figure 179.** Maximum principle tensile stresses along bridge transverse direction (t=45 days)

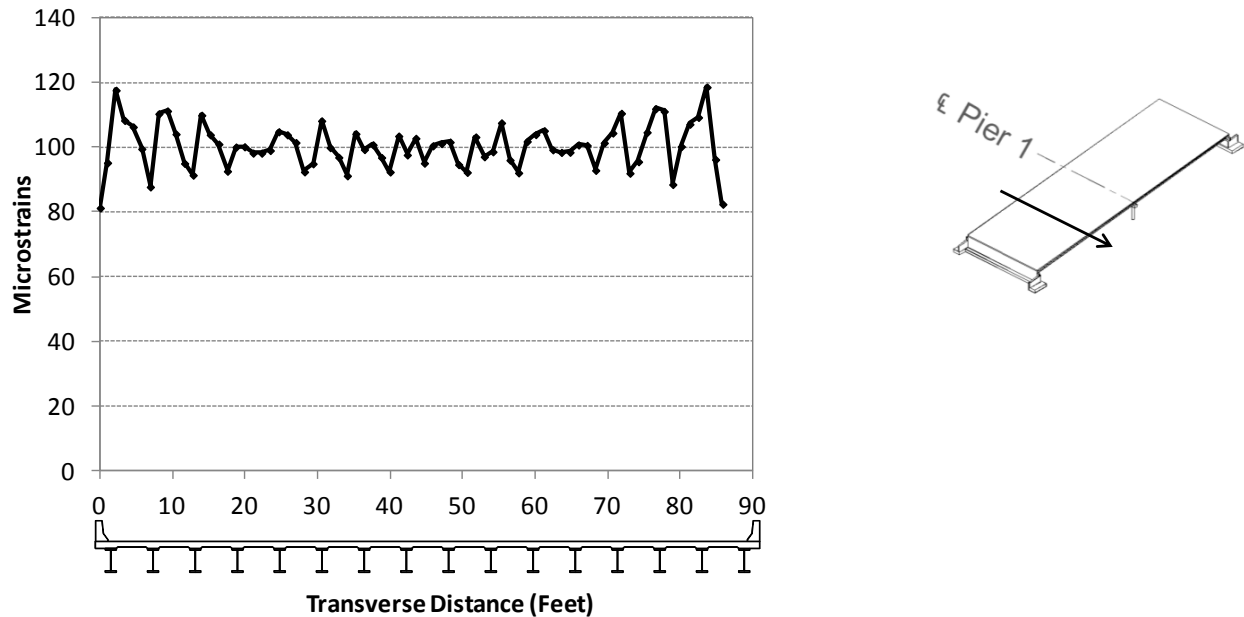


**Figure 180.** Maximum principle plastic strains along bridge transverse direction (time=45 days)

As shown, the bridge deck displaces in a “bowl-shaped” pattern along the transverse direction, with maximum displacement in the middle. The jumps in the plastic strain and tensile stresses through the width of the deck are likely due to the restraint provided by the girders and diaphragms. The overall stiffness of the steel girder bridge is increased due to the presence of diaphragms.

### 6.5.3 Concrete box beam bridge parametric study comparison results

As stated previously, the overall global behavior of the bridge remained the same for all the box beam bridge parametric analyses. To compare the outputs, maximum principal tensile stresses, maximum principal plastic strains, and vertical displacements were extracted at various locations and paths in the bridge deck. The nomenclature used in the results is summarized below in Table 24.

Selected results of the comparison study are shown in Figure 181 to Figure 193. As seen from these results the tensile stresses are higher near the top of the deck and decrease through the depth. The plastic strains penetrate roughly halfway through the depth of the deck. Reconfiguring the reinforcement arrangement had no effect on the stresses or plastic strains, while increasing the density produced slightly higher stresses and plastic strains. The lower-shrinkage mix had lower stress and strain values overall.

**Table 24.** Nomenclature used for box beam parametric study results

Parameter	Nomenclature used in plots of results
As-built model	“As-built”
Effect of using low-shrinkage slag mix	“Low-Shrinkage”
Effect of increasing the reinforcement	“Rebar Denser”
Effect of keeping the same reinforcement ratio with different configuration	“Rebar Re-Distribution”

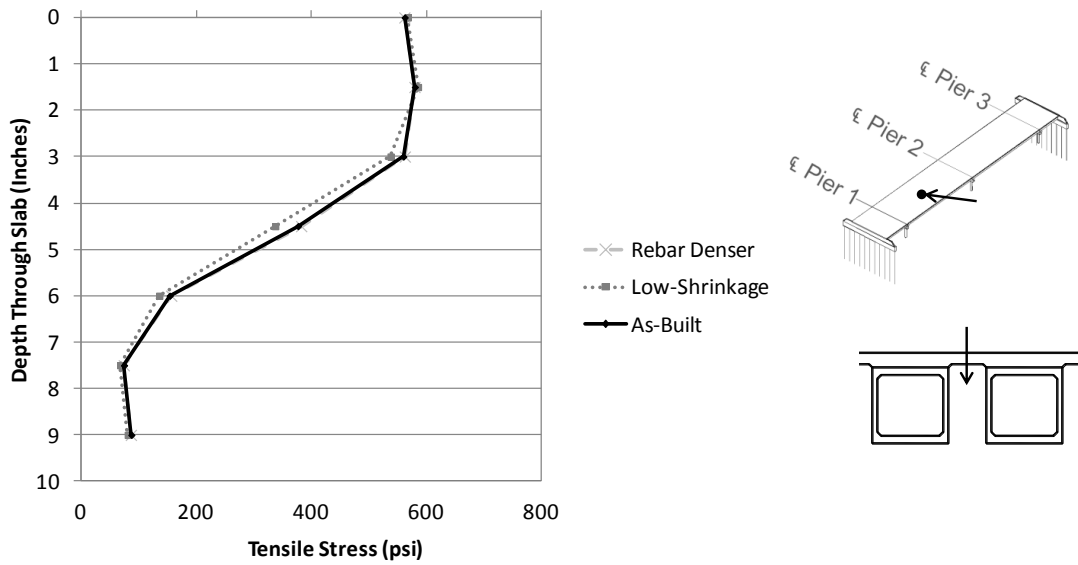


**Figure 181.** Max principal tensile stresses through the depth of the slab, between beams (t=45)

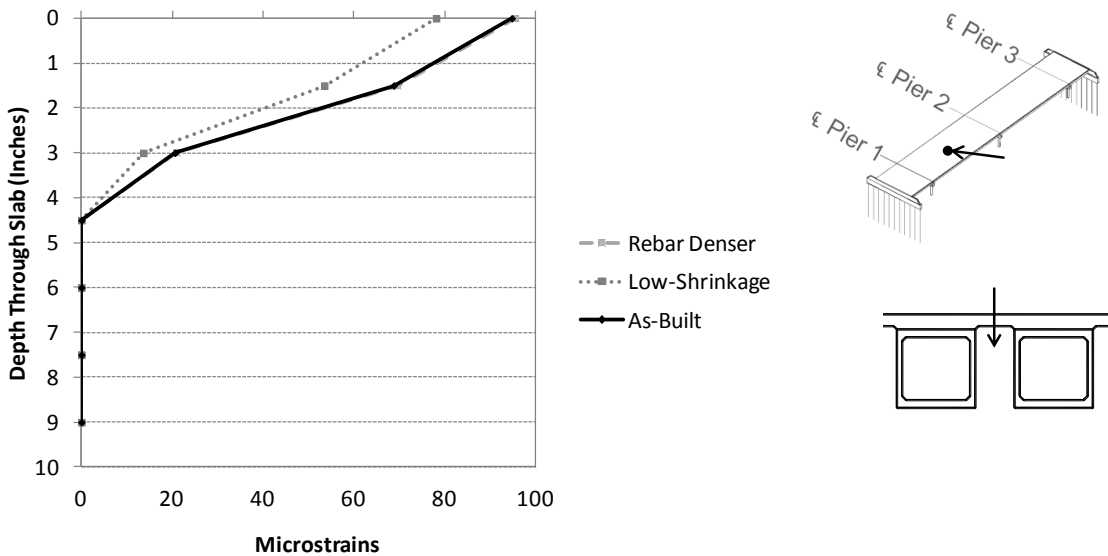


**Figure 182.** Max principal plastic strains through the depth of the slab, between beams (t=45)

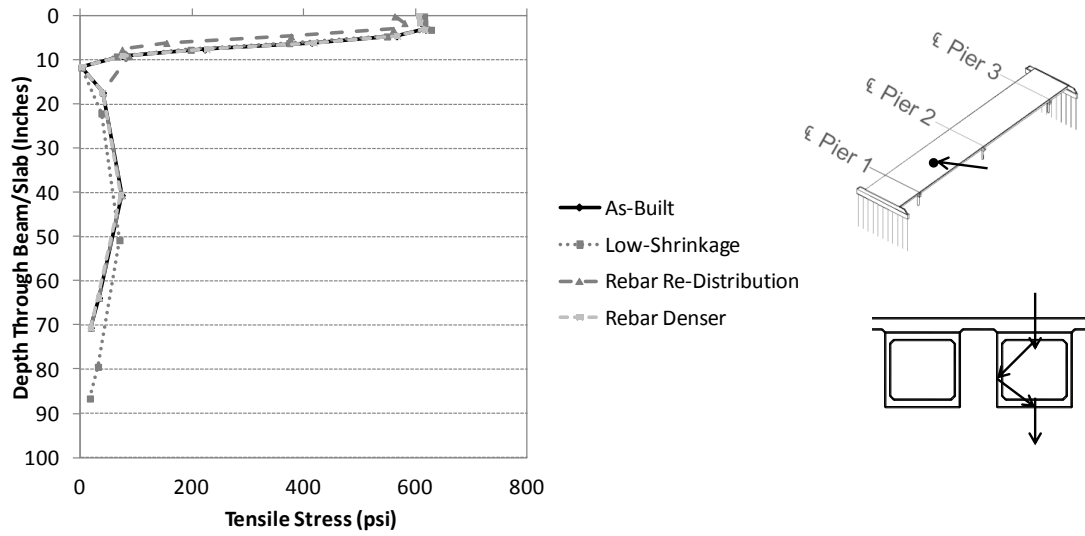


**Figure 183.** Max principal tensile stresses through depth of beam/slab assembly (t=45)

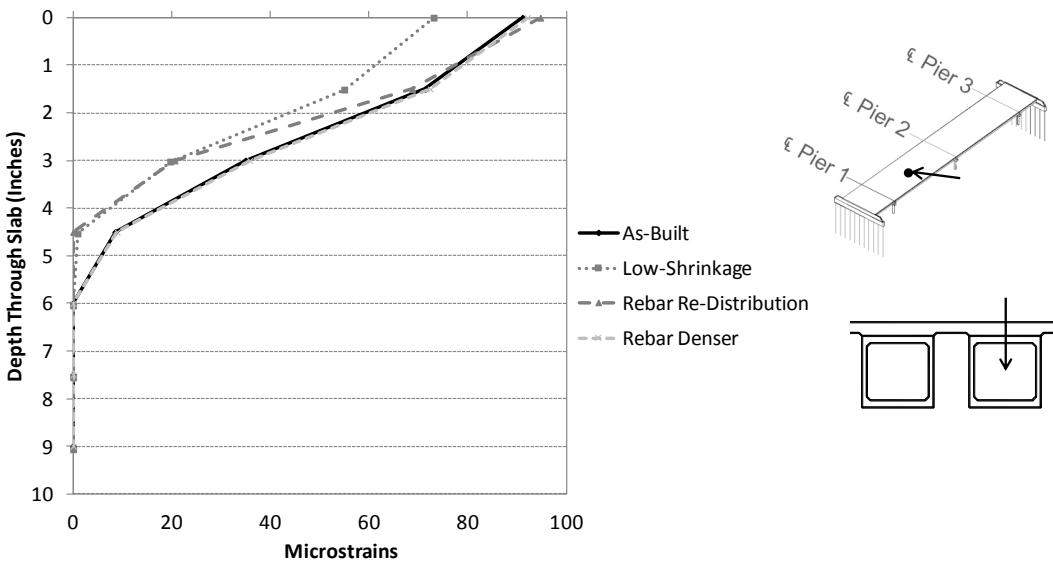


**Figure 184.** Max principal plastic strains through depth of slab, over beams (t=45)

The parametric analyses also show that the maximum principle tensile stresses are high in the deck, and then drop off significantly and remain fairly constant in the beams. Like in-between the beams, the plastic strains penetrate to about halfway through the depth of the deck. The stresses were slightly higher for the denser reinforcement configuration, while the plastic strains were lower for the lower-shrinkage mix.

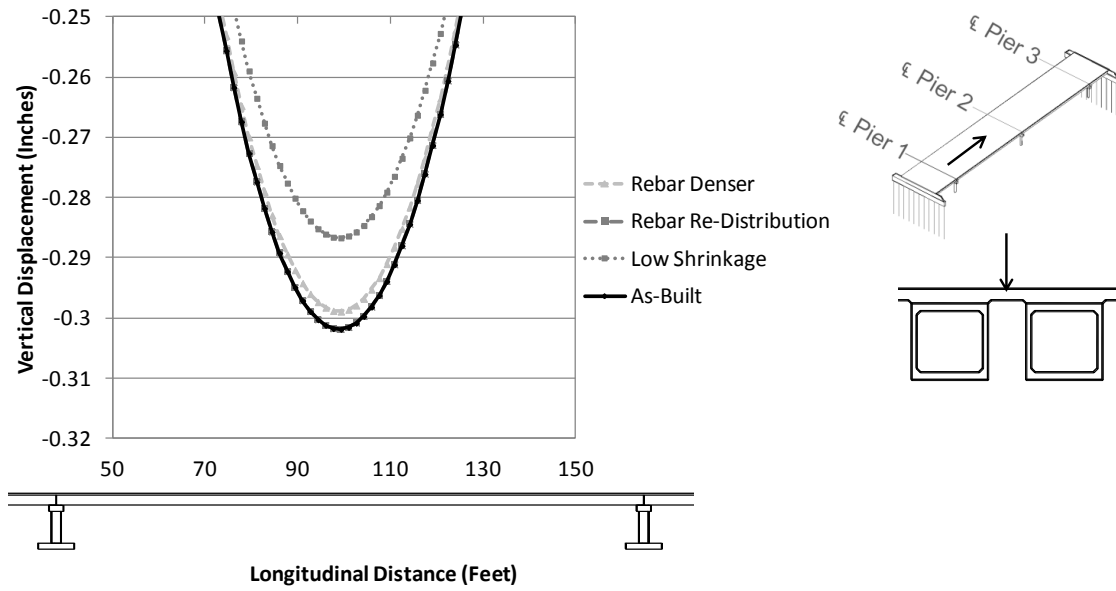


**Figure 185.** Vertical displacements along the longitudinal direction, span 2 (t=45 days)

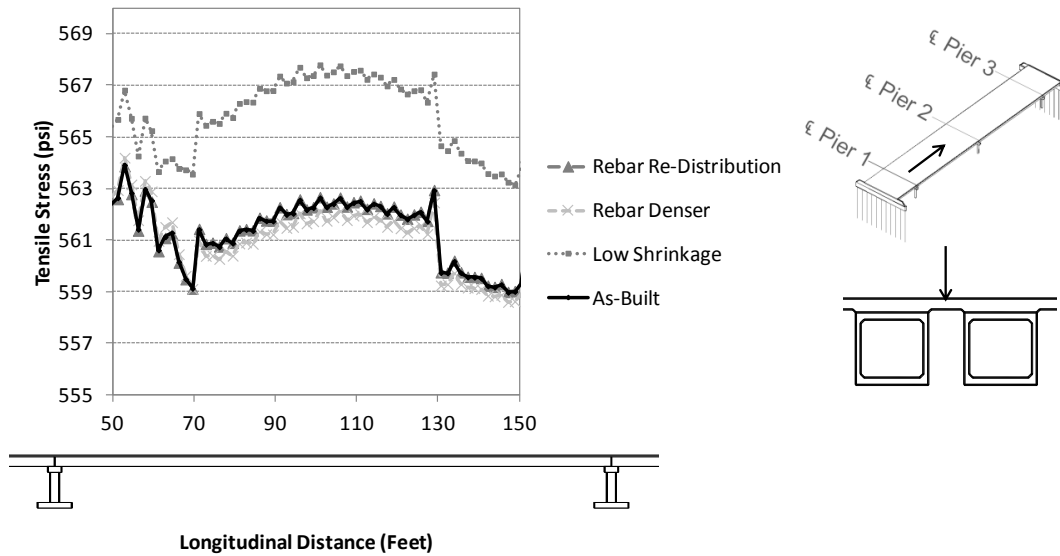


**Figure 186.** Max principal stresses along the longitudinal direction, span 2 (t=45 days)

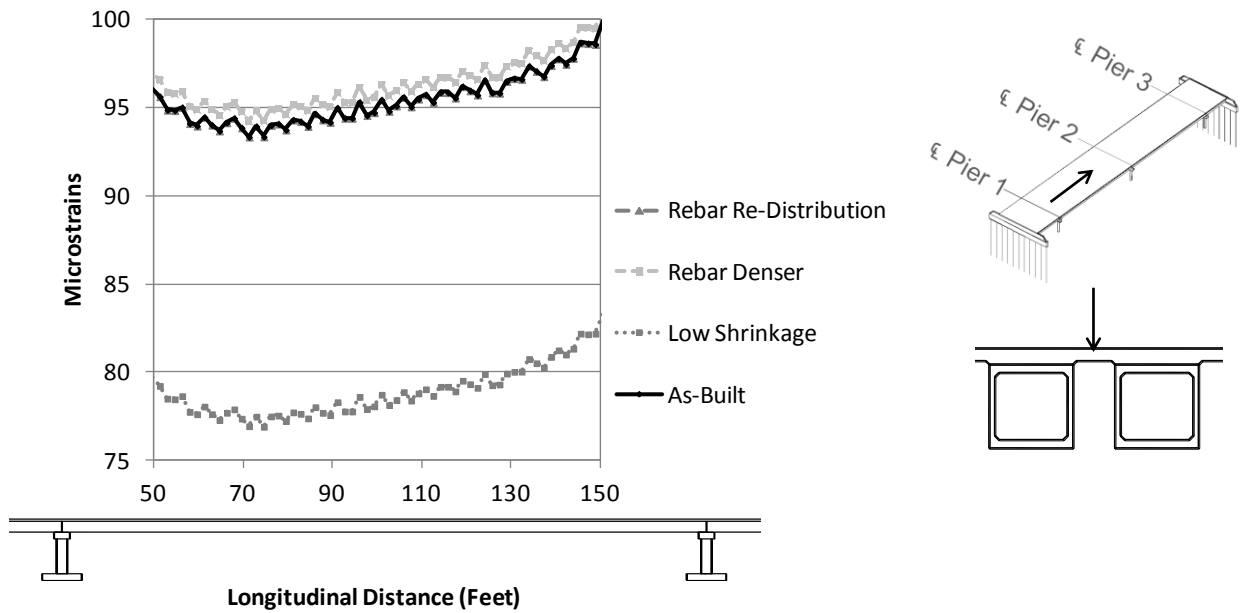


**Figure 187.** Max principal plastic strains along the longitudinal direction, span 2 (t=45 days)

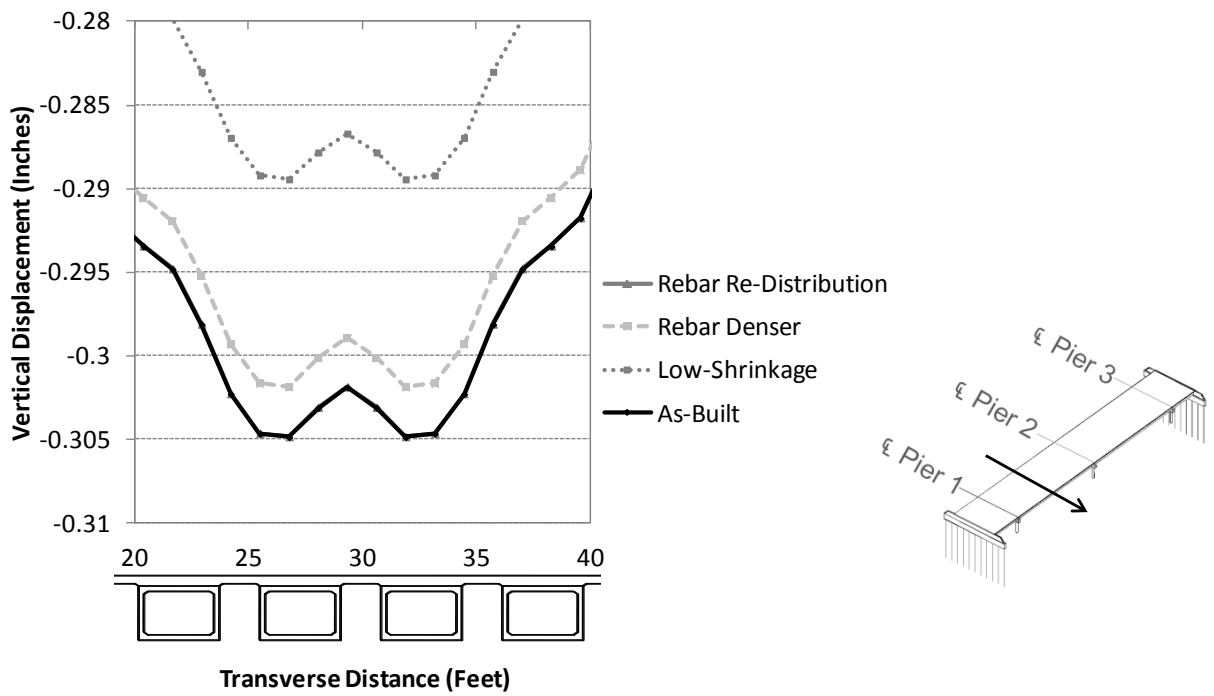


**Figure 188.** Vertical displacements along the transverse direction (t=45 days)

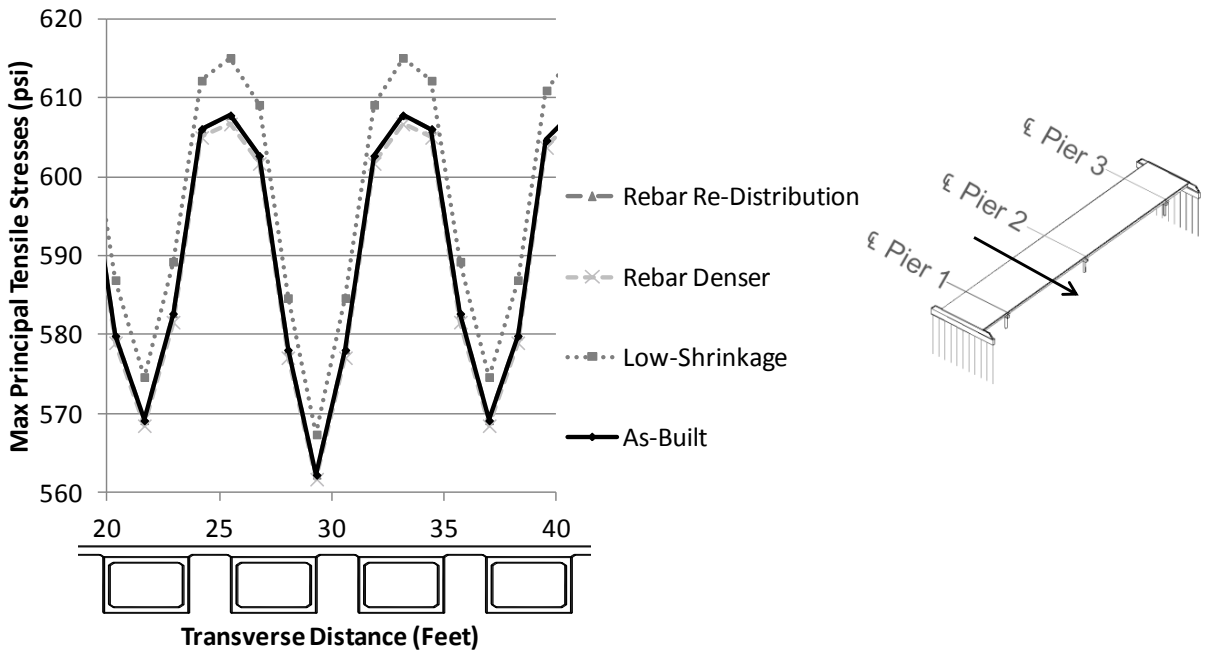


**Figure 189.** Max principal stresses along the transverse direction (t=45 days)

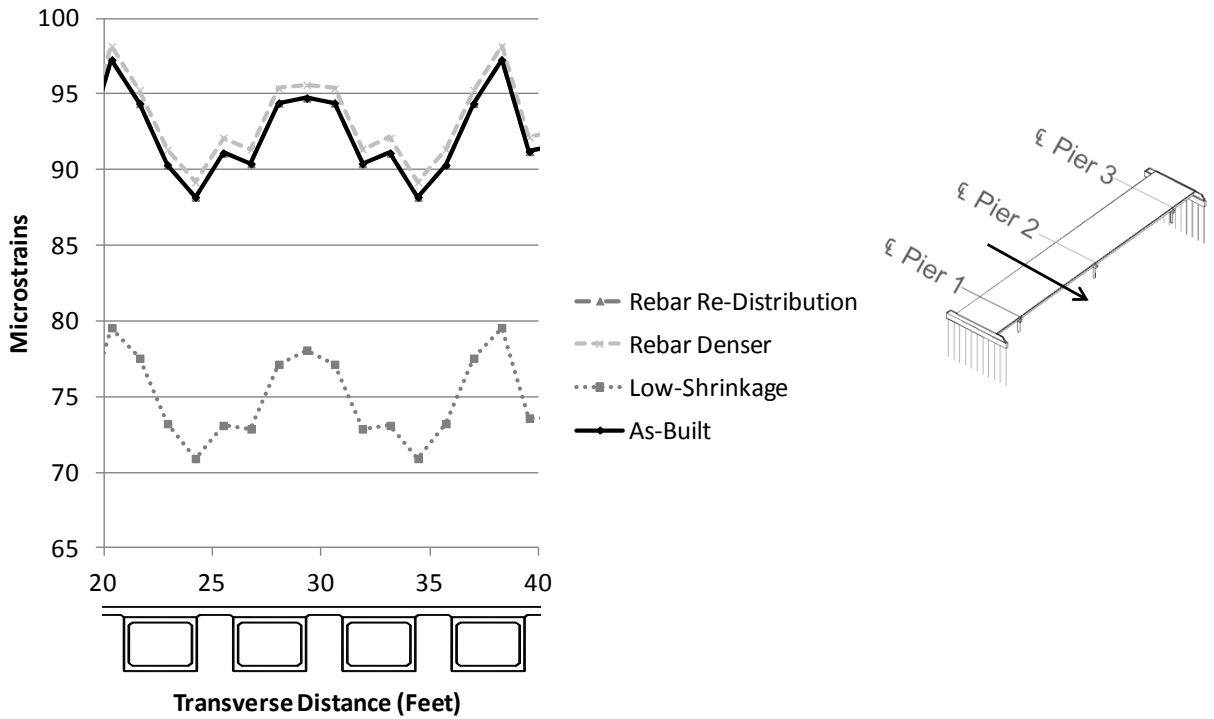


**Figure 190.** Max principal plastic strains along the transverse direction (t=45 days)

As shown in Figure 185 to Figure 190 above, reconfiguring the reinforcement had no effect on the vertical displacements, maximum principal stresses, or maximum principle plastic strains. The low-shrinkage mix had the lowest plastic strain values and the highest maximum principle stress values, which indicates the least amount of damage. The denser reinforcement configuration produced higher plastic strain values and lower stress values, indicating slightly more damage. The vertical displacements were lowest for the low-shrinkage mix, since induced loads are smaller. The denser reinforcement configuration also yielded slightly lower displacement values, due to the added restraint caused by the reinforcement.

Outputs through time on the top surface of the deck in the middle of span 2 are shown in Figure 191. As shown, there is an initial displacement at beginning of shrinkage, followed by a steady increase in displacement as shrinkage continues. This trend matches the behavior seen in the laboratory models. Overall, the as-built model has the highest displacement values, while the low-shrinkage mix has the lowest displacement values. Adding more reinforcement created additional restraint in the slabs, which also lowered the displacement values.

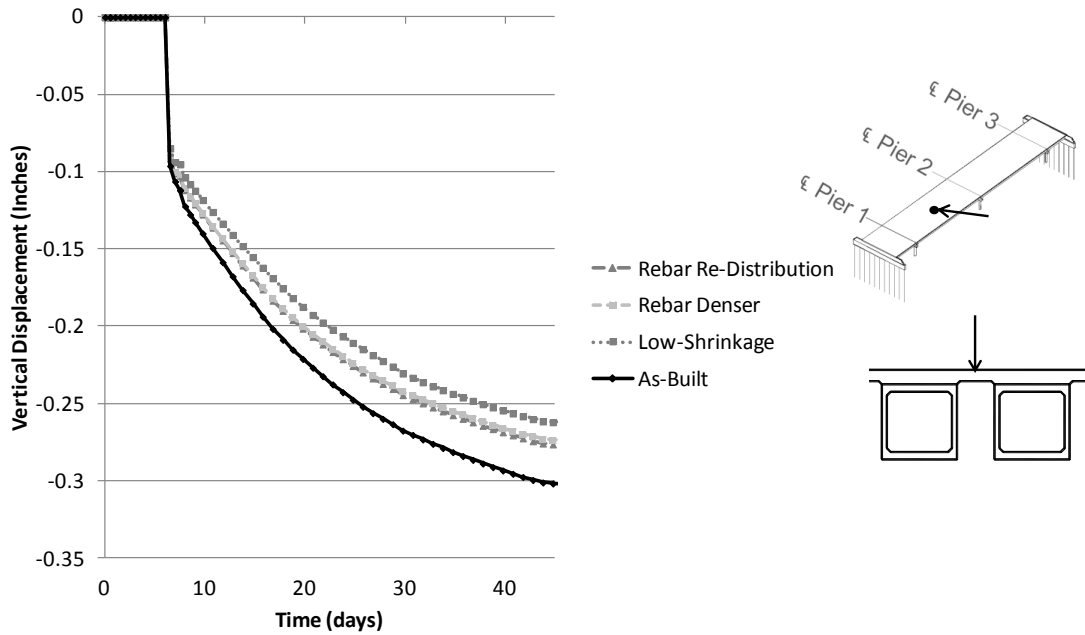


**Figure 191.** Vertical displacements through time, between beams, span 2



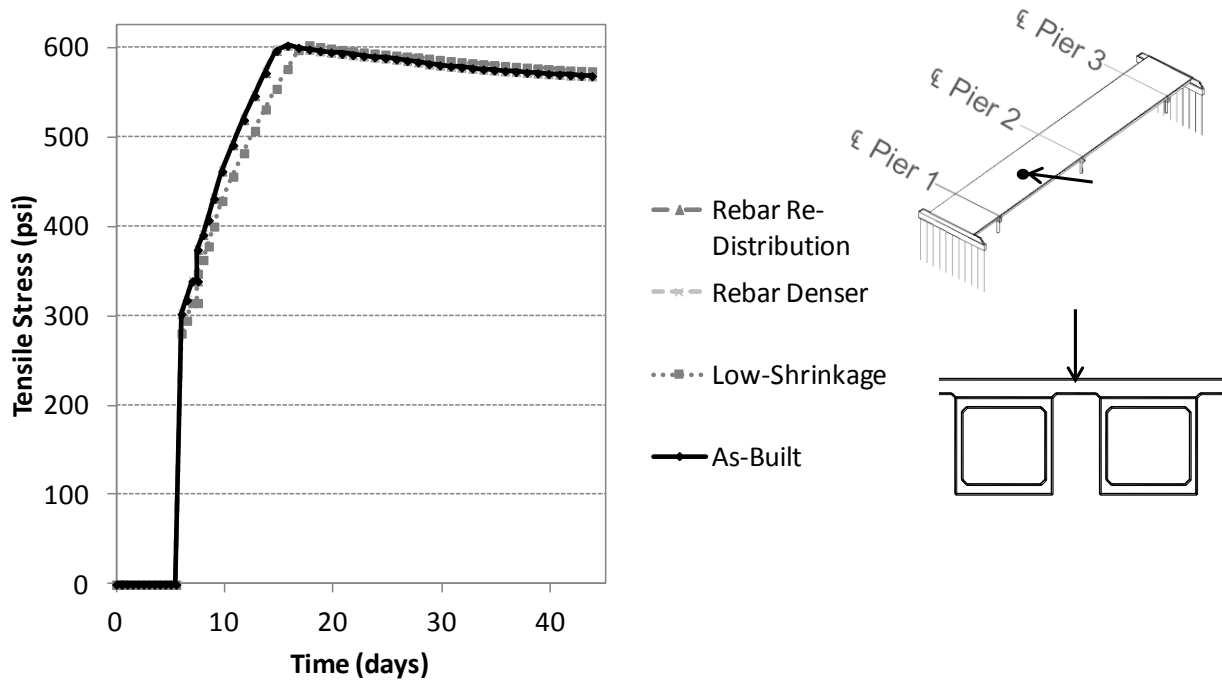


Figure 192. Max principal stresses through time, between beams, span 2

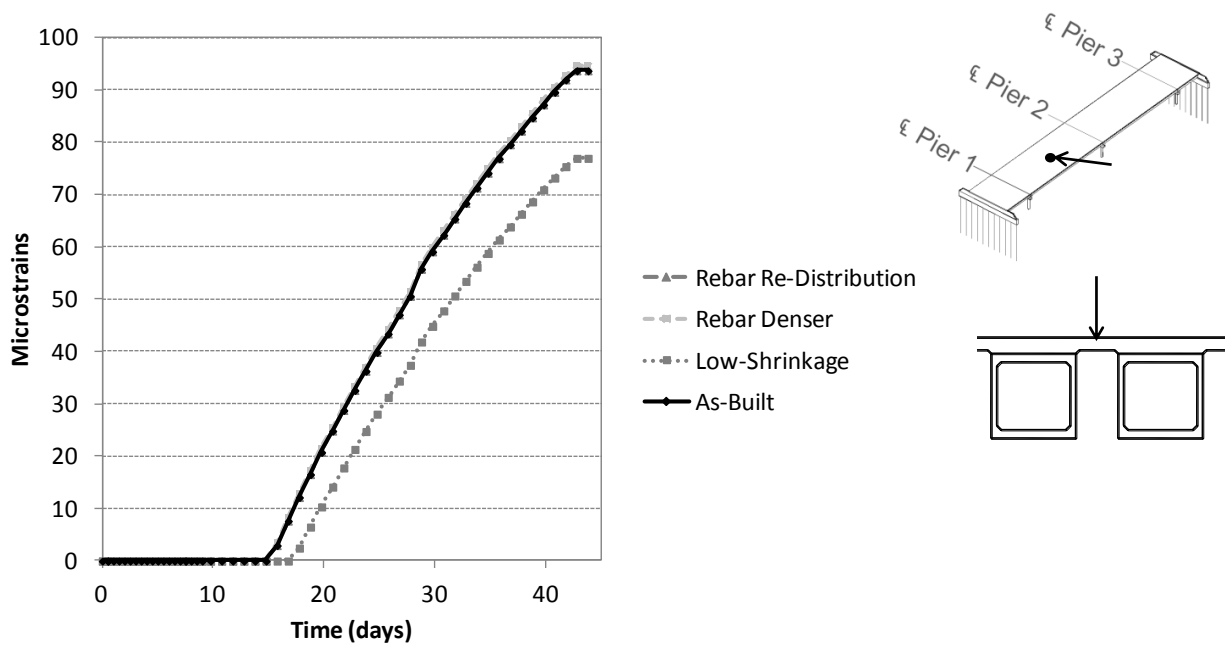


Figure 193. Max principal plastic strains through time, between beams, span 2

As shown, the maximum principal tensile stresses steadily grow until the concrete tensile strength is reached. At that point cracking occurs, and the stresses steadily decrease due to softening. The decrease in stress matches the increase in plastic strains, as the cracks continue to open.

The overall results of the parametric study for the box beam bridges are shown below in Table 25. Note that “time for cracking” is taken as the time for plastic strains to first begin to appear in the deck. This location was over the central pier.

**Table 25.** Box beam bridge parametric study overall results

<b>Analysis</b>	<b>Time for cracking</b>	<b>Maximum Plastic Strain Value</b>	<b>Maximum Vertical Displacement</b>
As-Built	13 days	281 $\mu$ -strain	-0.308 inches
Low-Shrinkage	16 days	249 $\mu$ -strain	-0.293 inches
Denser Rebar	12 days	284 $\mu$ -strain	-0.305 inches
Rebar Re-Distribution	13 days	281 $\mu$ -strain	-0.308 inches

Overall, the bridge with the low-shrinkage mix exhibited the best behavior. It had the lowest value of plastic strains at the end of the analysis as well as the latest time for cracking to occur. Increasing the amount of reinforcement by 50% created more restraint in the bridge deck, which lowered the time for cracking and increased the maximum plastic strain value at the end of the analysis. The effect of this, however, was very minimal. Re-distributing the deck reinforcement did not have a large effect on the bridge overall behavior. This is likely due to the way reinforcement was modeled in the simulation. The ‘rebar layer’ option in Abaqus uses the reinforcement information to modify the overall stiffness of the section, rather than implementing discrete reinforcement locations. Since the re-distribution of the reinforcement kept the same reinforcement ratio, the overall deck stiffness remained the same as in the as-built model, thus not having a large effect on the behavior.

#### 6.5.3.1 *Effect of Increasing Deck Reinforcement*

Increasing the amount of reinforcement by 50% created more restraint in the bridge deck, which lowered the time for cracking and increased the maximum plastic strain value at the end of the analysis. While this effect was very minimal, the results conflict with the conventional

wisdom for the effects of adding reinforcing steel. It would be expected that increasing the reinforcement in the deck would allow for more stresses to be accommodated by the steel, and thus produce less cracking. However, the analyses show the opposite effect.

To investigate the effect of reinforcing steel on concrete shrinkage cracking, small fixed “prism” models were created in Abaqus. The models were fully fixed at both ends, with uniform shrinkage temperature applied to the outside surfaces. The temperature followed the same temperature loading used for the ring test models, as shown in Figure 101. A schematic of the model is shown below in Figure 194.

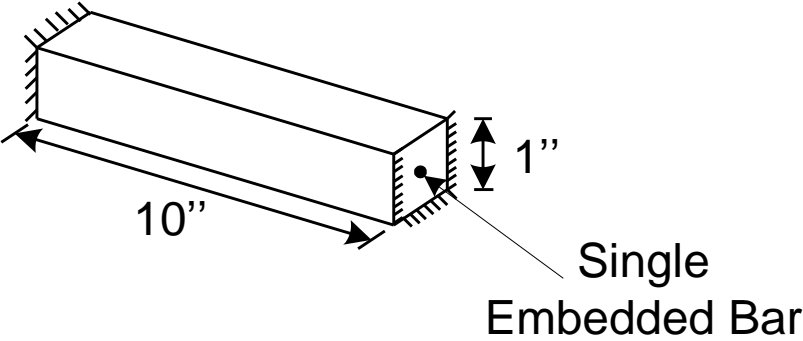
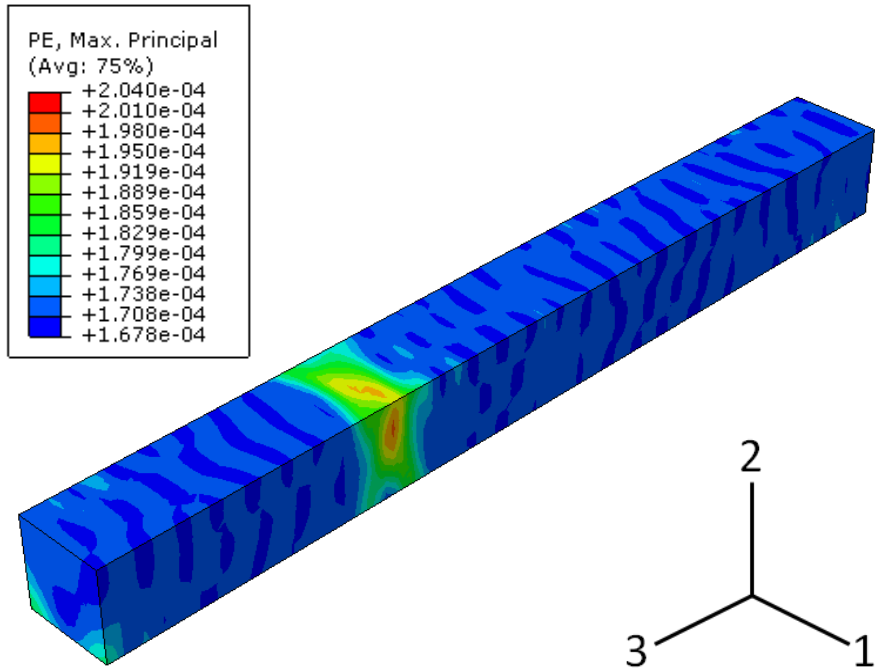
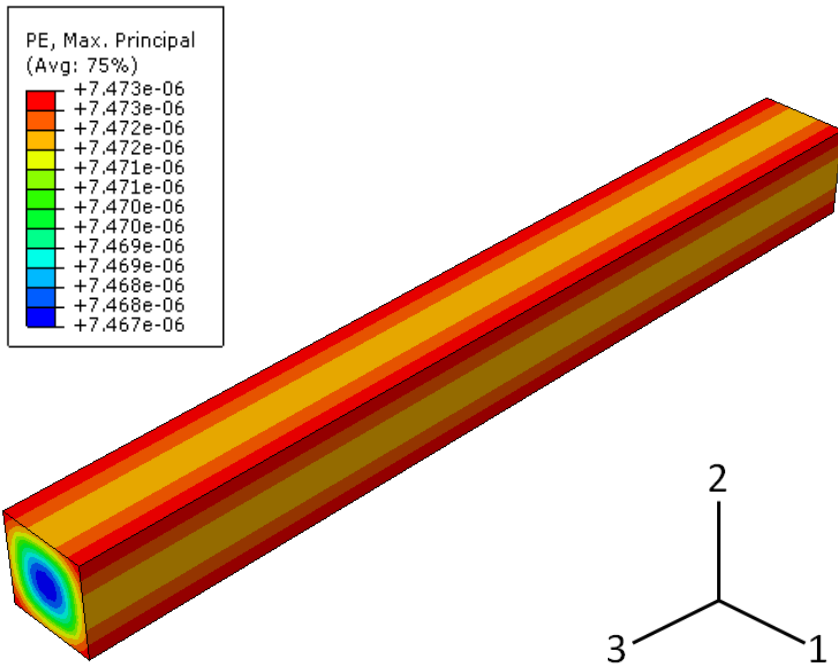


**Figure 194.** Prism model setup for investigating effect of reinforcement

As shown above in Figure 194, the effect of reinforcement was investigated by means of a single embedded bar in the middle of the prism. The analyses included a plain prism with no reinforcement, an embedded #3 bar, and an embedded #8 bar. Maximum principal plastic strain outputs for each analysis are shown below in Figure 195 to Figure 197.

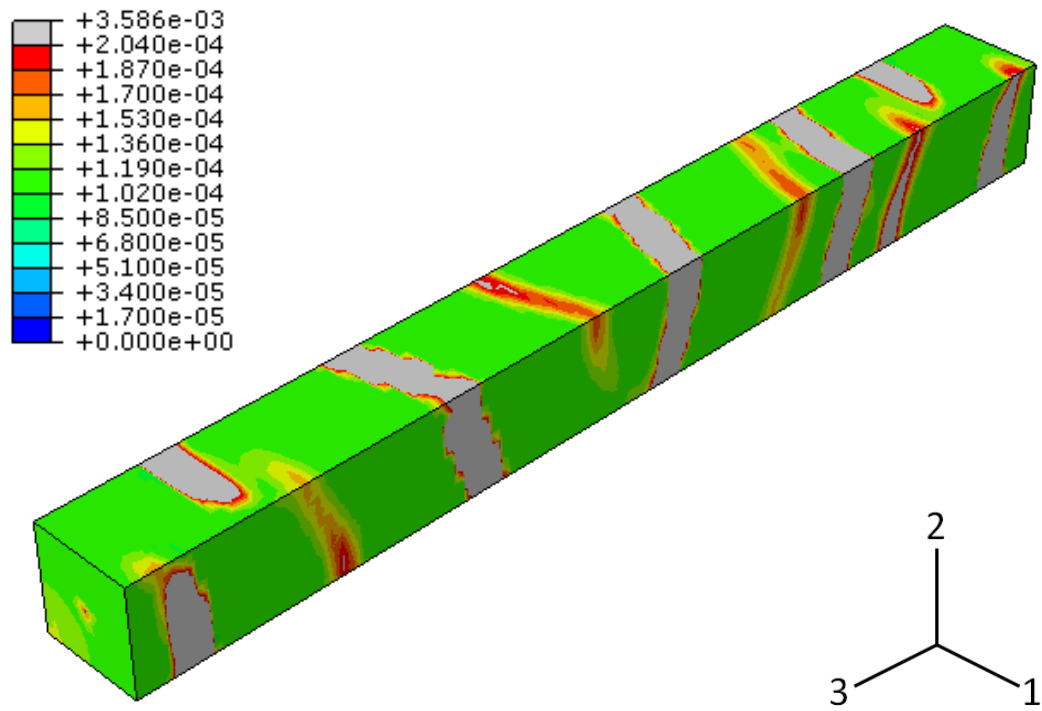


a) Time=30 days (end of analysis)

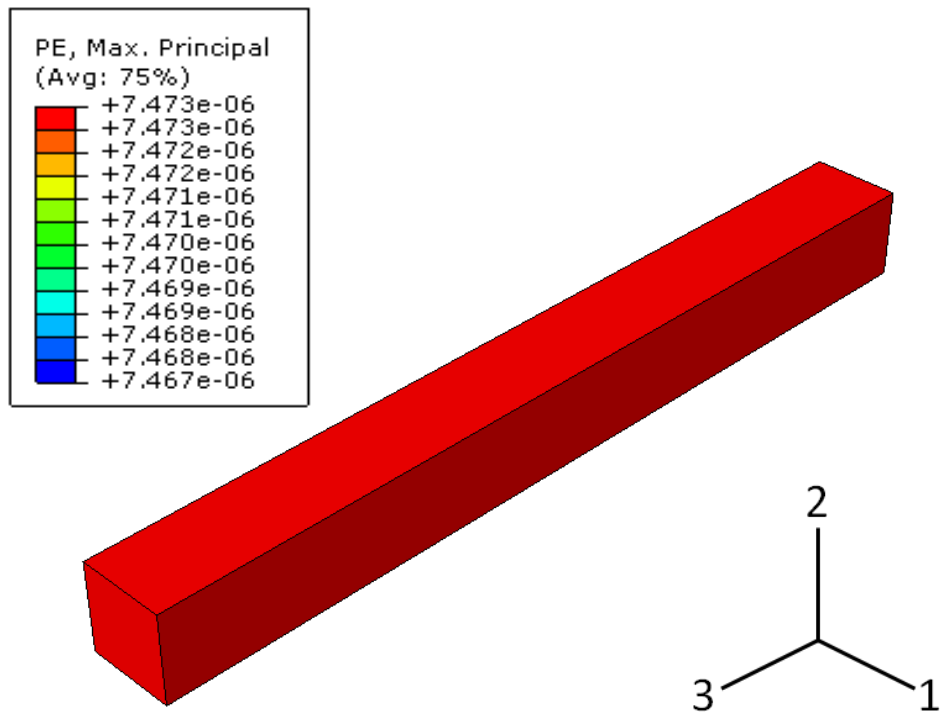


b) T=13.5 days (plastic strains begin to appear)

**Figure 195.** Maximum principal plastic strain output, unreinforced prism

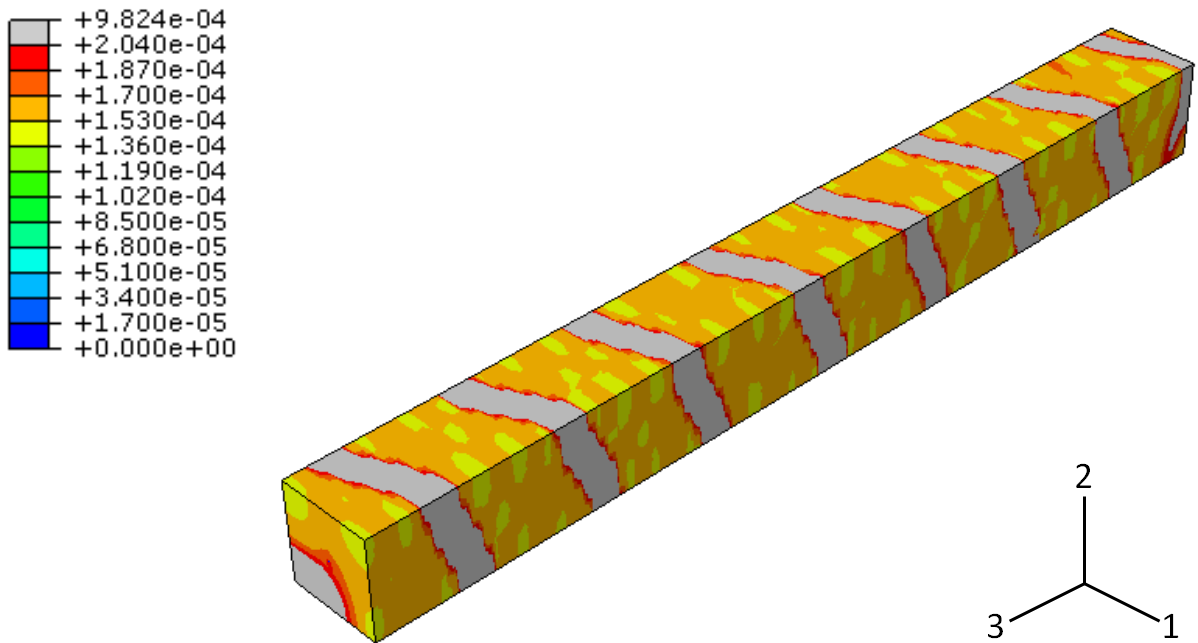


a) Time=30 days (end of analysis)

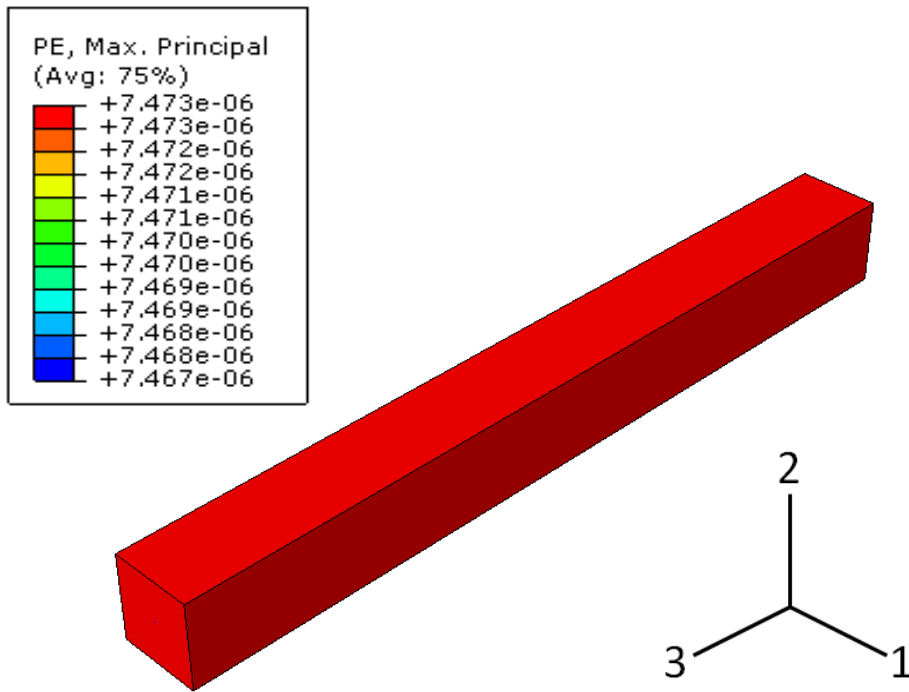


b) T=13.5 days (plastic strains begin to appear)

**Figure 196.** Maximum principal plastic strain output, #3 embedded bar



a) Time=27 days (end of analysis)



b) T=13.5 days (plastic strains begin to appear)

**Figure 197.** Maximum principal plastic strain output, #8 embedded bar

As shown above in Figure 195 to Figure 197, plastic strains begin to appear through the entire prism at a time of 13.5 days for all three models. This corresponded to a shrinkage strain of

175 $\mu$ -strain, and a temperature value of -30<sup>o</sup>F. The plastic remain uniform until a time of 23 days, after which high values and concentrations can be seen evenly-spaced through the length of the prism. When comparing the results at the end of the analysis, it can be seen that increasing the bar size produces slightly lower plastic strain values at a closer spacing.

To further determine the effects of increasing the bar size, plots through time were extracted for the maximum principal plastic strain and stress values. The stresses through time at the outside middle point of the prism are shown below in Figure 198.

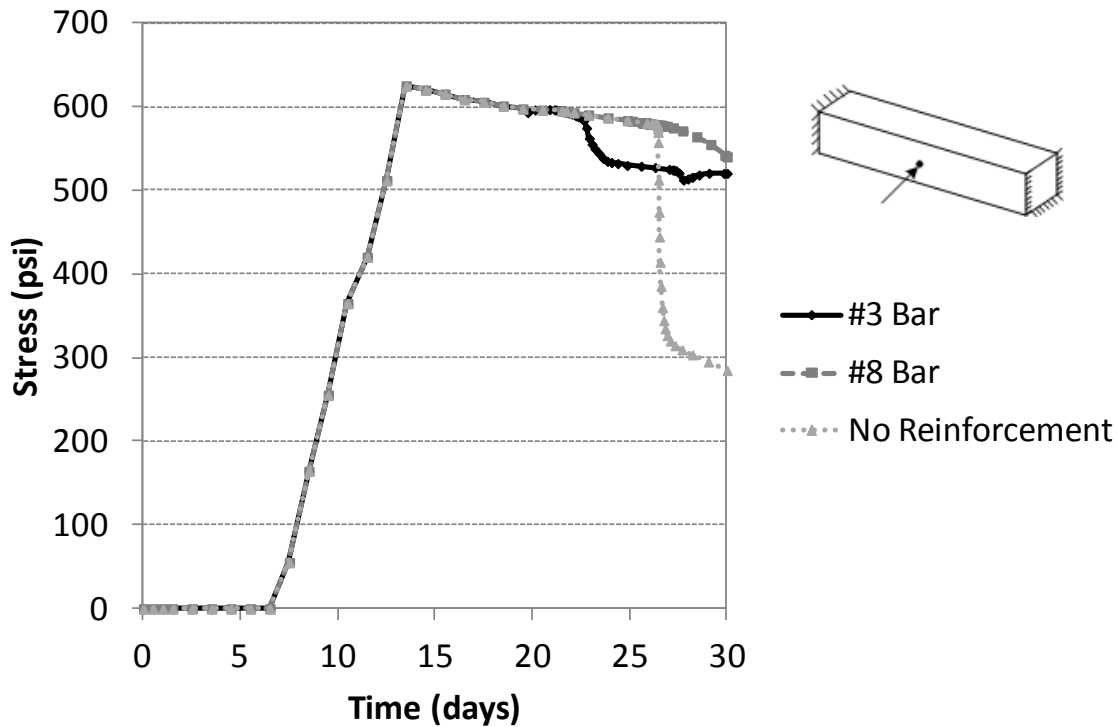


**Figure 198.** Development of stresses with time in prism

As shown in Figure 198, the most concrete softening occurred in the unreinforced model, which is indicated by the largest drop in stress. The prism with the #3 bar experienced slightly more softening than the prism with the #8 bar. Plastic strains were extracted along a longitudinal path on the outside edge of the prism at different times to determine the development of cracking, as shown below in Figure 199 and Figure 200.

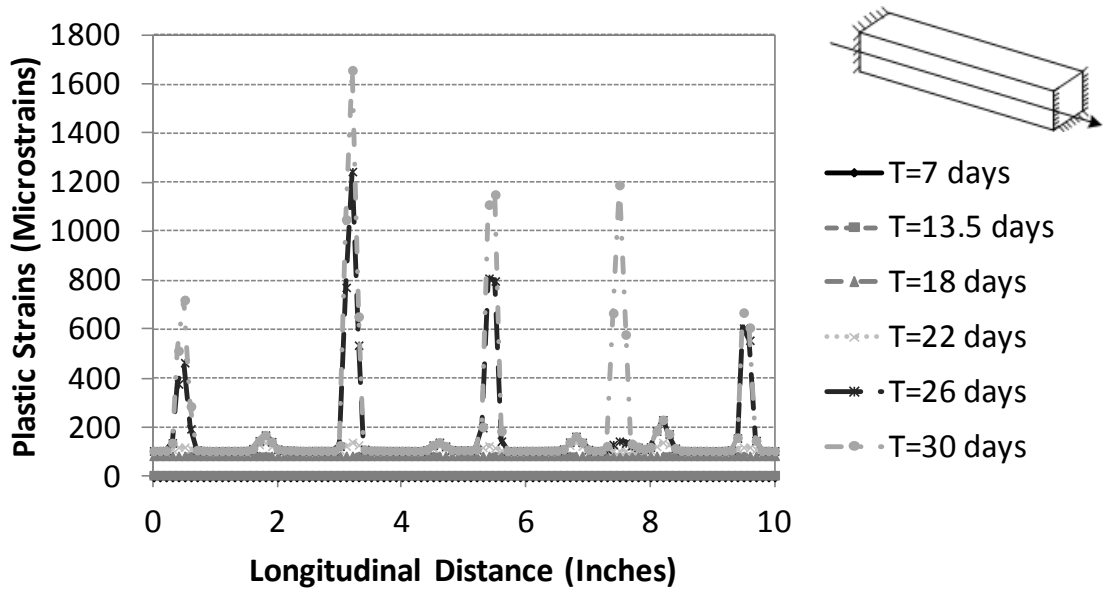


**Figure 199.** Prism with #3 reinforcement plastic strain output at various times

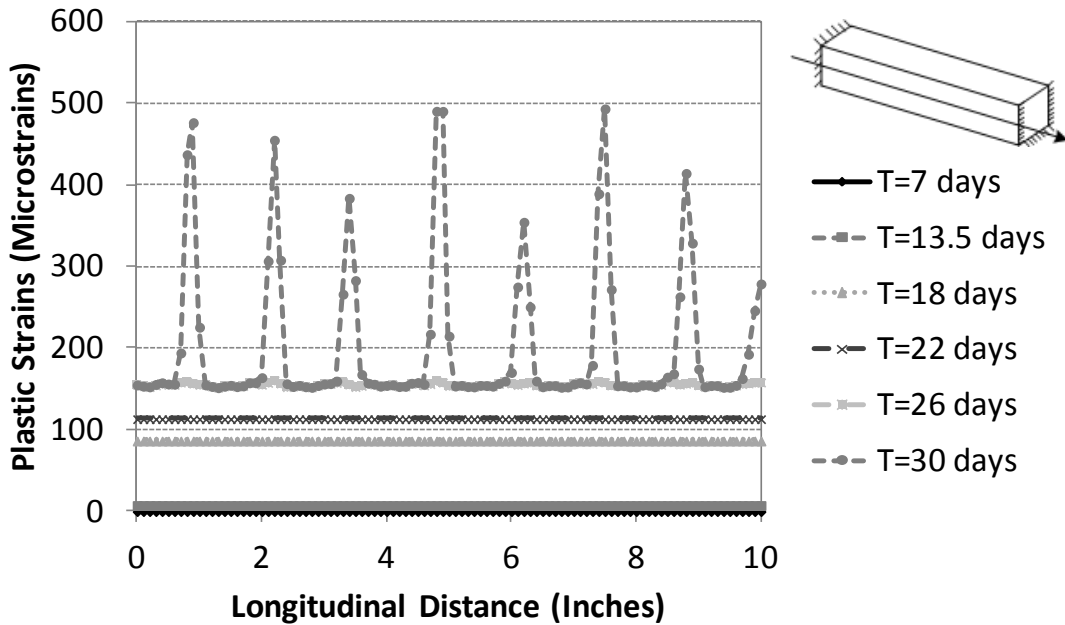


**Figure 200.** Prism with #8 reinforcement plastic strain output at various times

As seen above in Figure 199 and Figure 200, the prism with the #3 reinforcement had higher plastic strain values, with less cracking locations. The prism with the #8 reinforcement had more cracking locations, but lower plastic strain values than the prism with the #3 reinforcement. This behavior matches what was expected. If the bar size is increased, it would be expected that the crack widths would decrease, but the number of cracks would increase, which is seen in the



plots. Comparing the plastic strains at the concentrated areas of cracking, the larger plastic strain values in the model with the #3 bar can be seen, which is illustrated below in Figure 201.

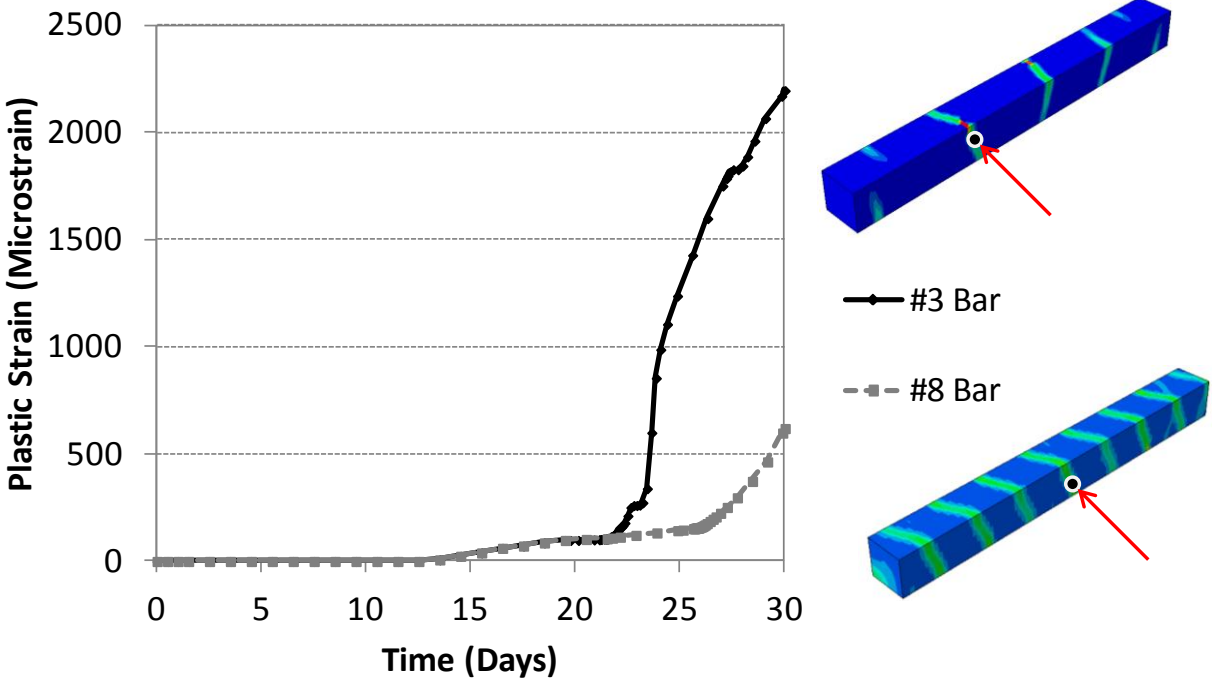


**Figure 201.** Prism plastic strain values with time in concentrated cracking areas

The longitudinal stresses through time in the bars were also extracted. It would be expected that the #8 bar would have lower stress values due to its increased area. The bar stress output is shown below in Figure 202.

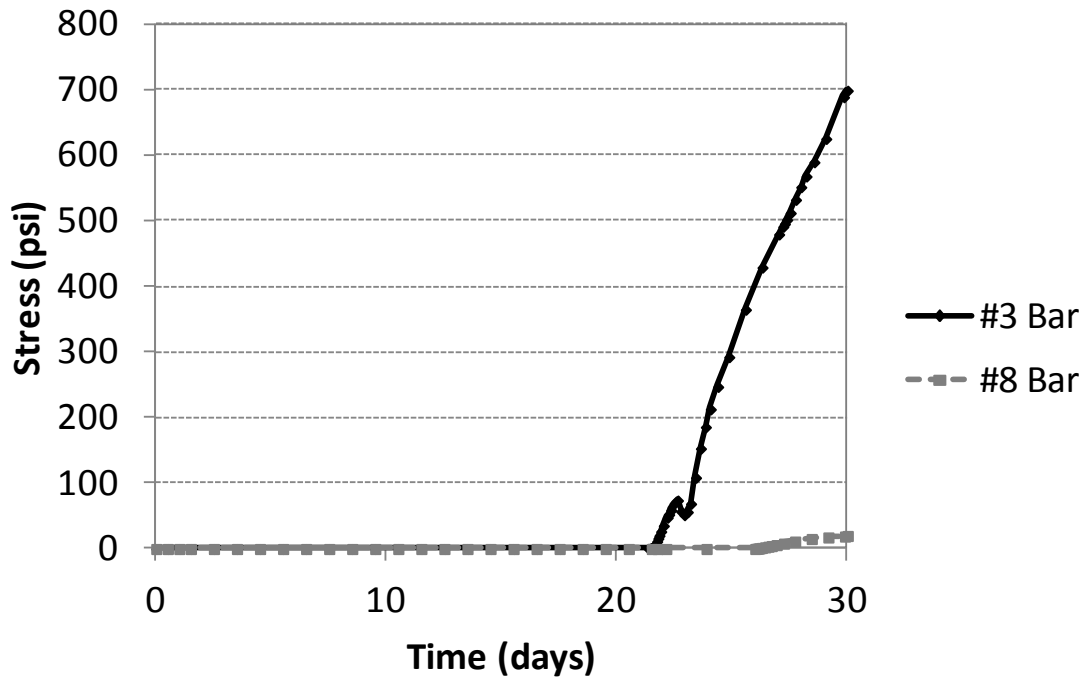


**Figure 202.** Prism reinforcing bar longitudinal stresses with time

Based on these analyses, it can be seen that the modeling approach is correct in terms of load sharing between the steel and the concrete. It would be expected that the larger the bar size, the lower the stresses in the bar, the decreased crack width, and the tighter spacing between cracks, all of which is captured in the models.

To investigate this issue further, the same prism models were run with a shell element and ‘rebar layer’ approach used to simulate the steel reinforcement. This was done since the ‘rebar layer’ approach was used in the full bridge models. The maximum principal plastic strain outputs at the end of the analysis are shown below in Figure 203 and Figure 204.

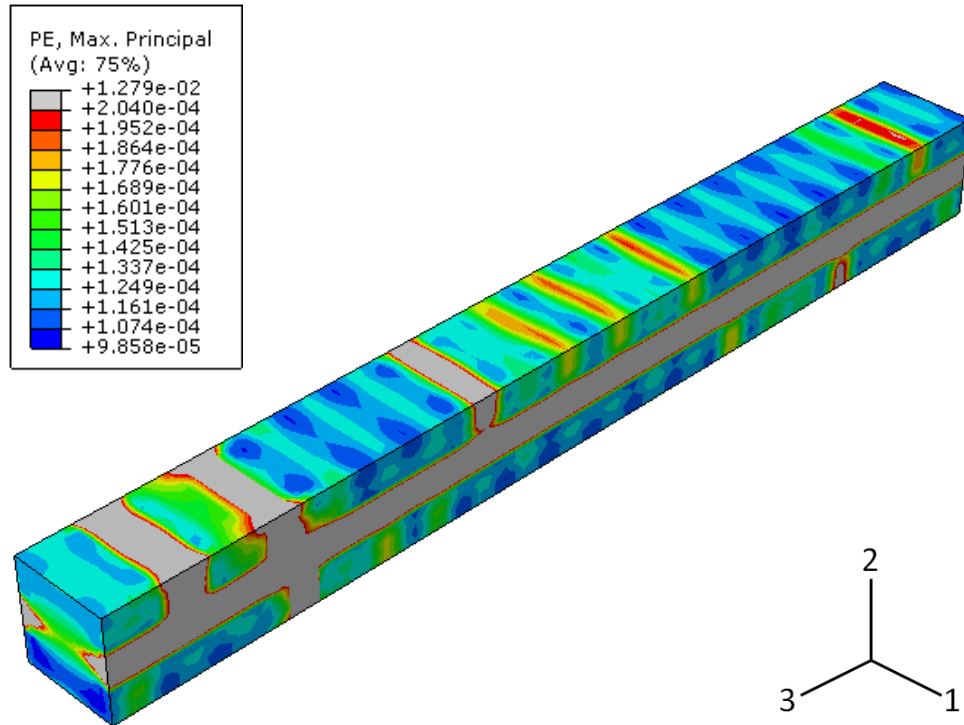


**Figure 203.** #3 prism with ‘rebar layer’ approach maximum principal plastic strains (t=30 days)

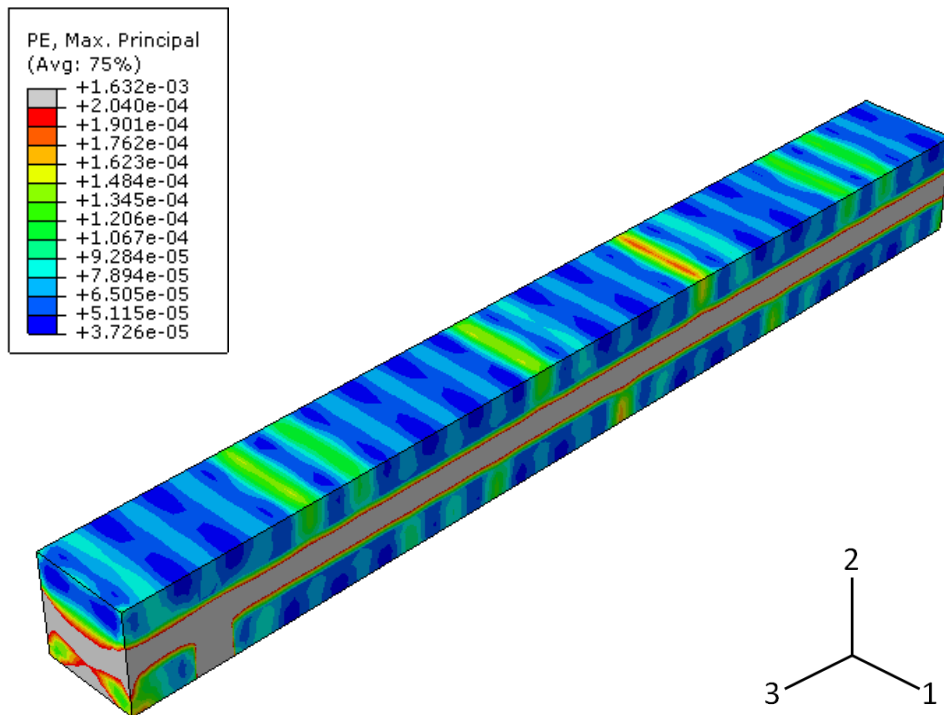


**Figure 204.** #8 prism with ‘rebar layer’ approach maximum principal plastic strains (t=30 days)

As seen in Figure 203 and Figure 204, using the rebar layer approach yields a slightly different plastic strain output. Since the rebar layer uses a smeared reinforcement approach,

where the reinforcement stiffness is spread across the entire shell section, the plastic strain values become concentrated at the location where the reinforcement is embedded. Even with this approach, it can still be seen that increasing the reinforcement bar size yields lower plastic strain values, and more cracking locations. To verify this, the plastic strains along the top edge of the prism were extracted at the end of the analysis and compared, as shown below in Figure 205.

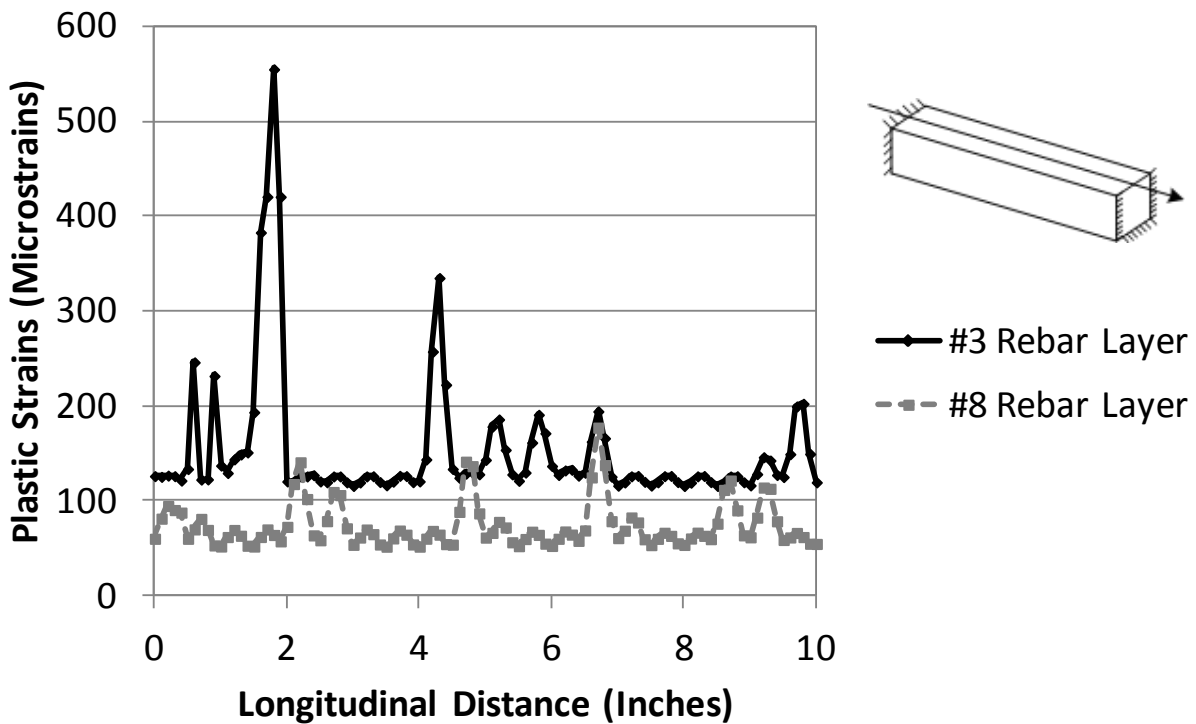


**Figure 205.** Plastic strains along longitudinal path for prisms with rebar layer approach (t=30)

As seen above in Figure 205, the plastic strain values are higher for the prism with the #3 rebar layer than the prism with the #8 rebar layer, which was expected. Although it is not as obvious as in the approach using the discrete embedded bar, it can be seen that the prism with the #8 rebar layer has more cracking locations, with lower overall plastic strain values.

In the full bridge models, the increase in plastic strain magnitudes that is seen with the increase in reinforcement can be attributed to the increased stiffness of the deck/girder system. In the full bridge deck, the girders create additional restraint, which produces higher plastic strain values with an increase in deck stiffness. The plastic strains are developed as a result of the restrained volume change due to shrinkage. In a real bridge deck, an increase in the reinforcement would lead to more discrete cracking locations, and lower overall crack widths.

However, the computational analysis uses a continuum model with strain/deformation control. When the stresses are high enough to induce plastic strains, cracking occurs throughout the entire model, and the analysis does not capture discrete crack locations. Therefore, while the models predict increased plastic strain values with added reinforcement, the crack widths and spacing would in reality be reduced with added reinforcement.

#### 6.5.4 Steel girder bridge parametric study comparison results

As with the box beam bridge, the overall global behavior of the steel girder bridge remained the same for all the parametric analyses. To compare the outputs, maximum principal tensile stresses, maximum principal plastic strains, and vertical displacements were extracted at various locations and paths in the bridge deck. The nomenclature used in the results is summarized below in Table 26.

**Table 26.** Nomenclature used for steel girder parametric study results

<b>Parameter</b>	<b>Nomenclature used in plots of results</b>
As-built model	“As-built”
Effect of changing abutment connection	“Non-integral”
Effect of changing the shear connector distribution	“Shear Stud”
Effect of changing the skew angle	“Skew Angle”

Selected results of the study are shown in Figure 206 to Figure 221. As shown, the tensile stresses are higher near the top of the deck, and decrease through the depth. The plastic strains penetrate roughly halfway through the depth of the deck, as in the box beam bridge. Increasing the shear connector spacing slightly lowered the maximum principal plastic strain values, as well as creating a non-integral connection at the abutment. Increasing the skew angle yielded slightly higher plastic strain values.

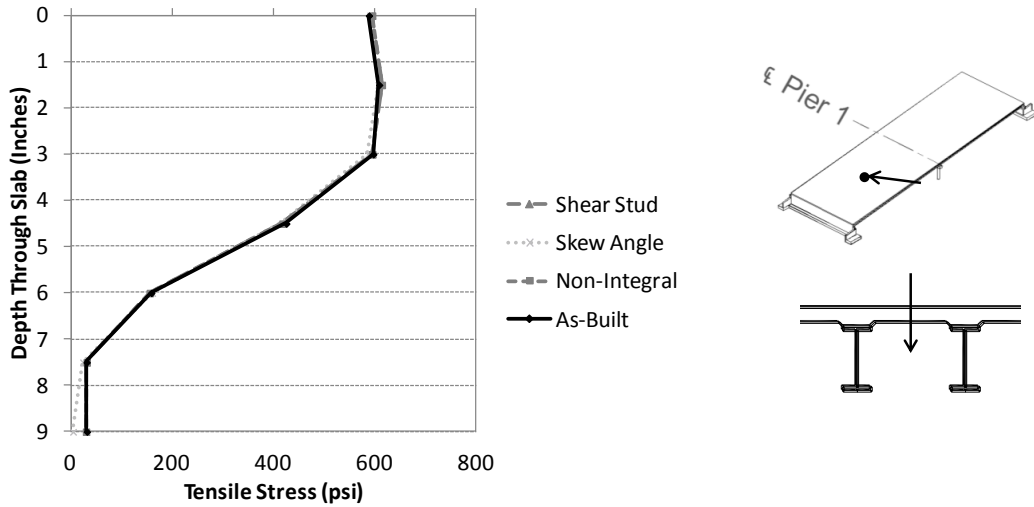


**Figure 206.** Max principal tensile stresses through the depth of the slab, between beams (t=45)

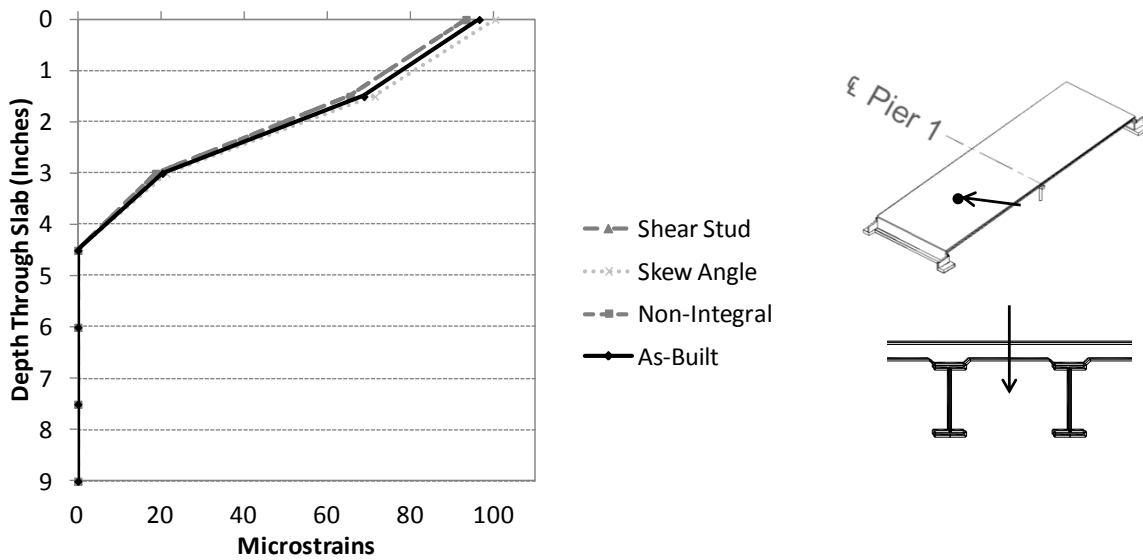


**Figure 207.** Max principal plastic strains through the depth of the slab, between beams (t=45)

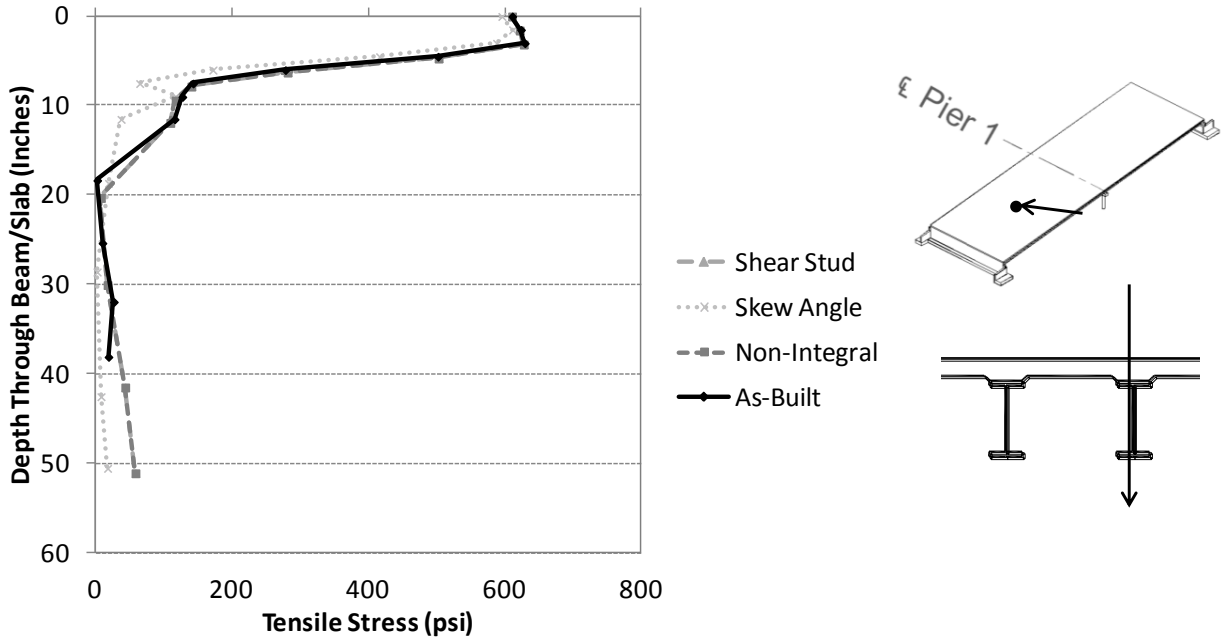


**Figure 208.** Max principal tensile stresses through depth of beam/slab assembly (t=45)

As shown, the maximum principle tensile stresses are high in the deck, and then drop off significantly and remain fairly constant in the beams. Like in-between the beams, the plastic strains penetrate to about halfway through the depth of the deck. The tensile stresses were slightly higher for the non-integral abutment connection and higher shear connector spacing, which corresponded to lower plastic strains. Increasing the skew angle also yielded slightly lower tensile stresses and higher plastic strains.

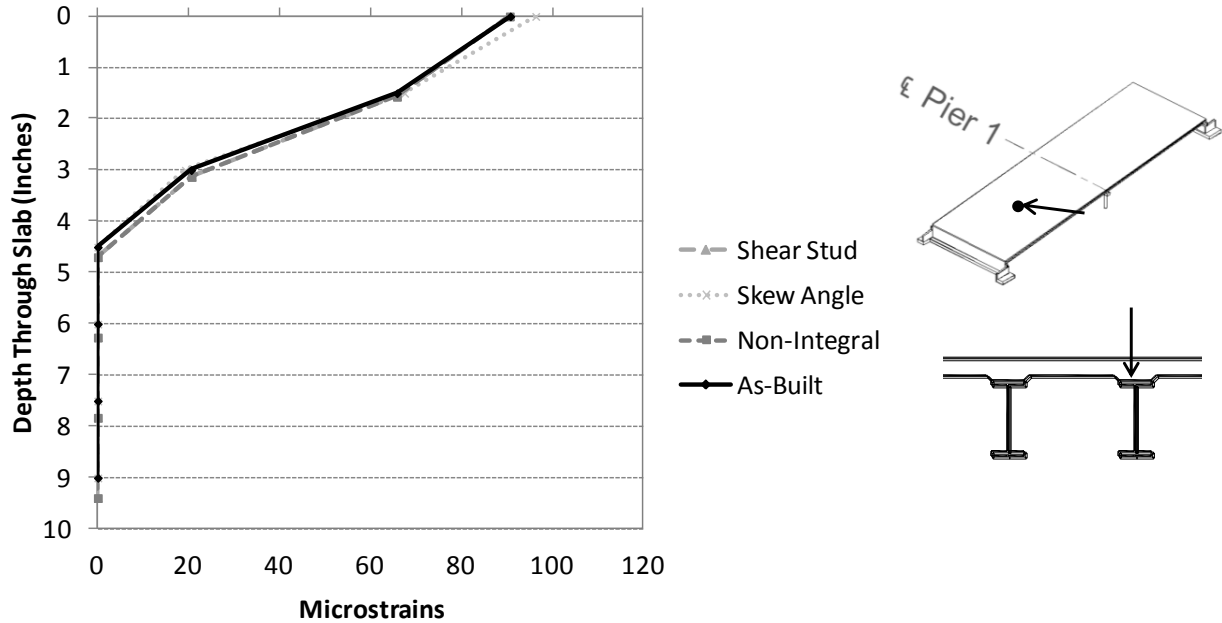


**Figure 209.** Max principal plastic strains through depth of slab, over beams (t=45)

As shown in Figure 210 to Figure 215 above, the non-integral abutment configuration yielded higher displacements, higher stresses, and lower plastic strains. The increased shear connector spacing configuration also yielded slightly higher displacements, higher stresses, and lower plastic strains, although not to the extent of the non-integral abutment configuration. Increasing the skew angle yielded lower displacements, lower stresses, and higher plastic strain values. The amount of overall restraint created by the non-integral abutment connection and increased shear connector spacing was lower than the as-built case, while increasing the skew angle produced a higher amount of restraint in the system.



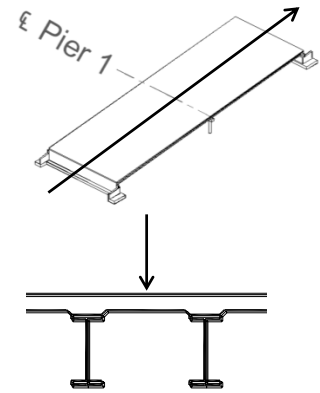
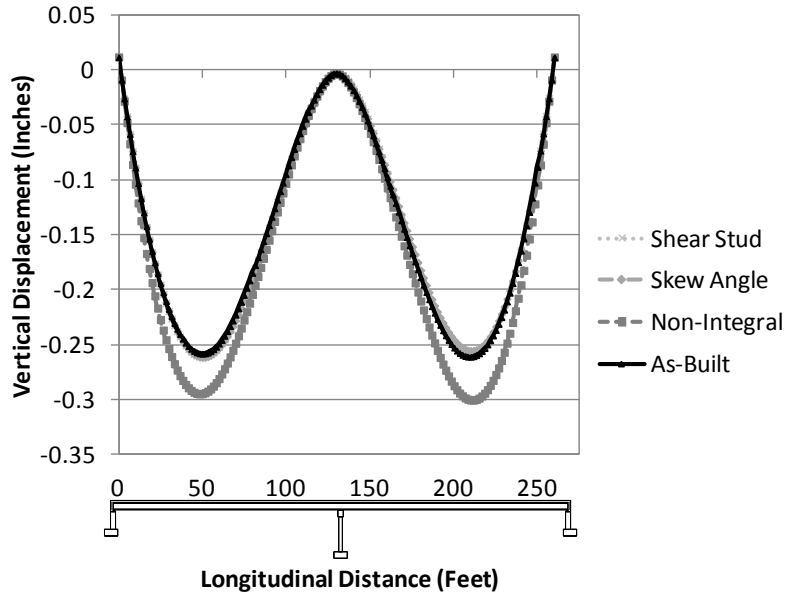


Figure 210. Vertical displacements along the longitudinal direction (t=45 days)

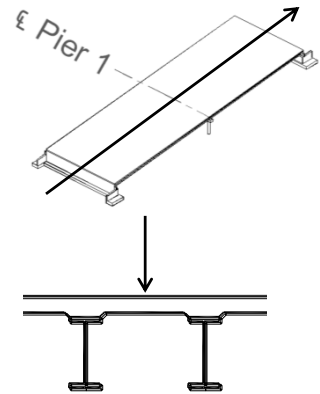
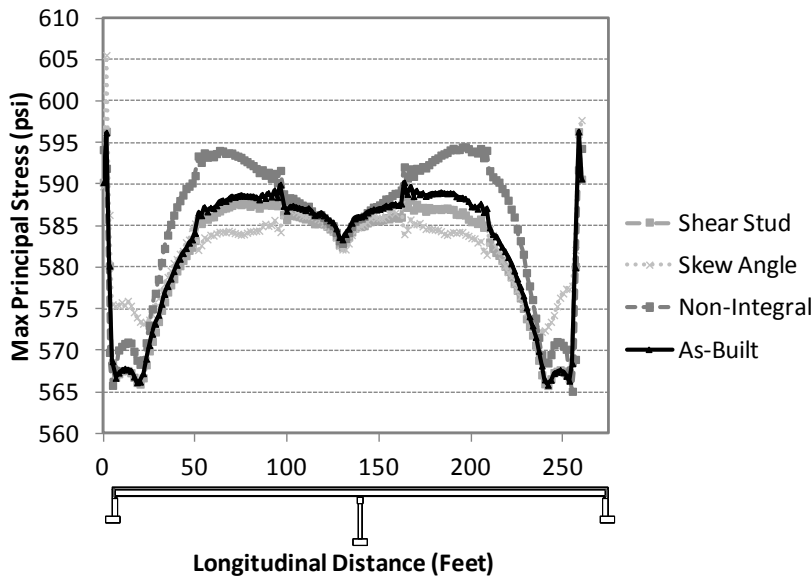
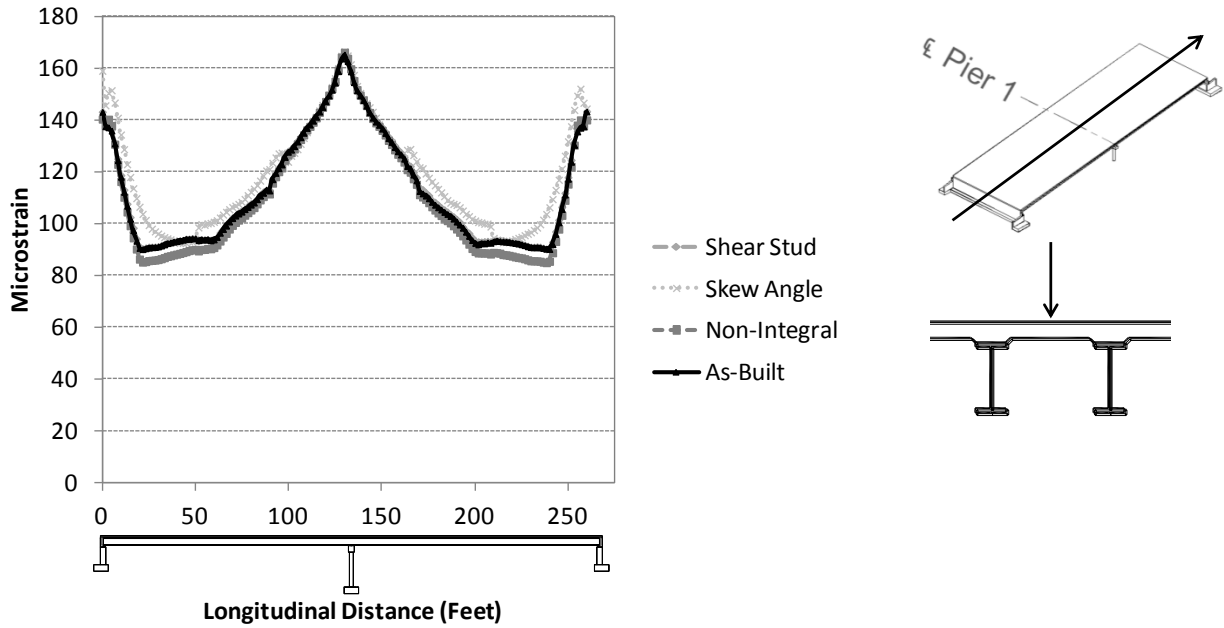
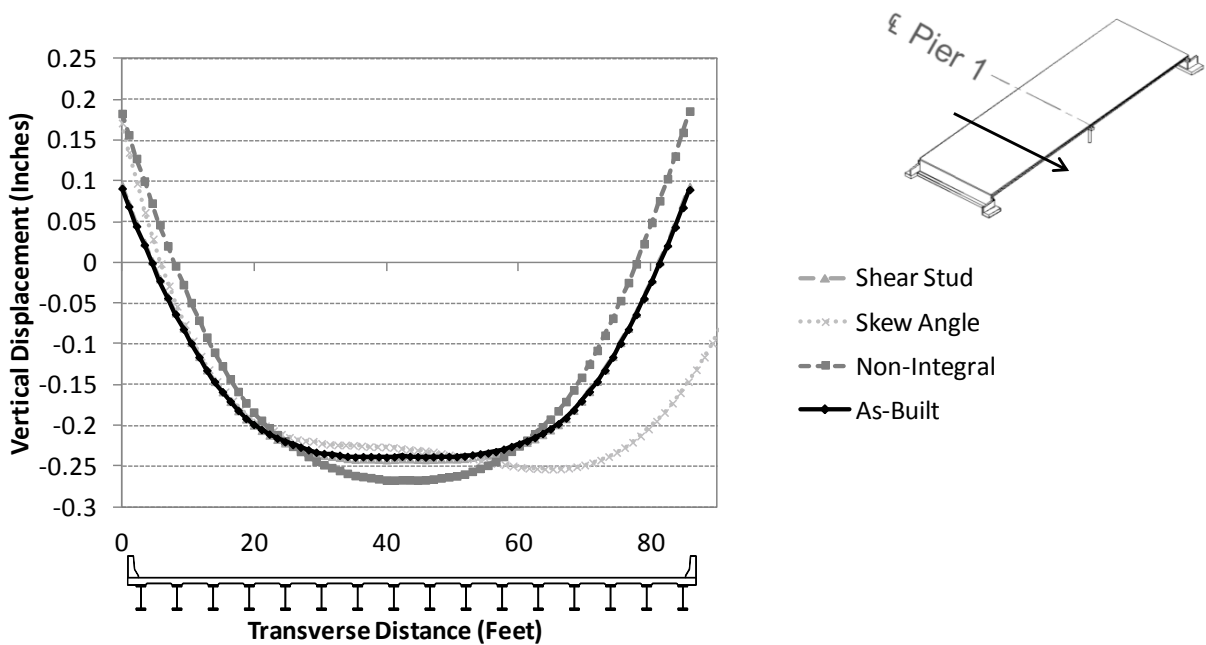


Figure 211. Max principal stresses along the longitudinal direction (t=45 days)



**Figure 212.** Max principal plastic strains along the longitudinal direction (t=45 days)



**Figure 213.** Vertical displacements along the transverse direction (t=45 days)

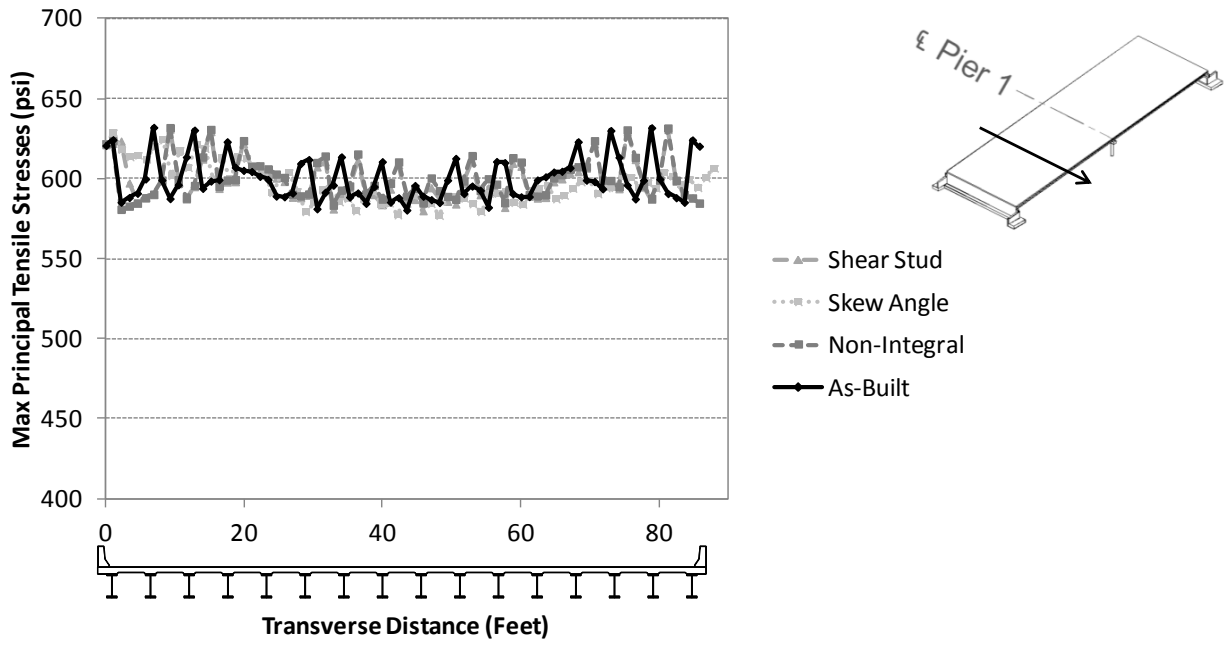


**Figure 214.** Max principal stresses along the transverse direction (t=45 days)

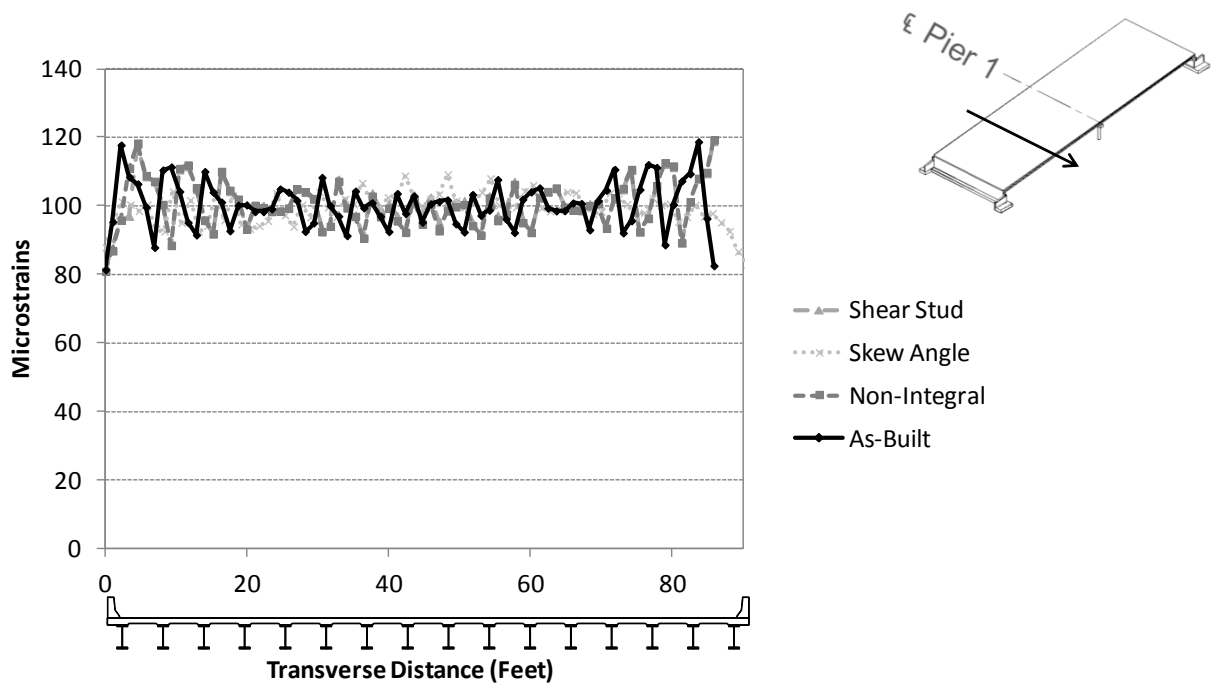


**Figure 215.** Max principal plastic strains along the transverse direction (t=45 days)

Outputs through time on the top surface of the deck in the middle of span 2 are shown in Figure 216. As shown, there is an initial displacement at beginning of shrinkage, followed by a steady increase in displacement as shrinkage continues. This trend matches the behavior experienced for the laboratory models.

Overall, the bridge with the non-integral abutment configuration had highest displacement values while the bridge with the skew had the lowest displacement values. The bridge with the higher shear stud spacing also had slightly higher displacement values. This occurred because the bridge with the non-integral connection had the lowest amount of overall restraint, which allowed for increased displacements. The skew angle created additional restraint in the bridge, which limited the displacement values.

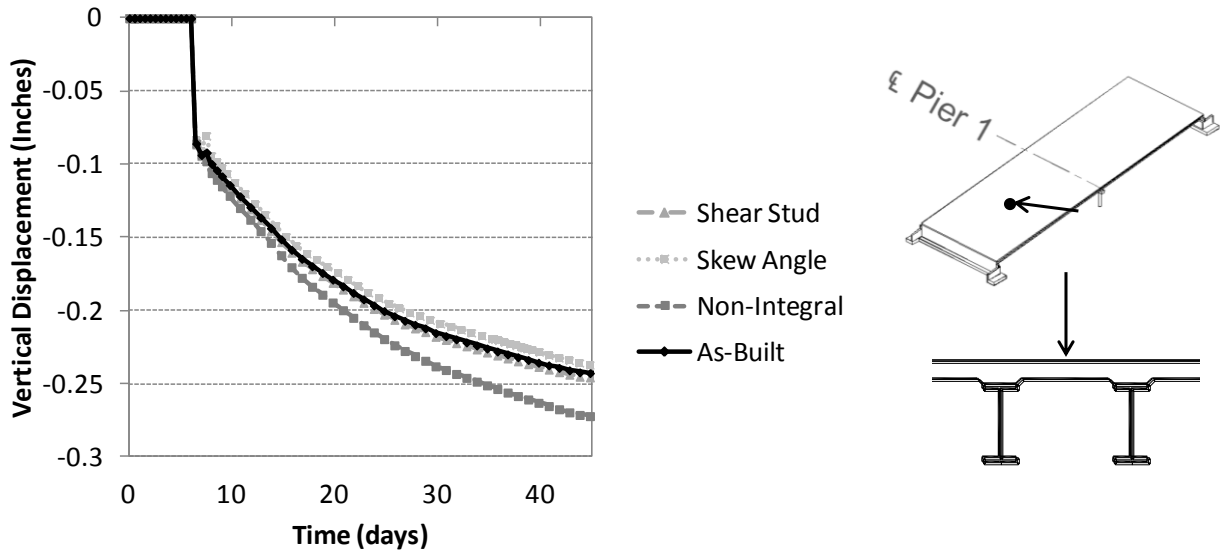


**Figure 216.** Vertical displacements through time, between beams

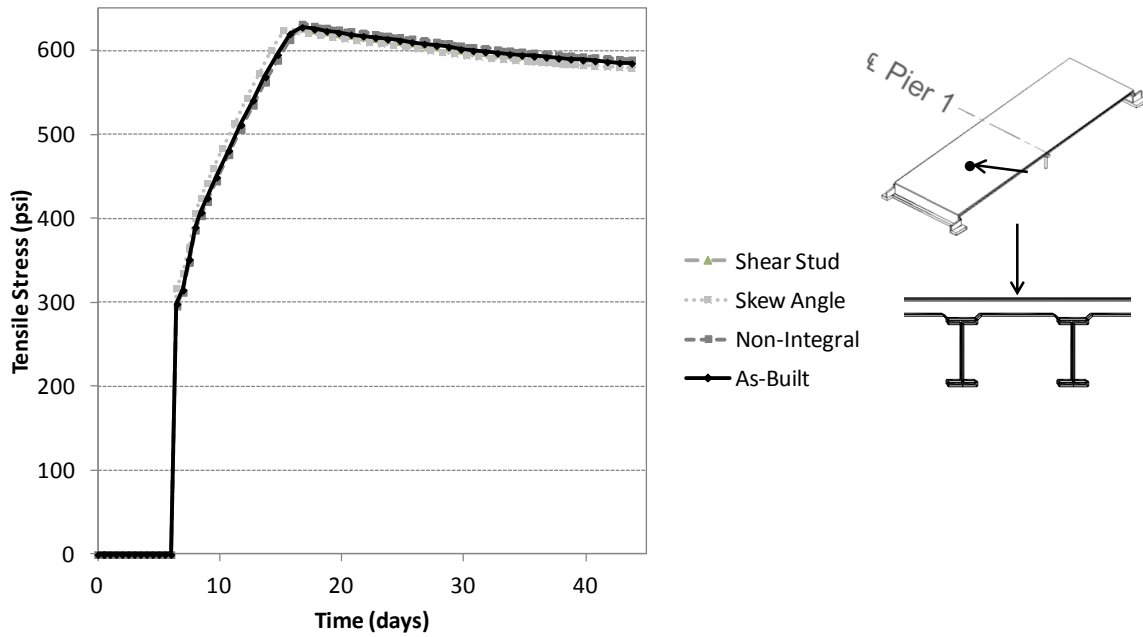


**Figure 217.** Max principal stresses through time, between beams

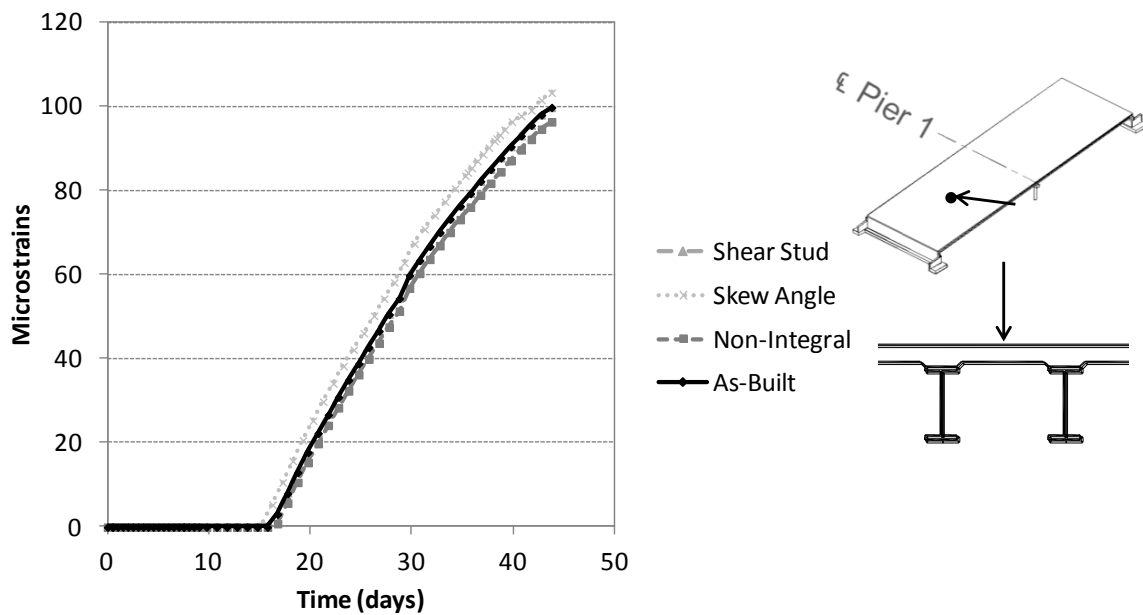


**Figure 218.** Max principal plastic strains through time, between beams, span 2

As shown, the maximum principal tensile stresses steadily grow until the concrete tensile strength is reached. At that point, cracking occurs, and the stresses steadily decrease due to softening. The decrease in stress matches the increase in plastic strains as the cracks continue to open. Overall, the non-integral abutment connection bridge had lower plastic strain values and higher stress values. The higher shear connector spacing bridge also had slightly lower plastic strain values and slightly higher stress values. Since the overall restraint in these configurations are slightly less than the as-built model, less cracking occurred, which yielded lower plastic strain values. The stress values were higher since less concrete softening took place. The skew angle bridge had higher plastic strain values and lower stress values. This bridge had more restraint than the as-built model, leading to more cracking and increased plastic strain values.

The overall results of the parametric study for the steel girder bridges are shown below in Table 27. Note that “time for cracking” is taken as the time for plastic strains to first begin to appear in the deck. This occurred in the region over the pier.

**Table 27.** Steel girder bridge parametric study overall results

<b>Analysis</b>	<b>Time for cracking</b>	<b>Maximum Plastic Strain Value</b>	<b>Maximum Vertical Displacement</b>
As-Built	13 days	170 $\mu$ -strain	-0.263 inches
Non-Integral	14 days	160 $\mu$ -strain	-0.301 inches
Shear Stud	13 days	167 $\mu$ -strain	-0.262 inches
Skew Angle	12 days	172 $\mu$ -strain	-0.281 inches

Increasing the shear stud spacing slightly improved the bridge performance, while skew angle produced more restraint and increased the maximum plastic strain value. Overall, the bridge with the non-integral abutment connection exhibited the best behavior. This bridge had the least overall amount of restraint, so it had the smallest plastic strain values at the end of the analysis and longest time for cracking to occur. Additionally, it had the largest maximum vertical displacement values, indicating the least amount of movement restraint.

#### 6.5.4.1 Effect of shear connector re-distribution

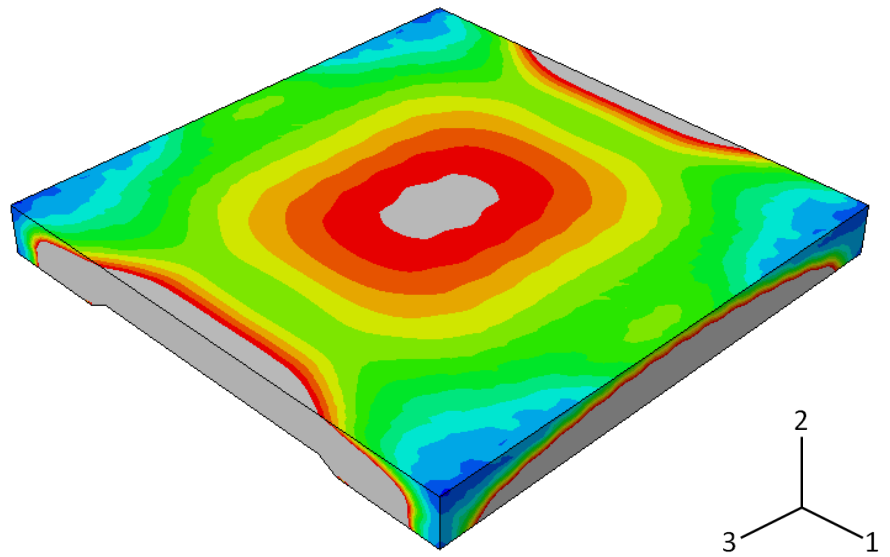
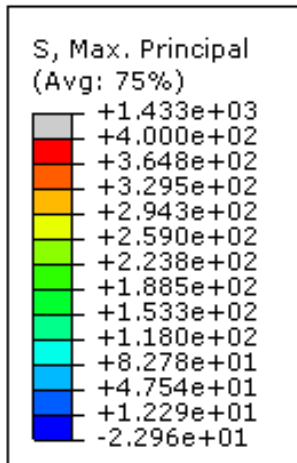
In the full bridge models for the parametric study the actual discrete shear studs were not modeled, so the full effect of shear stud size and volume was not able to be examined. Therefore, the lab sub-assembly models were utilized to examine the effect of size and volume. The shear stud size and spacing was compared between the as-built laboratory models (1.25''-diameter studs, spaced at 6'') with an arrangement with larger studs at greater spacing. The new size and spacing was calculated so that the total overall shear stud volume for each beam remained the same. The shear stud size and spacing examined using the lab sub-assembly models are summarized below in Table 28. Results from the analysis are shown below in Figure 220 to Figure 221. As shown, the stresses in the concrete were higher using the smaller shear studs at a closer spacing, while the overall vertical displacement values remained about the same. The additional amount of shear studs in the “as-built” model created more locations of restraint, which created higher overall stresses in the concrete.

**Table 28.** Shear stud size and volume determination for parametric study

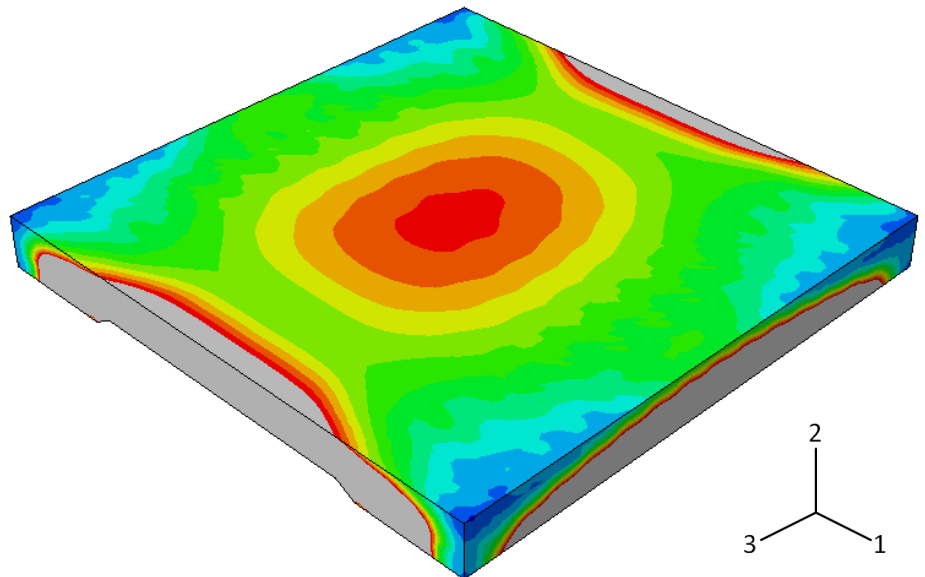
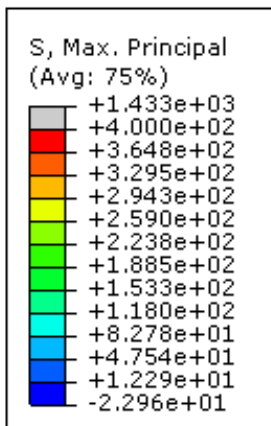
	<b>Stud Diameter</b>	<b>Stud Height</b>	<b>Stud Spacing</b>	<b>Stud Volume Per Beam</b>
<b>Detail 1 (as built)</b>	1.25''	6''	6''	419.71 in <sup>3</sup>
<b>Detail 2 (larger studs, larger spacing)</b>	1.5''	7''	10''	408.21 in <sup>3</sup>

#### 6.5.5 Effect of concrete tensile strength

As described in Section 5.3, a tensile strength of  $7.5\sqrt{f'_c}$  was defined for the concrete in the computational evaluations. Since the true tensile strength of concrete varies and is largely unknown, the effect of lowering the tensile strength was examined for the box beam “as-built” model. Instead of the original tensile strength of  $7.5\sqrt{f'_c}$ , a lower value of  $6.3\sqrt{f'_c}$  was used. The two analyses are compared below in Figure 222 to Figure 224. As shown, the overall bridge behavior remains the same when the concrete tensile strength is lowered. Lowering the tensile strength decreases the tensile stress values, since the maximum value that the stresses can reach before cracking occurs is lower. Additionally, lowering the tensile strength increases the magnitude of the plastic strain values, while lowering the time for cracking to occur.



a) Detail 1-Smaller Size and Spacing



b) Detail 2-Larger Size and Spacing

**Figure 219.** Maximum principal stress contours (time=30 days)



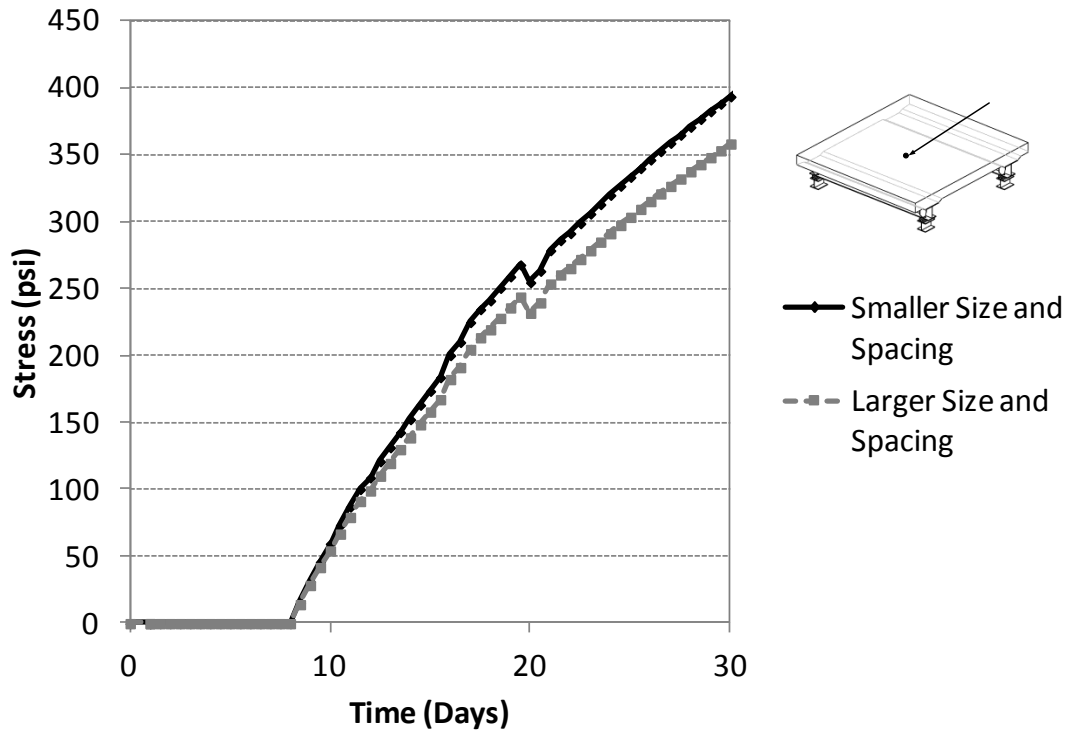


**Figure 220.** Concrete maximum principal tensile stresses, middle of the slab on top

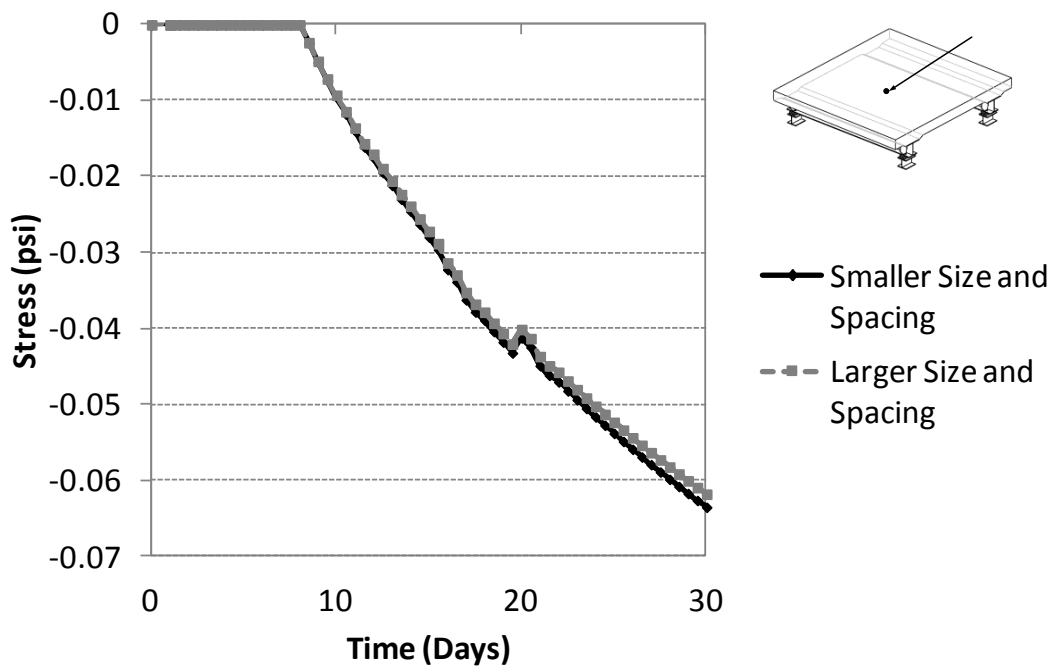


**Figure 221.** Vertical displacements, middle of slab on top

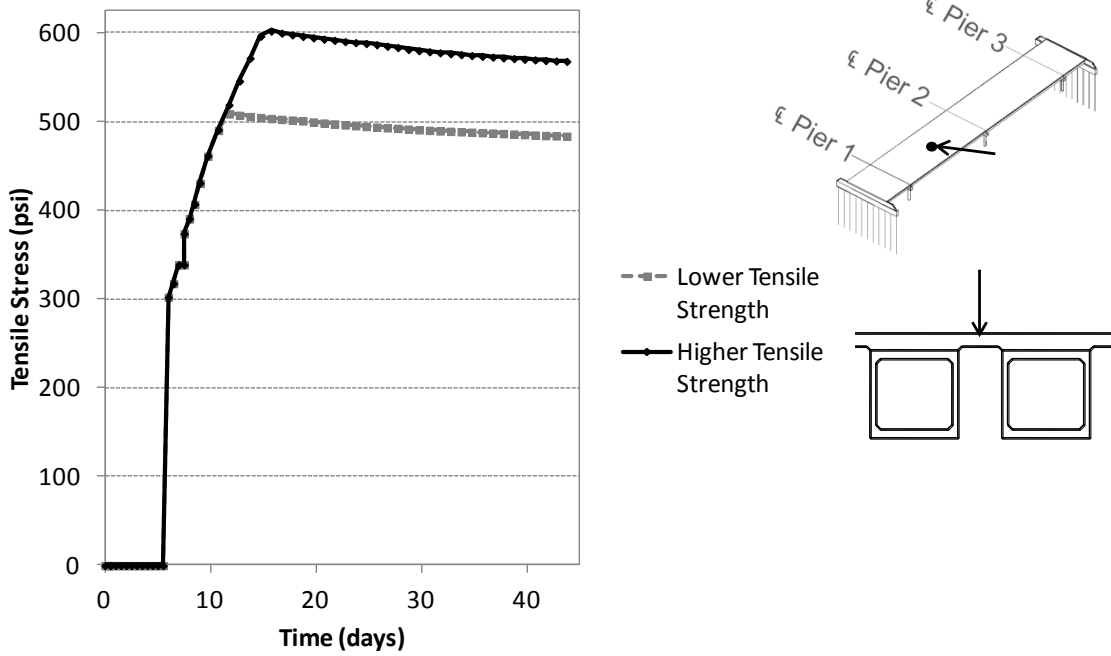


Figure 222. Maximum principle tensile stress values through time, tensile strength comparison

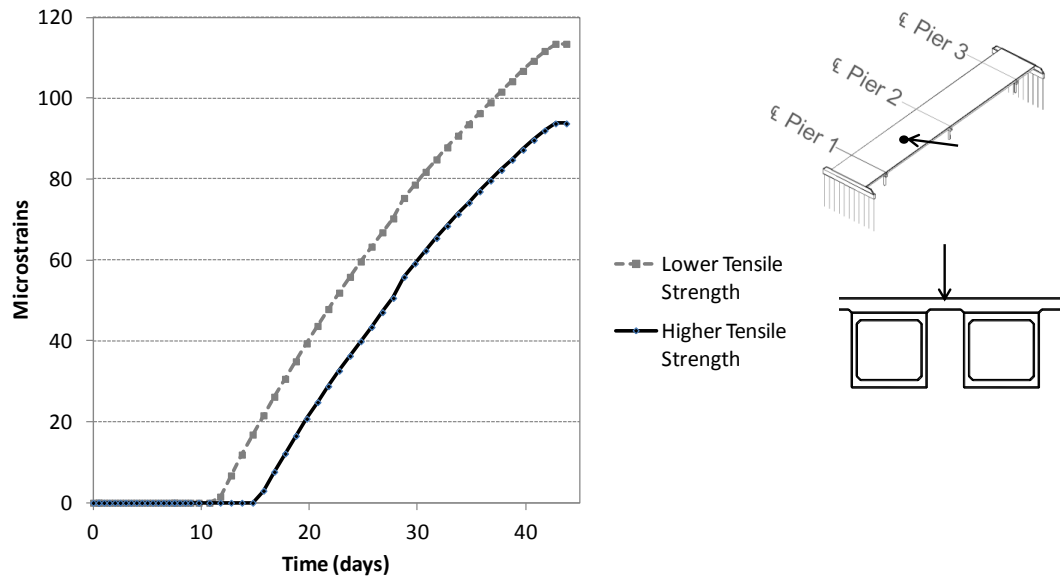
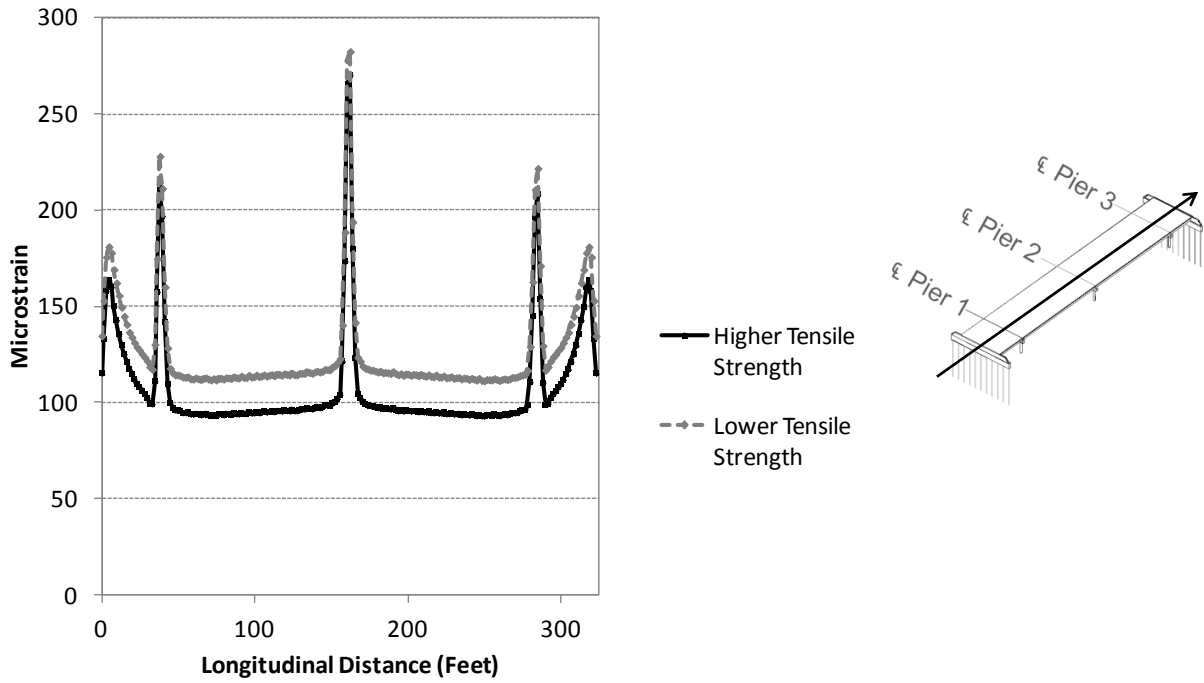
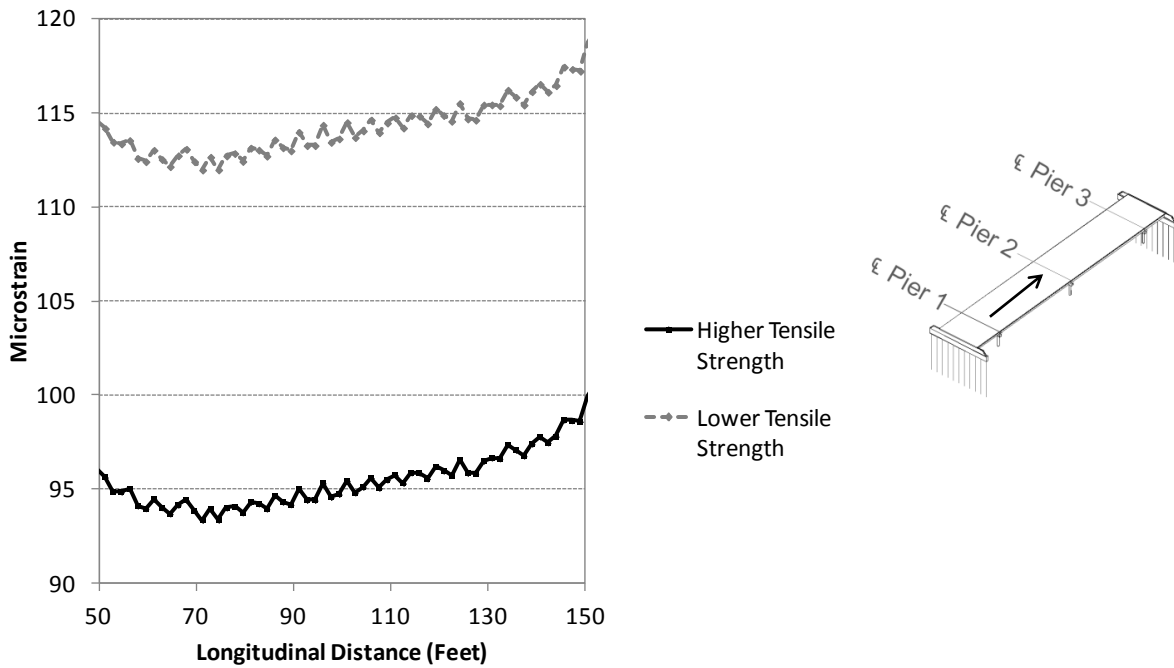


Figure 223. Maximum principle plastic strain values through time, tensile strength comparison



a) Entire length of bridge



b) Span 1

**Figure 224.** Maximum principle plastic strain values along longitudinal direction (t=45 days)

### 6.5.6 Discussion

Overall, the computational simulations were able to capture the damage and cracking patterns that were prevalent in the two prototype bridges in the field. The box beam model predicted both transverse cracking and longitudinal cracking throughout the bridge. Transverse cracking was predicted along the length of the entire bridge, with 3'-5' spacing between cracks. Longitudinal cracking was predicted between beams. Cracking originated in the negative moment regions, and then propagated to the rest of the bridge. These cracking patterns were observed during the field inspection of the M-57 over US-127 bridge. The steel girder predicted longitudinal and diagonal cracking at the abutments, and transverse cracking throughout the entire deck. Unlike the box beam bridge, longitudinal cracking was not predicted. This also matched the field observations during the inspection of the Kensington Road over I-96 bridge.

The steel and concrete “as-built” models exhibited similar behavior, and one bridge type did not perform significantly better than the other. Both bridges showed signs of cracking over the central pier at a time of around 13 days. Both bridges showed evidence of transverse cracking in the negative moment regions, over the piers, and also showed evidence of transverse cracking along the length of the spans. The steel girder bridge showed a higher concentration of transverse cracking in the regions over the piers, while the box beam bridge showed cracking that was more evenly-spaced. Both bridges also showed signs of longitudinal cracking and diagonal cracking at the two ends, over the abutments. Unlike the steel girder bridge, however, the box beam bridge showed longitudinal cracking along the length of the bridge, over the edges of the beams. Even with diaphragms, the steel girder bridge is much more flexible than the concrete bridge in the transverse direction, so this type of cracking did not occur.

For the parameters considered in the spread box beam bridge simulations, the low-shrinkage mix had the greatest effect on bridge behavior, as expected. Changing the distribution of reinforcement, while keeping the same reinforcement ratio, did not influence bridge behavior. Although the reinforcement was not discretely modeled which may have affected the results, it is predicted that changing the distribution will not influence the overall bridge performance. Increasing the amount of reinforcement actually produced slightly more cracking, which goes against conventional wisdom, and thus this issue is being examined further. This effect did not influence bridge behavior to a significant extent, and the changes in behavior produced by increasing the amount of reinforcement were small.

For the parameters considered in the steel girder bridge simulations, changing the abutment connection from fully-integral to non-integral had the greatest effect on the bridge behavior. Changing the abutment to non-integral greatly reduced the total restraint present in the bridge, and improved the overall performance. Fully-integral abutments only appear to work well if the foundation is supported by flexible piles, oriented in weak-axis bending. As expected, increasing the shear stud density also slightly improved the bridge performance, since it eliminated some of the areas of restraint. However, this did not have a very large effect on the overall bridge behavior. Increasing the bridge skew angle produced higher plastic strain values and reduced the time for cracking to occur. The skew angle likely created additional restraint in the bridge, which lowered the overall performance.

Overall, it can be seen that the restraint of concrete shrinkage is governed by both axial and bending behavior. The axial behavior is caused by the end restraint conditions at the abutment, while the bending behavior is caused by the curling motion that is induced by the restraint caused by the girders, shear connectors, and reinforcement. This is illustrated in Figure 225 and was illustrated for the lab models in Figure 130.

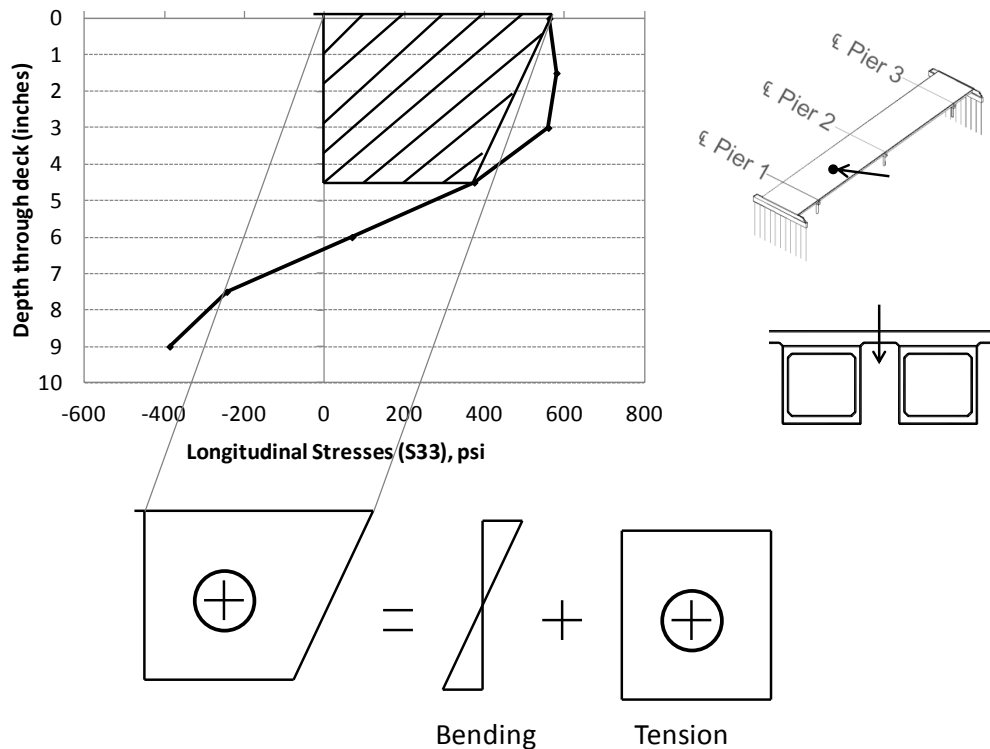


**Figure 225.** Longitudinal strains through the depth of the slab

As shown, the stresses in the top half of the deck, where cracking occurs in the simulations, is due to both axial and bending behavior. The bottom half of the deck can be seen to be in bending, with tensile stresses switching to compressive stresses. If the stresses through the top half of the deck are extracted, it can be seen that most of the stress is due to axial behavior, and the contribution of the bending stresses is minimal. This shows that the bending behavior of the slab due to curling does not control the cracking behavior, but it is instead governed by the axial effects due to the end restraint conditions. This explains why changing the design parameters at the global level (such as changing the abutment configuration and the bridge skew angle) had a greater impact than changing the design parameters at the sub-assembly level (such as the reinforcement arrangement and shear connector spacing).

Since the behavior is mostly dominated by axial restraint, the problem may be simplified to be analyzed as a slab on grade with restraints at the ends. As shrinkage is induced in the slab, cracking will occur at the mid-point, and then propagate to the quarter-points, until all of the stresses are relieved. This can also explain the presence of evenly-spaced transverse cracking in the bridge decks.

## 7 CONCLUSIONS AND RECOMMENDATIONS

### 7.1 Conclusions

While there are many factors that influence early-age deck cracking in jointless bridges, the most dominant source is restrained concrete shrinkage. As the concrete is restrained from movement, tensile stresses build up in the deck, causing cracking to occur. Restrained concrete shrinkage is dominated primarily by material properties and mix design, but bridge design factors can also greatly influence the amount of shrinkage restraint.

Overall, the research confirmed the hypothesis that the more restraint that is present in the bridge system, the greater the build-up of restrained tensile forces, and the more cracking that will occur. A field investigation showed that early-age transverse cracking occurs on both steel and concrete girder bridges, and that cracking is most prevalent in negative moment regions. Concrete box beam bridges also experience longitudinal cracking.

Computational simulations based on the finite element method were conducted to evaluate the effect of concrete shrinkage in full bridge systems, which were used to study the effects of design factors at the global level. The simulation approach was verified through experimentally-calibrated finite-element models. The following conclusions were drawn from the simulation parametric study on prototype jointless bridges.

- Shrinkage cracking was prevalent in both steel and concrete girder bridges. Concrete girder bridges experience both transverse and longitudinal cracking, while steel girder bridges experience only transverse cracking. With respect to restrained shrinkage cracking, one bridge type did not perform better than the other, and the overall behavior was similar.
- Higher inelastic strain values and more cracking occurred in bridges with more spans and more negative moment (pier) regions.
- Using a lower-shrinkage concrete mix helped reduce the magnitude of shrinkage loads, and thus reduced the amount of cracking. Changing the concrete mix had a larger influence on bridge behavior than changing the bridge design parameters.

- The effect of changing the amount of reinforcement and the reinforcement distribution was found to be minimal, and did not greatly influence the expected level of deck cracking.
- Designing a bridge with integral abutments and a rigid foundation greatly increased the restraint in the system and increased the amount of predicted cracking. This was seen in both the field investigation and the computational analysis for the full bridge models.
- Using larger shear studs at a larger spacing lowered the amount of restraint locations in the bridge, and slightly improved performance.
- Increasing the skew angle slightly lowered the overall bridge performance as indicated by an increase in the predicted deck cracking region near the abutment.
- Soil compaction level and foundation configuration greatly influences the overall stiffness of the bridge system, and is important to consider.
- The cracking behavior of the deck is primarily governed by the axial effects caused by the end restraint conditions and is not influenced greatly by the bending behavior and curling of the slab. For this reason, the bridge design parameters at the global level (abutment configuration and skew angle) have a much larger effect on bridge performance than the design parameters at the sub-assembly level (reinforcement arrangement and shear connector spacing).

## **7.2 Recommendations**

The following is recommended as a result of this research:

- Measures should be taken to provide the least amount of restraint possible in the bridge. The bridge simulations conducted in this study showed that the more restraint that is present, the more cracking that will occur in the deck. The shear connector density should be minimized as much as possible, although it should clearly be high enough to maintain composite action.
- Overall, cracking behavior is dominated by the axial demands caused by the end restraint conditions at the global level. Therefore, the global restraint features, such as the skew angle and abutment configuration, have a much larger effect on bridge performance than the restraint features at the sub-assembly level.



- Bridges supported by both steel and concrete beams are susceptible to deck cracking due to restrained concrete shrinkage. Thus, one bridge type is not seen as superior over the other with respect to this type of damage.
- The negative restraining effect when using fully-integral abutments (where the girders are cast into the abutment backwall) may be minimized by using a foundation supported on flexible piles oriented in weak-axis bending.
- Changing the reinforcement amount and distribution had a minimal effect on bridge performance, and maintaining the current design guidelines is recommended.
- Lowering the shear connector density slightly improved bridge performance. Increasing the shear stud size and spacing is recommended to provide less areas of restraint within the deck, and provide overall lower stress levels. However, the overall improvement was minimal, and care should be taken to ensure that composite action between the slab and beams is maintained.
- Increasing the bridge skew angle slightly reduces the overall performance of the bridge. Thus, large skew angles should be avoided as much as possible.
- Concrete mixture designs optimized for low shrinkage, such as the modified MDOT Grade D mix with the slag cement replacement, or the use of shrinkage reducing admixtures should be evaluated for their effect on minimizing early-age deck cracking on a full-scale bridge. However, care should be taken when evaluating the use of shrinkage reducing admixtures, as MDOT has found them to be detrimental in applications requiring entrained air for freeze-thaw durability. The strength behavior of the modified MDOT Grade D concrete mix was very similar to the normal Grade D mix, while the shrinkage characteristics were much better. Additionally, the price of the mix was comparable to the standard Grade D mix. The cracking potential and shrinkage magnitude was much smaller for the modified Grade D mix, and it is thus recommended for future construction.

## 8 REFERENCES

- [1] AASHTO, LRFD Bridge Design Specifications, American Association of State and Highway Transportation Officials, Washington, D.C., 2007
- [2] ACI Committee 209, 1992, “Prediction of Creep, Shrinkage, and Temperature Effects in Concrete Structure,” *American Concrete Institute*, Farmington Hills, MI, USA
- [3] American Institute of Steel Construction, “Steel Construction Manual”, *American Institute of Steel Construction*, 13<sup>th</sup> ed., 2005
- [4] American Petroleum Institute, “Recommended Practices for Planning, Designing, and Constructing Fixed Offshore Platforms-Working Stress Design,” *American Petroleum Institute*, 21<sup>st</sup> ed., 2000, pp. 70-71
- [5] American Society for Testing and Materials “Determining Age at Cracking and Induced Tensile Stress Characteristics of Mortar and Concrete under Restrained Shrinkage” C 1581-04, *ASTM International*, 2004
- [6] Alampalli, S., and Yannotti, A.P., “In-service Performance of Integral Bridges and Jointless Decks,” *Transportation Research Board*, No. 1624, 1998, pp. 1-7
- [7] Baluch, M.H., Mahmoud, I.A., and Rahman, M.K, “Thermo-Hygral Model for of Shrinkage Induced Stresses
- [8] Barr, B., and El-Baden, A., “Shrinkage properties of normal and high strength fibre reinforced concrete.” *Proceedings of Institute of Civil Engineers-Structures and Buildings*, 2003, pp. 15-25
- [9] Bonczar, C., Breña, S., Civjan, S., Crellin, B., and Crovo, D., “Field Data and FEM Modeling of the Orange-Wendell Bridge” *Proceedings of FHWA Integral Abutment and Jointless Bridges*, 2005, pp. 163-173
- [10] Burgueño, R, “Identification of Causes and Solution Strategies for Deck Cracking in Jointless Bridges,” *Michigan State University Department of Civil and Environmental Engineering*, May 2009, pp. 1-17
- [11] Chen, H.J., Peng, H.S., and Chen, Y.F., “Numerical Analysis of Shrinkage Stresses in a Mass Concrete” *Journal of the Chinese Institute of Engineers*, vol. 27, no. 3, 2004, pp. 357-365
- [12] Chen, T.C., and Ifju, P., “Modeling of Shrinkage Behavior in Cement Paste using Thermal-structural Interaction” *Proceedings of COMSOL Conference*, 2009, pp. 1-6

- [13] Collins, M.P., Mitchell, D., and MacGregor, J.G., "Structural Design Considerations for High Strength Concrete", *Concrete International*, Vol. 15, No. 5, May 1993, pp. 27-34
- [14] Faraji, S. and Ting, J.M., "Nonlinear Analysis of Integral Bridges, Finite-Element Model," *Journal of Geotechnical and Geoenvironmental Engineering*, May 2001, pp. 454-461
- [15] French, C.E., Eppers, L.J., Le, Q.T.C., and Haijar, J.F., "Transverse Cracking in Bridge Decks," *Minnesota Department of Transportation, Center for Transportation Studies*, January 1999, pp. 1-37
- [16] Frosch, R., Blackman, D., and Radabaugh, R., "Investigation of Bridge Deck Cracking in Various Bridge Superstructure Systems," *Federal Highway Administration-Joint Transportation Research Program*, January 2003
- [17] Hadidi, R., and Saadeghvaziri, M.A., "Transverse Cracking of Concrete Bridge Decks: State-of-the-Art," *Journal of Bridge Engineering*, Vol. 10, No. 5, 2005, pp. 503-510
- [18] Holt, E.E., and Janssen, D.J., "Influence of Early Age Volume Changes on Long-Term Concrete Shrinkage," *Transportation Research Record*, No. 1610, 1998, pp. 28-32
- [19] Kunin, J. and Alampalli, S., "Integral Abutment Bridges: Current Practice in the United States and Canada," *New York State Department of Transportation, Transportation Research and Development Bureau*, Special Report 132, June 1999
- [20] Lawver, A. French, C., and Shield, C.K., "Field Performance of Integral Abutment Bridge," *Transportation Research Record*, No. 1740, 2000, pp. 108-117
- [21] Li, Zo., Qi., M., Li, Za., And Ma, B., "Crack Width of High-Performance Concrete Due to Restrained Shrinkage." *Journal of Materials in Civil Engineering*, 1999, pp. 214-223
- [22] *Michigan Department of Transportation*, "Bridge Construction Plans-S03 of 63101." 2008, pp. 1-34
- [23] *Michigan Department of Transportation*, "Bridge Construction Plans-S08 of 47064." 2008, pp. 1-45
- [24] *Michigan Department of Transportation*, "Bridge Construction Plans-S14 of 29011." 2008, pp. 1-25
- [25] *Michigan Department of Transportation*, "Bridge Design Guides", 2011
- [26] *National Oceanic and Atmospheric Administration*, "Average Relative Humidity Values", *National Climactic Data Center*, 2002

- [27] *National Cooperative Highway Research Program*, “Manuals for the Design of Bridge Foundations,” *Transportation Research Board*, Report No. 343, 1991
- [28] Ramey, G.E., and Wolff, A.R., “Structural Design Acations to Mitigate Bridge Deck Cracking,” *Practical Periodical on Structural Design and Construction*, Vol. 2, No. 3, 1997, pp. 118-124
- [29] Russel, H.G., and Gerken, L.J., “Jointless Bridges—the Knowns and Unknowns,” *Concrete International*, Vol. 16, No. 4, 1994, pp. 44-48
- [30] Saadeghvaziri, M. A., and Hadidi R., “Transverse Cracking of Concrete Bridge Decks: Effects of Design Factors,” *Journal of Bridge Engineering*, Vol. 10, No. 5, 2005, pp. 511-519
- [31] Shah, B., “3D Finite Element Analysis of Integral Abutment Bridges Subjected to Thermal Loading,” Thesis, *Kansas State University, Department of Civil Engineering*, 2007, pp. 28-30
- [32] Shah, H.R., and Weiss, J., “Quantifying shrinkage cracking in fiber reinforced concrete using the ring test” *Materials and Structures Journal*, 2006, pp. 887-898
- [33] Shah, S.P. et. al, “Effects of Shrinkage-Reducing Admixtures on Restrained Shrinkage Cracking.” *ACI Materials Journal*, Vol. 89, No. 3, 1992, pp. 289-295
- [34] Schmitt, T.R., and Darwin, D., “Effect of Material Properties on Cracking in Bridge Decks,” *Journal of Bridge Engineering*, Vol. 4, No. 1, 1999, pp. 8-13
- [35] Simulia, ABAQUS/Standard v. 6.8.1
- [36] ABAQUS User’s Manual
- [37] Vecchio, J.V., and Collins, M.P., “The Modified Compression Field Theory for Reinforced Concrete Elements Subjected to Shear,” *ACI Structural Journal*, 1986 83(2), 219-231.
- [38] Wan, B., Foley, C., and Komp., J., “Concrete Cracking in New Bridge Decks and Overlays,” *Wisconsin Highway Research Program*, March 2010
- [39] William, G.W., Shoukry, S.N., Riad, M.Y., “Development of Early Age Shrinkage Stresses in Reinforced Concrete Bridge Decks,” *Mechanics of Time-Dependent Materials*, Vol. 12, No. 4, 2008, pp. 343-356
- [40] Wolde-Tinsae, A.M., Klinger, J.E., and White, E.J., “Performance of Jointless Bridges,” *Journal of Bridge Engineering*, Vol. 7, No. 5, 2002, pp. 276-289

## **9 APPENDICES**

*Please refer to separate document (available electronically).*



# REPORT APPENDIX

---

---

## IDENTIFICATION OF CAUSES AND SOLUTION STRATEGIES FOR DECK CRACKING IN JOINTLESS BRIDGES

by

David J. Stringer

Rigoberto Burgueño

Appendix to Report No. CEE-RR – 2012/04

July 2012

Research Report for MDOT under Contract No. 2009-0746/Z1  
SPR No. 108522

---

**Department of Civil and Environmental Engineering  
Michigan State University  
East Lansing, Michigan**

**TABLE OF CONTENTS**

Appendix A: MDOT Bridge Information for Field Investigation ..... 1

Appendix B: Field Inspection Detailed Results..... 10

Appendix C: Laboratory Slab Models Full Data Set ..... 92

Appendix D: Laboratory Full Data Comparison to Experimental Data ..... 114

## **Appendix A**

### **MDOT Bridge Information for Field Investigation**



<b>Bridge ID No.</b>	<b>Location</b>	<b>County</b>	<b>Date constructed</b>	<b>Date of inspection</b>	<b>Repair Actions taken</b>	<b>Skew (deg.)</b>	<b>Superstructure Type</b>	<b>Deck Forms</b>	<b>Crack Type</b>	<b>Transverse widespread?</b>	<b>Deck Rating (9-pt. scale)</b>	<b>Visit?</b>	<b>Reason</b>
19022-S03-3	I-96 eb over Grange Rd.	Clinton	2007	2008	None	21	Concrete I-beam	Metal SIP	Transverse and diagonal cracking throughout, transverse cracks in headers at the joints	Yes?	7	Yes?	Transverse cracking appears to be widespread, possibly visit based on close proximity
19022-S03-4	1-96 wb over Grange Rd.	Clinton	2007	2008	Epoxy sealer in cracks	21	Concrete I-beam	Metal SIP	Transverse and diagonal and longitudinal cracks in all spans, transverse cracks in headers	Yes?	7	Yes?	Transverse cracking appears to be widespread, possibly visit based on close proximity
23152-S06	Millett Rd. over I-96	Eaton	2001	2008	Epoxy sealer in cracks	6	Side by side box beam	None (side-by-side)	Longitudinal cracks along box beams, some transverse cracks	No	6	No	Cracking appears to be dominated by longitudinal cracks, it is not crack type we are interested in
23152-S07	I-96 wb over Canal Rd.	Eaton	2001	2009	Epoxy sealer in cracks	42	Side by side box beam	None (side-by-side)	Longitudinal cracks along box beams, transverse cracks at construction joints,	No	6	No	Skew angle is too large, mostly longitudinal cracking
23152-S08	I-96 eb over Canal Rd.	Eaton	2001	2009	Healer sealer in 2007	49	Side by side box beam	None (side-by-side)	Transverse cracking throughout entire bridge, longitudinal cracks over box beams	Yes	6	No	Contains cracking pattern of interest, skew angle is too large
23152-S09	I-96 wb over Lansing Rd.	Eaton	2001	2009	Epoxy sealer in cracks	5	Side by side box beam	None (side-by-side)	Transverse cracking throughout, some transverse cracking in barriers	Yes	6	Yes	Appears to have cracking pattern of interest, skew is not large, close proximity

<i>Bridge ID No.</i>	<i>Location</i>	<i>County</i>	<i>Date constructed</i>	<i>Date of inspection</i>	<i>Repair Actions taken</i>	<i>Skew (deg.)</i>	<i>Superstructure Type</i>	<i>Deck Forms</i>	<i>Crack Type</i>	<i>Transverse widespread?</i>	<i>Deck Rating (9-pt. scale)</i>	<i>Visit?</i>	<i>Reason</i>
23152-S10	I-96 eb over Lansing Rd.	Eaton	2001	2009	Epoxy sealer in cracks	5	Side by side box beam	None (side-by-side)	Transverse cracking and map cracking throughout, transverse cracking in barriers	Yes	6	Yes	Appears to have cracking pattern of interest, skew is not large, close proximity
33045-S02-3	I-496 eb over Pennsylvania Ave.	Ingham	2000	2009	None	15	Side by side box beam	None (side-by-side)	Transverse cracking over the piers, as well as longitudinal and diagonal cracking throughout	Yes	7	Yes	Appears to have cracking pattern of interest, skew is not large, close proximity
33045-S02-4	I-496 wb over Pennsylvania Ave.	Ingham	2000	2009	None	15	Side by side box beam	None (side-by-side)	Transverse cracks, spaced less than 5 feet, open transverse cracks on both piers	Yes	6	Yes	Appears to have cracking pattern of interest, skew is not large, close proximity
38101-B01	I-94 over Sandstone Creek	Jackson	1953, rehab in 2008	2009	None	20	Steel beams	None (removable forms used)	Some diagonal and transverse cracking, spalling at concrete patches, heavy map cracking	Yes	5	No	Appears to have cracking pattern of interest, but new overlay and widening may have dominated cracking
38101-S11	Hawkins Rd. over I-94	Jackson	1958, rehab in 2009	2009	None	0	Spread box beams	Metal SIP	New concrete deck replacement; no cracking yet observed, previously had longitudinal cracking	Yes?	8	Yes	While no official cracking inspection has been created, photos indicate possible cracking, and the new deck replacement would be of interest from the early-age standpoint
47064-S08	Kensington Rd. over I-96	Livingston	2009	2009	None	21	Steel girder	Metal SIP	New concrete deck replacement; some transverse cracking by construction joints, no extensive cracking for new deck	Yes?	9	Yes?	Photos indicate possible cracking, new deck of interest for early-age; however, extensive cracking not yet observed
58151-S01	Sterns Rd. over I-75	Monroe	2009	2009	None	0	Spread box beams	Metal SIP	New concrete deck replacement; no cracking yet observed, previously had many transverse cracks	Yes?	8	Yes?	Photos indicate possible cracking, new deck of interest for early-age; however, extensive cracking not yet observed

<i>Bridge ID No.</i>	<i>Location</i>	<i>County</i>	<i>Date constructed</i>	<i>Date of inspection</i>	<i>Repair Actions taken</i>	<i>Skew (deg.)</i>	<i>Superstructure Type</i>	<i>Deck Forms</i>	<i>Crack Type</i>	<i>Transverse widespread?</i>	<i>Deck Rating (9-pt. scale)</i>	<i>Visit?</i>	<i>Reason</i>
58152-B04-1	I-75 nb over The Huron River	Monroe	2009	2009	None	12	Steel beams	Metal SIP	Diagonal cracking, random cracking, numerous patches and spalling	No	7	No	Cracking appears to be random, photos do not indicate transverse cracking due to restrained shrinkage
58152-B04-2	I-75 sb over The Huron River	Monroe	2009	2009	None	12	Steel beams	Metal SIP	Transverse cracking adjacent to expansion joints, new deck in 2009, no extensive cracking noted	No	9	No	No extensive cracking was noted after construction
76011-B01	M-52 over The Looking Glass River	Shiawassee	2000	2009	Epoxy overlay	0	Spread box beams	Metal SIP	Epoxy overlay with diagonal, transverse, and longitudinal cracks,	Yes	6	Yes	Appears to have extensive cracking
81104-S09	Baker Rd. over I-94	Washtenaw	2007	2009	None	2	Side by side box beam	None (side-by-side)	Several longitudinal cracks throughout the deck	No	7	No	Cracking appears to be dominated by longitudinal cracks, it is not crack type we are interested in
81104-S10	Zeeb Rd. over I-94	Washtenaw	2002	2008	None	28	Side by side box beam	None (side-by-	Longitudinal cracks between box beams, some	No	7	No	Cracking appears to be dominated by longitudinal

								side)	transverse cracking parallel to construction joints				cracks, it is not crack type we are interested in
41026-S02	Walker Rd. over I-96	Kent	2006	2006 (part-width constr.)	None	6	Concrete Spread Box	Metal SIP	Transverse and longitudinal cracking	Yes	unknown	No	Part-width construction affected bridge performance
41064-B04	M-6 eb over Buck Creek	Kent	2001	2001 (immediately)	Epoxy sealer in cracks	0	Concrete I-beam	Metal SIP	Transverse cracking at the piers, longitudinal cracking at approaches	No	unknown	?	Visitation will be determined after seeing photos documenting the damage
41131-S06	44th Street over US-131	Kent	2009	2009 (part-width constr.)	None	11	Steel	Metal SIP	Transverse cracking throughout, concentrated at the piers	Yes	unknown	No	Part-width construction affected bridge performance
41064-S05	Burlingame Rd. Over M-6	Kent	2001	2009 (immediately)	None	11	Concrete I-beam	Metal SIP	Transverse cracking near middle pier, longitudinal at the ends of the bridge, map cracking throughout	No	unknown	?	Visitation will be determined after seeing photos documenting the damage
2nd submission													
Bridge ID No.	Location	County	Date constructed	Date of inspection	Repair Actions taken	Skew (deg.)	Superstructure Type	Deck Forms	Crack Type	Transverse widespread?	Deck Rating (9-pt. scale)	Visit?	Reason
56044-B04-3	US 10 eb over Sanford Lake	Midland	2008	2010	Latex overlay	unknown	Concrete I-beam	None (removable forms used)	New concrete deck replacement; several transverse and longitudinal cracks, spaced at	Yes	7	Yes	Several transverse cracks are evident from photos and inspection report

									10'				
56044-B04-4	US 10 wb over Sanford Lake	Midland	2008	2010	Latex overlay	unknown	Concrete I-beam	None (removable forms used)	New concrete deck replacement; no problems noted	No	9	No	No cracking problems are evident for new concrete deck construction
3rd submission													
Bridge ID No.	Location	County	Date constructed	Date of inspection	Repair Actions taken	Skew (deg.)	Superstructure Type	Deck Forms	Crack Type	Transverse widespread?	Deck Rating (9-pt. scale)	Visit?	Reason
11015-B01-3	I-94 eb over Galien River	Berrien	2008	2008	None	0	Spread box beams	Metal SIP?	No inspection report obtained; Some small transverse cracks near piers and west abutment	No	unknown	No	Based on provided comments, it appears transverse cracking is not widespread, no photos were provided
11015-B01-4	I-94 wb over Galien River	Berrien	2008	2008	None	0	Spread box beams	Metal SIP?	No inspection report obtained; some edge scaling at construction joints, new deck construction	No	unknown	No	Cracking does not appear to be widespread
39013-S03	Milham Rd. over US-131	Kalamazoo	1999	2008	None	10	Spread box beams	Metal SIP?	No inspection report obtained; scattered transverse cracking and some longitudinal cracks, extensive partial	Yes	unknown	Yes?	Cracking appears to be possibly of interest

									deck replacement				
78062-B01	M-86 over Swan Creek	Kalamazoo	2008	2009	None	0	Spread box beams	Metal SIP?	No inspection report obtained; scattered longitudinal cracks and some areas of map cracking	No	unknown	No	Does not appear to have transverse cracking
4th submission													
Bridge ID No.	Location	County	Date constructed	Date of inspection	Repair Actions taken	Skew (deg.)	Superstructure Type	Deck Forms	Crack Type	Transverse widespread?	Deck Rating (9-pt. scale)	Visit?	Reason
73171-B02-2	I-75 sb over Cass River	Saginaw	1961, rehab in 2006	2010	None	unknown	Steel Girder	Metal SIP	Transverse and longitudinal cracking in the deck surface	No	8	No	Cracking does not appear to be widespread, photos of the damage would be useful
73171-S08-2	I-75 sb over Genessee Ave.	Saginaw	1961, rehab in 2006	2010	None	unknown	Steel Girder	Metal SIP	Open cracking between construction joints, some longitudinal cracks	No	8	No	Transverse cracking does not appear to be widespread
5th submission													
50013-S03	25 Mile Rd. over M-53	Macomb	2009	2010	None	unknown	Spread box beams	Metal SIP	Transverse and horizontal cracks at pier area	No	8	Yes?	Some transverse cracking is evident from the photos, but it may not be

													widespread enough, deck is in good condition
63172-S05	Walton Blvd. over I-75	Oakland	1962, rehab date unknown	2010	None	unknown	Spread box beams	Metal SIP	Transverse and longitudinal cracks over pier, shrinkage cracking scattered throughout	Yes	8	Yes?	Some transverse cracking is evident, but it may not be widespread enough, deck is in good condition
Bridge ID No.	Location	County	Date constructed	Date of inspection	Repair Actions taken	Skew (deg.)	Superstructure Type	Deck Forms	Crack Type	Transverse widespread?	Deck Rating (9-pt. scale)	Visit?	Reason
6th submission													
unknown	I-196 over Mid-Michigan RR	Kent	2006	unknown	None	45	unknown	unknown	No inspection report obtained; extensive transverse cracking, spaced evenly across bridge	Yes	unknown	No	While the cracking is exactly the type we are looking for, the bridge has a large skew and experienced part-width construction
Other Bridges													
unknown	Halsted Rd. over I-696	unknown	unknown	unknown	unknown	unknown	unknown	unknown	unknown	unknown	unknown	unknown	*No information has been sent on these bridges except for the plans, these are

													bridges we are modeling
unknown	Chocolay River in U.P.	unknown	unknown	unknown	unknown	unknown	unknown	unknown	unknown	unknown	unknown	unknown	*No information has been sent on these bridges except for the plans, these are bridges we are modeling
29011-S14	M-57 over US-27	Gratiot	1999?	Unknown	Unknown	0	Spread box beams	Metal SIP?	No inspection report obtained; photos and plans sent; based on photos, widespread transverse cracking throughout entire	Yes	unknown	Yes	Based on the photos, it appears the bridge has widespread transverse cracking, somewhat close proximity to MSU, need bridge inspection report
									bridge				



## **Appendix B**

### **Field Inspection Detailed Results**

1: I-96 at Lansing Road

- Side-by-side concrete box beams
- 3-span, continuous deck for live-loading, simply supported beams
- *Mostly longitudinal cracking evident, spaced at the same spacing as the width of the beams (3-4 feet). Transverse cracking only evident at the construction joints, by the piers, and also at the approach slabs. Cracking is not likely due to restrained concrete shrinkage.*



**Figure 1.** Overall Bridge View



**Figure 2.** Cracking in deck fascia



**Figure 3.** Longitudinal cracks in the deck surface, near the approach slab



**Figure 4.** Overall deck view

2: I-496 at Pennsylvania Ave.

- Side-by-side concrete box beams
- 3-span, continuous deck for live-loading, simply supported beams
- *Cracking pattern was difficult to observe due to traffic on the freeway. Bridge was not crossed to obtain a detailed observation of the deck. Some vertical cracking was evident in the barrier walls, spaced evenly. Some transverse cracking was evident on the underside fascia of the deck, close to the piers. According to MDOT photos, it appears that longitudinal cracking is dominant in this bridge.*



**Figure 5.** Overall Bridge View



**Figure 6.** Transverse cracking in deck fascia



**Figure 7.** Overall bridge deck view



**Figure 8.** Cracking in approach pavement



**Figure 9.** Extensive cracking in barrier wall

3: M-52 over the Looking Glass River

- Spread concrete box beams
- 1-span, continuous deck and fully integral beams at the abutment.
- *There was some transverse cracking in the deck fascia, at the underside of the deck. The barrier walls experienced widespread vertical/transverse cracks. Both transverse and longitudinal cracking was evident in the deck.*



**Figure 10.** Bridge overall view





**Figure 11.** Bridge underside



**Figure 12.** Cracking in deck fascia



**Figure 13.** Vertical cracking in barrier wall, transverse cracking in the deck



**Figure 14.** Longitudinal crack in the deck



**Figure 15.** Transverse cracking in the deck



**Figure 16.** Longitudinal cracks



**Figure 17.** Large crack in barrier wall



**Figure 18.** Deck overall vie

5: M-57 over US-127\*

- Spread concrete box beams
- 4-span, continuous deck for live loading, simply supported beams (semi-integral abutment).
- *Some diagonal shear cracking was evident in the beams, near the piers. Transverse cracking was evident throughout the entire deck surface, spaced at every 3' to 4'. The cracking continued over the pier areas. The crack density was much greater in the area over the piers, or in the "middle" deck pour. According to the inspection reports, the cracks were previously sealed. As evident in the inspection, the cracking has continued through the seals.*

*\*This bridge shows the most evidence of evenly-spaced transverse cracking, and is likely the best prototype candidate for cracking due to restrained concrete shrinkage.*



**Figure 19.** Bridge overall view



**Figure 20.** Cracking in beams by the pier



**Figure 21.** Connection at the abutment



**Figure 22.** Overall bridge deck view



**Figure 23.** Bridge expansion joint and sleeper slab



**Figure 24.** Cracking in barrier wall



**Figure 25.** Transverse crack near construction joint





**Figure 26.** Transverse cracks in deck surface



**Figure 27.** Transverse cracking in deck



**Figure 28.** Transverse cracks in deck

7: I-96 over Grange Road

- Concrete I-beams
- 3-span, continuous deck for live-loading, simply supported beams
- *Some fairly widespread transverse/vertical cracking is evident in the concrete barrier walls. Some transverse cracking is evident in the bottom of the deck/deck fascia. The top deck surface did not have many evident signs of cracking. The bridge appears to be new/recently renovated.*



**Figure 29.** Overall bridge view



**Figure 30.** Cracking on underside of deck, by the pier area



**Figure 31.** Bridge deck underside



**Figure 32.** Overall bridge view



**Figure 33.** Bridge deck surface



**Figure 34.** Bridge deck surface (other side)

16: Hawkins Road over I-94

- Spread concrete box beams
- 2-span, continuous deck for live-loading, simply supported beams
- *Some fairly widespread transverse/vertical cracking is evident in the concrete barrier walls. The bottom of the deck/deck fascia does not have any signs of cracking. There is a large extent of transverse cracking in the area of the pier, near the middle of the bridge deck. Longitudinal cracking is evident throughout the bridge, spaced evenly at the same spacing of the beams.*

*\*This deck was replaced in 2009, and at the time of the inspection report there were no defects reported for the deck.*



**Figure 35.** Bridge overall view



**Figure 36.** Bridge underside



**Figure 37.** Longitudinal cracking in bridge surface



**Figure 38.** Close-up of longitudinal crack





**Figure 39.** Transverse cracking in pier area



**Figure 40.** Bridge surface overall view (note longitudinal cracks)



**Figure 41.** Transverse cracking in pier area



**Figure 42.** Transverse cracking in pier area



**Figure 43.** Bridge expansion joint (relatively clean of debris)

17: I-94 over Sandstone Creek

- Steel beams
- 3-span (small spans), continuous deck for live load, non-integral beams (beams are not cast into the abutment), rocker bearings at the ends, fixed bearings at the piers.
- Removable plywood forms used underneath.
- *Some cracking is evident on the underside of the deck, although it is not widespread. Some cracking is also evident in the concrete barrier walls. Not much cracking (longitudinal nor transverse) is evident in the bridge deck. The deck was difficult to observe due to traffic on the freeway.*



**Figure 44.** Bridge overall view



**Figure 45.** Semi-integral abutment detail



**Figure 46.** Bridge underside (note no SIP metal forms were used)



**Figure 47.** Cracking in barrier wall and deck fascia



**Figure 48.** Bridge expansion joint and approach slab (some cracking in approach)



**Figure 49.** Bridge deck surface (no notable cracks)



**Figure 50.** Bridge deck overall view

4: US-10 eb over Sanford Lake

- Spread Concrete I-girders (MI-1800 I-beam)
- 3-span, continuous deck for live-loading, continuous beams
- Removable plywood forms underneath
- *The eastbound side had significant longitudinal cracking throughout, and transverse cracking in the areas of the piers and approach slabs. The westbound side had no significant cracking in the bridge surface, some longitudinal cracking at the east approach.*



**Figure 51.** Overall Bridge View (Eastbound side)





**Figure 52.** Girder connection at the abutment

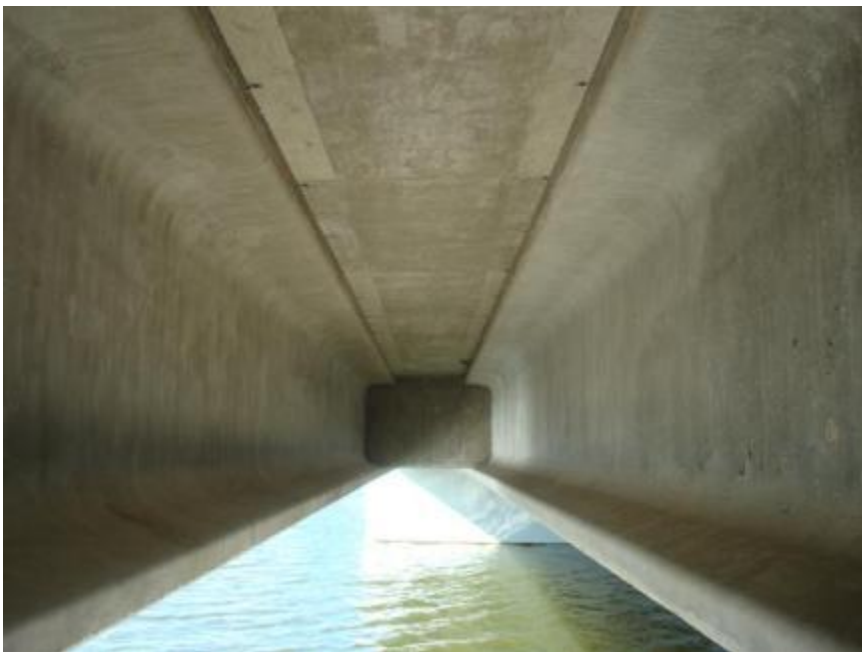


**Figure 53.** Bridge underside (note no SIP forms are used)



**Figure 54.** Deck approach slab and expansion joint (some longitudinal cracking)



**Figure 55.** Overall Bridge Deck View (Eastbound)



**Figure 56.** Longitudinal cracking in bridge deck



**Figure 57.** Transverse cracking near the first pier



**Figure 58.** Transverse cracking close-up



**Figure 59.** Additional transverse cracking at pier 2, as well as some longitudinal cracking



**Figure 60.** Identical designs for EB and WB sides

8: Kensington Rd. over I-96

- Steel girders
- 2-span, continuous deck for live loading, fully integral abutments, SIP metal forms underneath
- Sidewalk on west side of the bridge
- *Extensive transverse cracking is evident by construction joints, and close to the pier area. Longitudinal cracking is evident throughout the bridge deck. The barriers and sidewalk have extensive vertical/transverse cracking as well, some of which continued into the bridge deck as transverse cracks. Interestingly, this bridge was recently re-constructed (2009), yet it is experiencing a relatively high amount of cracking*



**Figure 61.** Bridge overall view



**Figure 62.** Bridge connection at the abutment (note that the steel girders sit on elastomeric bearings, and are cast into the abutment, similar to box-beam bridges we have seen)



**Figure 63.** Bridge underside overall view



**Figure 64.** Bridge deck overall view



**Figure 65.** Large transverse crack at the abutment





**Figure 66.** Close-up of transverse crack (note how it cracked through the repair)



**Figure 67.** Longitudinal cracks in the deck



**Figure 68.** Transverse/vertical cracking in sidewalk and barrier wall



**Figure 69.** Transverse cracking by construction joint



**Figure 70.** Transverse cracking in barrier continuing to deck surface

14: 26-Mile Rd. over M-53

- Spread concrete box beams
- 2-span, non-integral abutment (beams are not cast into abutment), continuous deck for live load, SIP forms used
- *There is a heavy amount of transverse cracking in the area of the pier, and scattered longitudinal cracking throughout the bridge. The longitudinal cracking is spaced at the same spacing of the beams. There is also evenly-spaced transverse cracking in the sidewalk/barrier wall (spaced at 3-4')*



**Figure 71.** Bridge overall view



**Figure 72.** Cracking in outside fascia of deck and barrier



**Figure 73.** Connection at the abutment (note that beam is not cast into abutment)



**Figure 74.** Bridge underside



**Figure 75.** Longitudinal cracking in approach slab



**Figure 76.** Cracking in barrier, at railing connection (typical)



**Figure 77.** Large longitudinal crack in deck surface



**Figure 78.** Heavy transverse cracking in pier area



**Figure 79.** Transverse cracking continuing into the sidewalk



**Figure 80.** Transverse and longitudinal cracking





**Figure 81.** Almost identical cracking in opposite approach slab

15: Walton Blvd. over I-75

- Spread concrete box beams
- 2-span, non-integral abutment (beams are not cast into abutment), continuous deck for live load, SIP forms used.
- *Heavy transverse cracking in pier area, scattered longitudinal cracking spaced at beam spacing. Evenly-spaced transverse/vertical cracks in barrier wall*

*\*This bridge design is very similar to 26-Mile Rd. over M-53, and the cracking pattern was also very similar*



**Figure 82.** Overall bridge view



**Figure 83.** Bridge underside



**Figure 84.** Connection at the abutment (same as 26-Mile Rd. over M-53)



**Figure 85.** Bridge surface overall view



**Figure 86.** Cracking in barrier wall (typical)



**Figure 87.** Longitudinal cracking in bridge surface



**Figure 88.** Longitudinal and transverse cracks in pier area



**Figure 89.** Transverse cracking in pier area



**Figure 90.** Transverse cracking in second span, near the abutment

6: Halsted Rd. over I-696

- Steel Girders
- 4-span, non-integral abutments, deck is continuous for live loading, SIP metal forms (this information was obtained from the bridge design plans)
- *Some cracking is evident in the barrier wall, spaced at 3-4'. Some transverse cracking in area of the piers, and a small amount of longitudinal cracking scattered throughout.*

*\*Overall, the deck appears to be in good shape, and is not in as bad of condition as noted by MDOT in previous meetings. The deck appears to have recently been re-constructed.*



**Figure 91.** Bridge overall view



**Figure 92.** Bridge surface view



**Figure 93.** Possible longitudinal crack in the middle (it was not clear in the investigation whether it was a crack or roughed surface)





**Figure 94.** Cracking in barrier wall, potential transverse crack in the middle



**Figure 95.** Evenly-spaced vertical cracking in barrier wall



**Figure 96.** Bridge deck surface

10: M-6 over Buck Creek

- Concrete I-girders (MI-1800 Girders)
- 4-span, continuous deck for live loading, non-integral abutments, SIP forms used underneath
- Relatively long spans compared to other bridges investigated
- Girder spacing varied (larger spacing in the middle, smaller spacing at the sides)
- *Extensive transverse cracking was evident in the second span, between pier 1 and the middle pier. Transverse cracking was also evident at the piers, in the negative moment region. Not much evidence of longitudinal cracking. Identical cracking pattern was evident in the two approach slabs.*



**Figure 97.** Bridge overall view



**Figure 98.** View of side of bridge



**Figure 99.** Transverse cracking bridge deck, near the abutment



**Figure 100.** Close-up of transverse cracks



**Figure 101.** Non-integral abutment detail (note that beams are not cast into the abutment)



**Figure 102.** Bridge underside view (girder spacing is larger in the left side of the photo)



**Figure 103.** Bridge deck surface overall view



**Figure 104.** Transverse cracking in bridge deck



**Figure 105.** Extensive and evenly-spaced transverse cracks



**Figure 106.** More transverse cracks in bridge deck



**Figure 107.** Transverse cracking in bridge deck



**Figure 108.** Large transverse crack at opposite abutment

11: 44<sup>th</sup> Street over US-131



- Steel beams
- 2-span, continuous deck, non-integral abutment, SIP forms used underneath
- Bridge has a unique shape (see photos, it is a rectangular bridge, with trapezoidal approaches)
- *Extensive transverse cracking evident at the pier area, evenly spaced transverse cracking in the east span. Some vertical cracking evident in the barrier wall. Not much evidence of longitudinal cracking.*



**Figure 109.** Bridge approach overall view



**Figure 110.** Cracking in barrier wall



**Figure 111.** Transverse cracking in pier area



**Figure 112.** Transverse cracking in-between pier and abutment



**Figure 113.** Transverse cracking in bridge deck



**Figure 114.** Bridge deck overall view



**Figure 115.** Bridge overall view



**Figure 116.** Non-integral beams/continuous deck at the abutment



**Figure 117.** Bridge underside view

12: Burlingame Rd. over M-6

- Concrete I-girders (MI-1800)
- 2-span, continuous deck for live loading, integral abutment
- *Heavy amount of longitudinal cracking, spaced evenly at girder spacing through the entire bridge. Some transverse cracking evident at the approaches and in the middle by the pier. Random map cracking throughout.*



**Figure 118.** Cracking in barrier wall (typical)



**Figure 119.** Diagonal cracking near the abutment



**Figure 120.** Transverse cracking in pier area



**Figure 121.** Transverse cracking at the pier area



**Figure 122.** Bridge underside





**Figure 123.** Connection at the abutment



**Figure 124.** Diagonal cracking near the abutment



**Figure 125.** Longitudinal cracking



**Figure 126.** Random/map cracking on the shoulder



**Figure 127.** Evenly-spaced longitudinal cracks



**Figure 128.** Longitudinal cracks running through entire deck

13: Milham Ave. over US-131

- Spread box beams
- 4-span, semi-integral abutment, continuous deck for live loading, part-width construction, SIP forms used except for the area where the part-width construction took place
- *Numerous transverse cracks in the underside where the part-width construction meets, numerous transverse cracks in the deck fascia and barriers. Widespread transverse cracking throughout, especially in the area by the piers and also in positive moment regions. Some longitudinal cracking evident throughout, scattered randomly.*

*\*Part-width construction may have had an effect on the cracking in this bridge*



**Figure 129.** Bridge overall view



**Figure 130.** Deteriorated outside/fascia of the bridge



**Figure 131.** Abutment connection detail



**Figure 132.** Bridge underside detail (note part-width construction area without SIP forms)



**Figure 133.** Transverse cracking in bridge underside



**Figure 134.** Transverse cracking



**Figure 135.** Cracking in barrier wall (typical)



**Figure 136.** Transverse cracking in bridge deck



**Figure 137.** Longitudinal/diagonal cracking near the abutment



**Figure 138.** Transverse cracking in the middle of the bridge





**Figure 139.** Transverse cracking in bridge deck and continuing into the sidewalk



**Figure 140.** Evenly-spaced transverse cracks



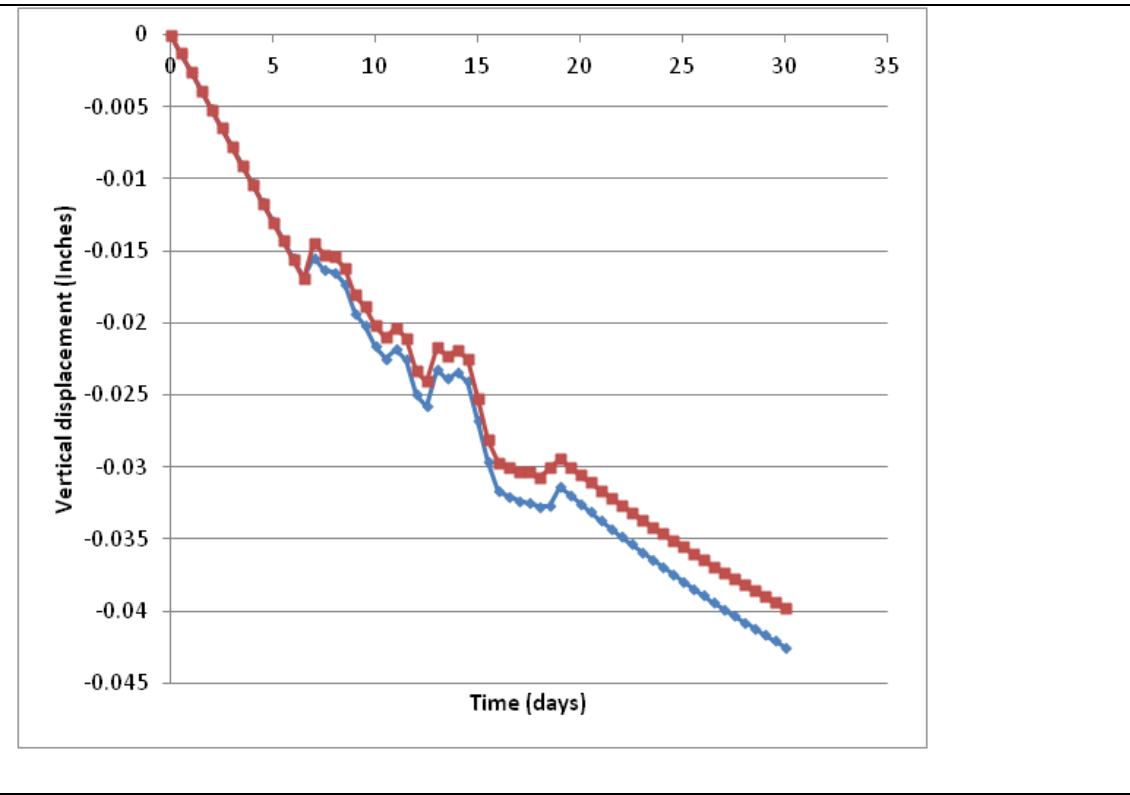
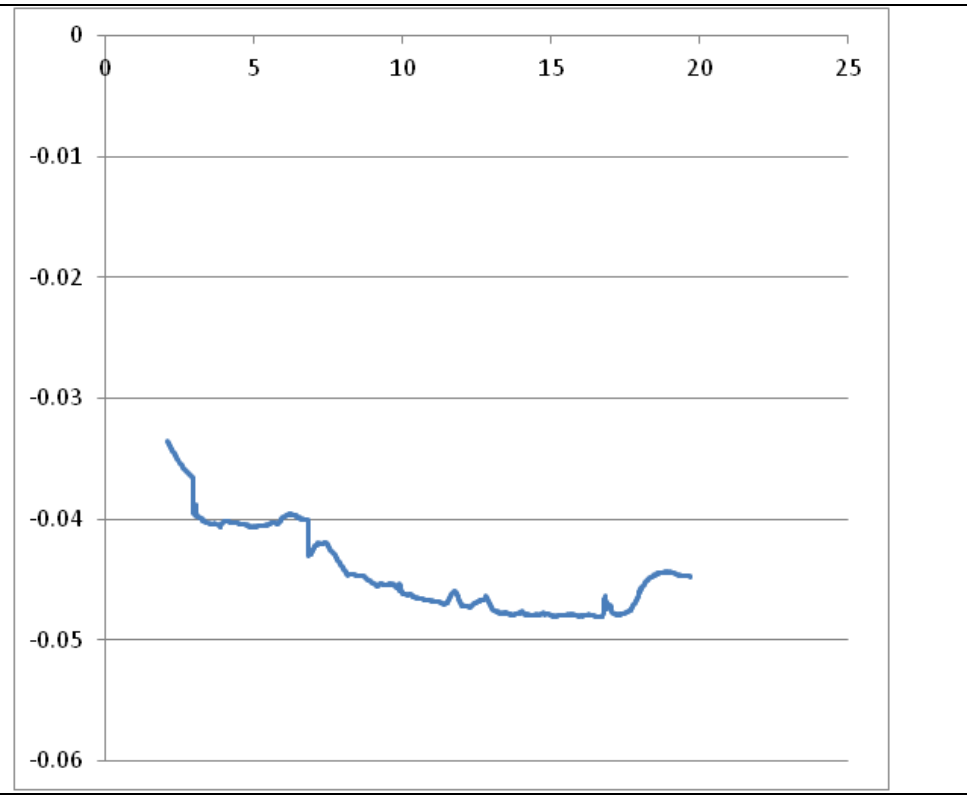
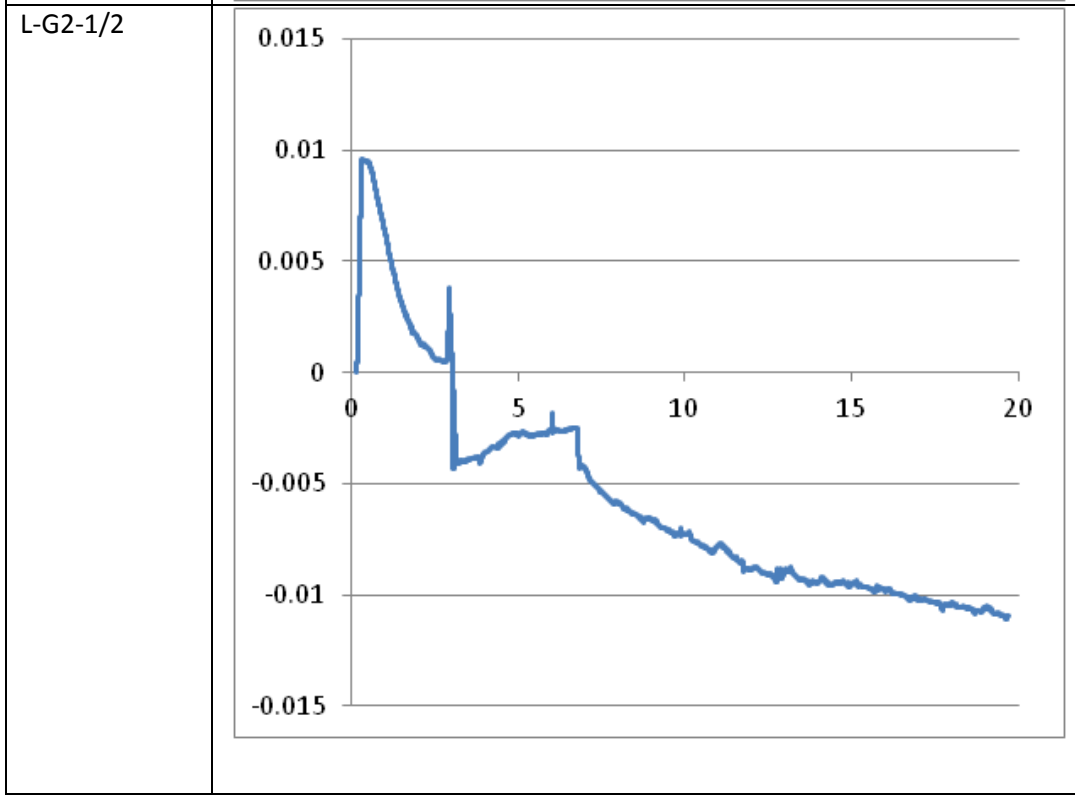
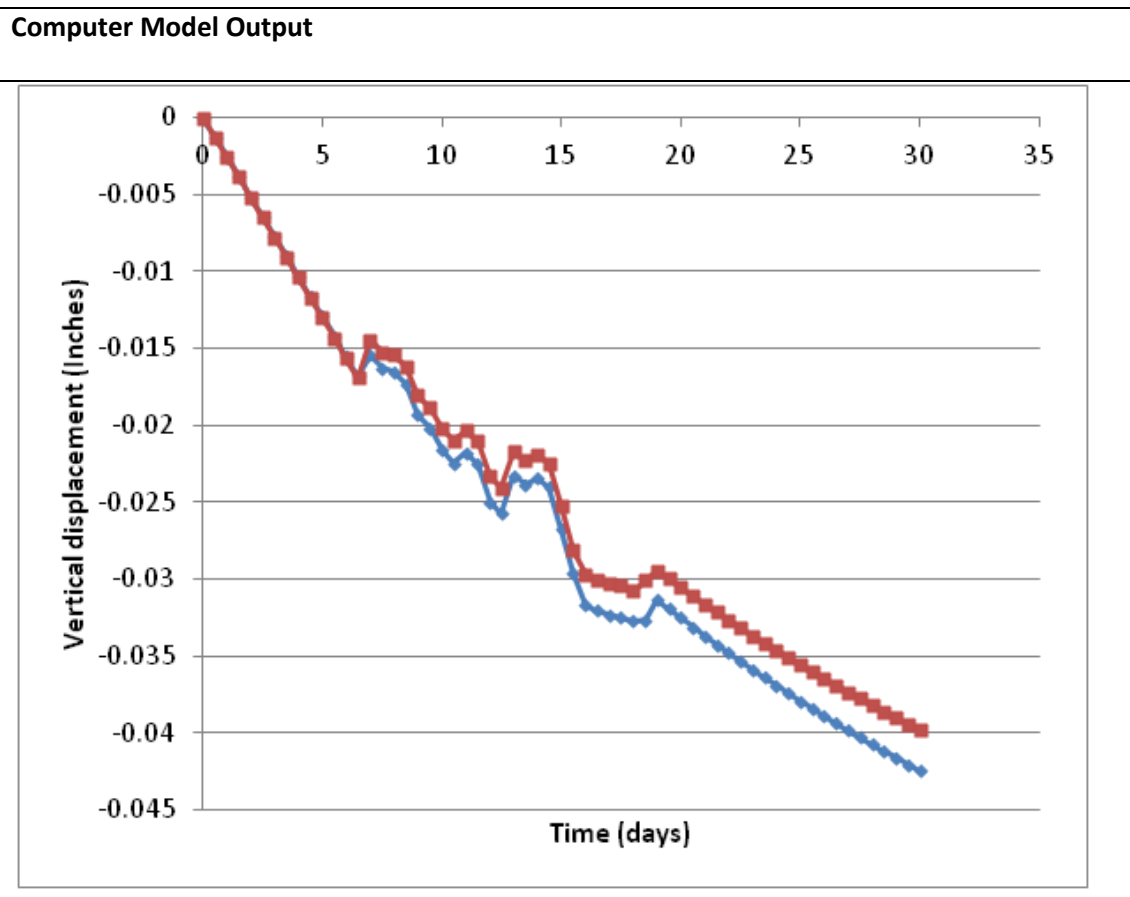
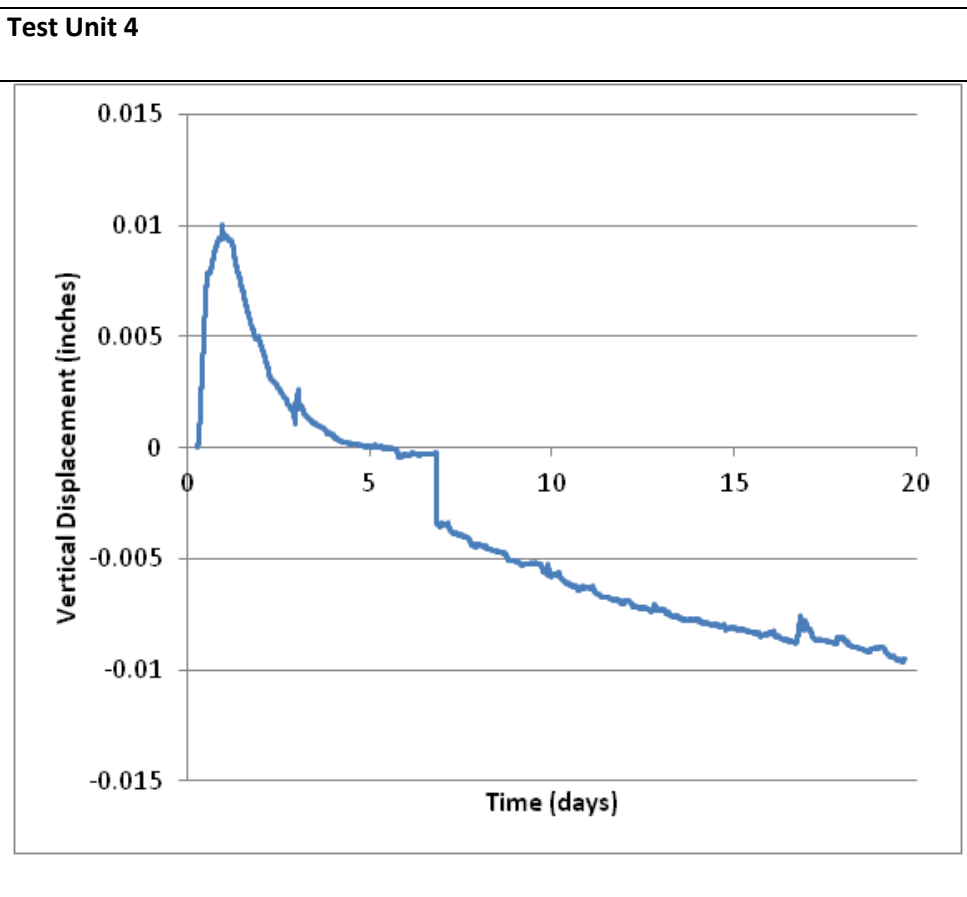
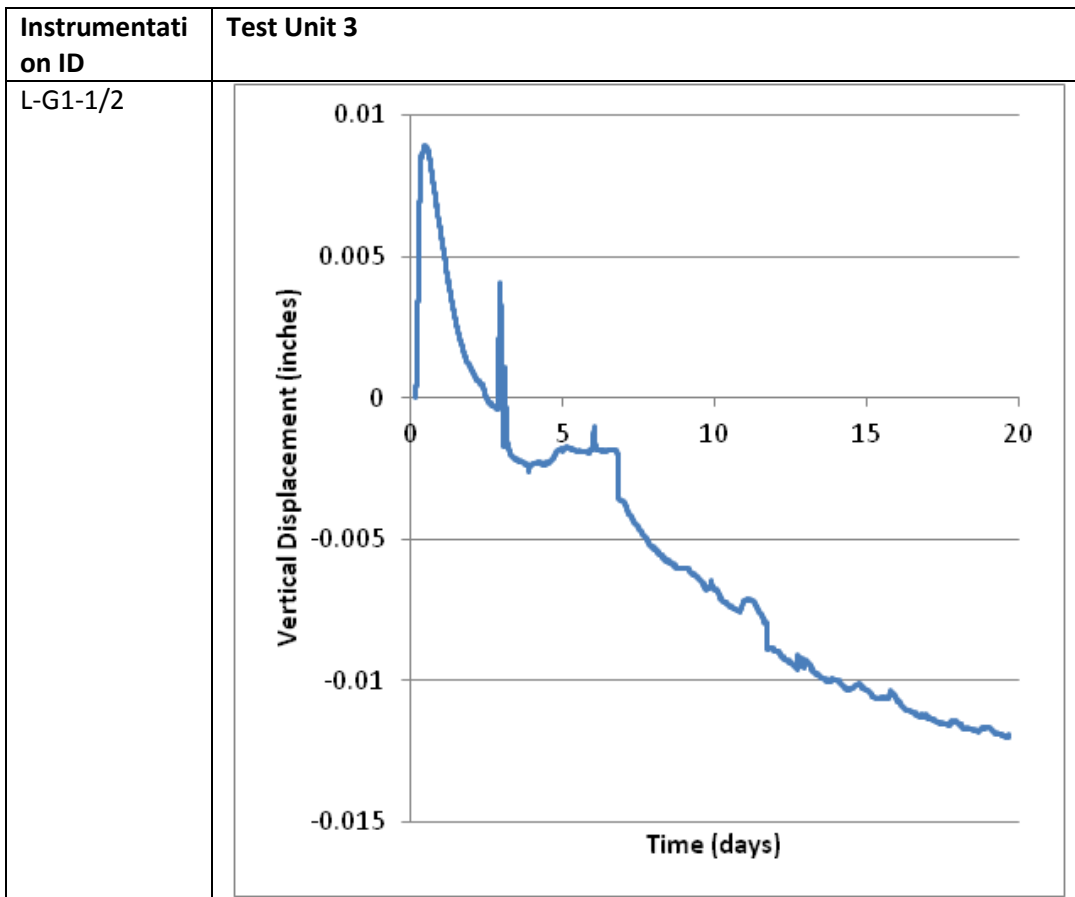
**Figure 141.** Random small longitudinal cracks



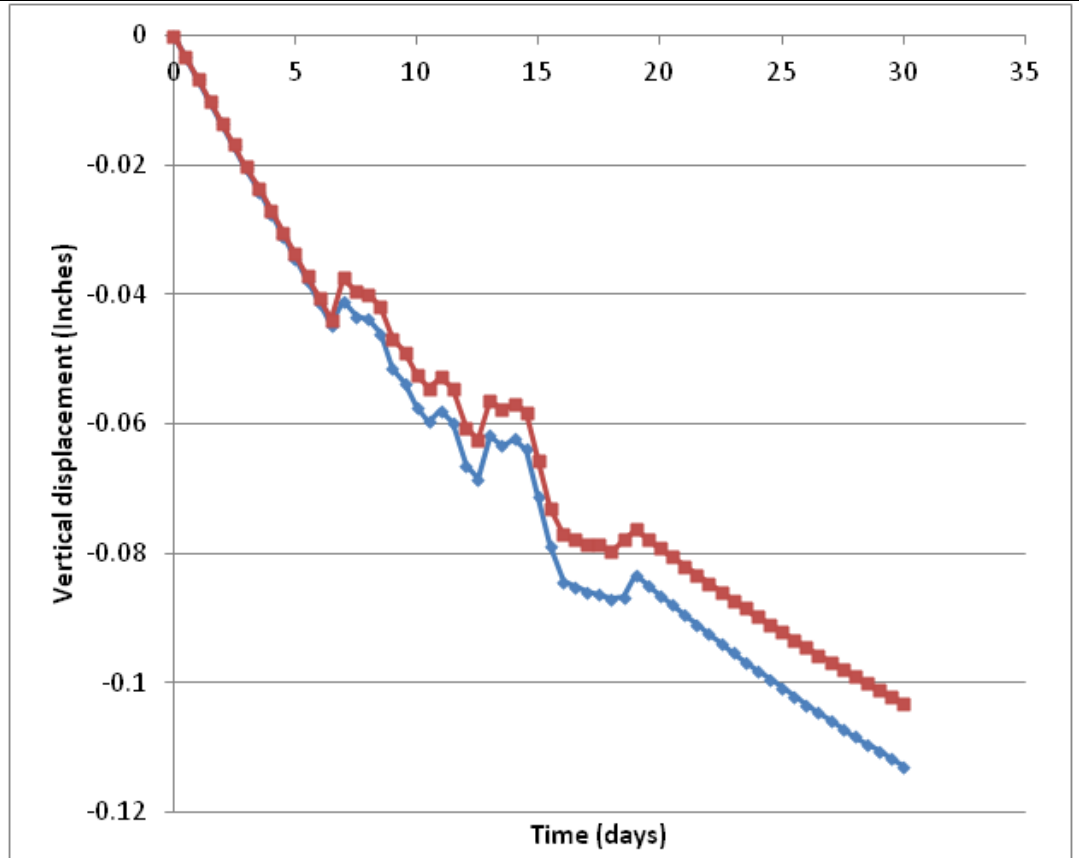
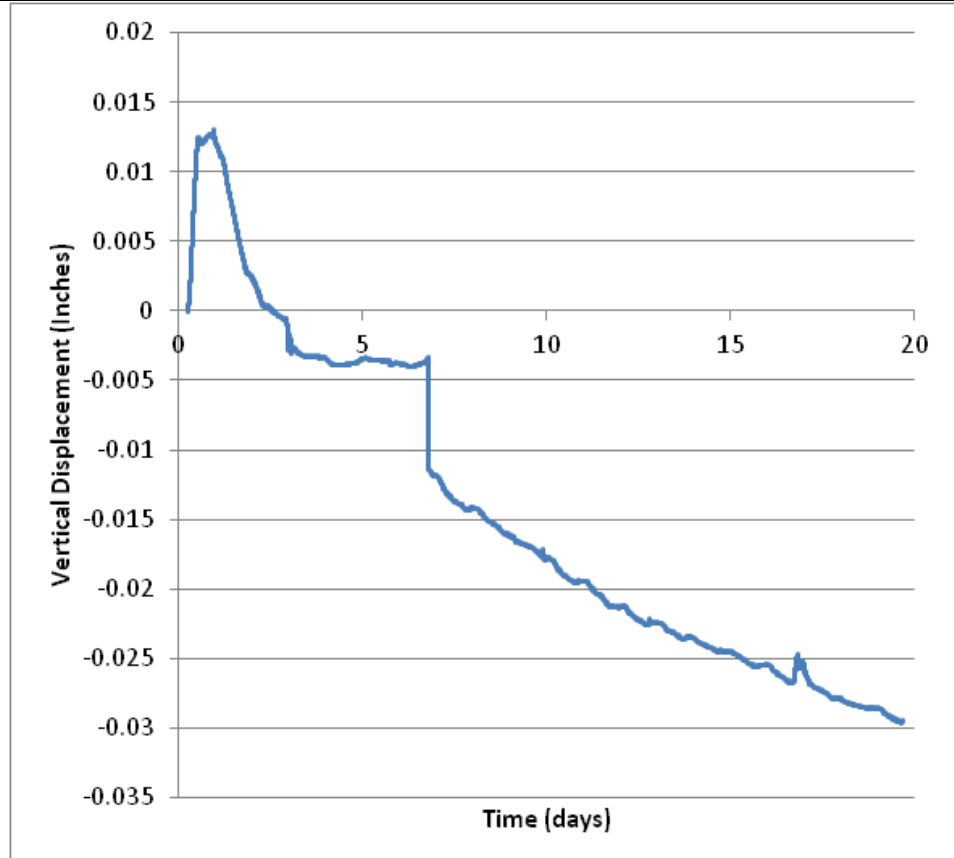
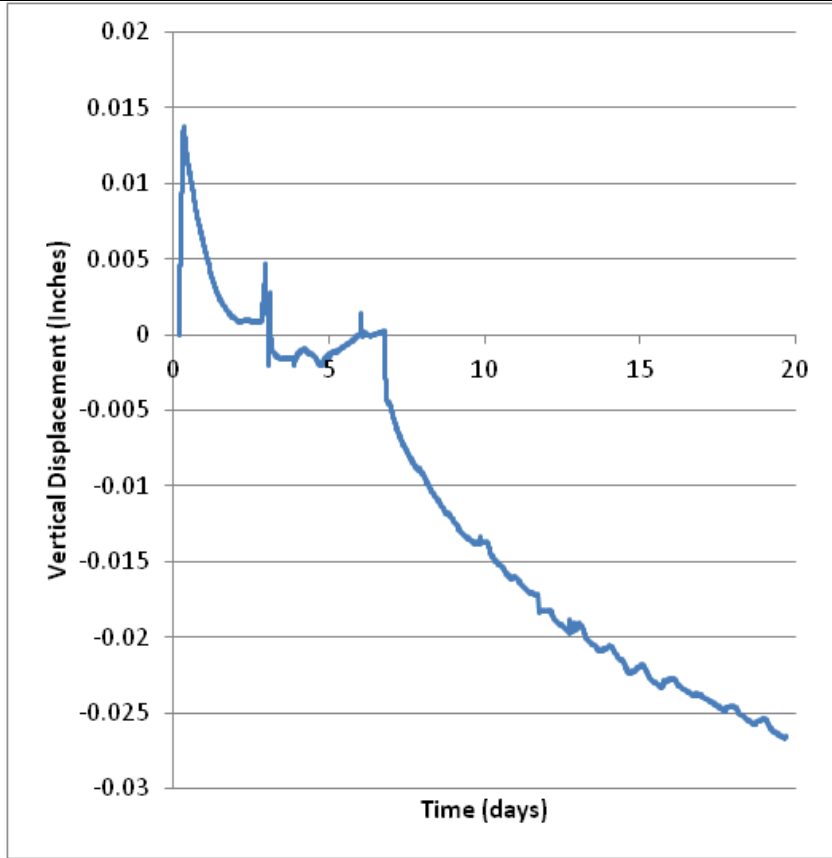
**Figure 142.** Bridge deck overall view

## **Appendix C**

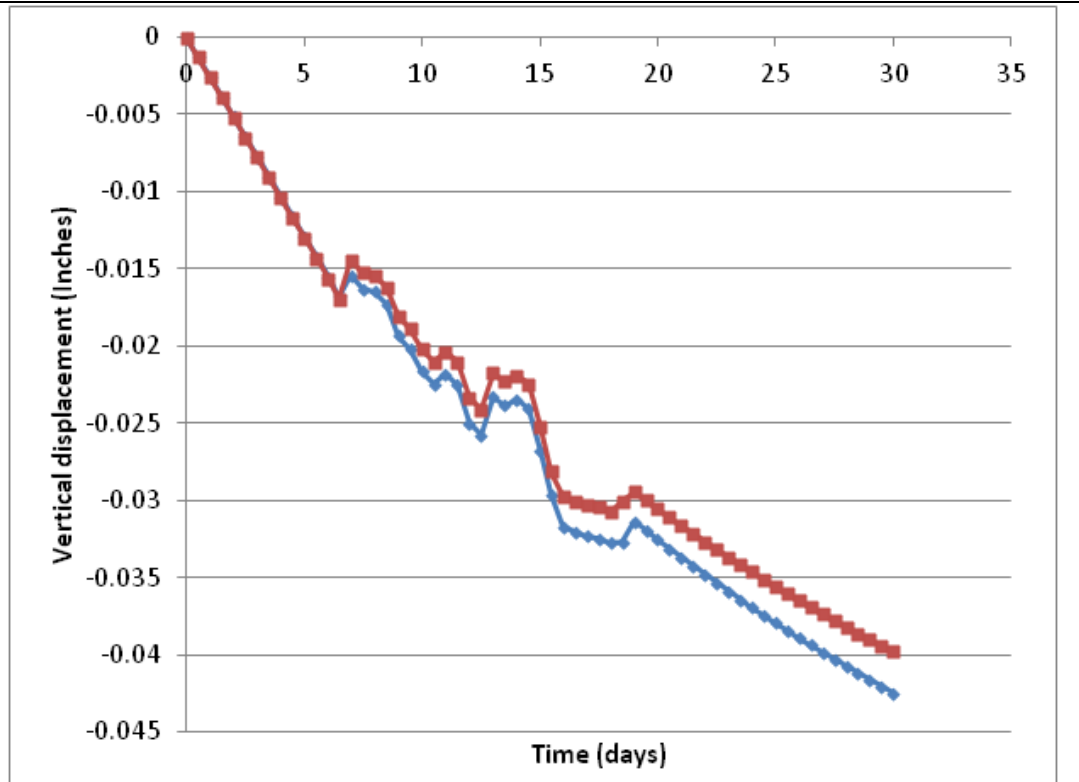
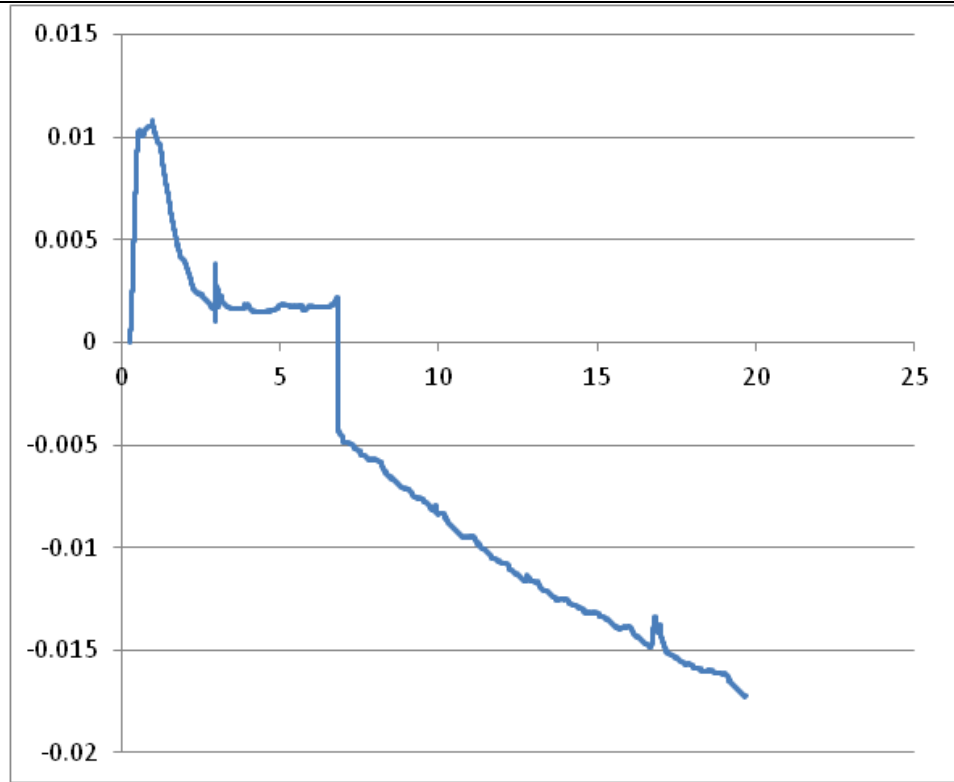
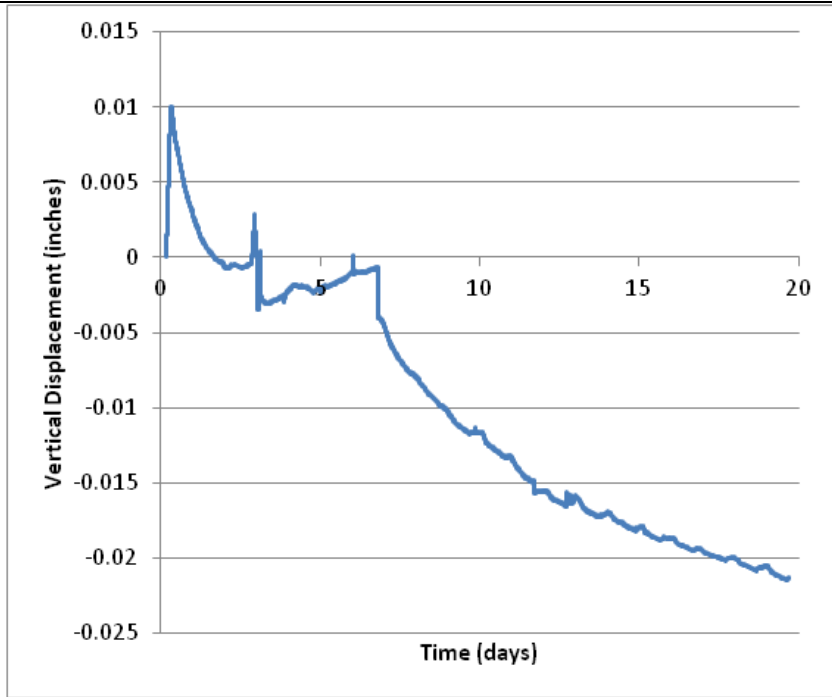
### **Laboratory Slab Models Full Data Set**



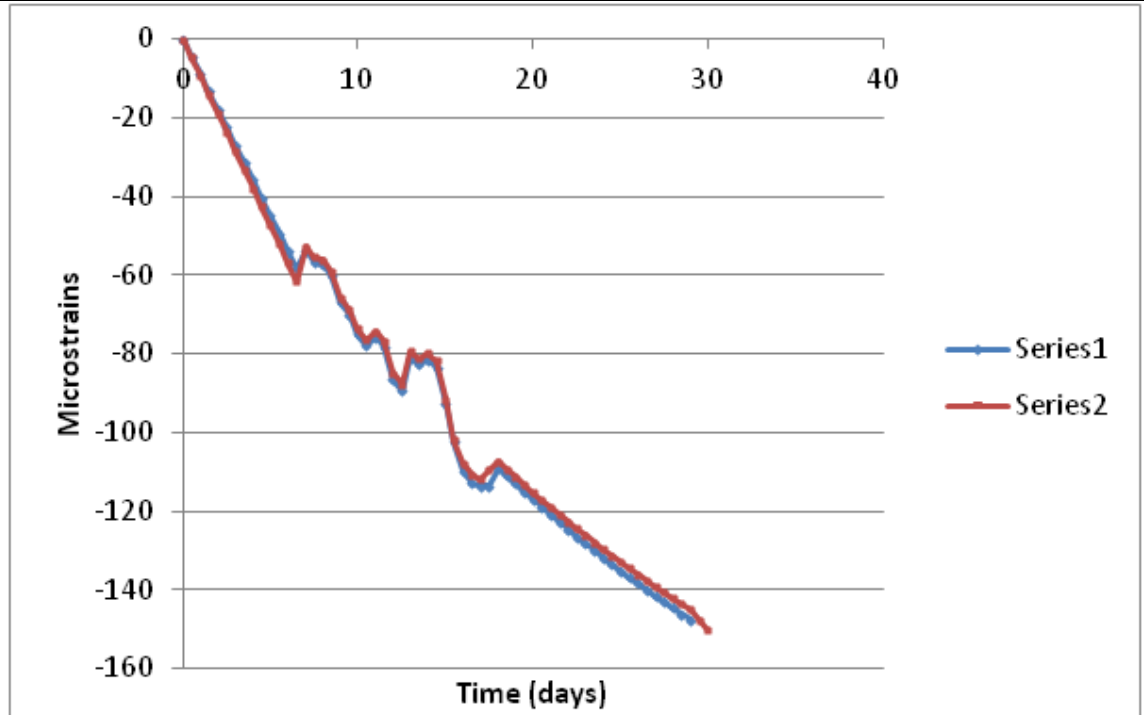
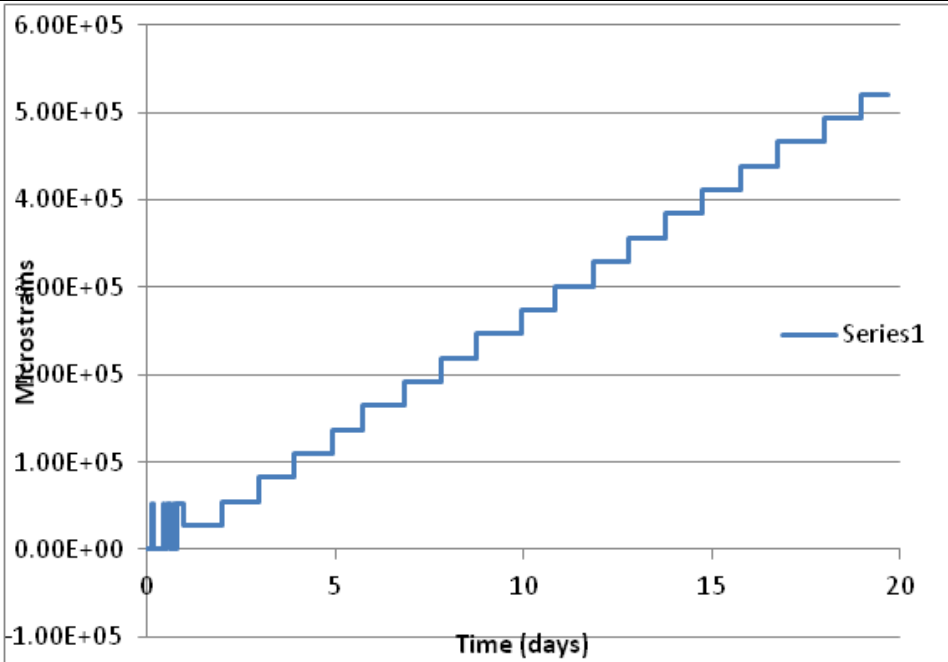
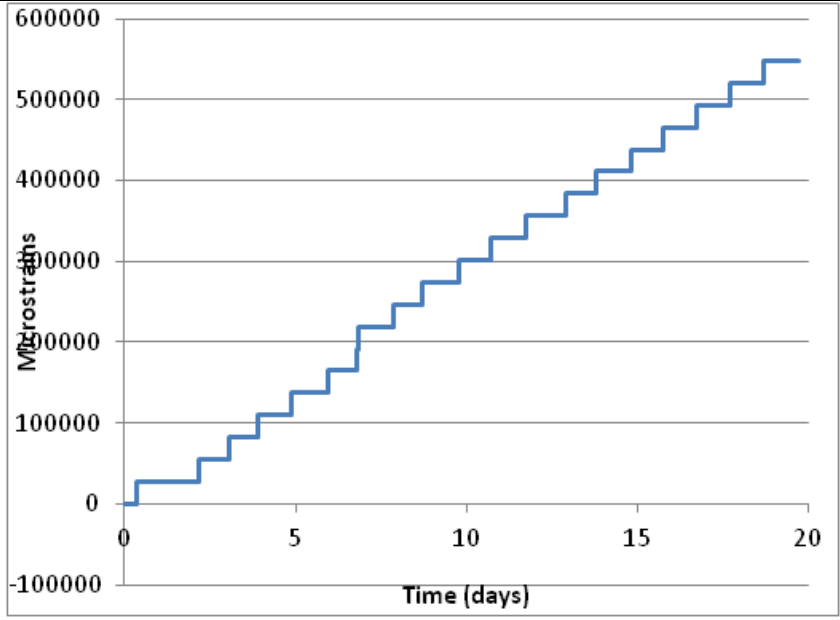
L-1/2-1/2



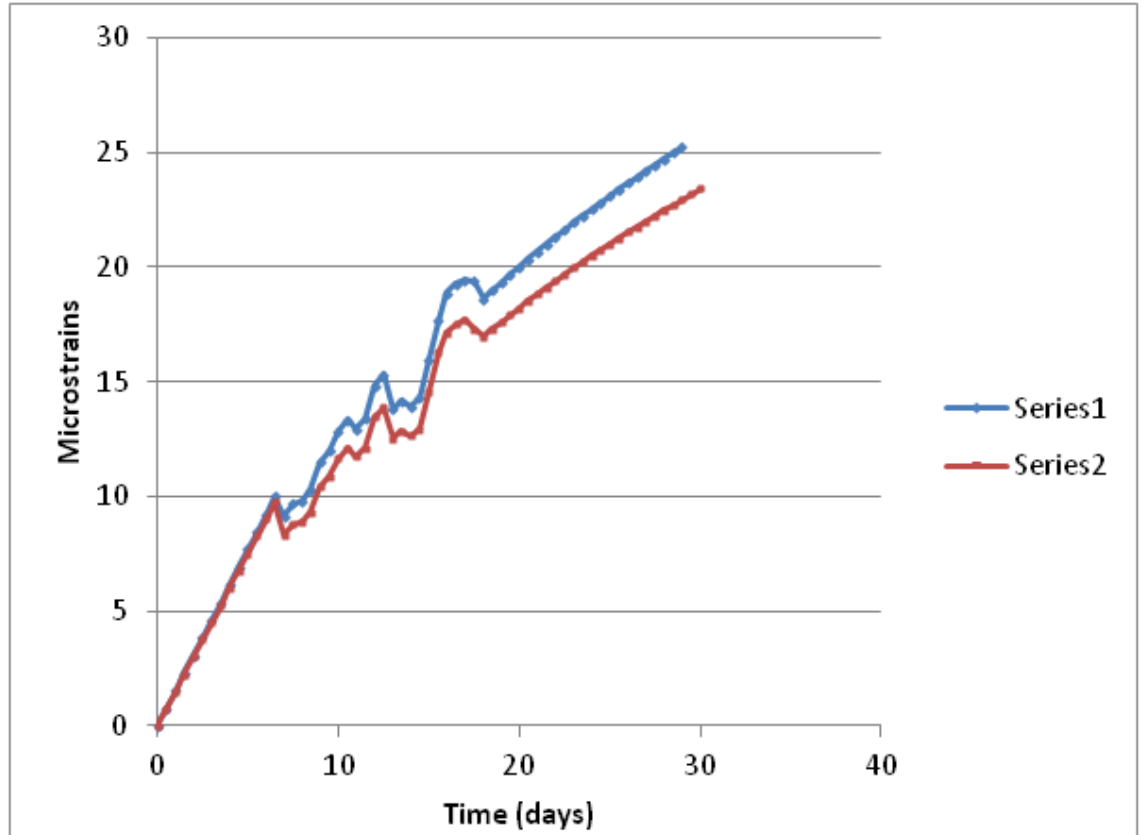
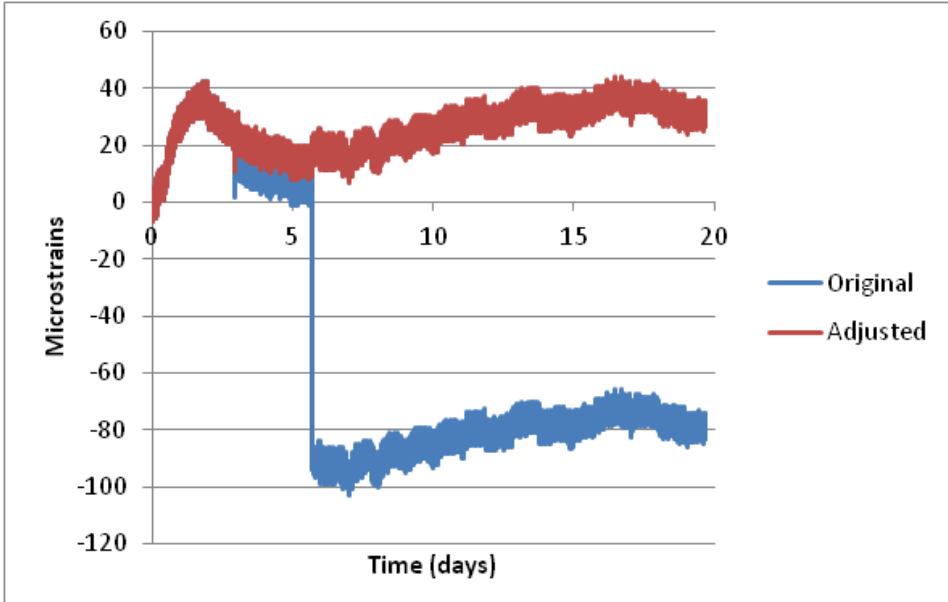
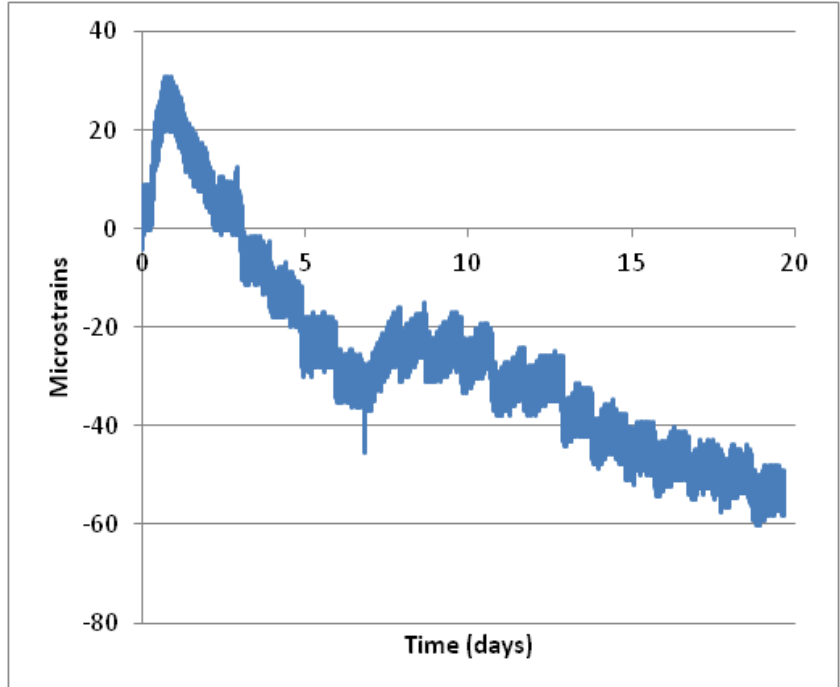
L-1/2-3/4



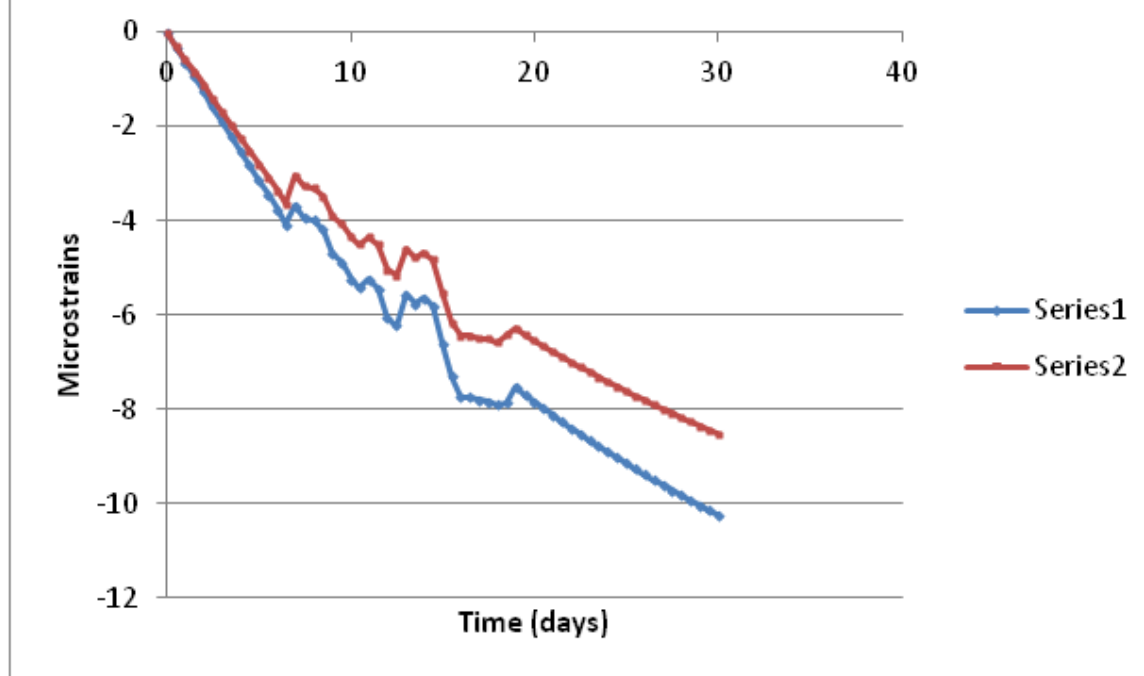
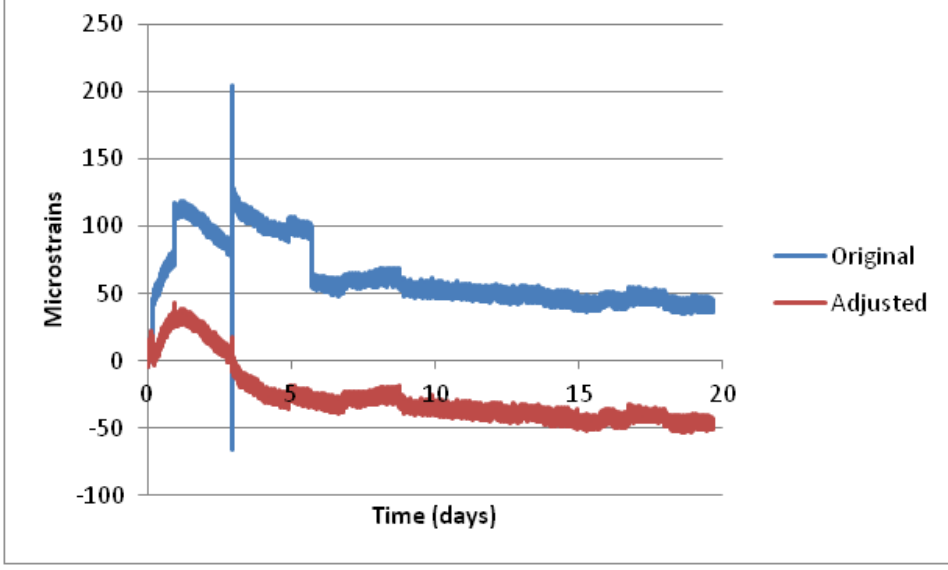
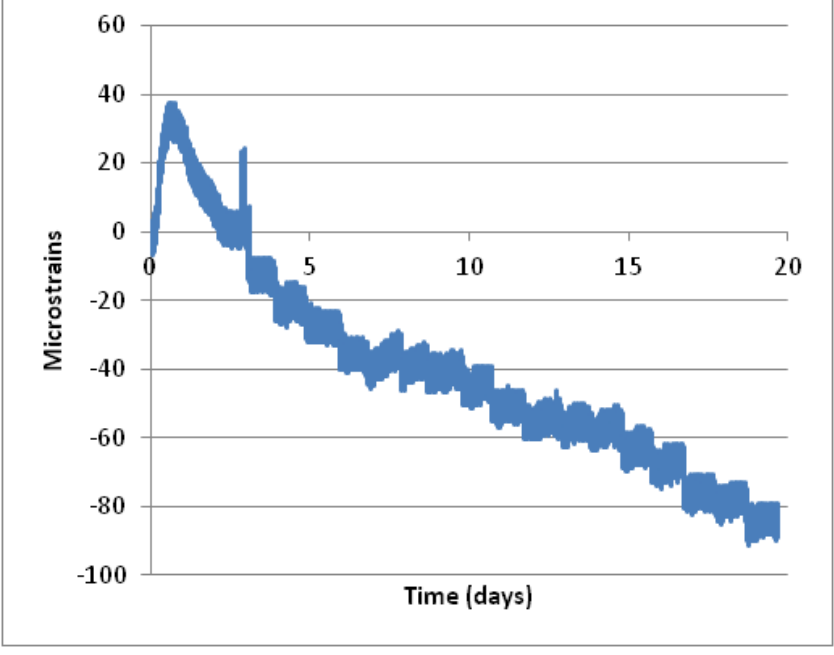
S-G1-TF-M-3/4-L



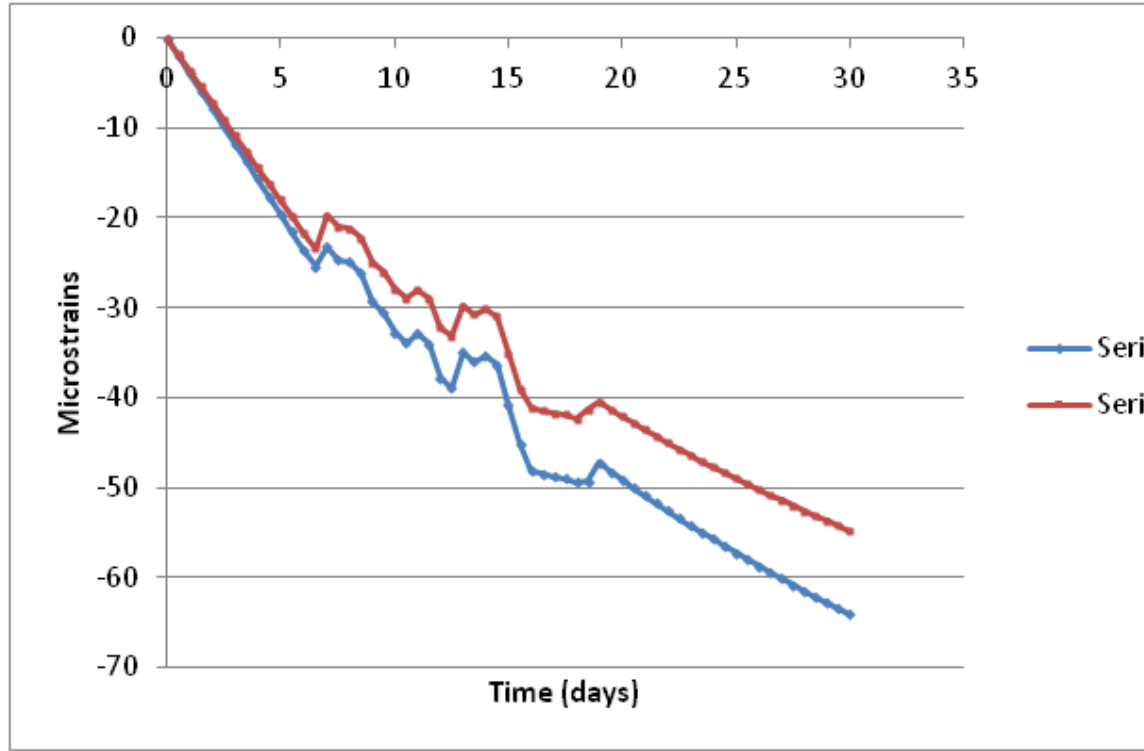
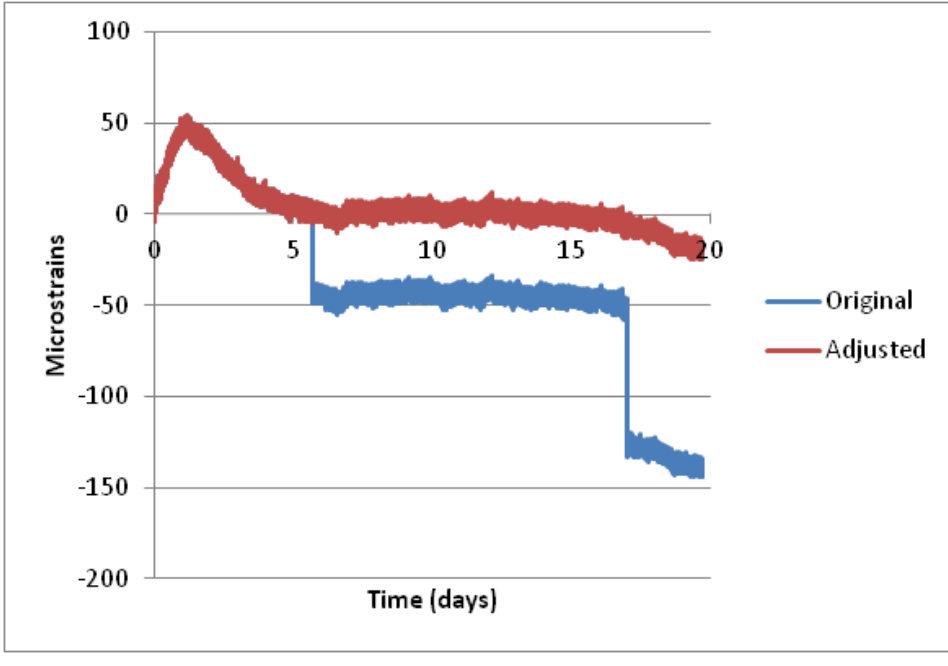
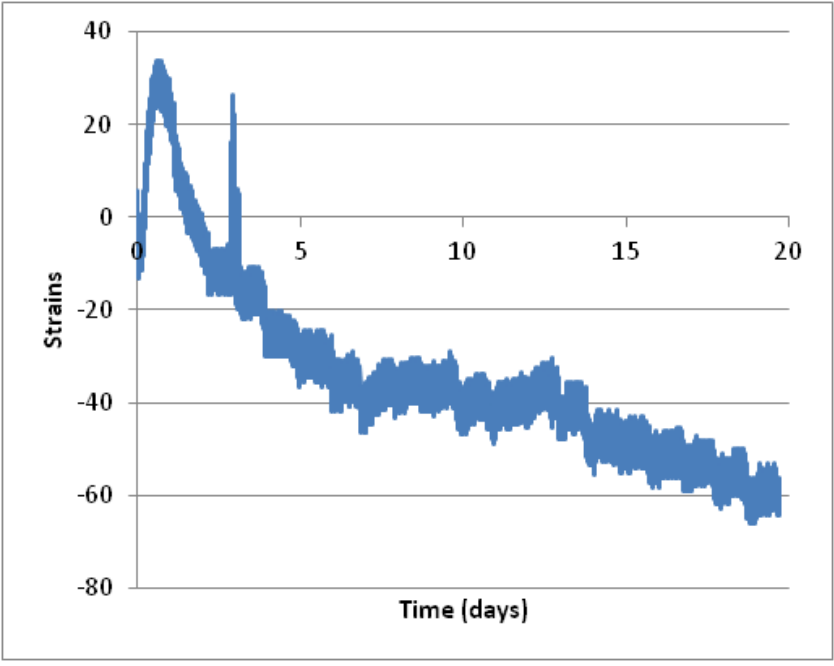
S-G1-Bf-M-3/4-L



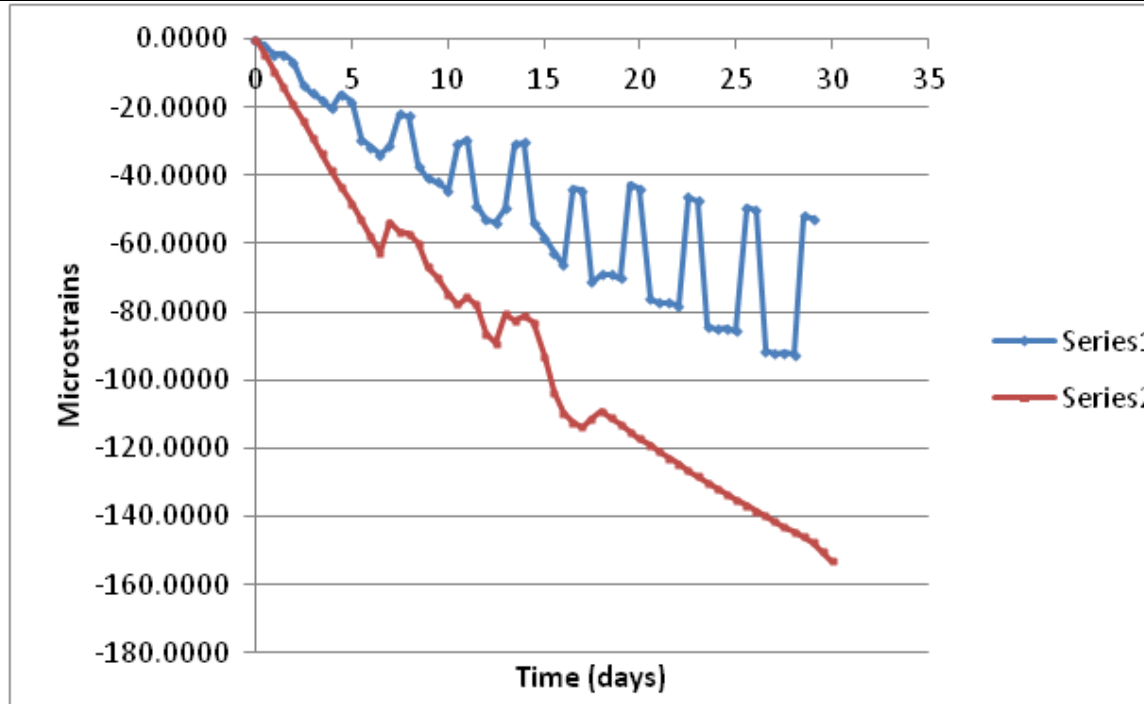
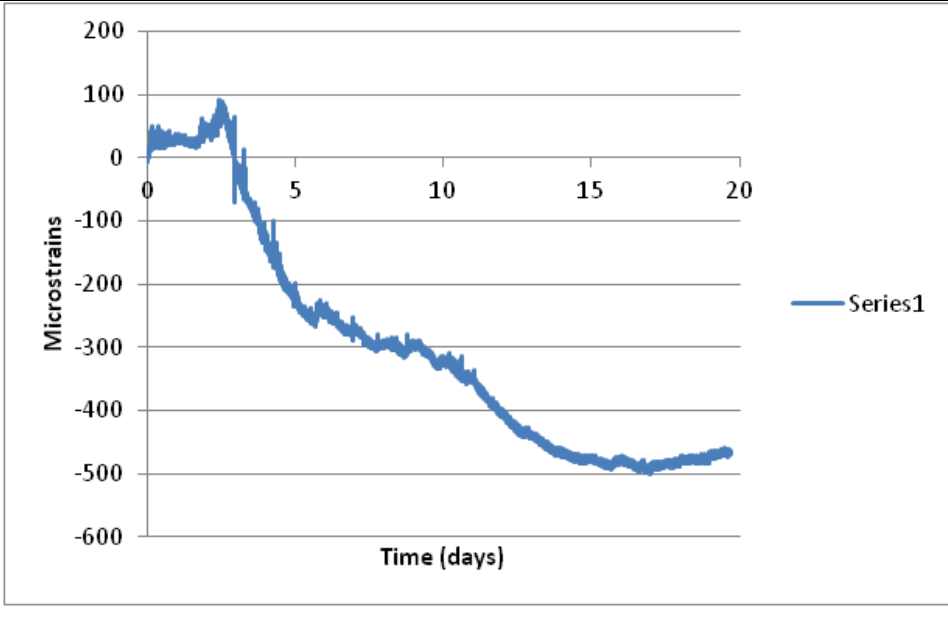
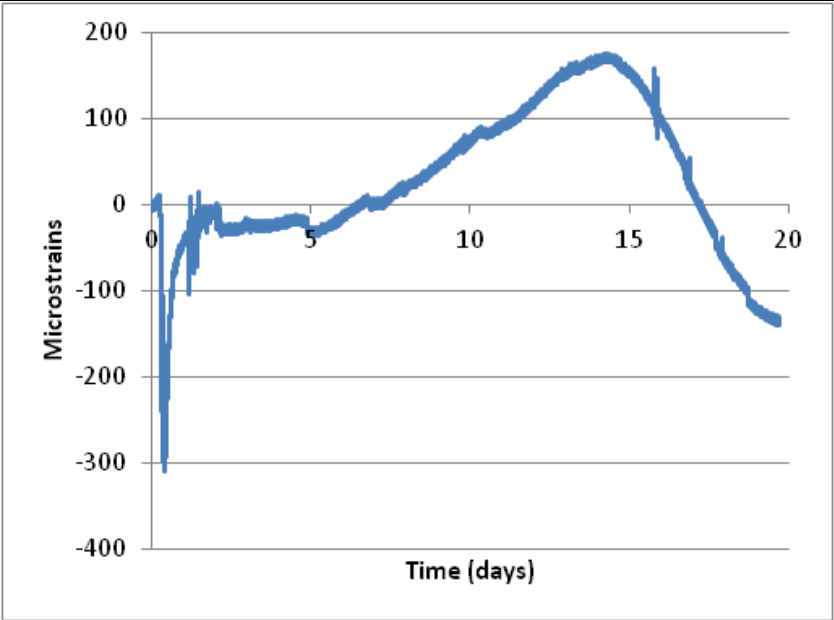
S-G1-W-O-3/4-L



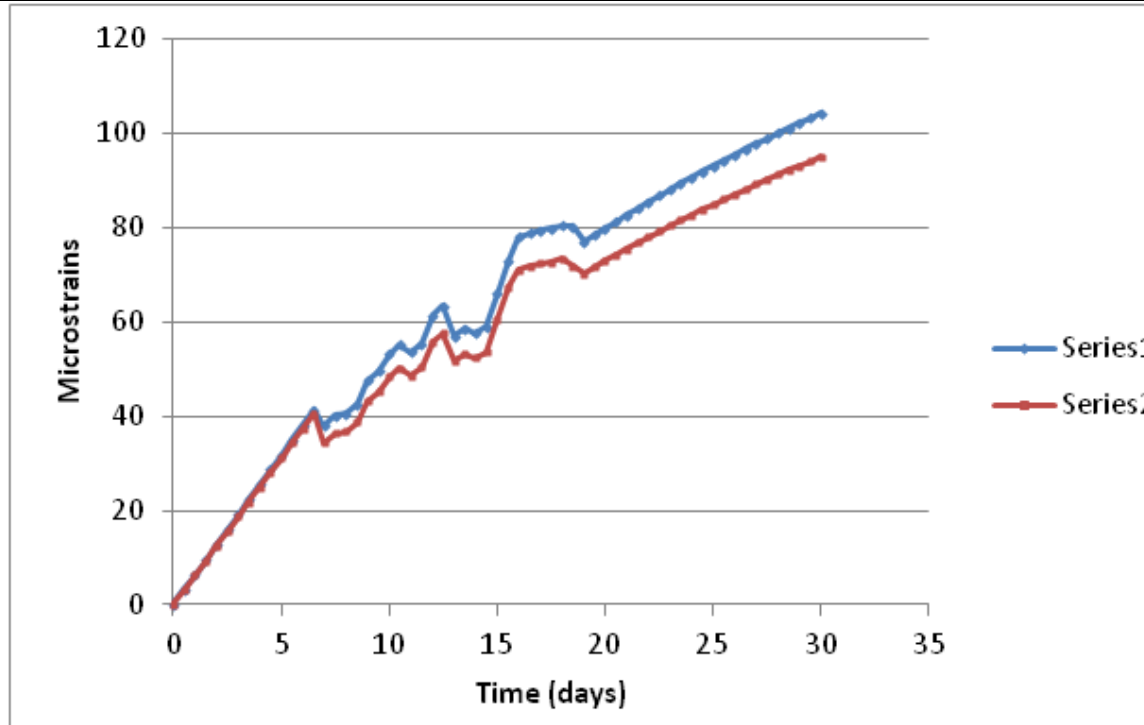
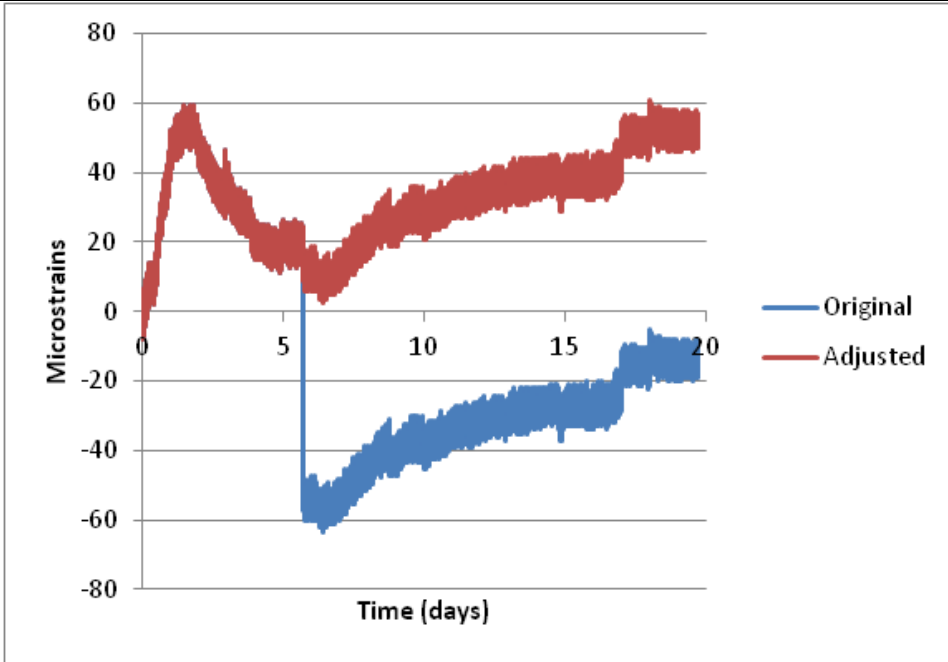
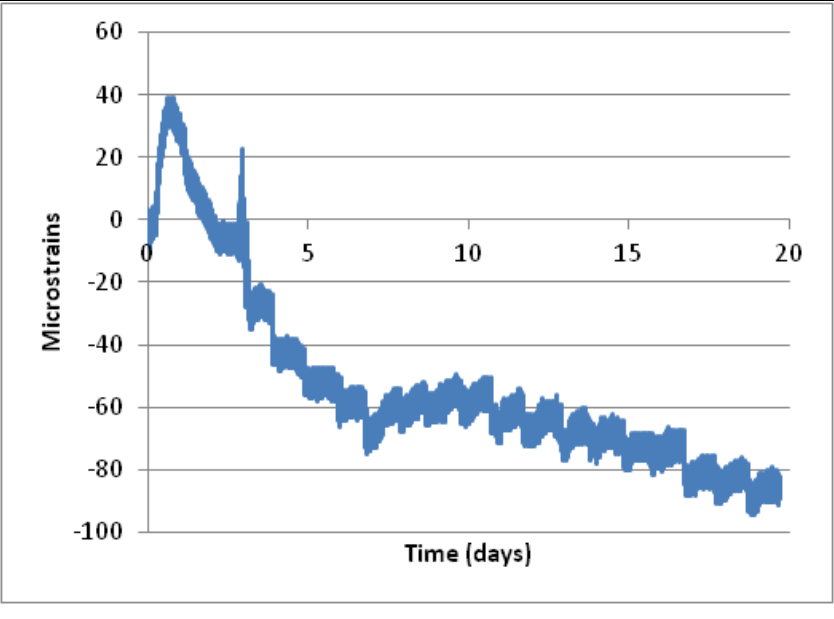
S-G1-W-O-1/2-L



S-G1-Tf-M-1/4-L

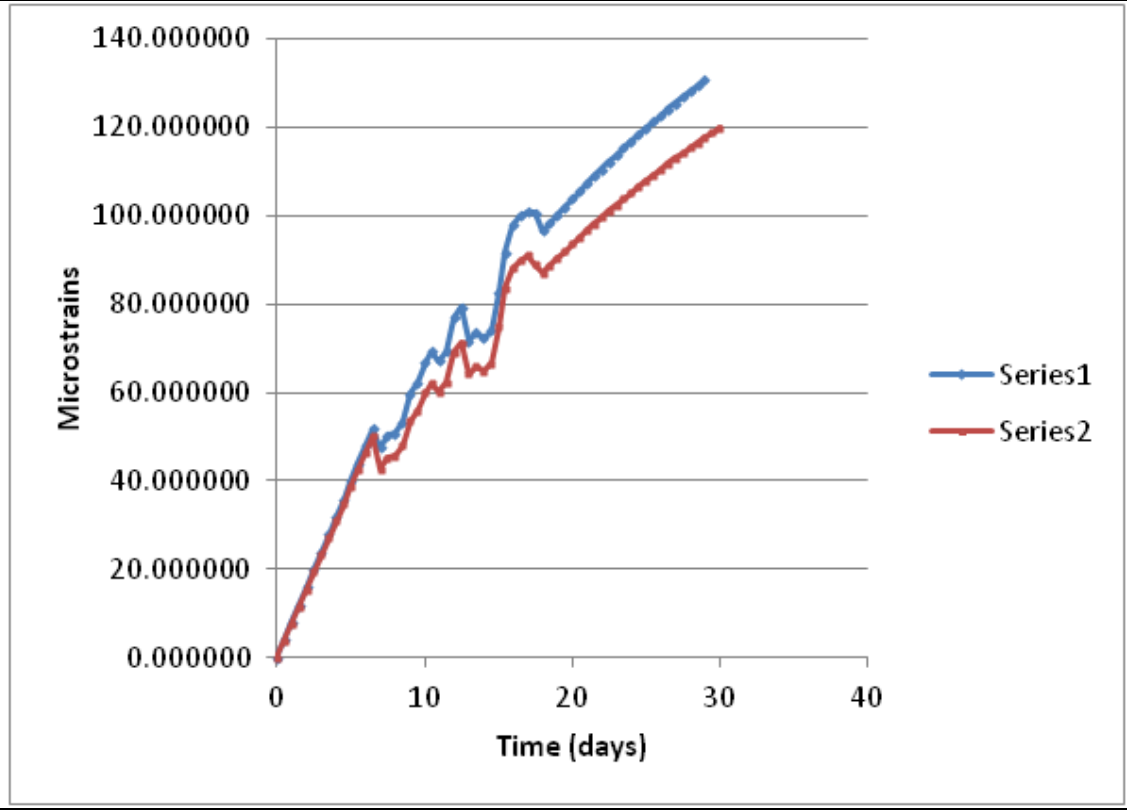
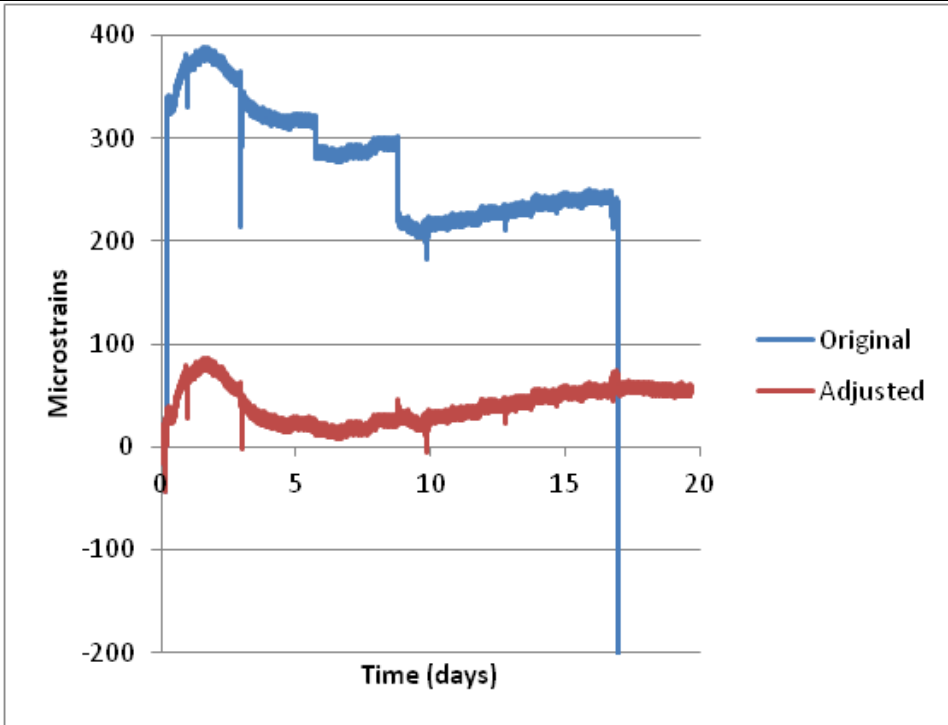
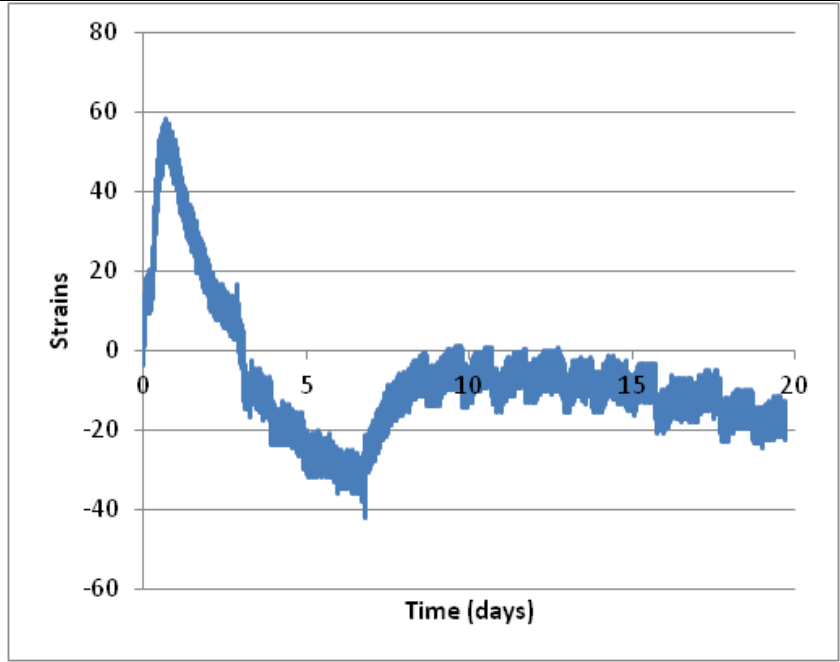


S-G1-Bf-I-1/2-L

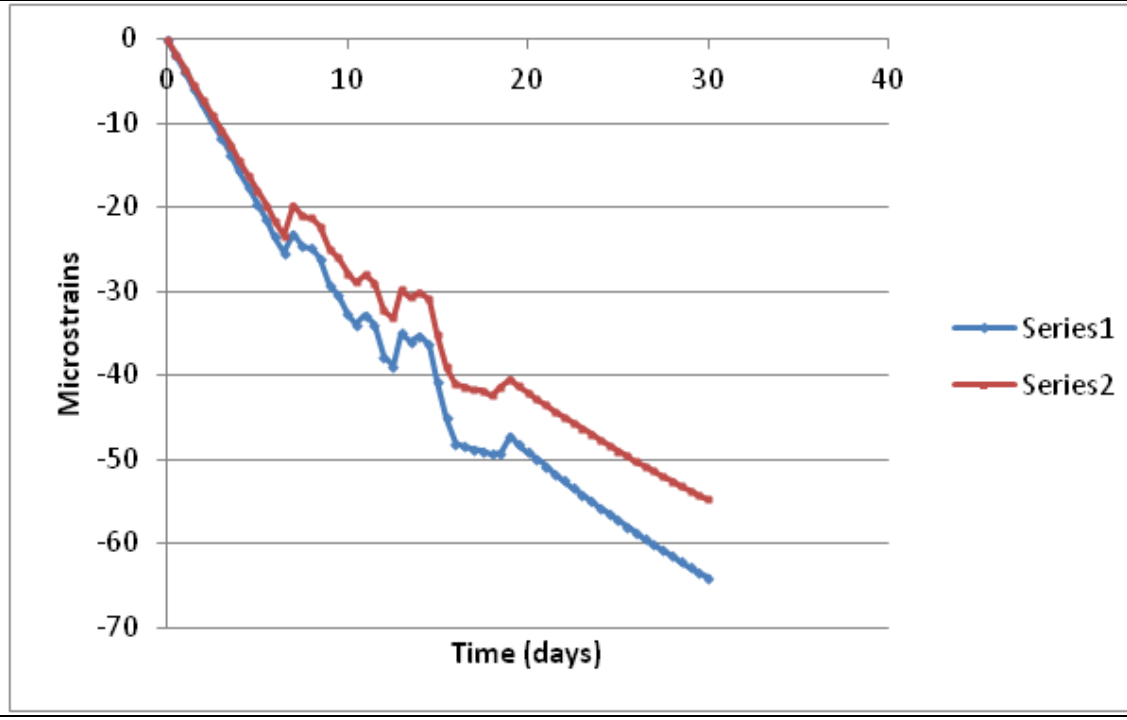
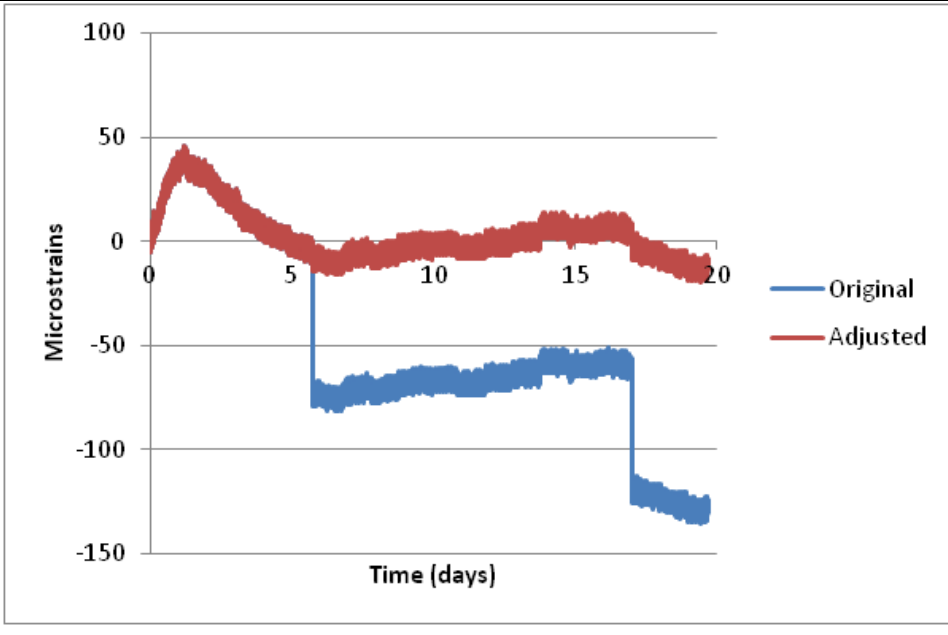
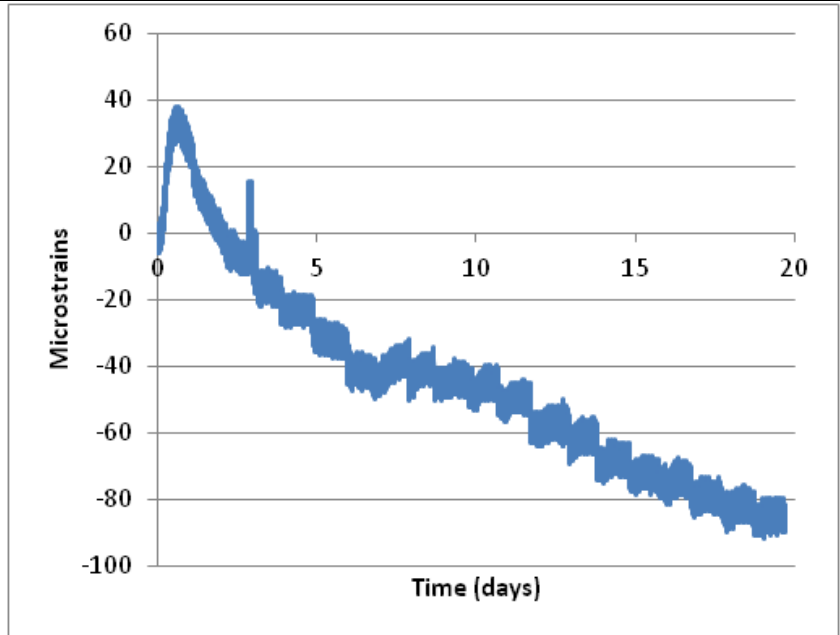




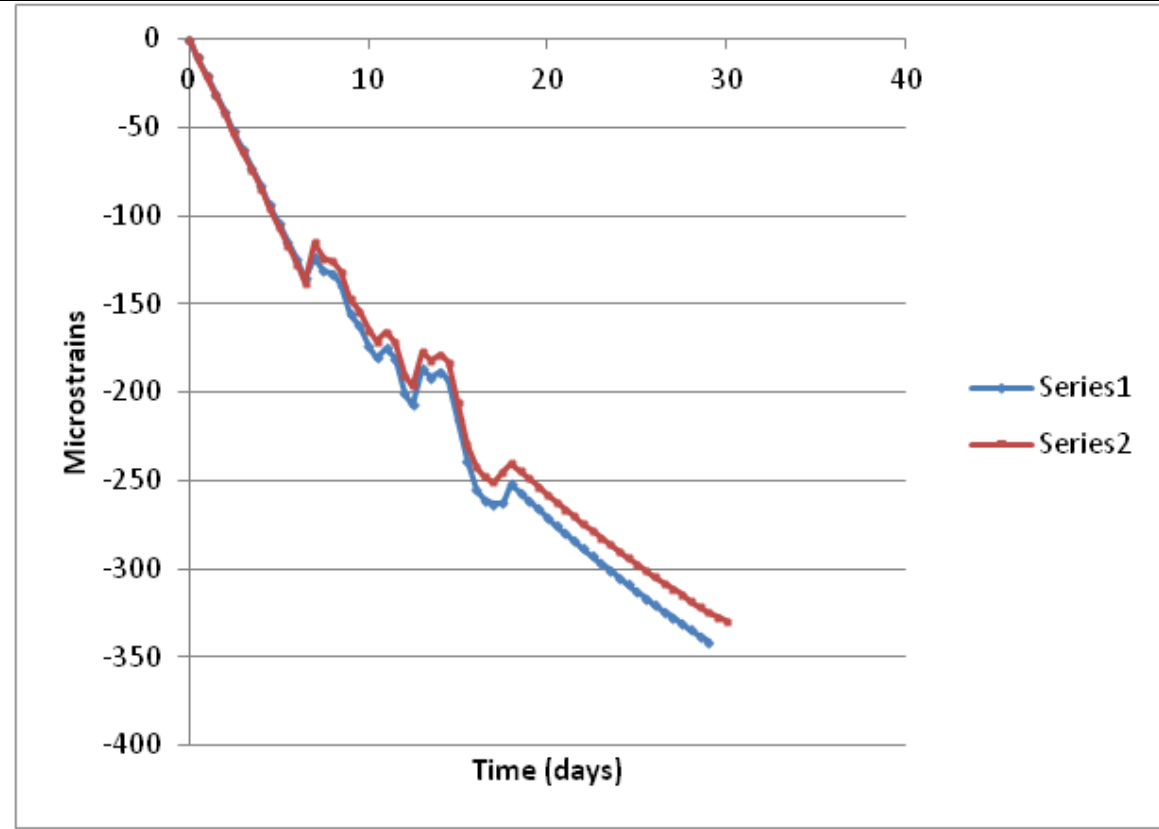
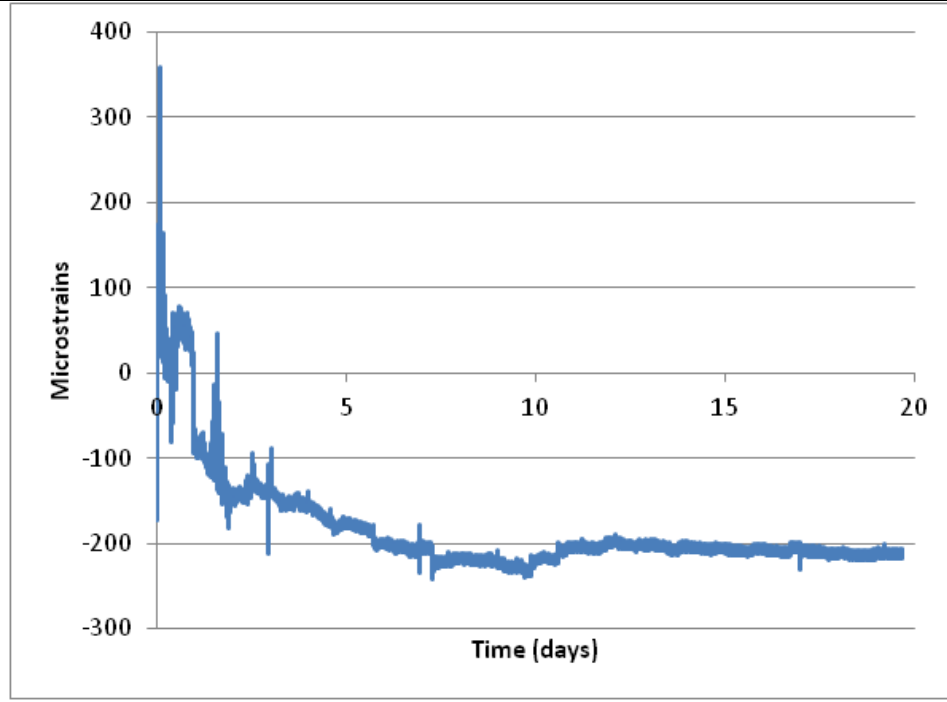
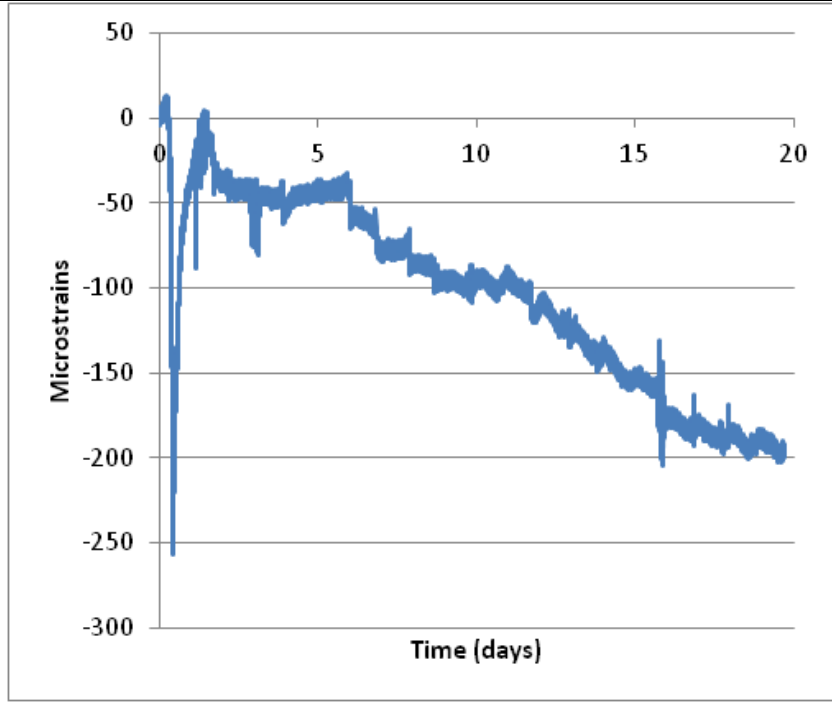
S-G1-Bf-M-1/2-L



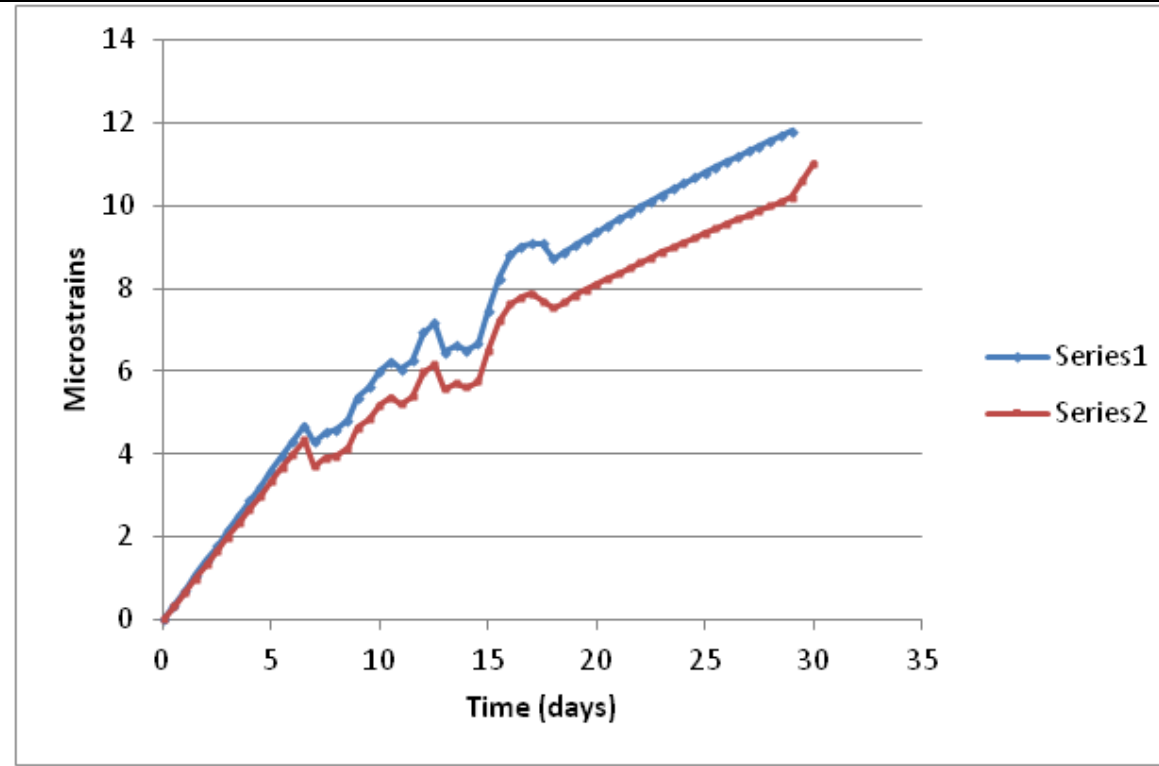
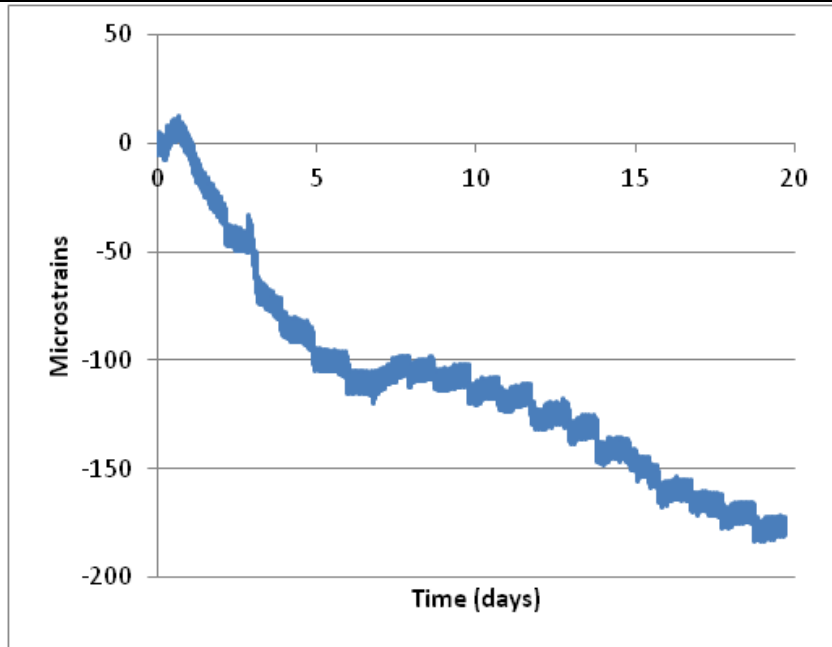
S-G1-W-I-1/2-L



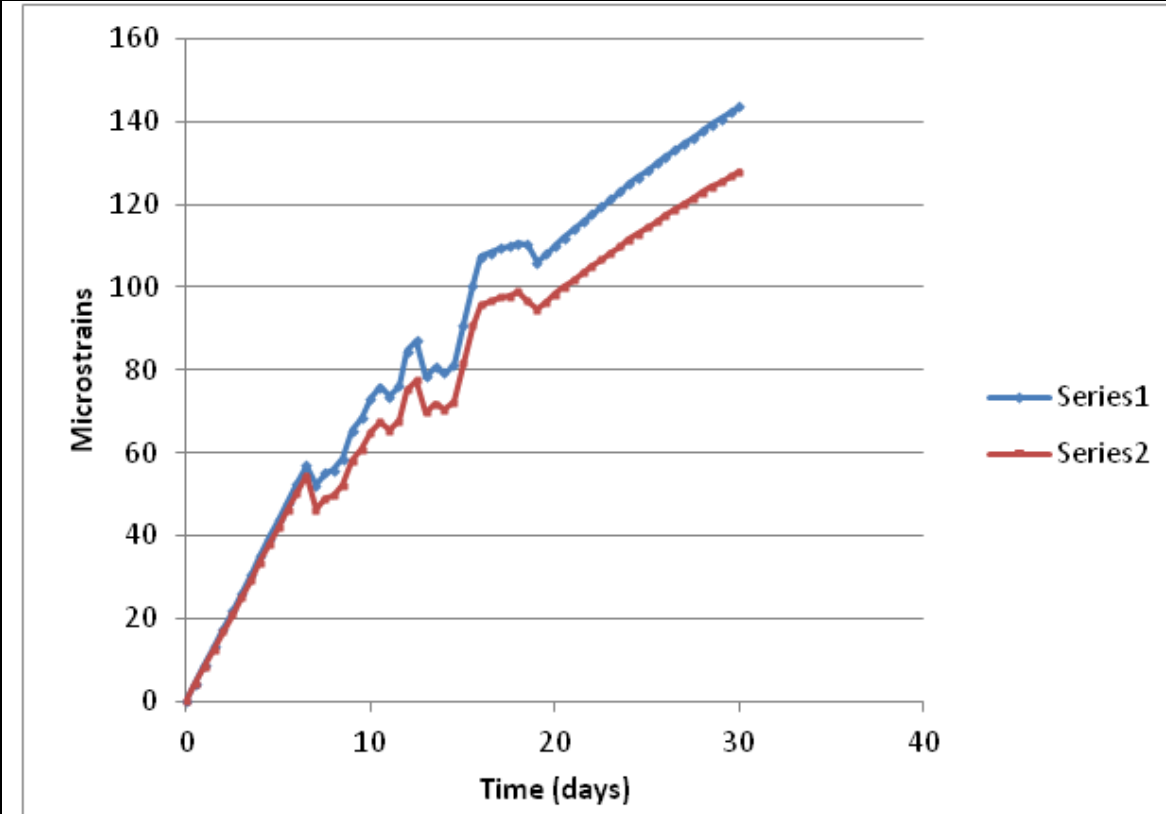
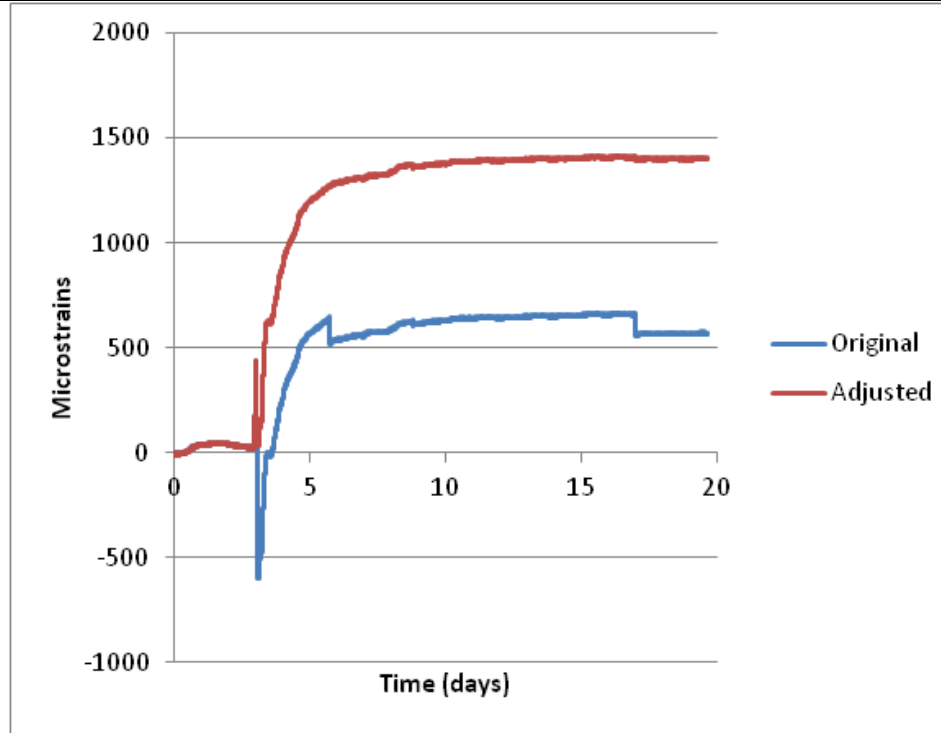
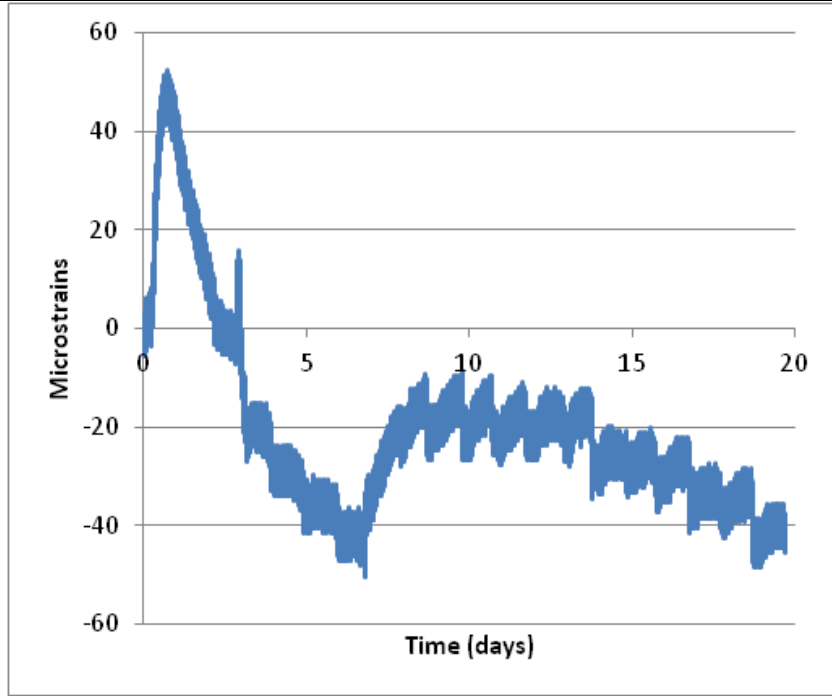
S-G1-Tf-M-1/2-L



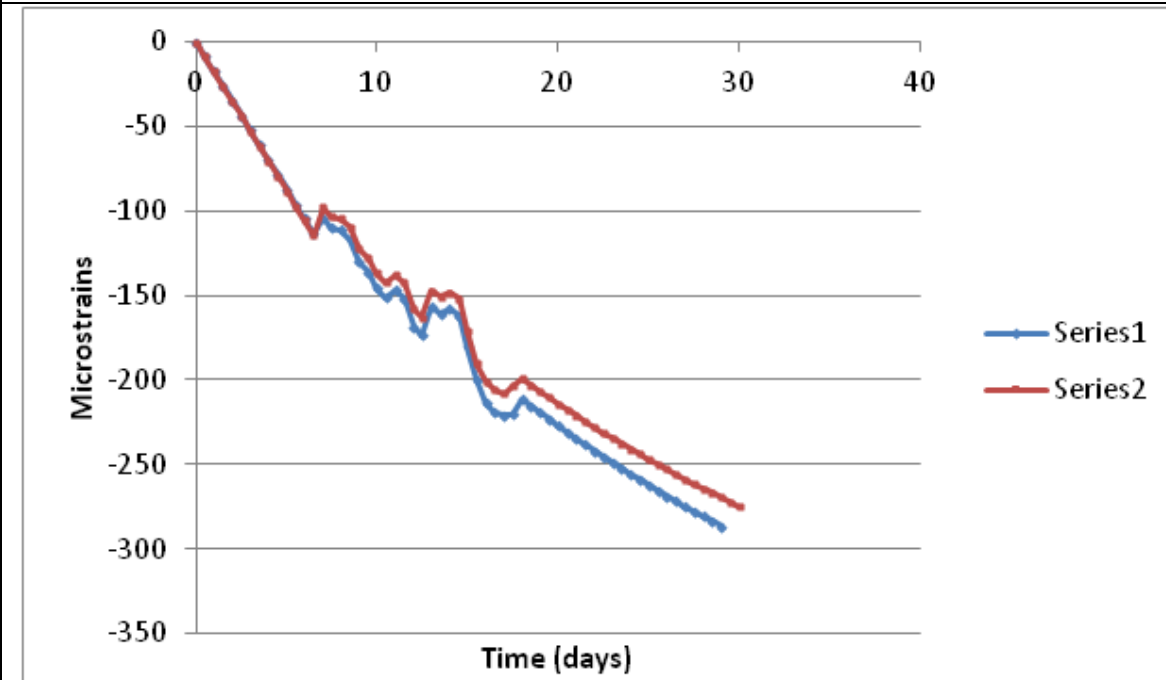
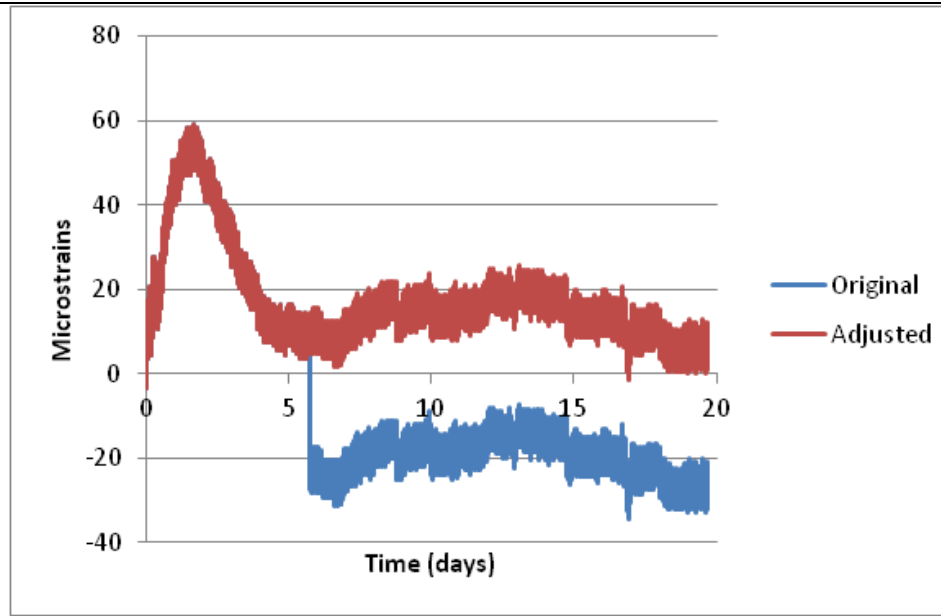
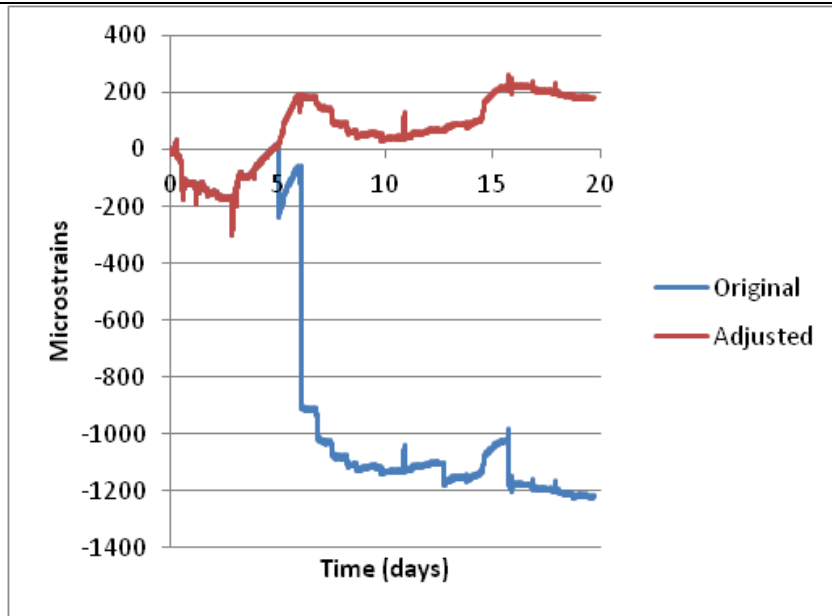
S-G1-Bf-M-1/4-L



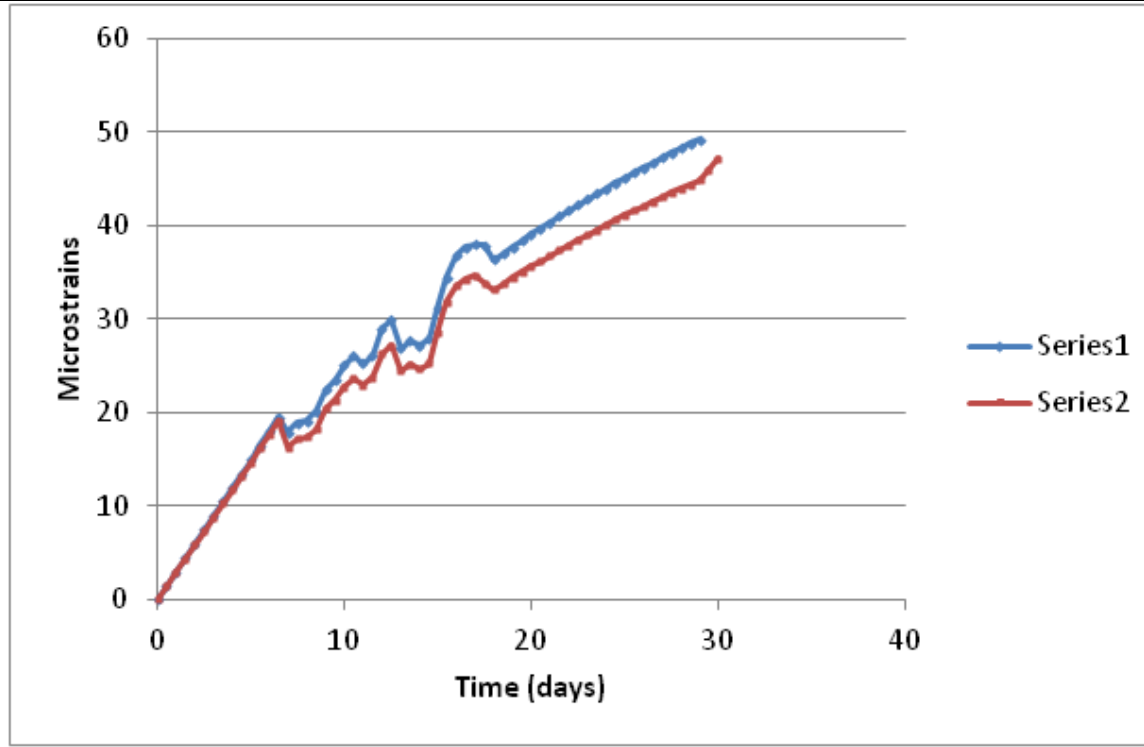
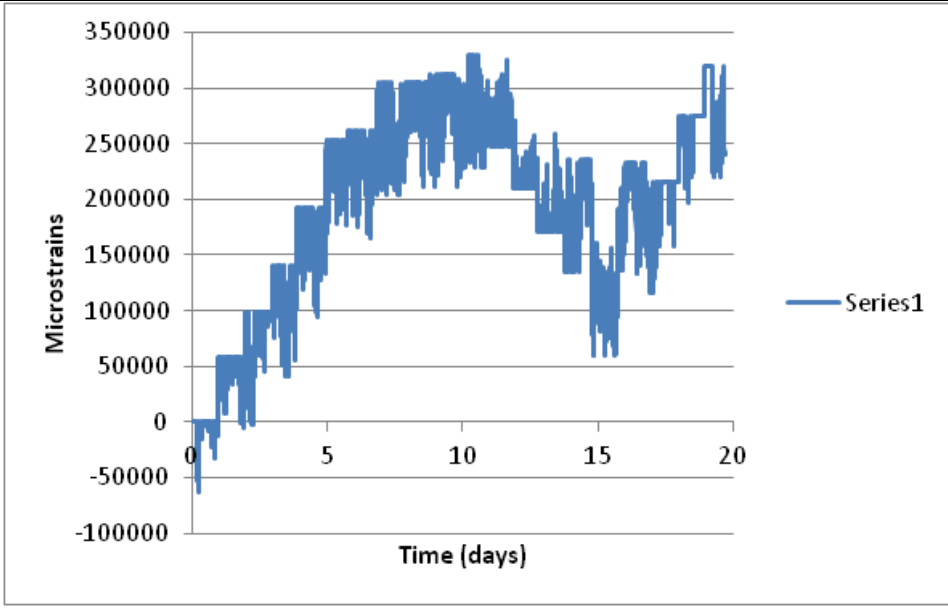
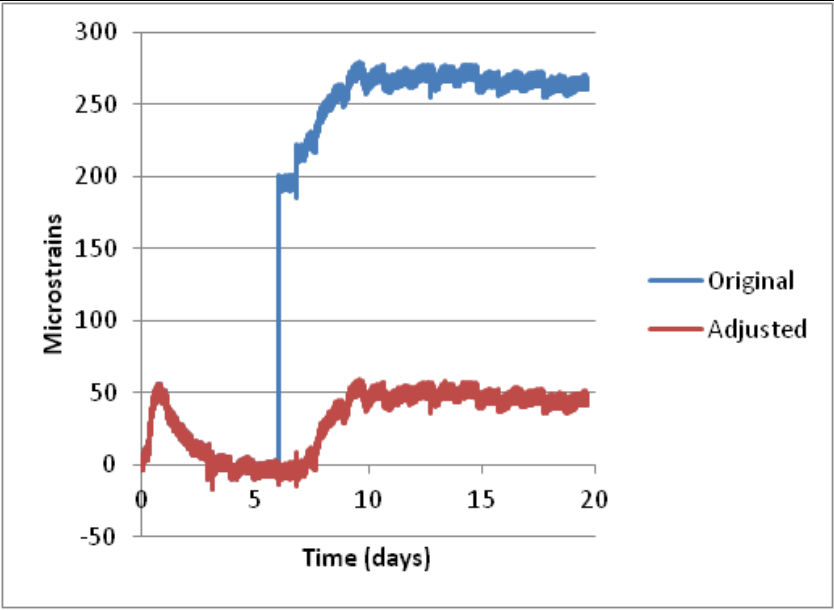
S-G1-Bf-O-1/2-L



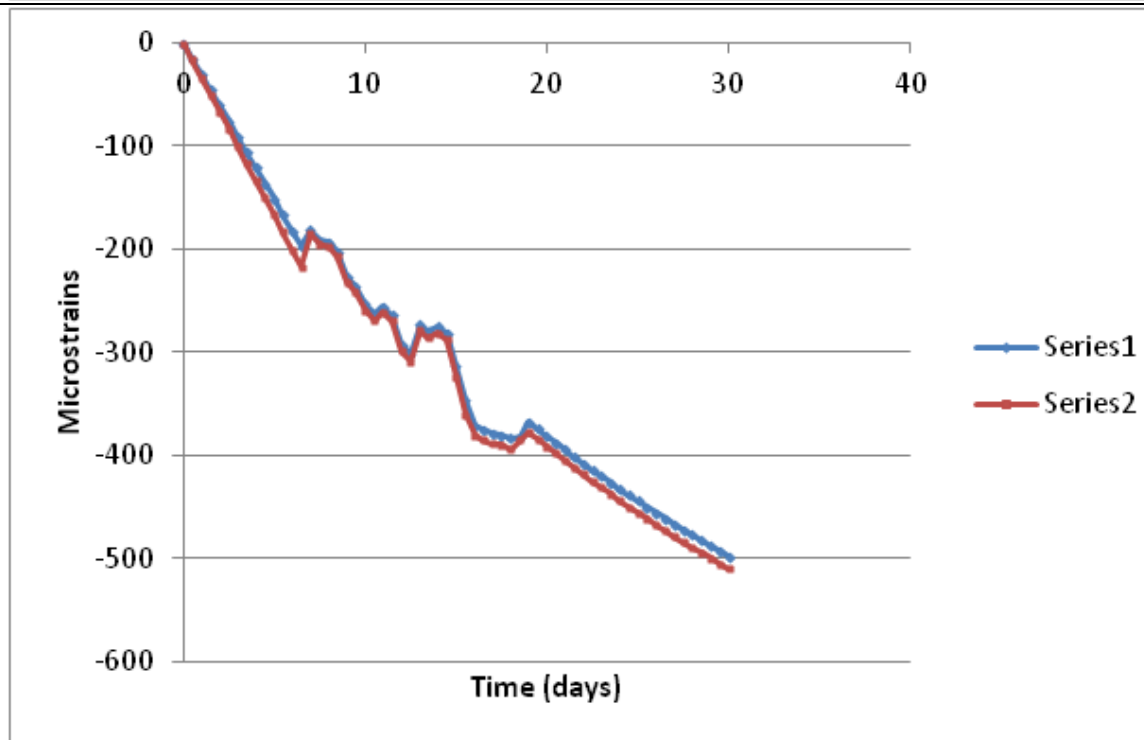
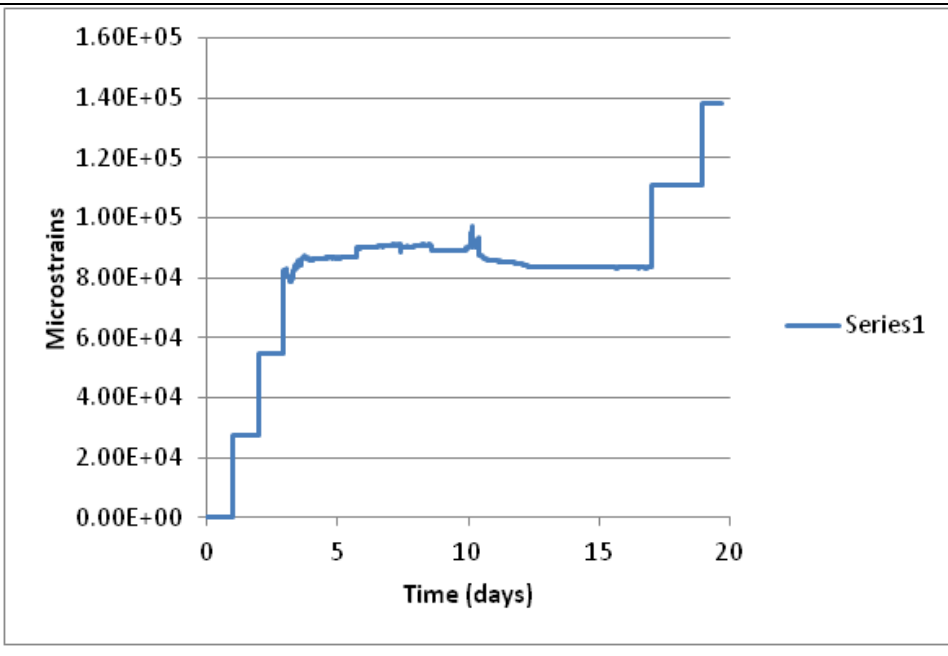
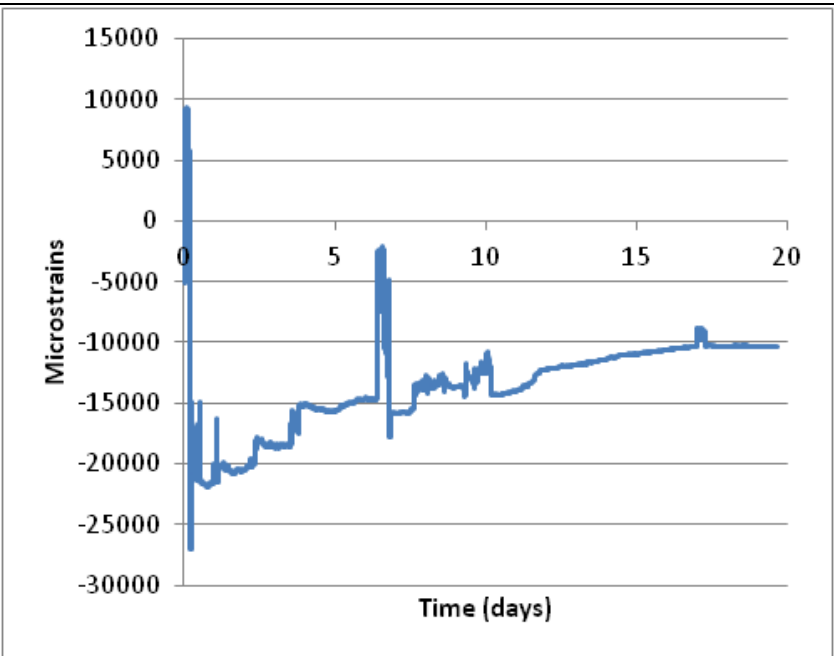
S-G2-Tf-M-1/2-L



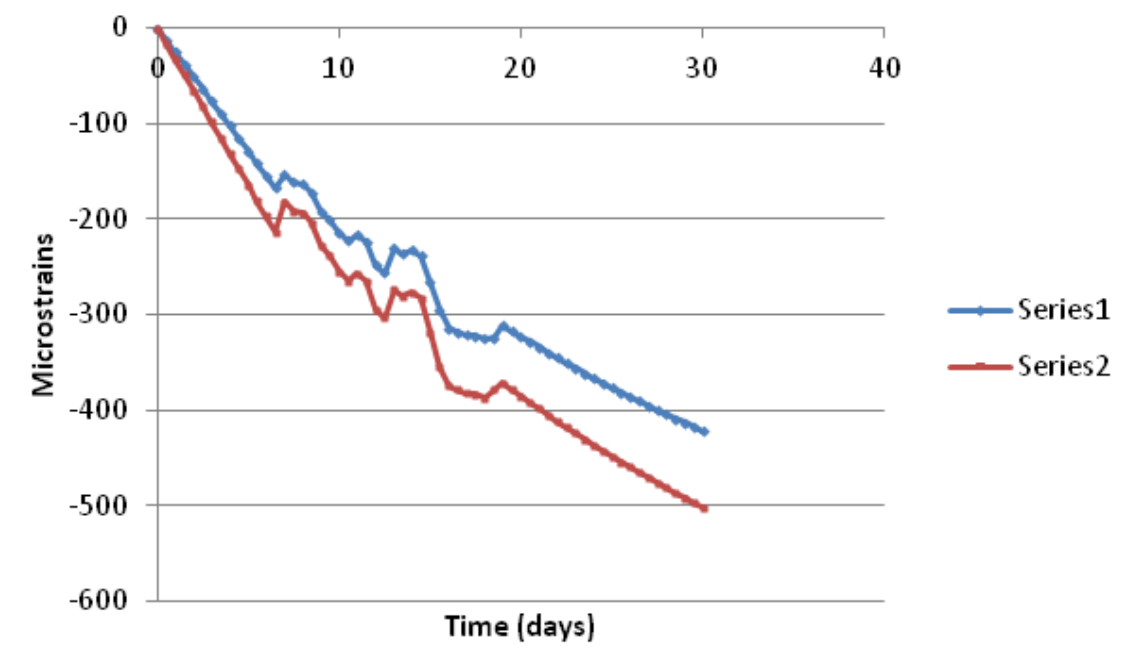
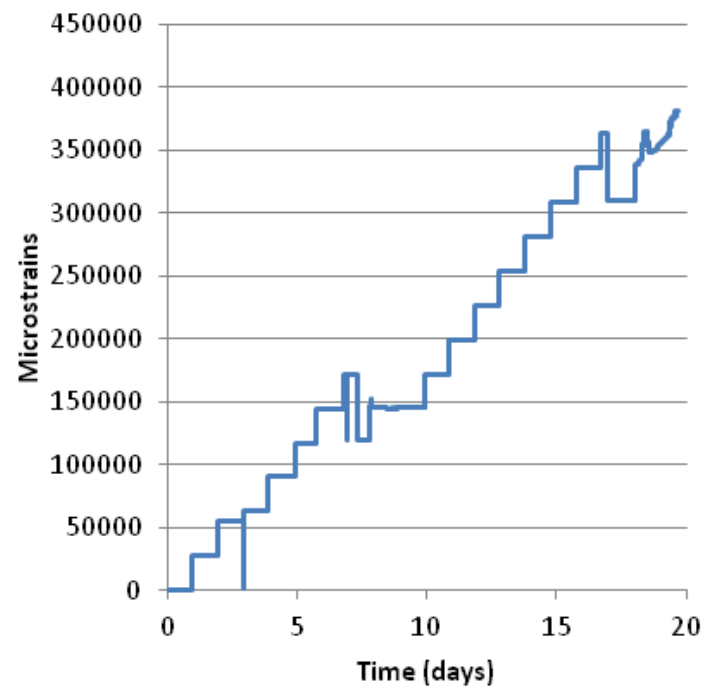
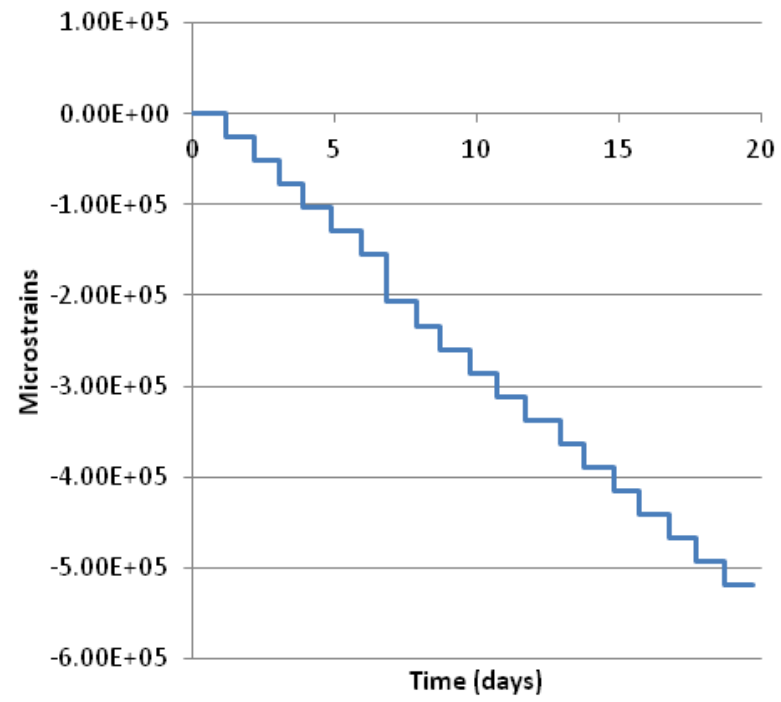
S-G2-Bf-M-1/2-L



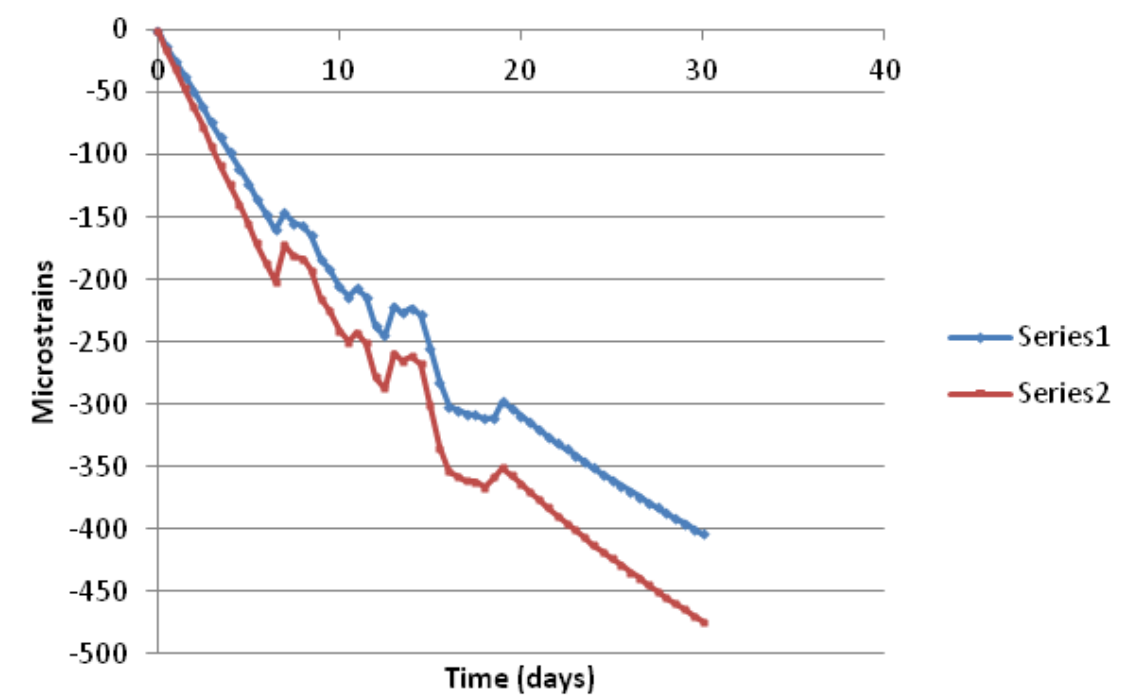
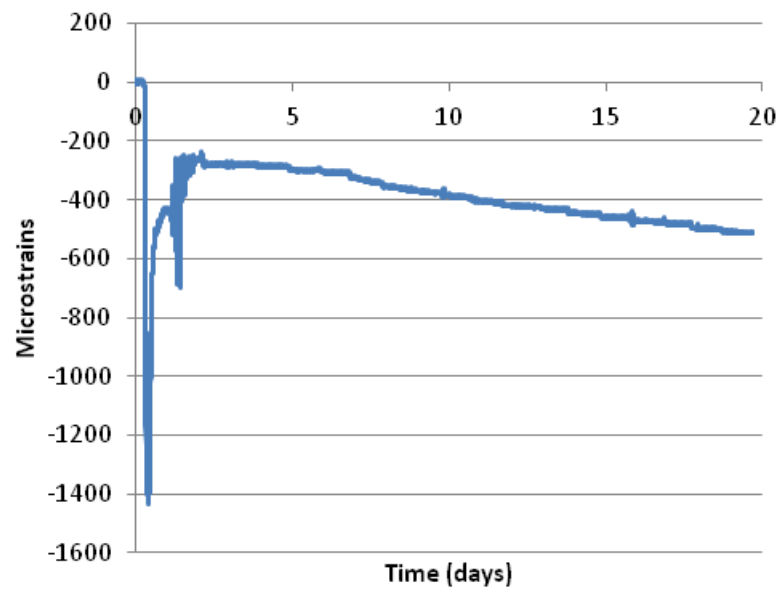
S-Tp-G1-1/2-L



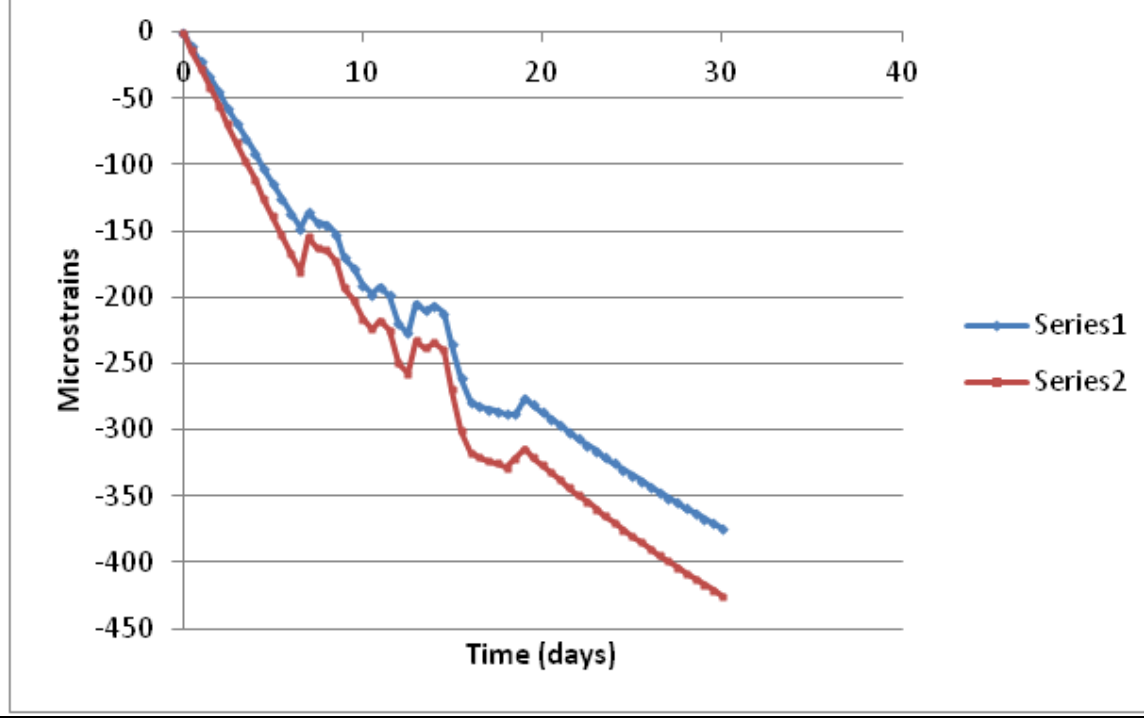
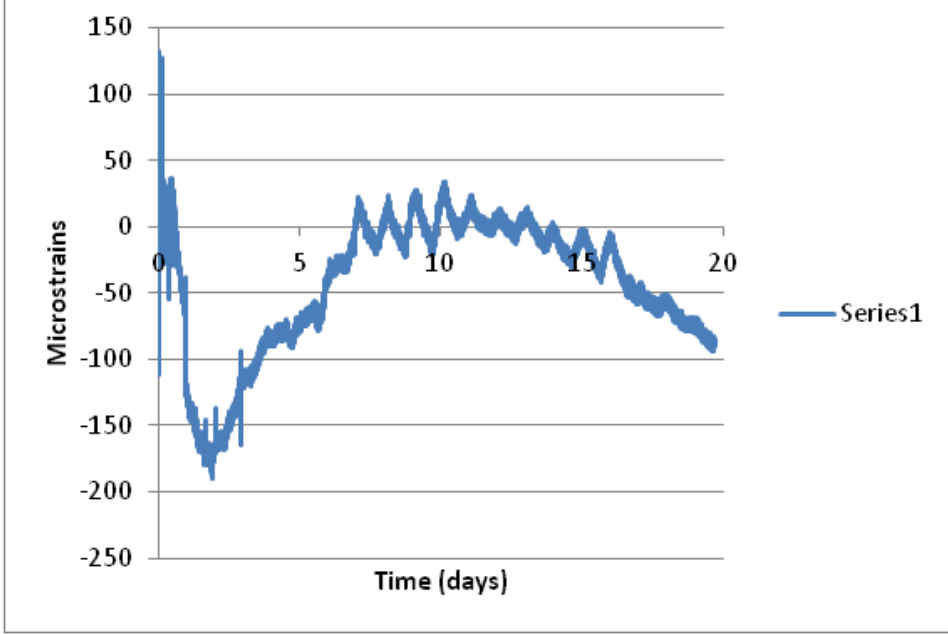
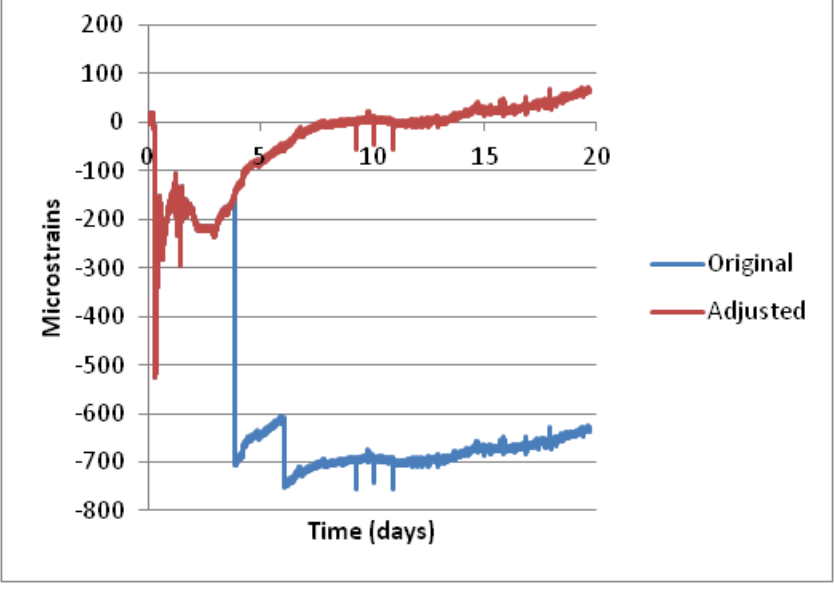
S-Tp-1/2-1/2-T



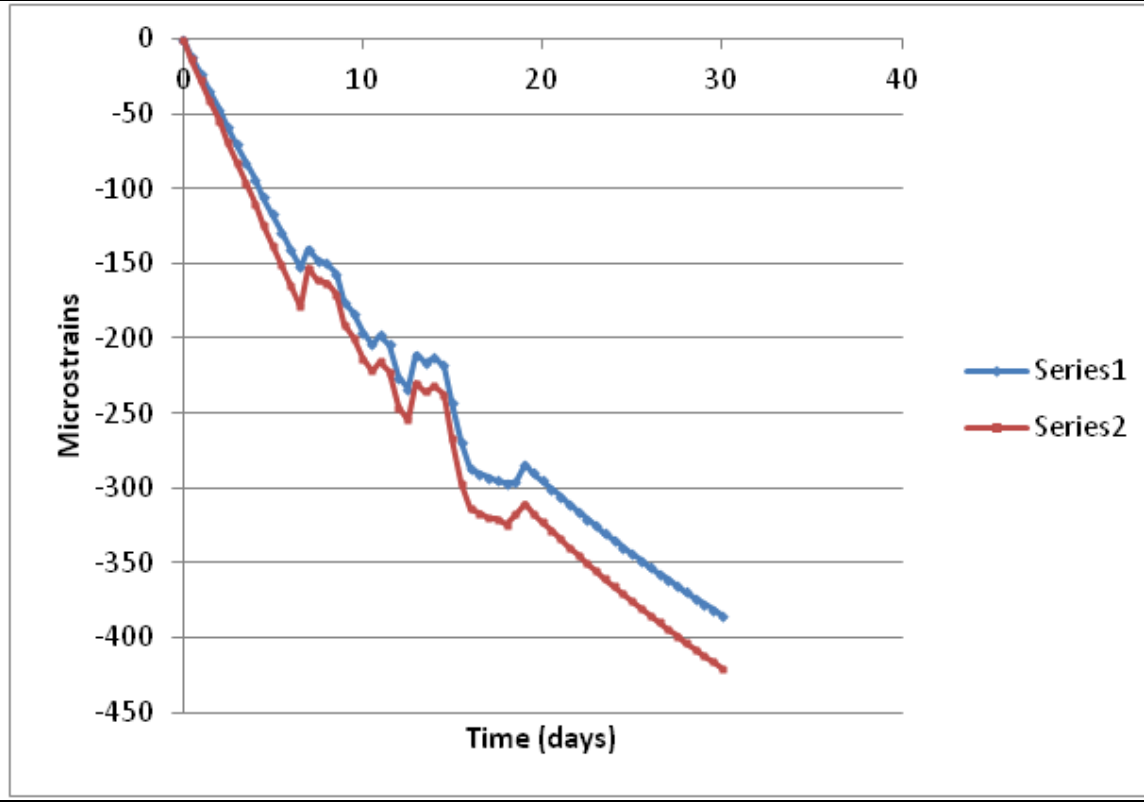
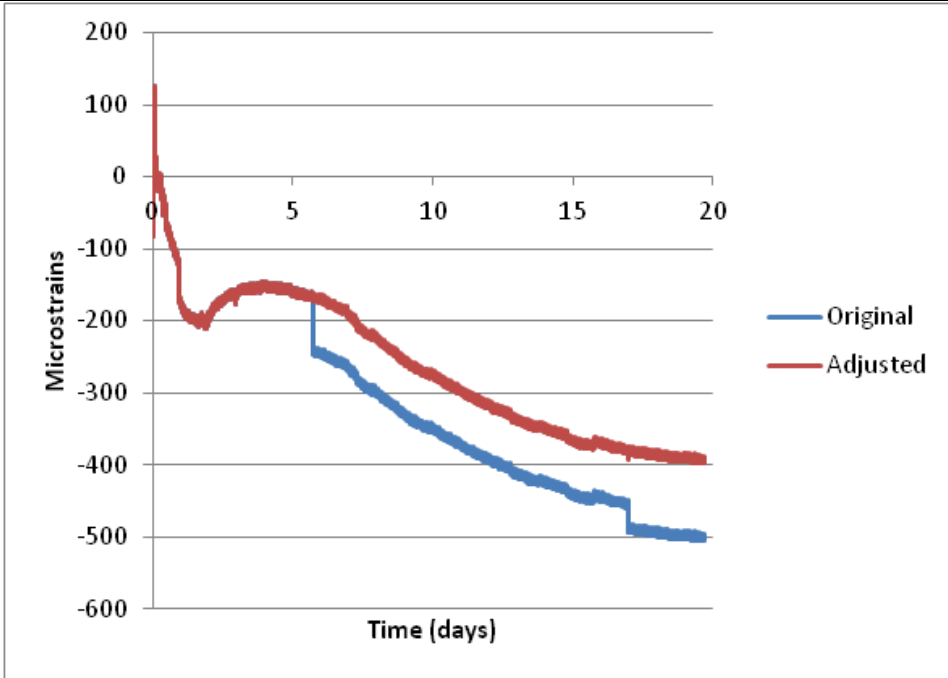
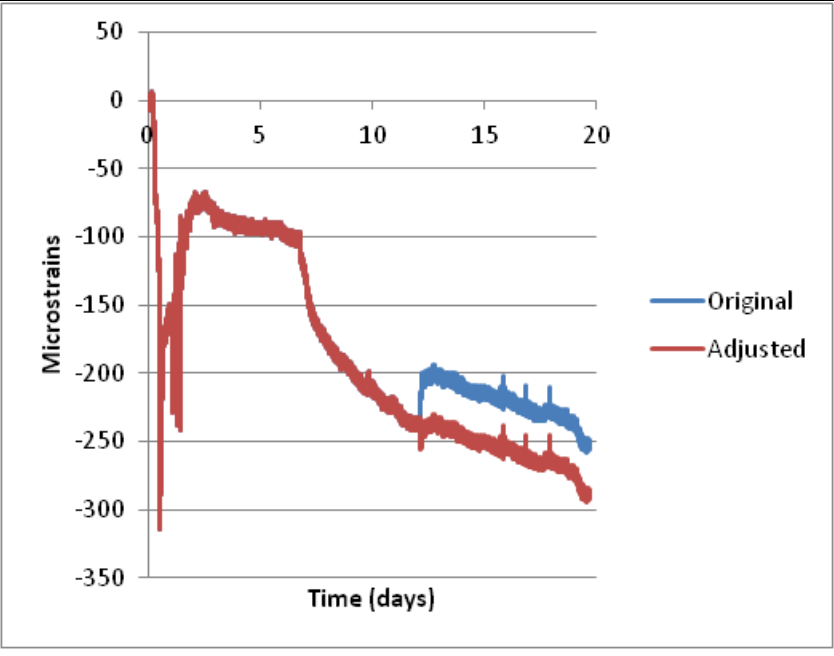
S-Tp-1/2-1/4-T



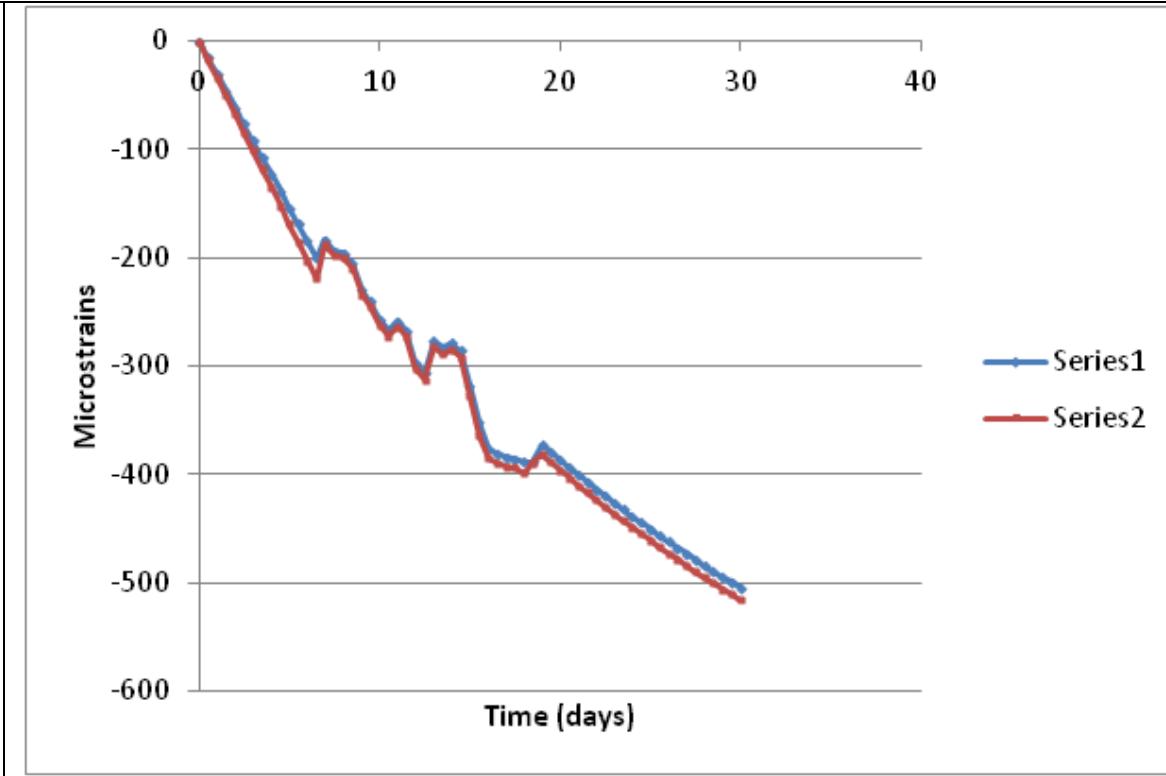
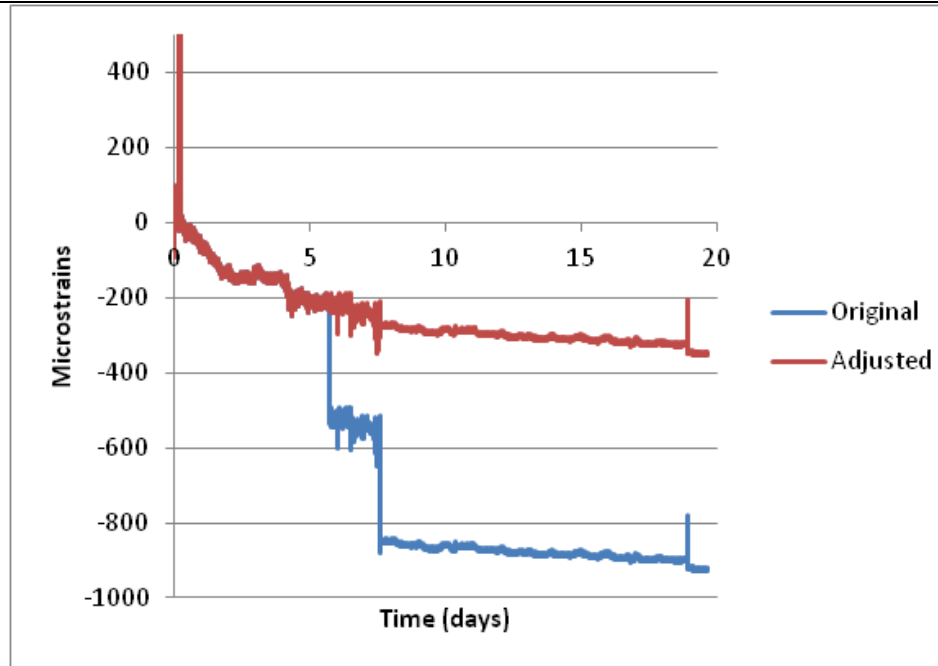
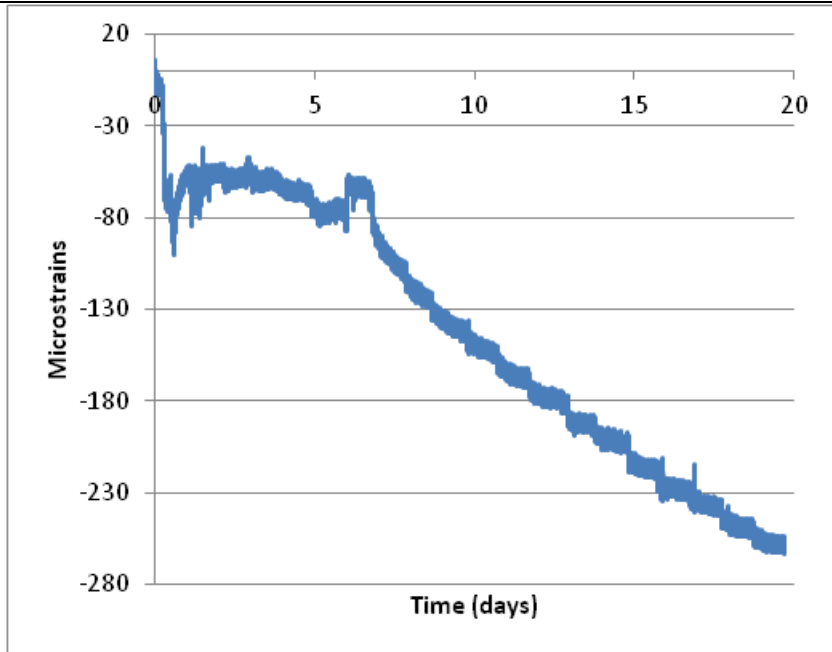
S-Tp-1/2-3/4-L



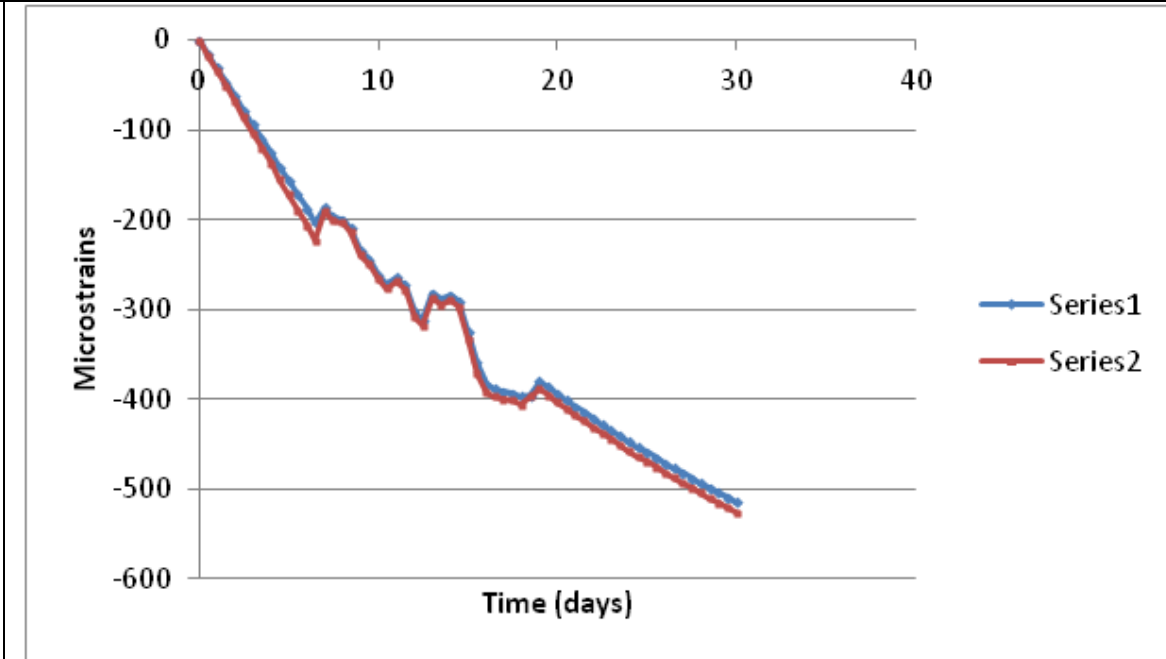
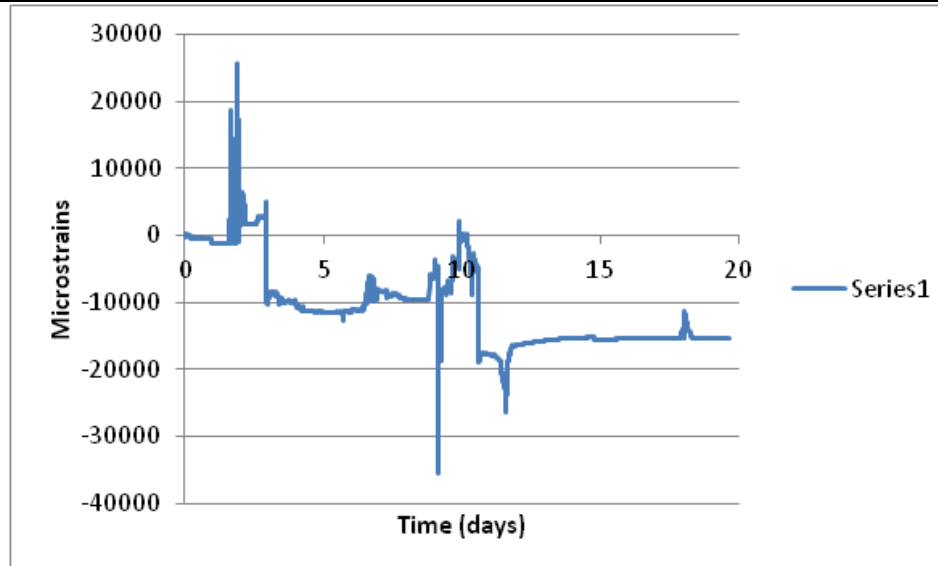
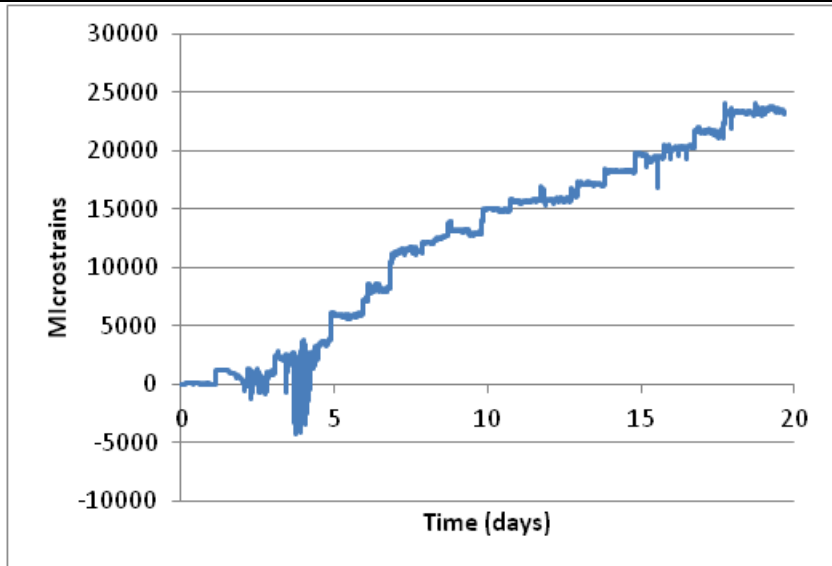
S-Tp-1/2-1/2-L



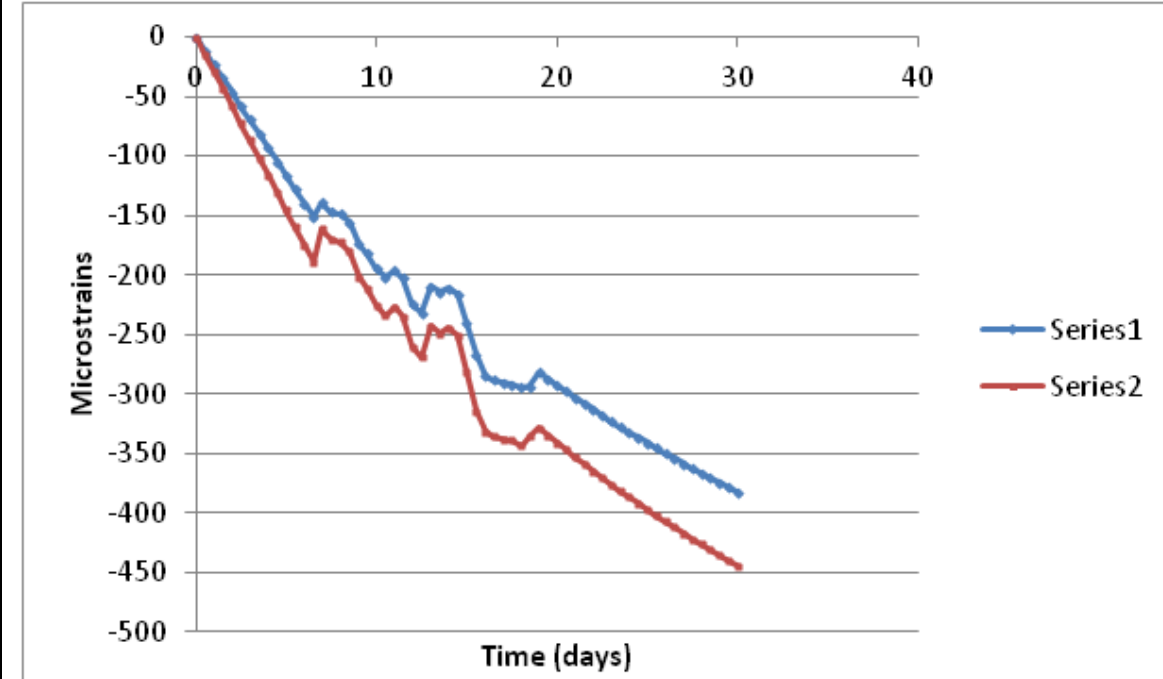
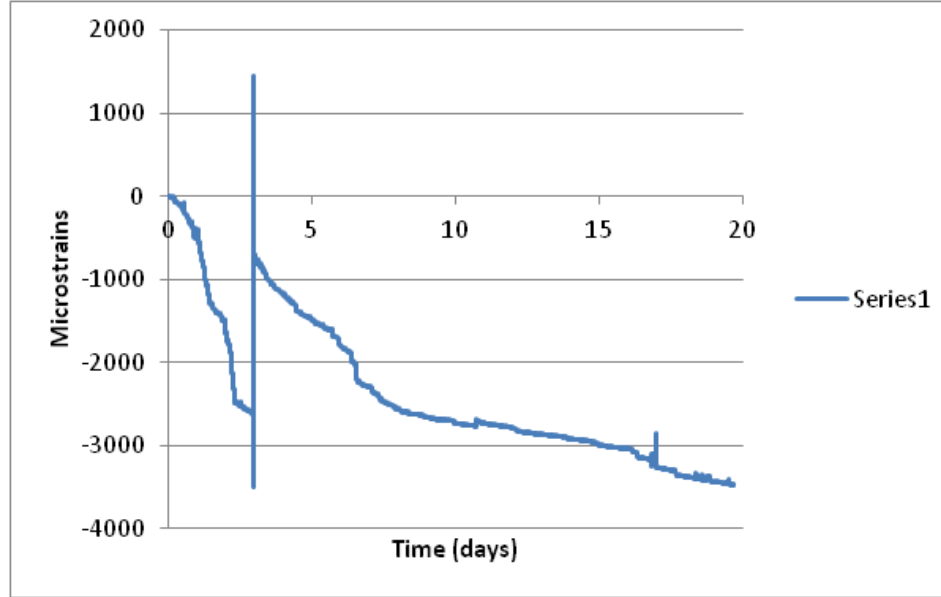
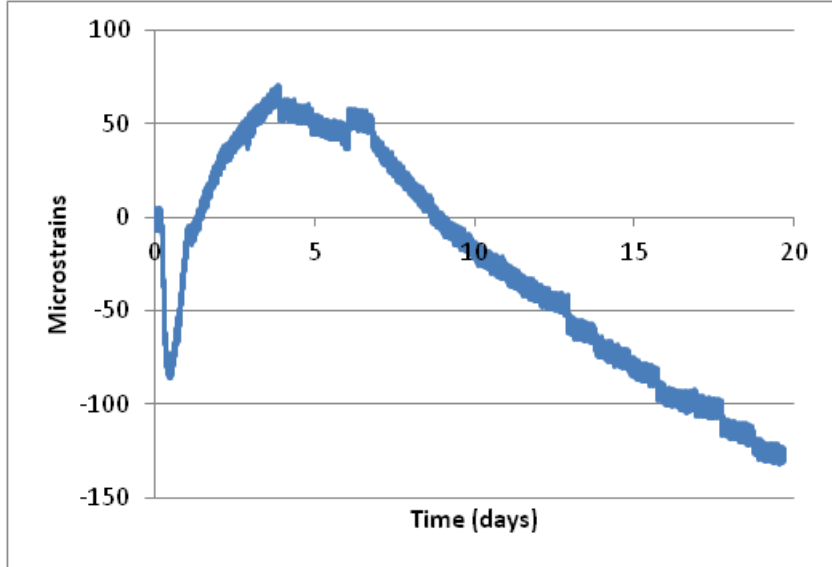
S-Tp-G2-1/2-L



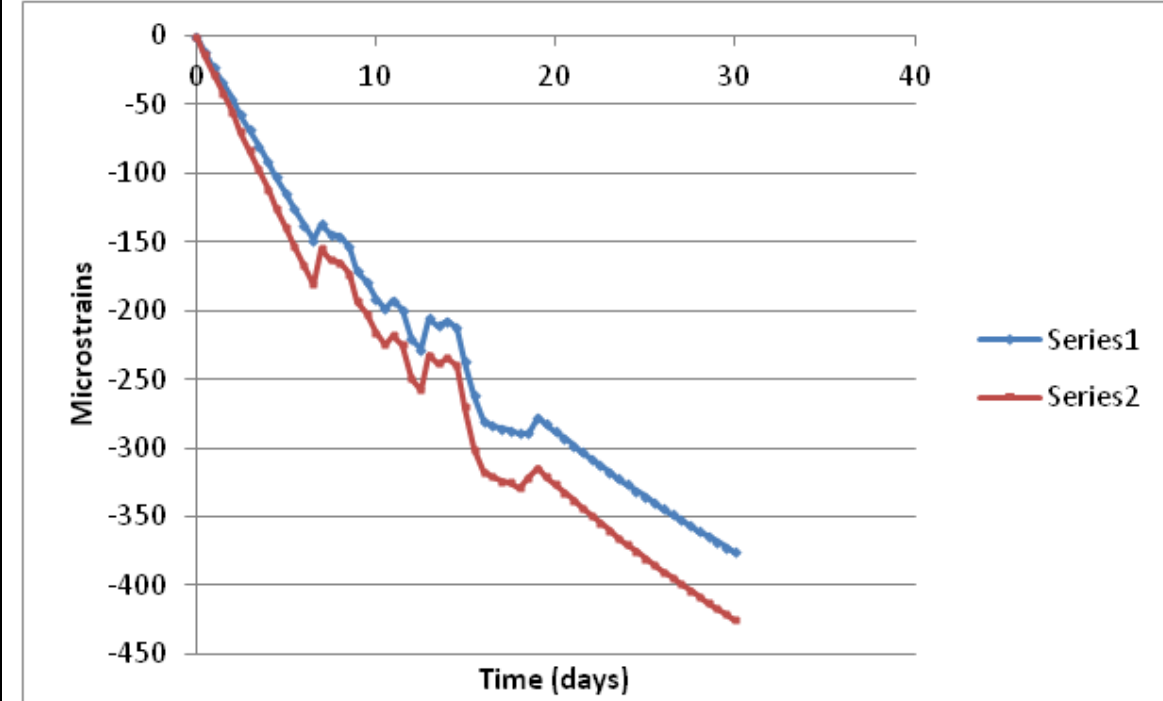
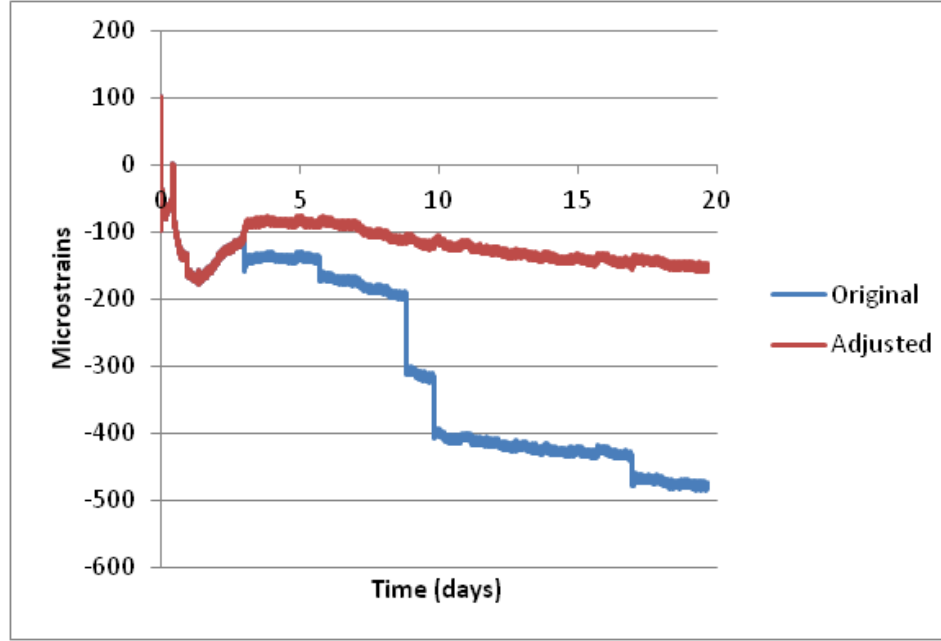
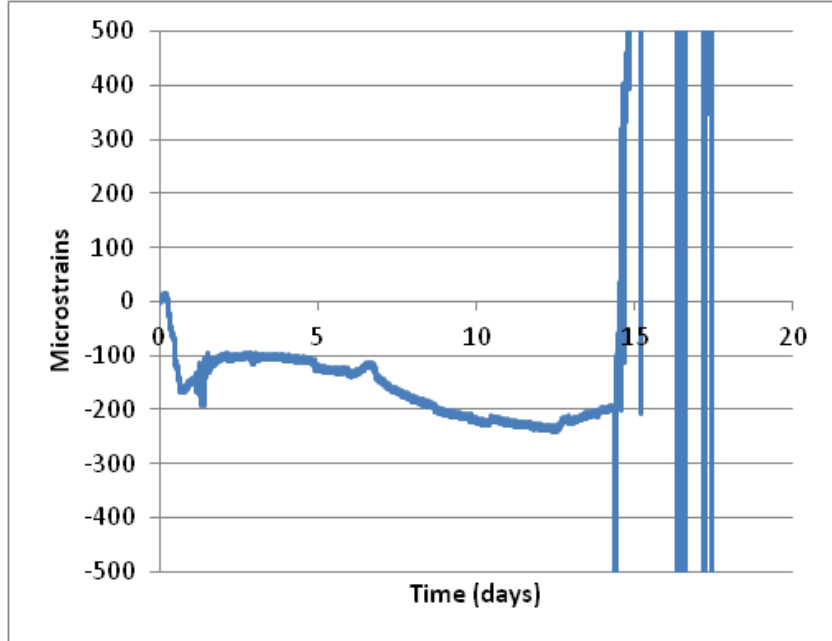
S-Tp-G1-3/4-L



S-Tp-1/3-3/4-L

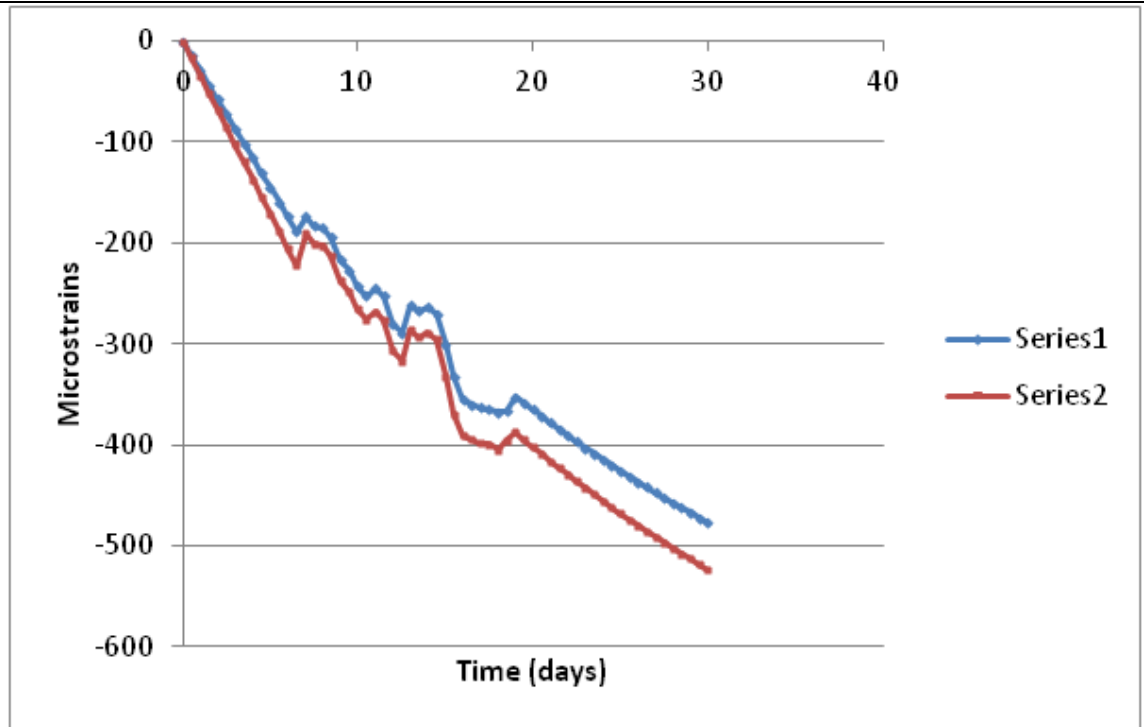
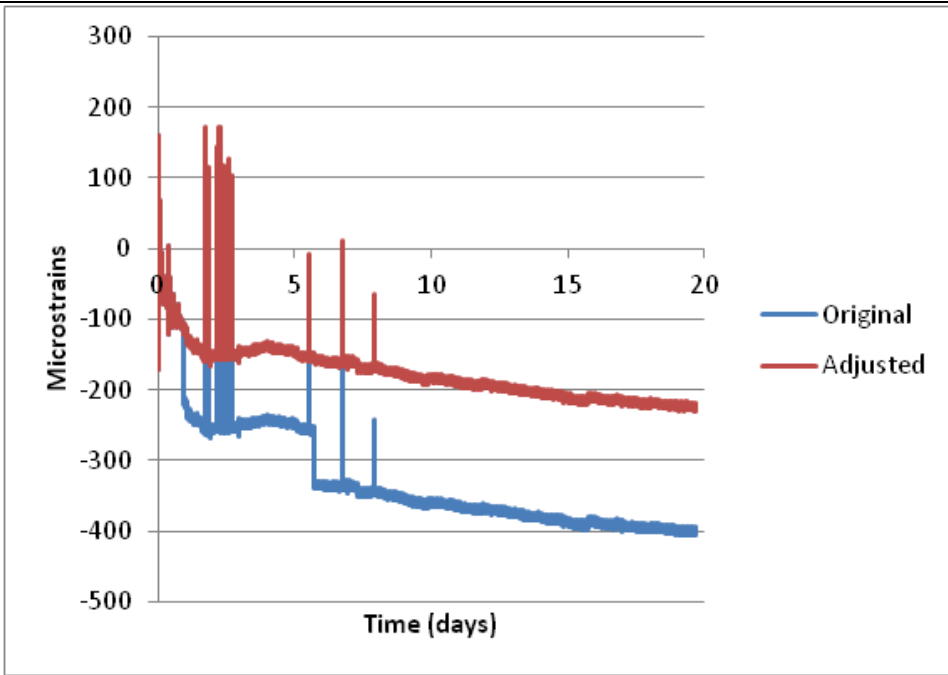
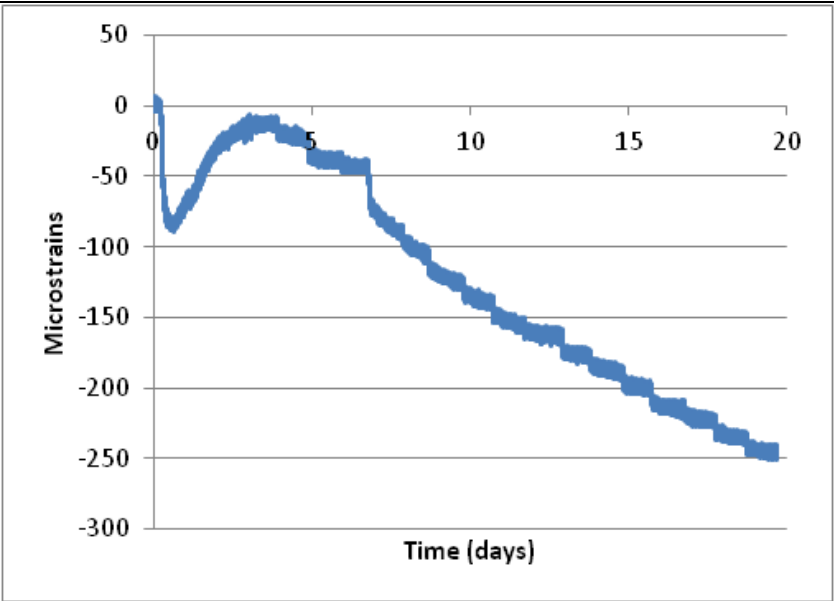


S-Tp-1/2-1/4-L

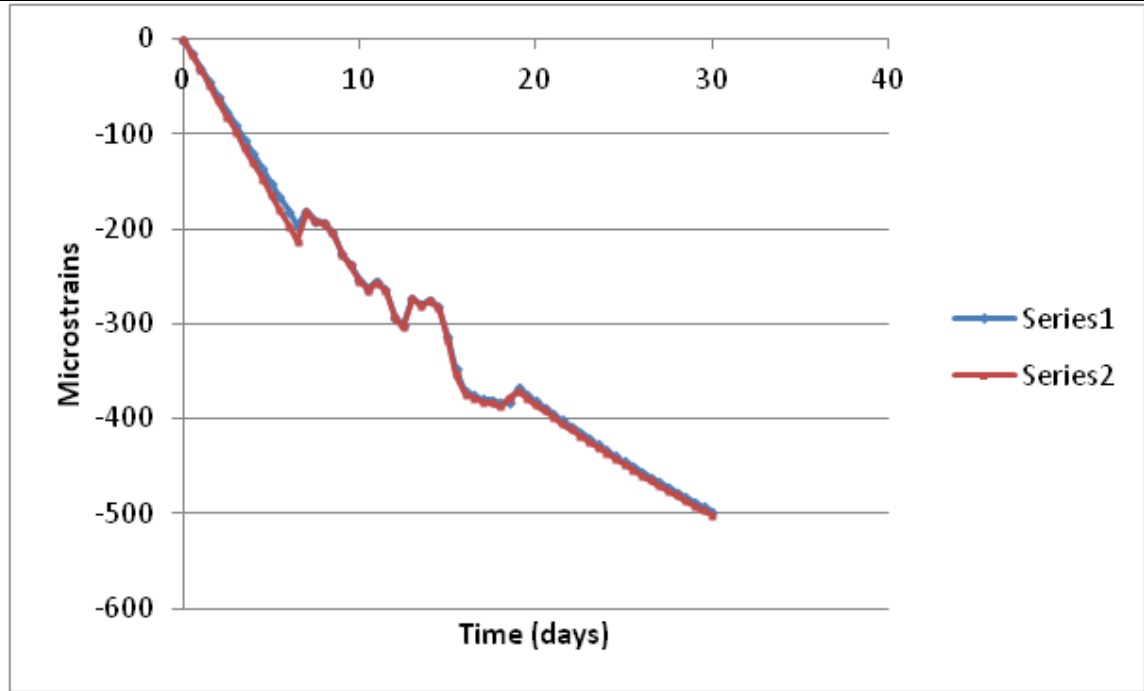
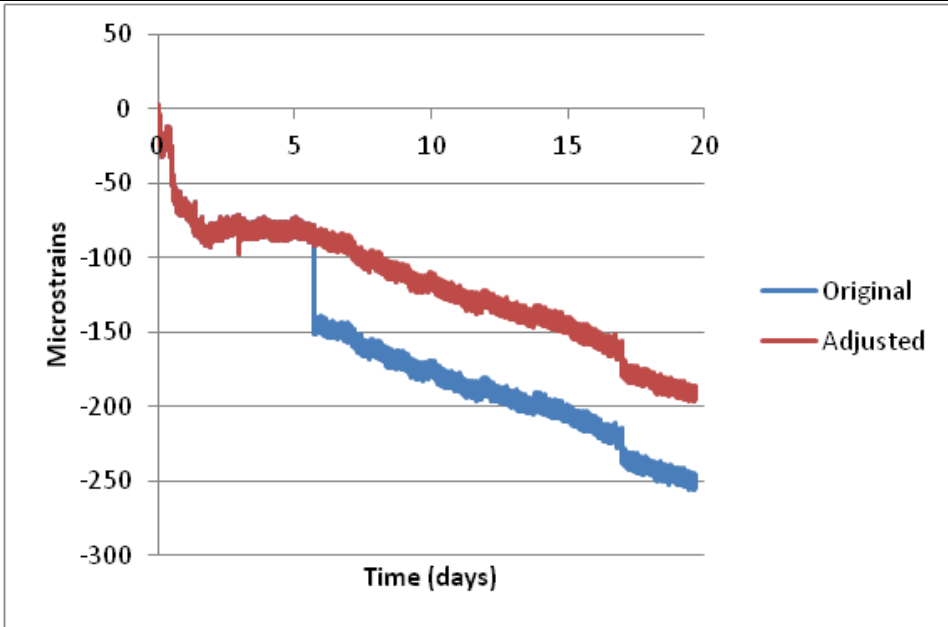
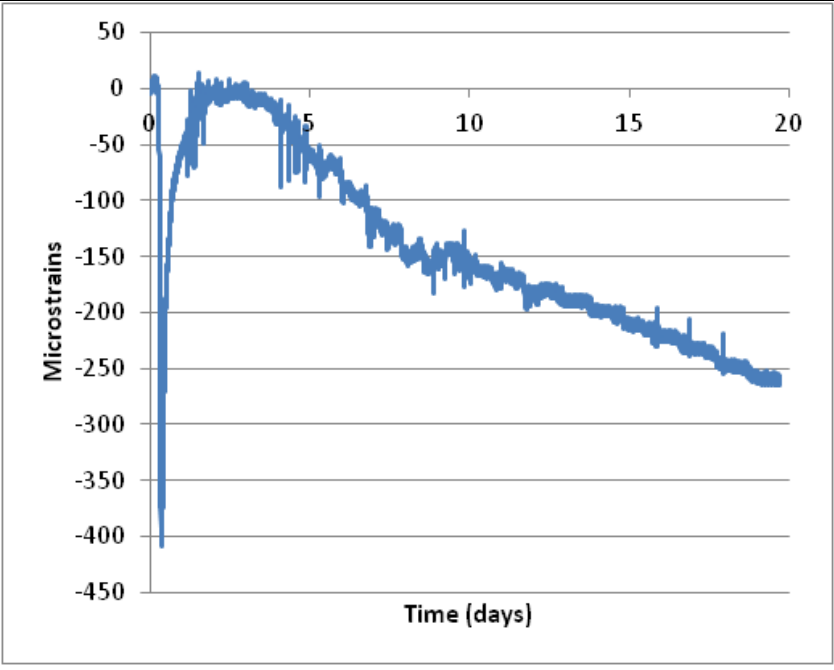




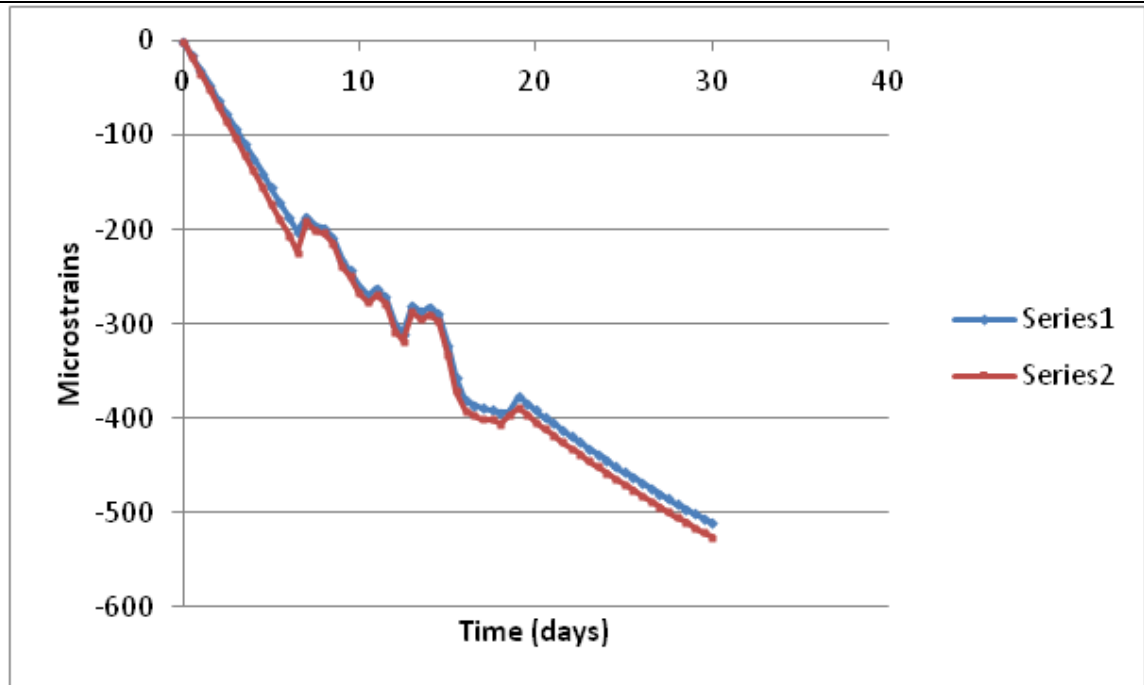
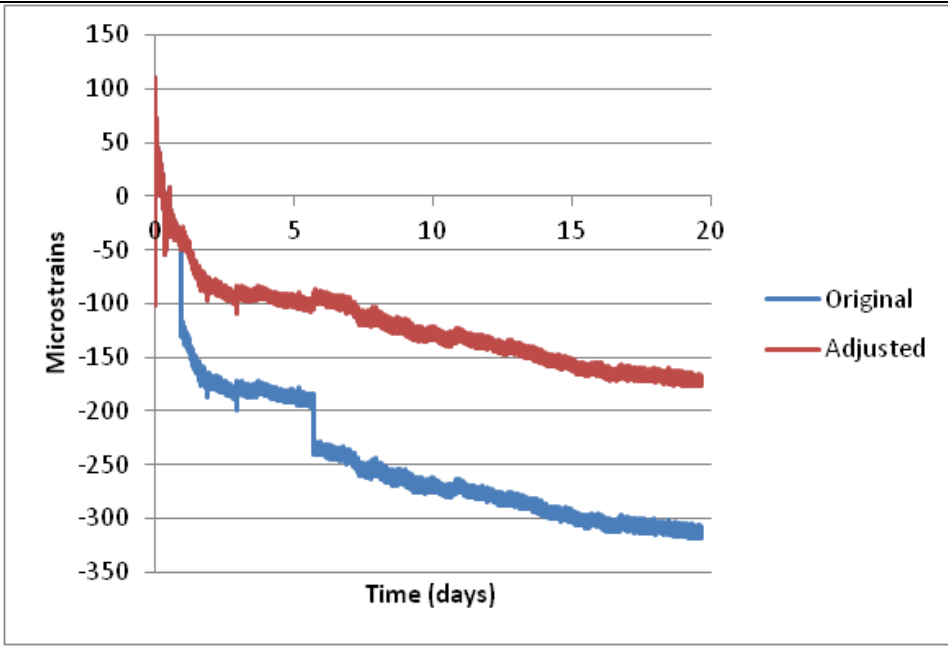
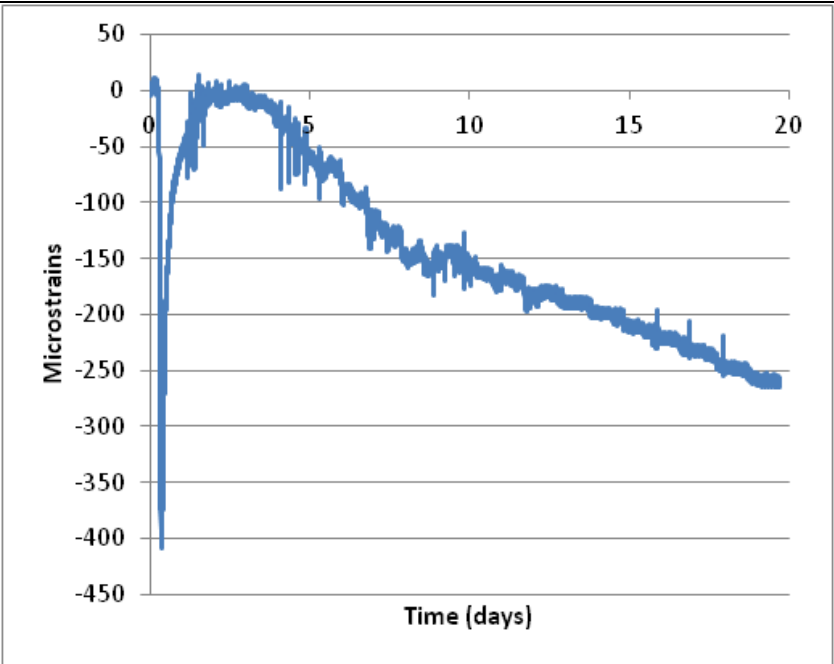
S-Tp-G1-1/4-T



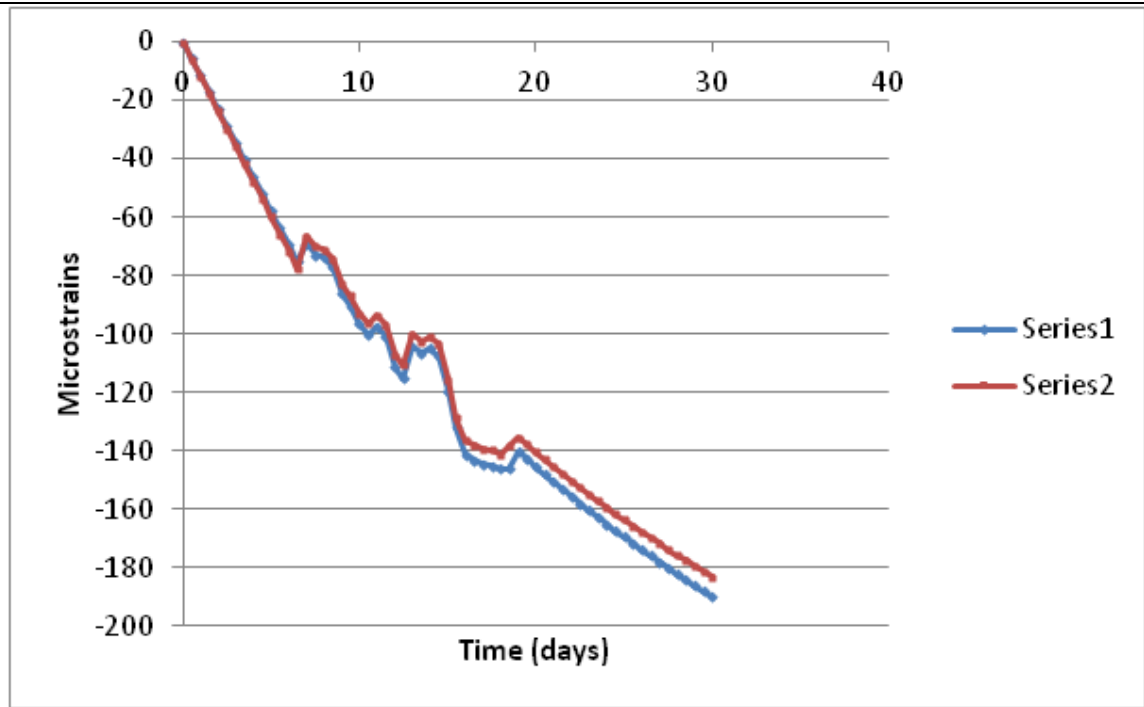
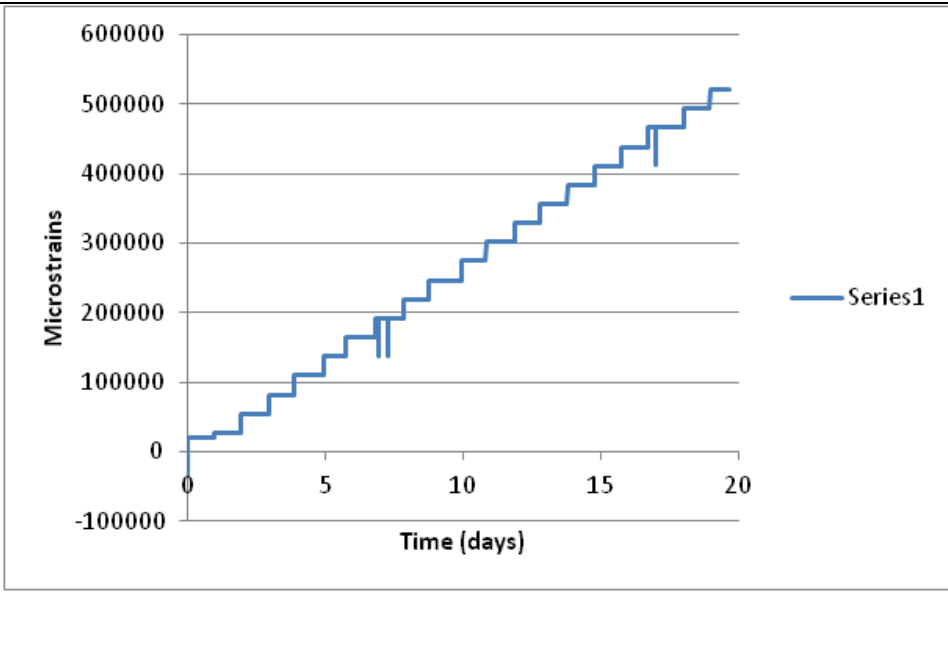
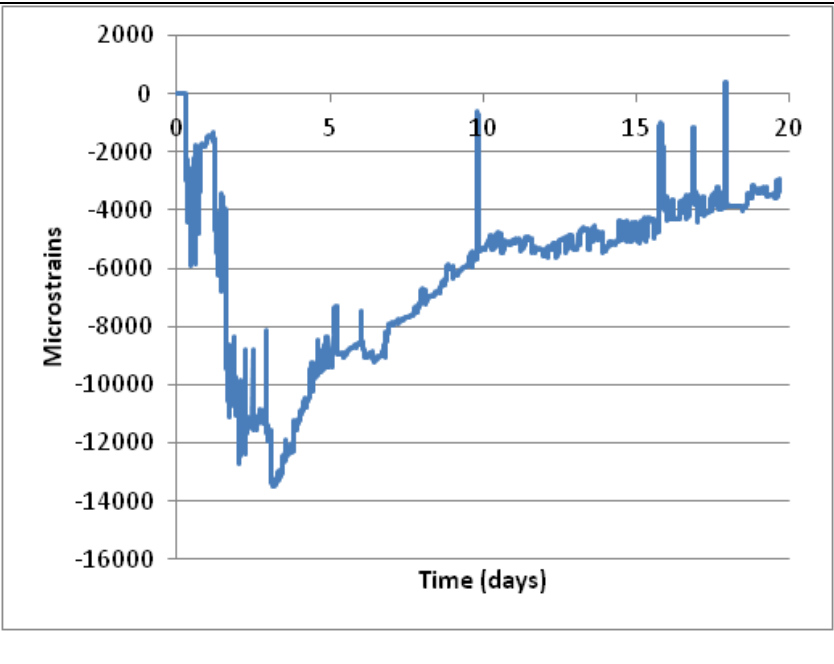
S-Tp-G1-1/2-T



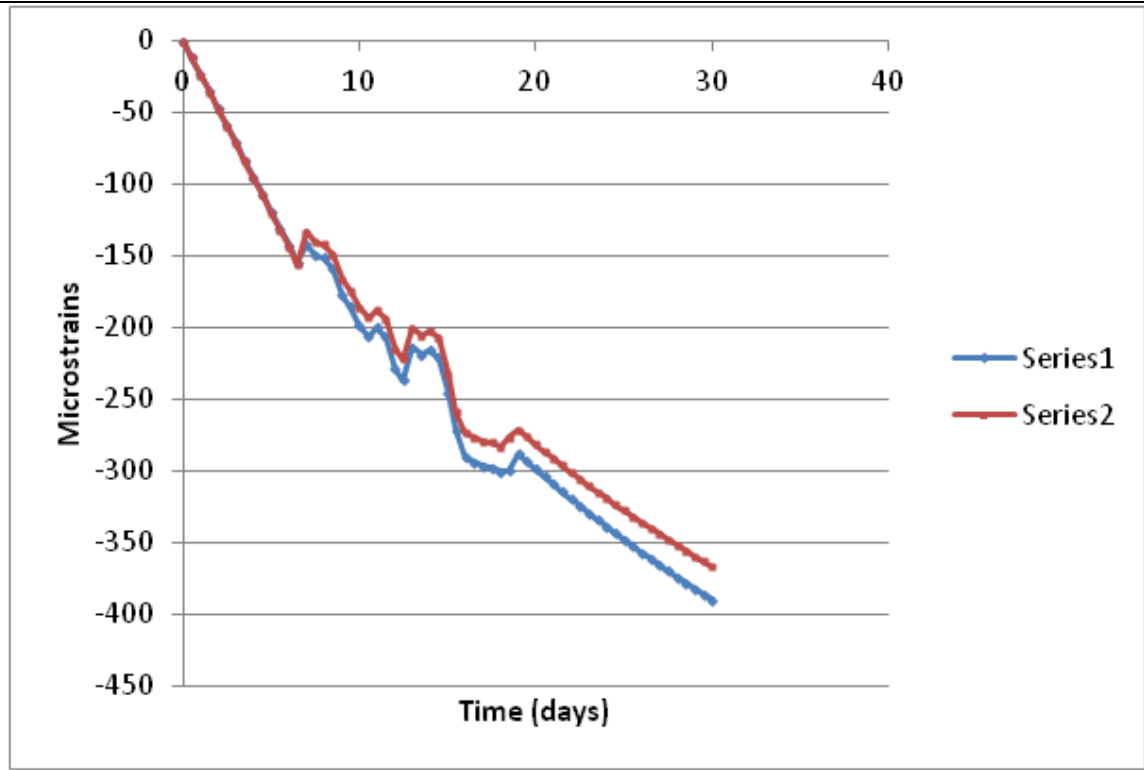
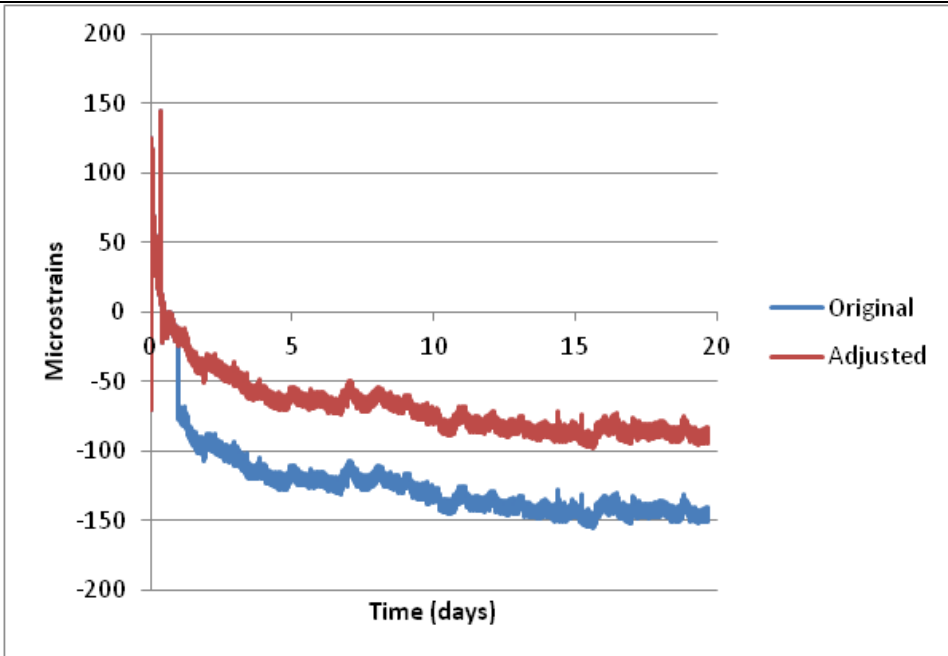
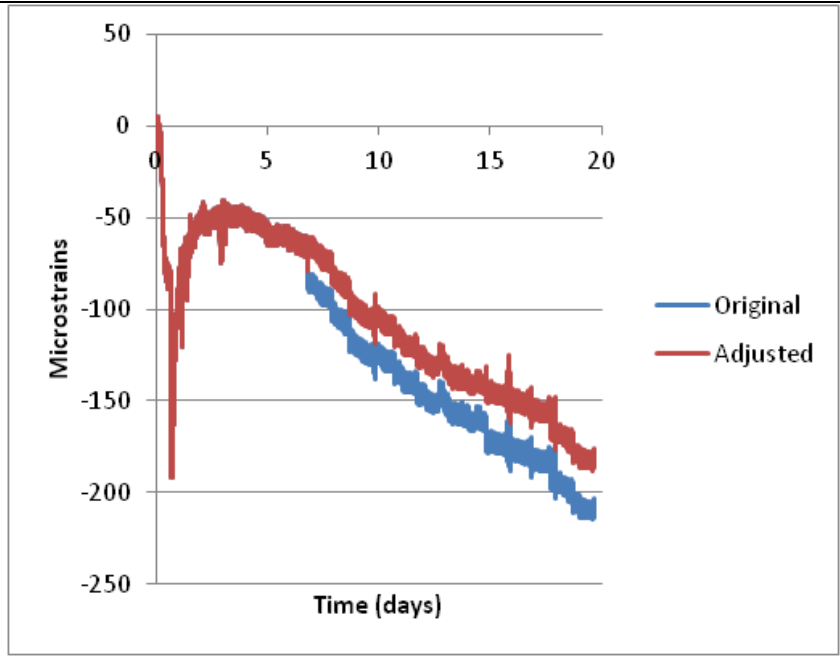
S-Tp-G1-1/4-L



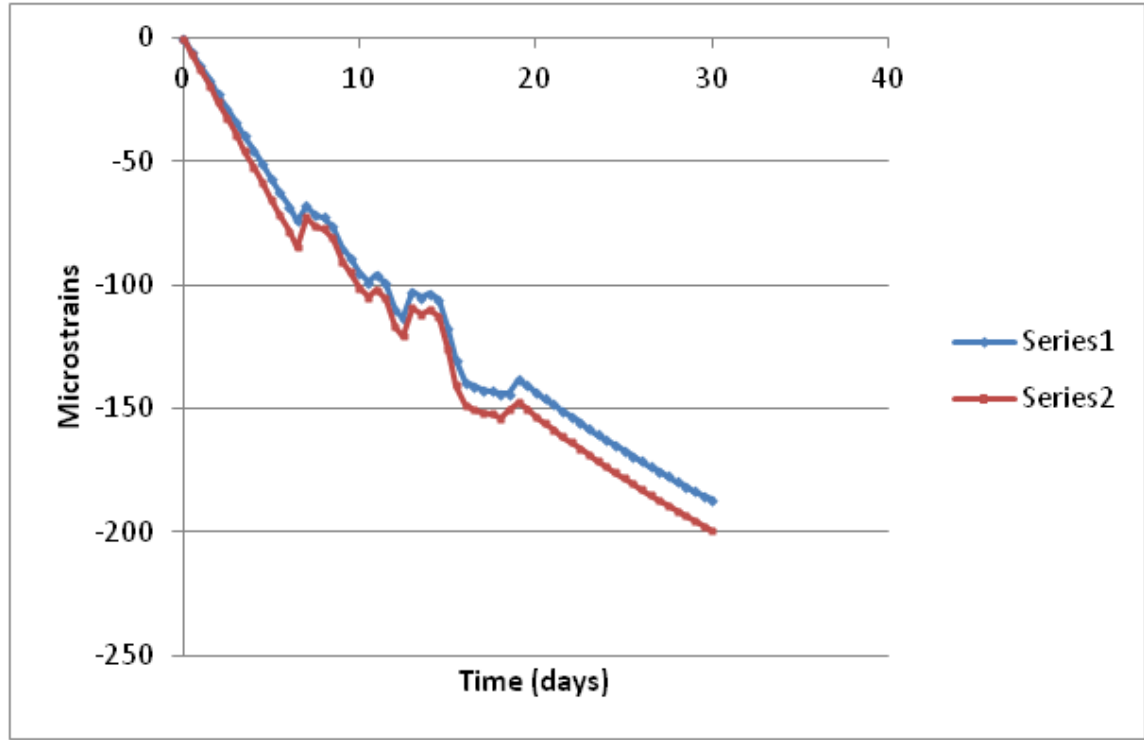
S-Bt-1/2-1/2-T



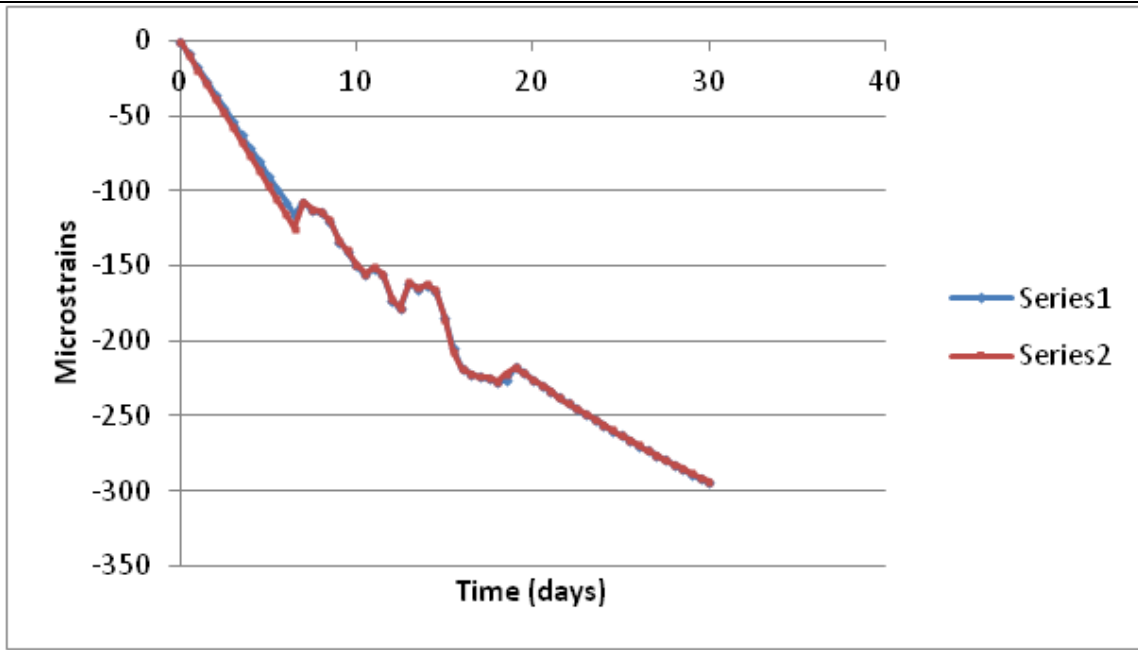
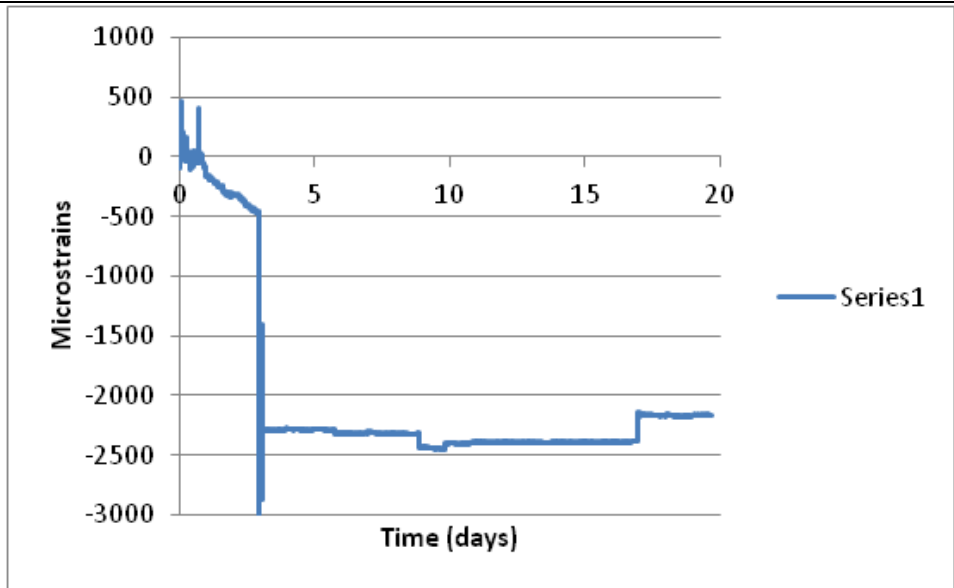
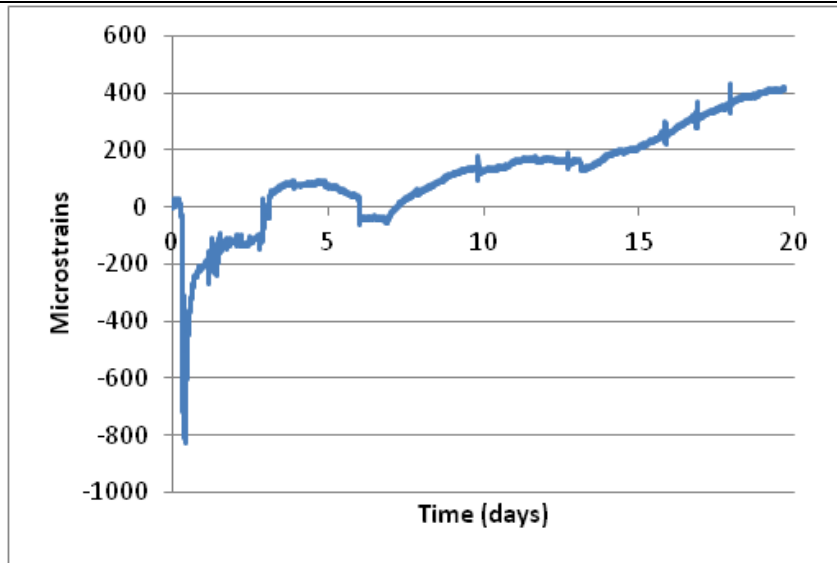
S-Bt-G2-1/2-L



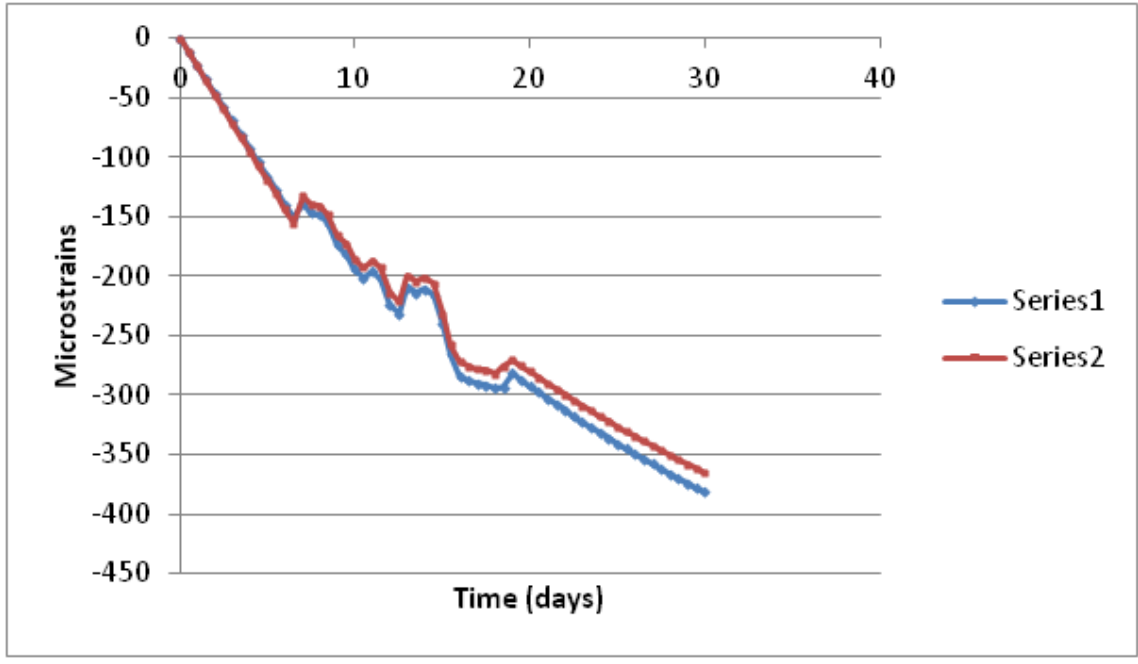
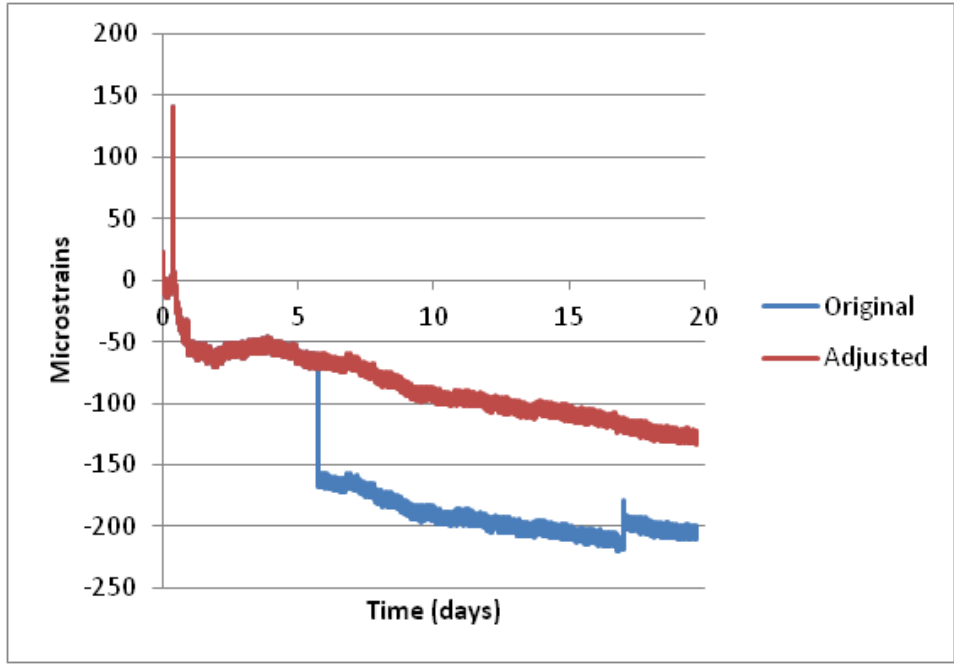
S-Bt-1/2-3/4-L



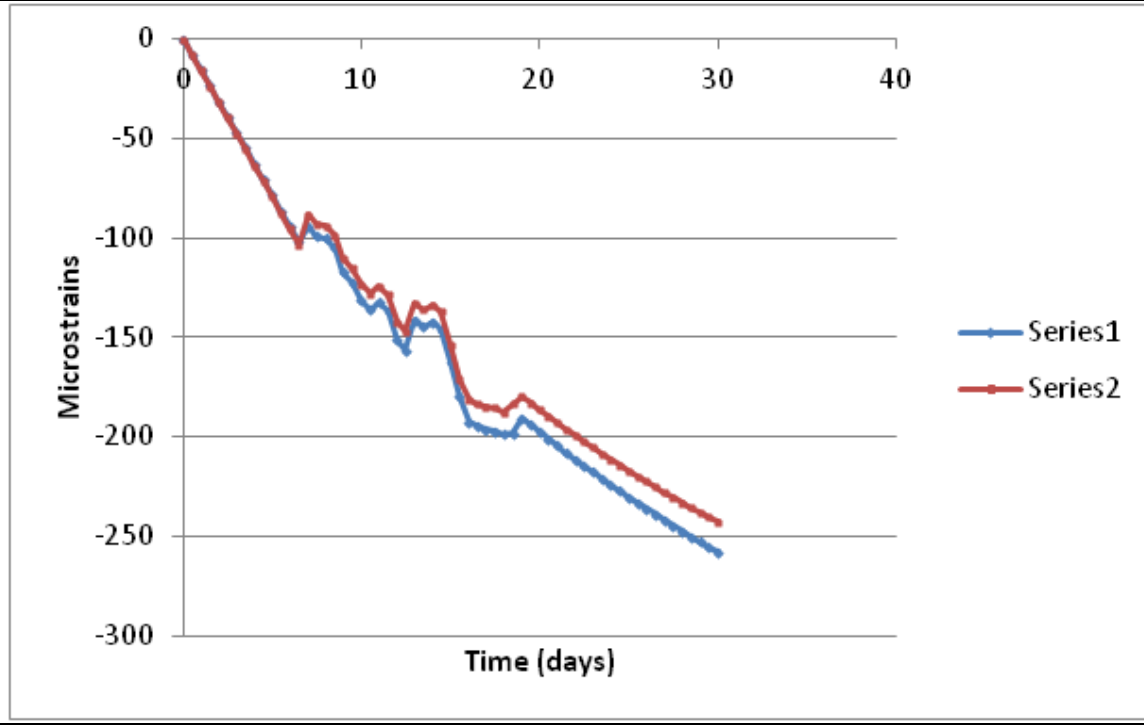
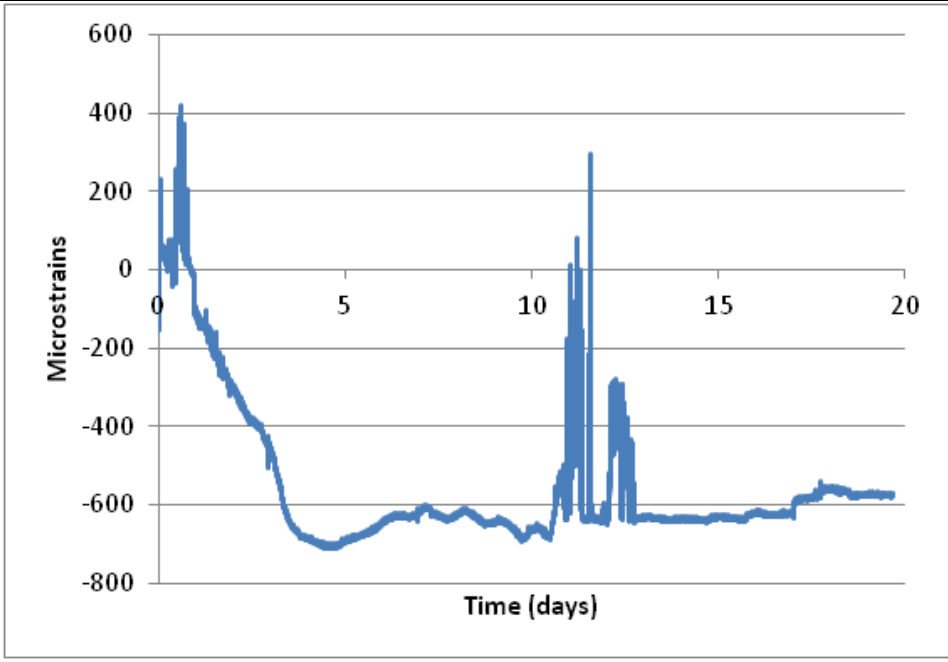
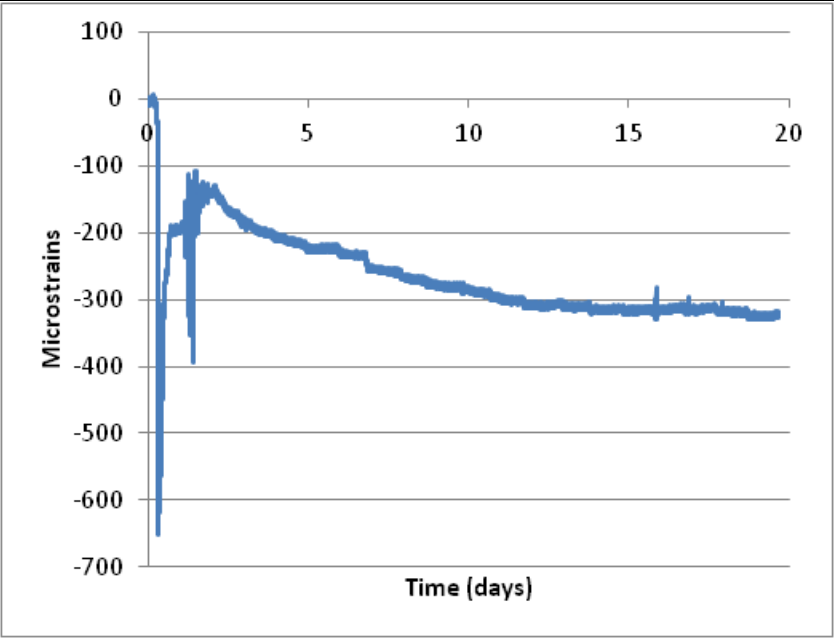
S-Bt-G1-1/4-T



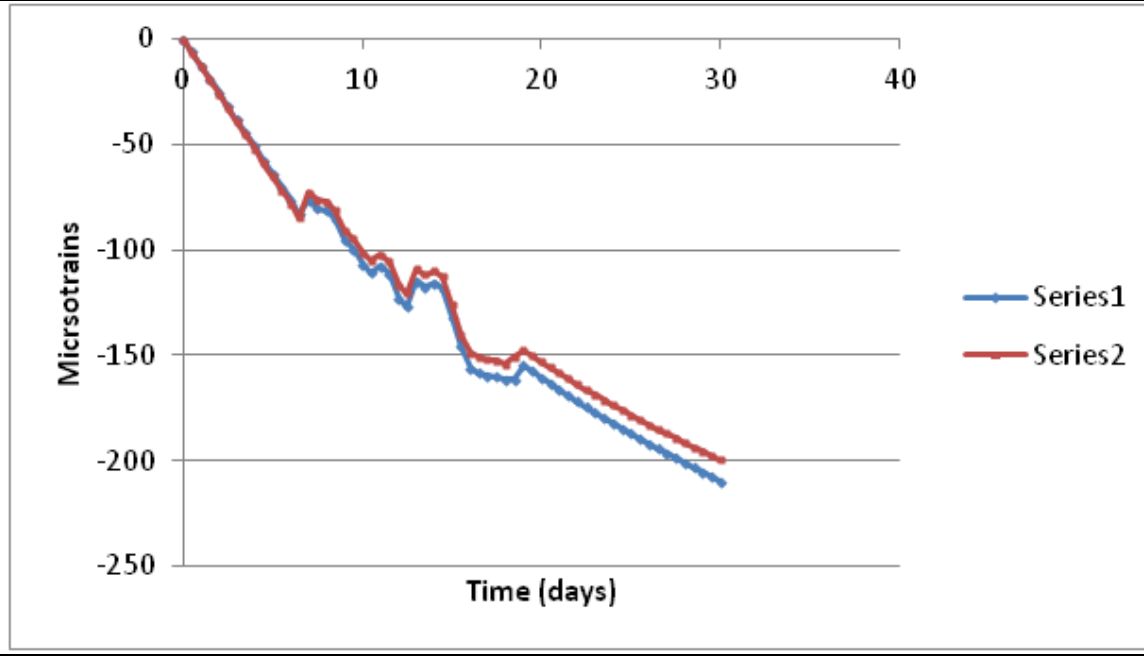
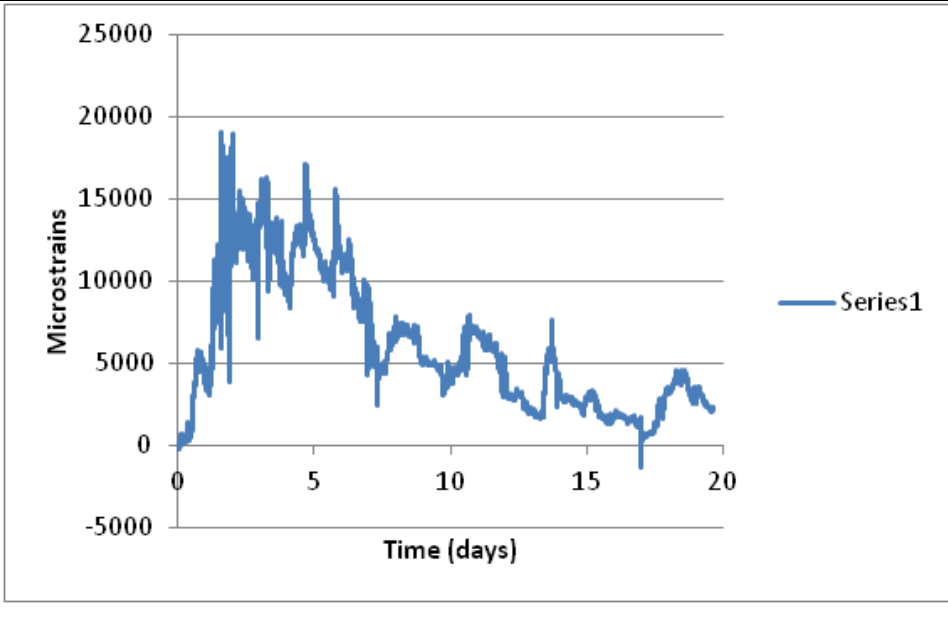
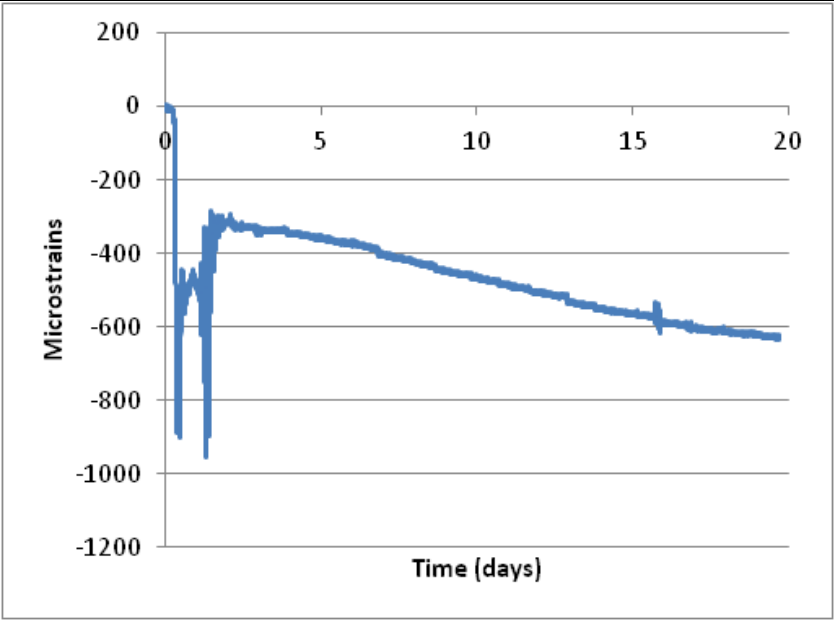
S-Bt-G1-1/4-L



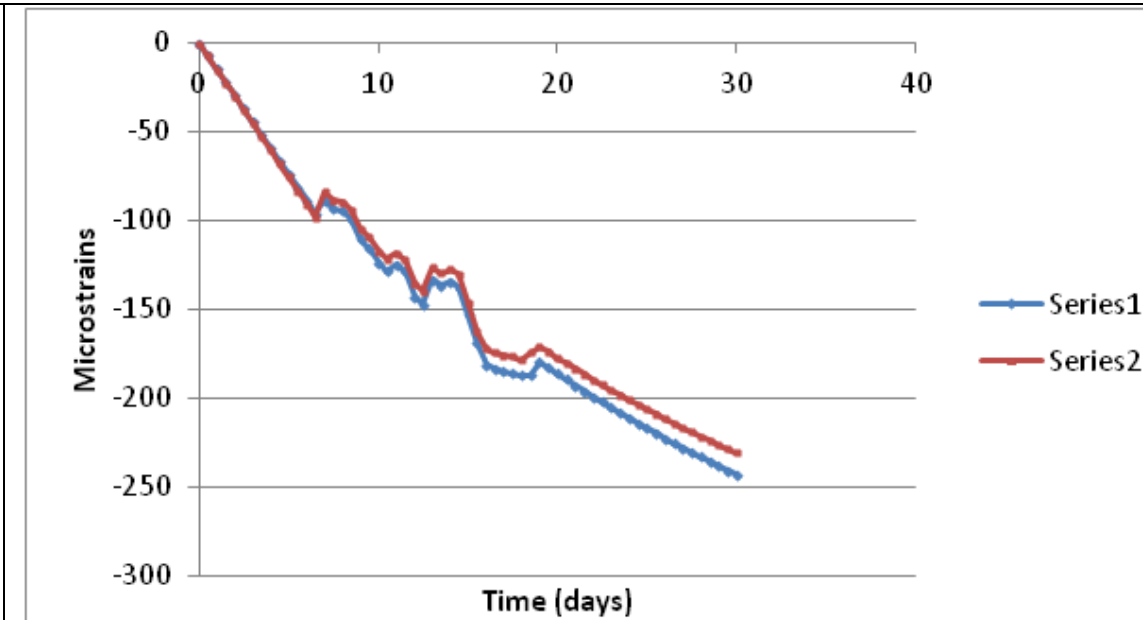
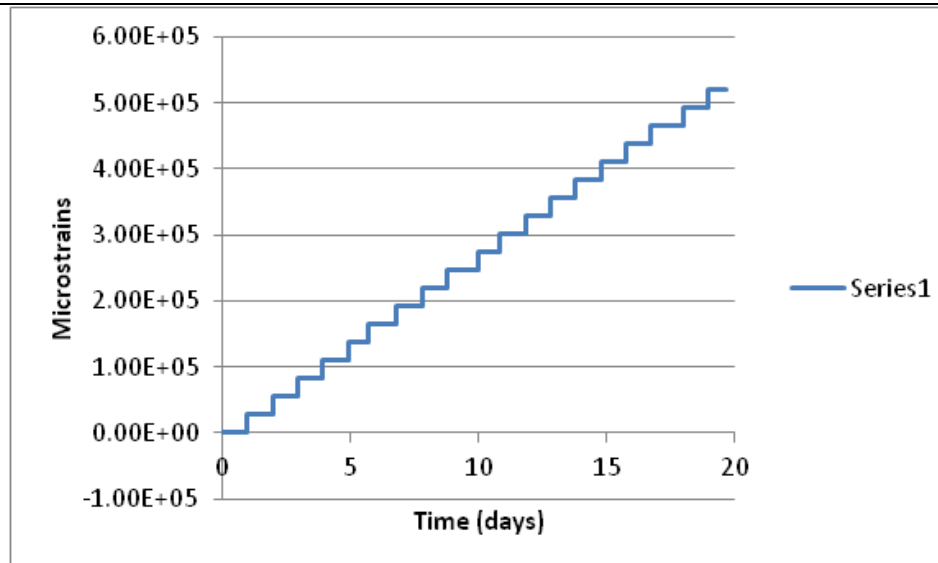
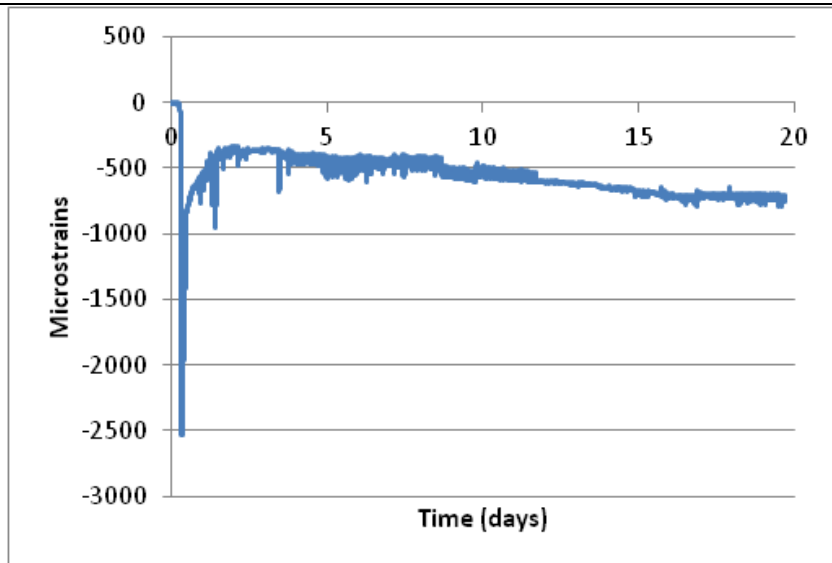
S-Bt-1/2-1/2-L



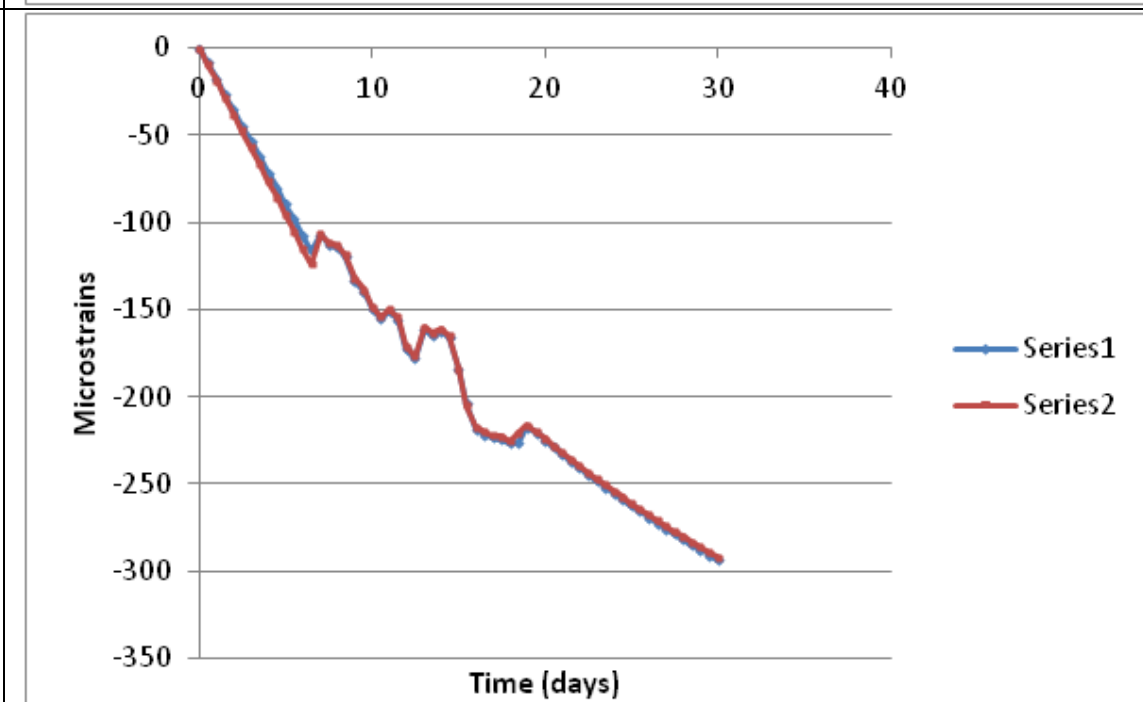
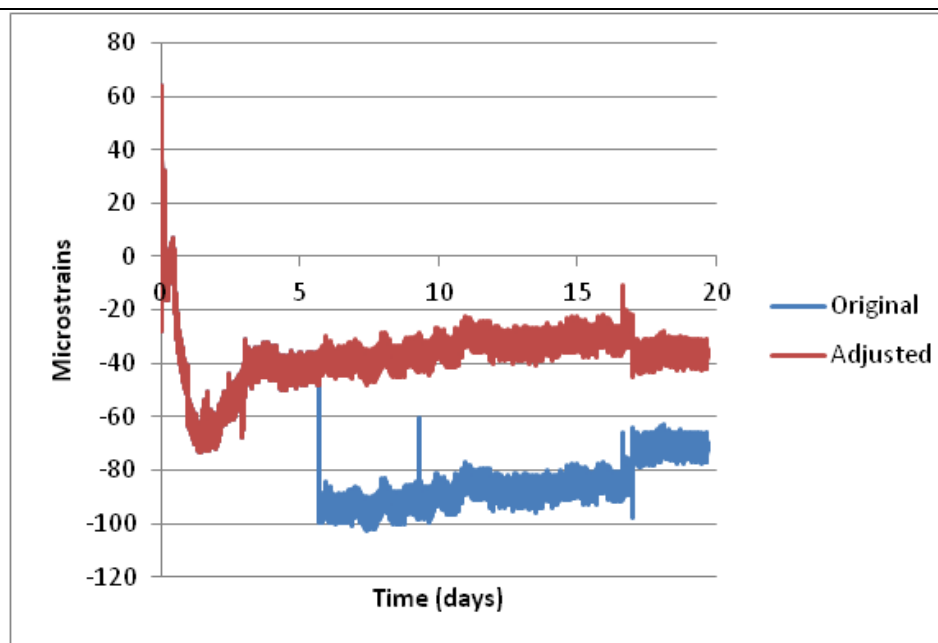
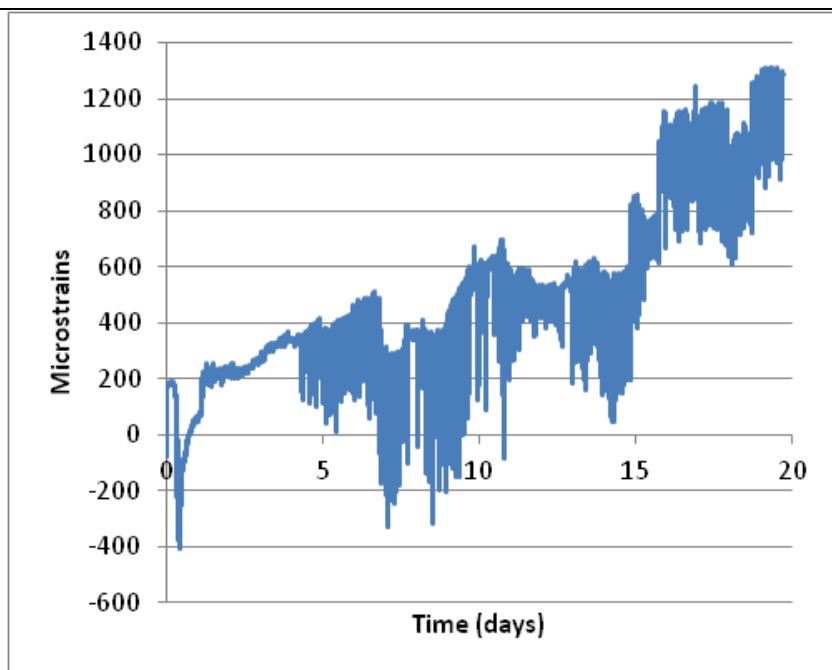
S-Bt-1/2-1/4-L



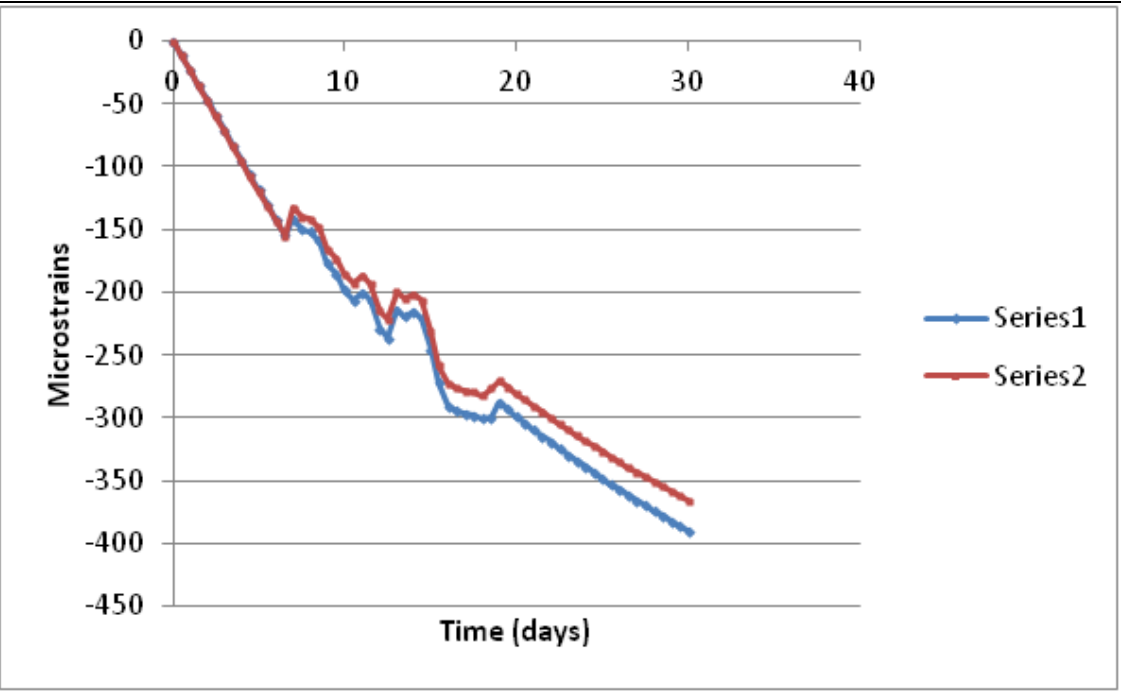
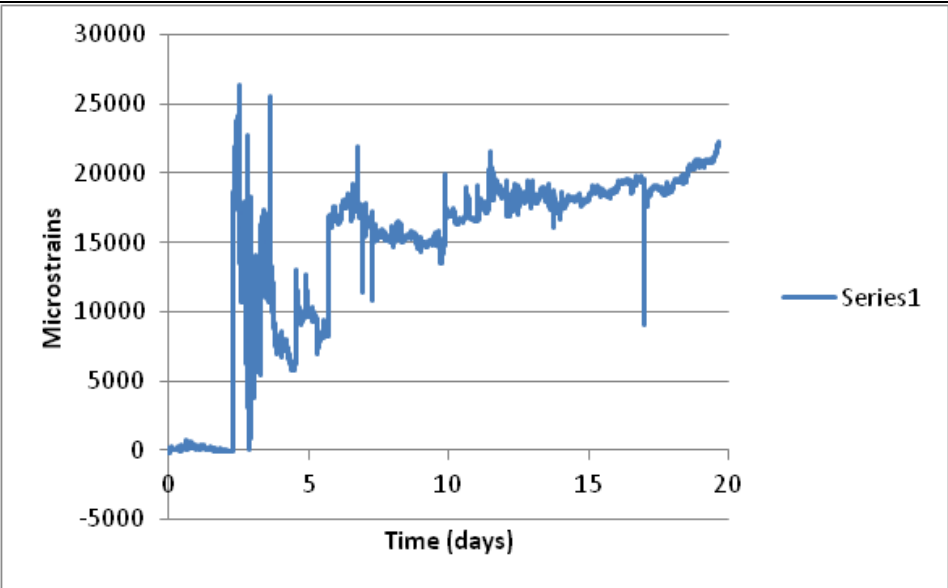
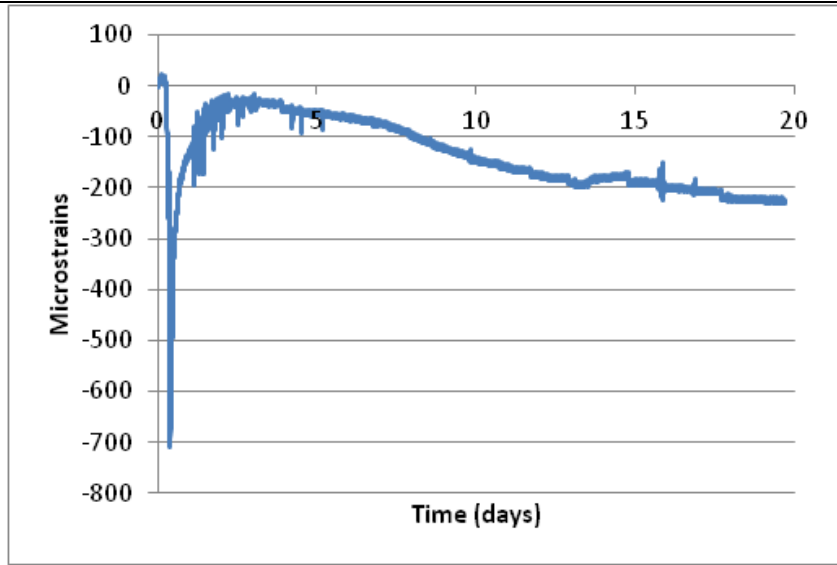
S-Bt-1/3-3/4-L



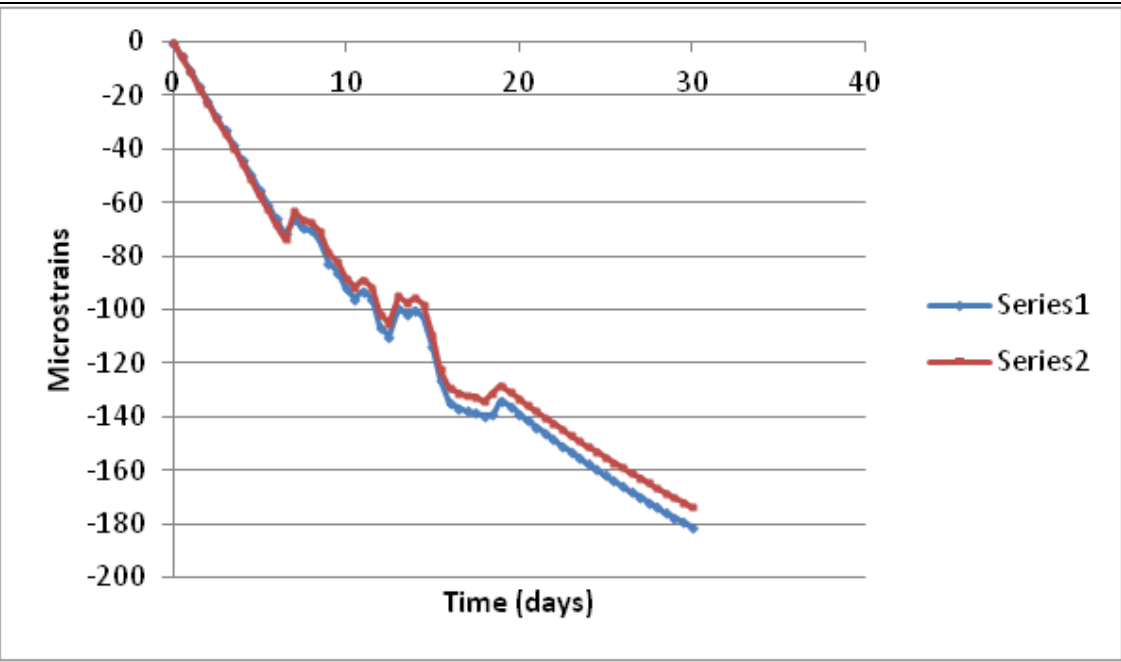
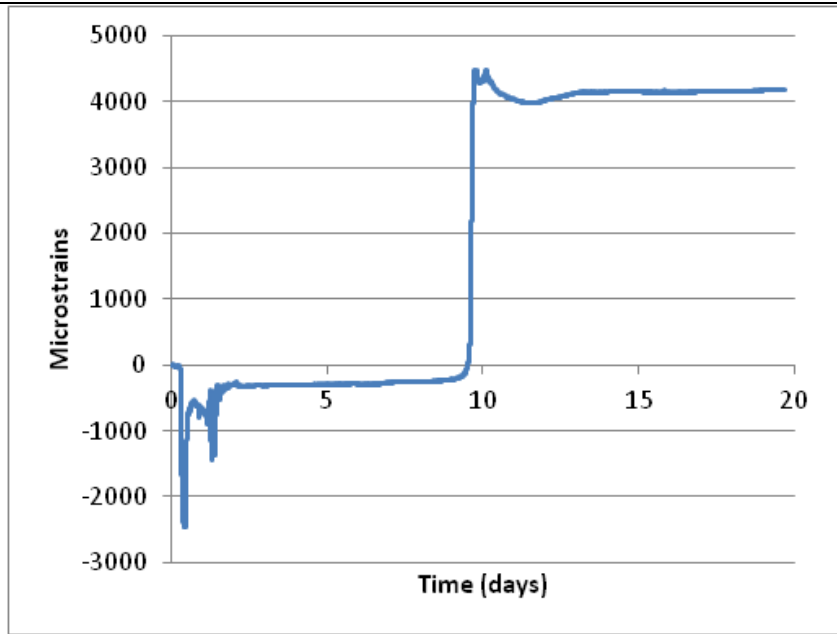
S-Bt-G1-1/2-T



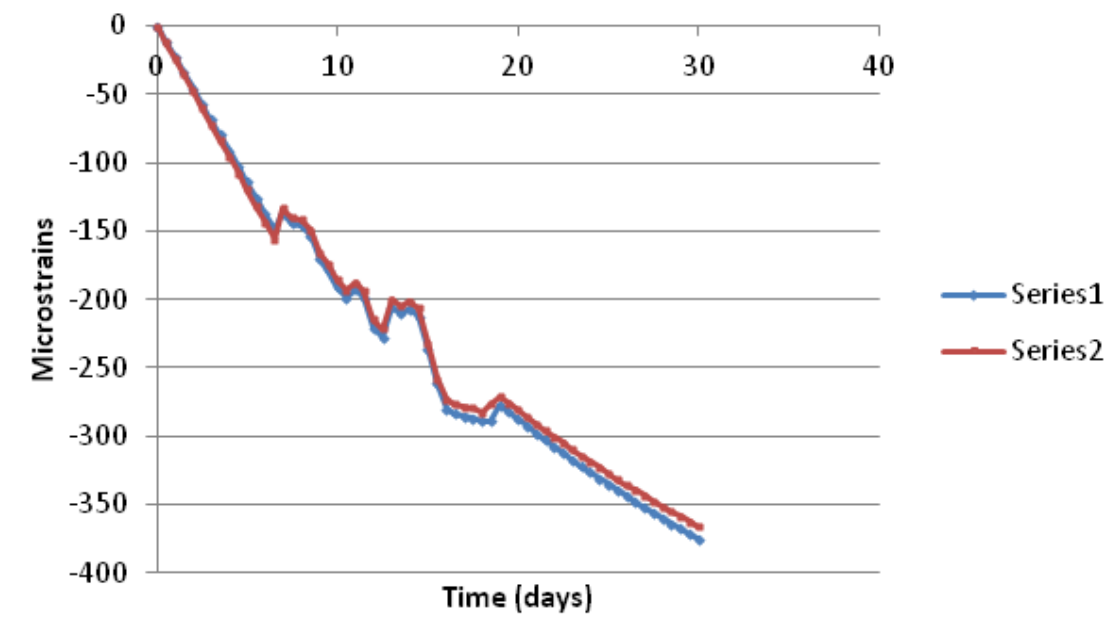
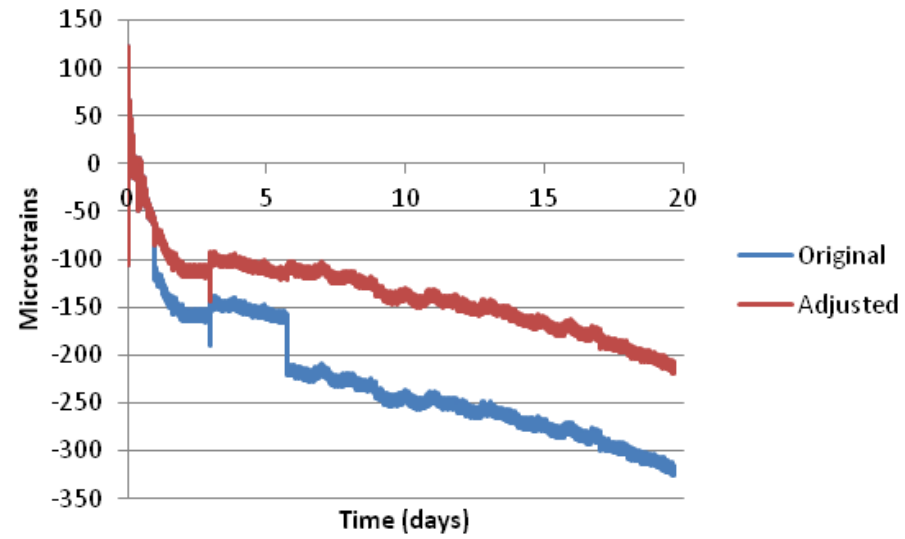
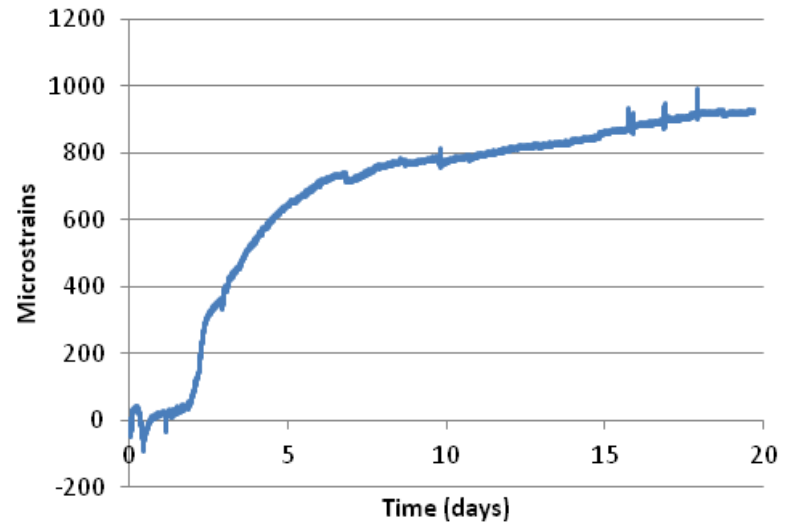
S-Bt-G1-1/2-L



S-Bt-1/2-1/4-T



S-Bt-G1-3/4-L



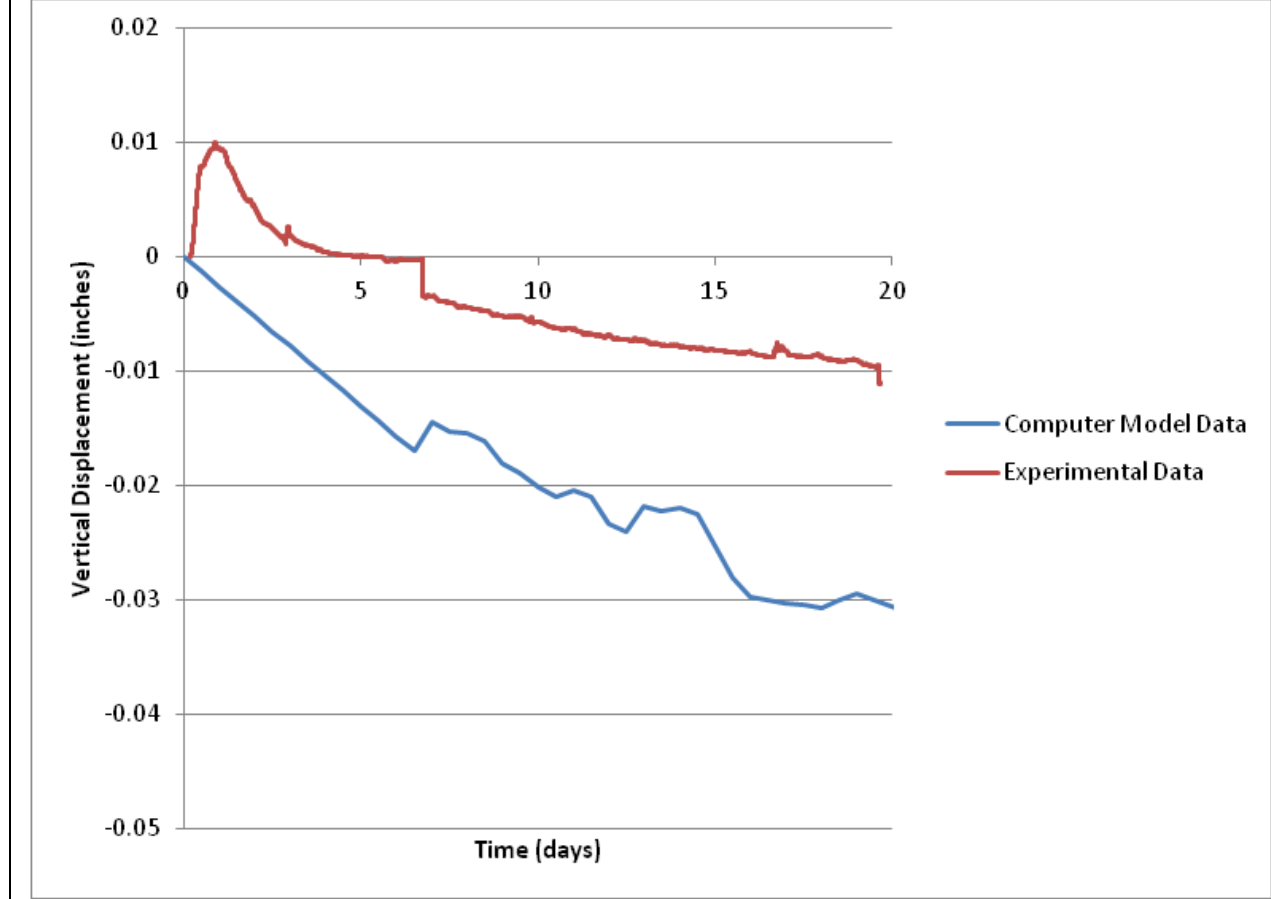
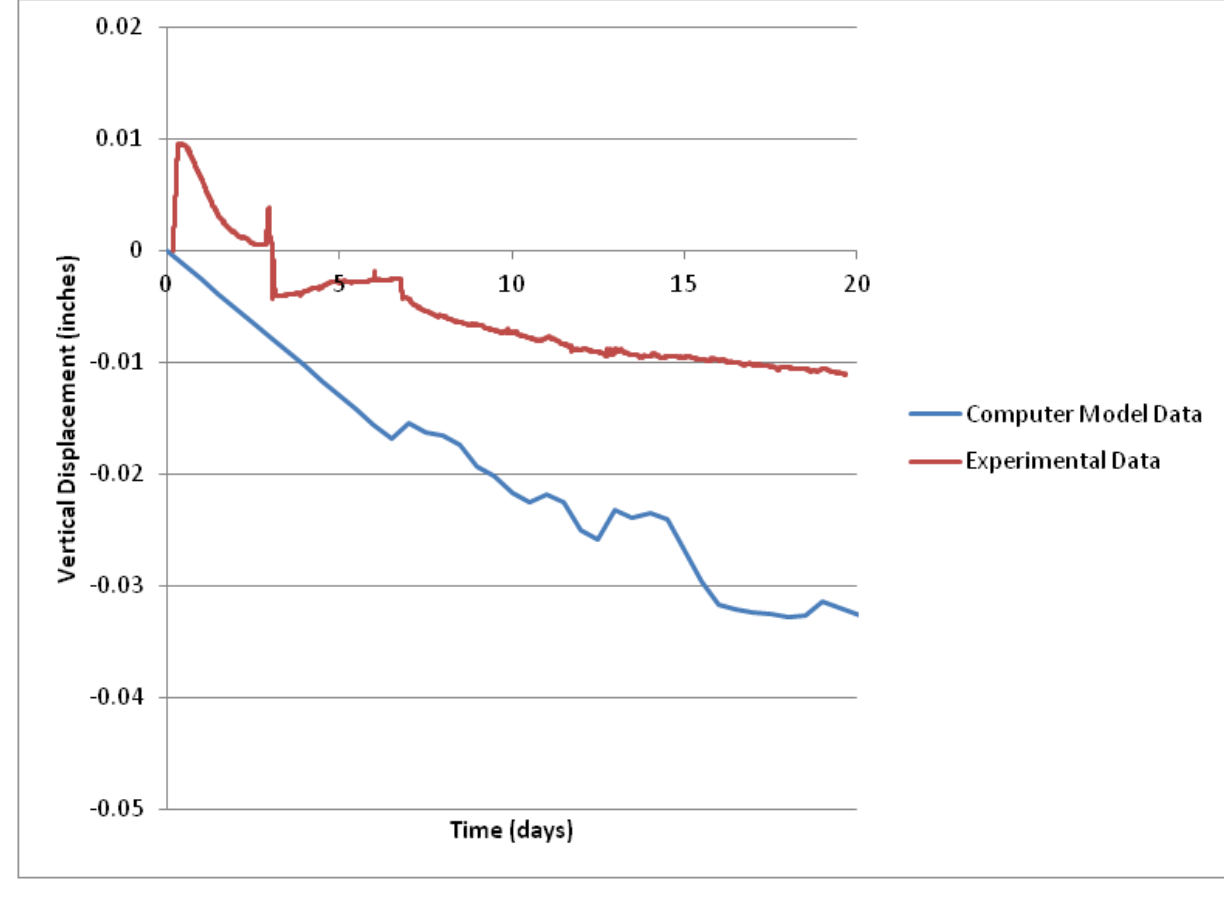


## **Appendix D**

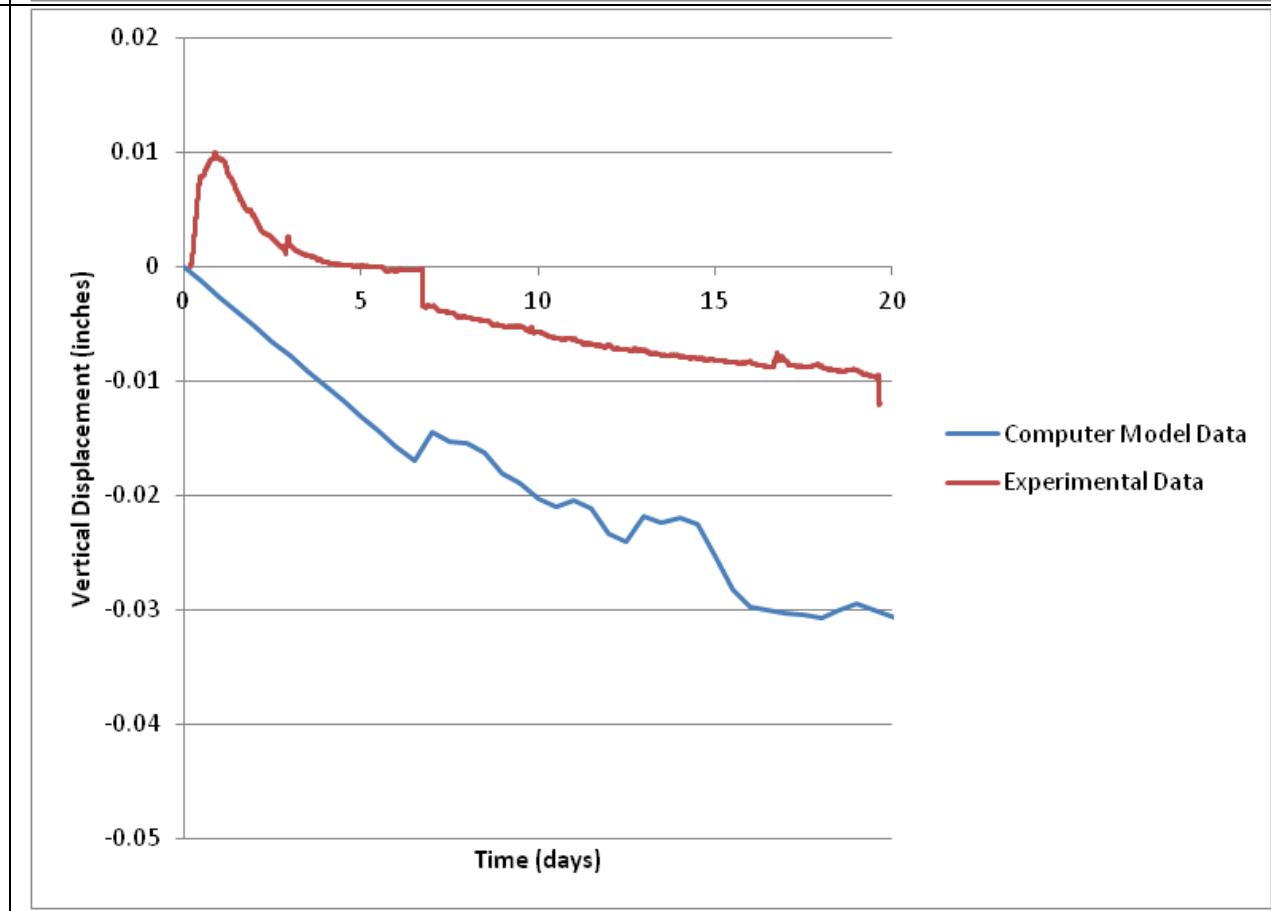
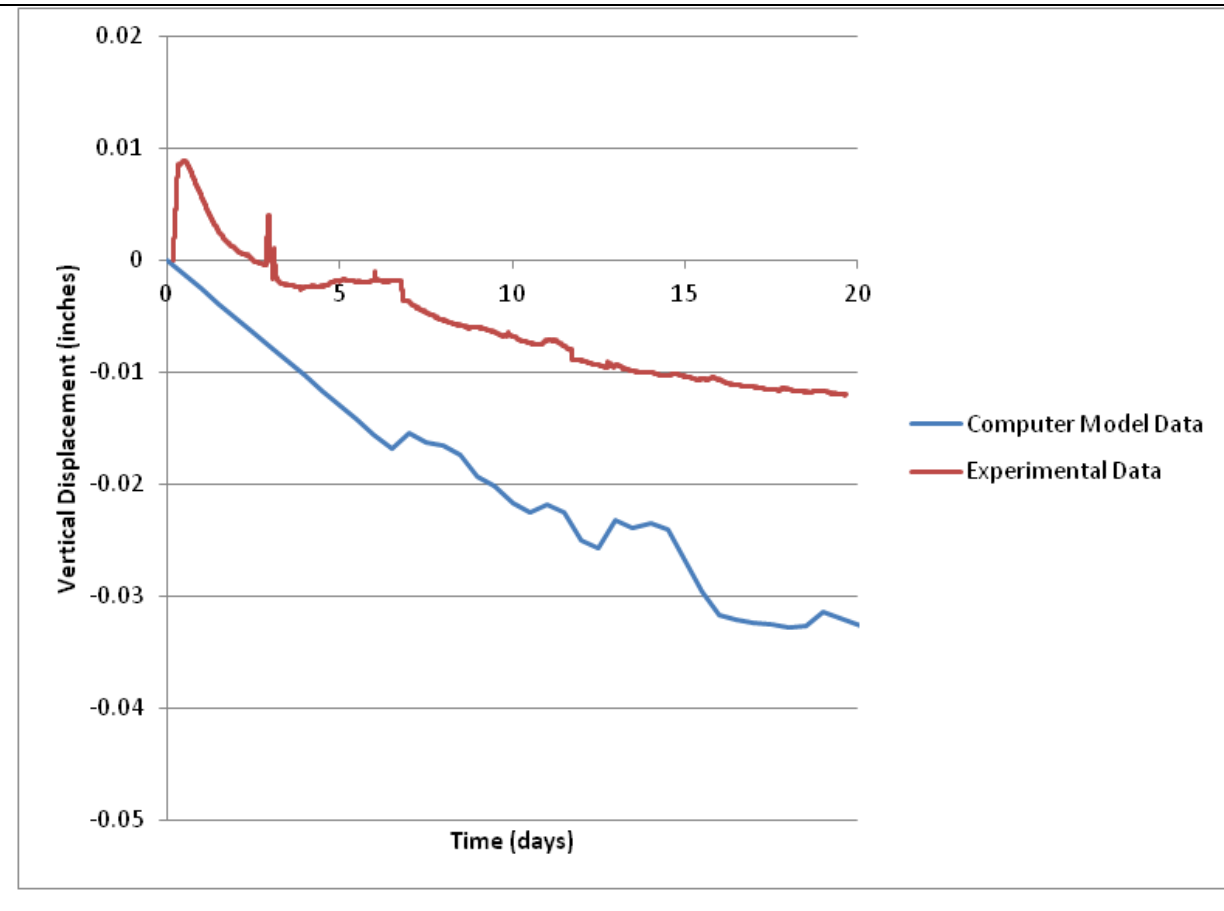
### **Laboratory Full Data Comparison to Experimental Data**

Instrumentation ID	Test Unit 3	Test Unit 4
--------------------	-------------	-------------

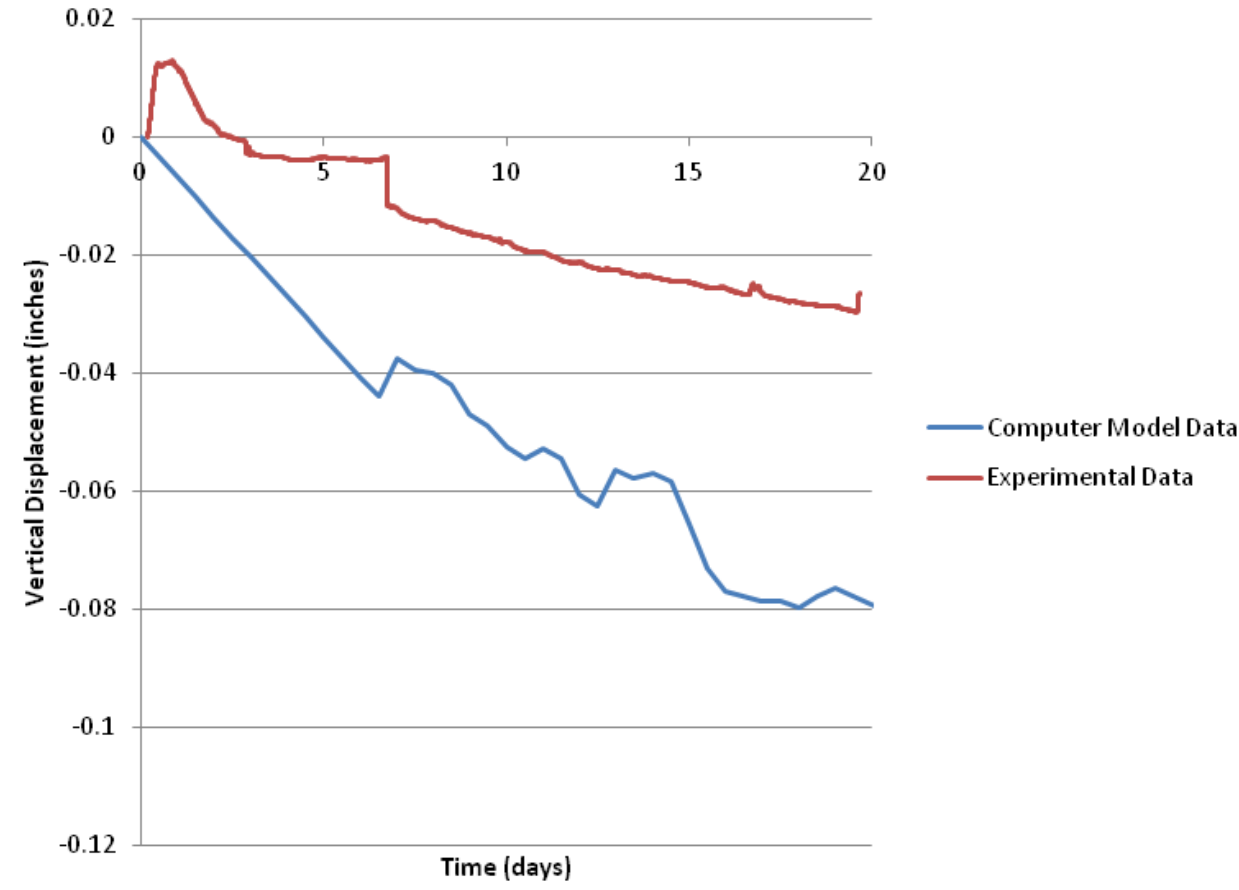
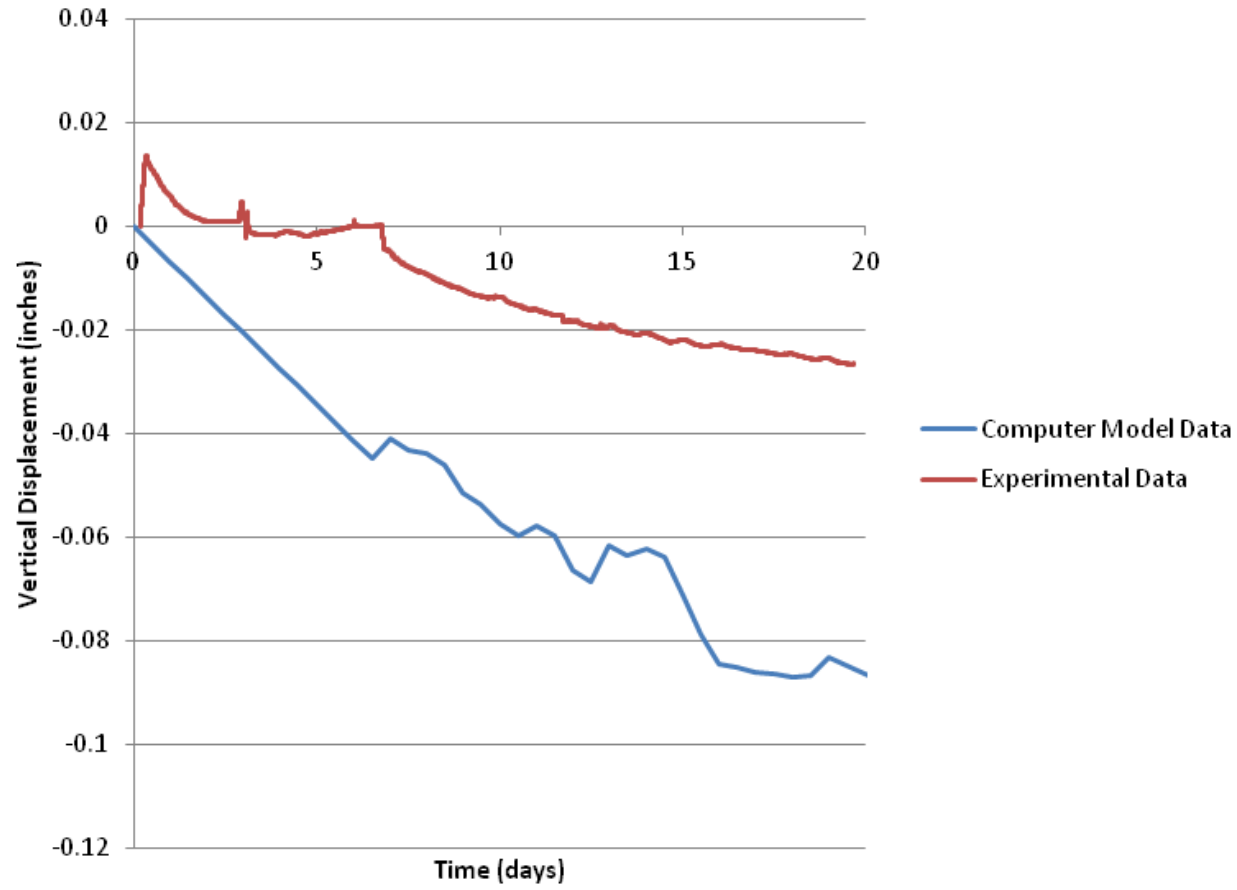
L-G1-1/2



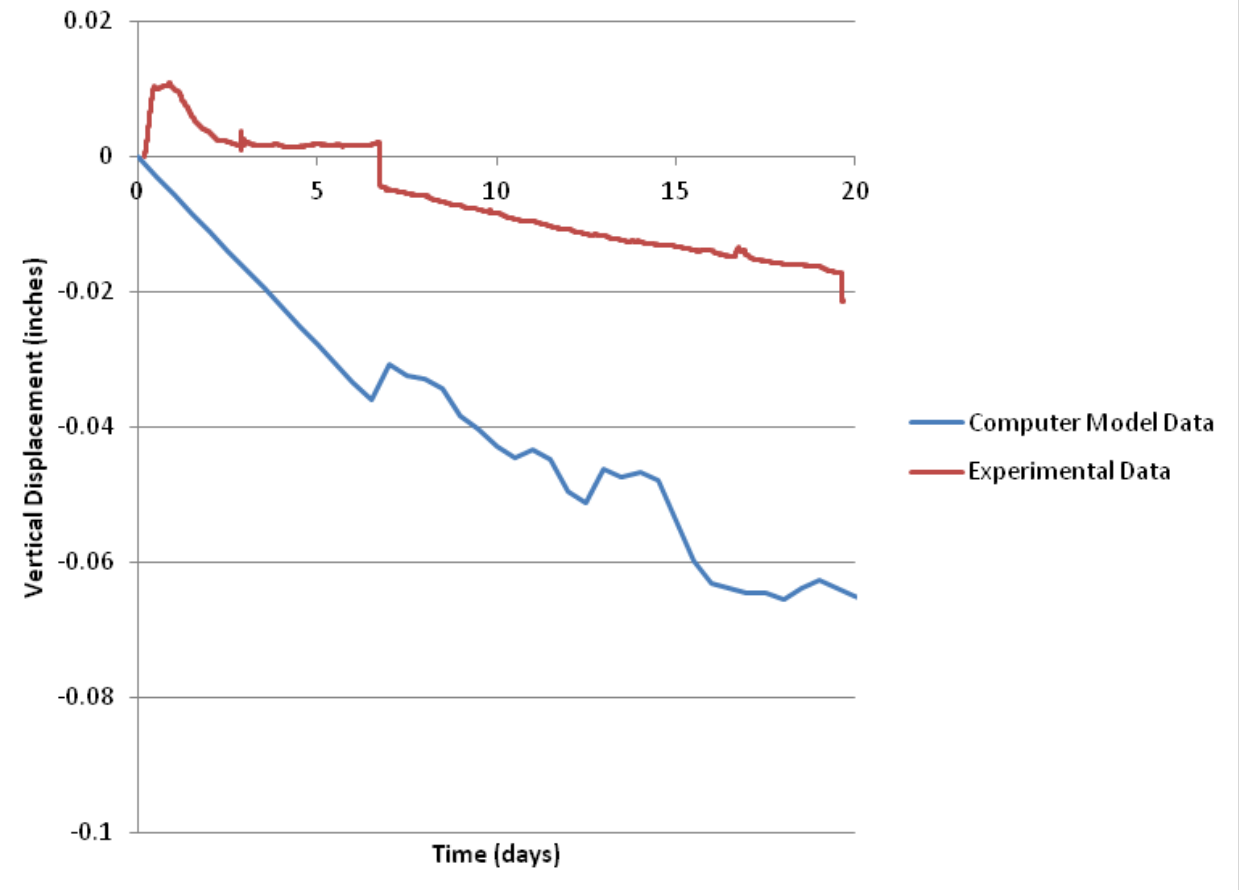
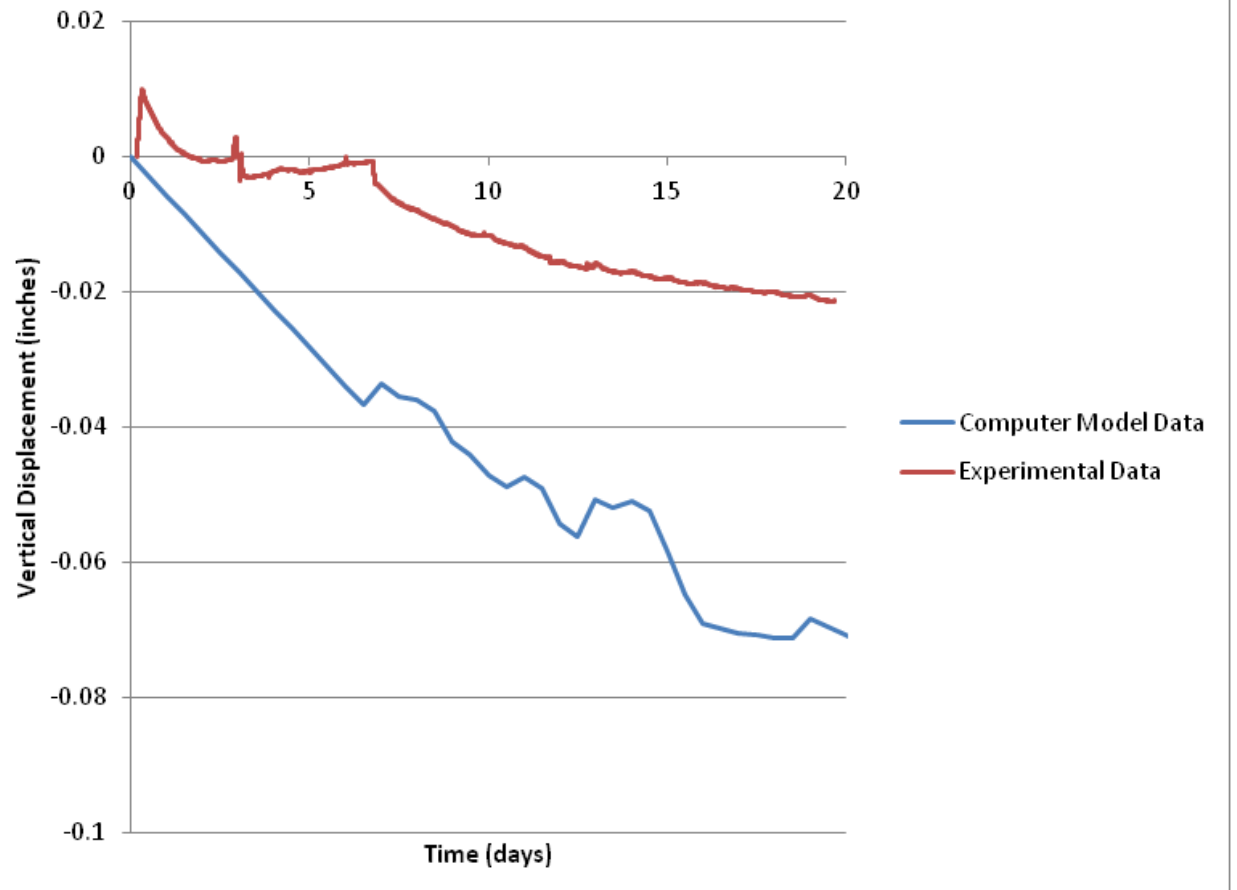
L-G2-1/2



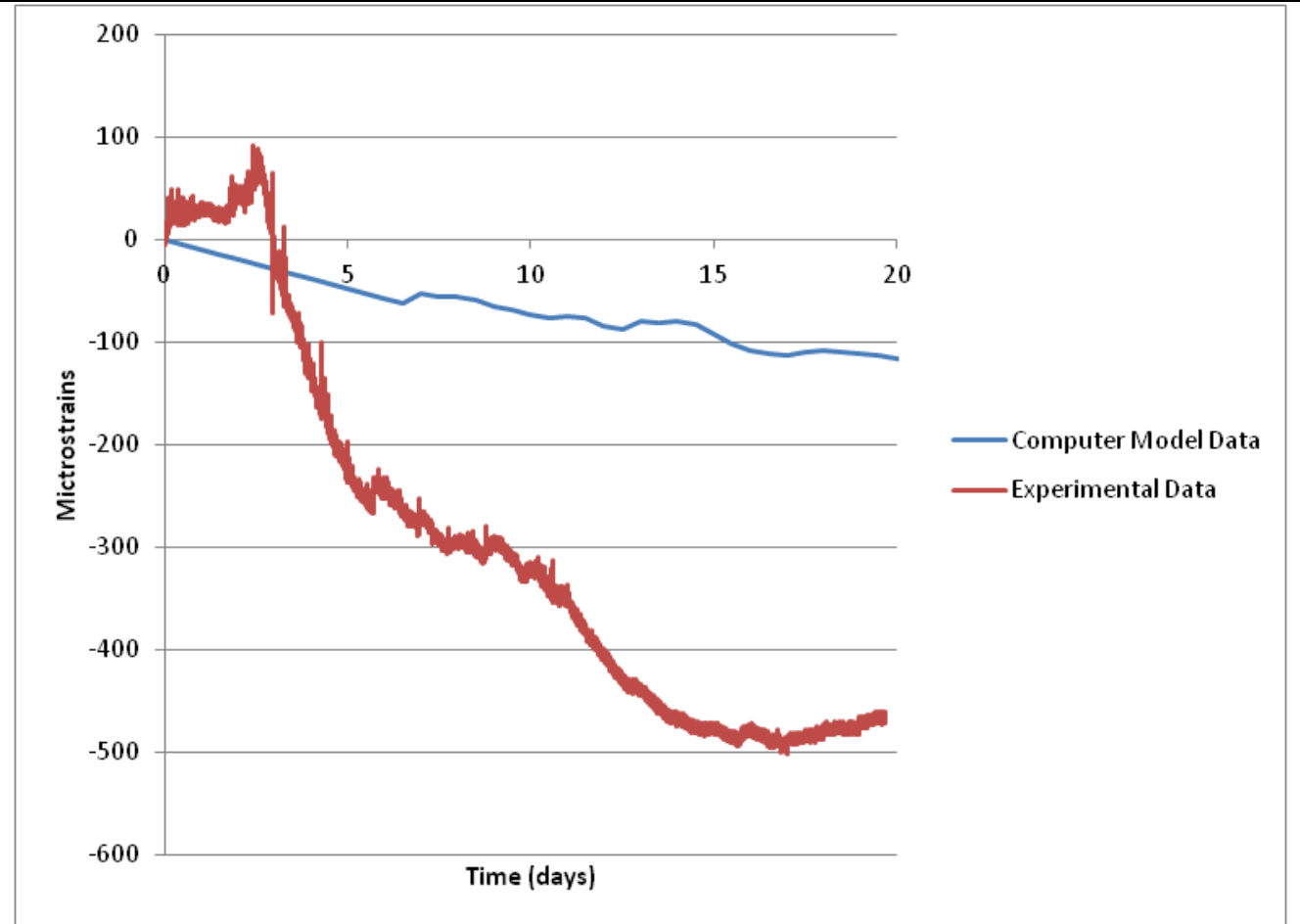
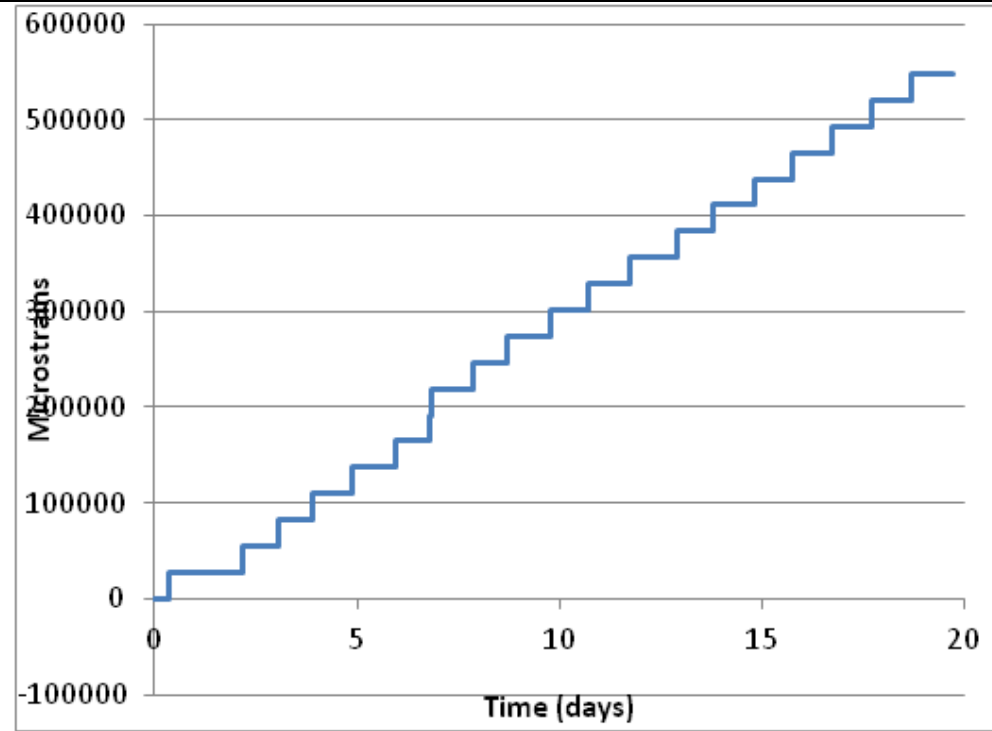
L-1/2-1/2



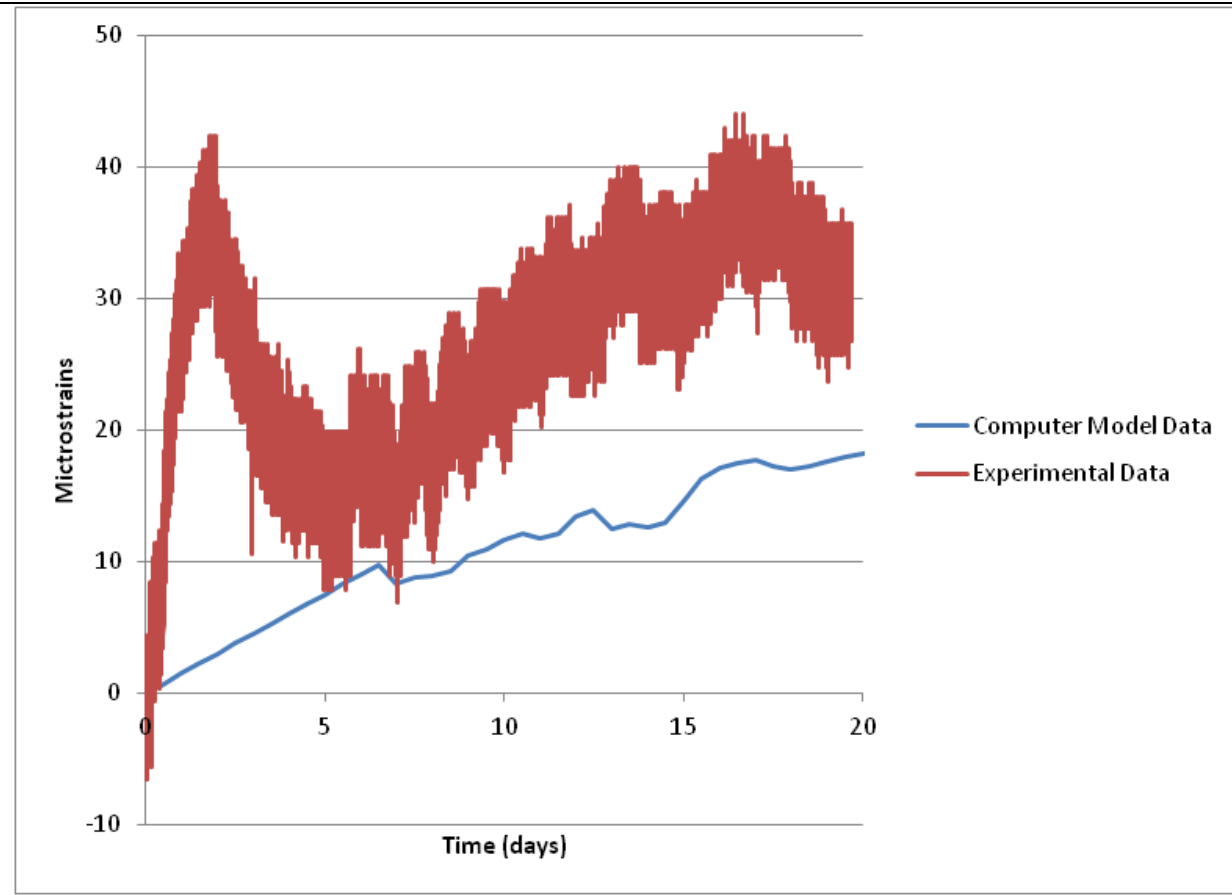
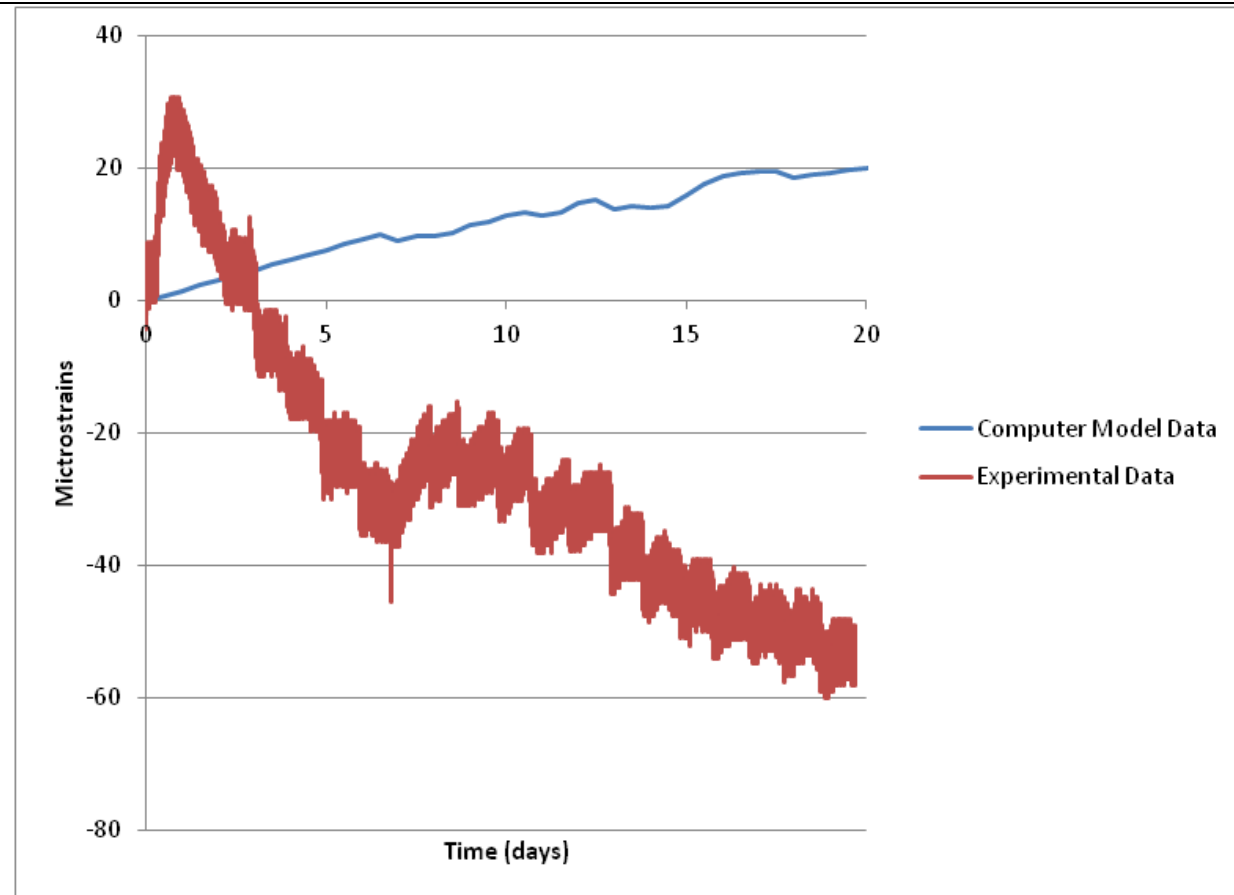
L-1/2-3/4



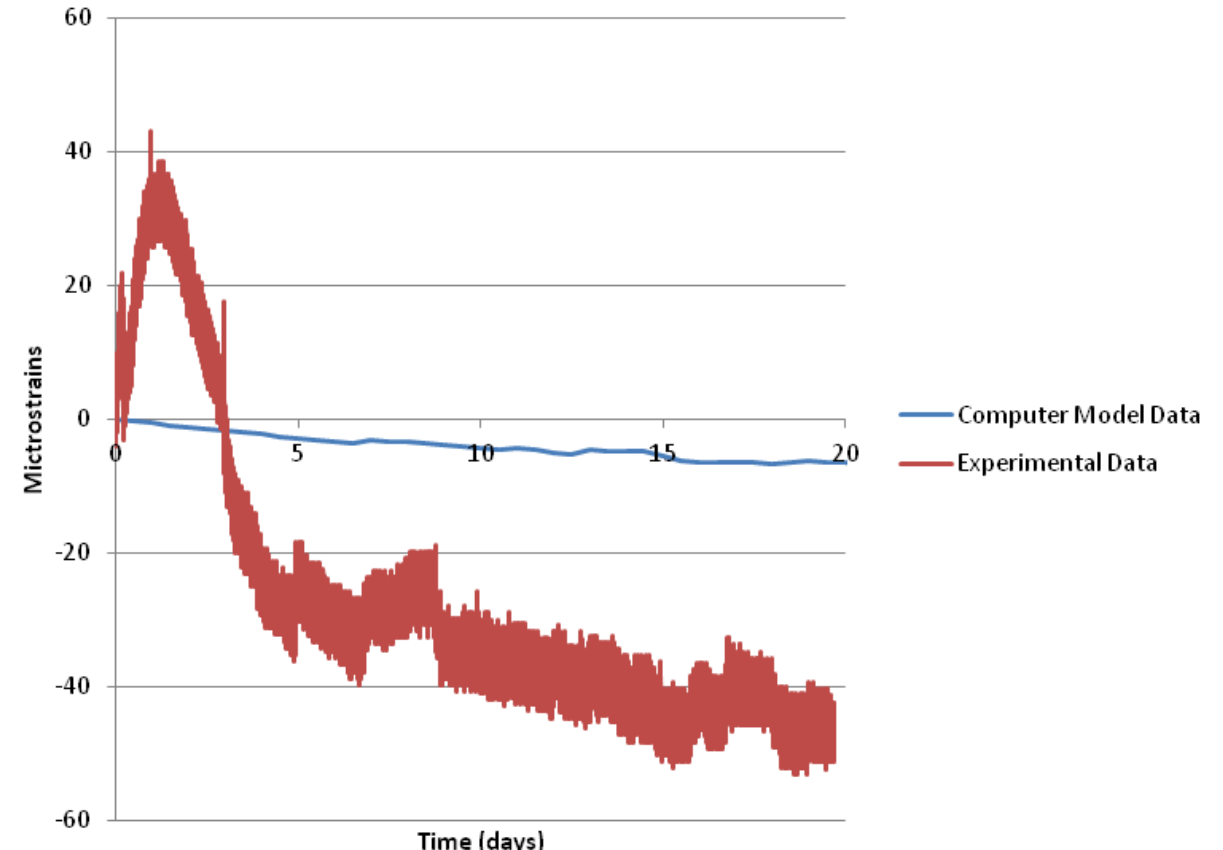
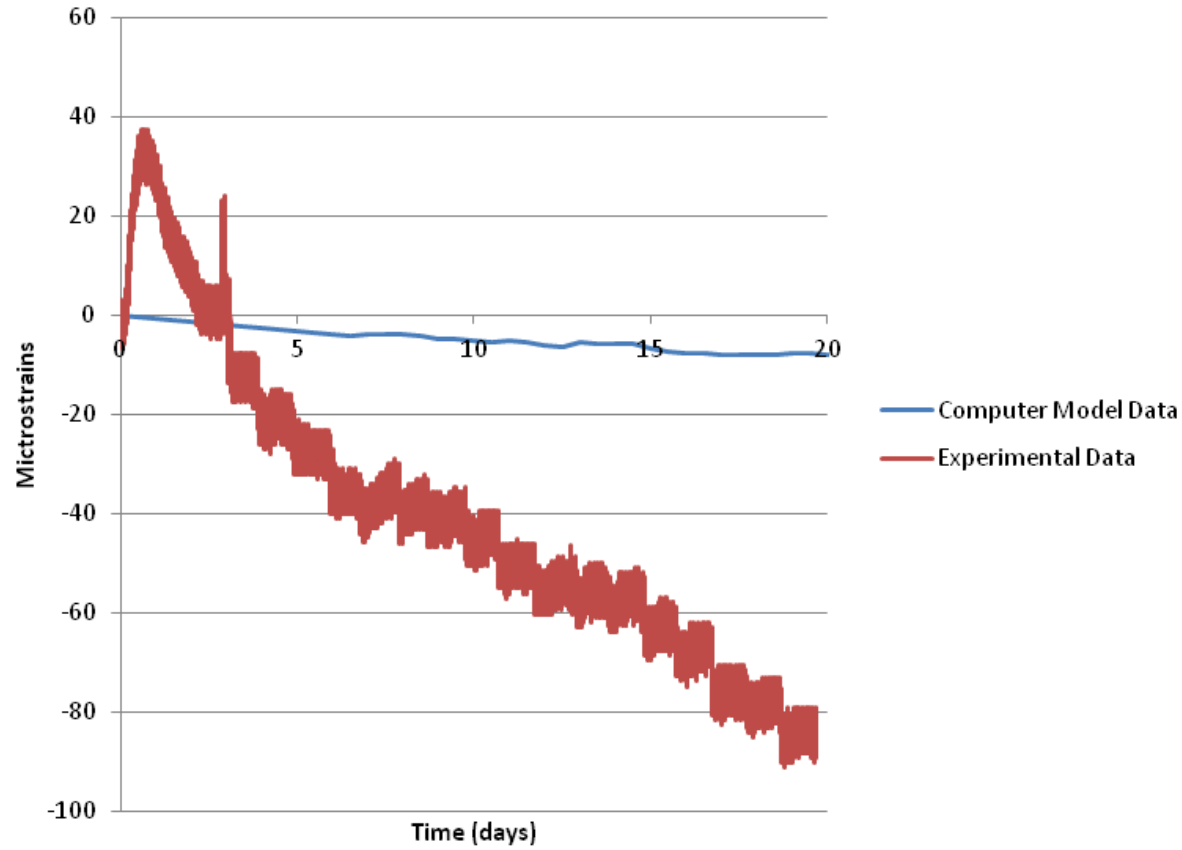
S-G1-Tf-M-3/4-L



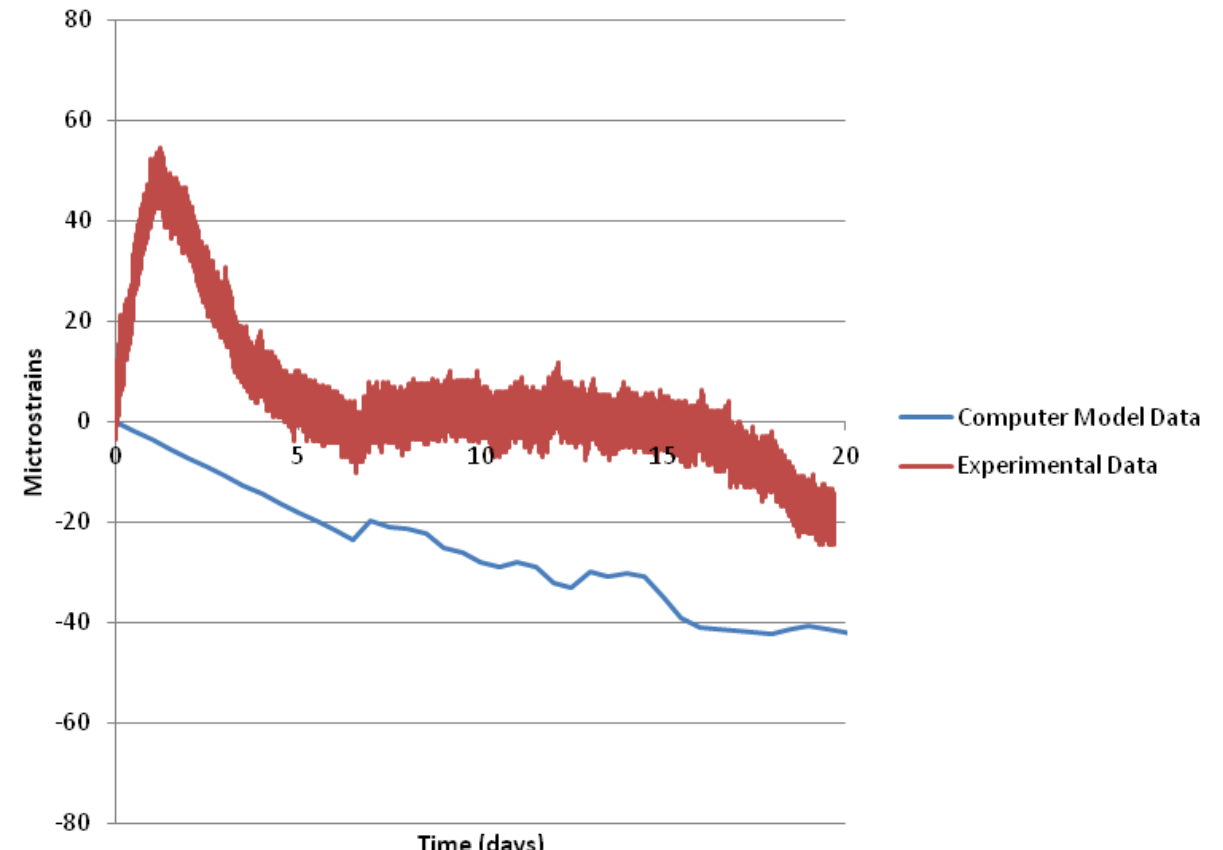
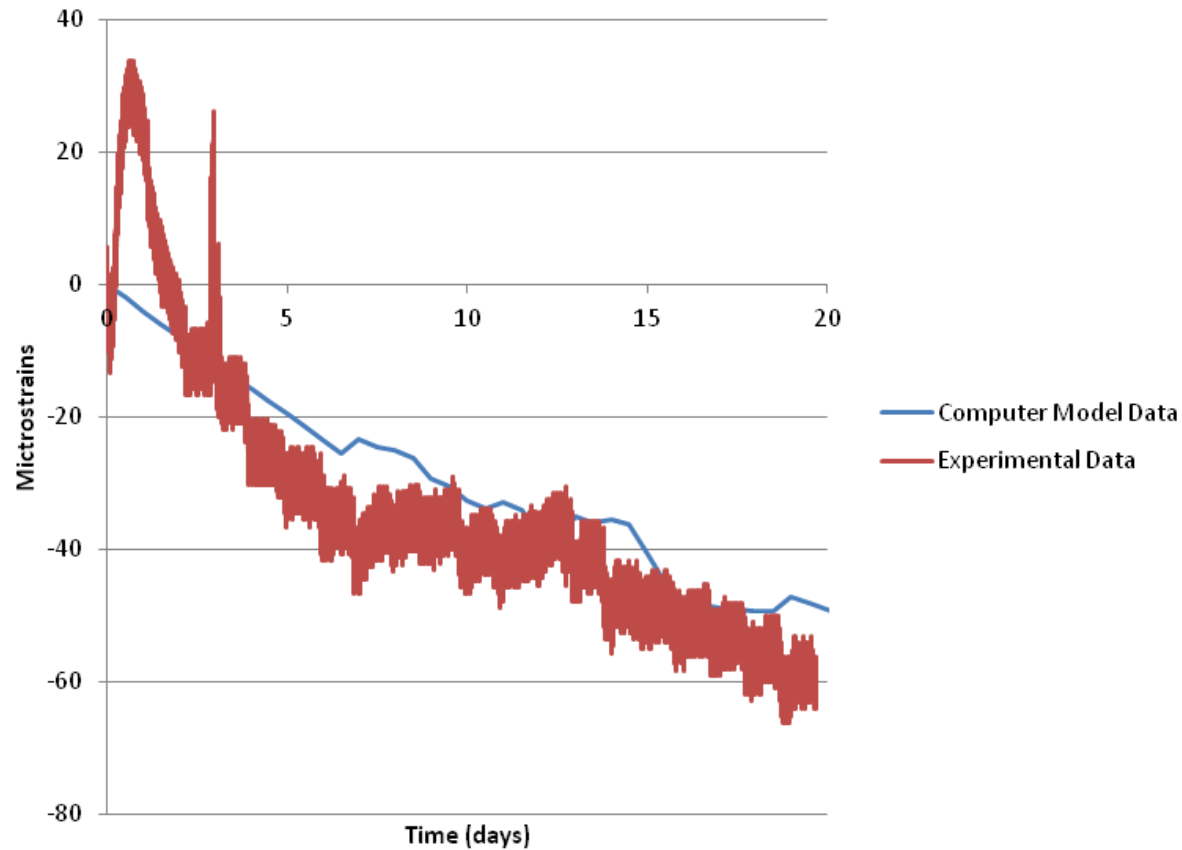
S-G1-Bf-M-3/4-L



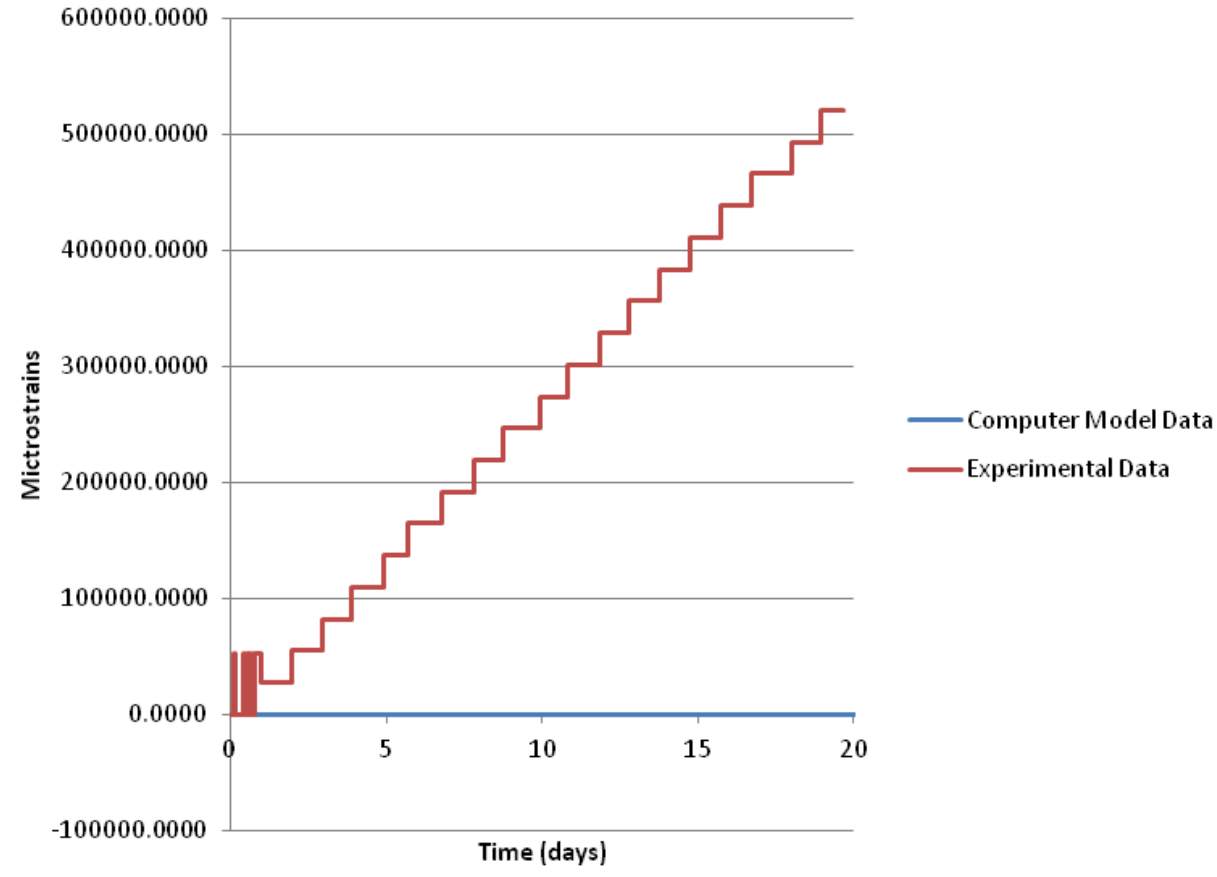
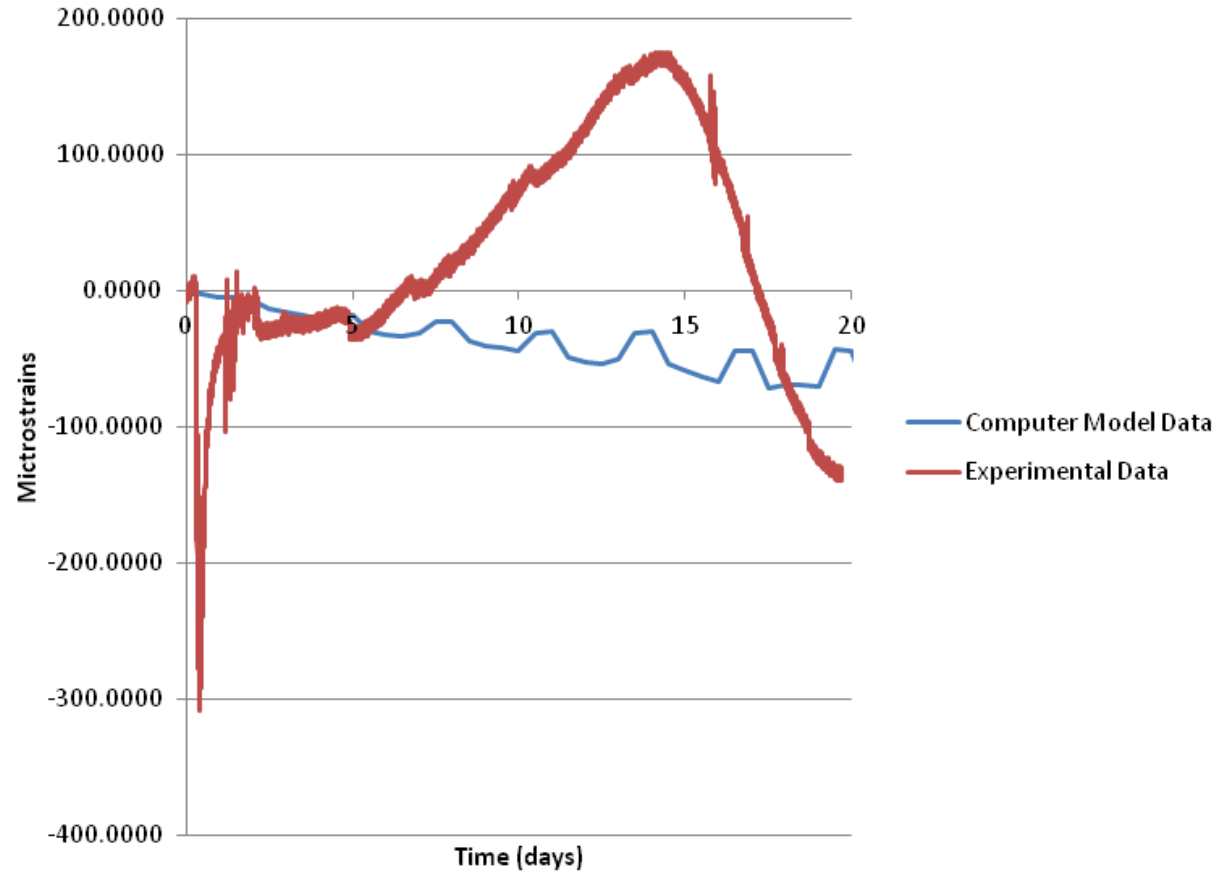
S-G1-W-O-3/4-L



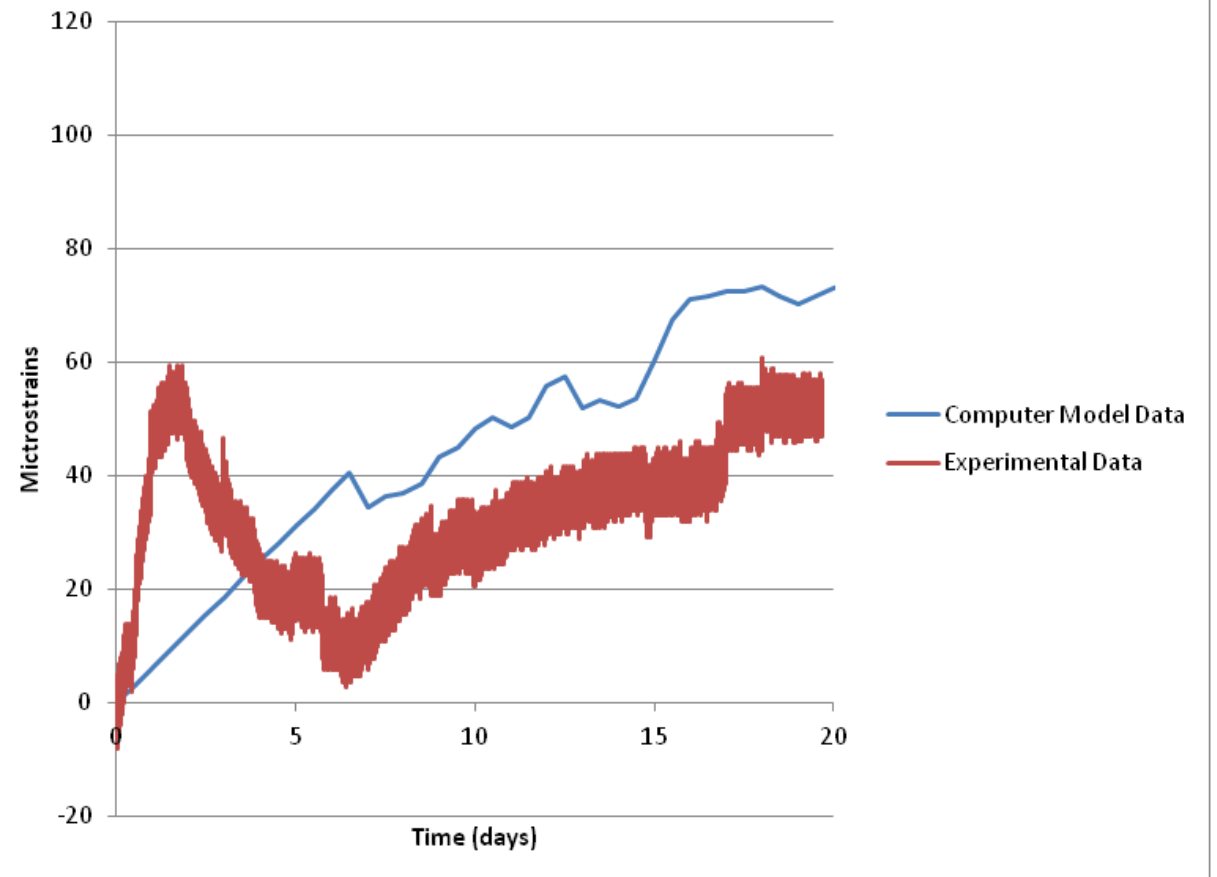
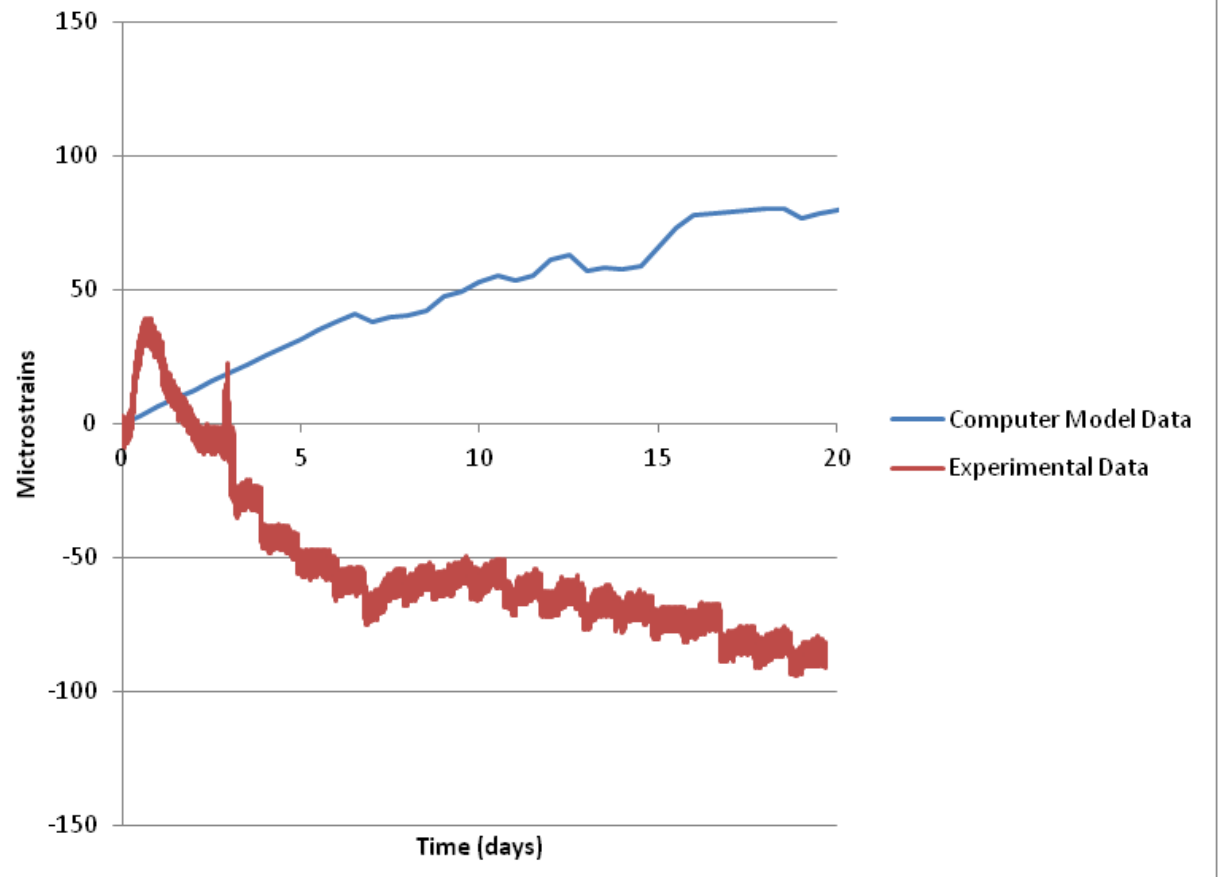
S-G1-W-O-1/2-L



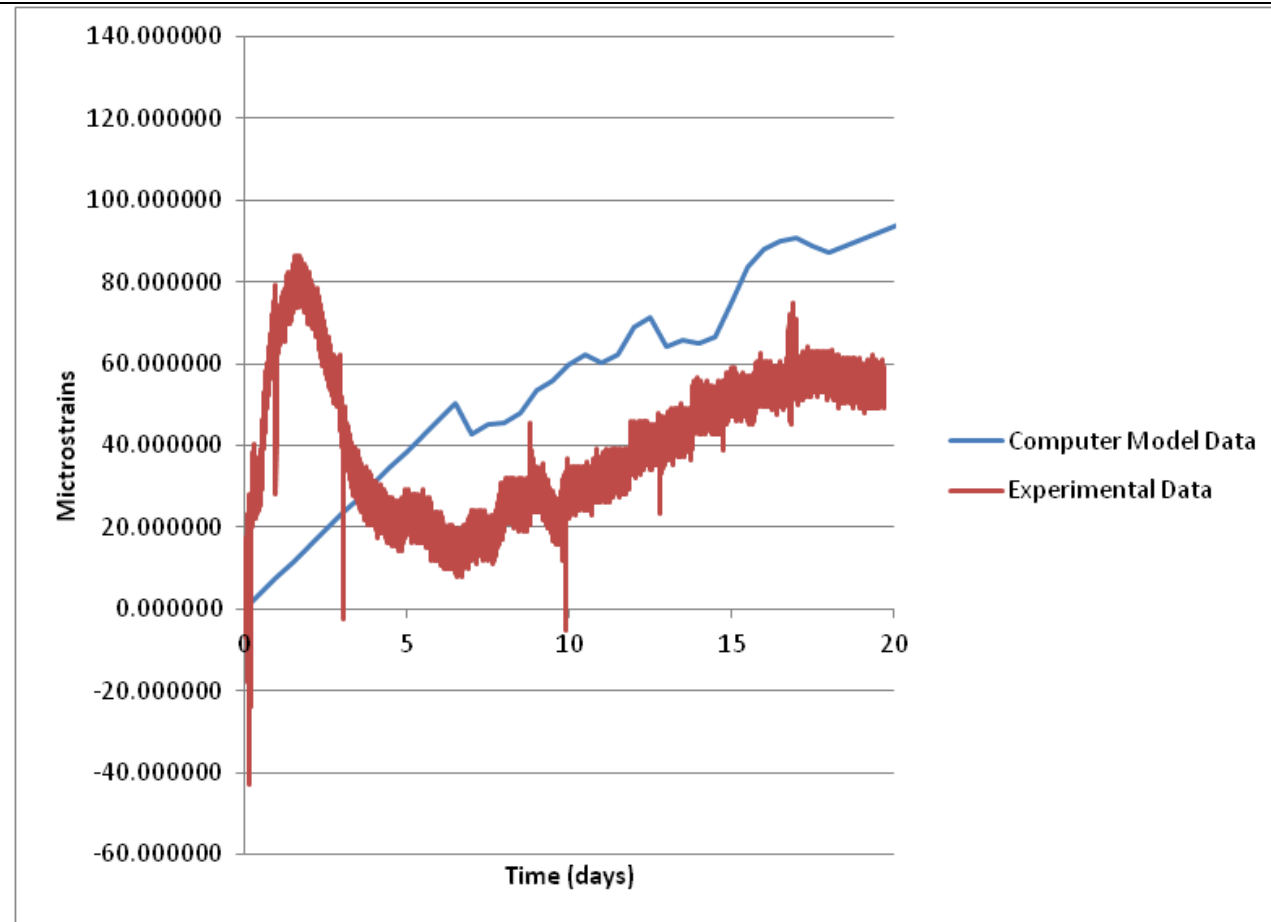
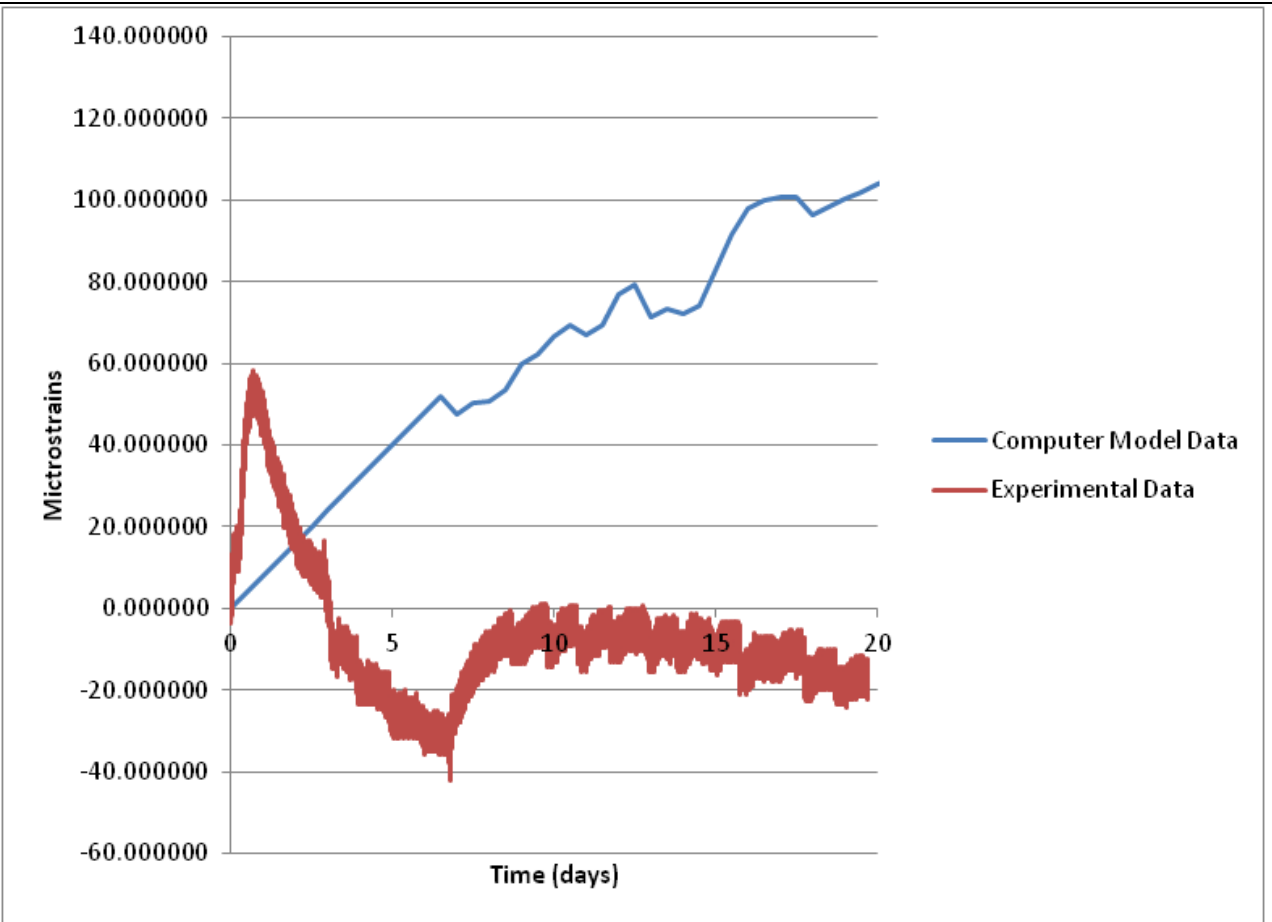
S-G1-Tf-M-1/4-L



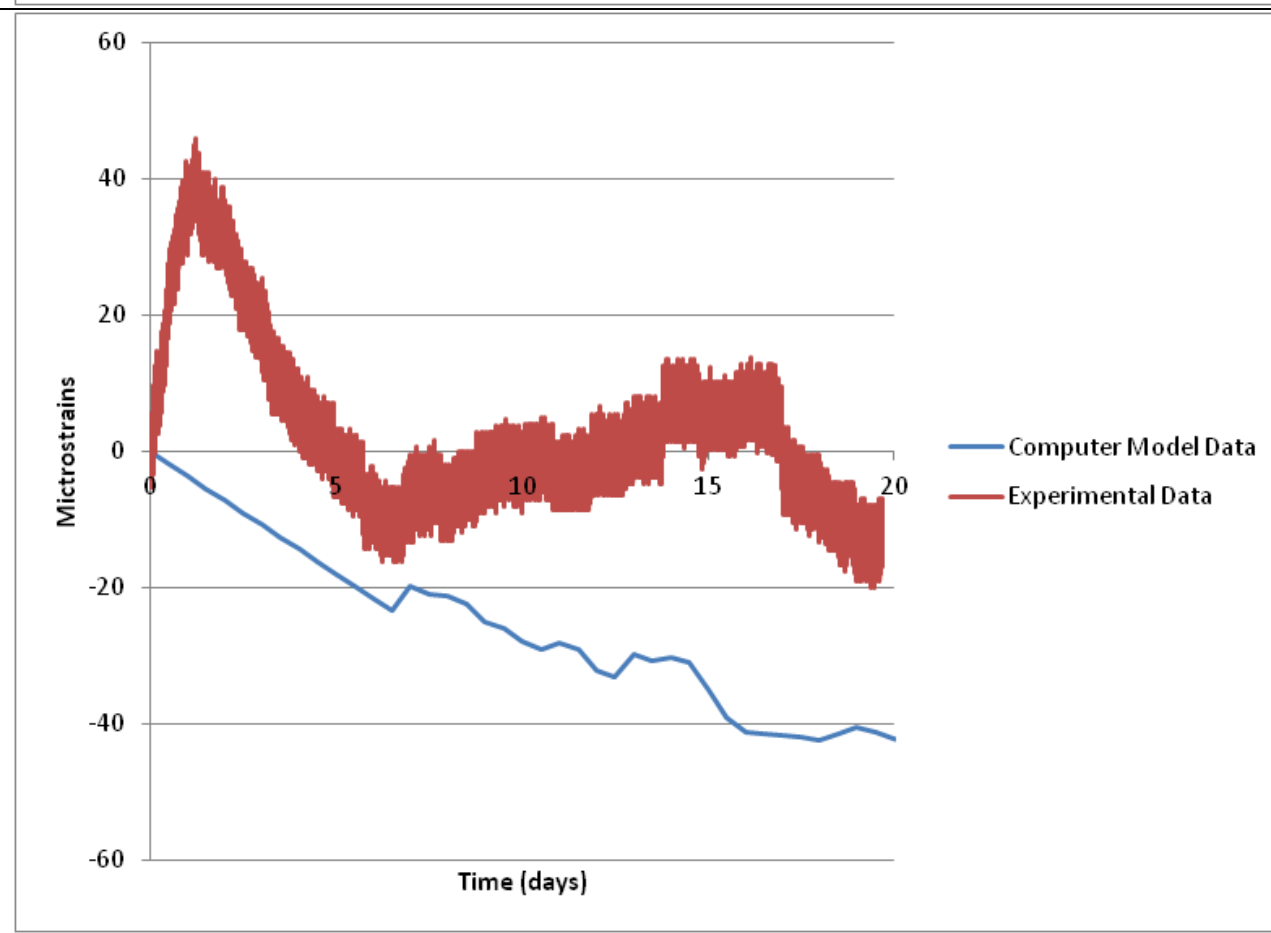
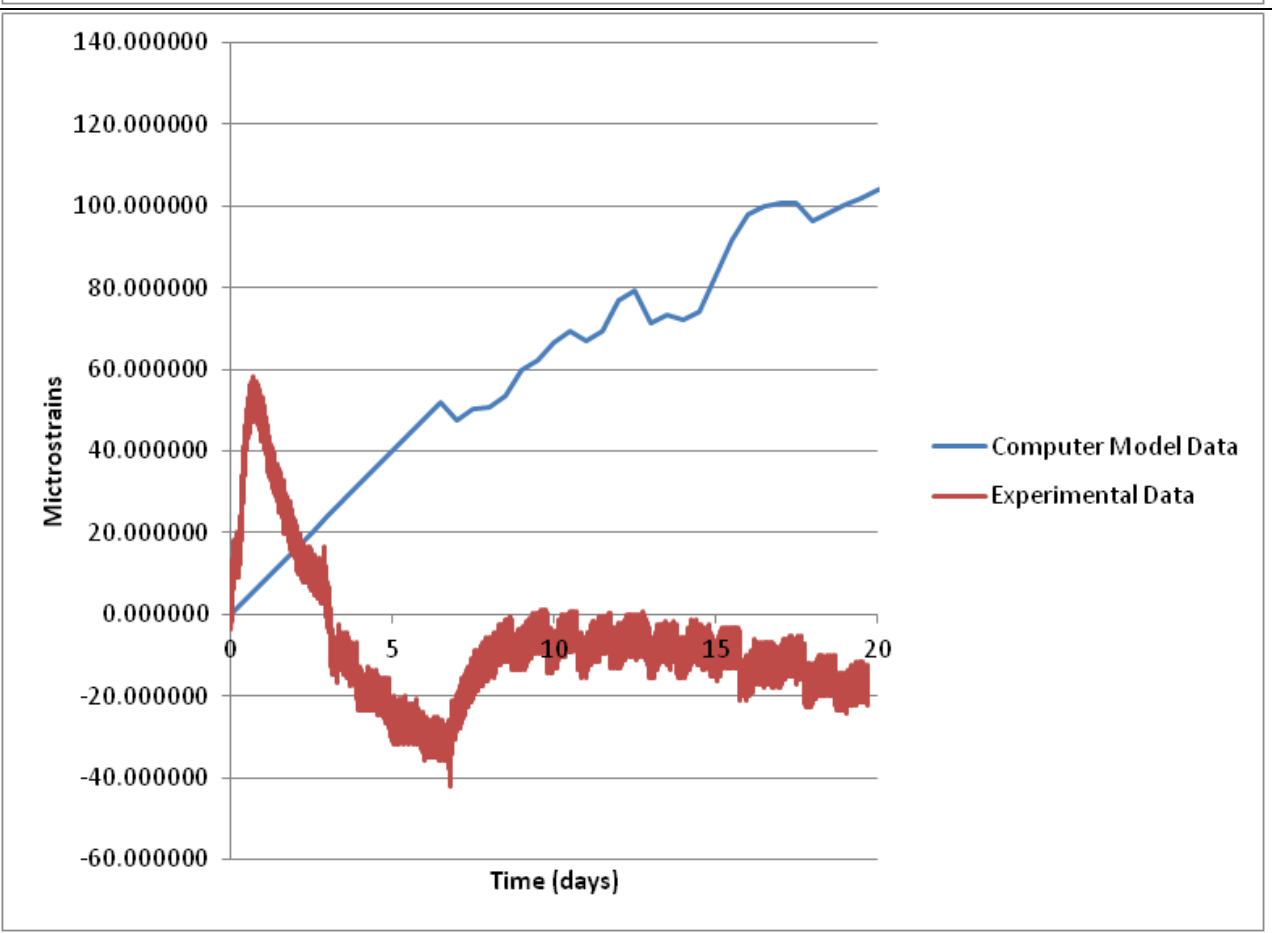
S-G1-Bf-I-1/2-L



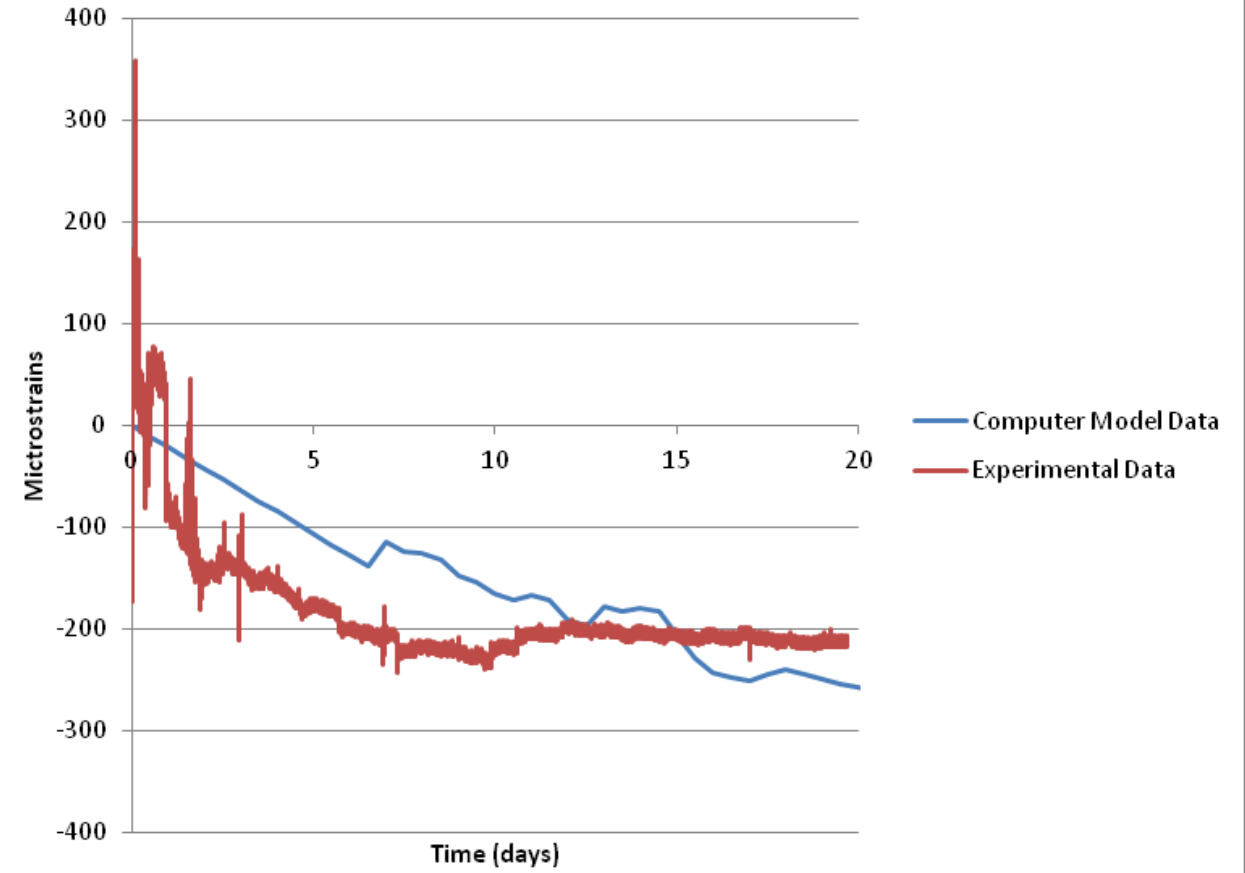
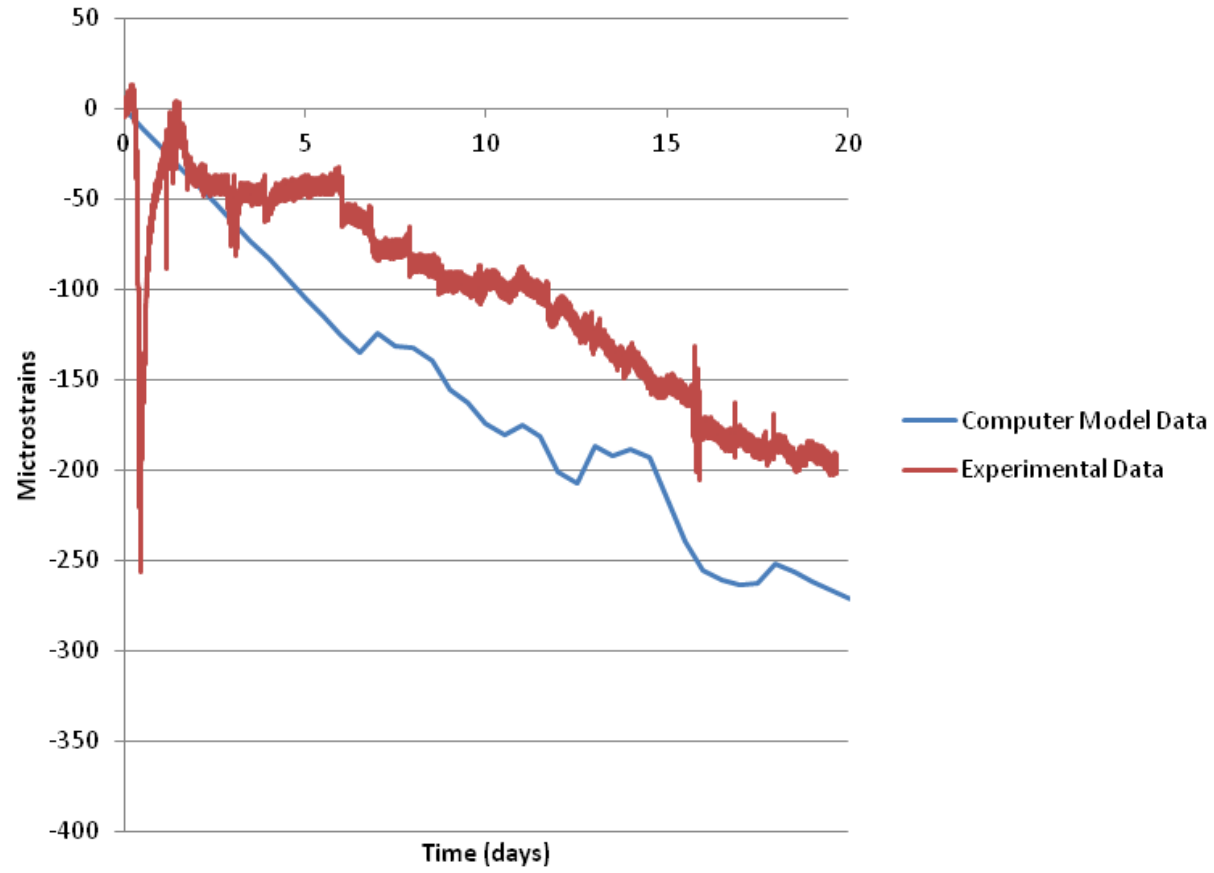
S-G1-Bf-M-1/2-L



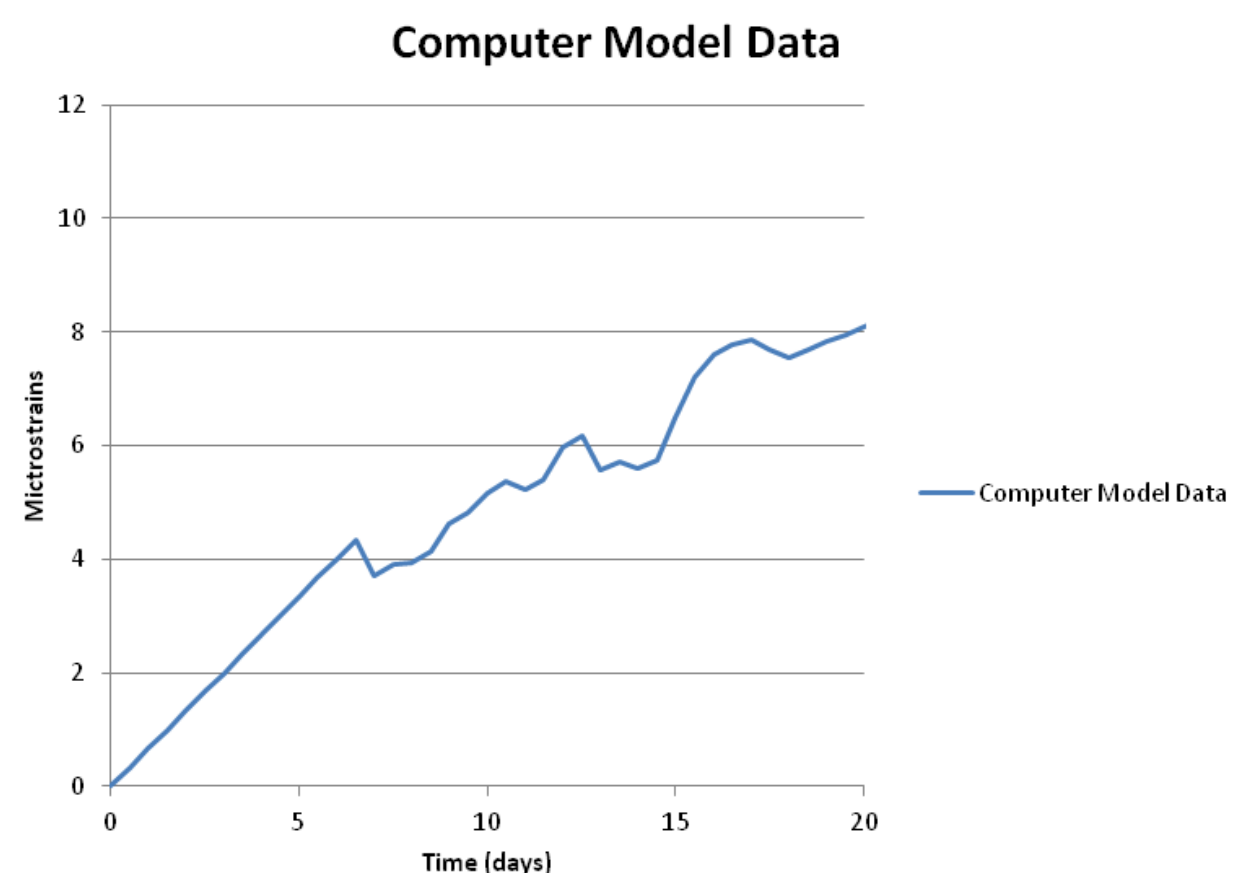
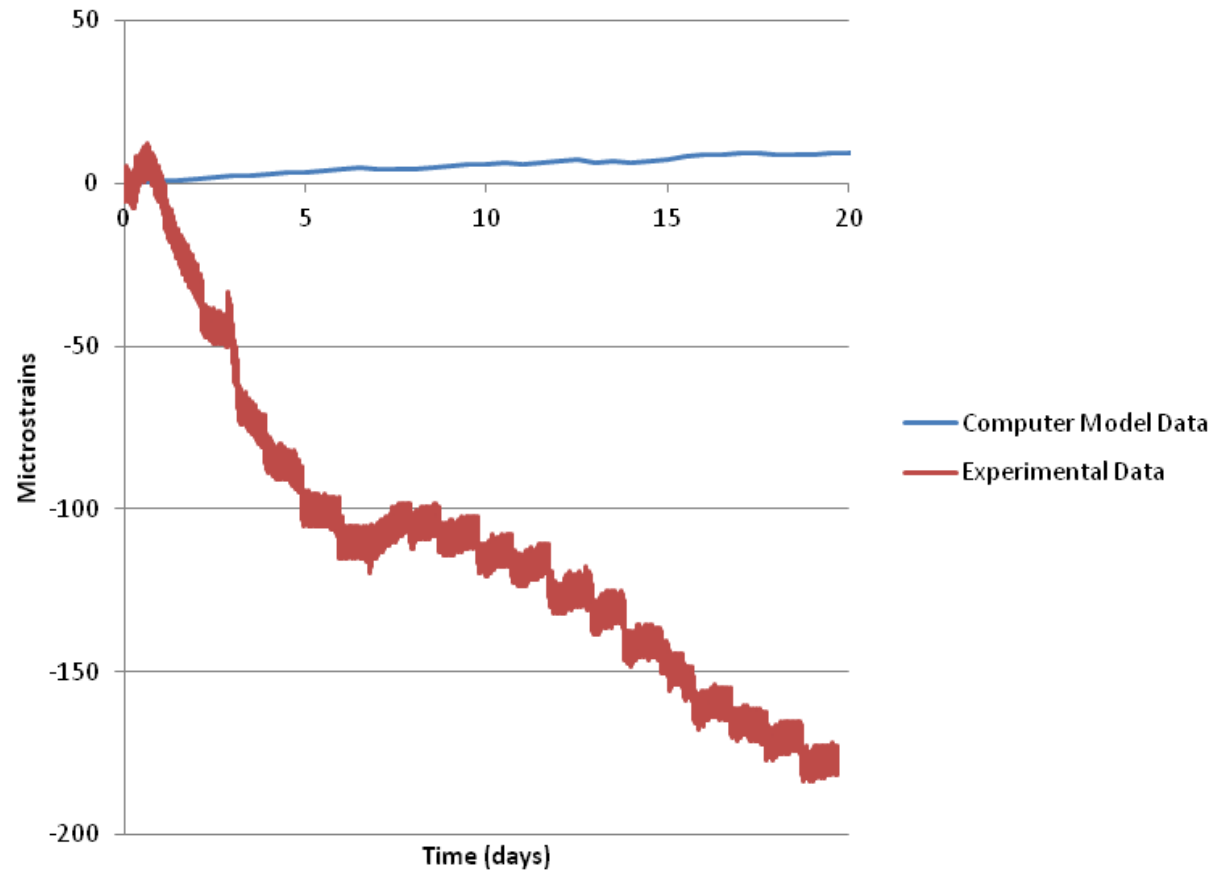
S-G1-W-I-1/2-L



S-G1-Tf-M-1/2-L

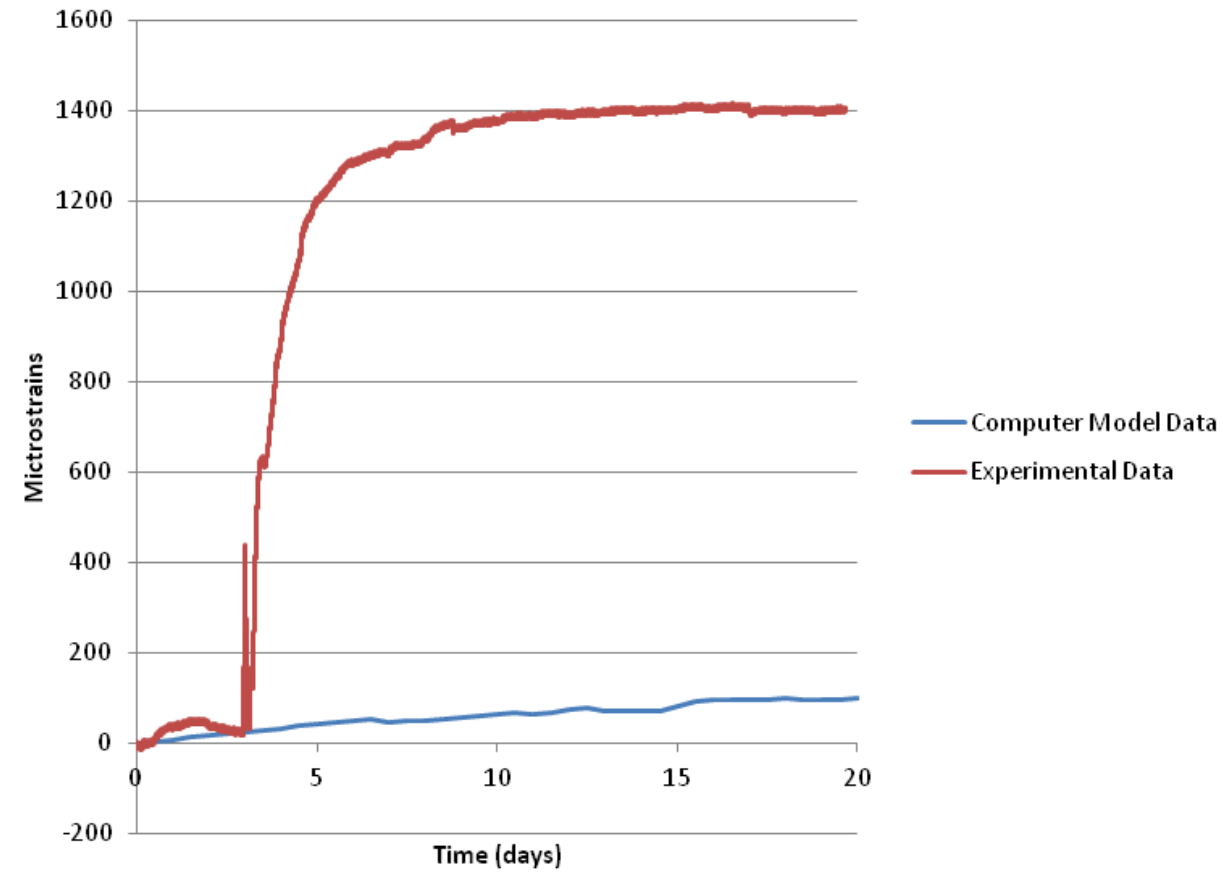
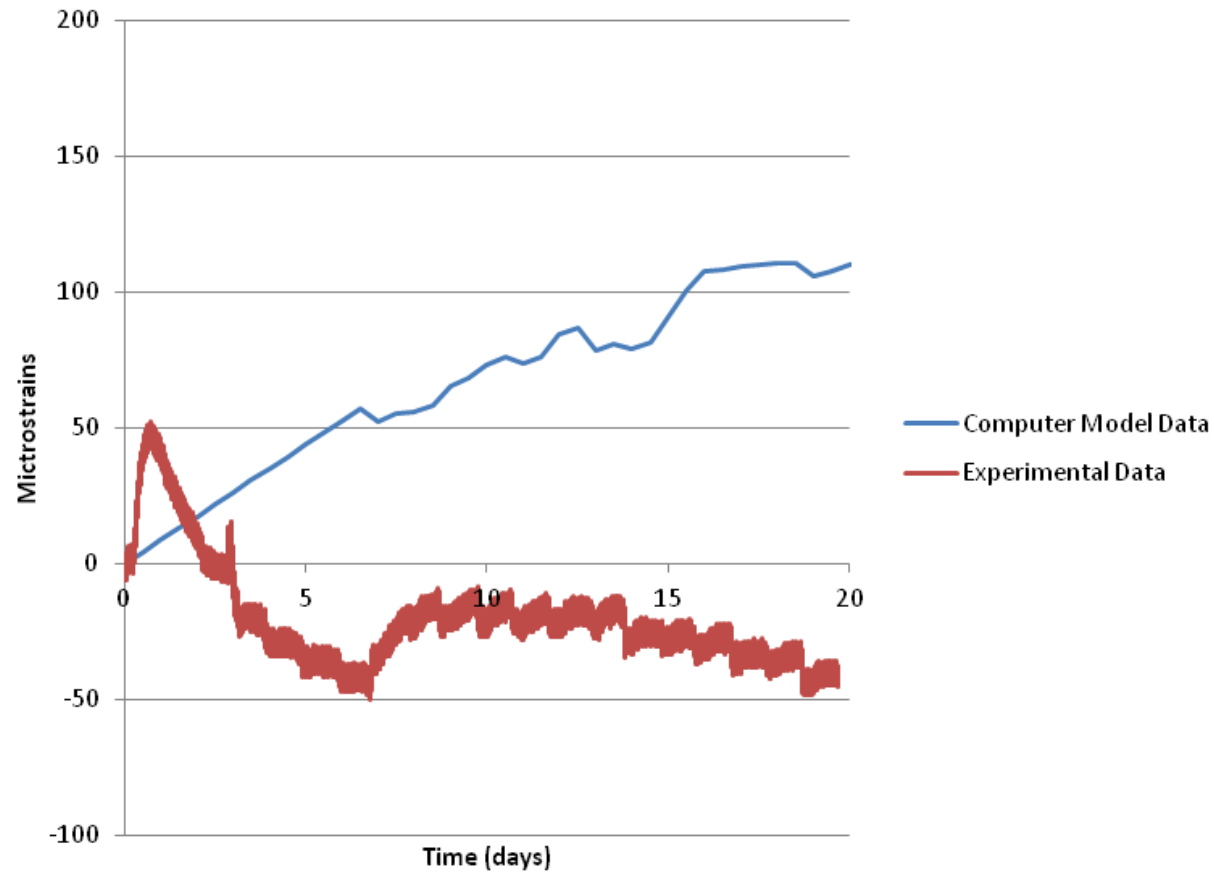


S-G1-Bf-M-1/4-L

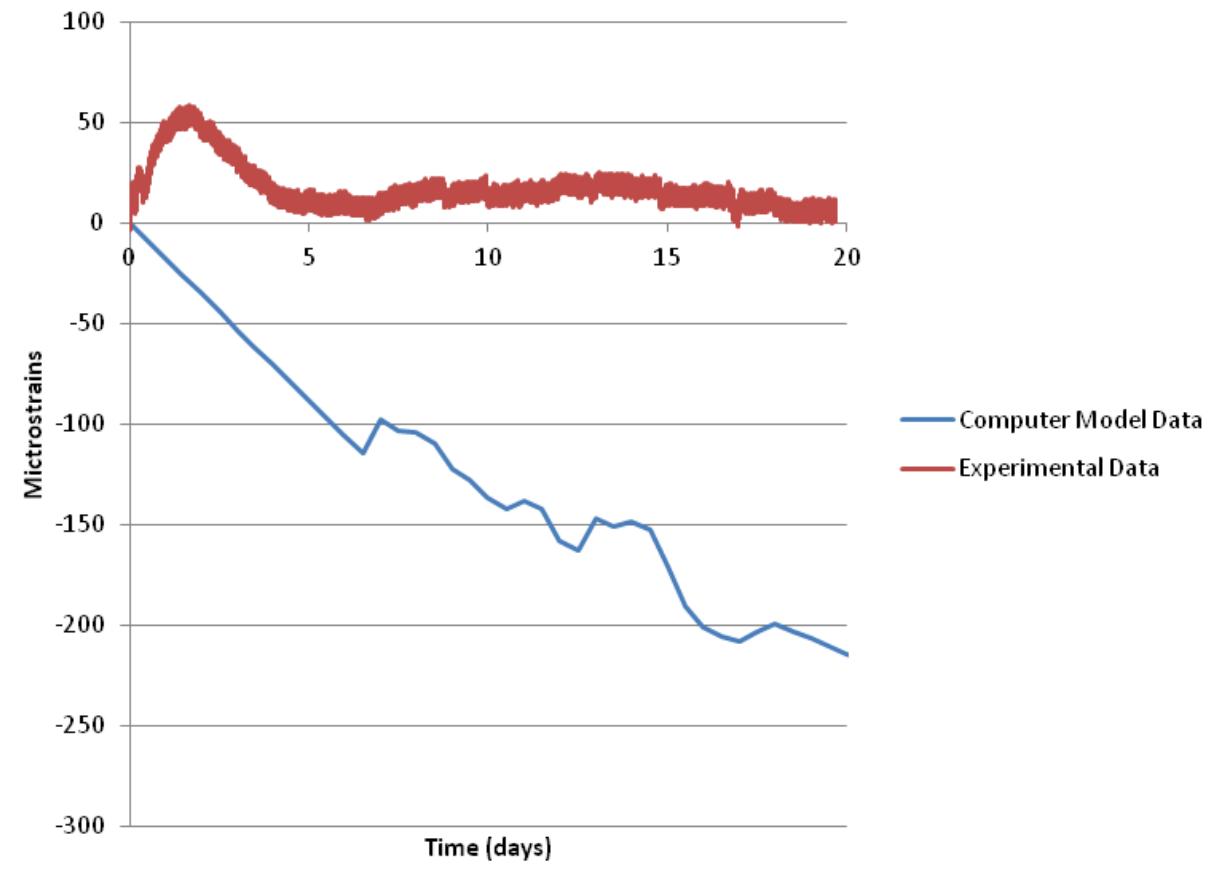
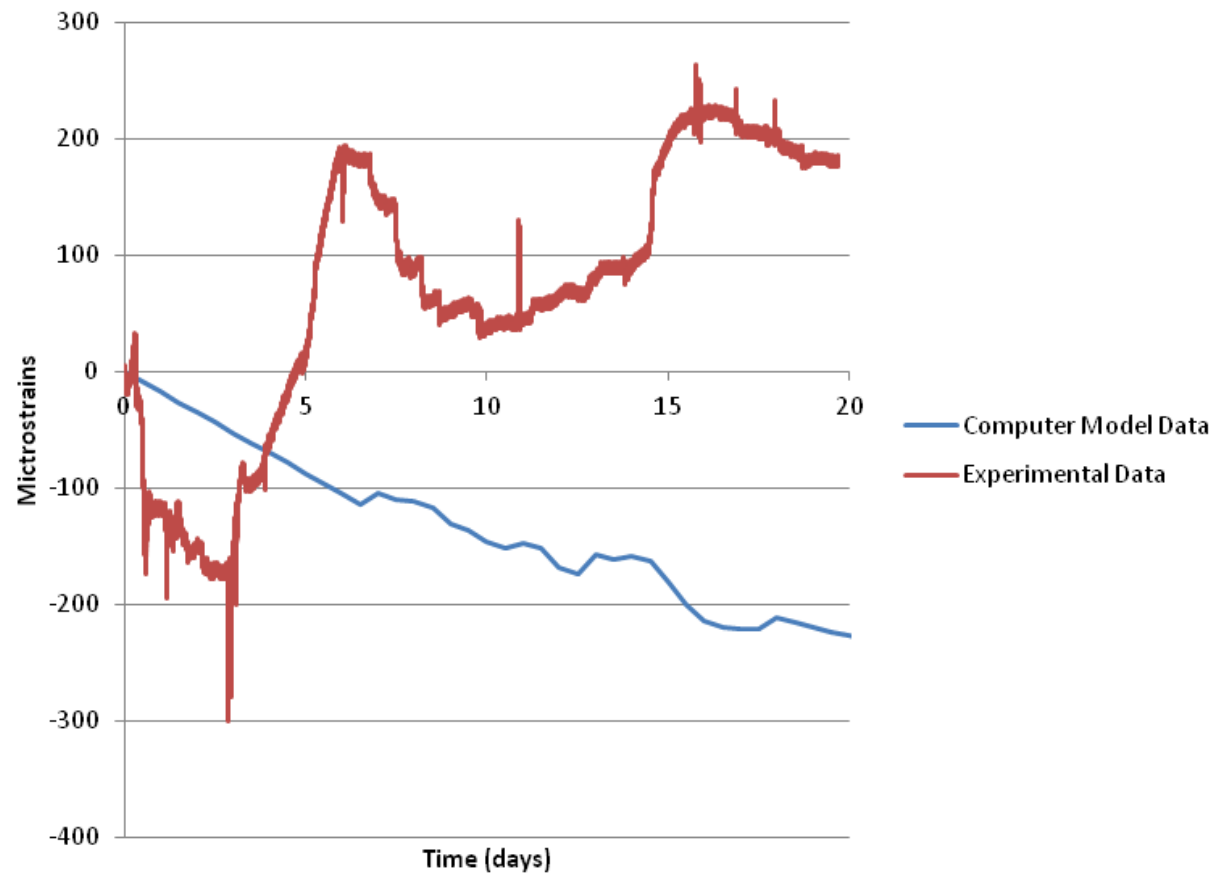




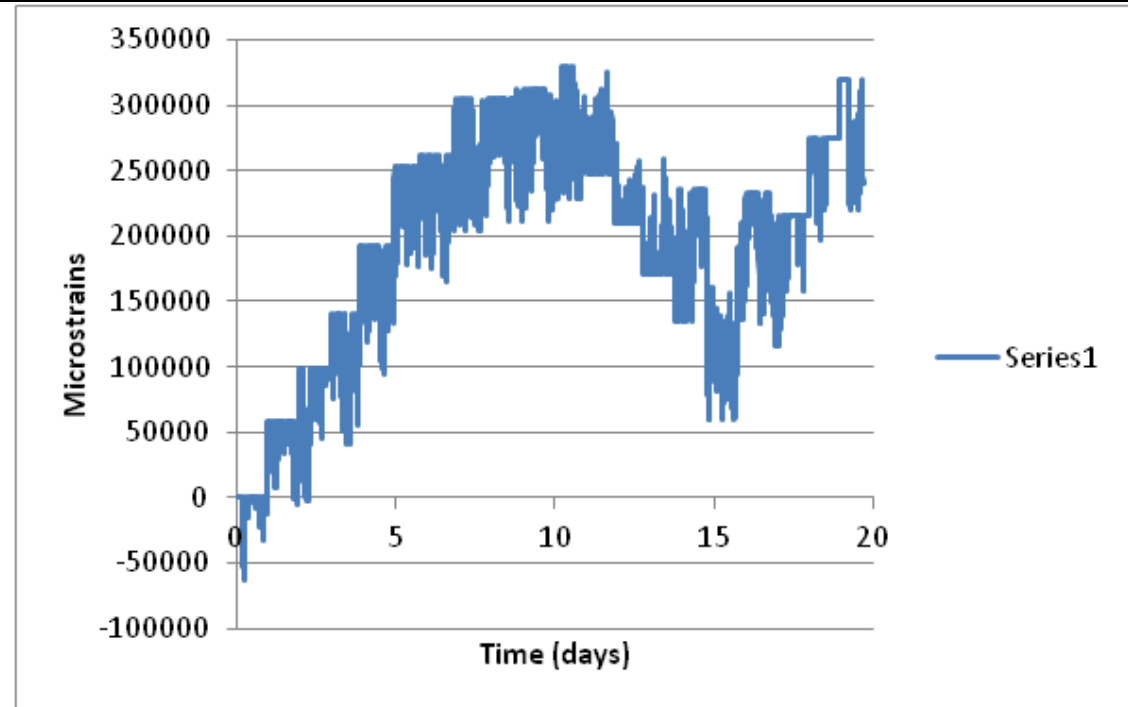
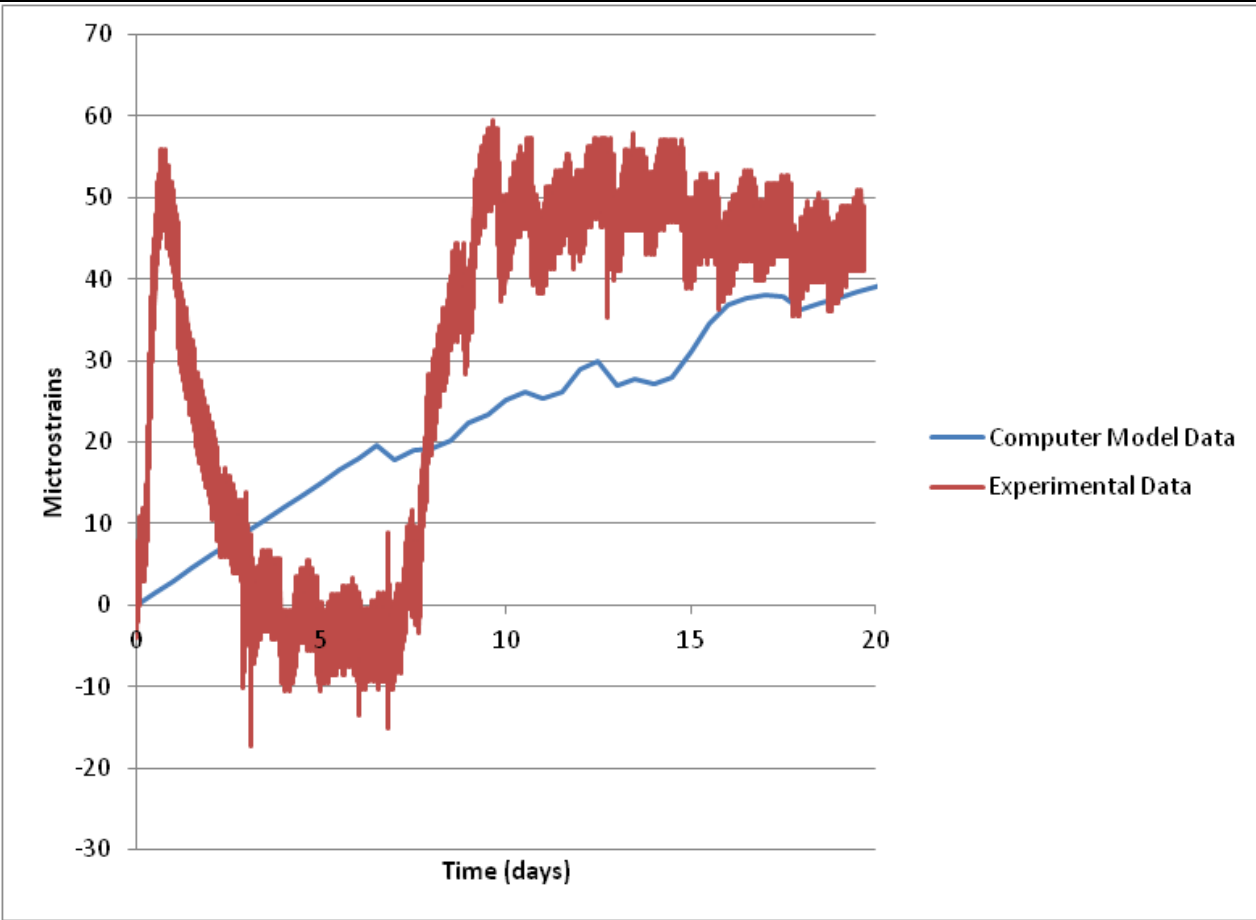
S-G1-Bf-O-1/2-L



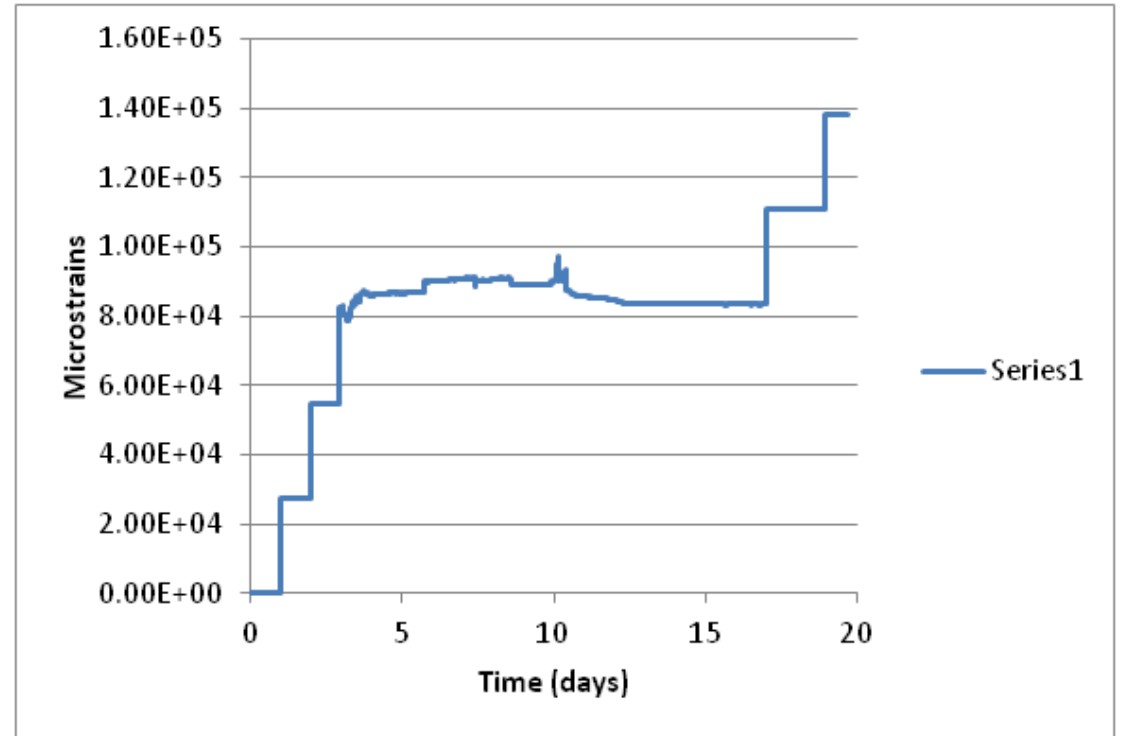
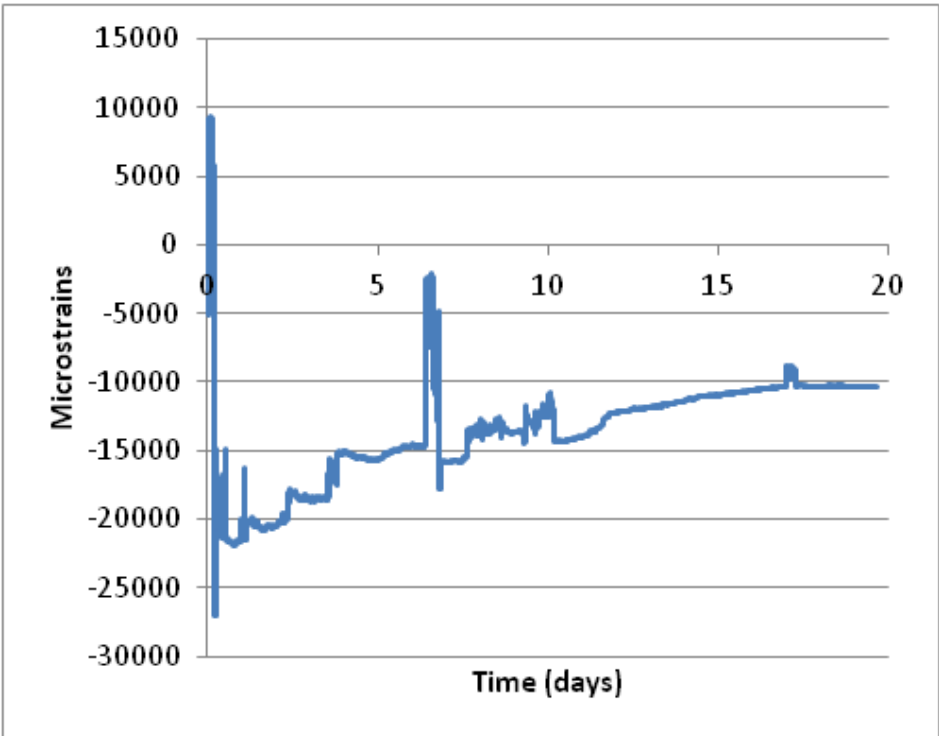
S-G2-Tf-M-1/2-L



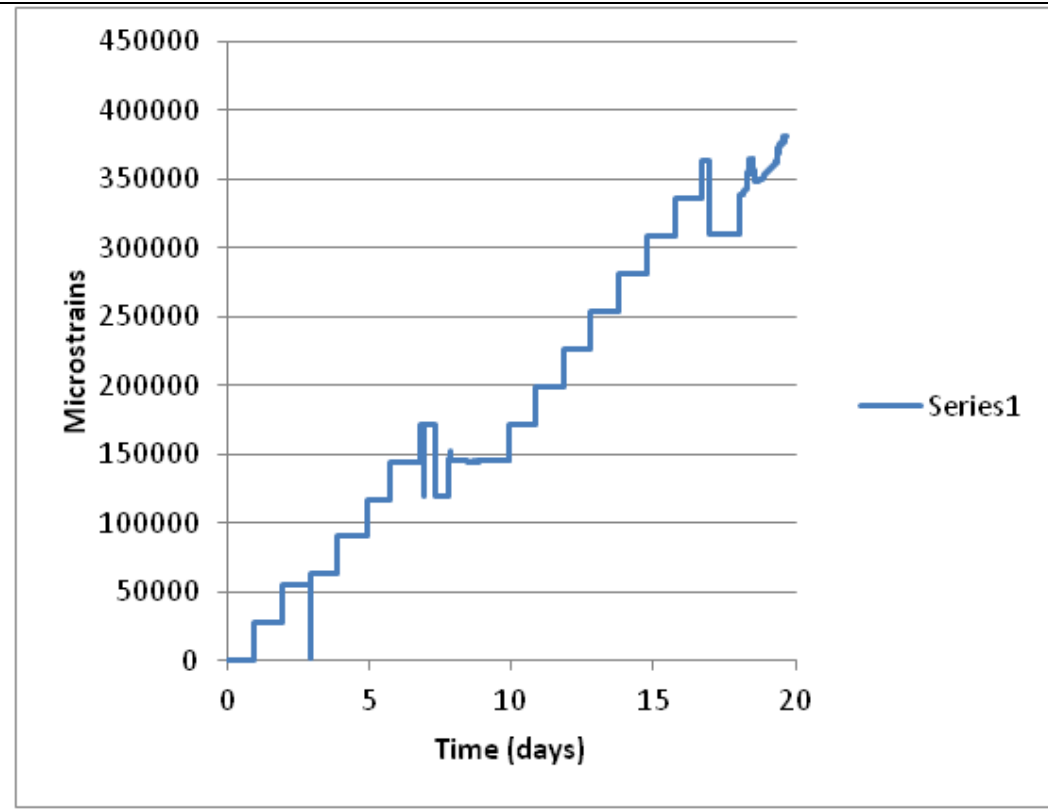
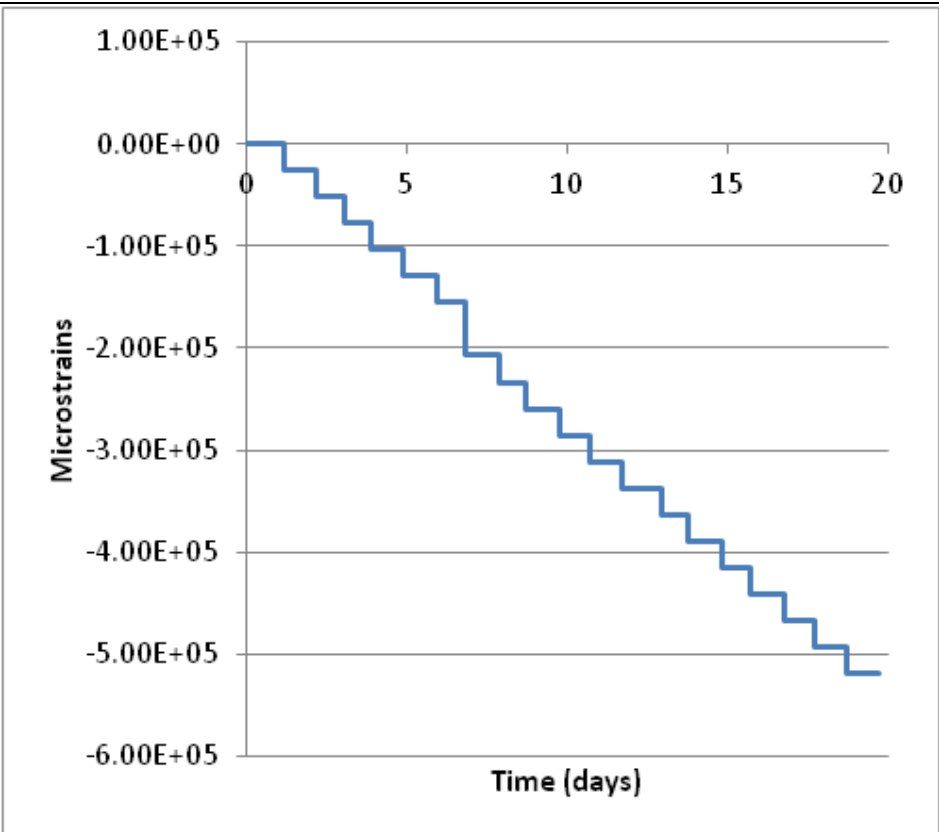
S-G2-Bf-M-1/2-L



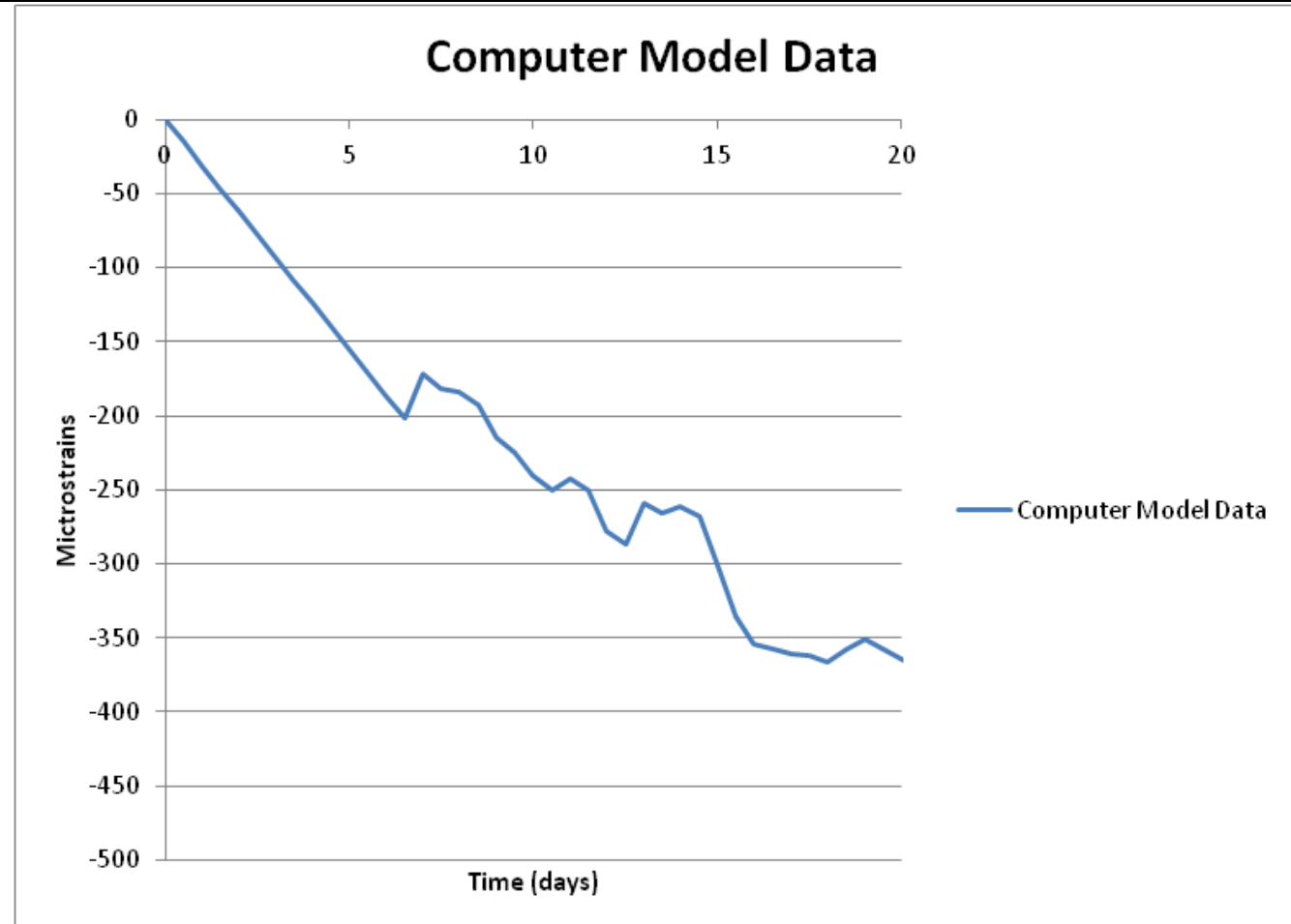
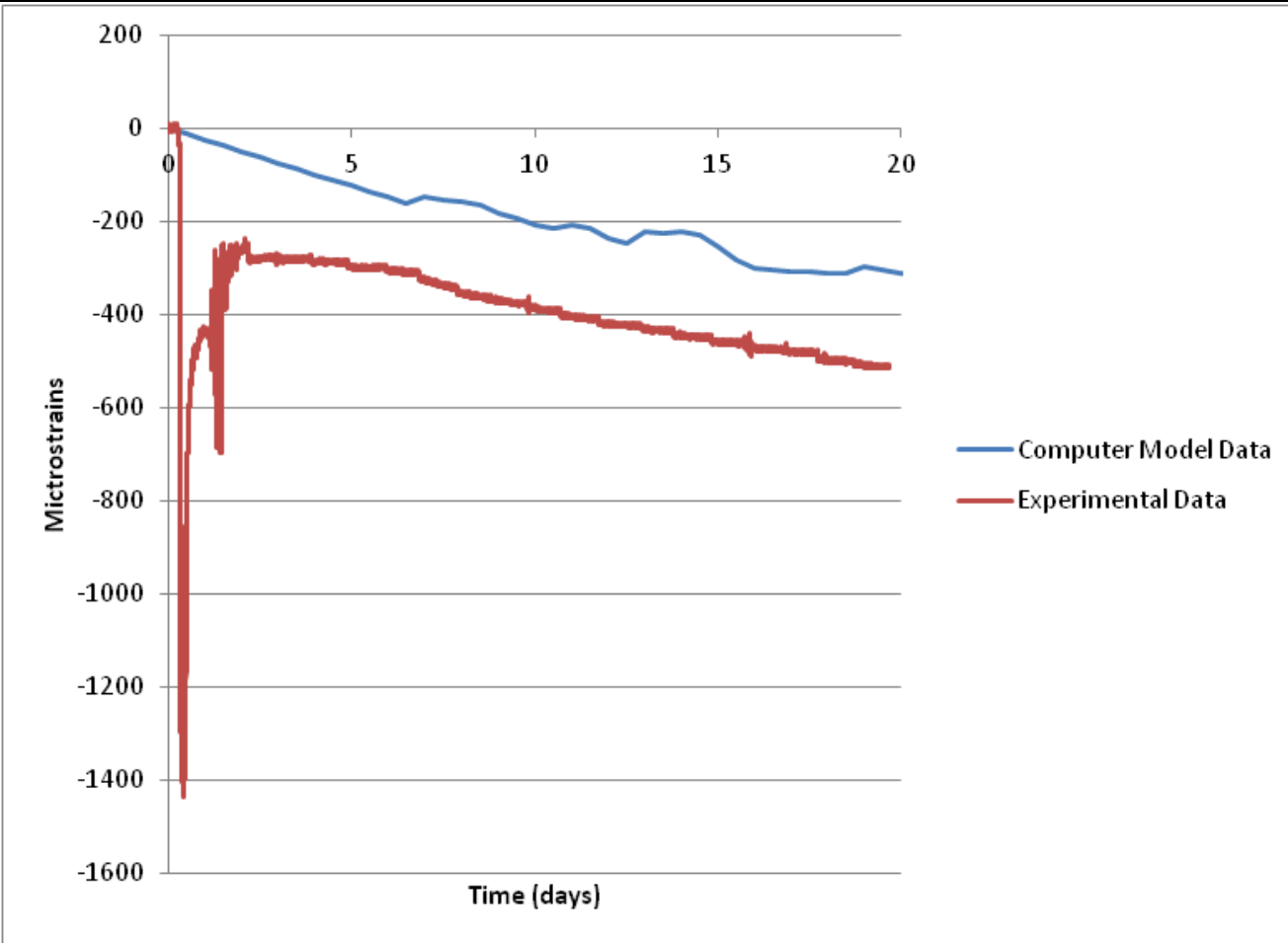
S-Tp-G1-1/2-L



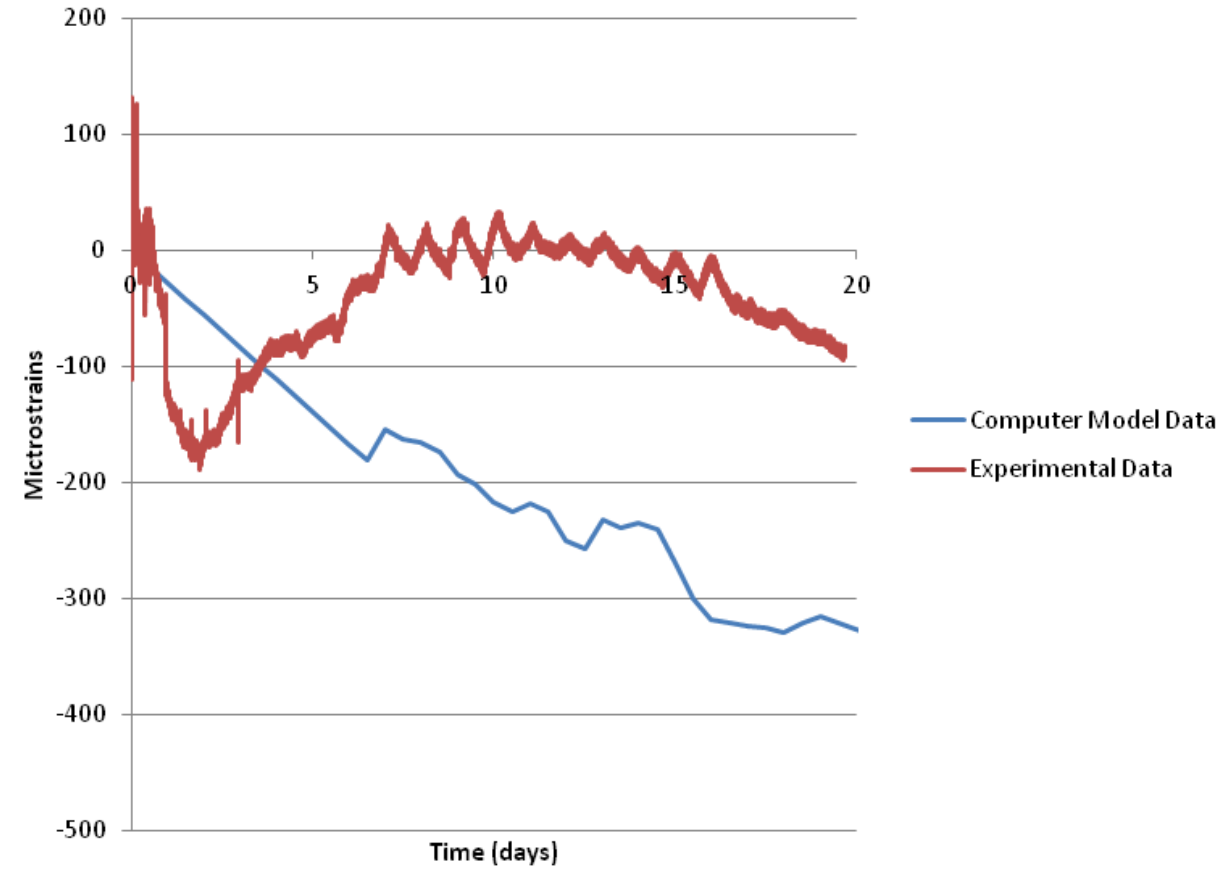
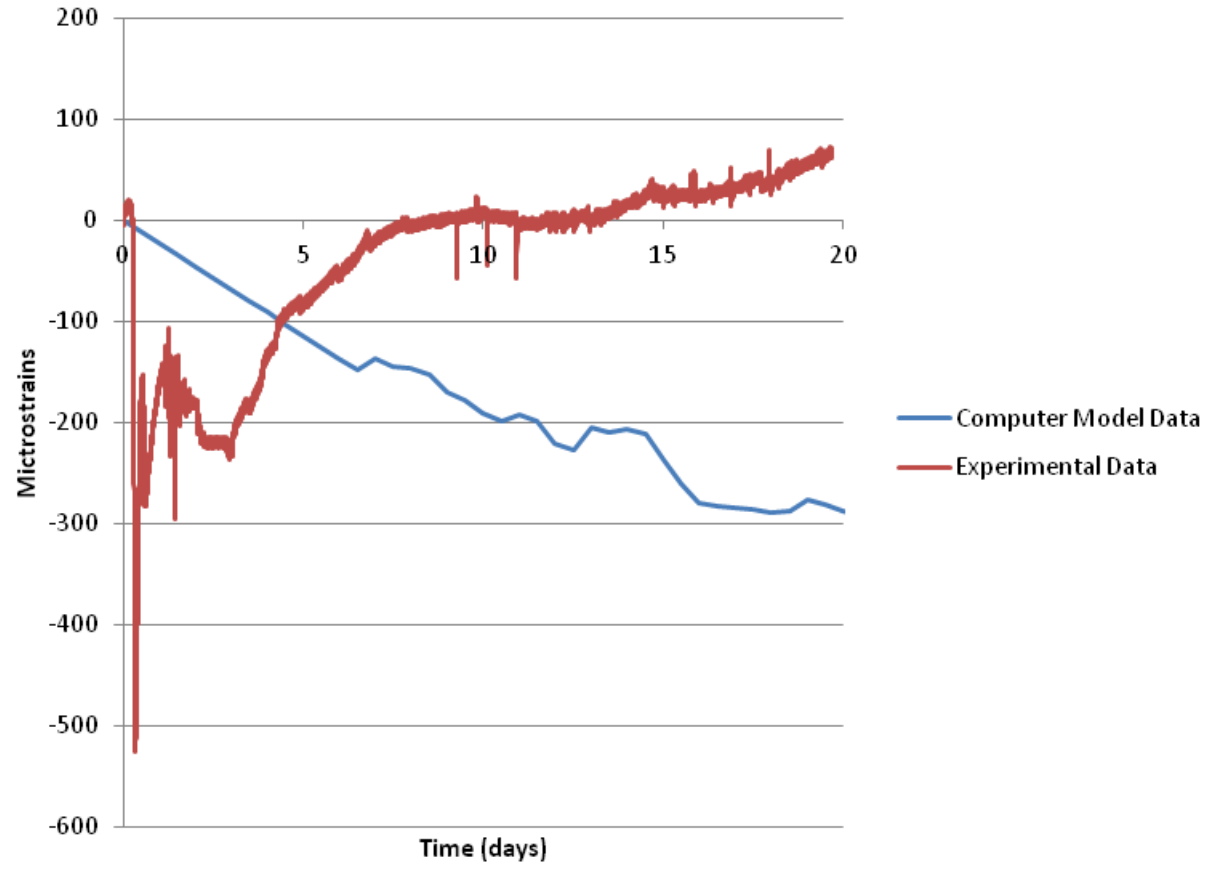
S-Tp-1/2-1/2-T



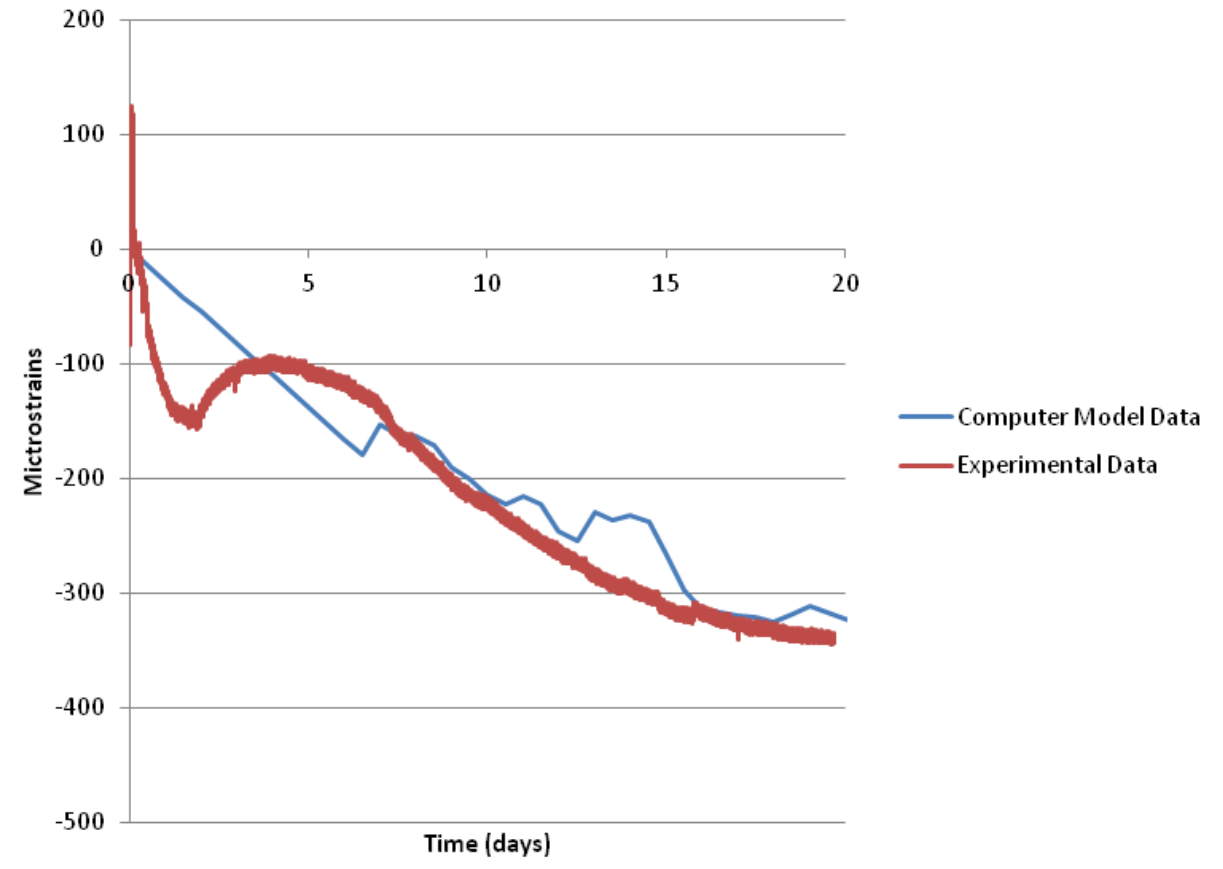
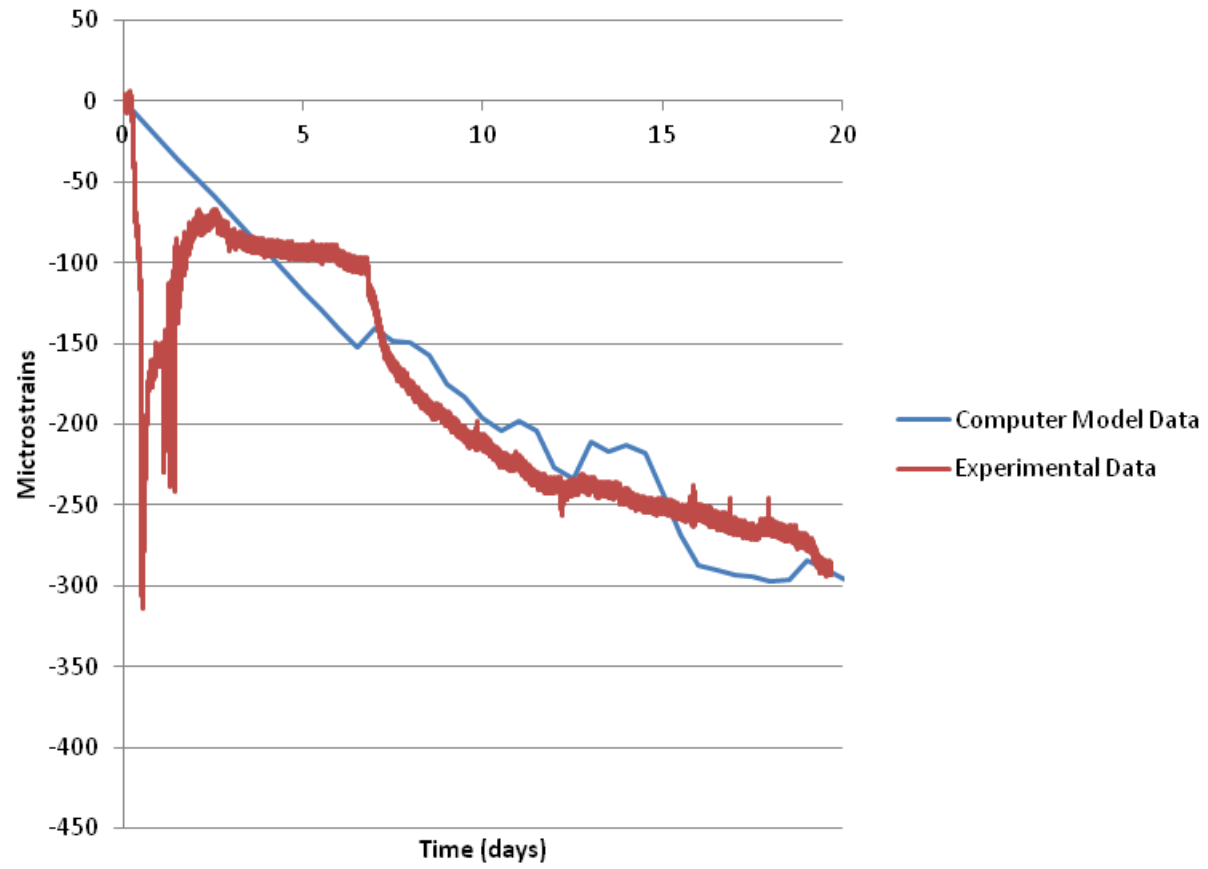
S-Tp-1/2-1/4-T



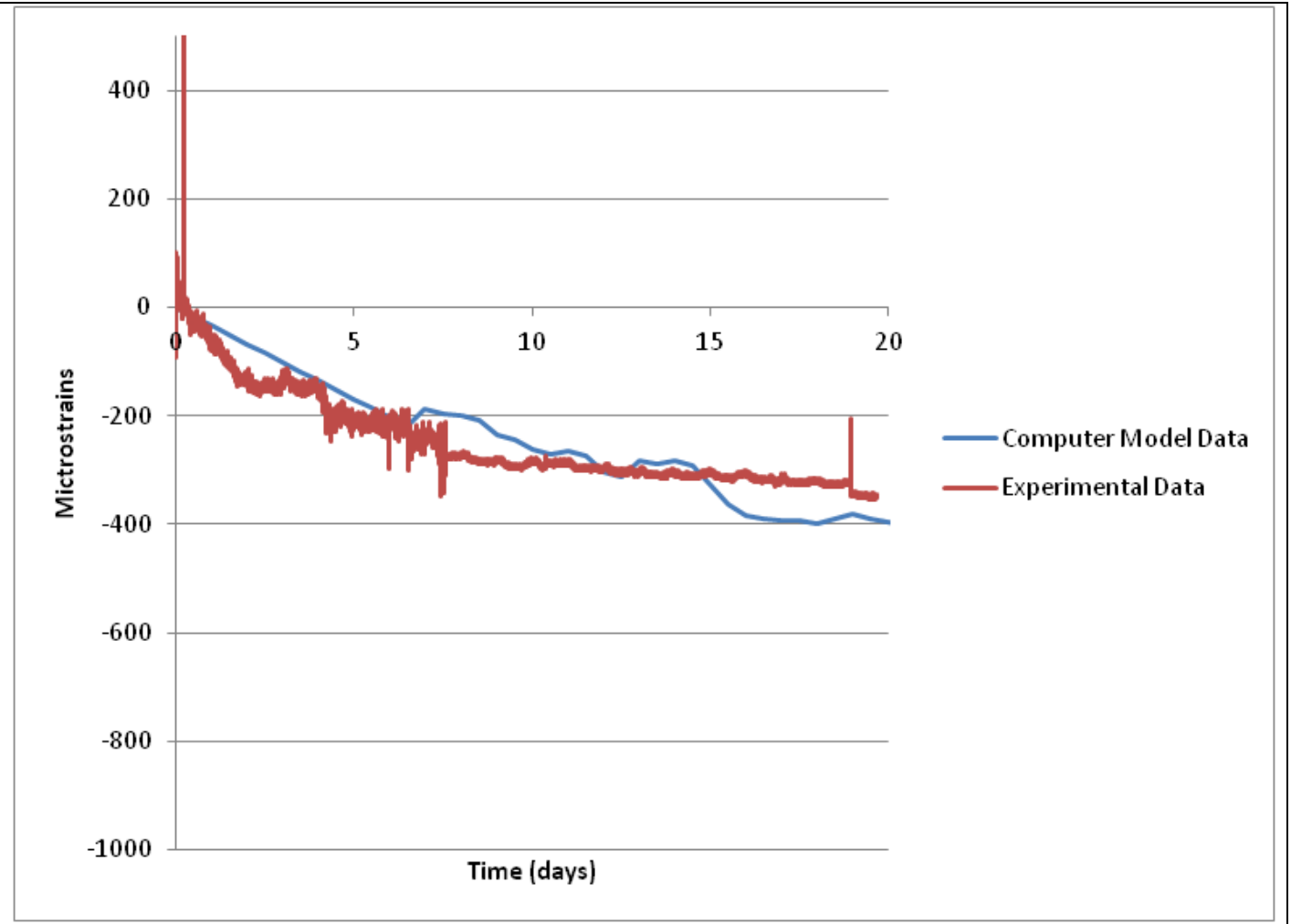
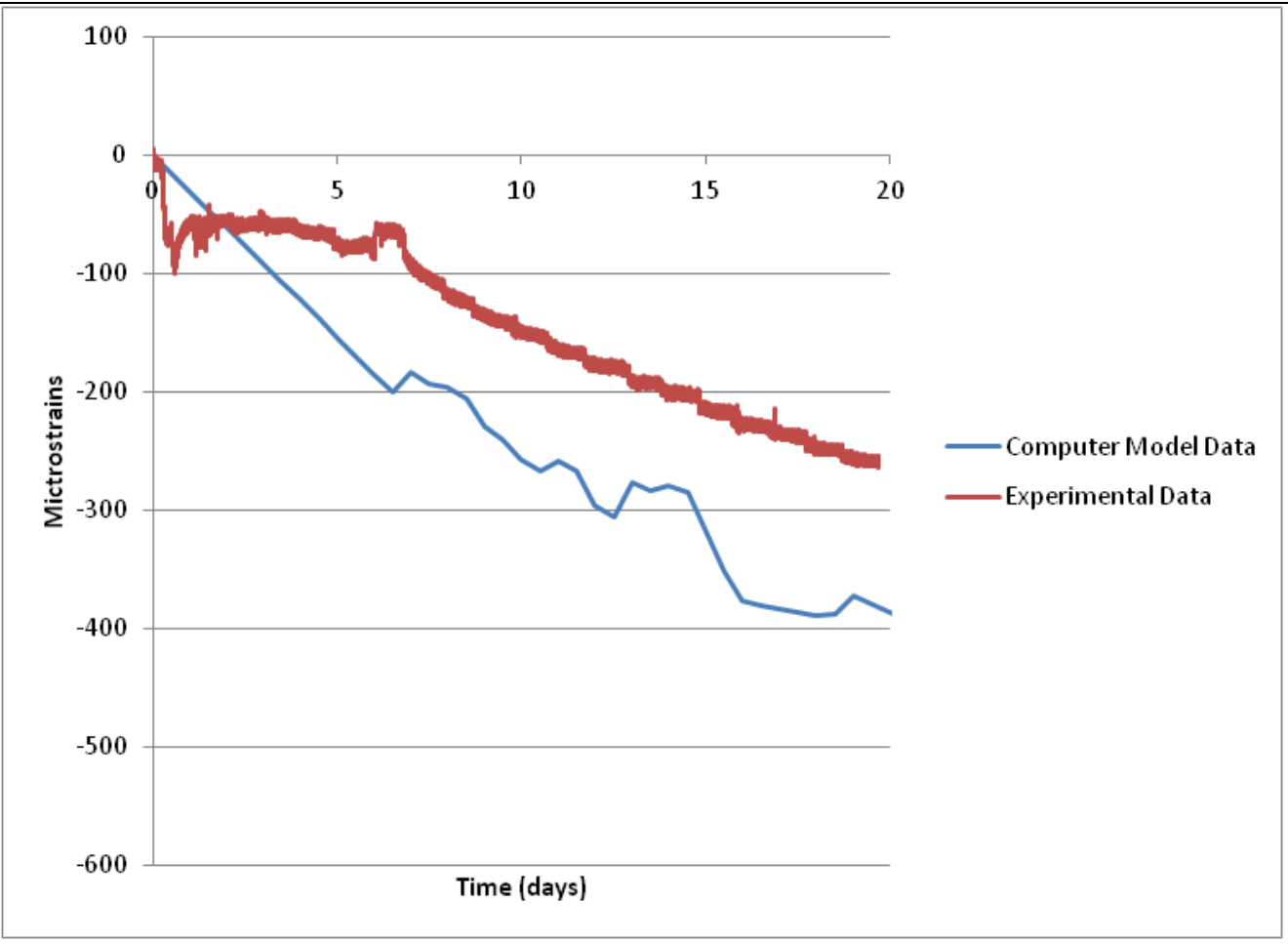
S-Tp-1/2-3/4-L



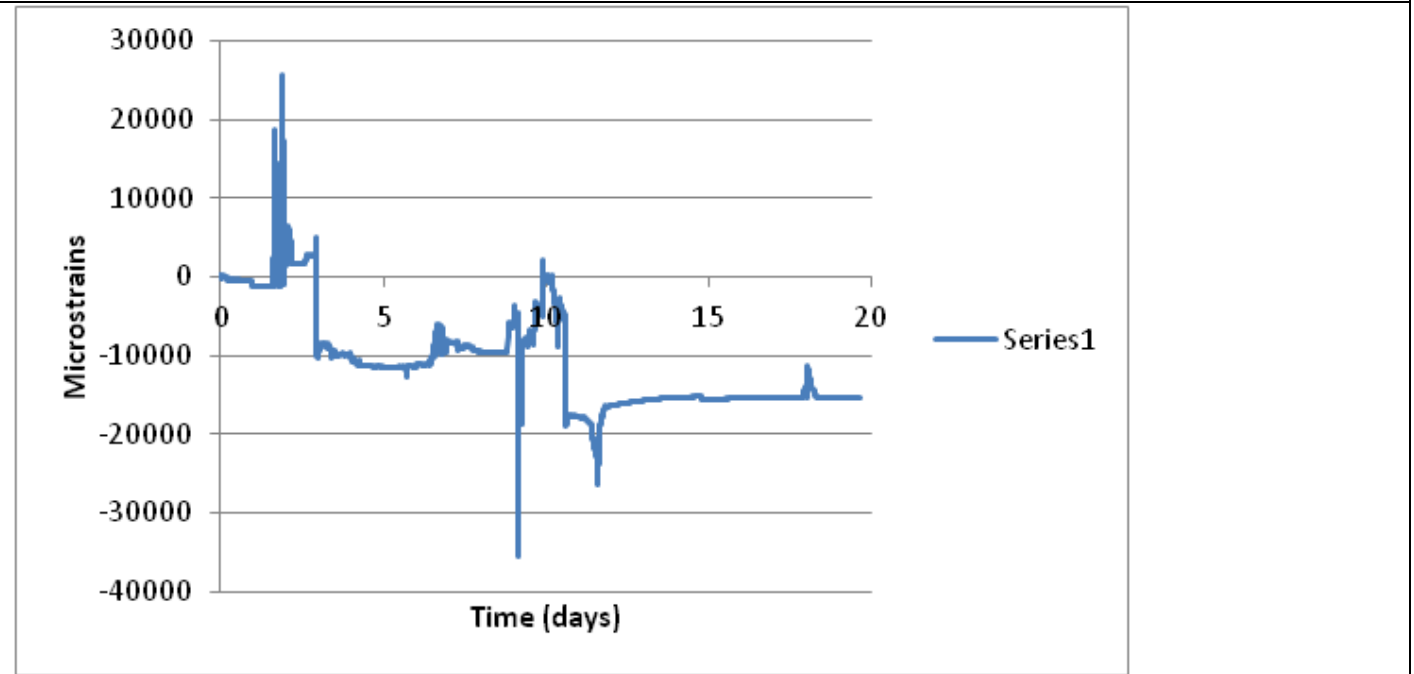
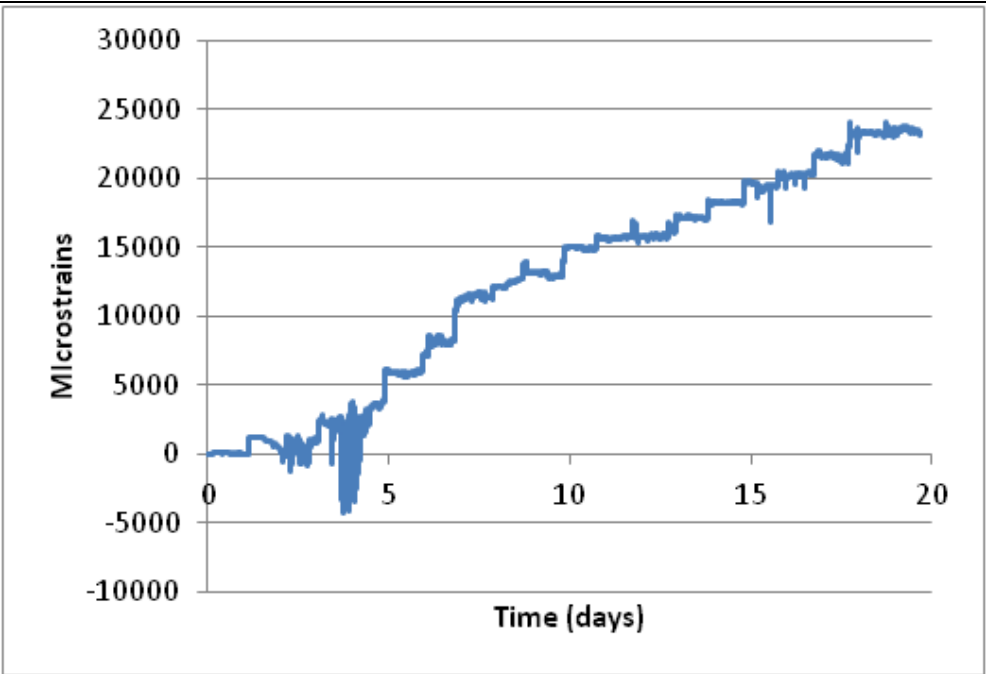
S-Tp-1/2-1/2-L



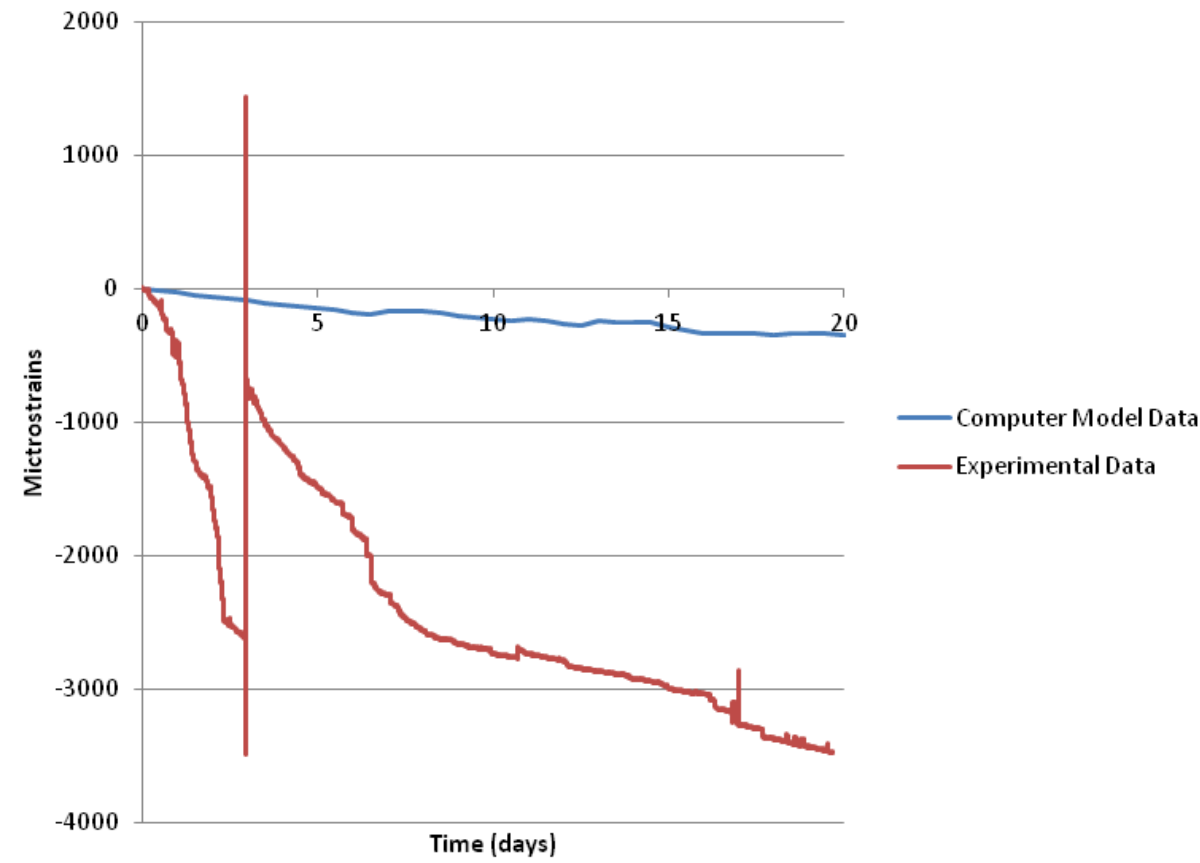
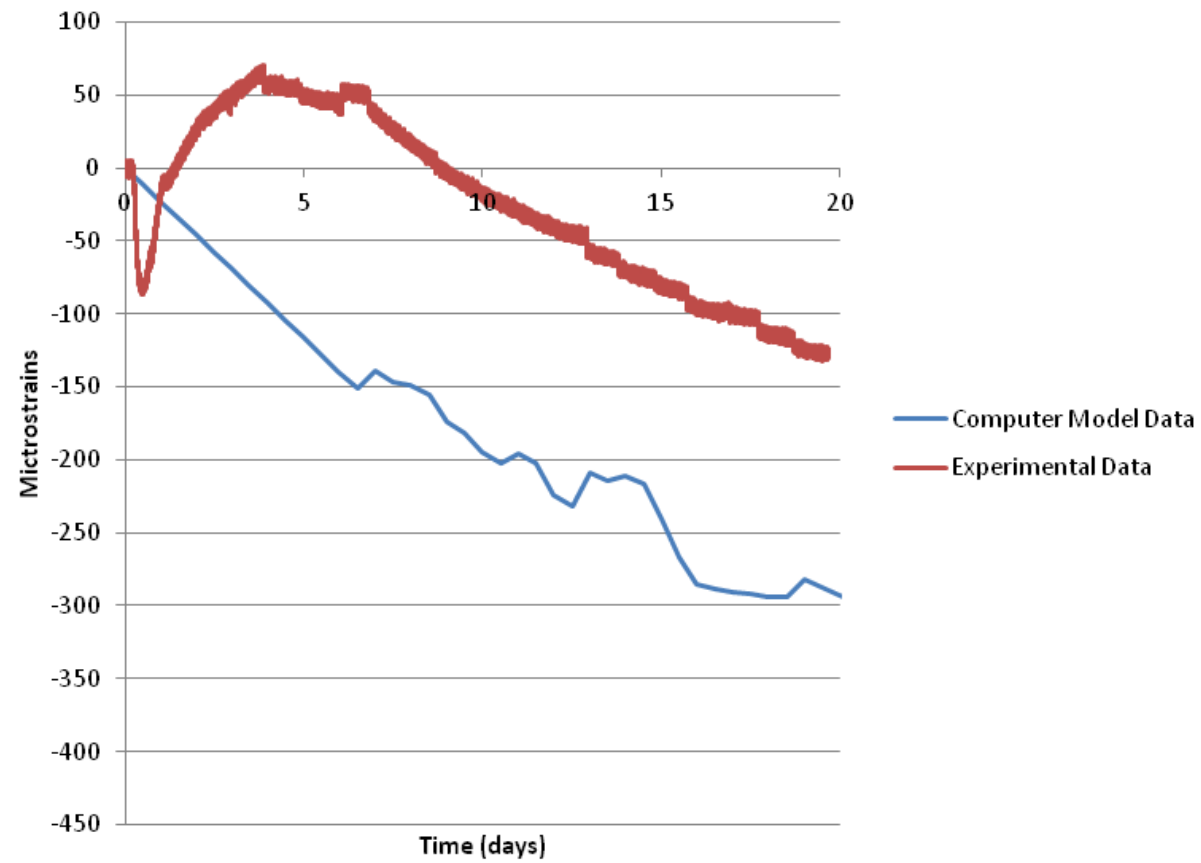
S-Tp-G2-1/2-L



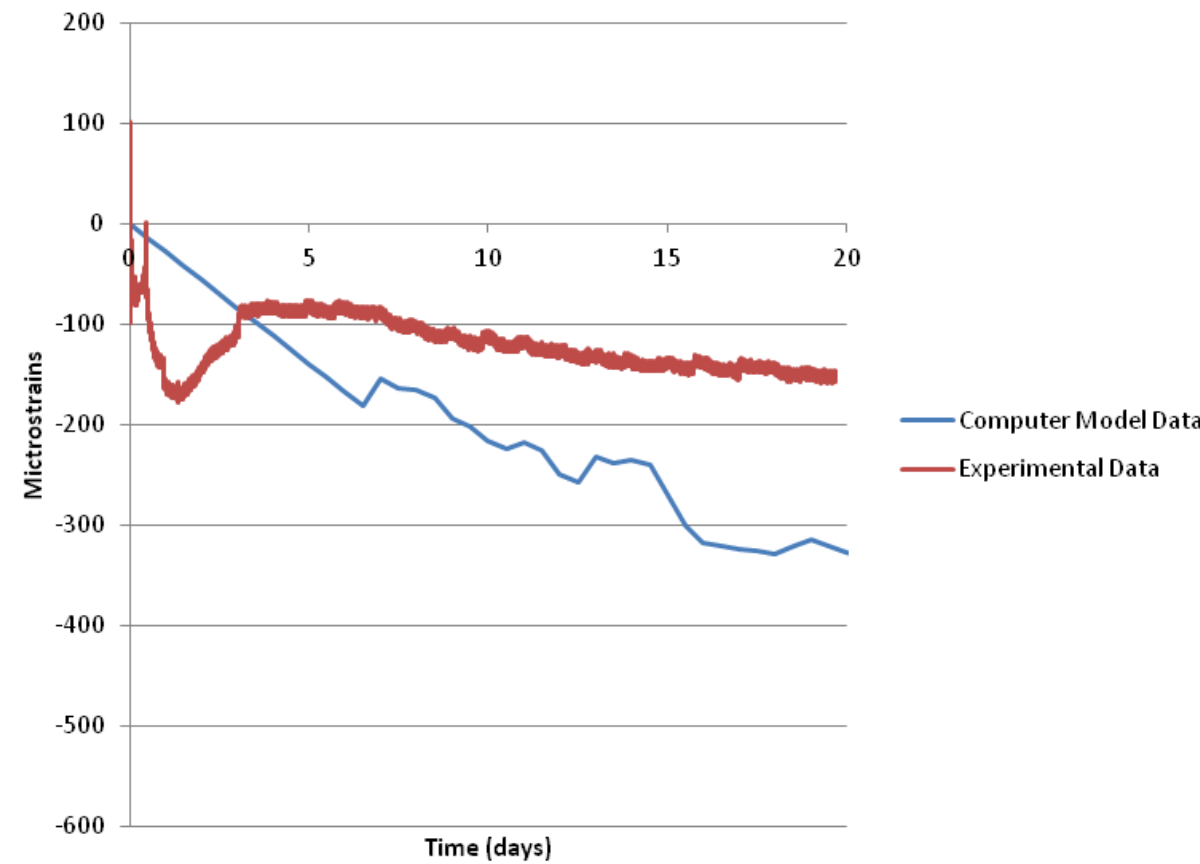
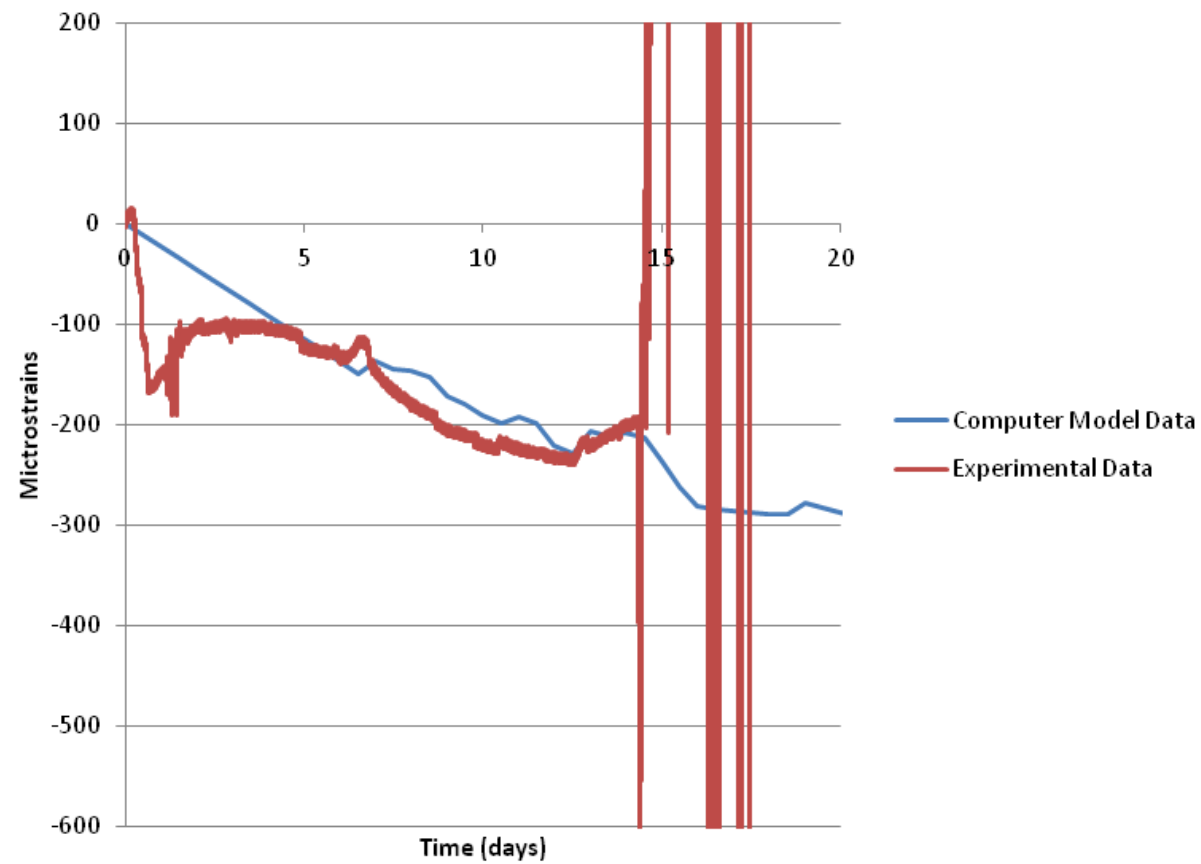
S-Tp-G1-3/4-L



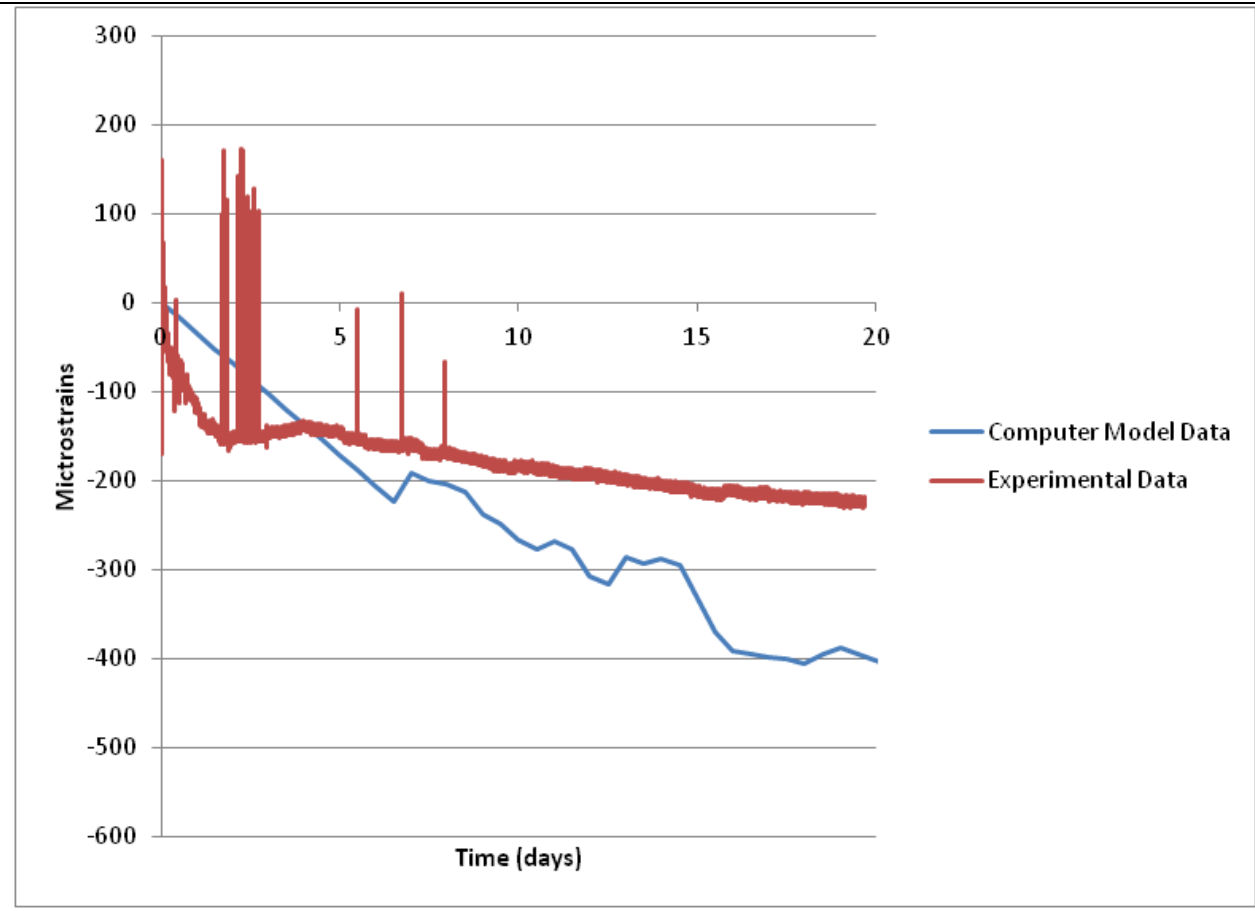
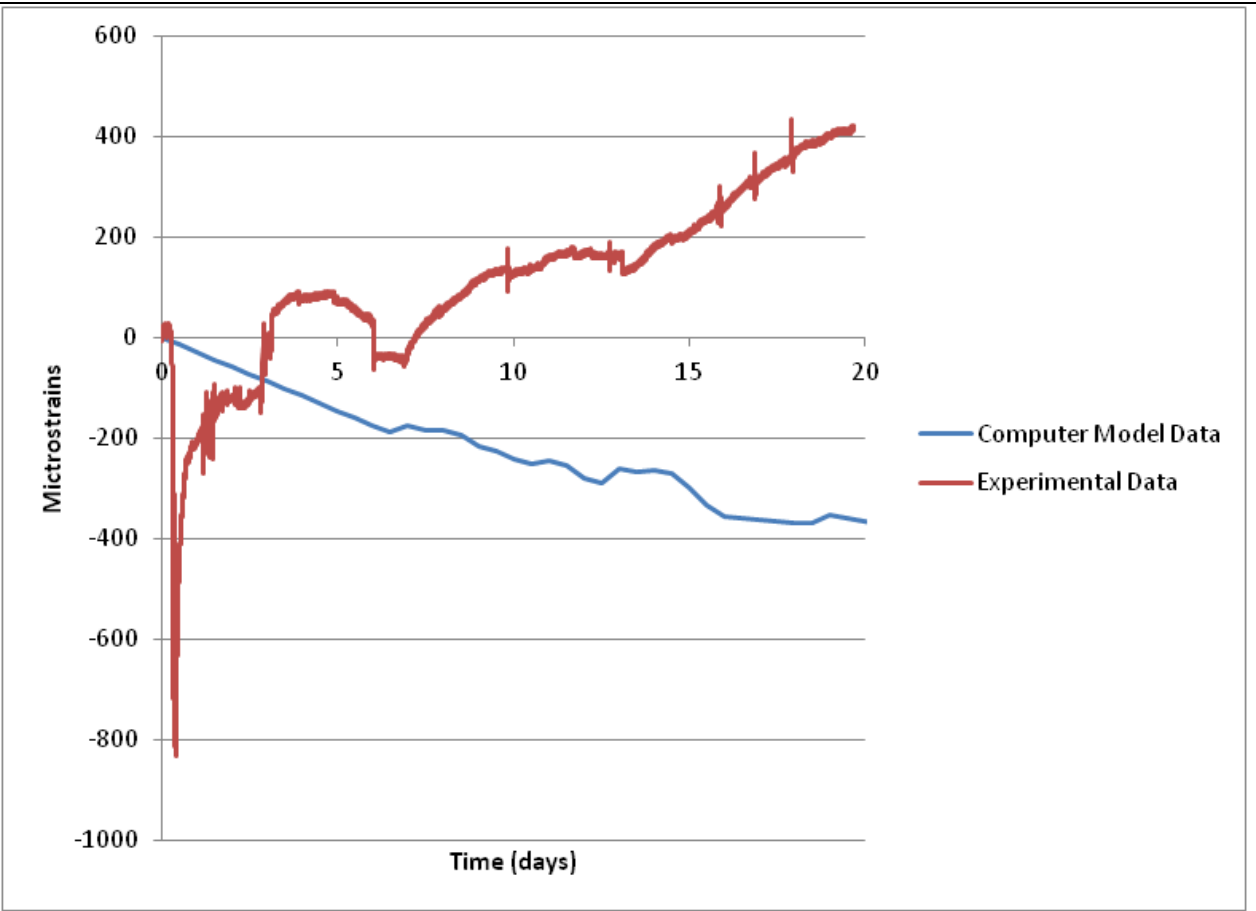
S-Tp-1/3-3/4-L



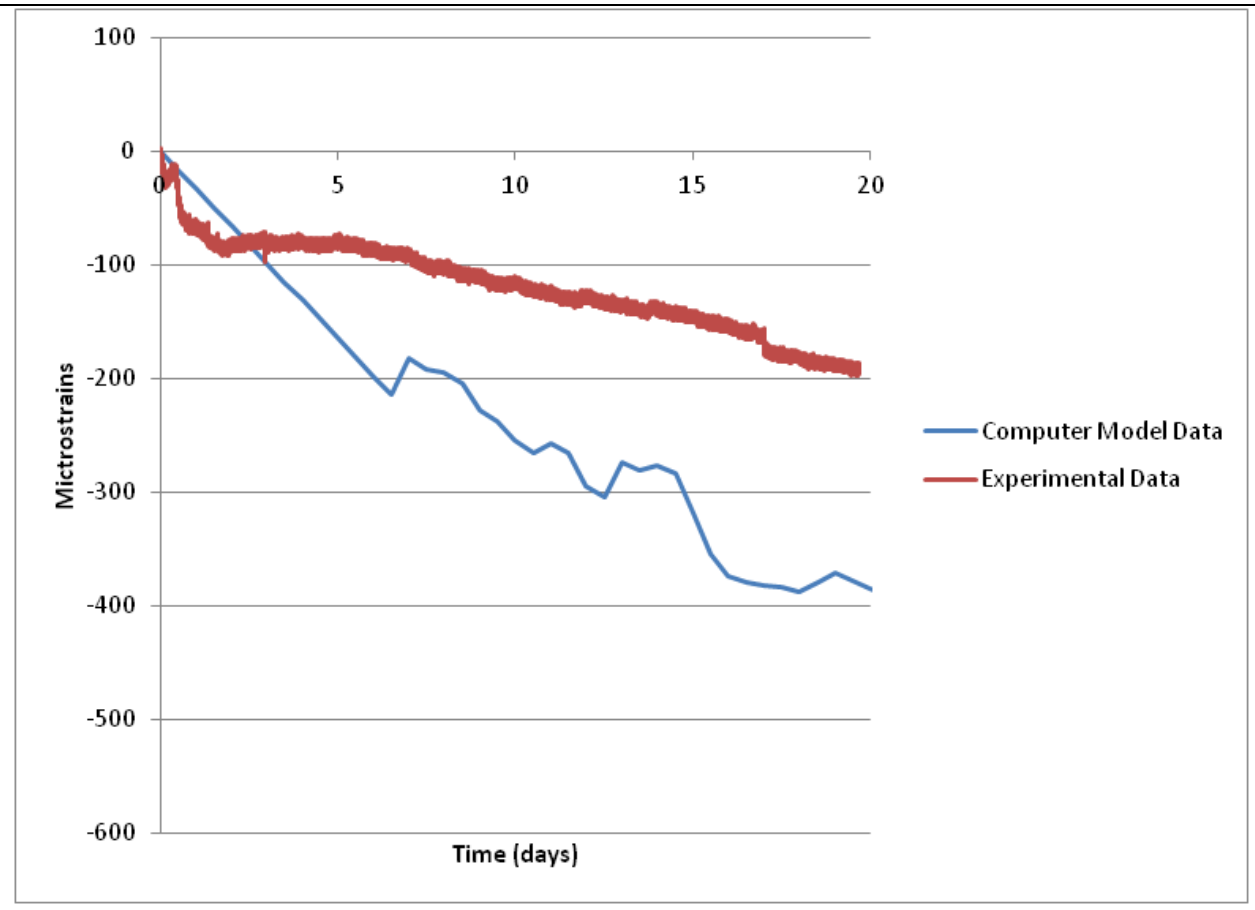
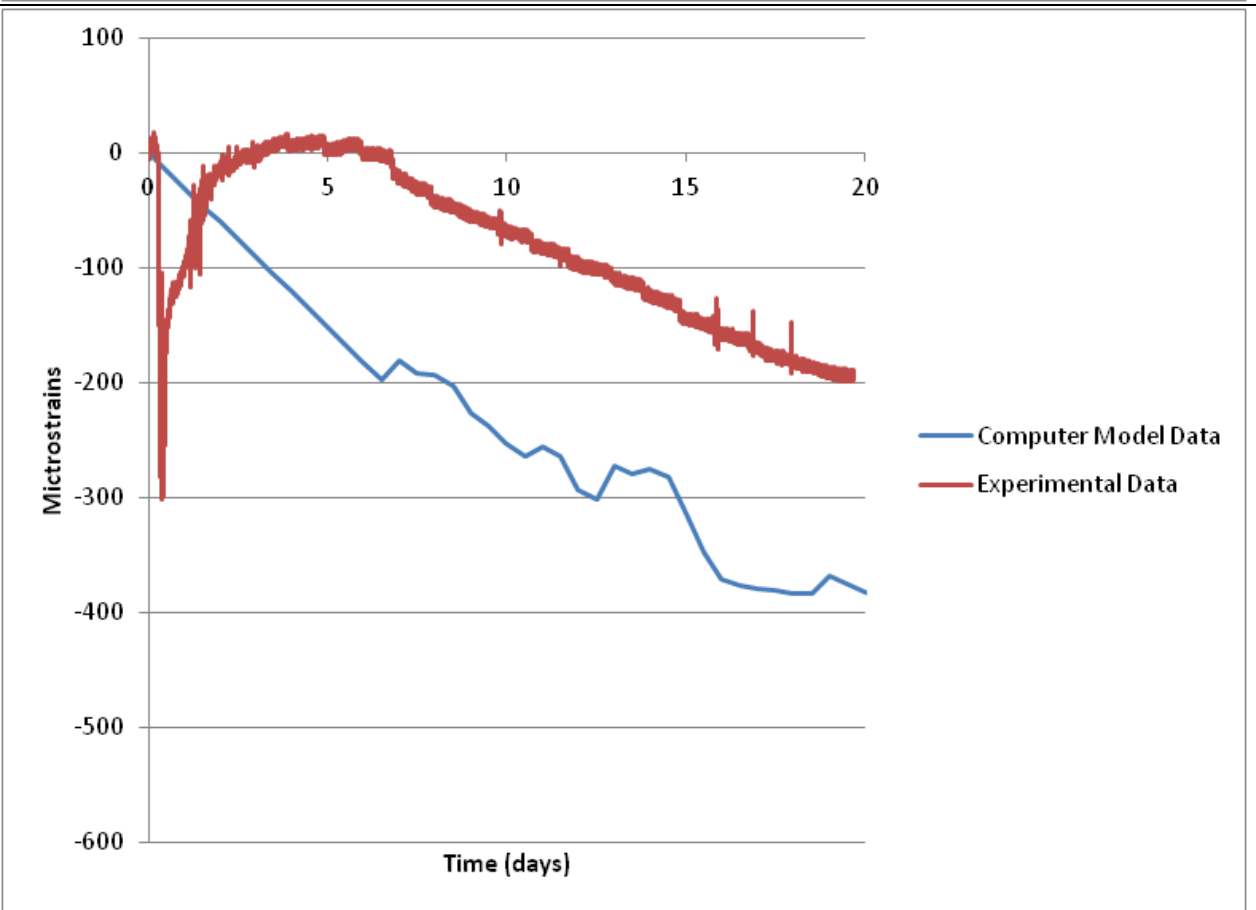
S-Tp-1/2-1/4-L



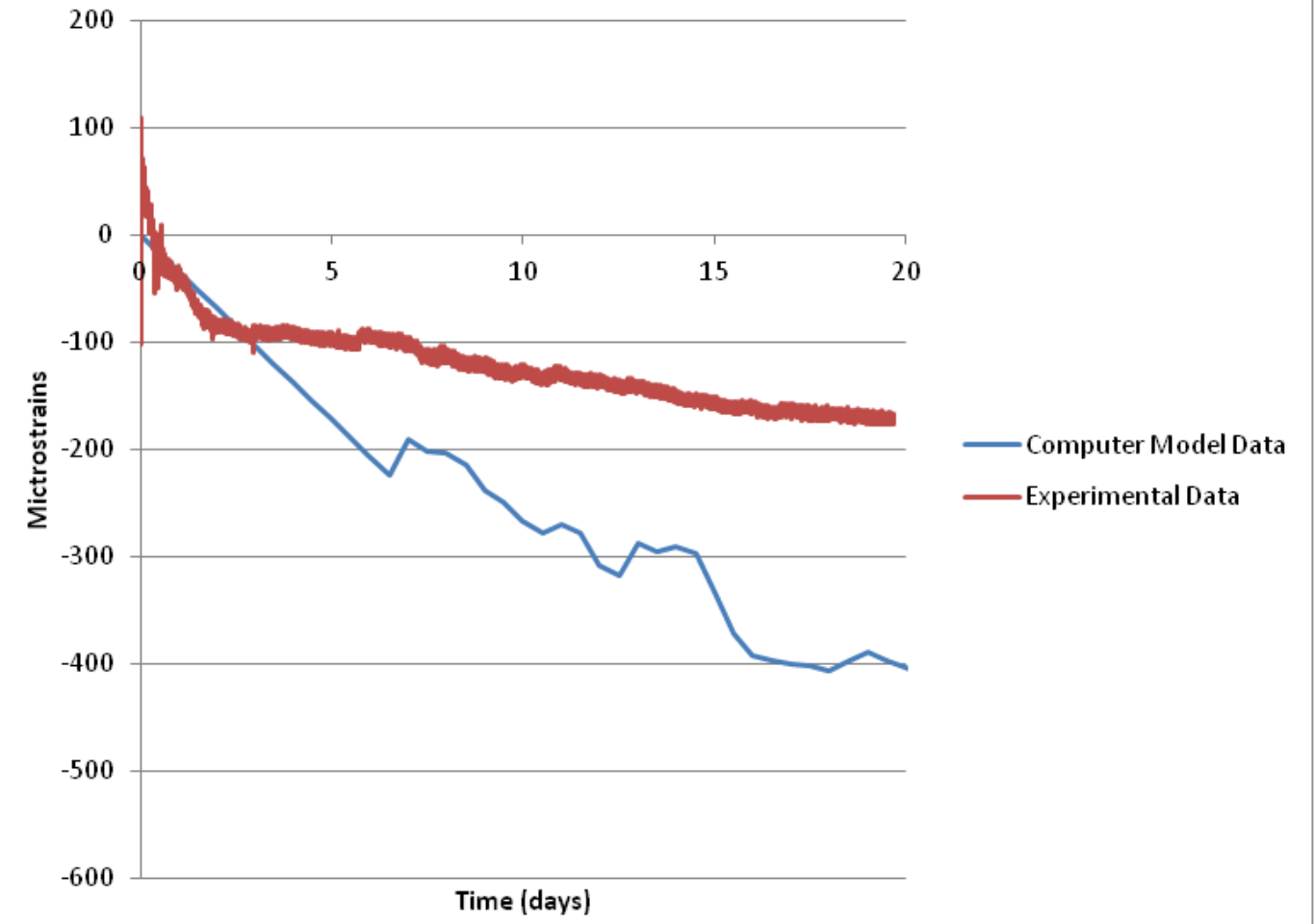
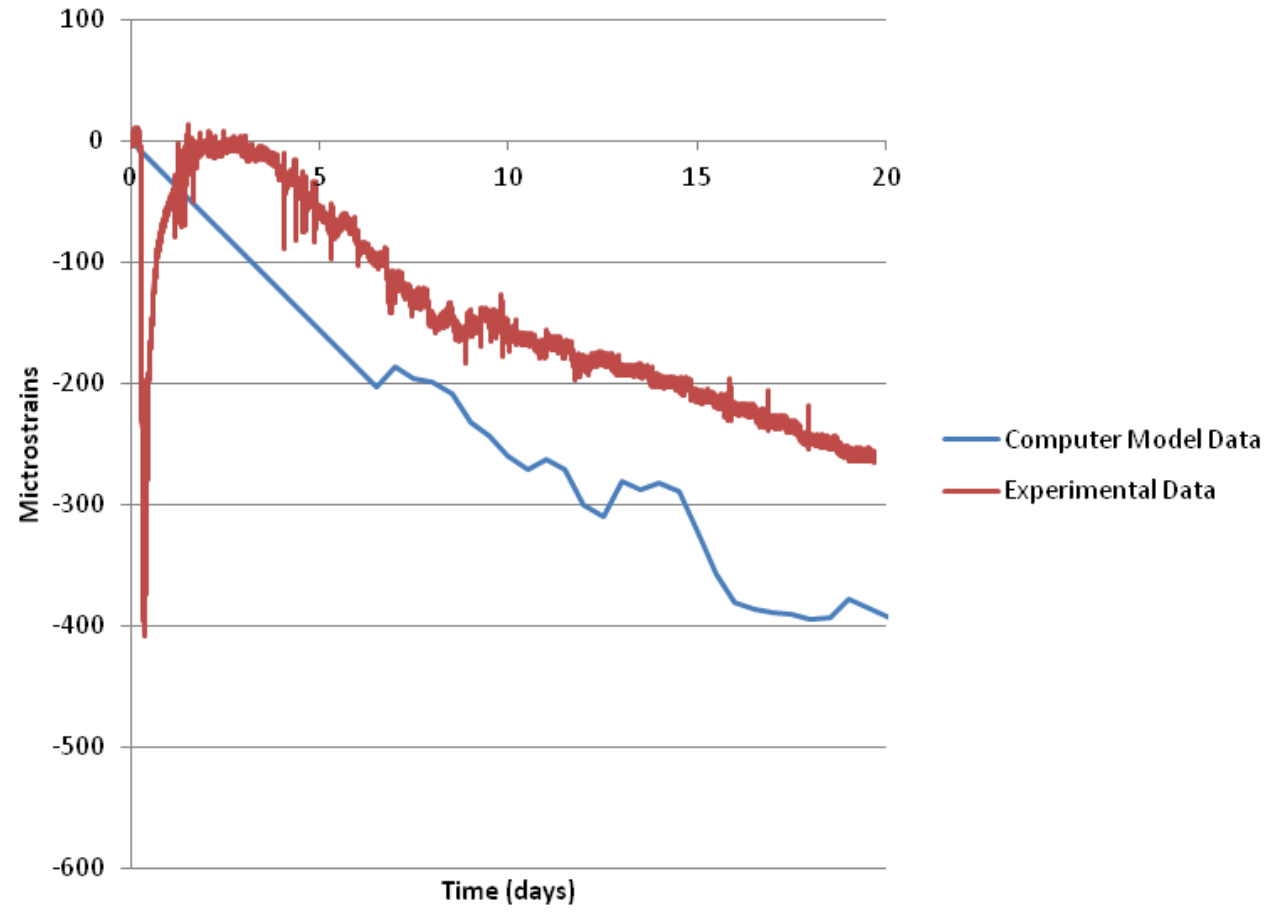
S-Tp-G1-1/4-T



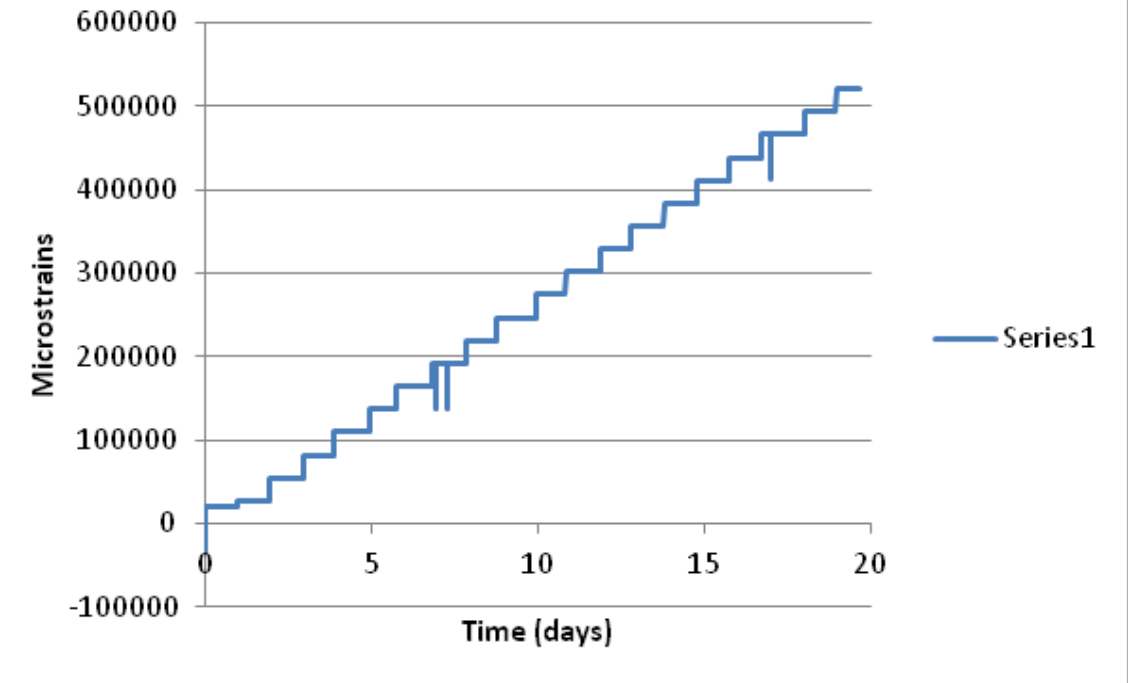
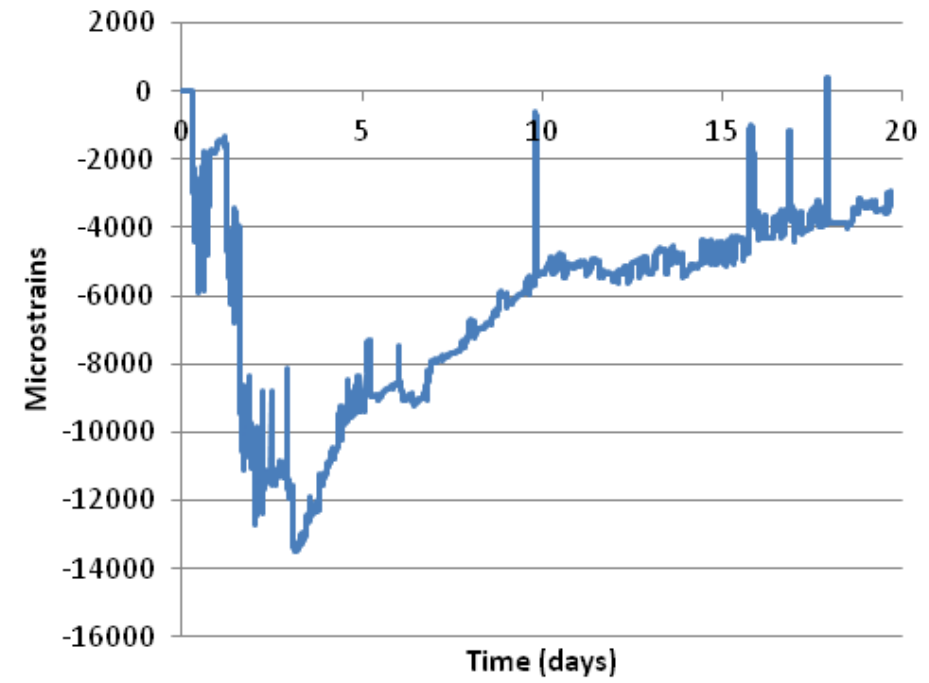
S-Tp-G1-1/2-T



S-Tp-G1-1/4-L

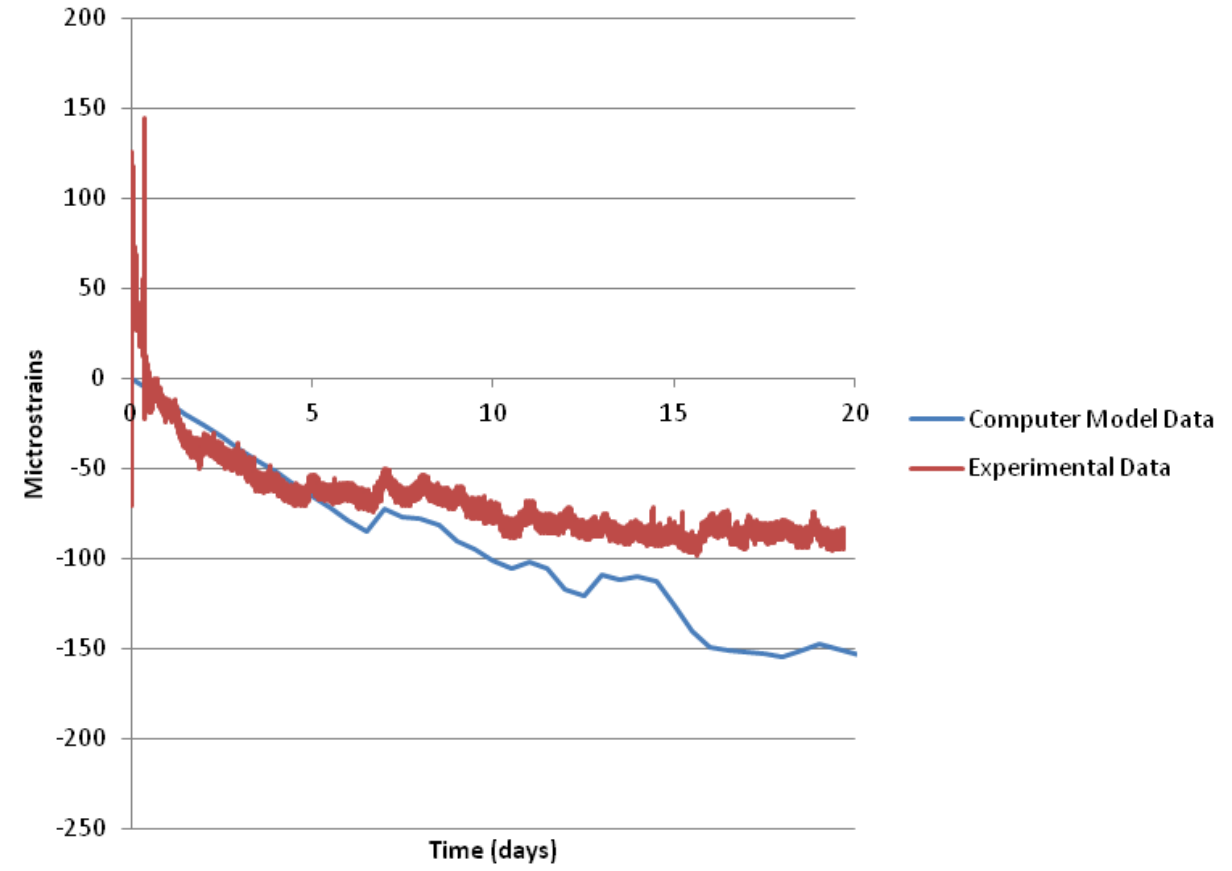
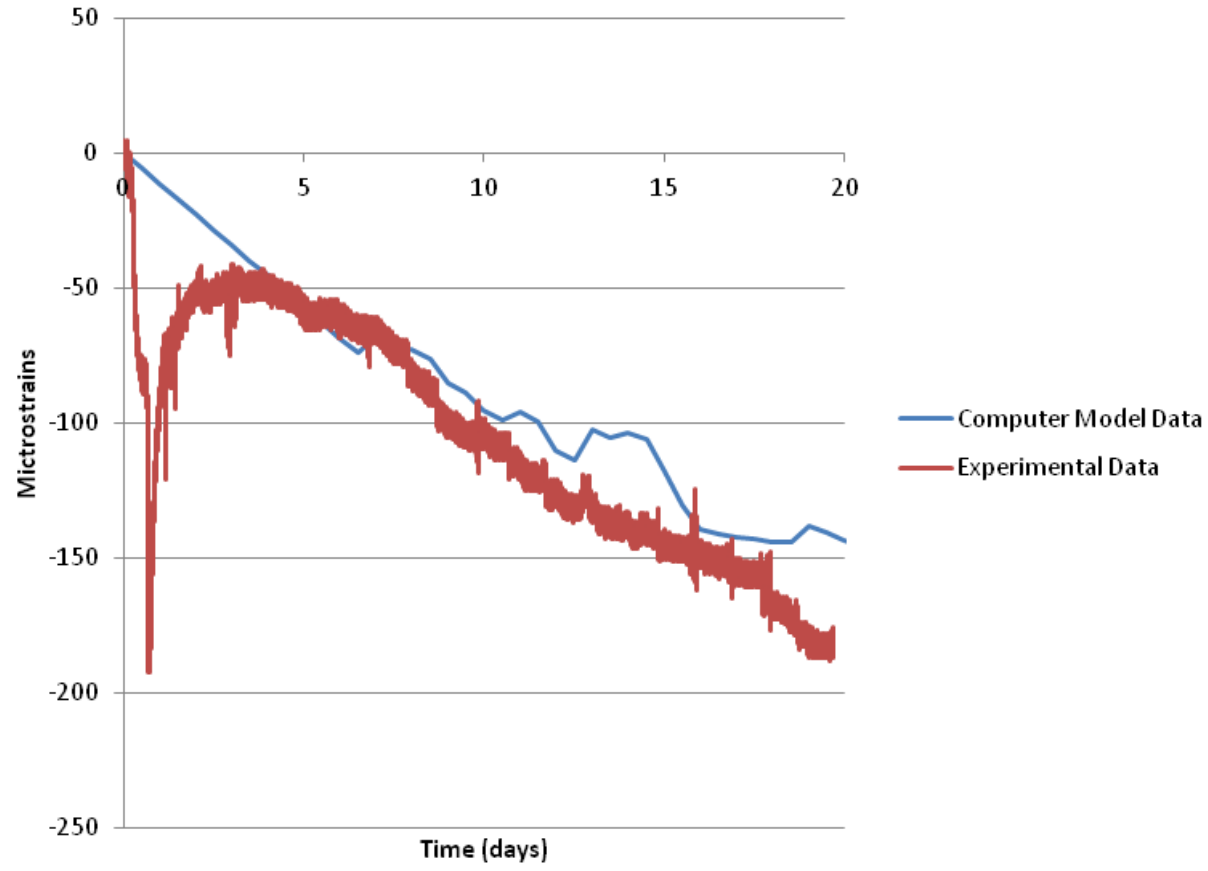


S-Bt-1/2-1/2-T

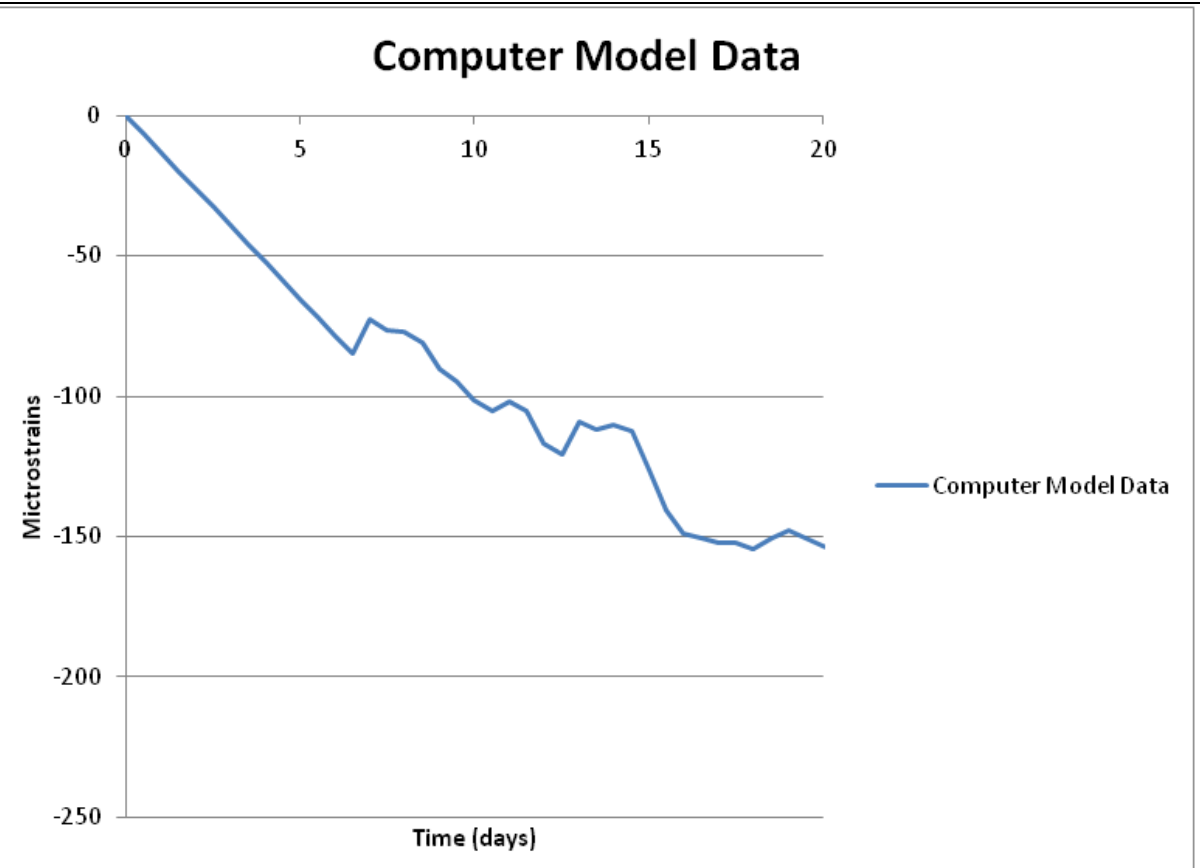
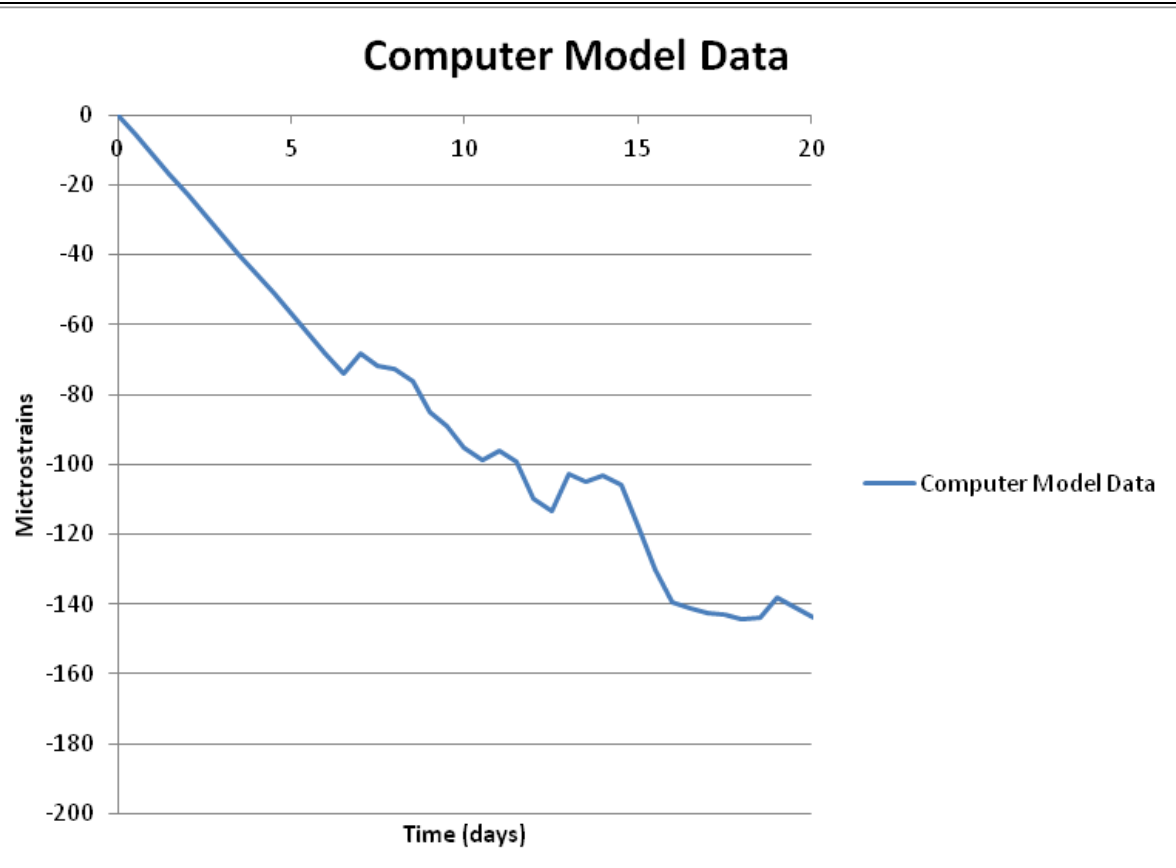




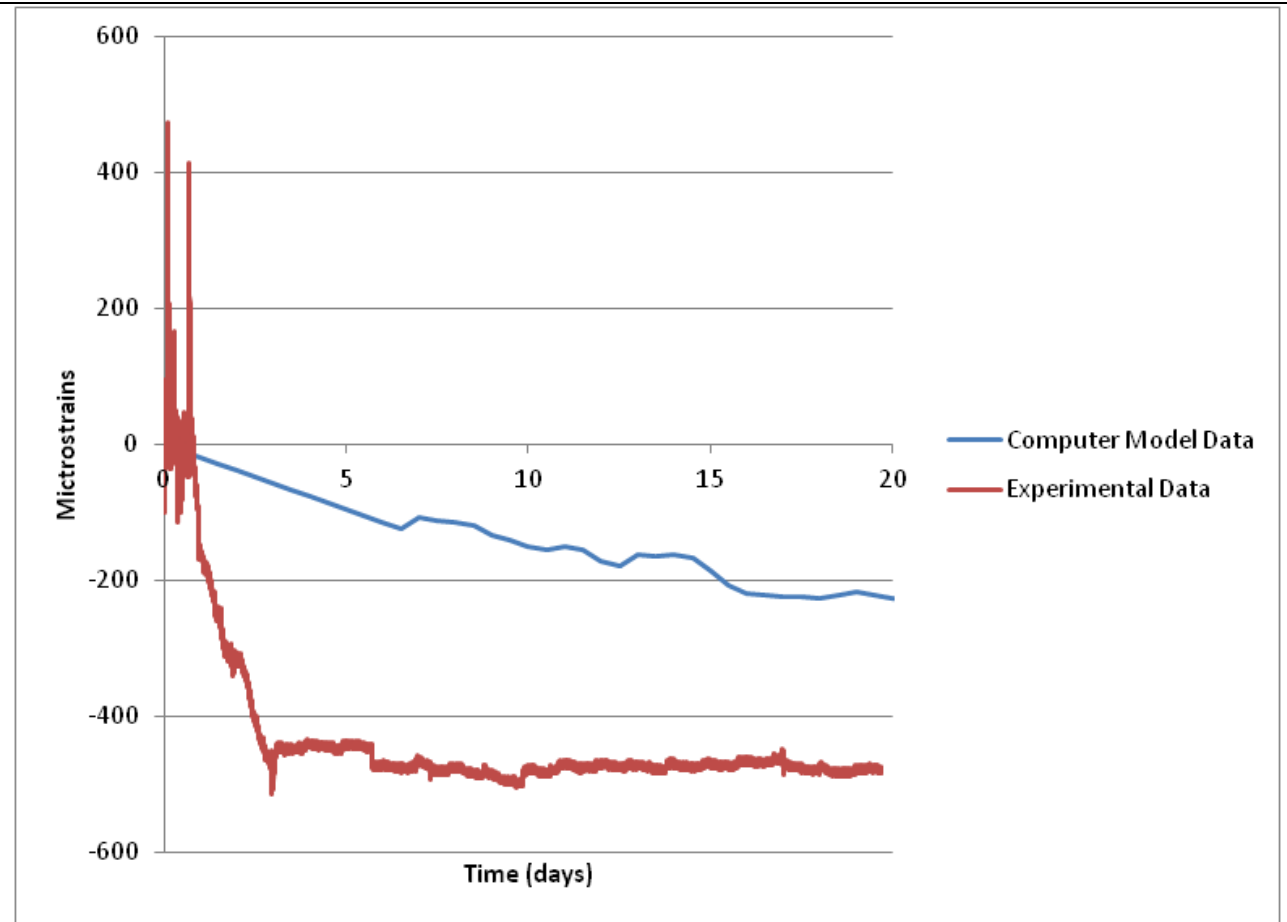
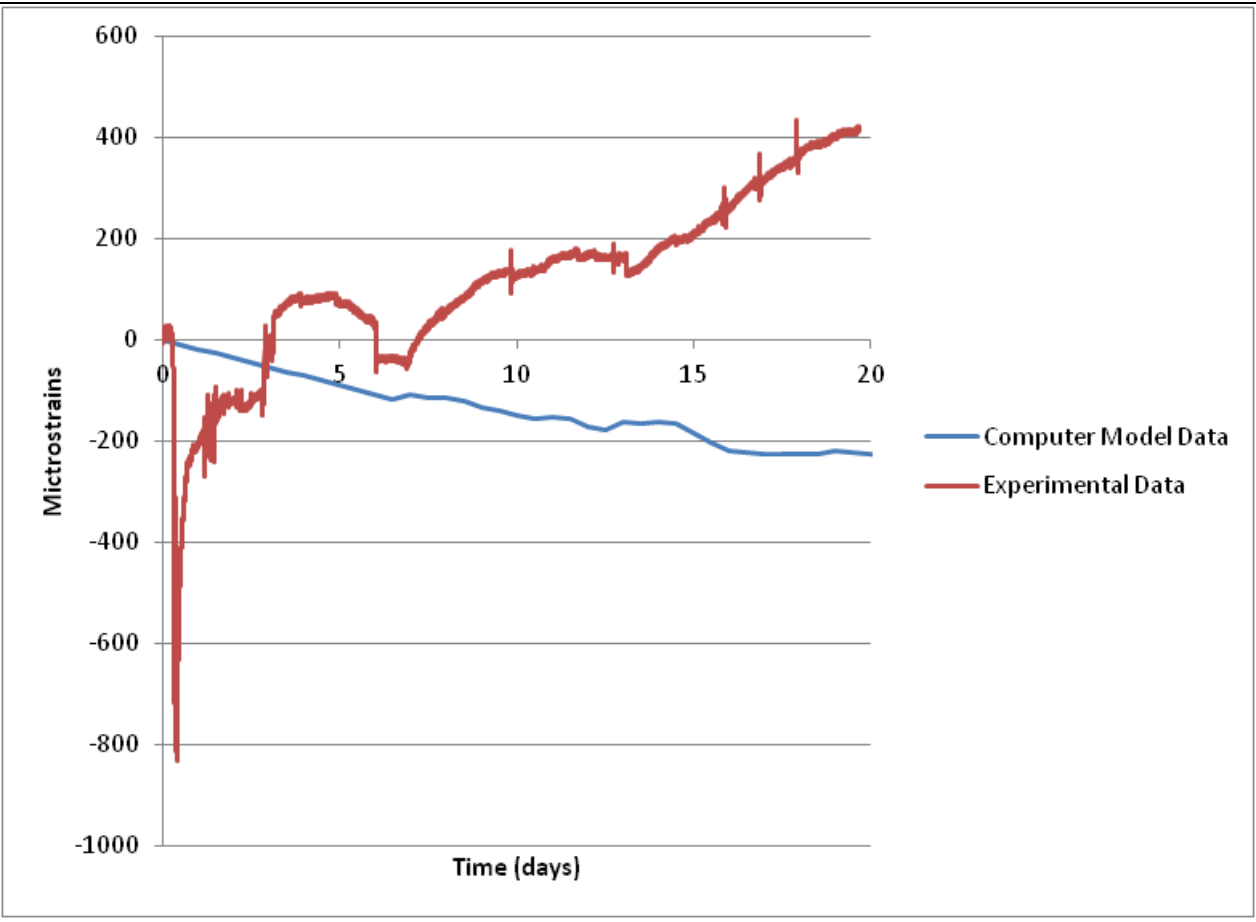
S-Bt-G2-1/2-L



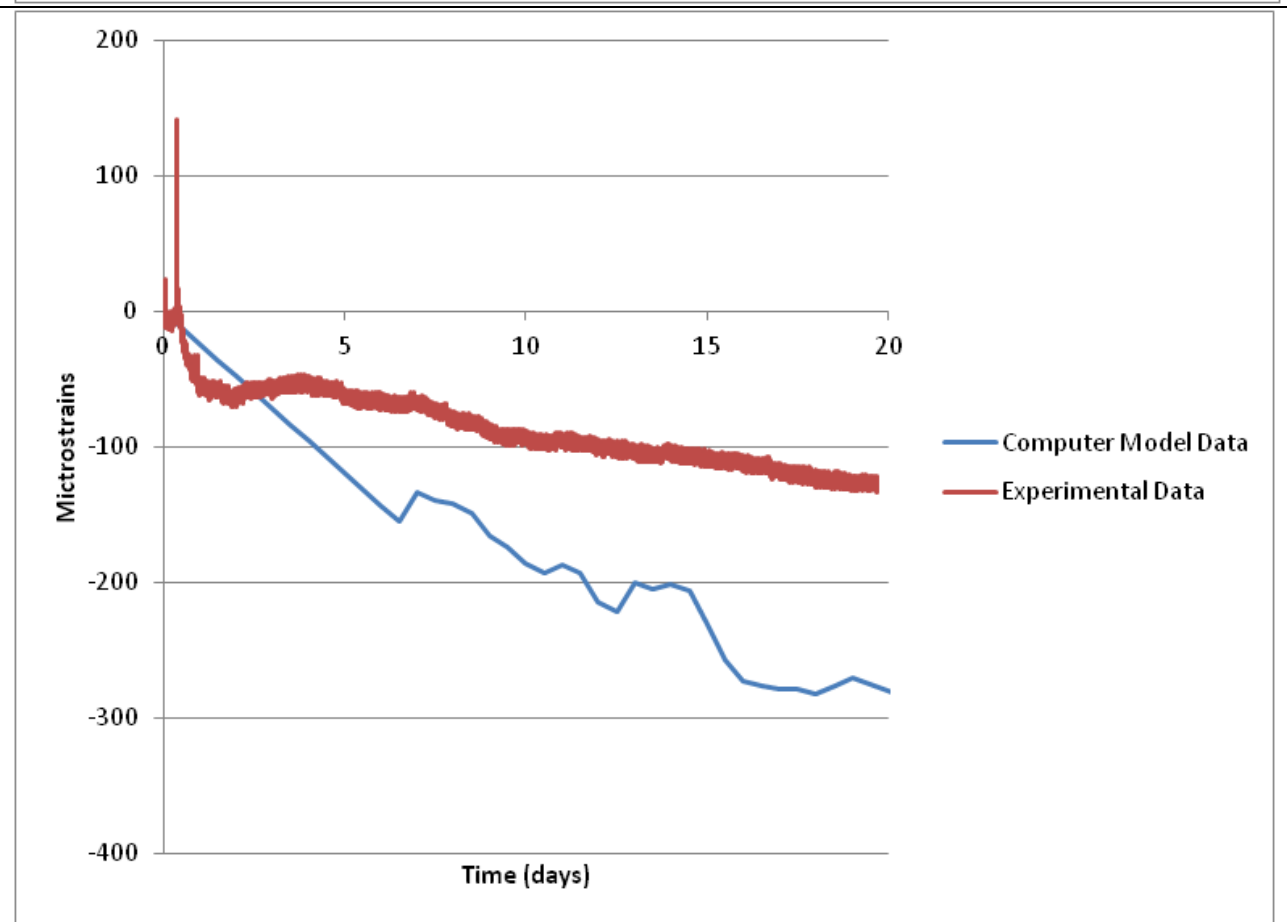
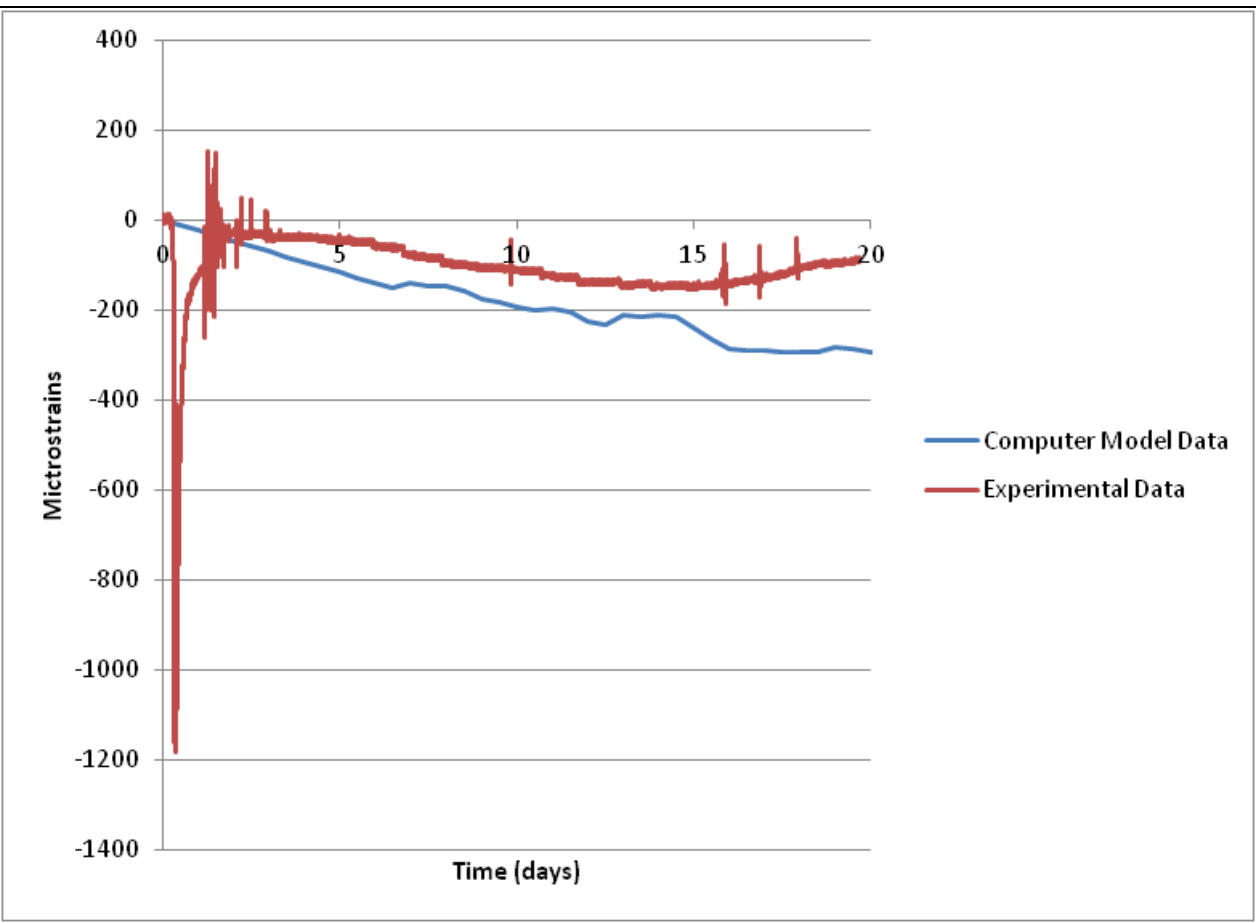
S-Bt-1/2-3/4-L



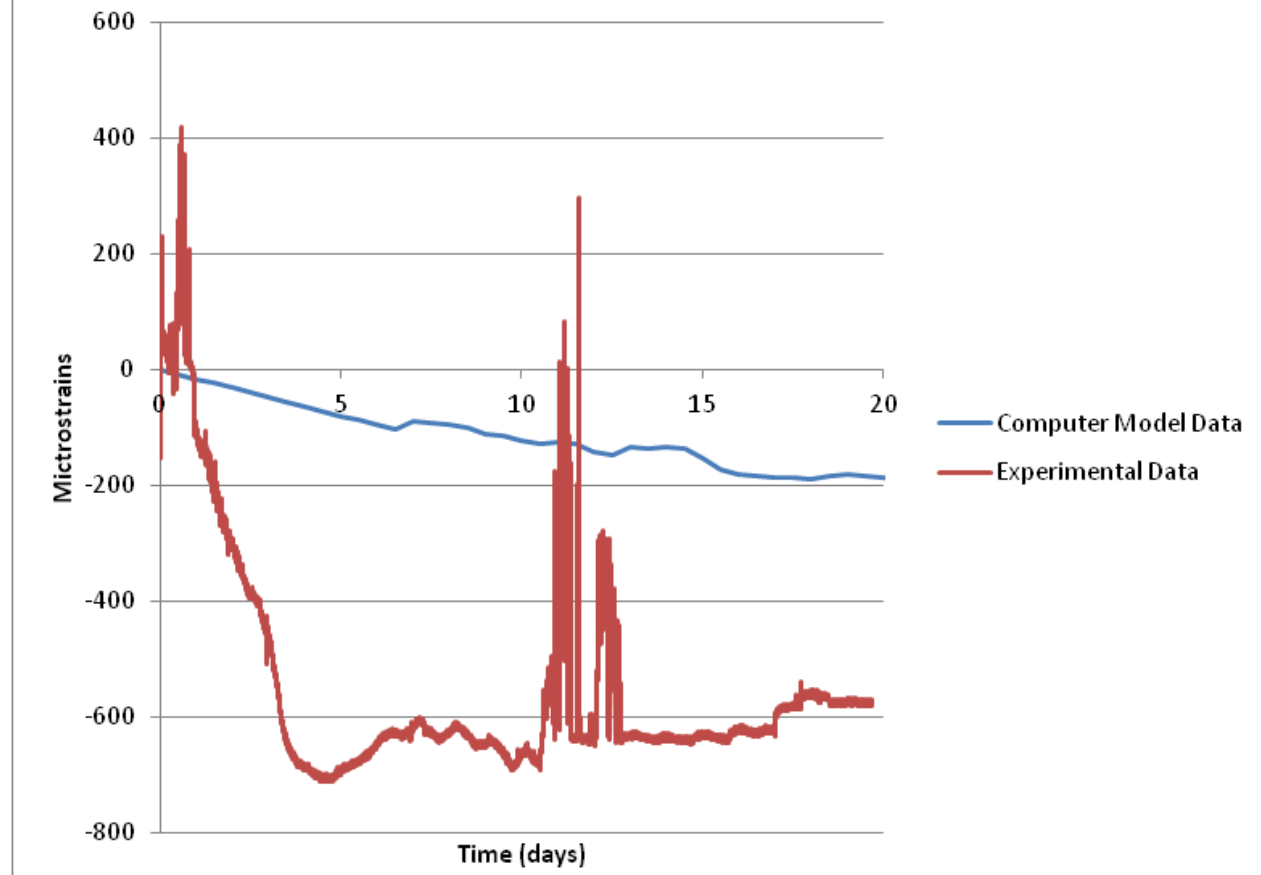
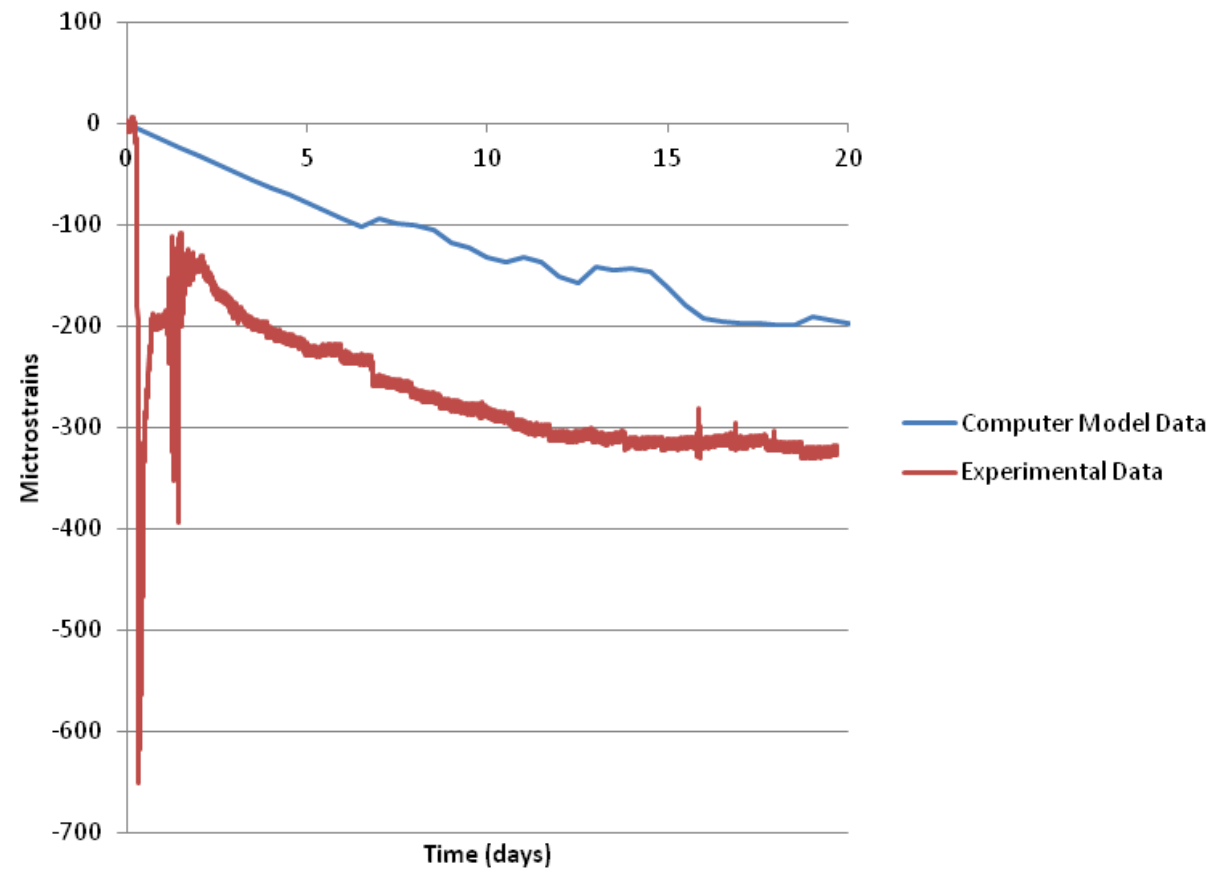
S-Bt-G1-1/4-T



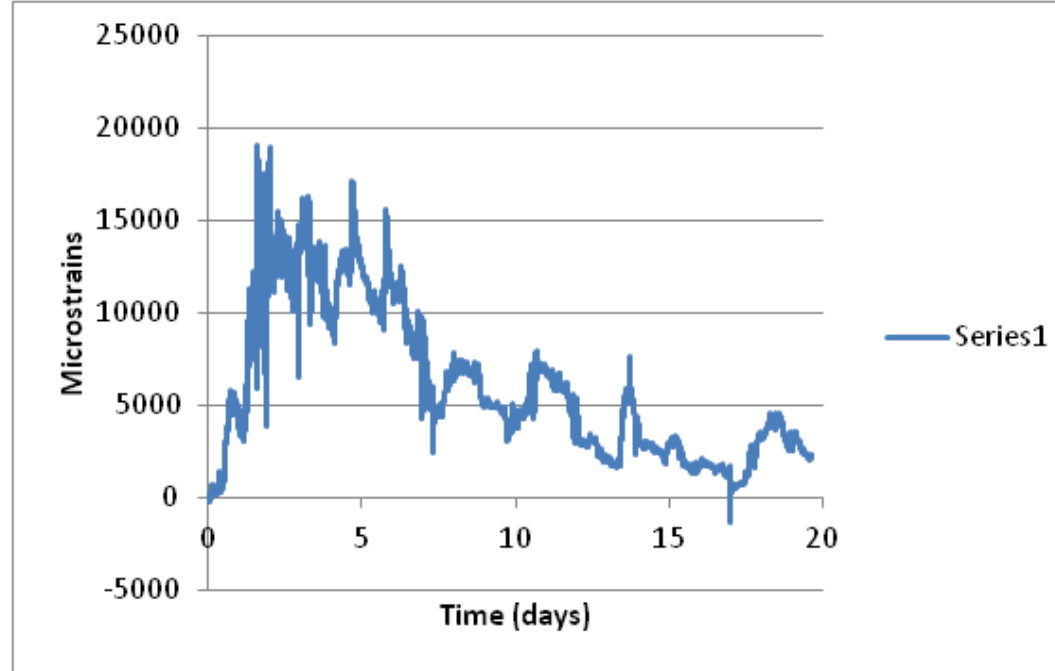
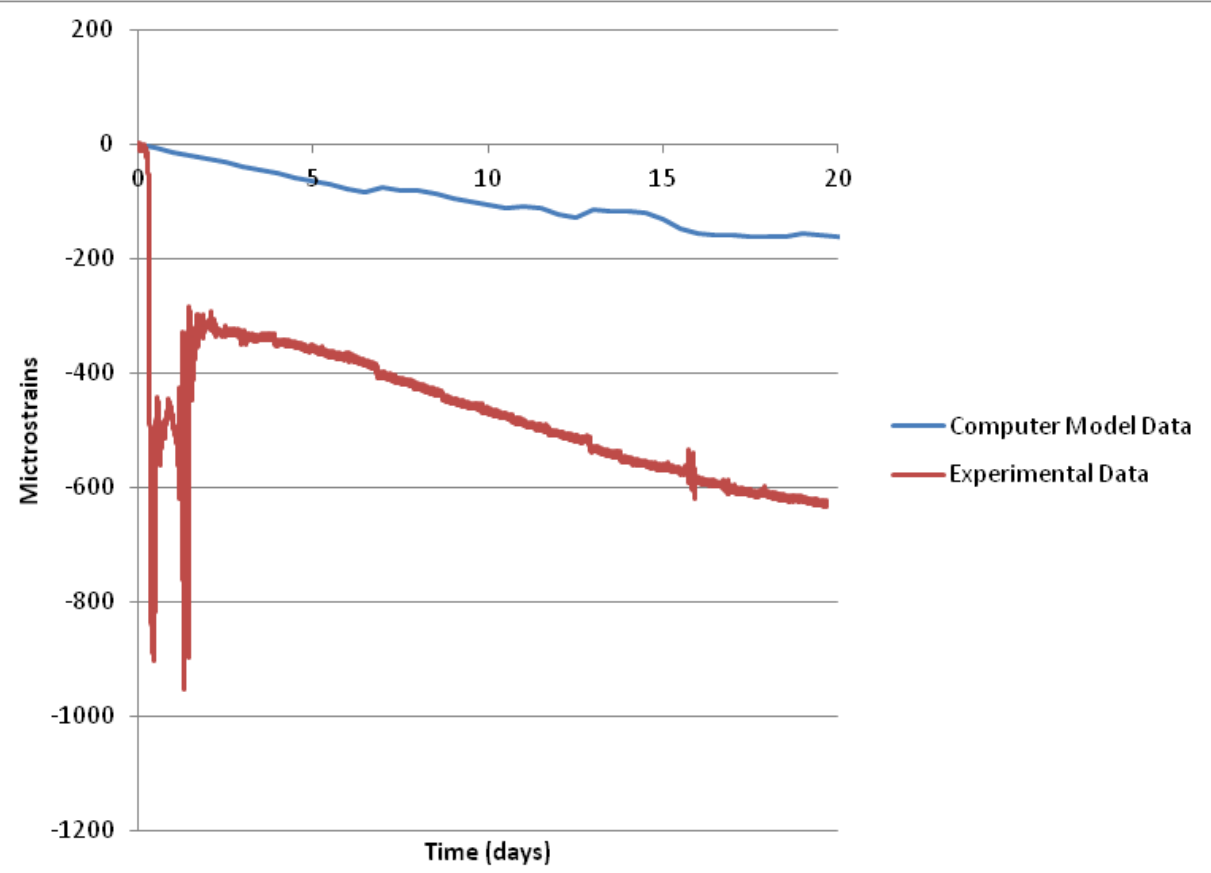
S-Bt-G1-1/4-L



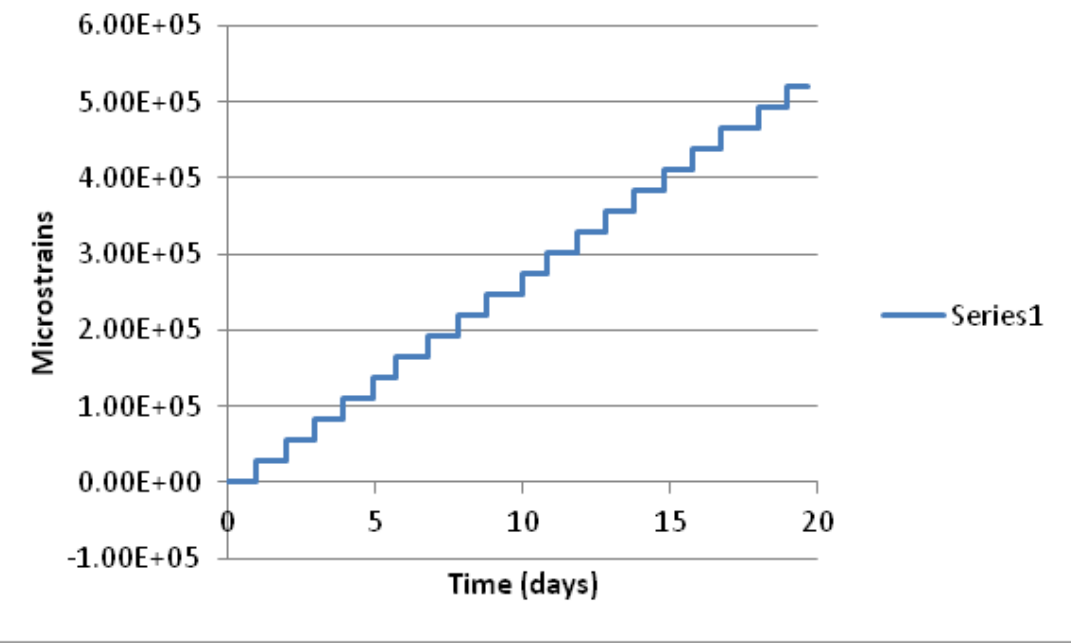
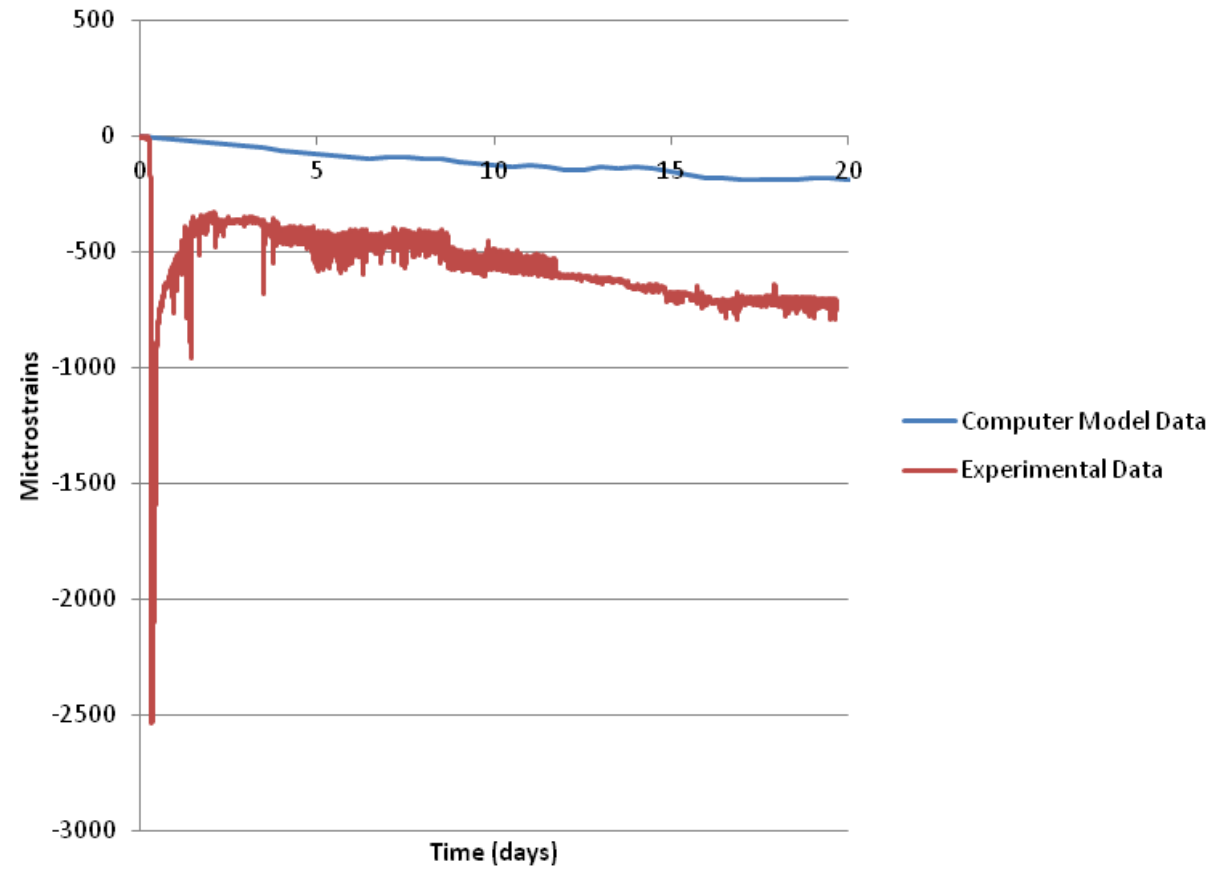
S-Bt-1/2-1/2-L



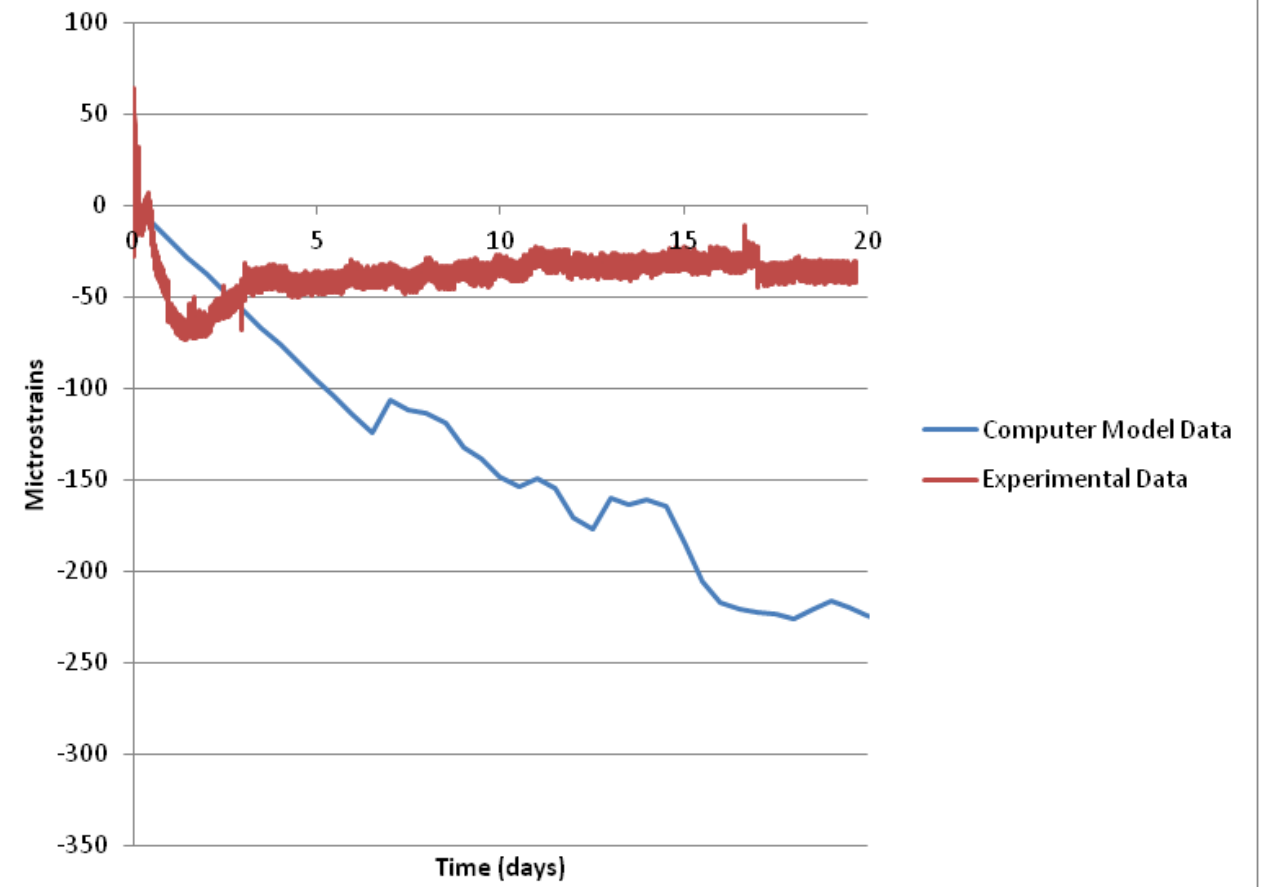
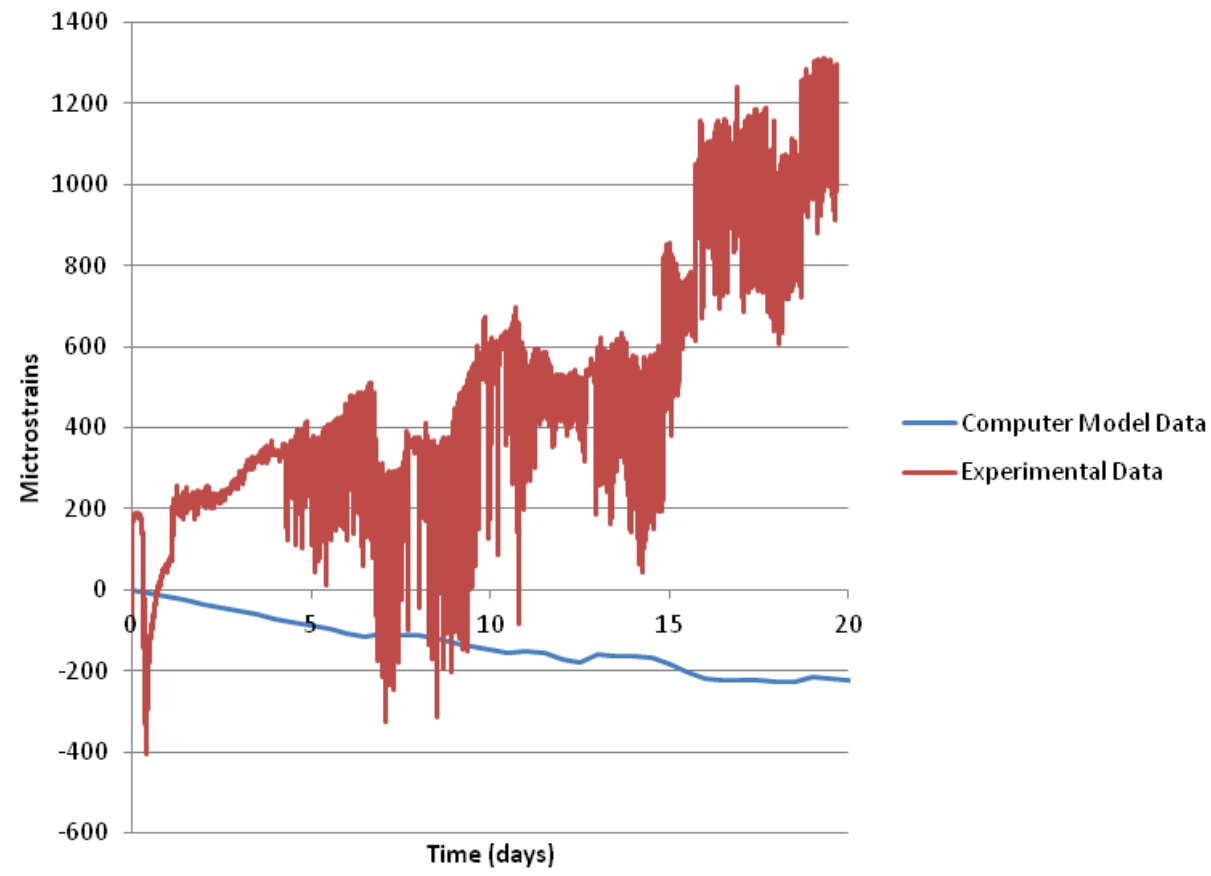
S-Bt-1/2-1/4-L



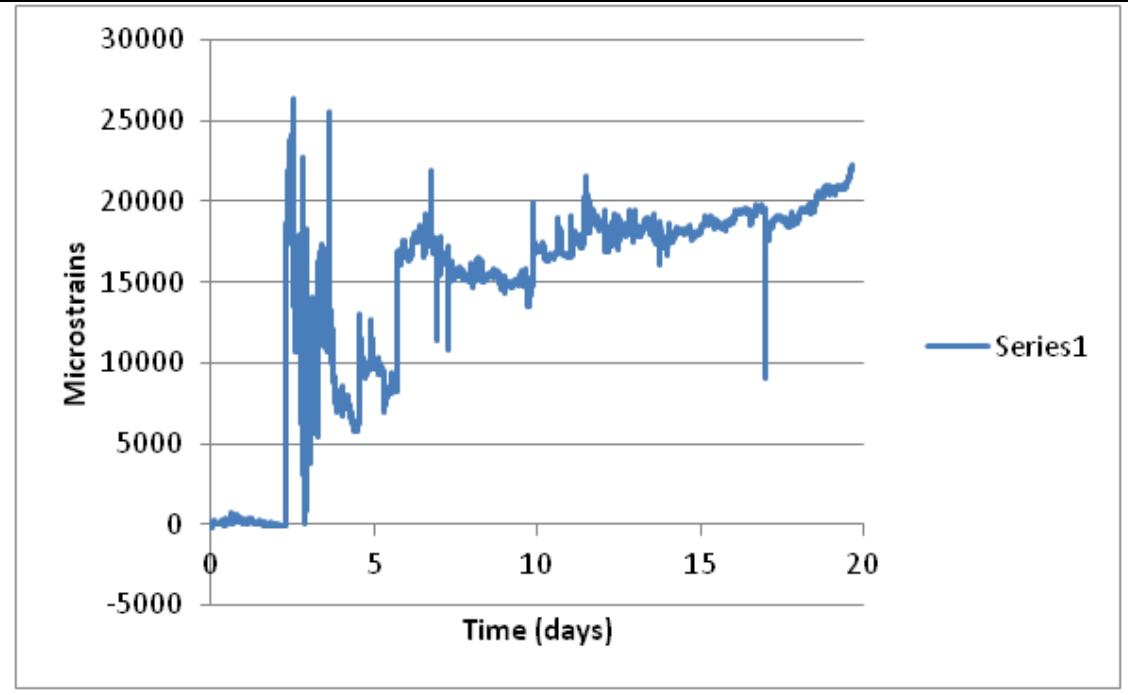
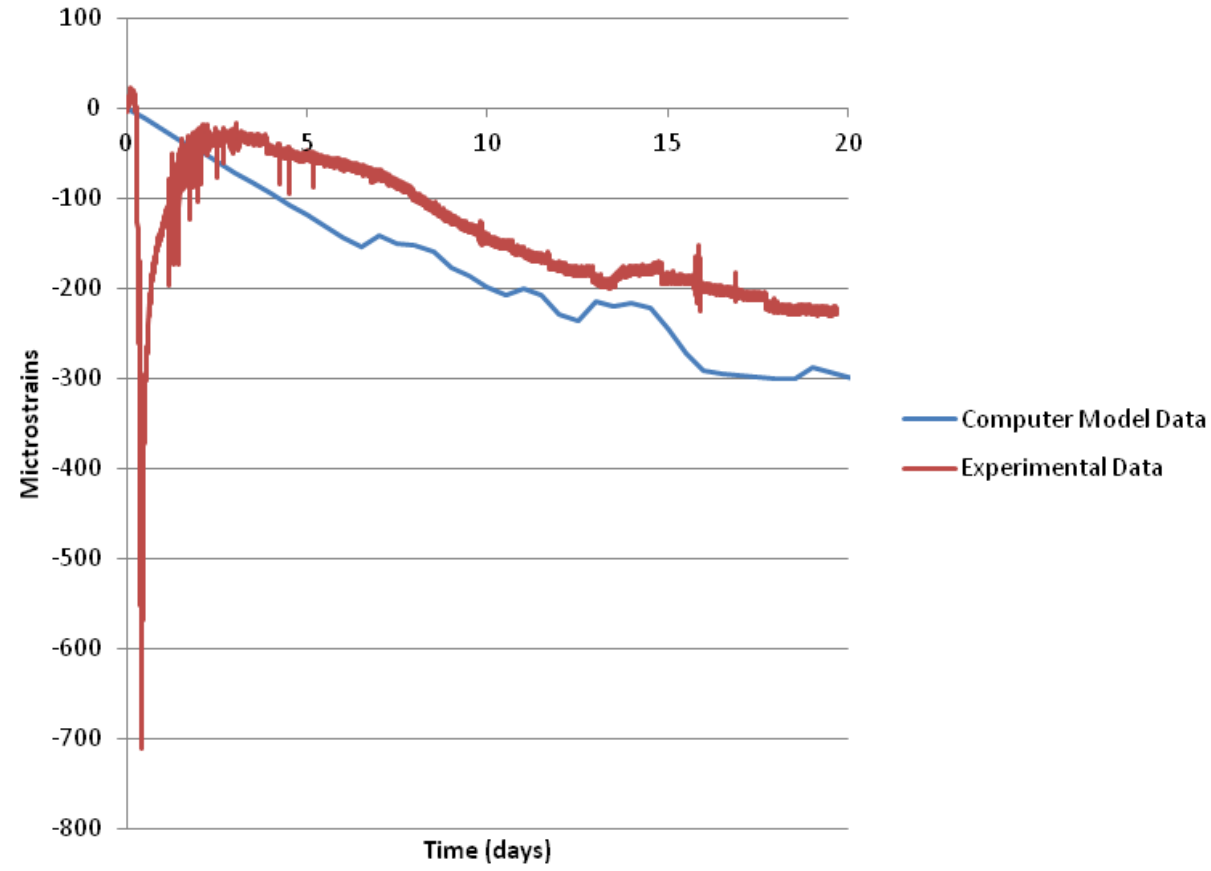
S-Bt-1/3-3/4-L



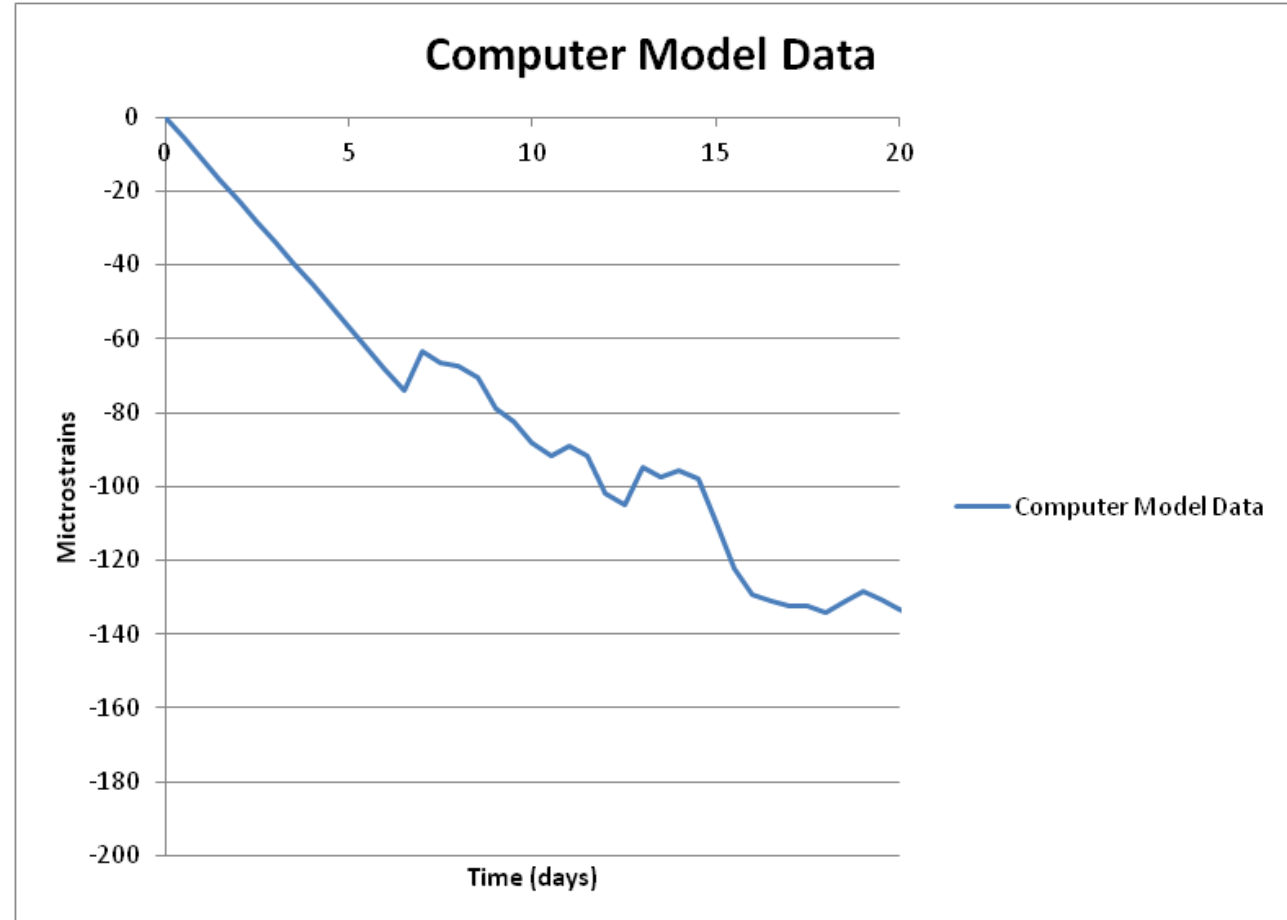
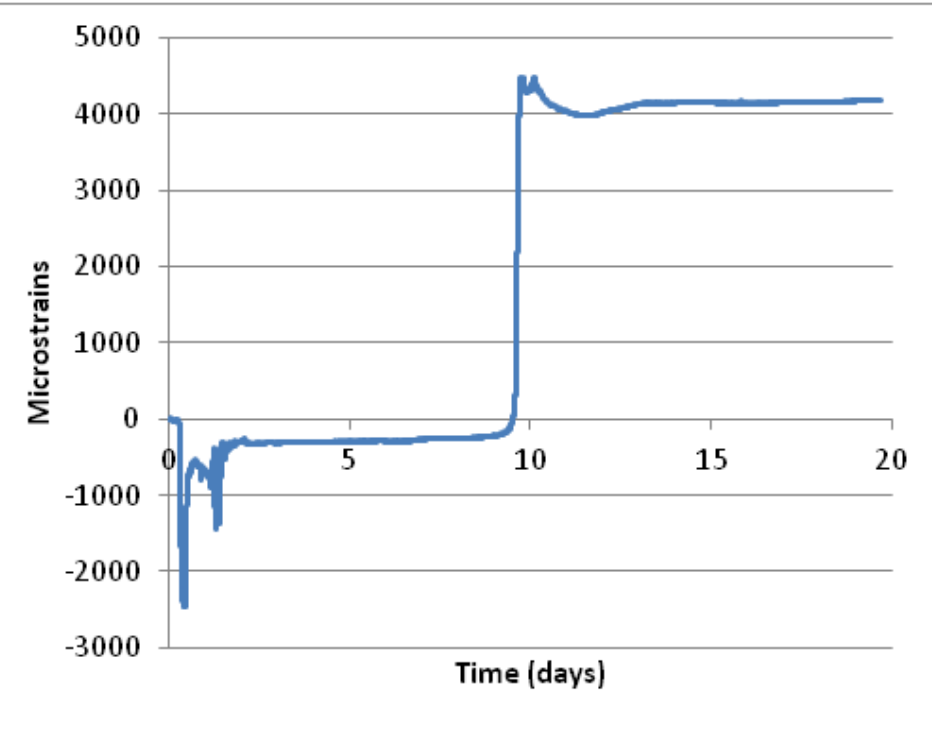
S-Bt-G1-1/2-T



S-Bt-G1-1/2-L



S-Bt-1/2-1/4-T



S-Bt-G1-3/4-L

